

Measurement of proton and  $\alpha$ -particle  
quenching in LAB based scintillators and  
determination of spectral sensitivities to  
supernova neutrinos in the SNO+ detector

DISSERTATION

zur Erlangung des akademischen Grades  
Doctor rerum naturalium  
(Dr. rer. nat.)

vorgelegt der  
Fakultät Mathematik und Naturwissenschaften  
der Technischen Universität Dresden

von  
Belina von Krosigk  
geboren am 17. 08. 1983 in Erlangen

**Gutachter:** Prof. Dr. Kai Zuber

Prof. Dr. Lothar Oberauer

**Datum der Einreichung:** 12. 03. 2015

**Datum der Disputation:** 26. 06. 2015



# **Measurement of proton and $\alpha$ -particle quenching in LAB based scintillators and determination of spectral sensitivities to supernova neutrinos in the SNO+ detector**

## **Abstract**

SNO+, the successor of the Sudbury Neutrino Observatory, is an upcoming low energy neutrino experiment, located in the 2 km deep laboratory SNOLAB, Canada. The spheric acrylic vessel in the detector center will contain 780 t of LAB. The main goal of SNO+ is the search for the neutrinoless double beta decay of  $^{130}\text{Te}$ , using a novel scintillator in which  $^{\text{nat}}\text{Te}$  is bound with an initial loading of 0.3% via water and a surfactant. Within this thesis, the first measurement of the  $\alpha$ -particle and proton quenching parameters of loaded and unloaded LAB is described. These parameters are crucial for an efficient background suppression, necessary to reach a sensitivity above the current limit in  $^{76}\text{Ge}$  of  $T_{1/2}^{0\nu} > 2.1 \times 10^{25} \text{ y}$  (90% C.L.). For 0.3% Te-loading, the quenching parameter obtained is  $kB = (0.0070 \pm 0.0004) \text{ cm/MeV}$  for  $\alpha$ -particles and  $kB = (0.0090 \pm 0.0003) \text{ cm/MeV}$  for protons. Additionally, the spectral sensitivity of SNO+ to supernova  $\bar{\nu}_e$ 's and  $(\bar{\nu})_{\mu,\tau}$ 's is determined for the first time, using inverse beta decay and  $\nu-p$  elastic scattering with the measured quenching parameters. The obtained sensitivity to the mean energy of  $\bar{\nu}_e$ 's is  $\langle E \rangle = 15.47^{+1.54}_{-2.43} \text{ MeV}$  and of  $(\bar{\nu})_{\mu,\tau}$ 's is  $\langle E \rangle = 17.81^{+3.49}_{-3.09} \text{ MeV}$ .

## **Messung des Proton und $\alpha$ -Teilchen Quenchings in LAB basierten Szintillatoren und Bestimmung der spektralen Sensitivität auf Supernova Neutrinos im SNO+ Detektor**

## **Kurzfassung**

SNO+, der Nachfolger des Sudbury Neutrino Observatorys, ist ein bevorstehendes Niederenergie-Neutrino-Experiment im 2 km tiefen Untergrundlabor SNOLAB in Kanada. Die Acryl-Kugel im Zentrum des Detektors wird mit 780 t LAB gefüllt werden. Das Hauptziel von SNO+ ist die Suche nach dem neutrinoless Doppelbetazerfall von  $^{130}\text{Te}$  mit einem neuartigen Szintillator, in dem  $^{\text{nat}}\text{Te}$  mit einer Anfangskonzentration von 0.3% über Wasser und ein Tensid gebunden wird. In dieser Arbeit wird erstmals die Messung der  $\alpha$ -Teilchen und Proton Quenching Parameter in diesem und in normalem LAB beschrieben. Die Parameter sind unverzichtbar für eine effiziente Untergrund Unterdrückung, die notwendig ist um auf das bestehende Limit in  $^{76}\text{Ge}$  von  $T_{1/2}^{0\nu} > 2.1 \times 10^{25} \text{ y}$  (90% C.L.) sensitiv zu sein. Der ermittelte Quenching Parameter bei 0.3% Te beträgt  $kB = (0.0070 \pm 0.0004) \text{ cm/MeV}$  für  $\alpha$ -Teilchen und  $kB = (0.0090 \pm 0.0003) \text{ cm/MeV}$  für Protonen. Zusätzlich wird erstmals die spektrale Sensitivität von SNO+ auf Supernova  $\bar{\nu}_e$ 's und  $(\bar{\nu})_{\mu,\tau}$ 's bestimmt über den inversen Betazerfall und die elastische  $\nu-p$  Streuung zusammen mit den gemessenen Quenching Parametern. Die ermittelte Sensitivität auf die mittlere Energie der  $\bar{\nu}_e$ 's ist  $\langle E \rangle = 15.47^{+1.54}_{-2.43} \text{ MeV}$  und der  $(\bar{\nu})_{\mu,\tau}$  ist  $\langle E \rangle = 17.81^{+3.49}_{-3.09} \text{ MeV}$ .



# Contents

<b>1</b>	<b>Introduction</b>	<b>1</b>
<b>2</b>	<b>Theory of scintillation in organic liquids</b>	<b>5</b>
2.1	Introduction . . . . .	5
2.2	Classification of organic scintillators . . . . .	6
2.3	Loaded organic scintillators . . . . .	7
2.4	The electron structure of organic molecules . . . . .	8
2.4.1	$\pi$ -electron states . . . . .	10
2.5	The processes of liquid scintillation . . . . .	13
2.5.1	Energy transfer . . . . .	14
2.6	Quenching . . . . .	16
2.6.1	Color and impurity quenching . . . . .	16
2.6.2	Oxygen quenching . . . . .	17
2.6.3	Ionization Quenching . . . . .	18
<b>3</b>	<b>Fundamentals of core collapse supernovae</b>	<b>23</b>
3.1	Classification . . . . .	24
3.2	Causes of core collapse . . . . .	25
3.3	Classic scenario of iron core collapse supernovae . . . . .	29
3.4	Occurrence of galactic core collapse supernovae . . . . .	38
3.5	Numercial modeling . . . . .	39
3.5.1	Neutrino spectra calculated in spherical symmetry by the Garching group . . . . .	42
3.6	Analytical supernova neutrino energy spectra . . . . .	46
<b>4</b>	<b>Neutrino Properties</b>	<b>51</b>
4.1	Flavor changing mechanisms in general . . . . .	52
4.2	Neutrino oscillations . . . . .	53
4.2.1	Oscillations in vacuum . . . . .	54
4.2.2	Oscillations in matter and the MSW effect . . . . .	58
4.3	Neutrinoless Double Beta Decay . . . . .	65

---

<b>5 The SNO+ experiment</b>	<b>71</b>
5.1 The SNOLAB underground laboratory . . . . .	72
5.2 The SNO+ detector . . . . .	72
5.3 The liquid scintillator of SNO+ . . . . .	73
5.3.1 LAB with PPO . . . . .	75
5.3.2 Neodymium-loaded LAB . . . . .	76
5.3.3 Tellurium-loaded water-surfactant-LAB . . . . .	76
5.3.4 Bis-MSB and perylene . . . . .	78
5.4 Scintillator purification . . . . .	78
5.5 Physics goals . . . . .	79
5.5.1 Double beta decay search . . . . .	79
5.5.2 Supernova neutrinos . . . . .	81
<b>6 Ionization quenching in LAB based scintillators</b>	<b>83</b>
6.1 Motivation . . . . .	83
6.2 Liquid scintillator compositions . . . . .	85
6.3 Experimental set-up . . . . .	87
6.3.1 Neutron field . . . . .	87
6.3.2 Liquid scintillator detector . . . . .	91
6.3.3 Read-out system . . . . .	92
6.4 Gamma calibration . . . . .	94
6.4.1 Measurement . . . . .	94
6.4.2 Simulation of the gamma response with GRESP7 . . . . .	97
6.4.3 Data analysis . . . . .	98
6.5 Beam data analysis . . . . .	106
6.5.1 Data cleaning . . . . .	107
6.5.2 Extraction of pulse-height spectra from quasi mono-energetic neutrons	114
6.5.3 Simulation of the neutron response with NRESP7 . . . . .	116
6.5.4 Light output resolution measured with neutron induced events . . .	117
6.5.5 Proton response . . . . .	120
6.5.6 Alpha response . . . . .	124
6.6 Adaption of Birks' law to the measured light responses . . . . .	129
6.6.1 Fit results using proton light responses . . . . .	134
6.6.2 Discussion of the measured proton Birks' parameters . . . . .	134
6.6.3 Fit results using $\alpha$ -particle light responses . . . . .	140
6.6.4 Discussion of the measured Birks' parameters of $\alpha$ -particles . . . .	141
6.7 Influence of the non-linearity of the electron light response . . . . .	143
6.8 Comparison of the alpha quenching results with independent LAB measurements . . . . .	144
6.8.1 Alpha quenching measurement with Sm-loaded LAB . . . . .	146
6.8.2 Alpha quenching measurement using SNO+ bucket source data . .	147
6.8.3 Comparison of the results from the three alpha quenching experiments	149

6.9 Comparison between the proton and alpha quenching parameter results . . . . .	151
6.10 Summary and outlook . . . . .	153
<b>7 Sensitivity of LAB scintillator detectors to supernova neutrinos</b>	<b>157</b>
7.1 Interaction channels in liquid scintillator . . . . .	160
7.1.1 Neutrino–proton elastic scattering ( $\nu$ – $p$ ES) . . . . .	160
7.1.2 Inverse beta decay (IBD) . . . . .	165
7.1.3 Neutrino–nucleus reactions on $^{12}\text{C}$ . . . . .	167
7.1.4 Neutrino–electron elastic scattering . . . . .	173
7.1.5 Summary . . . . .	174
7.2 Backgrounds . . . . .	175
7.2.1 Backgrounds to IBD events . . . . .	175
7.2.2 Backgrounds to $\nu$ – $p$ ES scattering events . . . . .	178
7.3 Reconstruction of neutrino energy spectra from IBD and $\nu$ – $p$ ES . . . . .	185
7.3.1 True neutrino and visible energy distributions . . . . .	185
7.3.2 Reconstructed neutrino energy distributions . . . . .	187
7.4 Fit to reconstructed neutrino energy spectra from IBD and sensitivities to spectral $\bar{\nu}_e$ parameters . . . . .	190
7.5 Fit to reconstructed neutrino energy spectra from $\nu$ – $p$ ES and sensitivities to spectral $\nu_x$ parameters . . . . .	195
7.5.1 Propagation of systematic uncertainties . . . . .	197
7.5.2 Fit results . . . . .	198
7.6 Influence of the trigger threshold, MSW effect, progenitor and equation of state on the $\nu$ – $p$ ES event yield . . . . .	204
7.7 Summary and outlook . . . . .	210
<b>8 Conclusions</b>	<b>213</b>
<b>A Natural decay chains and constants and non–SI units</b>	<b>215</b>
<b>B Spectra taken within the ionization quenching measurements</b>	<b>217</b>
B.1 Gamma calibration spectra . . . . .	217
B.2 Pulse–height over pulse–shape distributions . . . . .	236
B.3 Time–of–flight distributions . . . . .	237
<b>C Relativistic kinematics of the two–body <math>^{12}\text{C}(n,\alpha)^9\text{Be}</math> reaction</b>	<b>241</b>
<b>D Numerical neutrino energy reconstruction from the proton recoil spectrum</b>	<b>243</b>
D.1 Numerical solution of first–kind Volterra integral equations . . . . .	243
D.1.1 Application to a supernova event spectrum . . . . .	245
D.1.2 Propagation of statistical uncertainties . . . . .	248
<b>List of Acronyms</b>	<b>251</b>

<b>List of figures</b>	<b>252</b>
<b>List of tables</b>	<b>259</b>
<b>Bibliography</b>	<b>261</b>

# Chapter 1

## Introduction

Over the last decades, liquid scintillation detectors immensely gained in importance within the field of neutrino and astroparticle physics due to their power to detect the charged secondaries of neutrino interactions down to energies of  $\mathcal{O}(\text{keV})$  in realtime. The scintillation light yield scales with the energy of the charged particle, providing valuable kinematic information. The additional property of a signal pulse–shape dependence on the particle’s stopping power furthermore enables particle identification. The underlying effect is known as ionization quenching. With the evolution of both, detector technology and understanding of the scintillator properties, respective experiments grew in the second half of the last century from small–scale to multi–tonne detectors. Several large–scale liquid scintillator detectors with up to 1 kt scintillator mass are currently operational worldwide and multi–kilotonne detectors are being designed.

The SNO+<sup>1</sup> detector is a spherical, unsegmented 780 t liquid scintillator detector in the construction phase about to being commissioned. It is the successor experiment of SNO and located in Canada’s SNOLAB, which is one of the world’s deepest operating underground laboratories. SNO+ is a multi–purpose low–background detector with the principal objective to search for the neutrinoless double beta ( $0\nu\beta\beta$ ) decay of  $^{130}\text{Te}$ . For this purpose,  $^{\text{nat}}\text{Te}$  will be loaded into linear alkylbenzene (LAB) based scintillator after a measuring phase with unloaded LAB. Te–loading only became possible due to a novel technique, using water and a photoreactive surfactant (PRS) to bind Te stably in the solution. This state–of–the–art metal–loading technique is applied for the first time in the SNO+ experiment.

One of the goals of the unloaded scintillator phase of SNO+ is the measurement of the background spectrum without the contribution from the isotope itself. In order to build a profound background model and to develop efficient tagging techniques for the  $0\nu\beta\beta$  decay search, the energy dependent light yield functions of the charged particles have to be very well known in both, unloaded and Te–loaded scintillator. Since ionization

---

<sup>1</sup>SNO+: Sudbury Neutrino Observatory.

quenching affects the total light yield, the light yield function strongly varies between different particles and is reduced the stronger the higher the ionization energy loss of a particle.

Within this thesis, the light yield functions of protons and  $\alpha$ -particles, the most relevant ions in the context of SNO+ backgrounds, are measured with respect to the nearly unquenched electron response for six different LAB based scintillators with different fluor concentrations as well as with and without water plus PRS and with and without Te, to systematically investigate the influence of the different components. Additionally, two Nd-loaded LAB based scintillators are used, addressing the former goal of SNO+ to search for the  $0\nu\beta\beta$  decay of  $^{150}\text{Nd}$ . All light responses determined in this thesis are parameterized with one quenching parameter  $kB$ , or two parameters,  $kB$  and  $C$ , using Birks' law. These parameters are the basis of a correct light yield simulation in the SNO+ Monte Carlo (MC) and are indispensable for the analysis of future data. The quenching parameters of, for instance, LAB with 2 g/l PPO and 15 mg/l bis-MSB determined within this work in a one parametric fit are  $kB = (0.0096 \pm 0.0003) \text{ cm}/\text{MeV}$  for protons and  $kB = (0.0076 \pm 0.0003) \text{ cm}^2/\text{MeV}^2$  for  $\alpha$ -particles. The results of this thesis yielded the first publication of the proton quenching parameters for LAB based scintillators and the first measurement of ionization quenching in the novel kind of scintillator including water and PRS.

Despite the general, great progresses concerning the knowledge about liquid scintillator properties, some fundamental questions are still unanswered, like the question of whether the same quenching parameters do describe the light yield function of different ions but in the same liquid scintillator or not. Within this thesis, proton and  $\alpha$ -particle quenching is measured simultaneously under exactly the same conditions and only with internal particles, avoiding surface effects. This work thus offers an excellent opportunity to answer this question. For all compounds tested in this work, a  $4\sigma$ – $5\sigma$  difference between the Birks' parameter  $kB$  for protons and for  $\alpha$ -particles is observed in a one parameter fit, strongly disfavoring the hypothesis of the same parameter value for different ions in the same scintillator. This conclusion is also supported by the two parameter fit results.

It is furthermore an open question, how strongly the measurement conditions affect the observed ionization quenching parameters and, consequently, how transferable the results are from one experiment to another. Within the present work, the influence of the detector sensitivity to the electron light Cherenkov component on the observed quenching parameters is thoroughly discussed. It is this component, which can lead to significant differences between measurement results from different experiments. It is furthermore demonstrated that, under the same conditions concerning the Cherenkov light yield, results are transferable. The  $\alpha$ -particle quenching results from this work are for this purpose compared to two further and independent measurement results using LAB based scintillator, obtained with very different approaches. All results are in very good agreement.

---

On the basis of the measured proton quenching parameters, the sensitivity of large-scale LAB based scintillator detectors to the supernova  $\nu_\mu$ ,  $\bar{\nu}_\mu$ ,  $\nu_\tau$  and  $\bar{\nu}_\tau$  sum energy spectrum is determined, using  $\nu$ - $p$  elastic scattering. Joined in parallel is the determination of the spectral detector sensitivity to supernova  $\bar{\nu}_e$ 's via the inverse beta decay reaction. The results of the latter sensitivity study enter the analysis of the  $\nu$ - $p$  elastic scattering events. This work presents the first comprehensive sensitivity study of a combined measurement of these two reaction channels.

The thesis at hand is organized as follows: Sec. 2 gives an overview over the theory of scintillation in organic liquids. In Sec. 3 the fundamentals of core collapse supernovae are summarized and Sec. 4 gives an introduction to the basic neutrino properties in the Standard Model. The SNO+ experiment is shortly described in Sec. 5. Section 6 provides the detailed description of the ionization quenching measurement set-up and the data analysis, which is finalized with a thorough discussion of the results. In Sec. 7 the sensitivity of SNO+ and of a 20 kt LAB based detector to supernova neutrinos is determined. The thesis is completed with a conclusion given in Sec. 8.

All calculations in this thesis use natural and SI units unless stated otherwise. Deviating units are listed together with all natural constants relevant for this work in Appendix A, Tab. A.1. All references to figures, tables and equations in the appendix are preceded with a capital latter, referring to the respective chapter in the appendix.



## Chapter 2

# Theory of scintillation in organic liquids

### 2.1 Introduction

Hand in hand with his discovery of X-rays in 1895, Wilhelm C. Röntgen observed the luminescent behavior of barium platinocyanide crystals in the vicinity of his cathode ray tube [1]. As the scintillation light was appearing and vanishing in coincidence with the tube being switched on and off, Röntgen casually found a way to detect radiation with the additional advantage of an instantaneous response. The door was opened to scintillation detectors and the first inorganic scintillators, made of  $\text{CaWO}_4$  or  $\text{ZnS}$ , were used in the following years. Until today, tens of different inorganic scintillators have been developed [2]. Their advantage is a high light yield, their disadvantage are the slow decay times down to  $\mathcal{O}(\mu\text{s})$  and, in some cases, a hygroscopic behavior. In 1947, the first organic scintillators, crystalline napthalene and anthracene, were introduced by Hartmut Kallmann [3, 4]. Organic scintillators have decay times of  $\mathcal{O}(\text{ns})$  and are thus faster than inorganic solutions though with a lower light yield. To date, anthracene is the most efficient<sup>1</sup> pure organic scintillator known and its light yield is the standard reference value for comparisons. However, it cannot be grown in large crystals like napthalene, so John B. Birks started in the late 1940s studying mixed organic crystal scintillators containing only small amounts of anthracene [5]. In parallel, two more convenient types of organic scintillators, organic plastic and organic liquid scintillators (LSs), were developed [6, 7, 8], not suffering from limitations in size and shape. A further important step in the history of organic scintillators was the discovery of different light responses to different particles of the same energy. During Lieselott Herforth's investigations of the scintillating properties of solid and liquid organic compounds [9], the doctoral student of Kallmann observed the different time profile of the luminescent light pulse of organic scintillators after irradiation with  $\alpha$  and  $\beta$  particles, establishing the basis for  $\alpha/\beta$ -discrimination in today's commercial LS counters [10]. The underlying effect is known under the expression

---

<sup>1</sup>Scintillator efficiency is understood as the light output per unit particle energy.

of ionization quenching, described in detail in Subsection 2.6.3, forming one of the main subject areas of the thesis at hand.

The scintillators being examined within this dissertation are based on LAB, thus organic LSs. In the following, the main classes of organic scintillators are summarized, before the focus is directed on organic LSs. The basic physics of the processes causing light in organic liquids as well as processes reducing the light yield, relevant for this work, are recapitulated. More information can be found in the references [11, 12], which are the guideline for this chapter.

## 2.2 Classification of organic scintillators

Organic scintillators exist in the form of single- and multi-component systems. Depending on the amount of components, they are classified as unitary, binary or ternary systems. Systems with more than three components are in general possible, though they lack particular advantages and are barely applied. Examples for unitary systems are anthracene (pure crystal), LAB (pure liquid) and polystyrene (pure plastic), where only pure crystals are of practical use since the efficiencies of the other two types are too low. Though the emission spectra of liquid or plastic scintillators are red-shifted compared to their absorption spectra (see Fig. 2.1), an effect known as Stokes shift, the emission spectra of single-component scintillators generally still have a non negligible overlap with the absorption spectra. This leads to an increased opacity due to multiple absorption and reemission processes. To enhance the Stokes shift and thus reduce the losses by self-absorption, a second, and eventually third, organic component is usually added, forming binary and ternary systems. These one or two solutes, or fluors, are to efficiently absorb the light emitted by the primary component, the solvent, and to reemit it at longer wavelengths, where the solvent is transparent. Thus, solutes are also called wavelength-shifters. An illustrative presentation is given in Fig. 2.2 for LAB scintillators. Common primary solutes are e.g. 2,5-diphenyloxazole (PPO) and p-terphenyl and appropriate secondary solutes are e.g. p-bis-(o-methylstyryl)-benzene (bis-MSB) and 2,2'-p-phenylene-bis-(5-phenyloxazole) (POPOP). To avoid self-absorption by the solutes, they are admixed in a low concentration, which is typically at the percent level for primary solutes and at the sub-percent level for secondary solutes. While a primary solute is necessary to increase the quantum yield of the scintillator, a secondary solute is mainly to adapt the emitted wavelengths to the experimental needs and boundary conditions as, for instance, the peak sensitivity of the utilized photodetector, the transparency of detector parts and regions of high absorption by the specimen of interest. Besides the binary and ternary liquid and plastic solutions consisting of solvent, primary and possibly secondary solute, also binary crystal solutions exist (e.g. napthalene with anthracene). Although efficient scintillators, they are, however, more difficult to produce and less convenient in application and thus rarely used.

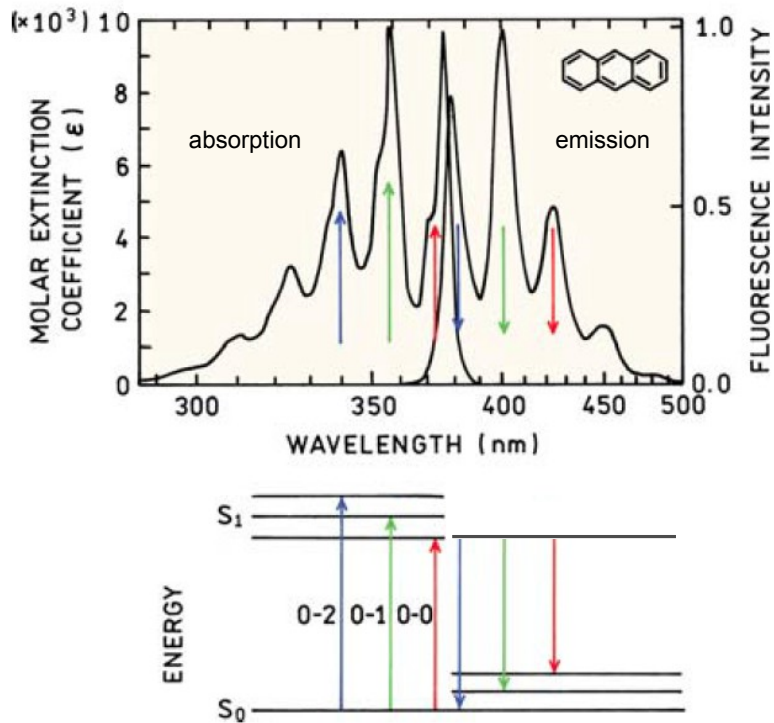


**Figure 2.1:** Absorption and fluorescence light emission spectrum of anthracene (from [13], modified). The numbers 0, 1, and 2 in the term scheme (bottom) denote vibrational levels, where the first number refers to the ground state  $S_0$  and the second to the first excited singlet state  $S_1$ . The species intrinsic molar extinction coefficient  $\epsilon$  defines the light absorption strength per molar concentration.

## 2.3 Loaded organic scintillators

The main constituents of organic scintillators are hydrogen, carbon and partly oxygen. However, these compounds can be additionally loaded with high- $Z$  elements attractive for different purposes. Standard hydrocarbon compounds show, for instance, no photopeak due to the low- $Z$  constituents and the respectively vanishing photoelectric cross section for typical gamma-ray energies. Adding e.g. lead or tin to the scintillator provides a certain fraction of photoelectric gamma ray conversion [15] turning organic scintillators into comparatively cheap and fast gamma-ray scintillators. Another interest in loading organic scintillators, especially in neutrino physics, arises from the interest in neutron detection as for example in the pioneering neutrino experiment by Clyde L. Cowan and Frederick Reines in 1956 [16] or in DayaBay<sup>2</sup> [17], one of the currently operating neutrino experiments. In these cases, elements like Cd or Gd are added to strongly increase the neutron capture cross section and thus the detection efficiency. Furthermore, an interest

<sup>2</sup>Named after the nuclear reactor complex in Daya Bay, China.

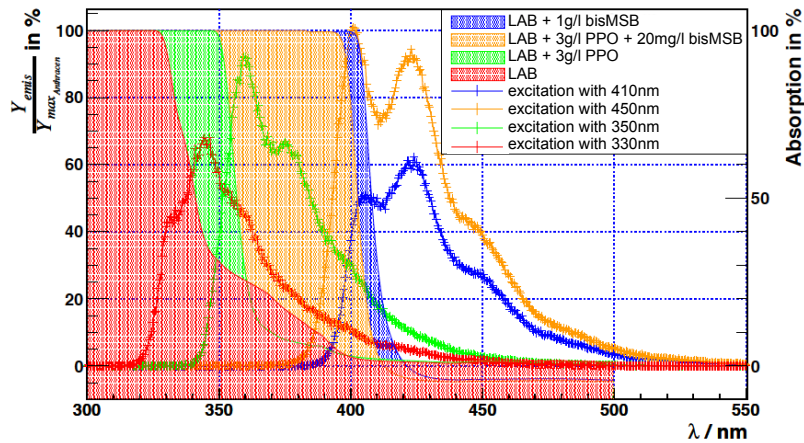


**Figure 2.2:** Absorption (filled areas and right ordinate) and fluorescence (crosses and left ordinate) spectra of LAB-based scintillators, taken from [14]. The spectra are for LAB as unitary system, in a binary system with PPO or bis-MSB as primary fluor and in a ternary system with PPO as primary and bis-MSB as secondary fluor. The same colors refer to the same compounds. The excitation wavelengths used in the fluorescence measurements are given in the legend.

can lie in the investigation of the loaded element itself. Organic scintillators can be loaded, for instance, with known double beta decaying isotopes to search for the  $0\nu\beta\beta$  decay. In the case of the SNO+, the elements of interest are Nd and Te. Details about the respective loading are given in Chapter 5.

## 2.4 The electron structure of organic molecules

Photoluminescence is understood as the emission of visible or ultraviolet (UV) light with a characteristic spectral shape after the absorption of radiation with normally higher energy. Whether an organic compound is luminescent or not thus depends on the energy levels of electrons in the molecules, i.e. the electron structure. In terms of molecular orbital theory, the individual atomic orbitals overlap in the formation of molecules and the electron probability density between the atoms increases, forming binding molecular orbitals, or decreases, forming anti-binding molecular orbitals. The component of the molecular orbital angular momentum in the direction of the internuclear axis is quantized and reduced to the values  $\lambda\hbar$  ( $\lambda = 0, 1, 2, \dots$ ). Following the spectroscopic notation pattern for atomic orbitals ( $s, p, d, \dots$ ), molecular orbitals are designated by  $\sigma, \pi, \delta, \dots$ , according to the value of  $\lambda$ . An example is given in Fig. 2.3.

In the case of organic molecules, the structure is largely determined by the electron structure of the C atom. Its ground state configuration is  $1s^22s^22p^2$ . The "binding" ground state configuration, however, is  $1s^22s2p^3$ , where one of the  $2s$ -electrons can be considered to be excited into a  $2p$ -state. In this configuration, carbon offers four valence electron orbitals (one  $2s$  and three  $2p$ ) of which a linear combination can contribute to

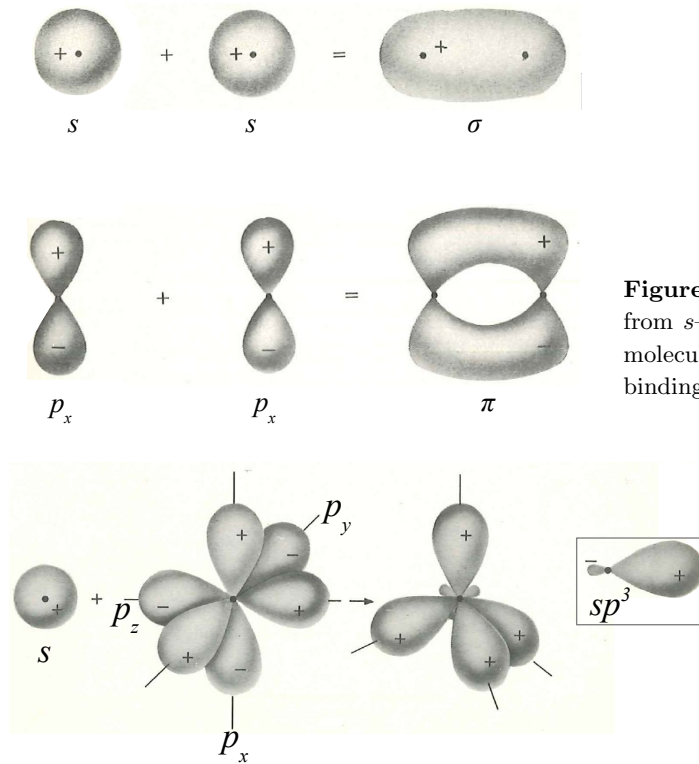


**Figure 2.3:** Binding molecular orbital formation from  $s$ - and  $p$ -orbitals in homonuclear diatomic molecules [18]. The  $x$ -axis is orthogonal to the binding axis of the nuclei and in the paper plane.

every molecule orbital. This phenomenon of hybridization occurs, if the atomic  $s$ - and  $p$ -levels are very close such that the resulting binding energy is larger than in the case of pure orbitals, like in C, and only if the atom forms a molecule with at least one other atom. Hydrocarbons can exhibit different C hybrid orbital configurations. However, only if the configuration contains a system of  $\pi$ -orbitals with delocalized electrons, the compound is luminescent. Localized  $\sigma$ -electrons are more tightly bound to the parent C atom than delocalized  $\pi$ -electrons and it thus requires more energy for their excitation. Only  $\pi$ -electrons can be excited with radiation of wavelengths in the visible or UV range and as a consequence emit light of similar wavelengths. In the  $sp^3$  hybridization as e.g. in methane ( $\text{CH}_4$ ), one  $s$ -orbital and three  $p$ -orbitals form four equivalent  $sp^3$  hybrid orbitals in one atom (see Fig. 2.4). The hybrid orbitals of the C atom form together with the  $1s$ -orbitals of the H atoms four binding  $\sigma$ -orbitals and no  $\pi$ -orbitals. Compounds with  $sp^3$  hybridization are non-luminescent and thus no scintillators. A second possible configuration is given by  $sp^2$  hybridization, where three equivalent  $sp^2$  hybrid orbitals are formed, leaving one of the original  $p$ -orbitals unchanged. In the simplest example benzene ( $\text{C}_6\text{H}_6$ ), inherent to e.g. LAB, the overlap of the  $sp^2$  hybrid orbitals with each others and with the H atoms lead to  $\sigma$ -bonds (see Fig. 2.5, left) and the pure  $p$ -orbitals of the C atoms form molecular  $\pi$ -orbitals (see Fig. 2.5, center and right) with six delocalized  $\pi$ -electrons. It is the excited states of these delocalized  $\pi$ -electrons, which are responsible for luminescence. Hydrocarbon molecules with this configuration are called aromatic and are the compounds of liquid organic scintillators. In the third possible configuration, resulting from  $sp$  hybridization

**Figure 2.4:**  $sp^3$  hybridization [18]. One  $s$ - and three  $p$ -orbitals form four  $sp^3$  hybrid orbitals in the same atom.

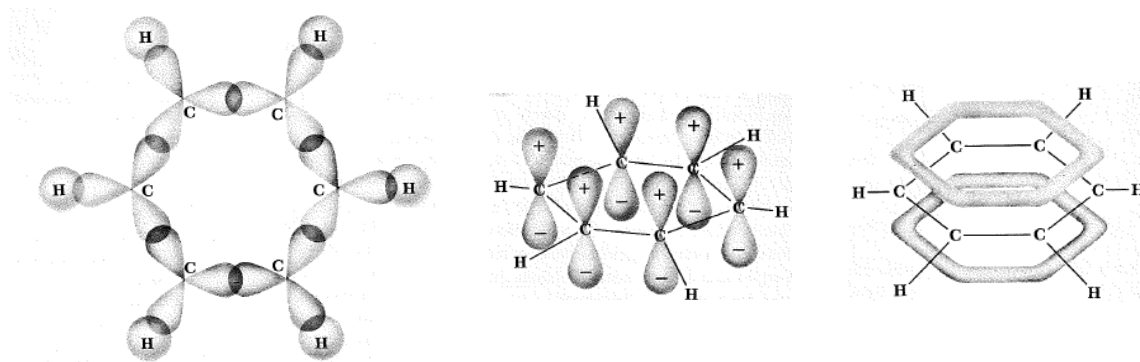


**Figure 2.5:** Benzene molecule ( $C_6H_6$ ) [18]. The overlap of the carbon  $sp^2$  hybrid orbitals with each others and with the hydrogen  $s$ -orbitals form  $\sigma$ -orbitals (left). Each C atom has a pure  $p_x$ -orbital occupied with one electron (center). The resulting binding molecular  $\pi$ -orbitals form a continuous electron distribution around the molecule with six delocalized electrons (right).

as e.g. in acetylene ( $C_2H_2$ ), the two unchanged atomic  $p$ -orbitals combine to molecular  $\pi$ -orbitals. These molecules are also luminescent.

#### 2.4.1 $\pi$ -electron states

The  $\pi$ -electron states of an organic molecule can be represented schematically as in Fig. 2.6. The energy of the levels depend on the spin orientation of the excited electron relative to the unpaired electron in the ground state, separating the electronic states into singlet (anti-parallel orientation) and triplet (parallel orientation) states. The ground state  $S_0$  is a singlet state followed by a series of excited singlet  $S_{1,2,3,\dots}$  and triplet states  $T_{1,2,3,\dots}$  up to the  $\pi$ -ionization energy  $I_\pi$ . The triplet states are always lower in energy than the respective singlet states according to the first Hund's rule<sup>3</sup>. Each level has vibrational sub-levels, typically denoted by a second suffix, e.g.  $S_{00,01,02,\dots}$  in the case of the ground state. The energy spacing between electronic levels is about  $2 - 4.5\text{ eV}$  and about  $0.1 - 0.2\text{ eV}$  between vibrational levels. At energies above the energy difference between  $S_3$  and  $S_0$  usually an additional sequence of  $\sigma$ -electron excited states exists. The presence of the  $\sigma$ -excited states disables the observation of any higher  $\pi$ -excited states in absorption spectrometry. The  $\pi$ -electronic absorption spectrum arises from fast transitions, taking  $\sim 10^{-15}\text{ s}$ , from the lowest vibrational sub-level of the ground state  $S_{00}$  to  $S_{10,11,12,\dots,20,21,\dots}$ . The optical transition from  $S_0$  to  $T_1$ , changing spin, is forbidden, however the triplet states are populated indirectly either by intersystem crossing – the radiationless transition between states of different multiplicities due to electron spin-flip – from  $S_1$  to  $T_1$ , or via ionization after which 75% of the ionized molecules recombine into triplet states. In the recombination processes, the production ratio of molecules in excited singlet and triplet states is about 1:3 corresponding to the spin multiplicities. In the case of excitation by ionizing particles, involving collisions and Coulomb interactions, the selection

<sup>3</sup>The term with the maximum multiplicity lies lowest in energy.

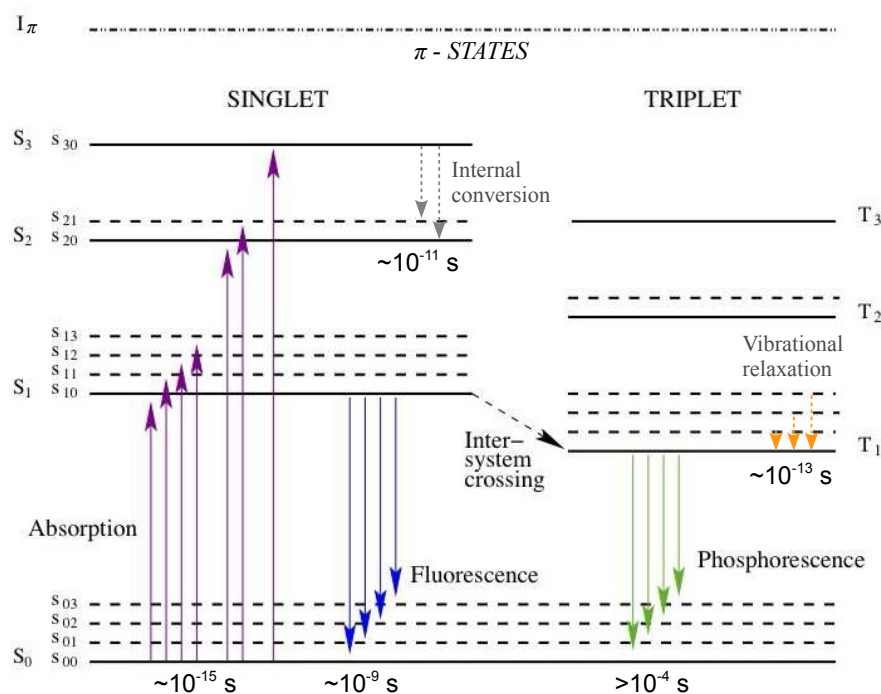


**Figure 2.6:** Energy levels of  $\pi$ -electrons in an organic molecule (Jablonski diagram) (from [11], modified).  $S_0$  denotes the ground state,  $S_{1,2,3}$  excited singlet states and  $S_{00,01,02,\dots,10,11,\dots}$  the corresponding vibrational sub-levels.  $T_{1,2,3}$  are excited triplet states and  $I_\pi$  is the ionization energy of the  $\pi$ -orbital. Solid lines illustrate radiative transfer, dashed lines non-radiative transfers.

rule that the spin does not change is potentially violated, leading to semi-forbidden transition as a result of the failure of spin-orbit coupling and the  $S_1 \rightarrow T_1$  transition strength increases.

Having absorbed radiation, the organic compound starts luminescing, where the luminescence appears in three types: fluorescence, phosphorescence and delayed fluorescence. Each type is shortly described in the following text passages.

Fluorescence corresponds to a radiative transition from  $S_1$  to  $S_0$  with a lifetime of  $\sim 10^{-8}$  to  $\sim 10^{-9}$  s. If states above  $S_1$  are excited, usually no radiative transitions into lower excited states or the ground state are observed due to rapid ( $\sim 10^{-11}$  s) internal conversion – the radiationless transition into a state of the same multiplicity at lower energy – between neighboring excited states. Also the period of molecular vibrations is with a duration of  $\sim 10^{-13}$  s much shorter, such that the molecule normally reaches thermal equilibrium through vibrational relaxation before emission and the transition into any of the ground state sub-levels takes place from  $S_{10}$ . The resulting characteristic vibrational structure of

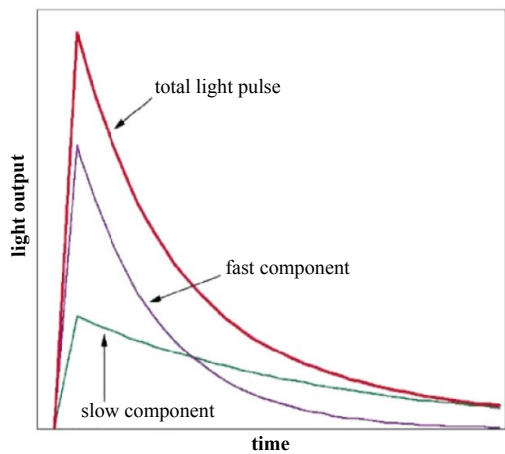


**Figure 2.7:** Time dependent scintillator light output consisting of a fast and a slow component from fluorescence and phosphorescence, respectively [19].

the fluorescence spectrum is visible in Fig. 2.1. The intensity  $I$  of the fluorescence light decays exponentially with time  $t$  as per

$$I(t) = I(0)f(t)e^{-t/\tau} \quad (2.1)$$

where  $\tau$  is the decay time. The function  $f(t)$  accounts for the finite rise time, for which an exponential behavior  $f(t) = -I(0)\exp(-t/\tau_{\text{rise}})$  is assumed in [20] and a Gaussian distribution in [21]

Phosphorescence refers to light emission at longer wavelengths than fluorescence, also decaying exponentially but with an orders of magnitude longer decay time of  $10^{-4}$  s up to seconds. Phosphorescence is explained with the existence of a metastable state at a level below  $S_1$ , here the first excited triplet state.  $T_1$  is long-lived since the transition into the singlet ground state is forbidden and involves spin reversal, severely slowing down the transition. The shape of the phosphorescence spectrum is similar to the fluorescence spectrum, since also in this case the transition can occur into any of the  $S_0$  sub-levels as sketched in Fig. 2.6. Fluorescence and phosphorescence are also known as fast and slow scintillation component of the observed scintillation light pulse, as shown in Fig. 2.7. Their relative intensities depend on the population frequentness of triplet states and therefore primarily on the ionization strength of the exciting radiation.

Delayed fluorescence is possible at room temperature or hotter. At these temperatures, molecules in  $T_1$ , or another metastable state, potentially acquire sufficient thermal energy during their excited lifetime to return to  $S_1$  instead of decaying into  $S_0$ . This luminescence process is called delayed fluorescence, because the subsequent  $S_1 \rightarrow S_0$  transition has the same spectrum as fluorescence but with a strongly increased period of  $> 10^{-6}$  s and a non-exponential decay behavior. This kind of delayed fluorescence is also called eosin-type delayed fluorescence and is not observed in scintillator molecules because of a relatively large energy gap. Delayed fluorescence that occurs in aromatic hydrocarbons, as notably in pyrene, is called pyrene-type delayed fluorescence. Responsible for this late fluorescence

light are triplet-triplet interactions in which two colliding molecules in excited triplet states form excimers, excited unstable dimers [22]. Some of these dissociate thermally into excited and ground state singlet monomer molecules and some fluoresce. The excimer fluorescence spectrum lacks the vibrational structure and is at longer wavelengths than the monomer fluorescent spectrum. p-type delayed fluorescence therewith shows additional features not present in the fast scintillation component.

## 2.5 The processes of liquid scintillation

In this section, the main physical processes taking place in the liquid scintillation mechanism of multi-component solutions are described. They are essential for the interpretation of the measurement results presented in Chapter 6. To follow the notation in [11, 12], solvent molecules are identified with  $X$ , primary solute molecules with  $Y$  and secondary solute molecules with  $Z$ . A ternary system therewith reads  $XYZ$ . Molecules in the first excited  $\pi$ -state are indexed with one asterisk, in a higher excited state with two asterisks and ions with the respective sign. The spin multiplicity is indicated with a prefixed superscript. Hence, a solvent molecule in the third excited singlet state  $S_3$ , for instance, reads  $^1X^{**}$ . Dimers are abbreviated with  $D$ , excimers thus with  $D^*$ .

The processes occurring, when energy is deposited in LS solutions, are subdivided into primary and secondary processes, where the first are processes that transfer energy from the traversing radiation into excitation or ionization energy of the solvent molecules  $X$  and the second are processes that compete for the excitation energy. Direct excitation of the usually low concentrated  $Y$  and  $Z$  is negligible. The processes are in detail:

### primary processes

- I) excitation of  $\pi$ -electrons, yielding
  - a)  $^1X^{*(*)}$ ,
  - b)  $^3X^{(*)}$ ,
- II) excitation of  $\sigma$ - or carbon 1s-electrons, yielding
  - a)  $\sigma^{(*)}$ ,
  - b)  $1s^{(*)}$ ,
- III) ionization, yielding
  - a)  $^2X^+ + e^-$ ,
  - b)  $F^+ + F^-$  (i.e. free radicals),

### secondary processes

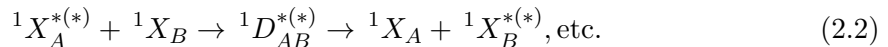
- IV) transfer between  $X$ 's, via
  - a) absorption and reemission,
  - b) collisional processes,

- V) transfer from  $X$  to  $Y$ , via
  - a) absorption and reemission,
  - b) collisional processes,
  - c) dipole–dipole coupling,
- VI) transfer from  $X$  or  $Y$  to  $Z$ ,
  - a) absorption and reemission,
  - b) collisional processes,
  - c) dipole–dipole coupling,
- VII) fluorescence,
- VIII) internal conversion,
- IX) intersystem crossing,
- X) excimer fluorescence,
- XI)  $D^{*(*)}$  dissociation into  ${}^3X^{*(*)}$  and  ${}^1X$ ,
- XII) excimer dissociation into  $2{}^1X$ ,
- XIII) phosphorescence.

Only a few percent of an ionizing particle’s energy is converted into fluorescence and phosphorescence light. The remainder is mostly dissipated thermally or in terms of lattice vibrations. The slow electrons from process IIIa produce secondary excitation and ionization (I–III) or recombine with any  ${}^2X^+$  yielding  ${}^1X^{**}$ ,  ${}^3X^{**}$  or  $\sigma^{**}$ , with  ${}^1X$  yielding  ${}^2X^-$  or with  $F^+$  yielding  $F$ . Note that the latter means a permanent damage reducing the scintillation efficiency. Thus, the superfluous exposition to radiation like daylight is to be avoided. The energy transfer processes IV and V are described in the next subsection, as well as the interplay of the main processes for a ternary system, which are schematically shown in Fig. 2.8.

### 2.5.1 Energy transfer

In an aromatic solvent, where the molar concentration is  $\sim 10^3 \text{ mol/m}^3$ , excited  ${}^1X^{*(*)}$  and unexcited  ${}^1X$  molecules collide with high frequency forming excited unstable dimers  ${}^1D^{*(*)}$ . The mean time between  ${}^1X^{*(*)}$  production and  ${}^1D^{*(*)}$  dissociation is  $\mathcal{O}(10^{-11} \text{ s})$ , two orders of magnitude larger than the fluorescence decay time. Besides emission and reabsorption processes (IVa), rapid excimer formation and dissociation (IVb)



is thus responsible for the excitation energy migration from one solvent molecule  $X_A$  to another one  $X_B$ . The efficiency is only reduced by possible dissociation ending in an excited triplet state (XI) or occurring radiationless into  $2{}^1X$  (XII) or by excimer fluorescence (XII).

In a binary system,  $Y$  is excited by radiative or non-radiative energy transfer from  $X^{*(*)}$ . Radiative transfer is the absorption and reemission of solvent fluorescence light

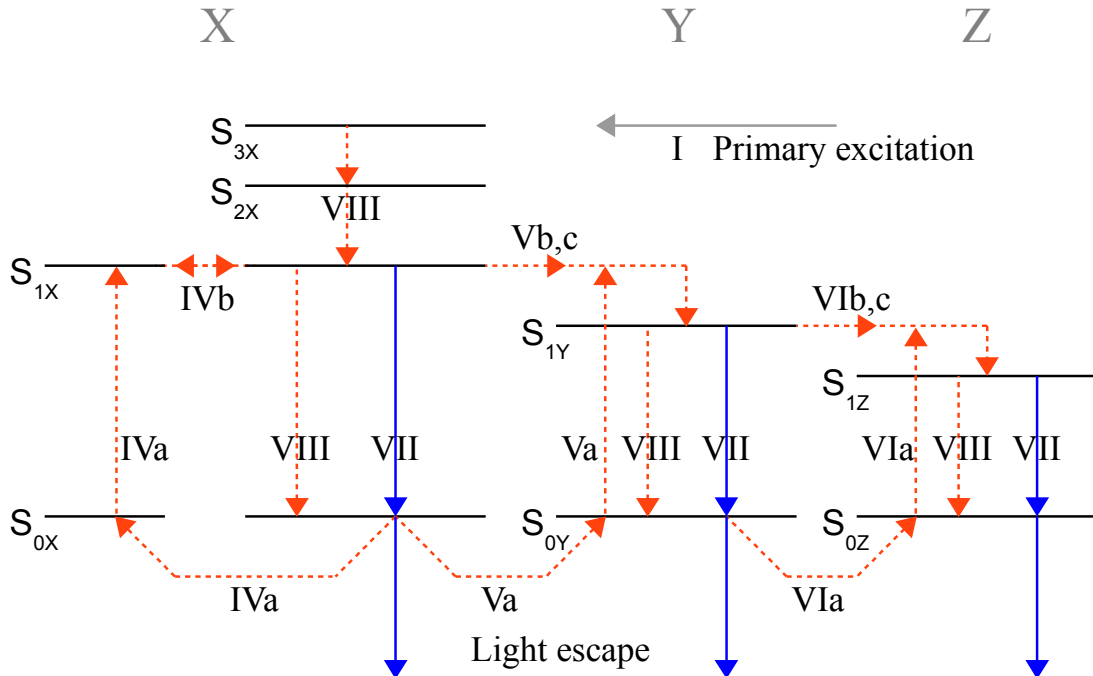


**Figure 2.8:** The main secondary processes in a ternary aromatic system  $XYZ$ , following solvent excitation. Only singlet states  $S$  are shown without their vibrational sub-levels. Solid lines represent fluorescence and dashed lines processes without light emission. The roman numbers refer to the individual processes listed and described in the text.

by  $Y$  (Va). Non-radiative transfer occurs by collisional migration (Vb) or by weak dipole-dipole coupling, also called Förster resonance energy transfer (Vc) [23, 24]. At the typical, low concentrations of the solute, only a combination of both non-radiative mechanisms is able to quantitatively explain the energy transfer from the excited solvent to the solute [25]. Non-radiative transfers are desired since the quantum yield of the solvent fluorescence is low. However, the transition rates of both, collisional processes and resonance energy transfer depend on the distance to a  $Y$  molecule. A higher solute concentration increases the transfer efficiency and thus the total light yield. An increase of the concentration, on the other hand, also increases self-absorption by other  $Y$  molecules and decreases the light yield. The optimum concentration therefore differs from binary system to binary system and needs to be determined experimentally.

Also  $Z$  in a ternary system is excited by the just mentioned radiative and non-radiative transitions (VIa-c). Direct solvent-solute transfer  $^1X^* \rightarrow ^1Z^*$  is in principle possible, however, since the  $Y$  concentration [ $Y$ ] is typically one to two orders of magnitude higher than the concentration [ $Z$ ], the transfer usually occurs from  $X^*$  to  $Y^*$  to  $Z^*$ . In the radiative transfer  $^1Y^* \rightarrow ^1Z^*$ , fluorescence is absorbed by  $^1Z$  before it can escape from the compound. Different from solvent fluorescence, primary solute fluorescence typically has

a high quantum yield and radiative transition forms an efficient transfer, while collisional and resonance transfer become less probable due to the large distances to  $Z$  molecules. The radiative transfer efficiency, though, also depends on  $[Z]$ , but in this case this can be compensated by the size of the detector. The probability that  ${}^1Y^*$  fluorescence light escapes through a thickness  $d$  (cm) before it is absorbed by the secondary solute  $Z$  is

$$\frac{I}{I(0)} = 10^{-\varepsilon[Z]d}, \quad (2.3)$$

where  $\varepsilon$  is the molar extinction coefficient of  ${}^1Z$  (see also Fig. 2.1) averaged over the  ${}^1Y^*$  fluorescence spectrum. An example with typical values is the interplay of PPO and POPOP, where  $\varepsilon \sim 3 \times 10^4$ , with  $[Z] = 1.33 \times 10^{-4} \text{ mol/m}^3$ . In this example, only about 1% of the PPO fluorescence escapes from 5 mm thickness, while the rest is absorbed by POPOP. The scintillator thickness is commonly larger in applications of scintillation counting, as is the case in the measurements presented in Chapter 6.

## 2.6 Quenching

Processes that reduce the quantum yield of a scintillator are called quenching. There are a number of different quenching mechanisms competing with different secondary scintillation processes or changing the ratios of primary processes described in the previous subsection. Depending on the kind of quenching, either the total scintillation light yield is reduced, keeping the time profile conserved or single components of the light pulse are affected, changing both, the intensity and the time profile. The quenching mechanisms important for this work are presented in more detail below.

### 2.6.1 Color and impurity quenching

Color quenching occurs, when the specimen itself or any impurity absorbs parts of the emitted scintillation light. In the standard situation, the foreign molecules are not luminescent and the absorbed spectral component is lost. The intensity decreases and the spectrum lacks, or is strongly reduced in, the respective wavelengths. The overall decay time does not change. If on the other hand the molecule does emit light in the visible or UV region, the intensity decreases less, but the spectral shape may change as well as the effective decay time.

Furthermore, any molecule  $M$  different from  $X$ ,  $Y$  or  $Z$  introduced to the compound also competes with the non-radiative energy transfer processes (IVb, Vb,c and VIbc) between the scintillator molecules, leading to impurity quenching. This also affects both, total and time-resolved fluorescence intensity, as an additional way of depopulating the excited state is created. Assuming, for the ease of explanation, a unitary system, the decay time  $\tau = \tau_X$  in Eq. 2.1 is derived from the sum of the rates  $k_{0X}$  of processes competing for the  ${}^1X^*$  excitation energy (IV,VII-XII) as per

$$\frac{1}{\tau_X} = k_{0X}. \quad (2.4)$$

The introduction of a molar concentration of  $M$  increases the total rate by  $k_M$ , the interaction rate with  $M$  molecules, and changes the decay time according to

$$\frac{1}{\tau_{XM}} = k_{0X} + k_M. \quad (2.5)$$

In case of binary or ternary systems, the above sum is extended by the rate parameter  $k_{XY}$  of solvent–solute energy transfer or  $k_{XY}$  and  $k_{YZ}$ , the rate parameter for solute–solute energy transfer. This type of impurity quenching is also referred to as dynamic to distinguish it from static impurity quenching, where  $M$  molecules form ground-state complexes with any of the fluorophores. These complexes can be excited but are normally not luminescent so that they do not contribute to the total fluorescence light yield. In this case, a molecule  $M$  effectively turns a molecule  $X$  non-luminescent and thus reduces the total light yield, but leaves the pulse decay time unchanged. It should be noted at this point that loaded elements (Section 2.3) are from this point of view impurities and lead to impurity and possibly also to color quenching.

One prominent dynamic quenching agent in LS experiments is oxygen. Oxygen is a special case of impurity quenching and commonly individually considered under the expression of oxygen quenching.

### 2.6.2 Oxygen quenching

It was first observed in 1938 that an increase of dissolved oxygen molecules  $O_2$  in LS solutions substantially reduces the light output [26]. The reduction is remarkably strong, since dioxide does not only lead to impurity quenching, but possesses further possibilities to quench. Being an electron acceptor, for instance, it tends to absorb slow electrons from solvent ionization processes (IIIa), which are then not available anymore for secondary excitations and ionizations. The overall light yield is reduced. Furthermore,  $O_2$  exhibits the seldom case of a triplet ground state with an energy difference to the first excited state that is with 0.98 eV smaller than the spacing of scintillator molecule states. Thus, excitation energy of aromatic hydrocarbons in triplet states, especially in the long-lived  $T_1$  state, is transferred to nearby<sup>4</sup> dioxide, returning the hydrocarbon into the ground state and exciting the oxygen molecule



The transition resulting in phosphorescence, or eventually fluorescence, is bypassed. Due to the highly preferred triplet–triplet state transition, oxygen always quenches if close enough to a triplet state excited scintillator molecule and strongly suppresses the slow scintillation

---

<sup>4</sup>Nearby in this context means that the molecular orbitals overlap.

component. On top of that, excited O<sub>2</sub> molecules are in a singlet state and thus chemically reactive, which may lead to peroxidation and thus the destruction of the original scintillator molecule.

### Elimination of dissolved oxygen from solutions

There are several methods to eliminate the dissolved oxygen from LS solutions. Three common ways of deoxygenation are ultrasonic degassing [27], vacuum distillation [28] and bubbling with N [26, 29] or Ar. For all measurements conducted within this work, N or Ar bubbling was used.

When non-saturated LS is exposed to air, more oxygen molecules diffuse into the solution than from it until thermodynamic equilibrium is reached. However, if the oxygenated scintillator is flushed with N or Ar, both gases are available with high oxygen-purity, the partial pressure of oxygen in the gas bubbles present in the solution can be considered to be zero. Oxygen therefore diffuses into the gas bubbles and escapes with them. The escape rate is thus roughly proportional to the total surface of the bubbles in the scintillator and the partial pressure of oxygen, which in turn is proportional to the oxygen concentration. Measurements have demonstrated that after about 20 min of nitrogen flushing with bubbles of about 4 mm diameter, no further oxygen diminishment is achieved [30]. Besides oxygen purity, it is important that the gas used for bubbling is not electron affine itself. Besides noble gases like Ar, N is one of the few gases for which electron capture is an endothermic process and therefore suitable for this method.

#### 2.6.3 Ionization Quenching

While the aforementioned quenching processes are induced by changes within the compound and are occurring independent of the source of excitation, ionization quenching strongly depends on the ionization energy loss of the traversing radiation and thus on the kind of particle. As stated earlier, ionized scintillator molecules  ${}^2X^+$  mainly recombine into triplet states and the more  $X$  are ionized, the more the fast scintillator component is suppressed and the slow component enhanced. As a consequence, the signal drafted in Fig. 2.7 has a more distinct tail for highly ionizing particles, like  $\alpha$ -particles, than for sparsely ionizing particles, like  $\beta$ -particles, as clearly visible in Fig. 2.9. Ionization quenching is a primary process and expected to be independent of any solute. This expectation has been confirmed within this thesis [32], as will be shown in Sec. 6.

Since the quantum yield of fluorescence is higher compared to phosphorescence, also the integrated light yield  $L$  is reduced. As long as interactions between the excited or ionized molecules are negligible, the light response is proportional to the particle energy  $E$  dissipated in the compound

$$L = SE, \quad (2.7)$$

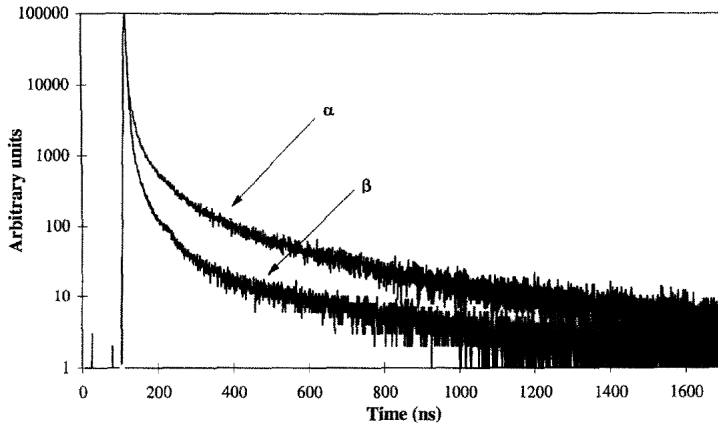


**Figure 2.9:** Averaged and peak normalized scintillation time profiles from  $\alpha$ - and  $\beta$ -particle excitation in PC with 1.5 mg/l PPO [31]. As  $\alpha$ -particle source,  $^{210}\text{Po}$  was used and the  $\beta$ -particles result from Compton scattering of  $\gamma$ 's from a  $^{137}\text{Cs}$  source.

or, in differential form,

$$\frac{dL}{dx} = S \frac{dE}{dx}, \quad (2.8)$$

where  $x$  is the path length in the scintillator and  $S$  the scintillation efficiency. The differential light yield  $dL/dx$  is also referred to as specific fluorescence and  $dL/dE$  is the differential scintillation efficiency. Equations 2.7 and 2.8 very well hold for fast electrons, which have a low energy loss per path length  $dE/dx$  and the individual excited or ionized molecules lay several molecular distances apart. For many of the standard organic liquid and plastic scintillators, linearity of the scintillation light yield has been observed down to about 100 keV [33, 34]. At lower energies,  $dE/dx$  is increased with respect to fast electrons and  $L$  rises non-linearly with  $E$ . For heavy charged particles like protons,  $\alpha$ -particles or other ions, that have a relatively high  $dE/dx$ , the deviation from linearity is even stronger, due to the high density of ionized and excited molecules along the particle's path.

In order to describe the non-linear behavior, Birks proposed the semi-empirical relation

$$\frac{dL}{dx} = S \frac{dE/dx}{1 + kB dE/dx}, \quad (2.9)$$

on the basis of measurements with anthracene crystals [35]. The specific ionization density is  $B dE/dx$ , where  $B$  is a constant.  $k$  is a quenching parameter accounting for the effect of ionization quenching and the product  $kB$  became known as Birks' parameter. For small  $dE/dx$ , Eq. 2.9 approximates Eq. 2.8 and for very large  $dE/dx$  Eq. 2.9 becomes

$$\frac{dL}{dx} \approx \frac{S}{kB} \quad (2.10)$$

and thus constant. Equation 2.9, commonly referred to as Birks' law, only considers unimolecular de-excitation. Bimolecular de-excitation and diffusion are neglected.

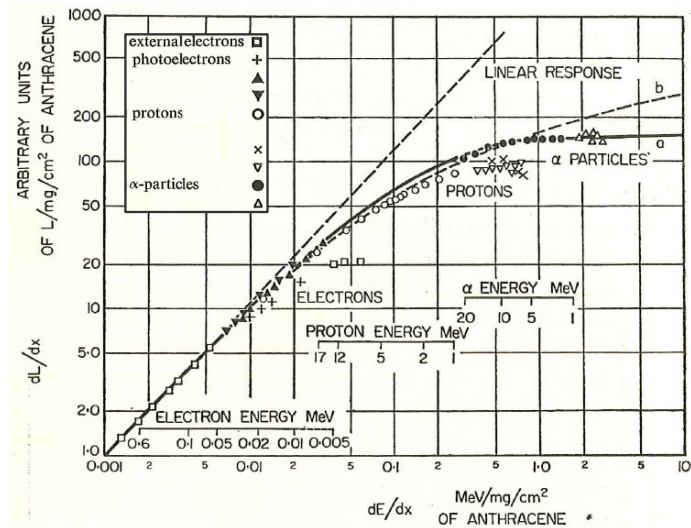


**Figure 2.10:** Specific fluorescence  $dL/dx$  as function of energy loss  $dE/dx$  for anthracene crystals [11]. Adapted to the data points are Eq. 2.9 with  $kB = 0.0053 \text{ cm MeV}^{-1}$  and  $S = 1040 \text{ MeV}^{-1}$  (a) and an equation taking bimolecular de-excitation into account, not considered here (b).  $dL/dx$  of low energy externally incident particles is lower than expected due to surface effects.

Figure 2.10 shows Eq. 2.9 as a function of  $dE/dx$  for fixed  $S$  and  $kB$  together with measurements of the differential light yield of slow and fast electrons, of protons and of  $\alpha$ -particles. The measurements were taken with anthracene crystals and confirm the linear light response Eq. 2.8 of fast electrons, followed by the non-linear behavior according to Eq. 2.9 of slow electrons, of protons and of  $\alpha$ -particles and an approximately constant differential light yield Eq. 2.10 for high  $dE/dx$ , mainly from slow  $\alpha$ -particles. Also the overall trend of an increasing deviation from linearity with increasing  $dE/dx$  is clearly evident. However, it appears that the value of  $kB$ , properly describing the  $\alpha$ -particles, is too low for protons contradicting a common assumption that the response of a particular organic compound to any ion is quantified by the same Birks parameter [36].

Regularly, instead of the derivatives  $dL/dx$  and  $dE/dx$ , the integrated light yield

$$L(E) = S \cdot \int_0^E \frac{dE}{1 + kB \left( \frac{dE}{dx} \right)} \quad (2.11)$$

is displayed as function of the particle energy, as shown in Fig 2.11. In this equation, the denominator quantifies the effect of ionization quenching. In [37], the effect of ionization quenching is described by a second order polynomial, instead of a first order polynomial like in Eq. 2.11. Since a higher order polynomial can only improve the agreement between an analytical description and data, Eq. 2.11 is sometimes encountered in its generalized form

$$L(E) = S \cdot \int_0^E \frac{dE}{1 + kB \left( \frac{dE}{dx} \right) + C \left( \frac{dE}{dx} \right)^2} \quad (2.12)$$

The coefficients of the polynomial are not interpreted in [37] and  $C$  simply parameterizes a quadratic correction term, added to Eq. 2.11.

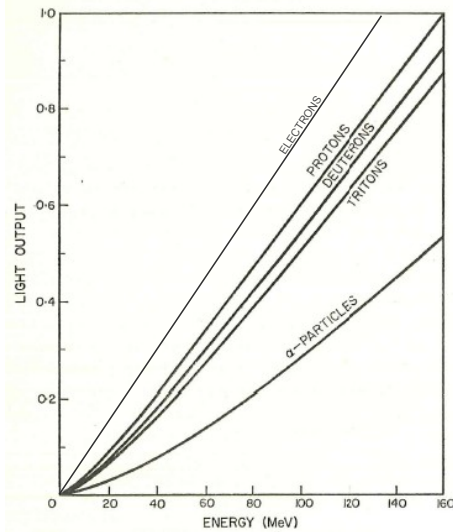


**Figure 2.11:** Calculated light output of NE102 plastic scintillators to electrons, protons, deuterons, tritons and  $\alpha$ -particles as function of kinetic particle energy, taken from [11] and slightly modified.

Even though the scintillation behavior is more complex in liquids than in crystals, Eq. 2.11 and 2.12 are generally successfully used to analytically describe LS data. However, it should be kept in mind that Eq. 2.11 is an unimolecular equation which is kept very simple for a description of a process as non-trivial as ionization quenching. In this process, a multitude of factors affect the time profile of the quenched pulse as the duration of ion recombination or the dissipation of vibrational energy to neighboring molecules. The equation is semi-empirical.

Others than the aforementioned quenching processes, the strength of ionization quenching is normally not quantified absolutely, but in relation to the light yield of a reference particle, which is typically an electron. The light yield in ionization quenching measurements thus is frequently represented in electron equivalent energy or as the ratio of ion response  $L_i$  to electron response  $L_e$  [38, 36]

$$Q_i(E) = \frac{L_i(E)}{L_e(E)}. \quad (2.13)$$

This equation is also referred to as quenching function of the ion  $i$ , or, if given for a discrete particle energy, as quenching factor.

### Surface effects

If organic crystal, plastic or liquid scintillators are excited from external ionizing particles with a short residual range  $r$  in the compound, excitation energy escapes and the observed specific fluorescence is less than expected from Eq. 2.9 and varies non-linearly with  $r$ . To account for this effect, Birks has introduced an energy dependent parameter  $\varphi$  [11], which describes the ratio of experimentally determined and theoretical (Eq. 2.9) specific fluorescence

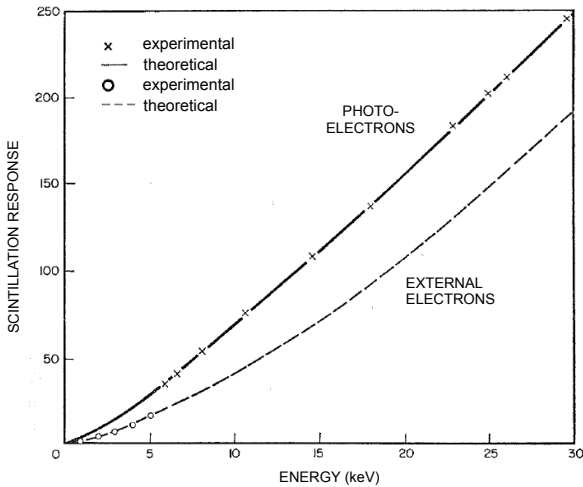


**Figure 2.12:** Light response as function of kinetic electron energy in anthracene crystals [11]. Eq. 2.15 is adapted to the data with  $\varphi = 1$  (solid line) for photoelectrons from  $\gamma$ -ray irradiation (crosses) [39] and  $\varphi$  as function of electron energy (dashed line) for external electrons (circles) [40].

$$\varphi = \frac{(dL/dx)_{exp}}{(dL/dx)_{theo}} \quad (2.14)$$

yielding

$$\frac{dL}{dx} = \varphi S \frac{dE/dx}{1 + kB dE/dx}. \quad (2.15)$$

The change in the light yield behavior due to surface effects has been experimentally determined for different scintillators and particles [11] and is exemplarily shown for electrons in anthracene in Fig. 2.12.

Further causes, besides excitation energy escape, are surface contaminations, surface aging and back-scattering of primary particles. Within this work, only internal charged particles were used to measure the respective light responses eluding surface effects. These effects have to be taken into consideration, though, when it comes to comparisons with results from authors using external particles.

## Chapter 3

# Fundamentals of core collapse supernovae

With the observation of solar and supernova (SN) neutrinos [41, 42, 43, 44] a new field of astrophysics has been opened. Recently, also the first ultra–high energy neutrino events of still unknown source have been observed well–above the atmospheric background [45]. In this field of particle astrophysics, neutrinos from galactic and extra–galactic sources play a key role, since they are an unparalleled probe of cosmological objects and their dynamics. The solely weakly interacting neutrinos traverse high densities and the photon–filled universe mainly unhindered and thus conserve valuable information like direction and energy.

A remarkable source of cosmic neutrinos of all flavors and types are core collapse supernovae (CCSNe), a subclass of SNe, as summarized in Sec. 3.1. Also CCSNe are further subdivided by their initiating cause, which is shortly discussed in Sec. 3.2. The aim within this work is the determination of liquid scintillator detector sensitivities to pivotal features of SN neutrino energy spectra. This chapter therefore focuses on the type of CCSNe that has comparatively well–predicted neutrino emission spectra, the so–called Type II SNe. This type represents the vast majority of CCSNe and is possible for O/Ne/Mg core as well as Fe core stars. The causes that can initiate stellar core collapse are outlined in Sec. 3.2. The results presented in Sec. 7 assume the collapse of an Fe core, giving more significance to these progenitors here. Details about the course of Fe core collapses ending in a Type II SN are given in Sec. 3.3 and their frequentness in the Milky Way in Sec. 3.4. Neutrino fluxes resulting from simulations and kindly provided by Hans–Thomas Janka and Lorenz Hüdepohl [46, 47], are shortly described in Sec. 3.5 and the analytical description of the neutrino spectra is discussed in Sec. 3.6. In the context of SN neutrinos,  $\nu_\mu$ ,  $\nu_\tau$ ,  $\bar{\nu}_\mu$  and  $\bar{\nu}_\tau$  are grouped as  $\nu_x$ , since they can only interact via the flavor and particle type independent neutral current (NC) reactions. If none of the flavors and types is distinguishable, the neutrinos are labelled as  $\nu$ . All constants and non–SI units used within this chapter are listed in Tab. A.1.

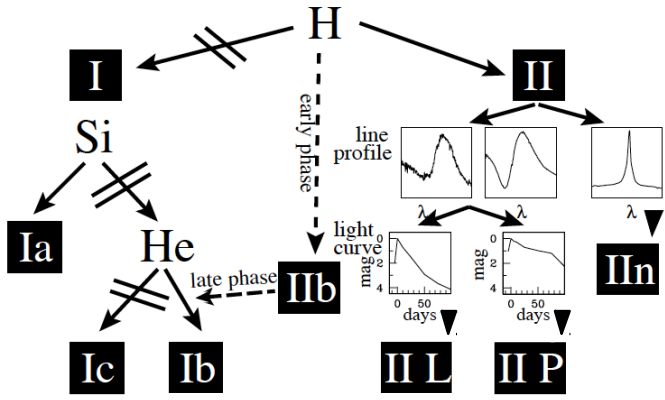


**Figure 3.1:** Supernova taxonomy using spectral features, light curve profiles and their evolution in time, taken from [50].

The drawback of supernovae as cosmological neutrino source is their rare occurrence, as outlined in Sec. 3.4, which is furthermore not reliably predictable in time. The last nearby CCSN, SN 1987A, occurred in February 1987 in the  $\sim 50$  kpc distant Large Magellanic Cloud. Despite the enormous distance, 24 neutrino events were counted on Earth in total with three<sup>1</sup> detectors: Kamiokande II<sup>2</sup>, IMB<sup>3</sup> and the Baksan Scintillator Telescope [42, 43, 44]. At that time, only  $\bar{\nu}_e$  were observed, as the total cross section for the inverse beta decay (IBD) reaction  $\bar{\nu}_e + p \rightarrow e^+ + n$  is the largest. Present-day and near-future low energy neutrino detectors are collectively sensitive to all neutrino flavors and types and an observation of SN neutrinos, especially from a galactic progenitor, will provide unprecedented information about still unknown mechanisms driving the explosion.

### 3.1 Classification

Historically, supernovae are classified according to the absorption lines in their emitted photon spectra and the shape and magnitude of the light curve, i.e. the light intensity as a function of time as seen by an observer on Earth without the influence of the atmosphere. A schematic overview is given in Fig. 3.1, which is followed in this section.

The key differentiator is the absence or presence of H lines in the optical spectrum dividing SNe into Type I and Type II, respectively. Both types are subdivided. If the near maximum spectrum of a Type I SN shows strong absorption due to Si, it is of Type Ia, if not, it is of Type Ib/c. Type Ib and c further distinguish SNe according to strong He

<sup>1</sup>Also LSD (Liquid Scintillator Detector) observed a five-neutrino excess above background [48]. However, the event happened about 5 hrs earlier and the source of the excess has never been clarified unambiguously [49].

<sup>2</sup>Kamioka Nucleon Decay Experiment.

<sup>3</sup>Irvine–Michigan–Brookhaven.

absorption features in the first case and weak or no features in the latter. The subdivision of Type II SNe is less simple and includes light curve profiles and their time evolution, as indicated in the right-hand side of Fig. 3.1. The spectrum of a Type I Ib SN evolves from Type II-like to the spectrum of a Type Ib SN, turning Type IIb into an intermediate class. Type IIP/L/n have a Type II spectrum throughout, with narrow lines (Type IIn) or without (Type IIP/L) and a light curve that reaches a plateau (Type IIP) or displays a linear decrease (Type IIL).

More details about spectral taxonomy are given in [50]. This classification, however, is based on the observed emission spectra and not on their cause: the progenitors' structure and the processes in the final stages of their life. The cause is, on the other hand, what defines whether an intense flux of neutrinos will be present or not. A more suitable classification in the sense of neutrino physics is therefore the distinction between SNe arising from explosive thermonuclear burning, also called runaway fusion, ignited on degenerate white dwarfs ( $\lesssim 9 M_{\odot}$ ) in a binary system (Type Ia) and SNe driven by the gravitational collapse of massive ( $\gtrsim 9 M_{\odot}$ ) single stars (Type II and Ib/c). Supernovae can be divided accordingly into thermal runaway supernovae and core collapse supernovae. Thermal runaway supernovae [51] will not be further discussed here as in this case most of the explosion energy is transferred into heavy element synthesis and kinetic energy of the ejecta and not into neutrinos. Whereas in a standard CCSN,  $> 99\%$  of the binding energy are expected to be released in the form of neutrinos and antineutrinos of all flavors [52].

## 3.2 Causes of core collapse

Core collapse can be initiated for different reasons: electron capture [54], excess of the Chandrasekhar mass limit [55], pair-instability [56] and photodisintegration [57]. The cause of a core collapse as well as the type of the resulting SN, if any, and the remnant left behind are largely determined by the mass  $M^*$  of the progenitor at birth and its metallicity<sup>4</sup>, as extensively discussed in [53] and illustrated in Fig. 3.2. The mass and metallicity range of primary interest within this thesis is the region in Fig. 3.2 associated with Type II SNe after Fe core collapse, i.e. initial progenitor masses of about  $(10 - 40) M_{\odot}$  over nearly the full range of metallicities. Closely related in the context of neutrino phenomenology is the mass region of O/Ne/Mg core collapse from about  $(9 - 10) M_{\odot}$ , completing the region of Type II SNe. Type II SNe form with nearly 90% [53] the vast majority of all CCSNe and their course is presently the best understood, which leads to the most profound predictions concerning the emitted neutrino fluxes. Type II SNe resulting from Fe core collapse are initiated by the excess of the Chandrasekhar limit, which is discussed in more detail in the next subsection. The other initiating scenarios are only outlined here, following Fig. 3.2, and the reader is pointed to the corresponding references for more details.

---

<sup>4</sup>The metallicity is the total mass fraction of elements heavier than helium in the star's initial matter.

### Electron capture supernova

Progenitors with masses of about  $(9 - 10) M_{\odot}$  have an O/Ne/Mg core that withstands the gravitational pressure by electron degeneracy<sup>5</sup> pressure. Mass, and thus the inward pressure, grows through phases of He and H shell burning and the density in the core increases. The consequently increasing electron Fermi energy together with low reaction thresholds leads to electron captures on Ne and Mg, reducing the degeneracy pressure. The core collapses and in doing so induces explosive oxygen fusion, leading to a Type IIP SN that results in a neutron star[54, 58]. Electron–capture SNe are accompanied by the emission of neutrinos [59, 60] and expected to represent up to  $\sim 30\%$  of all CCSNe [58, 61].

### Iron core collapse supernova after excess of the Chandrasekhar mass limit

In case of the more massive Fe core stars with about  $(10 - 100) M_{\odot}$ , the core becomes gravitational unstable, when its mass exceeds the Chandrasekhar mass limit [55] of

$$M_{Ch} \approx 1.457 \left( \frac{2}{\mu_e} \right)^2 M_{\odot} \quad (3.1)$$

and disintegration of the Fe–group isotopes in the core is promoted. In this equation,  $\mu_e = A/Z$  is the mean molecular weight per electron [55, 62] and  $A$  and  $Z$  are as usually the atomic mass and number. The progenitor mass region extends to higher masses in the case of moderate or high metallicity. The collapse results in a Type II, Type Ib/c or jet–powered SN, leaving a neutron star or black hole behind. In the latter case, the formation of the black hole causes a defined end to neutrino emission. Furthermore, at masses  $\gtrsim 40 M_{\odot}$  (blue dashed lines in Fig. 3.2), the collapsing star is unable to launch a shock wave and thus a SN without being driven by a jet. More details about jet–powered SNe are found in [53, 63]. For the earlier mentioned reasons, only Type II SNe due to the collapse of an Fe core progenitor are within the scope of this work. They represent with nearly 60% the largest fraction of all CCSNe and are often assigned as standard or ordinary CCSN. The details of the respective scenario are given in the subsequent section.

### Pulsational pair–instability and pair–instability supernova

Supermassive progenitors of roughly  $(100 - 260) M_{\odot}$  with vanishing metallicity encounter electron–positron pair production from high–energy photons. This instant reduces the thermal pressure necessary to sustain gravitational pressure and the core becomes unstable [56, 64]. If the initial mass is in the range of about  $(100 - 140) M_{\odot}$ , the primary contraction of the core does not launch a full collapse yet. During contraction, the core gets dense and hot enough to ignite oxygen fusion to heavier elements. This exothermic reaction induces a thermonuclear runaway explosion that has just enough energy to eject the outer

---

<sup>5</sup>Fermions reach degeneracy when their Fermi energy begins to exceed the thermal energy  $k_B T$ . In this state, matter is so dense that further compaction would require electrons to occupy the same energy states, which is forbidden by the Pauli exclusion principle.

layers [53, 65]. After the explosion, the residual core contracts to regain a stable burning state. When the temperature again reaches the pair-instability threshold, a second thermonuclear explosion occurs, once more shedding several solar masses of material. It is anticipated that a series of these mass loss pulses proceed until the remaining mass drops below  $\sim 100 M_{\odot}$  [53, 65] or the explosion is energetic enough to unbind the star. If the mass reduces to  $\lesssim 100 M_{\odot}$ , the temperature is too low to support pair-creation and the core undergoes normal core collapse. Since the mass of the formed Fe core is large and the entropy high, the remnant is most probably a black hole [53]. The pulsational period, that can last thousands of years, is also called pulsational pair-instability and is described in more detail in [65]. If the progenitor mass is between  $140 M_{\odot}$  and  $260 M_{\odot}$ , already the first thermonuclear runaway explosion is violent enough to disrupt the entire star. A true pair-instability SN occurs, leaving no remnant behind [53, 66]. For slightly higher metallicities, the mass limits shift to higher masses, as indicated by the brown diagonally hatched and red cross hatched areas in Fig. 3.2.

In the case of black hole formation, an enormous amount of energy ( $\sim 10^{55}$  erg) is expected to be released in the form of neutrinos [64, 67] with a sudden end of their emission. However, the occurrence of pair-instability SNe is assumed to be  $< 1\%$  of all CCSNe [53, 67] and the nature of a star's death due to pair-instability is neither fully understood nor in detail agreed on and an ongoing topic of intense research.

### Core collapse due to photodisintegration

At highest initial progenitor masses of  $\gtrsim 260 M_{\odot}$  and lowest metallicity, the hot stellar core can generate gamma rays energetic enough to directly commence photodisintegration in the center. This reaction is endothermic, no thermonuclear explosion occurs and the collapse continues to a very massive black hole ( $\gtrsim 100 M_{\odot}$ ) directly, without a SN [53, 57].

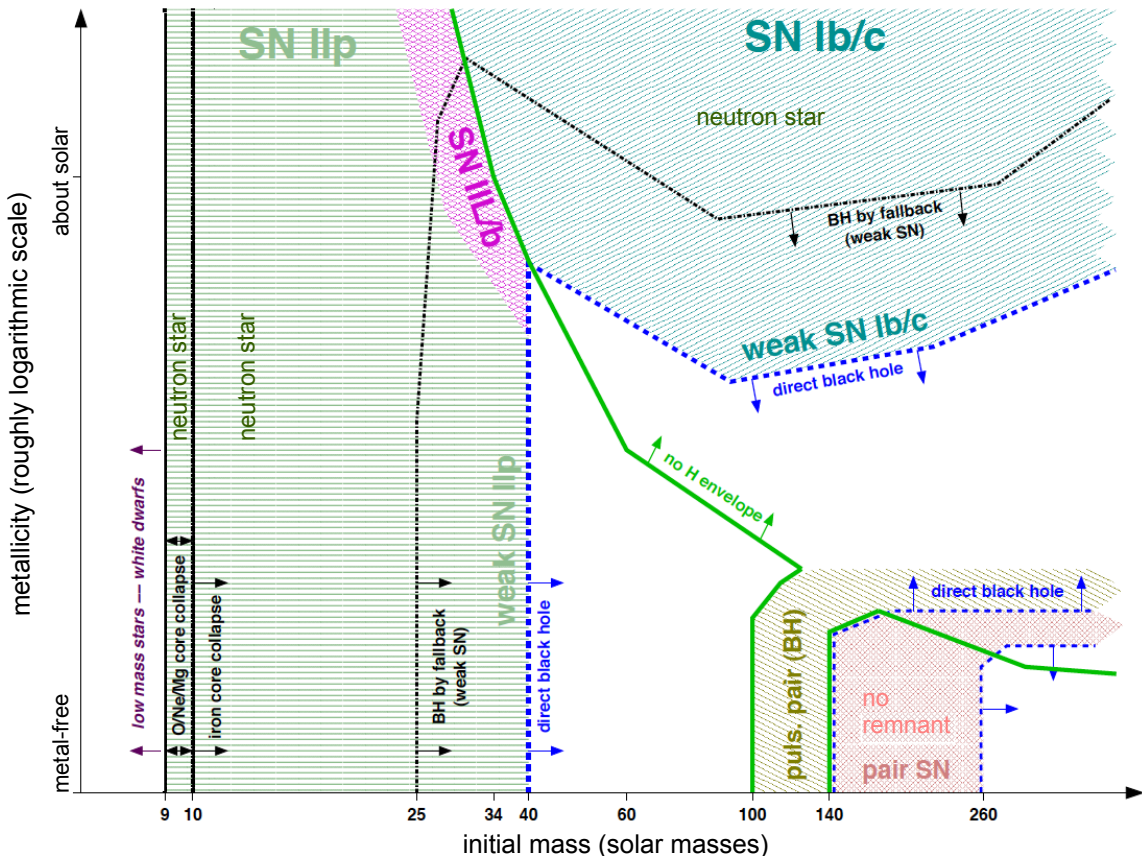


**Figure 3.2:** Remnants and SN type of non-rotating single massive stars as function of initial mass and metallicity (qualitatively). Below the thick green line, stars keep their hydrogen envelope, above they do not, consequently separating the regimes of Type II and Type I SNe. At the lowest shown masses (white strip at the very left), the cores do not collapse and white dwarfs are created. On the right of the two vertical black solid lines, neutron stars are created in O/Ne/Mg or Fe core collapses, until black hole (BH) formation by fallback of material onto the initial neutron star sets in (black dash-dotted line). Right of and below the black dash-dotted line, the remnant is always a BH, except in the red cross hashed area. This is the regime in which pair-instability SNe occur, which leave no remnant behind. The green vertically striped area indicates the domain of Type IIP SNe, which are expected to be weak and observationally faint due to  $^{56}\text{Ni}$  fallback at higher masses and lower metallicity. The purple cross hatching indicates the occurrence of Type IIL/b SNe that have a H envelope below  $2 M_{\odot}$ . The turquoise dashed area is the domain of Type Ib/c SNe, which are expected to be weak and faint at lowest included metallicity, again due to  $^{56}\text{Ni}$  fallback. In the white areas right of the blue dashed lines, no outgoing shock wave is launched and thus no "normal" (non-jet powered) SNe occur. In the brown diagonally hatched regime, pulsational pair-instability SNe occur that start their ejection before the core collapses. The picture and most of the caption is taken from [53]. The picture was slightly modified to include further information from [53].

### 3.3 Classic scenario of iron core collapse supernovae

Over tens of millions to billions of years the stability of the pre-collapse star against its own gravity is retained by central fusion of H to He. However, when H in the stellar core gets depleted and nuclear fusion slows down, the star contracts which in turn raises the temperature and density. As soon as both are high enough and as long as the stellar interior is not stabilized entering the regime of strong electron degeneracy, the next nuclear burning sequence is ignited in which three He nuclei fuse to C. The newly ignited nuclear fusions compensate the energy drain in radiation and neutrinos until the fuel gets again exhausted and contraction continues. Considering progenitor masses of about  $10 M_{\odot}$  to  $100 M_{\odot}$ , this process is repeated in successive stages of nuclear burning, producing increasingly heavier nuclei, until the last stage, Si burning, is reached. The core finally consists of the heavy ashes consisting of Fe-group elements which do not ignite. Figure 3.3 illustrates the resulting onion-like structure within a progenitor in its last throes, including the pauses of contraction at each burning sequence exemplarily assuming  $M^* = 25 M_{\odot}$ . The evolution speeds up considerably because each sequence releases progressively less thermal energy. Furthermore, when central temperatures reach  $T_c \sim 10^9$  K, which is after about the onset of C burning,  $e^+e^-$  pairs become abundant and consequent energy losses via  $\nu\bar{\nu}$  pair production scale up dramatically. At this point, neutrino losses are larger than radiation losses and the evolution of the core decouples from the one of the envelope. The maximum neutrino luminosity is reached during Si fusion [69].

Figure 3.4 sketches the conditions necessary to ignite the individual burning stages and the conditions that are reached by different progenitors. At lowest CCSN progenitor masses,  $8 M_{\odot} \lesssim M^* \lesssim 10 M_{\odot}$ , the stars reach electron degeneracy before they reach the Ne burning state. They thus do not synthesize heavier elements but develop O/Ne/Mg cores before they collapse.

#### Silicon burning

The rapid nucleosynthesis over the different burning stages chiefly advances via alpha processes, meaning by adding He nuclei to heavier nuclei. After a massive star has mainly S and Si in its core and when it further contracts until the core reaches  $\sim 3.3 \times 10^9$  K [69], Si burning sets in. At these temperatures, Si and other elements can be photodisintegrated and outgoing alpha particles can be captured, creating yet heavier elements. Si burning lasts about one day to a couple of days and  $^{56}\text{Ni}$ , made from  $^{28}\text{Si}$  plus  $7\alpha$  particles, which is identical to  $14\alpha$  particles, is the final fusion product with a binding energy per nucleon of  $(8642.71 \pm 0.20)$  keV/A [70]. Alpha capturing to reach the next isotope,  $^{60}\text{Zn}$  (15 alphas), with a binding energy of  $(8583.27 \pm 0.18)$  keV/A per nucleon requires energy instead of releasing any and thus does not take place in the stellar core. The  $\beta^+$  emitter  $^{56}\text{Ni}$  is the most tightly bound nuclei in the alpha process chain and decays with a half-life of about 6.08 days into  $^{56}\text{Co}$ , which further decays under the emission of another positron and with a half-life of about 77.27 days into the stable  $^{56}\text{Fe}$ . For this reason  $^{56}\text{Fe}$  is the

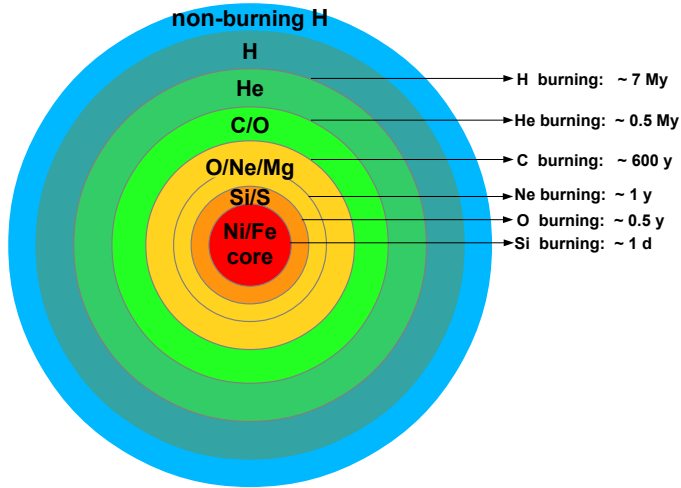


**Figure 3.3:** Schematic shell structure of a Type II supernova progenitor with Fe core, just prior to collapse. The burning stages are reached at the indicated boundaries between the zones. The time periods are calculated for a star of  $25 M_{\odot}$  [68]. Only the most abundant elements are indicated. The radial thickness of the layers is not drawn to scale.

most abundant metal in the universe though it is not the isotope of highest binding energy. This attribute is commonly falsely accredited to  $^{56}\text{Fe}$ , having  $(8790.32 \pm 0.01)$  keV/A, though it truly belongs to  $^{62}\text{Ni}$  with  $(8794.55 \pm 0.01)$  keV/A, which is not part of the alpha process chain. It is also not directly produced from  $^{56}\text{Fe}$ , as  $^6\text{He}$  or  $^3\text{H}$  would be necessary, which are unstable and basically not existing in the core.  $^{56}\text{Fe}$  even only comes at third place since also  $^{58}\text{Fe}$  has with  $(8792.22 \pm 0.01)$  keV/A a higher binding energy. Simply the fact that  $^{56}\text{Fe}$  represents the most common endpoint of nucleosynthesis in stars leads to this wrong conclusion.

The following paragraphs describe the final seconds of a standard CCSN, accompanied by a vast neutrino flux able to generate an event burst in low energy large scale neutrino detectors. They are thus described along with the time distribution of the neutrino luminosities shown in Fig. 3.5.

### Onset of the collapse and neutrino trapping

During the Si burning sequence, the generation of thermal energy by fusion, supporting the core against collapse under its own gravity, declines while the Fe core grows. Simultaneously the neutrino losses continue relentlessly. The stellar interior further contracts and degeneracy pressure of relativistic electrons takes over the support. The core finally becomes gravitational unstable when its mass exceeds the Chandrasekhar mass limit Eq. 3.1. It then typically has a radius of  $R_{\text{Fe}} \sim 3000$  km [72]. At the temperatures and densities reached at that point, two additional processes deprive the Fe core of its energy necessary to avoid collapse: photodisintegration and electron capture. At temperatures around  $10^{10}$  K, the hard ambient radiation shifts the nuclear statistical equilibrium (NSE)<sup>6</sup> towards photodisintegration. The radiation starts to break up Fe nuclei in the process

<sup>6</sup>The NSE is the equilibrium between strong interactions, synthesizing heavier nuclei, and photodisintegration, breaking the nuclei up, at  $T > 5 \times 10^9$  K and  $\rho \approx 10^9$  g/cm<sup>3</sup>.

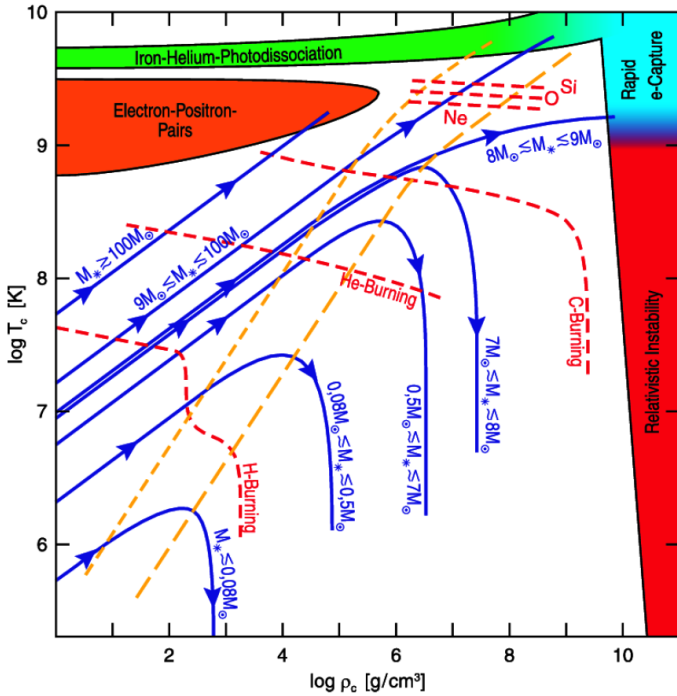


**Figure 3.4:** Central temperature  $T_c$  and central density  $\rho_c$  regimes of the final stages of massive stars. Colored areas are stellar death regions, labelled according to the initial cause of core collapse. Red dashed lines mark the necessary conditions for the next nuclear burning stage. Yellow lines indicate the beginning of degeneracy (short-dashed) and strong degeneracy (long-dashed) of the electron plasma. Blue lines schematically track the stellar evolution (ignoring wiggles and loops at the burning stages) according to the approximate progenitor's birth mass region. Stars not reaching a death zone stabilize by electron degeneracy, cool and form white dwarfs. The picture is taken from [67].



melting it down to He and free neutrons and thereby partially undoing millions of years of stellar evolution in less than one second. To overcome the binding energy of heavy nuclei, a great amount of thermal energy is consumed and the support against gravitational pull diminishes. The core further contracts and though the sustaining degeneracy pressure increases with growing density, so does the electron chemical potential. Thus, deep in the star's interior, electron capture reactions on heavy nuclei, predominantly on  ${}^{56}\text{Fe}$ ,



and on free protons



considerably accelerate. The electron gas pressure is reduced and energy is again carried away from the core in the form of neutrinos, where both effects are promoting the implosion. Additionally, the number of leptons is decreased. Note that in this phase, as long as the core density is below about  $(10^{11} - 10^{12}) \text{ g/cm}^3$ , the herein released  $\nu_e$  escape freely and with increasing luminosity, as shown in the left panel of Fig. 3.5 before the core bounce at the zero point of the time axis. The degree of deleptonization during the collapse depends on the matter composition including the free proton fraction and on the duration of the infall until the critical density is reached and neutrinos become trapped. Within numerical models of CCSNe, both aspects are connected to the equation of state (EOS) of nuclear matter used.

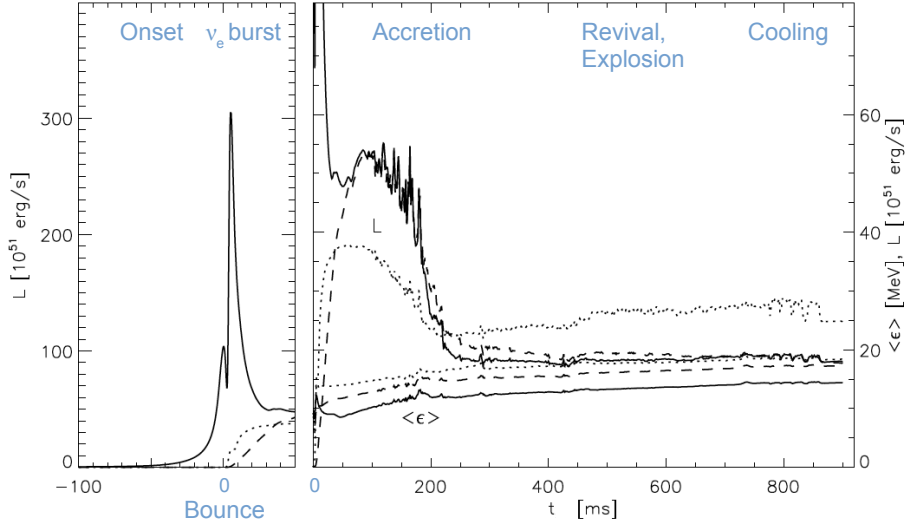


**Figure 3.5:** Exemplary evolution of  $\nu_e$  (solid line),  $\bar{\nu}_e$  (dashed line) and  $\nu_x$  (dotted line) luminosities  $\mathcal{L}$  time  $t$  resulting from simulation of a  $15 M_\odot$  progenitor star [71]. The explosion was obtained only after manipulation. The post–bounce phase (right) also shows the mean energies  $\langle E \rangle$  of the emitted neutrinos. The picture is taken from [71]. The cooling phase not fully shown lasts  $\gtrsim 10$  s with roughly exponentially decreasing luminosity.

After about 100 ms from the onset of instability, the inner part of the Fe core with a radius of  $\sim 100$  km exceeds densities of  $\sim 10^{11}$  g/cm<sup>3</sup>. The  $\nu_e$  produced in Eq. 3.3 and 3.4 are trapped in the collapsing material, since their mean free path becomes smaller than the inner core radius, leading to a sharp cut in the  $\mathcal{L}_{\nu_e}$  time evolution around  $t = 0$  ms in Fig. 3.5. Before the critical density is acquired, only about  $10^{51}$  erg are released in the form of  $\nu_e$ 's with a degenerate spectrum of high energy. The dominant source of matter opacity is coherent scattering of neutrinos. After neutrino trapping, the inner core collapses quasi homologously, i.e. with subsonic velocity proportional to the radius. At the same time, since the collapse of the inner core pulls off the support for the overlying material, the outer core collapses with supersonic free-fall velocity.

### Core bounce and shock formation

Within about 10 ms, the inner core shrinks into a sphere with  $R < 10$  km of mostly neutrons, overshooting the nuclear matter density  $\rho_0 \approx 2 \times 10^{14}$  g/cm<sup>3</sup> by about a factor of two [72]. The collapse comes to a sudden halt due to the repulsive component of the strong force and still infalling material rebounds, building up a shock front upon the clash with the outer core material that continues to crash down. At its propagation through the outer core, the emerging shock wave dissipates its energy by disintegrating the remaining layer of Fe-group material into free nucleons. Since the  $Q$ -value of electron captures on free protons is much larger than on neutron-rich nuclei, the electron capture rate escalates, generating a flood of  $\nu_e$  right behind the shock and increasing the number of neutrons. The newly born remnant,

commonly called protoneutron star (PNS), settles into hydrostatic equilibrium, while the further on supersonically infalling outer core material is abruptly decelerated within the shock. Having traversed the shock, the material propagates much slower towards the PNS, accreting it. The remnant is rapidly growing, developing an unshocked core and a shocked mantle.

### Deleptonization burst and shock stagnation

The outward moving shock wave is opaque to the electron capture  $\nu_e$ 's, having them piling up behind the shock front until it reaches a zone with  $\rho \approx 10^{11} \text{ g/cm}^3$  about 10 ms after the bounce [72]. At this radius, a large fraction of the neutrinos decouple and move out freely. This surface of last neutrino interaction is called neutrinosphere in analogy to the photosphere of a normal light emitting surface. The sudden release of leptons, carrying away energy of  $\mathcal{O}(10^{51} \text{ erg})$  in a few milliseconds from the core, is called deleptonization burst, or also neutronization burst, which leaves an unambiguous signature in the  $\mathcal{L}_{\nu_e}$  time spectrum in Fig. 3.5. The duration of the burst, though, which is defined by the duration of shock propagation, is too short to significantly reduce the electron lepton number and only the low-density outer zones of the PNS are neutronized. This phase presumably does not strongly depend on the progenitor, due to the universal character of the homologously collapsing inner core [62, 73].

The energy losses due to photodisintegration and the deleptonization burst severely weaken the shock. Once it was thought that the shock wave is vigorous enough to not only stop the collapse but to also expel the outer shells of the star, generating a prompt SN within a few hundreds of milliseconds. However, state-of-the art simulations of Fe core collapse cannot confirm the prompt explosion scenario [72]. The shock instead stalls  $\sim 100$  ms after the bounce at a radius of about  $(200 - 300) \text{ km}$  and matter continues to track through it being disintegrated [72, 74].

### Accretion phase

The PNS keeps on accumulating mass due to the infalling matter that successfully passes through the shock front. If more matter is accreted than degeneracy pressure of the nucleons can sustain, the PNS collapses into a black hole, presumably without a SN. Otherwise the nascent remnant keeps on growing throughout this phase of quasi-stationary accretion, until after  $\sim 500$  ms the shock wave is revived and the remaining outer peripheries ejected in a delayed SN explosion.

Right after core bounce and from the beginning of the accretion phase on, neutrinos of all flavors and types are thermally created, additionally to the  $\nu_e$  from Eq. 3.4. The material behind the shock front, mainly composed of free nucleons, electrons and photons, is heated by the accretion. The electron degeneracy is partly lifted in the hot PNS mantle and thus positrons are created, subsequently leading to the production of  $\bar{\nu}_e$  by positron

captures on neutrons

$$e^+ + n \rightarrow p + \bar{\nu}_e. \quad (3.5)$$

Neutrino–anti–neutrino pairs of all three flavors are produced [74] by nucleon–nucleon bremsstrahlung

$$N + N \rightarrow N' + N' + \nu + \bar{\nu}, \quad (3.6)$$

electron–nucleon bremsstrahlung

$$e^\pm + N \rightarrow e^{\pm\prime} + N' + \nu + \bar{\nu}, \quad (3.7)$$

$e^+e^-$  annihilation

$$e^+ + e^- \rightarrow \nu + \bar{\nu}, \quad (3.8)$$

plasmon decay

$$\gamma \rightarrow \nu + \bar{\nu} \quad (3.9)$$

and photoannihilation

$$\gamma + e^\pm \rightarrow e^\pm + \nu + \bar{\nu}. \quad (3.10)$$

$\nu_x$  are additionally created from the annihilation of electron neutrino–anti–neutrino pairs

$$\nu_e + \bar{\nu}_e \rightarrow \nu_{\mu,\tau} + \bar{\nu}_{\mu,\tau}. \quad (3.11)$$

Since  $\nu_e$  and  $\bar{\nu}_e$  are additionally created in the capture reactions Eq. 3.4 and Eq. 3.5, their luminosities are larger than the  $\nu_x$  luminosity in this phase and comparable to each other (see Fig. 3.5).

The created neutrinos have energies around 40 MeV according to the surrounding temperatures [74]. Hence  $\nu_x$  can only react via NC interactions while electron flavor neutrinos can additionally undergo charged current (CC) reactions, the inverse of Eq. 3.4 and Eq. 3.5, by which they are in fact dominated. The electron (anti-)neutrinos are kept in thermal equilibrium by these processes until they decouple from matter at the neutrinosphere, as illustrated in the upper panel of Fig. 3.6. Their spectrum is thus thermal and represents the matter temperature around that radius. Because the neutron density is higher than the proton density and thus the rate of electron captures Eq. 3.4 compared to positron captures Eq. 3.5, the  $\nu_e$  neutrinosphere is further outside and at lower temperatures than the  $\bar{\nu}_e$  neutrinosphere. The neutrinosphere picture is not exact, however, since the cross sections grow with  $E^2$  and various energy groups decouple at different radii and thus temperatures. The neutrinospheres have a finite thickness and the total neutrino spectra are averaged over several temperatures and thus only quasi-thermal.

The case with the  $\nu_x$  lays slightly different. They are kept in thermal equilibrium by creation and destruction through the NC reactions Eq. 3.6–3.10 and the inverse until these reactions freeze out. The thermalized neutrinos, though, do not yet stream off freely from this radial position. Following Fig. 3.6 and [75], this sphere is named energysphere,

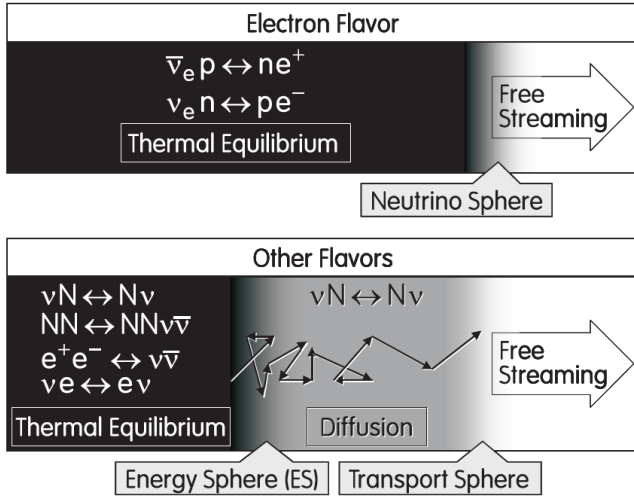


**Figure 3.6:** Schematic of neutrino spectra formation in the atmosphere of a supernova core [75].

after which the  $\nu_x$  are still trapped by  $\nu-N$  inelastic scattering. However, the energy transfer between neutrinos and the heavy non-degenerate nucleons at temperatures around 10 MeV [75] is inefficient. The  $\nu_x$  diffuse outwards, until their mean free path becomes large enough to leave the core unhindered from the neutrinosphere, or transportsphere in this depiction, before reaching thermal equilibrium with the colder matter at this sphere surface. The thermal neutrino spectra from the energysphere are thus smeared out and shifted to lower temperatures, until the neutrinos propagate freely. As a consequence, the spectral shape does not follow the one of a true black-body spectrum anymore, but was found to be pinched [75, 76], meaning reduced in the spectral width, and to have slightly smaller mean energy  $\langle E_{\nu_x} \rangle$ , as illustrated in Fig. 3.7. If the thermal spectrum is described by a Fermi-Dirac distribution, a so-called pinching parameter is thus introduced in order to account for this instance, as will be discussed in more detail in Sec. 3.6.

Since  $\nu_x$  have less sources of opacity than  $\bar{\nu}_e$ , they decouple closer to the core from matter. Following the hierarchy of the neutrinosphere radii  $R_\nu$ , the negative temperature gradient towards the outside of the remnant and the shift of  $\langle E_{\nu_x} \rangle$ , the mean energies of the  $\nu_e$ ,  $\bar{\nu}_e$  and  $\nu_x$  distributions are ordered according to

$$\langle E_{\nu_e} \rangle < \langle E_{\bar{\nu}_e} \rangle \lesssim \langle E_{\nu_x} \rangle. \quad (3.12)$$

In some early simulations, the smearing and downward adjustment of the  $\nu_x$  spectra was neglected for the sake of numerical simplicity and the neutrinos were assumed to have the same energy at the transportsphere as at the energysphere. The energy hierarchy was pronounced. With increasing interest in reliable neutrino spectra as observables, the modification of the  $\nu_x$  energies progressively entered simulations, mitigating the hierarchy.

The  $R_\nu$  are expected to be in this phase between 50 km and 100 km [72, 74], thus smaller than the radius of shock stagnation. When the still propagating shock has passed the individual neutrinospheres, the bulk of neutrinos produced right behind the shock front

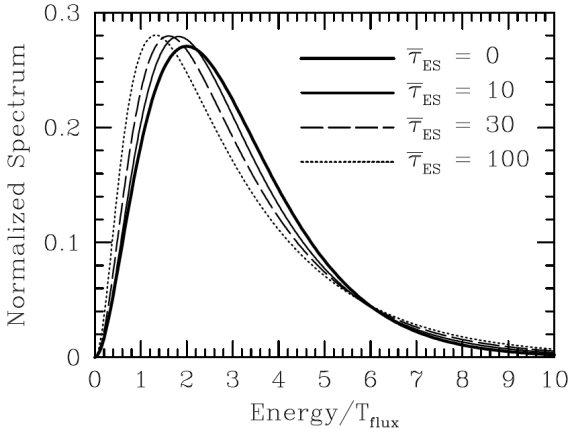


**Figure 3.7:** Comparison of pinched and unpinched thermal distributions, where  $\bar{\tau}_{ES}$  characterizes the distance between energy- and transportsphere.  $T_{\text{flux}}$  is the spectral flux temperature, which is the temperature of those neutrinos that stream. The figure and more details are found in [75].

streams out unhindered, leading to the luminosity hump in Fig. 3.5. Only the neutrinos with high energies are blocked by the increased matter density at the shock position due to a higher interaction rate. Neutrinos created deep inside the hot remnant take instead hundreds of milliseconds to propagate to the respective neutrinosphere and thus continue to stream out also after shock stagnation. The duration of the accretion phase as well as the details of the neutrino spectra depend on progenitor properties like its compactness<sup>7</sup> or mass profile. Additionally, the opacity of the shock to the highest neutrino energies further weakens the mean energy hierarchy Eq. 3.12.

### Delayed explosion and cooling

After shock stagnation, a SN can only follow, if the shock is revived being fed with about  $10^{50} - 10^{51}$  erg of energy [77]. The scenario of shock revival is still, and partly controversially, discussed [67] and a so far unknown combination of mechanisms including for instance neutrino-heating, convection, rotation and magnetic fields. Highly elaborate simulations world-wide show that commonly accepted assumptions are to date not able to explode Fe core progenitors throughout all possible masses. Within this thesis, spherically symmetric, i.e. one-dimensional, simulations performed at MPA Garching [47, 78] are used that are ending with the accretion phase and thus before the explosion. The simulation details are summarized in Sec. 3.5.1.

A mechanism assumed to strongly support the shock revival is the delayed neutrino-heating [72, 74, 79], in which a fraction of the neutrinos emitted from the neutrinospheres deposits its energy in the dense post-shock region. The largest energy deposition is due to  $\nu_e$  and  $\bar{\nu}_e$  captures on the free nucleons behind the shock, since the respective CC cross sections are larger than the NC cross sections. Neutrino-heating, though, is in tight competition with neutrino cooling through neutrino losses via the reactions Eq. 3.4–3.11. Close to the neutrinospheres, neutrino losses dominate, yielding in a cooling layer. As

<sup>7</sup>Compactness is defined as the ratio of a given mass to the radius enclosing this mass at the time of bounce [73]. A higher compactness is equivalent to a higher rate of infalling mass.

the cooling rate declines much faster with radius than the heating rate, heating starts to dominate at a certain point, the so-called gain radius  $R_g$ . Between  $R_g$  and the radial stalled shock position, neutrinos can deposit a substantial amount of energy and revive the shock wave, eventually initiating the stellar explosion. Neutrino-heating is sufficiently strong, if a critical neutrino luminosity  $L_{\nu,c}$  has been overcome [67, 80], which depends on the mass accretion rate  $\dot{M}$  and the neutron star mass  $M_{NS}$  as per

$$L_{\nu,c} \propto \beta^{-2/5} \dot{M}^{2/5} M_{NS}^{4/5}, \quad (3.13)$$

where  $\beta$  is the post-shock to pre-shock density ratio. The caveat of this mechanism is that, in spherical symmetry, it only yields explosions for O/Ne/Mg core progenitors, not for Fe core progenitors [77, 81]. Multi-dimensional models revealed that effects like a convective overturn [82, 83] in the gain layer of neutrino-heating or a standing accretion shock instability (SASI) [84] can support the neutrino-driven shock revival and lead to successful explosions. In multi-dimensional models, effects like these reduce  $L_{\nu,c}$  compared to 1D models [83, 85].

The delayed supernova scenario is widely accepted and considered as sort of a standard model of CCSNe [74]. The revival mechanism, though, is not yet conclusive and still under study. Neutrino-heating, aided by convective processes and hydrodynamic instabilities in the post-shock layer has become the most favored explanation for the majority of SN explosions. For further potential explosion mechanisms see [67].

Accretion and neutrino-heating stops after the take off of the shock wave and only diffuse losses of neutrinos created in Eq. 3.4–3.11 continue, further cooling the PNS down to its center. The luminosities decline roughly exponentially. After ten to tens of seconds, the nascent neutron star (NS) becomes transparent to neutrinos and their luminosities drop significantly [72]. Neutrino emission finally fades away, when no further neutrinos are created in the cooled-down NS. Though at the beginning of the cooling phase, a mild hierarchy of the mean energies as in Eq. 3.12 is observed, it dissolves seconds after the burst [67] into

$$\langle E_{\nu_e} \rangle \approx \langle E_{\bar{\nu}_e} \rangle \approx \langle E_{\nu_x} \rangle. \quad (3.14)$$

In the late cooling phase, the temperature profile within the PNS is flat and the neutrinospheres are close together, due to the dominance of neutral currents under the conditions in this stage [67], explaining the loss of hierarchy. The luminosities are of similar magnitude during the entire cooling phase. The neutrino emission characteristics in this phase are not expected to depend much on the progenitor mass [62].

Due to their only weakly interacting character, neutrinos are the most efficient in carrying away energy from the collapsing star. For the above described scenario of CCSN, neutrino emission is the cardinal energy drain. Only about 1% of the released gravitational

energy is used up in the shock wave and further less, namely 0.01%, is converted into electromagnetic radiation. The residual  $\sim 99\%$  are emitted as neutrinos totaling several  $10^{53}$  erg. While the optical emission takes a few hours to diffuse to the stellar surface and radiate away, intense neutrino emission starts already with the onset of the collapse and gives a direct imprint of the thermonuclear processes involved in the individual CCSN phases.

### Summary

A standard CCSN passes in less than 1 s through its final evolution stages in which a progenitor core with a radius of several thousand kilometers collapses into a hot, dense neutronrich sphere, the PNS, of some tens of kilometers radius. The PNS either further collapses into a black hole or forms within  $\sim 10$  s a NS about  $\sim 10$  km in radius. The evolution stages comprise the onset of instability, core bounce and shock formation, shock stagnation, quasi-stationary accretion, shock revival and explosion. The explosion is finally followed by up to several tens of seconds of cooling. These stages of the delayed explosion scenario, including cooling, are accompanied by a neutrino flux with basically three distinct phases. First visible is an intense, less than 100 ms short, high energy  $\nu_e$  burst with a degenerate spectrum that is mostly independent of the progenitor mass. The second part are approximately thermal  $\nu_e$ ,  $\bar{\nu}_e$  and  $\nu_x$  spectra throughout the  $\sim 500$  ms of accretion phase with increased luminosities at the beginning, and typically a hierarchy of  $\mathcal{L}_{\nu_e} \approx \mathcal{L}_{\bar{\nu}_e} > \mathcal{L}_{\nu_x}$  and  $\langle E_{\nu_e} \rangle < \langle E_{\bar{\nu}_e} \rangle \lesssim \langle E_{\nu_x} \rangle$ . In this case, the spectral shapes and magnitudes depend on the progenitor. The third part are thermal  $\nu_e$ ,  $\bar{\nu}_e$  and  $\nu_x$  spectra during the tens of seconds lasting cooling phase. These spectra have similar luminosities  $\mathcal{L}_{\nu_e} \approx \mathcal{L}_{\bar{\nu}_e} \approx \mathcal{L}_{\nu_x}$  that are roughly exponentially decreasing and show a vanishing hierarchy  $\langle E_{\nu_e} \rangle \approx \langle E_{\bar{\nu}_e} \rangle \approx \langle E_{\nu_x} \rangle$  after the first seconds of cooling. The total count of escaped neutrinos outnumber the original amount of leptons of the collapsed core by an order of magnitude.

At this point, no mechanisms that can change the neutrino flavor and thus the shape of the individual spectra are considered. They are discussed in Sec. 4.

## 3.4 Occurrence of galactic core collapse supernovae

The youngest known remnant from a CCSN in the Milky Way is Cassiopeia A in the constellation Cassiopeia. It was discovered in 1947 by radio detection [87]. The SN was of Type IIb and it is believed that its first light reached the Earth about 300 years ago. However, to the present day only one historical record of a potential observation of the faint SN has been found [88]. The collapse occurred at approximately 3.4 kpc distance, the progenitor star is unknown.

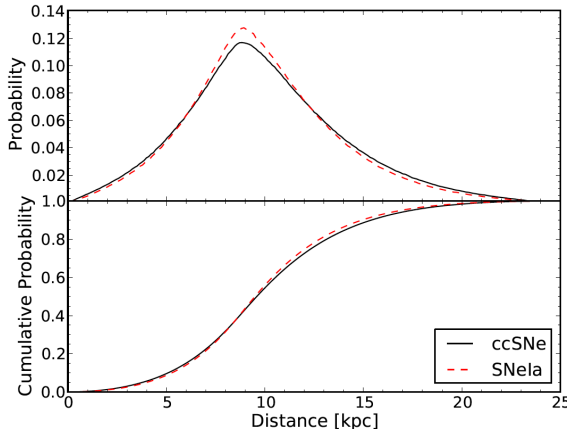


**Figure 3.8:** Differential (top) and cumulative (bottom) probability distribution of the distance of core collapse supernovae (ccSNe) and Type Ia supernovae (SNeIa) from Earth [86].

The last directly observed galactic SN appeared in 1604 [89], known as Kepler’s Supernova, in the constellation Ophiuchus about 6.1 kpc away from Earth. It was of Type Ia [90] and visible by naked eye. It is named after Johannes Kepler, whose observations written down in [91] track the event over one year. Since then and thus since the invention of the first observational instrument, the optical telescope, first recorded in 1608 in the Netherlands, no further galactic SN has been observed.

Motivated by the richness of information gained from a detection of CCSN signals like gravitational waves, electromagnetic radiation and neutrinos, the authors of [86] determined amongst others the probability distribution of the distance and the expected galactic CCSN rate. The rate expectation is found to be  $3.2^{+7.3}_{-2.6}$  per century. The distance distribution, shown in Fig. 3.8, peaks around 9 kpc from Earth. The generic distance for sensitivity studies is 10 kpc [92, 93, 94, 95], which is, given the above distribution, only about 1% less probable than the peak value and thus a reasonable assumption. For the ease of comparison, a distance  $d = 10$  kpc is also considered throughout this work.

The most promising massive single star candidate for a Type II SN in our galaxy is Betelgeuse, also known as  $\alpha$  Orionis, found in the constellation of Orion at  $d = (197 \pm 45)$  pc [96]. Betelgeuse is a  $\sim 10^7$  yr old red supergiant presumably in the C burning phase, thus nearing its final evolution stages. Its initial mass is uncertain, but expected to be  $(10 - 20) M_{\odot}$  [97]. Hence the star is likely to form an Fe core and ultimately explode in a Type IIb SN leaving a NS behind.

### 3.5 Numerical modeling

The foundation stone for hydrodynamic stellar modeling was laid in a debate between Stirling A. Colgate, co-developer of the hydrogen bomb<sup>8</sup> at the Lawrence Livermore

<sup>8</sup>Amongst others, Colgate investigated together with M. Johnson the resultant gamma rays and the fallout from H-bomb explosions and performed numerical calculations.

Laboratory, and Soviet scientists during the nuclear test ban negotiations in 1959 in Geneva [98]. Colgate stated, relating to the satellite surveillance of high altitude H–bomb explosions, that the detectors might be falsely triggered by the radiation emissions from a SN. This argument was slurred over by the Soviet Ambassador Semjon K. Zarapkin saying 'Who knows what a supernova would look like?'. Following this, and with the newborn interest in astrophysics, Colgate decided to continue his research on SN, even after the test of the Soviet > 50 Mt Tsar bomb in 1961 and the strong encouragement by Edward Teller to follow up on its detonation. Based on the work by Burbridge et al. [99], Colgate and Montgomery Johnson started to investigate the ultimate cause of a SN, supported by Subrahmanyan Chandrasekhar. With the first applications of numerical hydrodynamic codes to the problem of stellar collapse and explosion, they intended to determine whether thermonuclear detonation, as suggested in [99], can drive the explosion. However, the simulations, performed by Richard White, demonstrated that the explosion fails as the accompanying shock wave is not strong enough. Colgate and White started developing models of stars about to collapse and White generated a program combining software used to design bombs with EOSs for a star. The ultimate end point of a collapse was soon identified as a neutron star, a merely hypothetical object at that time, and the problems of its stiffness and the EOS became the central point of numerical hydrodynamic calculations. This research helped validate the parallel work of Chandrasekhar on mass limits of stable white dwarfs and moreover it revealed that a deposition of pre-emitted neutrinos as heat in the mantle aids the shock wave in blowing off the outer shells of the star. The idea of the neutrino–heating mechanism was born. In 1966 the research of Colgate, Johnson and White finally resulted in a seminal article [100], edited by Chandrasekhar.

James R. Wilson, originally working on numerical simulations for nuclear weapons, pursued the approach of neutrino transport from the center to the outer regions of the star [101]. He soon became a pioneer in computer-based numerical modeling of SN explosions and demonstrated the importance of neutrinos in the synthesis of heavy elements in SNe. The investigations of Colgate et al. and Wilson were further paralleled by the work of W. David Arnett [102] in hydrodynamic simulation of gravitational stellar collapse. In the course of his work he predicted in 1977 new types of SNe, namely type Ib/c [103].

During the approximately 40 years since the pioneering works, the accuracy of the numerical treatment within models and the input physics have been improved tremendously. The role of highly sophisticated models is to help understanding the genesis of neutron stars, black holes and heavy elements in SN explosions and to predict observables from these events such as gravitational waves, light curves, pulsar kicks or neutrino spectra. These tasks are strongly correlated with the more fundamental and long-standing question of how collapsing stars succeed to explode. As mentioned earlier, neutrinos seem to play a key-role in this quest. Originally, the transport of neutrinos was included in spherically symmetric simulations, but a constrain to spherical symmetry turned out to be insufficient to drive a successful explosion of progenitors with  $M^* > 10 M_\odot$ .

without making assumptions [104] that proved to be invalid under closer analyses [105]. However, also in the era of axially symmetric, i.e. two-dimensional, simulations, the first successful explosions in fully self-consistent models were only reported around the year 2000 [106, 107, 108, 109]. Some of the findings from 2D simulations are the basic confirmation of the neutrino-driven explosion mechanism and the reduction of the critical neutrino luminosity for explosions compared to spherically symmetric models due to effects like the SASI. Independent of the recent successes in 2D modeling, the simulations appear to be limited for at least some of the progenitor models. Thorough cross-checks and code comparisons are necessary and ongoing. Additionally, three-dimensional models are needed to explore the explosion mechanism in a more realistic environment and to test the reliability of the less computing power intense 2D calculations. First results of 3D models have been accomplished by the Garching group [77, 110].

In order to make reliable predictions of observables like neutrinos over the entire course of the SN event, self-consistent numerical simulations are necessary that include a stable solution of the explosion mechanism of Fe core collapse SNe. Though theory has made great progress in that direction, it is not yet at that point. The way things stand at the moment, factors like approximations in the neutrino transport, the degree of stiffness<sup>9</sup> of the nuclear EOS or the influence of multi-dimensional effects on the neutrino emission at  $t \gtrsim 100\text{ ms}$  [77] all influence the neutrino luminosities, mean energies and the shaping of the energy spectra, the key figures parameterizing the observable SN neutrino flux. The relation between these parameters and progenitor properties thus strongly depends on the settings in the models and it is thus not intended within this work to interpret the observed neutrino spectra. However, even though neutrino spectra from different calculations vary quantitatively and their interpretation suffers from this degeneracy, fundamental features of the neutrino fluxes are generic and overall trends comparable [77]. As long as the time evolutions of luminosities, mean energies and energy shapes agree qualitatively, detector sensitivities to the spectral parameters, determined based on a specific calculation, are valid across the different models. Qualitative agreement between neutrino spectra achieved in different 1D and 2D simulations has been tested and confirmed in various publications [111, 112, 113]. The scintillator detector sensitivities determined in Sec. 7 are based on an analytical description which is in agreement with simulations and introduced in Sec. 3.6. Additionally, spherically symmetric calculations, developed by the Core Collapse Modeling Group at the Max Planck Institute for Astrophysics in Garching [78], are used in Sec. 7 to study the variation of the neutrino event yield in the considered detectors, depending on for instance the progenitor mass or the EOS. A short overview over these simulations and the yielded neutrino spectra follow in the next subsection.

---

<sup>9</sup>"Stiff" in this context means, the remnant contracts slower [77]. The antonym is "soft". A stiffer EOS leads to a less compact remnant.

### 3.5.1 Neutrino spectra calculated in spherical symmetry by the Garching group

All SN models considered in this work were simulated at MPA Garching with the PROMETHEUS–VERTEX code [47, 112]. The simulations are spherically symmetric and cover the onset of the collapse, the core bounce and the accretion phase. None of the runs produced an explosion. The set of simulations from the Garching group is based on a selection of progenitor models from Woosley, Heger and Weaver [56] with mass  $M^* = 11.2, 12.0, 15.0, 17.6, 17.8, 20.0, 20.6, 25.0, 27.0$  and  $40.0 \text{ M}_\odot$  as well as one older model from Woosley and Weaver [114] with  $M^* = 15.0 \text{ M}_\odot$ . The calculations were performed with the softer EOS of Lattimer and Swesty [115] with a nuclear incompressibility of 220 MeV, denoted by **ls220**, and the stiffer EOS of Shen [116], denoted by **shen**. For the  $40.0 \text{ M}_\odot$  progenitor, only a model using **shen** exists. Of the publicly available EOSs, **ls220** agrees the best with constraints from nuclear theory and astrophysical observations [73].

The resulting neutrino flux tables [46] provide the time-dependent luminosity  $\mathcal{L}$  (Fig. 3.9–3.11), mean energy  $\langle E \rangle$  (Fig. 3.12–3.14) and second and third energy moment  $\langle E^2 \rangle$  (Fig. 3.15–3.17) and  $\langle E^3 \rangle$  at more than 1000 timesteps between about  $-0.276 \text{ s}$  and  $0.497 \text{ s}$  post-bounce time  $t$  for every SN model mentioned above and for  $\nu_\alpha = (\nu_e, \bar{\nu}_e, \nu_x)$ . In the following,  $\alpha$  represents any of all six neutrino types. The values given in the tables were extracted from  $(400 - 500) \text{ km}$  in the simulation’s output and transformed to a resting observer’s frame at infinity, including the small effect of gravitational redshift from that radius.

Two important aspects in view of the figures are to be noted. First, none of the observables is constant or nearly constant over time, except  $\langle E_{\nu_x} \rangle$  and  $\langle E_{\nu_x}^2 \rangle$  for one or two of the progenitors and preferably the **shen** EOS. Therefore, observables from instantaneous neutrino signals and their time-integrated values must be distinguished carefully and integration over time implies the summation of a set of different quasi-thermal spectra. The resulting sum spectra are not necessarily as well reproduced by a quasi-thermal analytical description as a spectrum from a shorter time period with approximately constant spectral properties. The significance of the deviation and consequences for the interpretation of neutrino data depends on the one hand on the SN itself and on the other hand on the event statistics in the detector. Second, a direct comparison of the neutrino signals derived from models run with **ls220** and run with **shen** show a quantitative difference in the spectra. As mentioned in Sec. 3.3, the duration of the accretion phase and the neutrino emission during this phase depends on progenitor properties like its compactness. A more compact NS is hotter and thus leads to increased luminosities and higher mean energies. The compactness on the other hand is affected by the stiffness of the EOS and lower the stiffer the equation. Furthermore influenced by the EOS is the position of the neutrinospheres, which evolves typically at larger radii, and thus in a colder environment, if **shen** is applied compared to runs with **ls220** [73]. The neutrinos thus thermalize at different temperatures. These

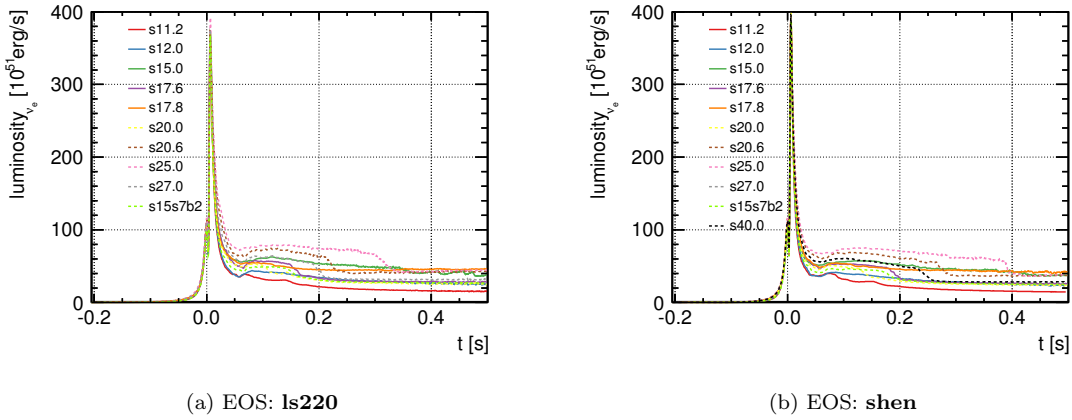


**Figure 3.9:** Electron neutrino luminosity  $\mathcal{L}_{\nu_e}$  time  $t$  for different progenitors and EOSs, using the tables from [46]. The legend denotes the model, implying the progenitor mass.

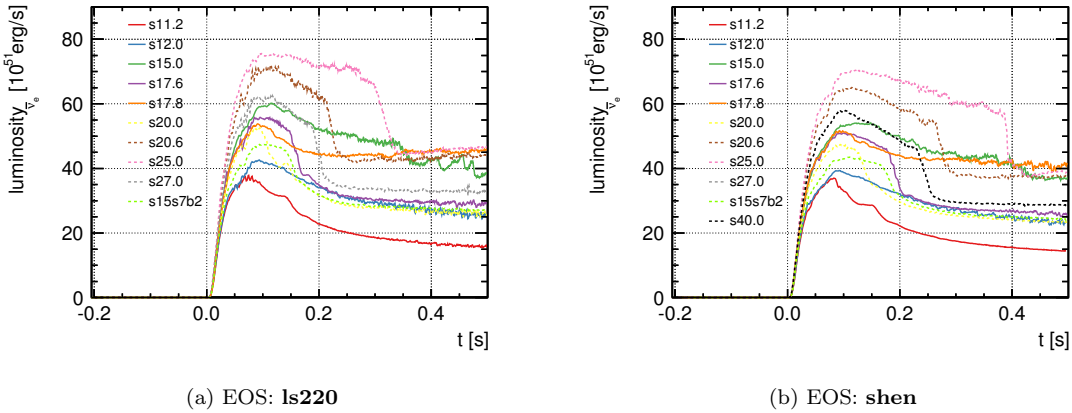


**Figure 3.10:** Electron anti-neutrino luminosity  $\mathcal{L}_{\bar{\nu}_e}$  time  $t$  for different progenitors and EOSs, using the tables from [46]. The legend denotes the model, implying the progenitor mass.

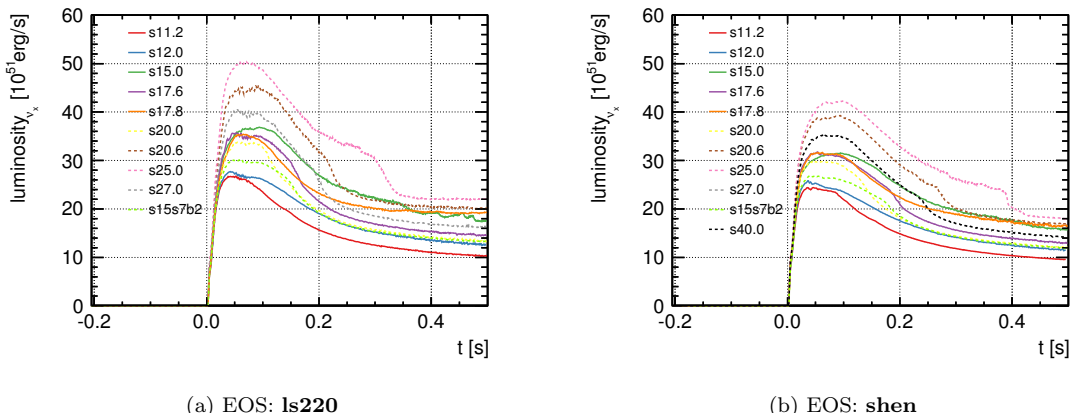


**Figure 3.11:** Muon/tau (anti-)neutrino luminosity  $\mathcal{L}_{\nu_x}$  time  $t$  for different progenitors and EOSs, using the tables from [46]. The legend denotes the model, implying the progenitor mass.

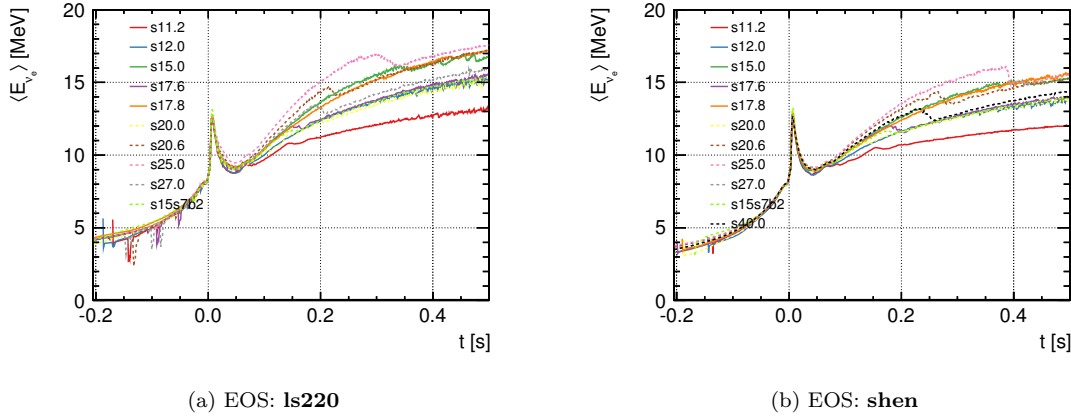


**Figure 3.12:** Electron neutrino mean energy  $\langle E_{\nu_e} \rangle$  time  $t$  for different progenitors and EOSs, using the tables from [46]. The legend denotes the model, implying the progenitor mass.

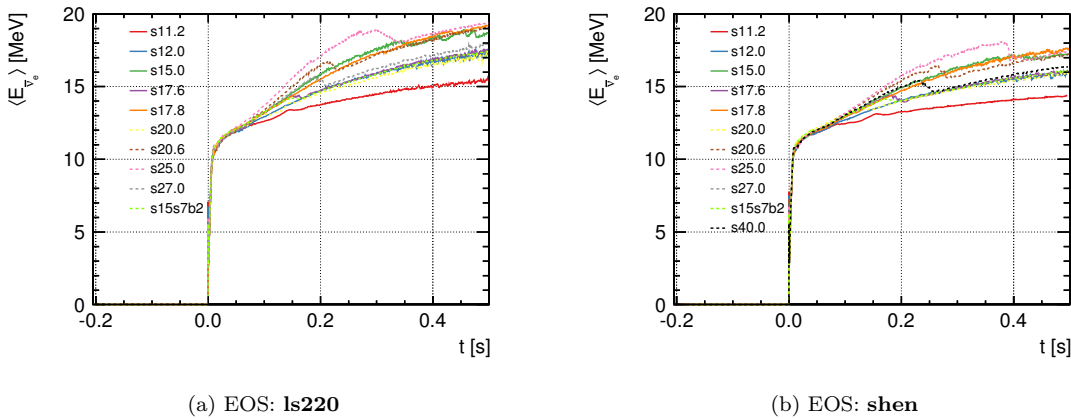


**Figure 3.13:** Electron anti-neutrino mean energy  $\langle E_{\bar{\nu}_e} \rangle$  time  $t$  for different progenitors and EOSs, using the tables from [46]. The legend denotes the model, implying the progenitor mass.

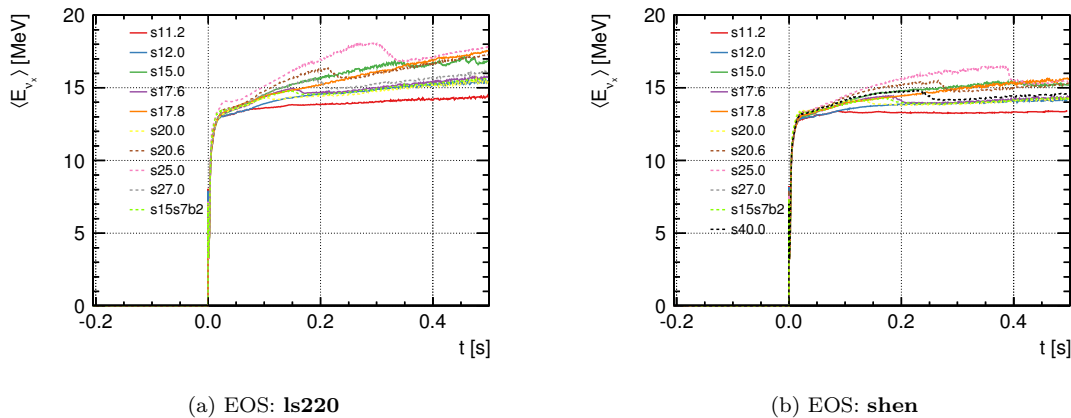


**Figure 3.14:** Muon/tau (anti-)neutrino mean energy  $\langle E_{\nu_x} \rangle$  time  $t$  for different progenitors and EOSs, using the tables from [46]. The legend denotes the model, implying the progenitor mass.

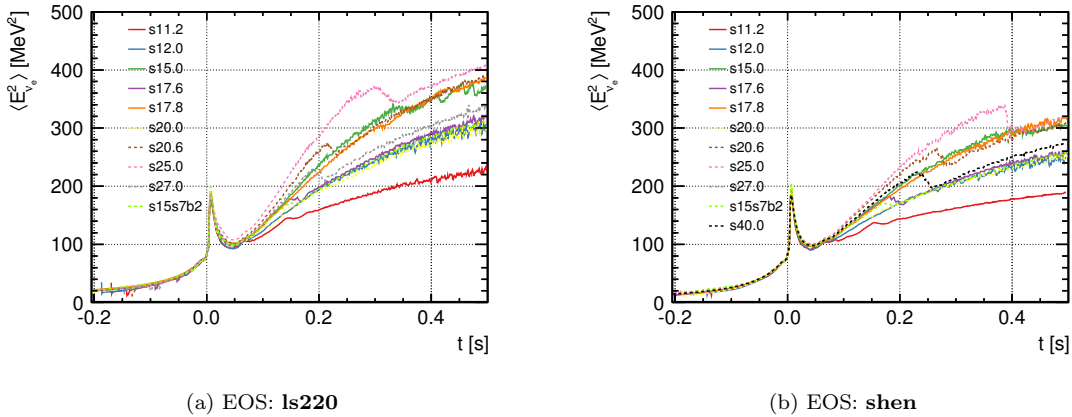


**Figure 3.15:** Electron neutrino second energy moment  $\langle E_{\nu_e}^2 \rangle$  time  $t$  for different progenitors and EOSs, using the tables from [46]. The legend denotes the model, implying the progenitor mass.

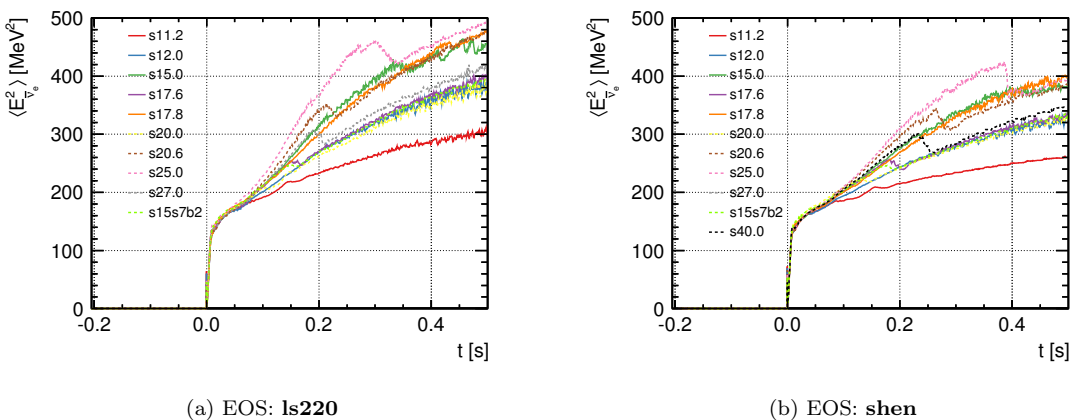


**Figure 3.16:** Electron anti-neutrino second energy moment  $\langle E_{\bar{\nu}_e}^2 \rangle$  time  $t$  for different progenitors and EOSs, using the tables from [46]. The legend denotes the model, implying the progenitor mass.

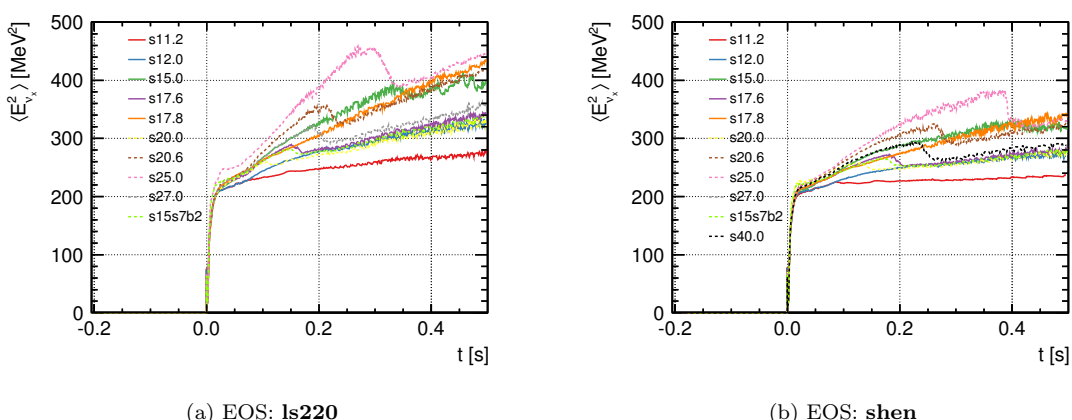


**Figure 3.17:** Muon/tau (anti-)neutrino second energy moment  $\langle E_{\nu_x}^2 \rangle$  time  $t$  for different progenitors and EOSs, using the tables from [46]. The legend denotes the model, implying the progenitor mass.

and further aspects of the EOSs influence the signal parameters shown in Fig. 3.9–3.17 and underline the dependency of the observables on model assumptions, making a physics interpretation at least difficult. An accurate measurement of the spectral parameters, on the other hand, will enable to disfavor, or at best exclude, assumptions. The determination of parameters from an observed SN neutrino flux naturally requires a common parameterization, which is presented in the next section.

### 3.6 Analytical supernova neutrino energy spectra

The double differential neutrino flux per time  $t$  and energy  $E$  streaming off the hot PNS is given by

$$\frac{d^2\Phi_\alpha}{dEdt} = N_\alpha(t)\varphi_\alpha(E, t). \quad (3.15)$$

The number of neutrinos  $N_\alpha$  at time  $t$  is determined from the time-dependent neutrino luminosity  $\mathcal{L}_\alpha$  and mean energy  $\langle E_\alpha \rangle$  according to

$$N_\alpha(t) = \frac{\mathcal{L}_\alpha(t)}{\langle E_\alpha \rangle(t)}. \quad (3.16)$$

$\varphi_\alpha$  is the normalized time-dependent energy distribution  $f_\alpha$

$$\varphi_\alpha(E, t) = \frac{f_\alpha(E, t)}{\int_0^\infty f_\alpha(E, t)dE}. \quad (3.17)$$

As the spectral distribution is expected to be approximately thermal after core bounce, it is often parameterized by a Fermi–Dirac function,

$$f_\alpha(E, t) = \frac{E^2}{e^{E/T_\alpha(t)-\eta_\alpha(t)} + 1}, \quad (3.18)$$

including a so-called degeneracy parameter  $\eta_\alpha$ . This parameter accounts for the spectral pinching mentioned at the end of Sec. 3.3. If the neutrinos were in thermal equilibrium the moment they escape, the degeneracy parameter would be  $\eta = 0$ . The observed pinching, though, is only reproducible with  $\eta \neq 0$ , where different  $\eta_\alpha$  for  $\nu_e$ ,  $\bar{\nu}_e$  and  $\nu_x$  reflect the different coupling to matter. Expanding  $\langle E \rangle/T$  up to the second order of  $\eta$  [117], the neutrino temperature  $T_\alpha$  is related to the mean energy as per

$$\frac{\langle E \rangle}{T} \approx 3.1514 + 0.1250\eta + 0.0429\eta^2 \quad (3.19)$$

and thus  $\langle E \rangle \approx 3.1514T$  in local thermodynamic equilibrium (LTE).

To characterize the amount and direction of spectral pinching, a pinching parameter  $p$  is introduced in [75] with

$$p_\alpha(t) \equiv \frac{1}{a} \frac{\langle E_\alpha^2 \rangle(t)}{(\langle E_\alpha \rangle(t))^2}, \quad (3.20)$$

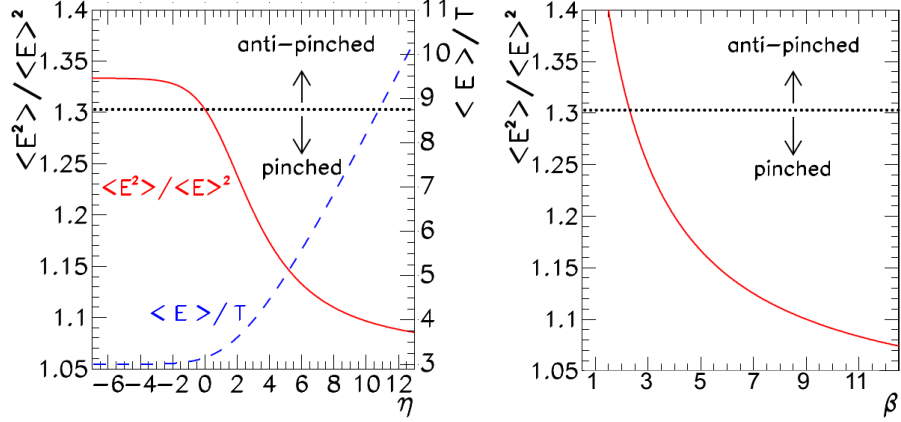


**Figure 3.18:** The left panel shows the ratio  $\langle E^2 \rangle / \langle E \rangle^2$  (red solid line and left label) and  $\langle E \rangle / T$  (blue dashed line and right label) for the Fermi–Dirac distribution Eq. 3.18 as a function of the degeneracy parameter  $\eta$ . The black dotted line gives the value of  $\langle E^2 \rangle / \langle E \rangle^2$  at thermodynamic equilibrium, i.e. for no pinching. The right panel shows the behavior of  $\langle E^2 \rangle / \langle E \rangle^2$  over the  $\beta$  parameter in the Garching parameterization Eq. 3.22.

where the ratio of the second moment over the squared mean energy  $\langle E^2 \rangle / \langle E \rangle^2$  is closely related to the width of the distribution. The parameter  $a$  is given by

$$a \equiv \left. \frac{\langle E_\alpha^2 \rangle(t)}{(\langle E_\alpha \rangle(t))^2} \right|_{\text{LTE}} = \text{const.} \quad (3.21)$$

in thermal equilibrium. Assuming a Fermi–Dirac distribution with  $\eta = 0$  yields  $a \approx 1.3029$  [117]. The spectral shape is that of a black–body, if  $p = 1$ . If the high and low energy tails are relatively suppressed, then  $p < 1$  and the spectrum is pinched. In the opposite case, the spectrum is anti–pinched and  $p > 1$ . The correlation between the ratio  $\langle E_\alpha^2 \rangle / \langle E_\alpha \rangle^2$  and  $\eta$  is shown in Fig. 3.18 in the left panel. It is clear from this figure that the Fermi–Dirac distribution cannot unambiguously reproduce anti–pinched spectra from the mean energy and second moment information, since  $\langle E_\alpha^2 \rangle / \langle E_\alpha \rangle^2$  is not associated with an explicit  $\eta$  at  $\eta < 0$ .

Since the physical motivation for a Fermi–Dirac distribution – the assumption of thermalized neutrinos – does not hold, an alternative parameterization of the spectral shape is considered in [117], motivated by analytic simplicity:

$$f_\alpha(E, t) = \left( \frac{E}{\langle E_\alpha \rangle(t)} \right)^{\beta_\alpha(t)} \exp \left[ -(\beta_\alpha(t) + 1) \frac{E}{\langle E_\alpha \rangle(t)} \right]. \quad (3.22)$$

In this case the distribution is not characterized by  $T_\alpha$  and  $\eta_\alpha$ , but by  $\langle E_\alpha \rangle$  and a shape parameter  $\beta_\alpha$  which is related to the pinching parameter Eq. 3.20 through

$$\frac{\langle E_\alpha^2 \rangle(t)}{(\langle E_\alpha \rangle(t))^2} = \frac{2 + \beta_\alpha(t)}{1 + \beta_\alpha(t)}. \quad (3.23)$$

The equation for  $\beta_\alpha$  directly follows, yielding

$$\beta_\alpha(t) = \frac{2(\langle E_\alpha \rangle(t))^2 - \langle E_\alpha^2 \rangle(t)}{\langle E_\alpha^2 \rangle(t) - (\langle E_\alpha \rangle(t))^2}. \quad (3.24)$$

In LTE  $\beta \approx 2.3$  and both distributions, Eq. 3.18 and Eq. 3.22, agree. The advantage of the latter description comes into play in the case of non-thermal SN neutrino spectra, where it shows no asymptotic behavior of  $\langle E_\alpha^2 \rangle / \langle E_\alpha \rangle^2$ , as shown in the right panel of Fig. 3.18. Therefore it can reproduce also anti-pinched spectra, while a Fermi-Dirac distribution is not well-defined in this regime, as mentioned above. For this reason, the parameterization Eq. 3.22 is used throughout this work. Using the time distribution of  $\langle E_\alpha \rangle$  and  $\langle E_\alpha^2 \rangle$  from the Garching tables, the time evolution of  $\beta_\alpha$  is calculated for each neutrino type and shown in Fig. 3.19–3.21. Note that  $\beta_\alpha$  is not constant over time until about the end of the accretion phase.

The normalized distribution  $\varphi_\alpha$  (Eq. 3.17), derived from the parameterization Eq. 3.22, reads

$$\varphi_\alpha(E, t) = \frac{(1 + \beta_\alpha(t))^{1+\beta_\alpha(t)}}{\Gamma(1 + \beta_\alpha(t))} \frac{E^{\beta_\alpha(t)}}{(\langle E_\alpha \rangle(t))^{\beta_\alpha(t)+1}} \exp\left[-(\beta_\alpha(t) + 1)\frac{E}{\langle E_\alpha \rangle(t)}\right], \quad (3.25)$$

where the integration of Eq. 3.22 follows Ref. [47]. Using Eq. 3.25 and 3.15, the time-integrated neutrino flux  $dN_\alpha/dE$  becomes

$$\begin{aligned} \frac{d\Phi_\alpha}{dE} &= \int_{t_a}^{t_b} \frac{d^2\Phi_\alpha}{dEdt} dt = \frac{\varepsilon_\alpha}{\langle E_\alpha \rangle} \varphi_\alpha(E) \\ &= \varepsilon_\alpha \frac{(1 + \beta_\alpha)^{1+\beta_\alpha}}{\Gamma(1 + \beta_\alpha)} \frac{E^{\beta_\alpha}}{\langle E_\alpha \rangle^{\beta_\alpha+2}} \exp\left[-(\beta_\alpha + 1)\frac{E}{\langle E_\alpha \rangle}\right], \end{aligned} \quad (3.26)$$

where the total energy  $\varepsilon_\alpha$  is the time-integrated luminosity  $\varepsilon_\alpha = \int_{t_a}^{t_b} \mathcal{L}_\alpha dt$ . A simplified variant of the normalized parameterization Eq. 3.25 is suggested in [92], reading

$$\varphi_\alpha(E, t) = \frac{128}{3} \frac{E^3}{(\langle E_\alpha \rangle(t))^4} e^{-4E/\langle E_\alpha \rangle(t)}, \quad (3.27)$$

where  $\beta_\alpha \equiv 3 = \text{constant}$  for all neutrino types and flavors. The total flux at a distance  $d$  from the SN is then given by

$$\frac{d^2\Phi}{dEdt} = \frac{1}{4\pi d^2} \sum_\alpha N_\alpha(t) \frac{128}{3} \frac{E^3}{(\langle E_\alpha \rangle(t))^4} e^{-4E/\langle E_\alpha \rangle(t)} \quad (3.28)$$

and the time-integrated flux, or fluence, by

$$\frac{d\Phi}{dE} = \frac{2.35 \times 10^{13}}{\text{cm}^2 \text{MeV}} \sum_\alpha \frac{\varepsilon_\alpha}{d^2} \frac{E^3}{\langle E_\alpha \rangle^5} e^{-4E/\langle E_\alpha \rangle}. \quad (3.29)$$

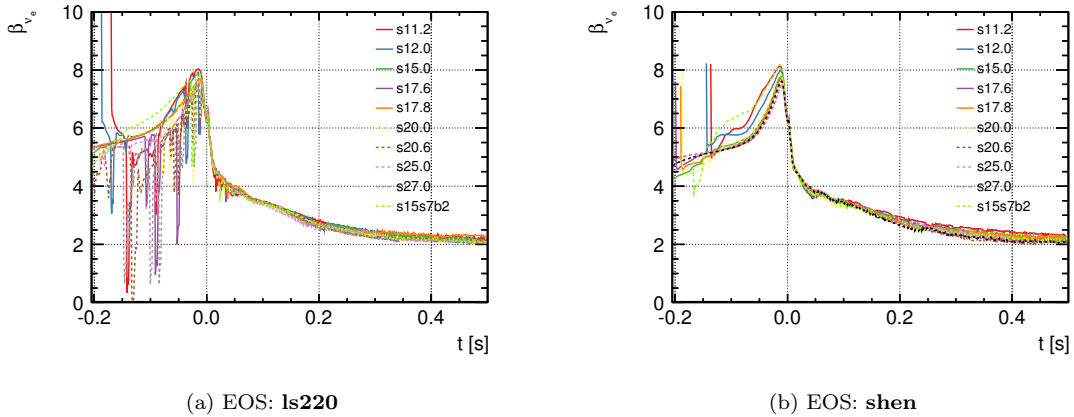


**Figure 3.19:** Electron neutrino energy shape parameter  $\beta_{\nu_e}$  time  $t$  for different progenitors and EOSs, using the tables from [46]. The legend denotes the model, implying the progenitor mass.

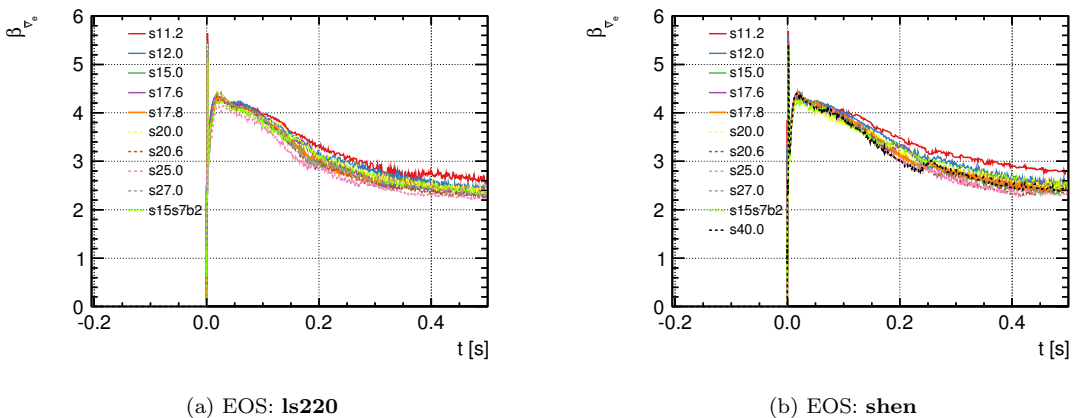


**Figure 3.20:** Electron anti-neutrino energy shape parameter  $\beta_{\bar{\nu}_e}$  time  $t$  for different progenitors and EOSs, using the tables from [46]. The legend denotes the model, implying the progenitor mass.

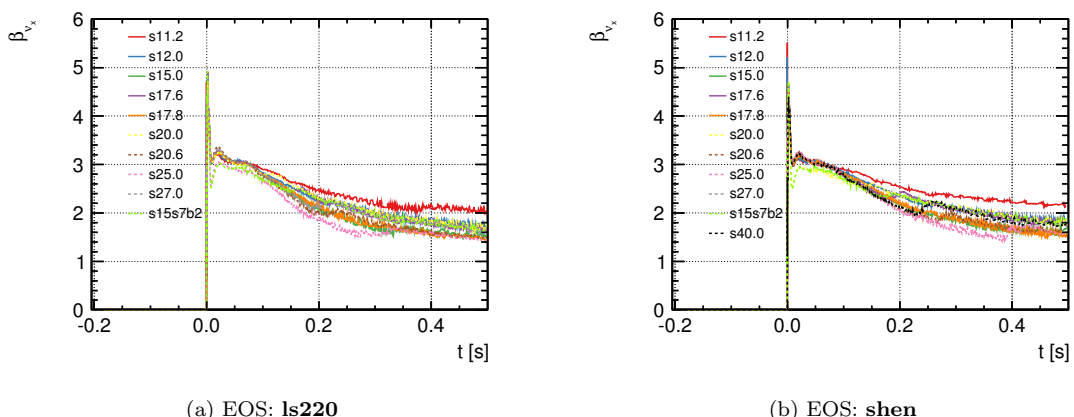


**Figure 3.21:** Muon/tau (anti-)neutrino energy shape parameter  $\beta_{\nu_x}$  time  $t$  for different progenitors and EOSs, using the tables from [46]. The legend denotes the model, implying the progenitor mass.

In this representation, the energies are given in MeV,  $d$  in 10 kpc and  $\varepsilon_\alpha$  in  $10^{52}$  erg [92]. Though this description of the neutrino fluence is only a rough approximation, since the assumption of  $\beta_\alpha = 3 = \text{constant}$  does not hold, regarding Fig. 3.19–3.21, its simplicity and universality makes it a useful tool to determine benchmarks and comparative values. The deviation of this approximation from the time-integrated spectrum taking the time-dependency of  $\beta$  into account depends on the neutrino flavor and to a smaller extend on the progenitor and SN model (see Fig. 3.19–3.21).

Neutrinos are subject to various flavor changing mechanisms, which partly modify the observed spectra on Earth. Both, the simulated spectra as well as predictions using the analytical description of this section thus must be altered accordingly. The different flavor changing effects, which are possible under the extreme and unique conditions during a SN, are discussed in Sec. 4.

## Chapter 4

# Neutrino Properties

This chapter summarizes properties of and effects on neutrinos relevant for SN neutrino observations. These are, for example, neutrino oscillations and additional flavor changing mechanisms occurring under the extreme conditions in a collapsing stellar core. Thereby the focus lays on effects possible during the early phases of core collapse up to the approximate end of the accretion phase, the time interval on which the results in Sec. 7 are based. In this phase, the neutrino signal properties are largely independent of the still unknown details of the explosion mechanism. Additionally outlined in this chapter is the process of neutrinoless double beta ( $0\nu\beta\beta$ ), the primary physics interest of SNO+ and main motivation for the  $\alpha$ -quenching measurements, presented in Sec. 6.

Throughout this work, three active neutrino flavors are considered, following the constraint to  $2.92 \pm 0.05$  light neutrino generations by the invisible  $Z^0$  decay width, as measured in LEP<sup>1</sup> experiments [118, 119] at CERN<sup>2</sup>. Light in this context means, the neutrinos have a mass  $m_\nu < m_Z/2$ , where  $m_Z$  is the  $Z^0$  mass. Active neutrinos are neutrinos that couple to the gauge bosons of the weak interaction in contrast to sterile neutrinos, which do not take part in any of the fundamental interactions of the Standard Model (SM) except gravity and which are up to now solely hypothetical particles. Furthermore, neutrinos within this thesis are considered as ultra-relativistic with  $m_\nu \ll p_\nu$ . This assumption is valid since even low energy neutrino detectors like SNO+ have a threshold of at least  $\sim 100$  keV and the total mass of active neutrinos is  $\sum_3 m_\nu < (0.23 - 0.66)$  eV at 95% C.L., according to the constraints published by the Planck collaboration in 2014 [120]. For the conservative limit, Planck data on the cosmic microwave background (CMB) temperature power spectrum is combined with CMB data from WMAP<sup>3</sup> [121] and ACT<sup>4</sup> [122]. The low limit additionally includes Planck data on Baryon Acoustic Oscillations [120]. Similar neutrino mass limits have been determined by a multitude of further experiments and are listed in [118]. Additionally, first claims of an exclusion of  $\sum_3 m_\nu = 0$  exist, as e.g. in [123].

---

<sup>1</sup>Large Electron Positron collider.

<sup>2</sup>Conseil Européen pour la Recherche Nucléaire.

<sup>3</sup>Wilkinson Microwave Anisotropy Probe.

<sup>4</sup>Atacama Cosmology Telescope.

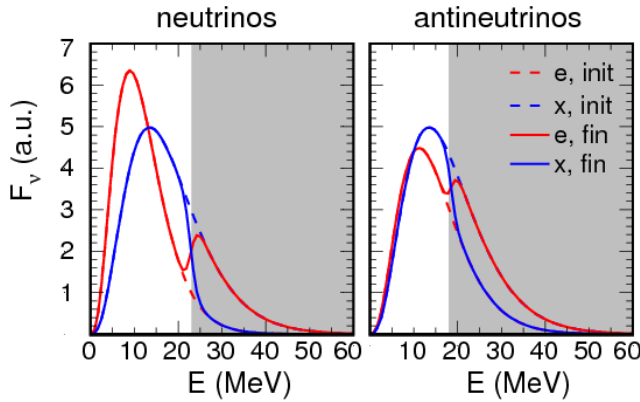


**Figure 4.1:** Energy spectra of supernova electron (anti-)neutrinos (e) and muon and tau (anti-)neutrinos (x) before (dashed lines) and after (solid lines) collective oscillations in the two-flavor sector [124]. The grey regions represent the range in which spectral swap occurs.

## 4.1 Flavor changing mechanisms in general

Supernova neutrinos observed on Earth are subject to a multitude of flavor changing mechanisms: the Mikheyev–Smirnov–Wolfenstein (MSW) effect, also called matter effect, the shock wave effect, the neutrino collective (self–interaction) effect, turbulence effects [125, 126] and the Earth matter effect [127, 128]. The matter effect in Earth is considered separately from the matter effect in the SN environment, since the occurrence of both is fully decoupled and their impacts are different.

The MSW effect on neutrinos emanating from the neutrinosphere and passing through the ordinary matter of the stellar envelope is a neutrino oscillation phenomenon and has been widely discussed [129, 130, 131, 132]. It has been shown that the respective flavor transitions occur at two different radii, which are both much larger than the neutrinosphere radii. Since the shock wave gets stalled further inside, near the neutrinospheres, the MSW effect occurs in a static density environment throughout the accretion phase and the flavor transition calculation is straight forward, which is outlined in Sec. 4.2.2.

As the revived shock wave propagates through the outer regions, though, the density dynamically varies with a steep gradient and the probabilities of flavor conversion are strongly modified [133, 134, 135]. Consequent shock wave effects occur only after shock revival and are most prominent at post bounce times  $t > 1\text{ s}$  [135]. They are thus not relevant for this work.

Another flavor changing mechanism occurs further inside the core, where the neutrino density is tremendous and neutrino–neutrino interactions lead to self–induced flavor conversions, dominating the flavor changing mechanisms [47, 136, 137, 138]. This collective effect typically occurs between the neutrinosphere and the MSW region. In this, rapid conversions between all flavors can occur coherently over a large energy range, depending on the original SN emission features [47, 139, 140, 141]. An example of how collective effects potentially modify SN neutrino energy spectra is shown in Fig. 4.1. The named

dependency is opposed to a general characterization of the SN neutrino signal from the original neutrino fluxes. Furthermore the flavor dynamics of neutrino collective effects are highly non-trivial and far from being fully understood at the moment. In the early SN phases, however, relatively stable conditions are expected. Collective flavor transitions are inevitably absent during the deleptonization burst of only  $\nu_e$  and matter suppressed in the subsequent accretion phase, according to works based on spherical symmetric SN models [142, 143]. Studies over a wide range of SN models, including multi-dimensional models, are still missing though, necessary to corroborate and generalize this conclusion. Given the current status, collective effects are not considered in the thesis at hand.

The last flavor changing mechanism within the star to be mentioned here are turbulence effects. These effects arise from turbulences in the mantle, which break the statics of the matter profile and thus alter the conditions for the MSW effect. According to [126, 144], large amplitude turbulences of about  $\gtrsim 10\%$  obscure the signal features induced by the MSW, as well as by the shock wave and collective effect and bring in new spectral features. Though large amplitudes are necessary for the shock revival, demanding multi-dimensional SN models, they are not yet present in the early post bounce phases considered in this work.

To sum up, the herein investigated phases of the SN from collapse to the approximate end of matter accretion form a comparatively stable environment in terms of the flavor composition of the signal. Only the well-understood neutrino matter oscillations incorporating the MSW effect in a static density profile have to be considered, which is explained in the following section. This instance, though, cannot be adopted for a flavor dependent neutrino observation over the entire time of the burst signal.

Finally, the neutrino signal is additionally affected if the neutrinos are seen through a large fraction of the Earth. However, a recent study in [145], using state-of-the-art simulations and the last missing mixing angle  $\theta_{13}$ , expects this effect not to be observable, unless the detectors are of large scale and the SN is very close by. The target masses considered are 400 kt water, 50 kt liquid scintillator and 100 kt liquid Ar and the distance, at which a difference between Earth shadowed and un-shadowed neutrino fluxes is resolvable, is 0.2 kpc. This distance is relatively unlikely (see Fig. 3.8) and the flux difference expected is  $< 2\%$ , a precision that is not yet accessible for the initial flux predictions. Thus also Earth matter effects [127, 128] are not further discussed here.

## 4.2 Neutrino oscillations

The phenomenon of neutrino oscillations is a quantum mechanical effect, changing the flavor, and thus lepton family number, of a neutrino as it propagates. The probability of flavor conversion from flavor  $\alpha$  to  $\beta$  is called oscillation probability  $P_{\nu_\alpha \nu_\beta}$  and the one of flavor preservation is called survival probability  $P_{\nu_\alpha \nu_\alpha} = 1 - \sum_{\beta \neq \alpha} P_{\nu_\alpha \nu_\beta}$ . The probabilities differ, when neutrinos travel through vacuum and matter. Neutrino oscillations were

originally proposed around 1960 by Bruno Pontecorvo in the form of  $\nu - \bar{\nu}$  oscillations in analogy with  $K_0 - \bar{K}_0$  oscillations [146], when the existence of three neutrino flavors was not yet known. Oscillations between active neutrino flavors are generated by the interference of neutrinos with different masses, which are generated and detected coherently due to their extremely small mass splittings. A finite neutrino mass as well as the violation of lepton family number is not foreseen in the SM, though also not forbidden by any of its fundamental gauge symmetries.

For full consistency of the derivation, neutrino oscillations would have to be described by a wave packet treatment [74]. A simpler approach is the plane wave approximation, which leads to the same results for the probabilities and is used in the following abridged derivation.

#### 4.2.1 Oscillations in vacuum

Neutrinos couple to the weak gauge bosons in the form of orthonormal eigenstates  $|\nu_\alpha\rangle$  ( $\alpha = e, \mu, \tau$ ) to the lepton number operator  $L_\alpha$ :

$$L_\alpha |\nu_\beta\rangle = \delta_{\alpha\beta} |\nu_\beta\rangle. \quad (4.1)$$

In other words, they are created and detected as pure weak flavor eigenstates. These eigenstates have no fixed mass and are thus not necessarily identical with the orthonormal eigenstates  $|\nu_i\rangle$  ( $i = 1, 2, 3$ ) to the mass operator  $M$ , the mass eigenstates:

$$M |\nu_i\rangle = m_i \delta_{ij} |\nu_i\rangle. \quad (4.2)$$

The neutrino masses  $m_i$  are the eigenvalues in this representation. The flavor and mass basis are related by a unitary mixing matrix  $U$  as per

$$|\nu_\alpha\rangle = \sum_{i=1}^3 U_{\alpha i}^* |\nu_i\rangle, \quad |\nu_i\rangle = \sum_{\alpha=e,\mu,\tau} U_{\alpha i} |\nu_\alpha\rangle, \quad (4.3)$$

where  $U$  is also known as PMNS matrix, named after B. Pontecorvo, Z. Maki, M. Nakagawa und S. Sakata. A flavor eigenstate is consequently a coherent superposition of mass eigenstates and vice versa, where the components are weighted by the entries of  $U^{(*)}$ . The assignment of  $U$  and its complex conjugate  $U^*$  in Eq. 4.3 is arbitrary.  $U$  is typically parameterized by three angles and three complex phases according to

$$U = \begin{pmatrix} c_{12}c_{13} & s_{12}c_{13} & s_{13}e^{-i\delta} \\ -s_{12}c_{23} - c_{12}s_{23}s_{13}e^{i\delta} & c_{12}c_{23} - s_{12}s_{23}s_{13}e^{i\delta} & s_{23}c_{13} \\ s_{12}s_{23} - c_{12}s_{23}s_{13}e^{i\delta} & -c_{12}s_{23} - s_{12}c_{23}s_{13}e^{i\delta} & c_{23}c_{13} \end{pmatrix} D(\epsilon_1, \epsilon_2), \quad (4.4)$$

with  $s_{ij} = \sin \theta_{ij}$  und  $c_{ij} = \cos \theta_{ij}$  and  $i \neq j$ . The three  $\theta_{ij}$  are mixing angles,  $\delta$  is a Dirac CP<sup>5</sup> violating phase and  $\epsilon_1$  and  $\epsilon_2$  are two Majorana CP violating phases. The diagonal

---

<sup>5</sup>CP stands for the combined charge conjugation (C) and parity (P) symmetry.

matrix  $D(\epsilon_1, \epsilon_2) = \text{diag}(1, e^{i\epsilon_1/2}, e^{i\epsilon_2/2})$  is not present, if neutrinos are Dirac particles. The nature of neutrinos, Dirac or Majorana, has not been ascertained yet and is amongst others the motivation for the search of neutrinoless double beta decays (see Sec. 4.3). In the framework of neutrino oscillations, though, the submatrix  $D(\epsilon_1, \epsilon_2)$  in Eq. 4.4 cancels out and the Majorana phases thus do not enter the calculations. For this reason, the reduced form of Eq. 4.4, in which  $D(\epsilon_1, \epsilon_2) = \mathbf{1}$ , is used from here on. The CP phase is  $0 \leq \delta \leq 2\pi$  and non-zero, when neutrino oscillations violate the CP invariance. The mixing angles are  $0 \leq \theta \leq \frac{\pi}{2}$ .

The time dependent Schrödinger equation

$$i \frac{\partial}{\partial \tau_i} |\nu_i(\tau_i)\rangle = \mathcal{H}_0 |\nu_i(\tau_i)\rangle, \quad (4.5)$$

with  $\mathcal{H}_0$  being the Hamiltonian in the mass basis in vacuum and  $\tau_i$  the neutrino proper time, is solved by the mass eigenstates:

$$|\nu_i(\tau_i)\rangle = e^{-im_i\tau_i} |\nu_i\rangle, \quad \text{with} \quad |\nu_i(0)\rangle = |\nu_i\rangle. \quad (4.6)$$

These states hence determine the neutrino evolution, which read in the lab frame

$$|\nu_i(t, L)\rangle = e^{-i(E_i t - p_i L)} |\nu_i\rangle. \quad (4.7)$$

Thus a neutrino initially produced in the flavor state  $|\nu_{ini}\rangle = |\nu_\alpha\rangle$  and having propagated a time  $t$  and a distance  $L$  in vacuum relative to the laboratory system is in the state

$$|\nu_{fin}(t, L)\rangle = \sum_{\beta=e,\mu,\tau} \sum_{i=1}^3 U_{\alpha i}^* U_{\beta i} e^{-i(E_i t - p_i L)} |\nu_\beta\rangle, \quad (4.8)$$

using Eq. 4.3. The probability amplitude  $\psi_{\alpha\beta}(t, L) = \langle \nu_\beta(t, L) | \nu_\alpha \rangle$  for this transition is

$$\begin{aligned} \langle \nu_{fin}(t, L) | \nu_{ini} \rangle &= \langle \nu_\beta | \sum_{\beta=e,\mu,\tau} \sum_{i=1}^3 U_{\alpha i}^* U_{\beta i} e^{-i(E_i t - p_i L)} |\nu_\alpha\rangle \\ &= \sum_{i=1}^3 U_{\alpha i}^* U_{\beta i} e^{-i(E_i t - p_i L)}, \end{aligned} \quad (4.9)$$

making use of the orthonormality relation  $\psi_{\alpha\beta}(0) = \langle \nu_\beta | \nu_\alpha \rangle = \delta_{\alpha\beta}$ . For ultra-relativistic neutrinos with  $m_i \ll p_i$ , the following approximations are justified:

$$t \approx L, \quad p \approx E \quad (4.10)$$

and thus

$$E_i = \sqrt{m_i^2 + p_i^2} \approx p_i + \frac{m_i^2}{2p_i} \approx E + \frac{m_i^2}{2E}, \quad (4.11)$$

assuming that each eigenstate has the same energy  $E_i = E$  and  $E$  is real. With Eq. 4.10–4.11 the amplitude Eq. 4.9 can be written as

$$\psi_{\alpha\beta}(L) = \sum_{i=1}^3 U_{\alpha i}^* U_{\beta i} e^{-i \frac{m_i^2}{2E} L}. \quad (4.12)$$

The transition probability from  $|\nu_\alpha\rangle$  to  $|\nu_\beta\rangle$  is the square of the absolute amplitude and thus

$$\begin{aligned} P_{\nu_\alpha\nu_\beta}(L) &= \left| \sum_{i=1}^3 U_{\alpha i}^* U_{\beta i} e^{-i \frac{m_i^2}{2E} L} \right|^2 \\ &= \sum_{i,j} U_{\alpha i}^* U_{\beta i} U_{\alpha j} U_{\beta j}^* e^{-i \frac{\Delta m_{ij}^2}{2E} L} \\ &= \delta_{\alpha\beta} - 4 \sum_{i>j} \Re(U_{\alpha i}^* U_{\beta i} U_{\alpha j} U_{\beta j}^*) \sin^2 \left( \frac{\Delta m_{ij}^2 L}{4E} \right) \\ &\quad \pm 2 \sum_{i>j} \Im(U_{\alpha i}^* U_{\beta i} U_{\alpha j} U_{\beta j}^*) \sin \left( \frac{\Delta m_{ij}^2 L}{2E} \right), \end{aligned} \quad (4.13)$$

with  $\Delta m_{ji}^2 \equiv m_j^2 - m_i^2$ . The last step makes use of the unitarity relation  $UU^\dagger = 1$  of the mixing matrix and thus  $\sum_i U_{\alpha i} U_{\beta i}^* = \delta_{\alpha\beta}$ . Equation 4.13 defines the oscillation probability if  $\alpha \neq \beta$  and the survival probability if  $\alpha = \beta$ . The minus sign in front of the imaginary part refers to the oscillation probability of anti-neutrinos  $P_{\bar{\nu}_\alpha \bar{\nu}_\beta}$ . This part is zero and thus  $P_{\nu_\alpha \nu_\beta} = P_{\bar{\nu}_\alpha \bar{\nu}_\beta}$ , if the CP symmetry is conserved. It is evident from Eq. 4.13 that neutrino oscillations only occur, if  $\Delta m_{ji}^2 \neq 0$ , in other words if not all neutrinos have the same mass. The observation of neutrino oscillations excludes that all neutrinos are massless. The mixing angles and the Dirac phase enter the measurable oscillation or survival probability Eq. 4.13 via the mixing matrix  $U$  given in Eq. 4.4. Since the probability also depends on the neutrino energy  $E$  and the distance  $L$  between neutrino source and detection, the experimental settings comprising  $L$ ,  $E$  and the neutrino species, determine the detector sensitivity to the oscillation parameters  $\Delta m_{ji}^2$ ,  $\theta_{ij}$  and  $\delta$  with  $i, j = 1, 2, 3$  considering three active neutrino flavors. The neutrino sources are either of natural kind or artificially created, where the first group is dominated by solar  $\nu_e$  [147], atmospheric  $\overline{\nu}_{\mu,e}$  [148] and supernova  $\overline{\nu}_{\tau,\mu,e}$  [49, 149] and the second group by accelerator  $\overline{\nu}_\mu$  [150] and reactor  $\bar{\nu}_e$  [151]. Historically, the first oscillation parameters measured, proving the existence of neutrino oscillations, are named after the respective neutrino source solar and atmospheric. The results from these experiments have shown that  $0 < \Delta m_{\text{sol}}^2 \ll |\Delta m_{\text{atm}}^2|$  [152]. Since the numbering of massive neutrinos  $\nu_i$  is arbitrary, the association of these squared mass differences with any  $\Delta m_{ji}^2$  is it as well. Most commonly, the smaller squared mass splitting is referred to  $\Delta m_{21}^2$ , and thus  $\Delta m_{\text{sol}}^2 \equiv \Delta m_{21}^2$  with  $m_1 < m_2$ . The three squared mass splittings are correlated via  $\Delta m_{21}^2 + \Delta m_{32}^2 - \Delta m_{31}^2 = 0$ , implying that  $\Delta m_{31}^2 \approx \Delta m_{32}^2$  and thus  $\Delta m_{\text{atm}}^2 \approx \Delta m_{31}^2 \approx \Delta m_{32}^2$ . Oscillation experiments are not yet sensitive to the sign of  $\Delta m_{31(32)}^2$ , leaving three possible

ordering schemes of the neutrino masses: normal hierarchy (NH), inverted hierarchy (IH) and a quasi degenerate (QD) scenario in case the lightest neutrino mass is  $m_{\text{lightest}} \gtrsim 0.1 \text{ eV}$  [118]. In the latter scenario, the neutrino masses are much larger than the squared mass splittings and thus in practice

$$m_{\text{lightest}} \approx m_1 \approx m_2 \approx m_3 \gtrsim 0.1 \text{ eV}. \quad (4.14)$$

In the numbering convention employed, NH refers to

$$\begin{aligned} m_{\text{lightest}} &= m_1 < m_2 \ll m_3, \\ m_2 &= \sqrt{m_1^2 + \Delta m_{\text{sol}}^2} \approx 0.0086 \text{ eV}, \\ m_3 &= \sqrt{m_1^2 + \Delta m_{\text{sol}}^2 + |\Delta m_{\text{atm}}^2|} \approx 0.048 \text{ eV}, \end{aligned} \quad (4.15)$$

and IH to

$$\begin{aligned} m_{\text{lightest}} &= m_3 \ll m_1 < m_2, \\ m_1 &= \sqrt{m_3^2 + |\Delta m_{\text{atm}}^2|} \approx 0.048 \text{ eV}, \\ m_2 &= \sqrt{m_3^2 + |\Delta m_{\text{atm}}^2| + \Delta m_{\text{sol}}^2} \approx 0.048 \text{ eV}. \end{aligned} \quad (4.16)$$

In the same convention, the solar mixing angle is assigned to  $\theta_{12}$  and the atmospheric mixing angle to  $\theta_{23}$ . The numerical values in Eq. 4.15 and 4.16 are derived from existing data from all types of oscillation experiments, which allows to determine  $\Delta m_{21}^2$ ,  $|\Delta m_{31(32)}^2|$ ,  $\theta_{12}$ ,  $\theta_{23}$  and  $\theta_{13}$  in a global fit [153], as summarized in Tab. 4.1. Neither a measurement of the CP violating phases in the mixing matrix Eq. 4.4 has been possible so far, nor the confirmation or exclusion of any of the three mass ordering schemes. It should be noted, however, that recent global analyses yield  $\delta/\pi = 1.08_{-0.31}^{+0.28}$  [153] or  $\delta/\pi = 1.67_{-0.77}^{+0.37}$  [154], although the  $1\sigma$  uncertainties are still large.

One explicit example for Eq. 4.13 is the  $\nu_e$  survival probability

$$\begin{aligned} P_{\nu_e \nu_e}(L) &= 1 - \frac{1}{2} \cos^4 \theta_{13} \sin^2 2\theta_{12} \left( 1 - \cos \left( \frac{\Delta m_{21}^2}{2E} L \right) \right) \\ &\quad - \frac{1}{2} \sin^2 2\theta_{13} \left( 1 - \cos \left( \frac{\Delta m_{31}^2}{2E} L \right) \right) \\ &\quad - \frac{1}{2} \sin^2 \theta_{12} \sin^2 2\theta_{13} \left( \cos \left( \frac{\Delta m_{31}^2}{2E} L \right) - \cos \left( \frac{\Delta m_{21}^2 + \Delta m_{31}^2}{2E} L \right) \right), \end{aligned} \quad (4.17)$$

particularly interesting for neutrinos from the Sun, as they are exclusively produced as  $\nu_e$ . All other explicit forms of Eq. 4.13 are found in [155], for instance. If the argument of the cosine in Eq. 4.17 is

$$\frac{\Delta m^2}{2E} L \gg 1, \quad (4.18)$$

**Table 4.1:** 3-neutrino oscillation parameters from a global fit of current (2014) data [118]. If the value in inverse hierarchy (IH) is different from the value in normal hierarchy (NH), it is added in brackets.  $\Delta m^2$  is defined as  $\Delta m^2 = m_3^2 - (m_2^2 + m_1^2)/2$ . Thus,  $\Delta m^2 = \Delta m_{31}^2 - \Delta m_{21}^2/2 > 0$  in NH, and  $\Delta m^2 = \Delta m_{32}^2 + \Delta m_{21}^2/2 < 0$  in IH [153].

Parameter	Best fit $\pm 1\sigma$	$3\sigma$ range
$\Delta m_{21}^2 [10^{-5}\text{eV}^2]$	$7.54^{+0.26}_{-0.22}$	$6.99 - 8.18$
$ \Delta m^2  [10^{-3}\text{eV}^2]$	$2.43 \pm 0.06$	$(2.38 \pm 0.06)$
$\sin^2 \theta_{12}$	$0.308 \pm 0.017$	$0.259 - 0.359$
$\sin^2 \theta_{23}$	$0.437^{+0.033}_{-0.023}$	$(0.455^{+0.039}_{-0.031})$
$\sin^2 \theta_{13}$	$0.0234^{+0.0020}_{-0.0019}$	$(0.0240^{+0.0019}_{-0.0022})$
		$0.0176 (0.0178) - 0.0295 (0.0298)$

only the average of the cosine function is observable, which is zero. Thus for solar neutrinos, where  $|\Delta m_{31}^2| \gg 2E/L$ , the measurable average survival probability is given by

$$\langle P_{\nu_e \nu_e}(L) \rangle = \cos^4 \theta_{13} \left( 1 - \sin^2 2\theta_{12} \sin^2 \left( \frac{\Delta m_{21}^2}{4E} L \right) \right) + \sin^4 \theta_{13}. \quad (4.19)$$

#### 4.2.2 Oscillations in matter and the MSW effect

The presence of matter, as in the Sun, Earth or a SN, can significantly change the neutrino oscillation probability. Interactions of neutrinos with the particles forming the matter give rise to a potential  $V$  that is not present in vacuum. Intuitively, this changes the total neutrino energy and hence the Hamiltonian in Eq. 4.5 and the consequent derivation of the oscillation probability. In general, the Hamiltonian is the sum of a kinetic energy component  $\mathcal{H}_0$  and a potential energy, or interaction, component  $\mathcal{H}_I$ ,

$$\mathcal{H} = \mathcal{H}_0 + \mathcal{H}_I, \quad (4.20)$$

with

$$\mathcal{H}_0 |\nu_i\rangle = E_i |\nu_i\rangle \quad \text{and} \quad \mathcal{H}_I |\nu_\alpha\rangle = V_\alpha |\nu_\alpha\rangle. \quad (4.21)$$

Note that  $E_i$  is the kinetic energy of massive neutrinos and the vacuum Hamiltonian  $\mathcal{H}_0$  in the mass eigenbasis, while  $V_\alpha$  is the effective potential felt by flavor neutrinos due to weak currents and  $\mathcal{H}_I$  thus in the flavor eigenbasis. The potential is the sum of CC and NC contributions from coherent forward scattering reactions<sup>6</sup>. In ordinary matter<sup>7</sup> only electron flavor neutrinos are affected by the CC potential  $V_{CC}$ , so that

$$V_\alpha = \delta_{\alpha e} V_{CC} + V_{NC}^n + V_{NC}^p + V_{NC}^e = \delta_{\alpha e} V_{CC} + V_{NC}^n. \quad (4.22)$$

<sup>6</sup>If the scattering is not forward, the neutrinos are off the source-detector axis and not observed.

<sup>7</sup>Ordinary matter is composed of nucleons and electrons only, in contrast to matter with significant non-electron leptonic (muon, tau, neutrinos) or photon content. Furthermore it is electrically neutral, implying an equal number of protons and electrons.

The NC potential in the electrically neutral ordinary matter reduces to the potential induced by neutrons  $V_{\text{NC}}^n$ , since the potentials by protons  $V_{\text{NC}}^p$  and electrons  $V_{\text{NC}}^e$  cancel out. Notice that radiative corrections introduce charged lepton mass-dependent contributions to the matter potentials that resolve the degeneracy of the NC potentials, strongly complicating the formalism. The remaining potentials are given by

$$V_{\text{CC}}(r) = \pm \sqrt{2} G_F N_e(r) \quad \text{and} \quad V_{\text{NC}}^n(r) = \mp \frac{G_F}{\sqrt{2}} N_n(r), \quad (4.23)$$

where the upper sign refers to neutrinos and the lower sign to anti-neutrinos [74].  $G_F$  is the Fermi constant in units of eV cm<sup>3</sup> (see Tab. A.1) and  $N_e$  and  $N_n$  are the local electron and neutron number densities in (1/cm<sup>3</sup>). The radial position  $r$  assumes radial symmetry of the density profiles.  $N_e$  is related to the matter density  $\rho$  via the electron fraction  $Y_e$ , the number of electrons per baryon, as per

$$N_e(r) = \rho(r) \frac{Y_e(r)}{m_N}, \quad (4.24)$$

where  $m_N$  is the average nucleon mass in grams.

Similar to the situation in vacuum, the Schrödinger differential equation describes the time evolution of neutrinos. An initial neutrino flavor state  $|\nu_\alpha\rangle$  obeys the evolution equation

$$i \frac{\partial}{\partial t} |\nu_\alpha(t)\rangle = \mathcal{H} |\nu_\alpha(t)\rangle. \quad (4.25)$$

The time evolution of the amplitude of a transition  $|\nu_\alpha\rangle \rightarrow |\nu_\beta\rangle$  directly follows, using Eq. 4.3 and 4.21:

$$i \frac{\partial}{\partial t} \psi_{\alpha\beta}(t) = \sum_{\eta} \left( \sum_i U_{\beta i} E_i U_{\eta i}^* + \delta_{\beta\eta} V_{\beta} \right) \psi_{\alpha\eta}(t). \quad (4.26)$$

Taking again advantage of the relativistic approximations Eq. 4.10–4.11, the evolution equation in space becomes

$$\begin{aligned} i \frac{\partial}{\partial L} \psi_{\alpha\beta}(L) &= \left( p + \frac{m_1^2}{2E} + V_{\text{NC}}^n \right) \psi_{\alpha\beta}(L) \\ &+ \sum_{\eta} \left( \sum_i U_{\beta i} \frac{\Delta m_{i1}^2}{2E} U_{\eta i}^* + \delta_{\beta\eta} \delta_{\eta e} V_{\text{CC}} \right) \psi_{\alpha\eta}(L). \end{aligned} \quad (4.27)$$

The first term is separated out, since  $V_{\text{NC}}^n$  is the same for all neutrinos and only generates a phase, common to all flavors. This phase can be eliminated by a phase shift, which has no influence on the oscillation probability [74], leaving only the second term. The reduced equation in matrix form then reads

$$i \frac{\partial}{\partial L} \Psi_\alpha = \frac{1}{2E} \left( U \mathcal{M}^2 U^\dagger + \mathcal{A} \right) \Psi_\alpha \quad (4.28)$$

with

$$\Psi_\alpha = \begin{pmatrix} \psi_{\alpha e} \\ \psi_{\alpha \mu} \\ \psi_{\alpha \tau} \end{pmatrix}, \quad \mathcal{M}^2 = \begin{pmatrix} 0 & 0 & 0 \\ 0 & \Delta m_{21}^2 & 0 \\ 0 & 0 & \Delta m_{31}^2 \end{pmatrix}, \quad \mathcal{A} = \begin{pmatrix} A_{CC} & 0 & 0 \\ 0 & 0 & 0 \\ 0 & 0 & 0 \end{pmatrix} \quad (4.29)$$

and

$$A_{CC}(r) \equiv 2EV_{CC}(r) = \pm 2\sqrt{2}EG_F N_e(r). \quad (4.30)$$

The plus sign refers to  $\nu_e$  and the minus sign to  $\bar{\nu}_e$  (see also Eq. 4.23). The new effective Hamiltonian

$$\mathcal{H}_F = \frac{1}{2E} (U \mathcal{M}^2 U^\dagger + \mathcal{A}), \quad (4.31)$$

entering Eq. 4.28 in the flavor basis, can only be diagonalized in a new basis, the matter mass basis.

For the diagonalization of  $\mathcal{H}_F$  and the derivation of the oscillation probability in matter, two-neutrino mixing is considered with only  $\nu_e$ ,  $\nu_\mu$  and  $\nu_1$ ,  $\nu_2$  taking part and with  $\nu_e$  being the initial neutrino. The effect of matter on the probability is well-described in this scheme, which is much simpler than the three-neutrino case. In this scenario, which is discussed in detail in [74],  $U$  from Eq. 4.4 reduces to a two-dimensional rotational matrix

$$U = \begin{pmatrix} \cos \theta & \sin \theta \\ -\sin \theta & \cos \theta \end{pmatrix}, \quad (4.32)$$

where  $\theta_{12} \equiv \theta$ . With Eq. 4.36 and  $\Delta m^2 \equiv \Delta m_{21}^2$ , the effective Hamiltonian Eq. 4.31 becomes

$$\mathcal{H}_F = \frac{1}{4E} \begin{pmatrix} -\Delta m^2 \cos \theta + A_{CC} & \Delta m^2 \sin \theta \\ \Delta m^2 \sin \theta & \Delta m^2 \cos \theta - A_{CC} \end{pmatrix}, \quad (4.33)$$

having neglected a common phase

$$\exp \left[ -i \frac{\Delta m^2 L}{4E} - \frac{i}{2} \int_0^L V_{CC}(x) dx \right]. \quad (4.34)$$

The matrix Eq. 4.33 is diagonalized by the orthogonal transformation

$$U_M^T \mathcal{H}_F U_M = \mathcal{H}_M = \frac{1}{4E} \text{diag}(-\Delta m_M^2, \Delta m_M^2), \quad (4.35)$$

where  $\mathcal{H}_M$  is the effective Hamiltonian in the matter mass basis,  $U_M$  the effective unitary mixing matrix in matter

$$U_M = \begin{pmatrix} \cos \theta_M & \sin \theta_M \\ -\sin \theta_M & \cos \theta_M \end{pmatrix} \quad (4.36)$$

and  $\Delta m_M^2 \equiv m_{M2}^2 - m_{M1}^2$  the effective squared mass splitting, with

$$\Delta m_M^2 = \sqrt{(\Delta m^2 \cos 2\theta - A_{CC})^2 + (\Delta m^2 \sin 2\theta)^2}. \quad (4.37)$$

The effective mixing angle in matter  $\theta_M$  in Eq. 4.36 is given by

$$\tan 2\theta_M = \frac{\tan 2\theta}{1 - \frac{A_{CC}}{\Delta m^2 \cos 2\theta}}. \quad (4.38)$$

### The MSW effect

It follows from Eq. 4.38 that  $\tan 2\theta_M \rightarrow +\infty$ , and thus  $\theta_M \rightarrow \pi/4$ , if

$$A_{CC} = \Delta m^2 \cos 2\theta \equiv A_{CC}^R. \quad (4.39)$$

In other words, the mixing can become maximal, enabling total flavor transition, even if the mixing angle is small as will be demonstrated in this paragraph. This resonance effect is called matter effect, or also MSW effect in honor of Stanislav Mikheyev, Alexei Smirnov and Lincoln Wolfenstein and their pioneering work [129, 156, 157]. It follows from Eq. 4.30 that the resonance is reached at a resonance electron density

$$N_e^R = \frac{\Delta m^2 \cos 2\theta}{2E \sqrt{2} G_F}. \quad (4.40)$$

The squared matter mass splitting at  $A_{CC}^R$  becomes

$$\Delta m_M^2|_R = \Delta m^2 \sin 2\theta \quad (4.41)$$

and thus minimal. The behavior of  $\theta_M$  and  $\Delta m_M^2$  as they pass the resonance density is shown in Fig. 4.2. If at the given mixing parameters  $N_e \gg N_e^R$ , the effective mixing angle  $\theta_M$  is nearly  $90^\circ$ , as visible in Fig. 4.2a, and a  $\nu_e = \cos \theta_M \nu_1 + \sin \theta_M \nu_2$  is produced as quasi pure  $\nu_2$ . When the neutrino propagates towards lower densities, it crosses the resonance where the energy gap  $\Delta m_M^2$  is minimal (see Fig. 4.2b). If transitions between the states  $\nu_2$  and  $\nu_1$  are negligible, the evolution is said to be adiabatic and the neutrino remains in the  $\nu_2$  state on its way to decreasing densities. The necessary conditions for an adiabatic evolution are typically summarized in the so-called adiabaticity parameter  $\gamma$  [156, 74], which is defined at the resonance radius  $r^R$  as

$$\gamma|_R = \frac{\Delta m^2 \sin^2 2\theta}{2E \cos 2\theta} \left| \frac{1}{N_e(r)} \frac{dN_e(r)}{dr} \right|_{r=r^R}^{-1}. \quad (4.42)$$

If  $\gamma \gg 1$ , the resonance is crossed adiabatically, if  $\gamma \approx 1$  it is crossed nonadiabatically and maximum violation of adiabaticity is reached at the minimum value of  $\gamma$ . Adiabaticity thus depends on the oscillation parameters and the density profile and is generally fulfilled in stars as the Sun [74] or in temporary static SN environments [131], using the measured solar mixing parameters. In this case, the neutrino leaves the dense environment and enters vacuum as  $\nu_2 = \sin \theta \nu_e + \cos \theta \nu_\mu$ , which is in the case of a small mixing angle almost

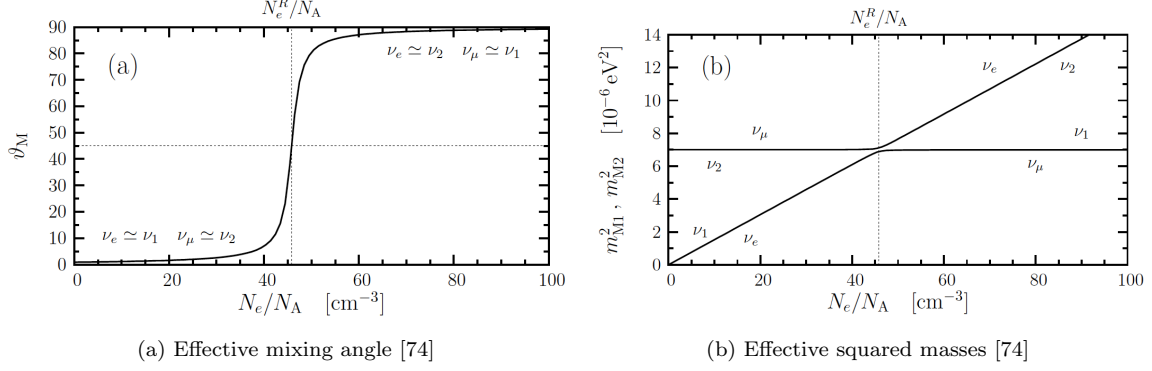


**Figure 4.2:** Evolution of the effective mixing angle  $\theta_M$  and squared masses  $m_{M2}^2$  and  $m_{M1}^2$  in matter as functions of the electron density  $N_e$  over Avogadro's constant  $N_A$ , for  $m_1 = 0$ ,  $\Delta m^2 = 7 \times 10^{-6} \text{ eV}^2$ ,  $\sin^2 2\theta = 10^{-3}$ ,  $E = 1 \text{ MeV}$  and the resonance electron density  $N_e^R$  from Eq. 4.40 [74]. Solid lines show the eigenvalues in the effective matter basis for two active neutrinos.

a pure  $\nu_\mu$  state. Thus nearly complete flavor conversion  $\nu_e \rightarrow \nu_\mu$  can occur in spite of a small mixing angle, the case when the MSW effect is most striking.

Sticking to the example of the electron survival probability, it reads in the case of adiabatic evolution through matter

$$\begin{aligned} P_{\nu_e \nu_e}^{\text{adiabatic}}(L) &= \frac{1}{2} + \frac{1}{2} \cos 2\theta_M^{\text{ini}} \cos 2\theta_M^{\text{fin}} \\ &\quad + \frac{1}{2} \sin 2\theta_M^{\text{ini}} \sin 2\theta_M^{\text{fin}} \cos \left( \int_0^L \frac{\Delta m_M^2(x)}{2E} dx \right), \end{aligned} \quad (4.43)$$

where  $\theta_M^{\text{ini}}$  and  $\theta_M^{\text{fin}}$  are the effective angles at the creation and detection point, respectively [74]. If  $L$  is very large, such that  $\int_0^L \frac{\Delta m_M^2(x)}{2E} dx \gg 1$ , as is the case for astrophysical neutrino sources, the second term averages to zero, equivalent to the situation in Eq. 4.17–4.19. Furthermore, if the neutrino does not travel a significant distance through the Earth before detection,  $\theta_M^{\text{fin}}$  coincides with the vacuum mixing angle  $\theta$ . The observed average survival probability then becomes

$$\langle P_{\nu_e \nu_e}^{\text{adiabatic}}(L) \rangle = \frac{1}{2} + \frac{1}{2} \cos 2\theta_M^{\text{ini}} \cos 2\theta. \quad (4.44)$$

Only the MSW effect is able to explain the otherwise too large  $\nu_e$  deficit of solar neutrinos observed on Earth [158]. Since a resonance in normal matter, where  $A_{\text{CC}} > 0$  for electron neutrinos (see Eq. 4.30), is only possible if  $\Delta m^2 \cos 2\theta > 0$  (see Eq. 4.39), the measurement of the solar mixing angle of  $\theta_{12} \approx 33.6^\circ$  (see Tab. 4.1) fixes the positive sign of  $\Delta m_{21}^2$ . In case of a negative sign, the resonance would instead occur in the anti-neutrino channel.

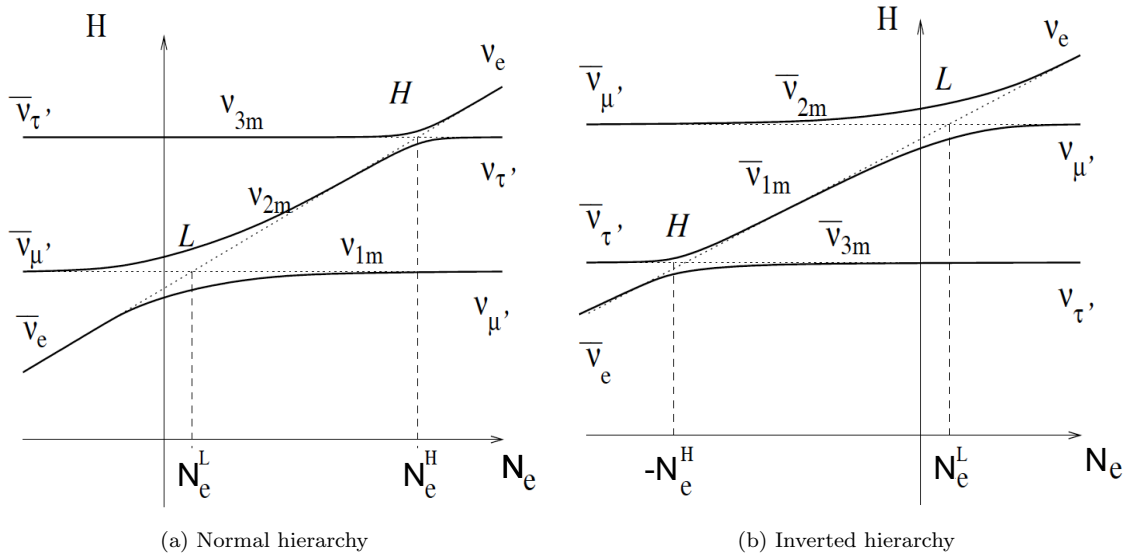


**Figure 4.3:** Level crossing schemes for the normal (a) and inverted (b) mass hierarchy and three active neutrinos. Solid lines show the eigenvalues in the effective matter basis as function of the electron number density  $N_e$ . Dashed lines correspond to energies of the flavor levels. The region with  $N_e > 0$  refers to neutrinos, the one with  $N_e < 0$  to anti-neutrinos (see Eq. 4.30). The two crossings are the low-resonance (L) and high-resonance (H), associated with the mixing parameters  $(\theta_{12}, \Delta m_{21}^2)$  and  $(\theta_{13}, \Delta m_{31}^2)$ , respectively [131, 159].

The matter densities reached in a SN exceed the maximum solar density of 162.2 g/cm<sup>3</sup> [160] by several orders of magnitude with an initial matter density profile [135] of typically

$$\rho_0(r) \approx 10^{14} \cdot \left( \frac{r}{1\text{km}} \right)^{-2.4} \frac{\text{g}}{\text{cm}^3}. \quad (4.45)$$

Such a profile provides a second density layer at which the MSW effect occurs, as illustrated in Fig. 4.3. The two resonances are referred to as low-resonance (L) and high-resonance (H), located at  $N_e^R(\theta_{12}, \Delta m_{21}^2)$  in the first and  $N_e^R(\theta_{13}, \Delta m_{31}^2)$  in the second case, following Eq. 4.40. The corresponding radial positions are given by Eq. 4.24, using Eq. 4.40, Eq. 4.45 and the relevant mixing parameters. Depending on the mass hierarchy, the H-resonance is crossed by neutrinos (Fig. 4.3a) or anti-neutrinos (Fig. 4.3b), while the L-resonance is in both cases crossed by neutrinos. The neutrino passages through the L- and H-resonance regions are adiabatic during the first second of the burst, before shock wave effects occur [135] and given the measured oscillation parameters [131] listed in Tab. 4.1.

In the early SN phases considered in Sec. 7, phase effects on the survival probability are negligible<sup>8</sup> and it is thus sufficient to propagate the probabilities from the neutrinospheres to the Earth instead of the probability amplitudes. For this intend it is convenient to make

<sup>8</sup>Besides the shock wave, the CP-violating Dirac phase can introduce phase effects. However, they are negligible at tree level and as long as the  $\bar{\nu}_\mu$  and  $\bar{\nu}_\tau$  fluxes are identical at their emission from the neutrinosphere [161]. The assumed equality is justified in Sec. 3 and becomes only invalid when the flavor of the neutrinos are changed already before they decouple from matter.

use of the equality of the  $\nu_\mu$  and  $\nu_\tau$  fluxes and perform a rotation of the neutrino states ( $|\nu_e\rangle, |\nu_\mu\rangle, |\nu_\tau\rangle$ )  $\rightarrow$  ( $|\nu_e\rangle, |\nu_x\rangle, |\nu_y\rangle$ ):

$$\begin{aligned} |\nu_x\rangle &= \cos\theta_{23}|\nu_\mu\rangle - \sin\theta_{23}|\nu_\tau\rangle, \\ |\nu_y\rangle &= \sin\theta_{23}|\nu_\mu\rangle + \cos\theta_{23}|\nu_\tau\rangle. \end{aligned} \quad (4.46)$$

This rotation diagonalizes the  $(\nu_\mu, \nu_\tau)$  submatrix of  $\mathcal{H}_F$  Eq. 4.31, comprising the elements  $H_{F,ij}$  with  $i, j = 2, 3$ . The other off-diagonal elements of the effective Hamiltonian are approximately zero at high matter densities [131, 94] and the Hamiltonian becomes diagonal. This means the flavor eigenstates ( $|\nu_e\rangle, |\nu_x\rangle, |\nu_y\rangle$ ) at production coincide with the matter eigenstates ( $|\nu_{M1}\rangle, |\nu_{M2}\rangle, |\nu_{M3}\rangle$ ) in the dense environment of neutrino creation during a CCSN. The same considerations are valid for anti-neutrinos. Under these assumptions, the neutrino fluxes  $F = (F_e, F_\mu, F_\tau)^T$  observable on Earth are calculated from the initial neutrino fluxes  $F^0 = (F_e^0, F_x^0, F_y^0)^T$  at the neutrinospheres via

$$F = \frac{1}{4\pi d^2} \mathcal{D} \mathcal{P}_f F^0, \quad (4.47)$$

where only flavor changes due to the MSW effect are taken into consideration [94, 131]. As usual in this work,  $d$  is the distance of the SN from Earth. The matrix  $\mathcal{P}_f$  is the MSW flip probability matrix

$$\begin{aligned} \mathcal{P}_f &\equiv \begin{pmatrix} P_{e1} & P_{x1} & P_{y1} \\ P_{e2} & P_{x2} & P_{y2} \\ P_{e3} & P_{x3} & P_{y3} \end{pmatrix} \\ &= \begin{pmatrix} P_H P_L & 1 - P_L & (1 - P_H) P_L \\ P_H (1 - P_L) & P_L & (1 - P_H) (1 - P_L) \\ 1 - P_H & 0 & P_H \end{pmatrix} \end{aligned} \quad (4.48)$$

with  $P_H$  and  $P_L$  being the matter state flip probabilities at the H-resonance and L-resonance. The second equality holds for neutrinos and NH. The derivation of the matrix elements is found in [131]. Setting  $P_H = 1$  yields the respective matrix for neutrinos in IH, where no H-resonance layer exists for neutrinos (see Fig. 4.3). Since for anti-neutrinos and NH no resonance is encountered at all, the anti-neutrino matrix is consistent with the identity matrix  $\bar{\mathcal{P}}_f^{\text{NH}} = \mathbf{1}$ . If the masses are in IH,  $\bar{\mathcal{P}}_f$  follows from Eq. 4.48 by replacing  $P_L$  with  $1 - \bar{P}_L$  and  $P_H$  by  $\bar{P}_H$ . As discussed above, both resonances are crossed adiabatically in typical SN density profiles at  $t \lesssim 1$  s. The flip probabilities are thus approximately zero

and the three affected matrices reduce to

$$\mathcal{P}_f^{\text{NH}} \approx \begin{pmatrix} 0 & 1 & 0 \\ 0 & 0 & 1 \\ 1 & 0 & 0 \end{pmatrix}, \quad \mathcal{P}_f^{\text{IH}} \approx \begin{pmatrix} 0 & 1 & 0 \\ 1 & 0 & 0 \\ 0 & 0 & 1 \end{pmatrix}, \quad \bar{\mathcal{P}}_f^{\text{IH}} \approx \begin{pmatrix} 0 & 0 & 1 \\ 0 & 1 & 0 \\ 1 & 0 & 0 \end{pmatrix}. \quad (4.49)$$

The (anti-)neutrinos leave the star's surface as mass eigenstates and the corresponding wave packets diverge over the typical distances from a SN to Earth [131]. The coherence between the mass eigenstates is lost, no further oscillation effects occur and the fluxes arriving at the Earth are identical with the fluxes at the surface of the star up to a geometrical factor included in Eq. 4.47. The neutrinos are observed as flavor eigenstates. This is taken into account in Eq. 4.47 by the matrix

$$\mathcal{D} = \begin{pmatrix} |U_{e1}|^2 & |U_{e2}|^2 & |U_{e3}|^2 \\ |U_{\mu 1}|^2 & |U_{\mu 2}|^2 & |U_{\mu 3}|^2 \\ |U_{\tau 1}|^2 & |U_{\tau 2}|^2 & |U_{\tau 3}|^2 \end{pmatrix}, \quad (4.50)$$

which contains the probabilities of a flavor eigenstate  $|\nu_\alpha\rangle$  to be in the mass eigenstate  $|\nu_i\rangle$  with  $|\langle\nu_\alpha|\nu_i\rangle|^2 = |U_{\alpha i}|^2$  and  $\sum_i |U_{\alpha i}|^2 = 1$ . The matrix product  $\mathcal{D}\mathcal{P}_f$  in Eq. 4.47 yields the matrix of the final survival probabilities used in Sec. 7.

### 4.3 Neutrinoless Double Beta Decay

The neutrinoless double beta decay is the main physics topic of SNO+. However, it is not directly subject to this thesis. For this reason, only the very basics of the physics behind this process are given here to complete the presentation of SNO+ in Sec. 5 and to motivate the quenching measurements presented in Sec. 6. For a deeper understanding the reader is referred to [162, 163].

Double beta decay, the coincident occurrence of two  $\beta^-$  decays in one nucleus, was first proposed by Maria Goeppert–Mayer in 1935 [164]. Two years later, Ettore Majorana demonstrated that the theoretical results remain unchanged if the neutrino is its own anti-particle [165], i.e. a Majorana particle, which lead to the proposal by Wendell H. Furry in 1939 that in this case the reaction can proceed without the emission of any neutrino [166]. In this instance, however, the total lepton number is violated and an observation of the process a prove of physics beyond the SM. Double beta decay in general is a second-order process and hence its half life is much longer than that of typical single beta decays. It is only experimentally observable, if the single beta decay is energetically forbidden while double beta decay is allowed. This is the case for even–proton even–neutron number nuclei that have a higher binding energy than their odd–odd neighbors due to proton–pair and

neutron–pair spin–couplings. Only the nucleus two proton numbers higher has a larger binding energy than the mother isotope, enabling double beta decay. In total, 35 naturally occurring double beta decay isotopes, with forbidden or suppressed  $\beta$  decay, exist [74].

The search for the  $0\nu\beta\beta$  addresses especially two long long-standing open questions in particle physics: the Dirac or Majorana nature of the neutrinos and the magnitude of their masses. As depicted in the above section, the squared mass differences  $\Delta m_{ij}^2$  are known with increasing precision from neutrino oscillation experiments, demanding non-zero neutrino masses. However, the absolute values of the mass basis eigenvalues in Eq. 4.2 are not resolvable in these experiments and thus neither the average neutrino masses

$$m_\alpha = \sqrt{\sum_i m_i^2 |U_{\alpha i}|^2}. \quad (4.51)$$

As of now, only upper limits of these masses are accessible from cosmology, tritium decay,  $\tau$  decay and pion decay measurements [152], which are at best of  $\mathcal{O}(\text{eV})$ , as mentioned at the beginning of this chapter. It is furthermore mentioned in the previous section, that non-zero neutrino masses are not foreseen in the SM. Finite neutrino masses are not, or at least not only, of SM Higgs origin. Amongst the proposed neutrino mass generation mechanisms, the seesaw mechanism is most favored [167, 168], in which small neutrino masses are created by physics beyond the SM in which the total lepton number conservation is violated at a scale that is much larger than the electroweak scale. In this scenario, the neutrinos with definite masses are of Majorana type, allowing the lepton number violating  $0\nu\beta\beta$  decay of even–even nuclei

$$N(A, Z) \rightarrow N(A, Z + 2) + e^- + e^-, \quad (4.52)$$

shown in form of a Feynman diagram in Fig. 4.4. The knowledge of the nature of neutrinos, Majorana or Dirac, is crucial for the understanding of the origin of neutrino masses at the eV-scale, which is several orders of magnitude below the quark and charged lepton mass scales. Thus large, ultra–low background experiments, like SNO+, set themselves to search for this process.

The general expression of the observable total decay width is

$$\Gamma^{0\nu} = \frac{1}{T_{1/2}^{0\nu}} = G^{0\nu}(Q, Z) |M^{0\nu}|^2 \frac{|m_{\beta\beta}|^2}{m_e^2}, \quad (4.53)$$

where  $G^{0\nu}$  is a known phase space integral with  $Q$  being the  $Q$ –value, both being listed for several candidate  $0\nu\beta\beta$  isotopes in Tab. 4.2.  $m_e$  is the electron mass and  $M^{0\nu}$  the nuclear matrix element (NME) corresponding to the diagram in Fig. 4.4. The neutrino masses and mixing in the standard parameterization Eq. 4.4 enter the matrix element in the form of the effective Majorana mass

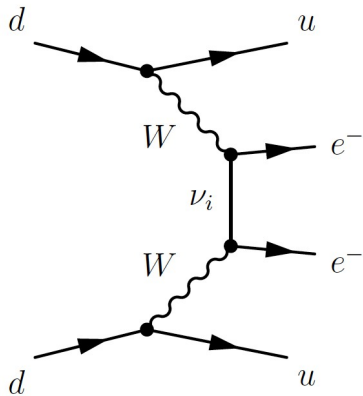


**Figure 4.4:** Feynman diagram of the particle transition inducing  $0\nu\beta\beta$  decay.

$$\begin{aligned} |m_{\beta\beta}| &= \left| \sum_i m_i U_{ei}^2 \right| \\ &= \left| m_1 \cos^2 \theta_{12} \cos^2 \theta_{13} + m_2 \sin^2 \theta_{12} \cos^2 \theta_{13} e^{i\epsilon_1} + m_3 \sin^2 \theta_{13} e^{i(\epsilon_2 - 2\delta)} \right|, \end{aligned} \quad (4.54)$$

which is bracketed out from  $M^{0\nu}$  [162]. In contrast to neutrino oscillations,  $0\nu\beta\beta$  decays also depend on the CP-violating Majorana phases in agreement with the lepton number violating nature of this process. The three neutrino masses  $m_{1,2,3}$  in Eq. 4.54 can be expressed in terms of the lightest neutrino mass  $m_{\text{lightest}}$  and the two measured squared mass splittings  $\Delta m_{\text{sol}}^2$  and  $\Delta m_{\text{atm}}^2$ , considering the three mass scale schemes in Eq. 4.14–4.16. The respective allowed regions of the effective Majorana mass as function of the lightest neutrino mass are shown in Fig. 4.5. Note that the underlying oscillation parameters and uncertainties used in [162] marginally differ from those listed in Tab. 4.1. The oscillation parameter uncertainties, leading together with the unknown CP-violating phases to the  $1\sigma$ ,  $2\sigma$  and  $3\sigma$  contours in Fig. 4.5, are propagated as uncorrelated in [162], but taking into account the asymmetry of uncertainties. In case of IH,  $|m_{\beta\beta}|$  is basically independent of  $m_{\text{lightest}}$  until the lightest neutrino mass nears the region of QD mass ordering, where  $|m_{\beta\beta}|$  rises linearly with  $m_{\text{lightest}}$ . The allowed  $|m_{\beta\beta}|$  range in case of NH is at least one order of magnitude below the allowed region in case of IH. The difference in the ranges for normal, inverted and quasi degenerate neutrino mass ordering opens up the possibility to gain information about the ordering scheme from a measurement of the effective Majorana mass.

The Majorana mass, however, is not directly measurable, but is deduced from a measurement of the  $0\nu\beta\beta$  half life  $T_{1/2}^{0\nu}$ , following Eq. 4.53. Since also the NME enters this equation, it has to be calculated, which is a non-trivial many-body problem. Currently, the main methods used for the calculation are the Quasi-particle Random Phase Approximation (QRPA) [170, 171], the Energy Density Functional method (EDF) [172, 173], the Projected Hartree-Fock-Bogoliubov approach (PHFB) [174], the Interacting Boson Model-2 (IBM-2) [175] and the Large-Scale Shell Model (LSSM) [176, 177]. Current results from the named approaches are summarized in Fig. 4.6 for different double beta

**Table 4.2:** Phase space factor  $G^{0\nu}$ , ground state to ground state transition  $Q$ -value, natural abundance and experimentally determined half lives of the ordinary double beta decay  $T_{1/2}^{2\nu}$  of candidate  $0\nu\beta\beta$  isotopes. The half lives are the latest compilation of results as of December 2014, taken from [118]. The first uncertainties are statistical, the second systematic, if two uncertainties are given. The rest of the table is adapted from [162, 163, 169].

$\beta\beta$ decay	$G^{0\nu}$	$Q$	nat. abund.	$T_{1/2}^{2\nu}$
	[ $10^{-14} \text{ y}^{-1}$ ]	[MeV]	[%]	[ $10^{21} \text{ y}$ ]
$^{48}\text{Ca} \rightarrow ^{48}\text{Ti}$	6.4	4.27226(404)	0.187	$0.044_{-0.004}^{+0.005} \pm 0.004$
$^{76}\text{Ge} \rightarrow ^{76}\text{Se}$	0.6	2.039061(7)	7.8	$1.84_{-0.08}^{+0.09} {}^{+0.11}_{-0.06}$
$^{82}\text{Se} \rightarrow ^{82}\text{Kr}$	2.7	2.99512(201)	9.2	$0.096 \pm 0.003 \pm 0.010$
$^{96}\text{Zr} \rightarrow ^{96}\text{Mo}$	5.6	3.35037(289)	2.8	$0.0235 \pm 0.0014 \pm 0.0016$
$^{100}\text{Mo} \rightarrow ^{100}\text{Ru}$	4.4	3.03440(17)	9.6	$0.00711 \pm 0.00002 \pm 0.00054$
$^{116}\text{Cd} \rightarrow ^{116}\text{Sn}$	4.6	2.81350(13)	7.6	$0.029_{-0.003}^{+0.004}$
$^{128}\text{Te} \rightarrow ^{128}\text{Xe}$	0.1	0.86587(131)	31.7	$7200 \pm 400$
$^{130}\text{Te} \rightarrow ^{130}\text{Xe}$	4.1	2.52697(23)	34.5	$0.7 \pm 0.09 \pm 0.11$
$^{136}\text{Xe} \rightarrow ^{136}\text{Ba}$	4.3	2.45783(37)	8.9	$2.165 \pm 0.016 \pm 0.059$
$^{150}\text{Nd} \rightarrow ^{150}\text{Sm}$	19.2	3.37138(20)	5.6	$0.00911_{-0.00022}^{+0.00025} \pm 0.00063$
$^{238}\text{U} \rightarrow ^{238}\text{Pu}$	3.4	1.14498(125)	99.3	$2.0 \pm 0.6$

isotopes. As obvious from this figure, a large discrepancy exists between the NME values calculated with different methods, entering the determination of  $|m_{\beta\beta}|$ .

Of the 35 double beta decaying isotopes, eleven have been experimentally observed undergoing the ordinary two-neutrino double beta ( $2\nu\beta\beta$ ) decay [152] (see Tab. 4.2). For the  $0\nu\beta\beta$ , only upper limits currently exist. The GERDA<sup>9</sup> experiment, using  $^{76}\text{Ge}$ , reached in 2013 a half life limit of  $2.1 \times 10^{25} \text{ y}$  at 90% confidence level after  $21.6 \text{ kg}\cdot\text{y}$  exposure [178]. This is currently the most stringent  $^{76}\text{Ge}$  half life limit, strongly disfavoring the controversial claim of the  $0\nu\beta\beta$  decay observation by a subgroup of the HDM<sup>10</sup> collaboration [179]. A combined analysis of the Ge results in [178], including the HDM and IGEX<sup>11</sup> results, yields a lower limit of  $3.0 \times 10^{25} \text{ y}$ . This result refers to a range for the upper limit on the Majorana mass of  $|m_{\beta\beta}| < (200 - 400) \text{ meV}$  [178], considering various NME calculations. Additionally, limits at 90% confidence level on  $T_{1/2}^{0\nu}$  of  $^{136}\text{Xe}$

<sup>9</sup>GERmanium Detector Array.

<sup>10</sup>Heidelberg–Moscow.

<sup>11</sup>International GERmanium eXperiment.

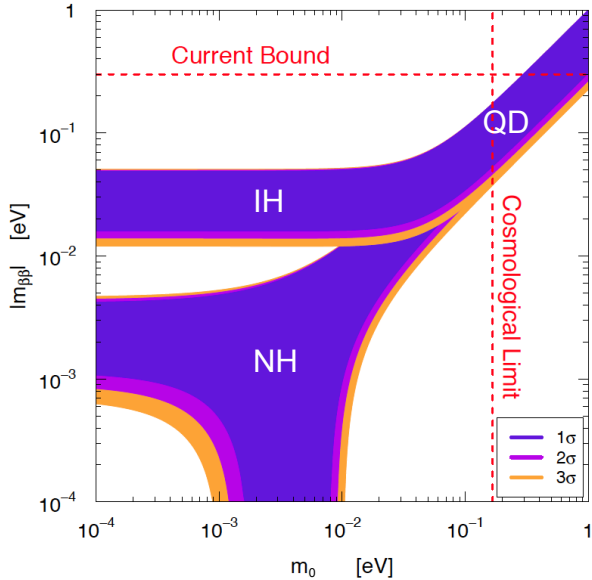


**Figure 4.5:** Effective Majorana mass  $|m_{\beta\beta}|$  as function of the lightest neutrino mass  $m_{\text{lightest}}$  in the normal (NH) and inverted (IH) hierarchy as well as in the quasi degenerate (QD) ordering (see Eq. 4.14–4.16). The value of  $\theta_{13}$  measured by the Daya Bay collaboration [17] is considered. The explicit underlying oscillation parameters and uncertainties are found in [162], from where the original figure is taken. They are the same within the uncertainties as in Tab. 4.1.

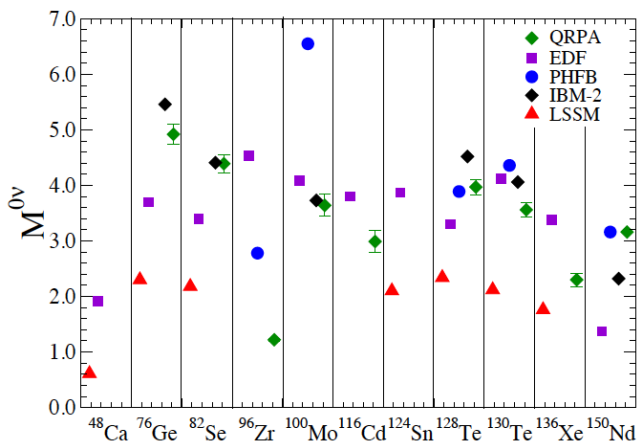


**Figure 4.6:** Values of  $0\nu\beta\beta$  decay matrix elements  $M^{0\nu}$ , calculated with different methods, named in the text. The figure is taken from [162].

are reported by the KamLAND<sup>12</sup>–Zen<sup>13</sup> and EXO–200<sup>14</sup> collaborations of  $1.9 \times 10^{25}$  y [180] and  $1.1 \times 10^{25}$  y [181], respectively. The upper limit on the Majorana neutrino mass, reported by EXO–200 [181], ranges from (190 – 450) meV.

Since the  $0\nu\beta\beta$  is an extremely rare process, detectors must not only have a large isotopic mass, but also a minimal background level and a very-well understood background model around the region of interest (ROI). Typically the majority of backgrounds stems from detector intrinsic radioactivity, including  $\alpha$  decays, as will be outlined in the context of SNO+ in Sec. 5. Also proton recoils add up to the SNO+  $0\nu\beta\beta$  decay backgrounds, though to a smaller extend. To determine the background model for SNO+, the responses

<sup>12</sup>Kamioka Liquid scintillator AntiNeutrino Detector.

<sup>13</sup>KamLAND Zero-neutrino double-beta decay.

<sup>14</sup>Enriched Xenon Observatory.

of the scintillator to the individual charged particles have to be measured, since they differ depending on the particle's ionization strength, as explained in Sec. 2. The response to protons and  $\alpha$  particles relative to  $\beta$  particles has been measured within this work, as described in detail in Sec. 6.

## Chapter 5

# The SNO+ experiment

SNO<sup>1</sup> was the deepest multi-tonne underground detector of its time [182], located in the Canadian SNOLAB. With the ability to not only detect electron neutrinos but also muon and tau neutrinos, SNO solved the long-standing solar neutrino problem of a strongly reduced electron neutrino flux from the Sun compared to theoretical expectations [183]. SNO+ is the follow up experiment of SNO, replacing the 1kt heavy–water target with  $\sim$ 0.78 kt of liquid scintillator and taking advantage of the already existing SNO infrastructure. However, due to the conversion from a Cherenkov detector into a scintillator detector, several upgrades and developments are needed to be able to handle the scintillator and to achieve the physics goals of the experiment. Currently, SNO+ is in the final phase of construction and has accomplished first test runs of data taking. A first commissioning phase with the detector being filled with light–water is scheduled for the beginning of the year 2015 before the water target is replaced by pure LS. The start of the  $0\nu\beta\beta$  phase with loaded LS is expected in 2016.

The target replacement, elaborate scintillator purification techniques and the use of ultra–clean materials shift the former SNO detector threshold to lower energies and provide ultra low backgrounds. For this reason, SNO+ is amongst others capable of observing low energy solar neutrinos, geo neutrinos, reactor neutrinos and possibly neutrinos from a SN. After a data taking phase with pure scintillator, a further phase is scheduled in which the scintillator is loaded with  $^{nat}Te$ . In this phase, SNO+ will search for the  $0\nu\beta\beta$  decay of  $^{130}Te$ , the main physics goal of the experiment. Originally the isotope of interest was  $^{150}Nd$ . However, after a novel loading technique was developed at the Brookhaven National Laboratory (BNL) [184, 185], enabling also the loading of LS with Te, and after thorough, collaboration–wide investigations on both elements, the collaboration decided in 2013 to change to  $^{130}Te$ . The main motivation for the change in isotopes is the higher expected half–life sensitivity of SNO+ using  $^{130}Te$  instead of  $^{150}Nd$ .

The underground laboratory is introduced in Sec. 5.1 and the detector in Sec. 5.2.

---

<sup>1</sup>Sudbury Neutrino Observatory.

The liquid scintillators used in SNO+ are described in detail in Sec. 5.3. Te-loading and Nd-loading are outlined, since scintillator with both loadings was used for the quenching measurements presented in Sec. 6. The purification of the LS is described in Sec. 5.4. Concluding, the  $0\nu\beta\beta$  search and observation of SN neutrinos in SNO+ are sketched in Sec. 5.5. Only these physics goals are described here, since they are the goals the thesis at hand is mostly related to.

## 5.1 The SNOLAB underground laboratory

The SNOLAB facility is an underground laboratory situated 2 km deep in the Vale Creighton Mine near Sudbury, Ontario, Canada. It is currently the second deepest operating physics laboratory world-wide [186]. In the past ten years, the original SNO detector site [182] was enlarged to a 5 000 m<sup>2</sup> facility forming today's SNOLAB, supported by a surface main building with preparatory laboratories, a workshop, a warehouse and offices. The entire underground facility is a large single cleanroom of class 2000<sup>2</sup>, enabling together with the 6080 m.w.e. of rock shielding the observation of low energy neutrinos and the searches for  $0\nu\beta\beta$  decays and dark matter. At present several experiments following, or planning to follow, these goals are housed by SNOLAB.

## 5.2 The SNO+ detector

The SNO+ detector, illustrated in Fig. 5.1, is installed in a barrel-shaped 34 m deep and  $\leq 22$  m wide cavity, which is sealed against the ingress of radon with an Urylon radon liner. The center of the detector is formed by a 12 m diameter acrylic vessel (AV) of 5 cm thickness which will contain about 0.78 kt of liquid scintillator. The AV is connected to the deck area via a cylindrical neck and supported by a hanging rope system. It is surrounded by a photomultiplier tube support structure (PSUP), a 17.8 m diameter geodesic stainless steel frame holding more than 9000 8“-photomultiplier tubes (PMTs). Each PMT is equipped with a reflective collar [182]. This configuration yields a solid angle coverage of about 54%. The entire volume outside the AV is filled with  $\sim 7$  kt of ultra-pure water, of which about 1.7 kt are between AV and PSUP and 5.3 kt are outside the PSUP, together shielding against radioactivity from mainly the PMTs, the ropes and the rock. The outer water volume is monitored by approximately 100 outward looking PMTs on the PSUP.

Changing the active medium within the AV from heavy-water to liquid scintillator raised new demands to the detector. In contrast to heavy-water, the LS has a lower density than the surrounding light-water shielding and will be subjected to buoyancy. An additional rope-net system anchoring the vessel to the cavity floor is necessary (see Fig. 5.1). The installation has been successfully completed at the beginning of the

---

<sup>2</sup>Cleanroom class 2000 means that  $\leq 2000$  particles with a diameter of  $\geq 0.5 \mu\text{m}$  are found per ft<sup>3</sup> of air, where 1 ft = 30.48 cm.

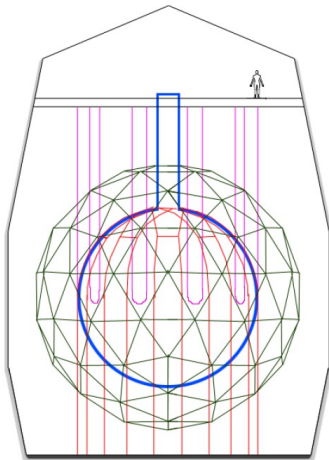


**Figure 5.1:** Schematic view of the SNO+ detector [187]. The acrylic vessel and neck are shown in blue. The PMT support structure is shown in green, with the PMTs omitted for visibility. The hold-down and hanging ropes are shown in red and pink respectively. The grey horizontal lines with the person on top mark the deck. The enclosing black contour below the deck sketches the cavity. The drawing is roughly to scale.

year 2012, using 40 mm diameter ropes made from high purity Tensylon. To match the background target levels of SNO+, the ropes of the former hanging system were replaced by Tensylon ropes as well, which have a diameter of 20 mm. Also the AV has to be as free from radioactivity as possible. To remove dust contamination that deposited after the heavy-water drain, the inner and outer surface has been thoroughly washed. To avoid new infiltration of mine air, which is laden with radon, a cover gas system has been installed sealing the neck. Electronics and data acquisition are upgraded including a re-designed trigger system and an increased data rate capacity to meet the one to two orders of magnitude higher light yield compared to heavy-water as well as the higher event rate. Some boards and several dead PMTs have been repaired or replaced and dead electronic channels have been re-mapped.

The solvent chosen for the liquid scintillator is LAB, as it satisfies the different requirements of the experiment. This solvent is chemically compatible with acrylic, low in toxicity and environmentally safe. It has a comparatively high flash point of 130° C and a high purity is achievable. Furthermore, LAB is readily available as it is a standard component in the production of detergents. SNO+ LAB will be delivered from the Petresa plant in Bécancour [188], Quebec, since Petresa performs purification steps that other producers skip and provides in this way the purest and most transparent LAB of all tested by SNO+. As primary solute PPO will be used in a concentration of 2 g/l. This value was experimentally determined and found to be the optimal compromise between light yield and self-absorption (see Sec. 2.5.1). The total light yield of this solution reaches  $\sim 10\,000$  photons/MeV [189]. As secondary solute bis-MSB and perylene are being investigated and the concentration is likely to be around 15 mg/l.

### 5.3 The liquid scintillator of SNO+

The liquid scintillator in SNO+ will be a solution based on LAB. In the original scheme, assuming  $^{150}\text{Nd}$  as the isotope for the double beta decay phase, LAB was supposed to

be the solvent and 2 g/l of the solute PPO were to be added. No secondary solute was planned, since Nd partly absorbs light of wavelengths typical for the emission spectrum of secondary wavelength shifters. The planned concentration of  $^{nat}\text{Nd}$  was 0.1% in the first data taking phase, intended to be increased to 0.3% in a later phase. Aiming now for the observation of the  $0\nu\beta\beta$  decay of  $^{130}\text{Te}$  instead, the solution had to be modified. While LAB can be loaded with Nd via organo–metallic loading [190], which leaves only LAB plus Nd before mixing it with any solute, a new technique [184, 185] had to be developed to load liquid scintillator with Te. The state-of-the-art compound for SNO+ is LAB scintillator with telluric acid, water and an amine-based surfactant binding the water with the LAB molecules. At the starting concentration of 0.3%  $^{nat}\text{Te}$ , the solution contains about (1.5–1.7)% H<sub>2</sub>O and  $\sim 5\%$  PRS. Preliminary studies have shown that loadings up to a few percent are possible, maintaining decent optical properties. The primary solute is also in Te-loaded LS 2 g/l PPO. Since Te has no absorption lines in the relevant wavelength region, a secondary solute will be added in order to shift the emission spectrum to higher wavelengths, which match the PMT sensitivity better. The candidate solutes are bis–MSB and perylene with a concentration around 15 mg/l. In this work, the ionization quenching in normal LAB with and without Nd as well as in water–surfactant–LAB (wsLAB) with and without Te were measured and hence all solutions and components described in this section. All components are listed in Tab. 5.1 together with properties, relevant for this work.

**Table 5.1:** Overview over the components present in loaded and unloaded SNO+ scintillators. All densities assume 19°C. At the given accuracy, the density of LAB is valid over a range of  $\gtrsim 10^\circ\text{C}$  [191].

Compound	Description	Molecular weight [g/mol]	Molecular formula	Density [g/cm <sup>3</sup> ]
LAB	solvent	235	C <sub>17.1</sub> H <sub>28.3</sub>	0.86
PPO	1 <sup>st</sup> solute	221.25	C <sub>15</sub> H <sub>11</sub> NO	1.06
Bis–MSB	2 <sup>nd</sup> solute	310.44	C <sub>24</sub> H <sub>22</sub>	1.10
Perylene	2 <sup>nd</sup> solute	252.31	C <sub>20</sub> H <sub>12</sub>	1.30
PRS	surfactant	375.767	C <sub>20.3</sub> H <sub>37.6</sub> NO <sub>3</sub> S	1.05
Water		18	H <sub>2</sub> O	1.00
Nd	specimen	144.24	Nd	7.01
Te acid	specimen	229.64	H <sub>6</sub> O <sub>6</sub> Te	3.07

### 5.3.1 LAB with PPO

Linear alkylbenzene is a family of organic compounds. During the production of LAB, the purified linear mono–olefines<sup>3</sup>  $C_nH_{2n}$ , gained from paraffin, react with benzene in the presence of a catalyst forming the LAB molecules. One benzene molecule,  $C_6H_6$ , consists of six carbon atoms joined in a ring and 6 hydrogen atoms attached to each carbon atom. The final molecular formula of LAB then reads  $(C_6H_5)C_nH_{2n+1}$ . This formula varies due to a varying number  $n$  of C atoms, with typically  $n = 10 – 16$ . The composition of LAB [188, 192], produced by Petresa Canada Inc. and used for SNO+, is given in Tab. 5.2 in first order accuracy and with  $n = 10 – 13$ . This results in an average molecular formula  $(C_6H_5)C_{11.1}H_{23.3}$ , or identically  $C_{17.1}H_{28.3}$ . The real composition may always differ slightly due to catalyst aging.

**Table 5.2:** Approximate mass fraction of different LAB molecules in the SNO+ LAB solvent [28].

Molecular formula	Mass fraction [%]
$C_{16}H_{26}$	20.4
$C_{17}H_{28}$	43.2
$C_{18}H_{30}$	33.4
$C_{19}H_{32}$	1.8
$C_{15}H_{24}$	1.2

2,5-diphenyloxazole (PPO) is an oxazole<sup>4</sup> derivative that forms well-crystallizing salts. Stirring it in LS, PPO dissolves. The chemical formula of this fluor is  $C_{15}H_{11}NO$ . Commercially available PPO generally has a high potassium contamination [193], but is provided in different grades of radiopurity. A special high purity PPO is produced for low background experiments.

Considering the natural isotopic abundances of H, C, N and O, the densities of the main isotopes in the LS are calculated and listed in Tab. 5.3. Also given are the resulting number fractions of the individual isotopes. The addition of 15 mg/l bis-MSB does not change the results at the given accuracy.

<sup>3</sup>Olefines, also known as alkenes, are unsaturated chemical compounds that contain at least one carbon–carbon double bond.

<sup>4</sup>Oxazole is a five-membered heterocyclic compound, a ring structure with five atoms of at least two different elements. In this case the heteroatoms are N and O.

**Table 5.3:** Isotope density and number fraction in LAB + 2 g/l PPO, considering an average composition of H<sub>28.360</sub>C<sub>17.195</sub>N<sub>0.002</sub>O<sub>0.002</sub> and an average LS density of 0.863 g/cm<sup>3</sup> at 15 °C [188, 192]. Only isotopes with densities  $\geq 1 \times 10^{18}$  /cm<sup>3</sup> are used. The number fractions are relative to the sum of the listed isotopes.

Isotope	Density	Number fraction
	[ $\times 10^{22}$ /cm <sup>3</sup> ]	[%]
<sup>1</sup> H	6.2751	62.241
<sup>2</sup> H	0.0007	0.007
<sup>12</sup> C	3.7633	37.327
<sup>13</sup> C	0.0419	0.415
<sup>14</sup> N	0.0005	0.005
<sup>16</sup> O	0.0005	0.005

### 5.3.2 Neodymium–loaded LAB

For the synthesis of Nd–LAB, a single–stage solvent–solvent extraction<sup>5</sup> procedure was developed at BNL to form a stable compound of the inorganic Nd and the organic liquid. In this procedure, the metal reactant neodymium chloride hexahydrate (NdCl<sub>3</sub>·6H<sub>2</sub>O) and the carboxylic acid reactant TMHA, 3,5,5–trimethyl–hexanoic acid (C<sub>9</sub>H<sub>18</sub>O<sub>2</sub>), are separately dissolved in water having their pH–values controlled by HCl and NH<sub>4</sub>OH, respectively. The two reactants are added together, forming an organo–Nd complex in aqueous medium, which is extracted into the organic LAB. The resulting Nd–LAB was found to be stable over several years at a Nd concentration of 1%. However, since Nd reduces the transparency of the scintillator, an initial loading of 0.1% was planned for SNO+ and respective samples have been investigated in the course of this work. Using elaborate purification techniques, the metal–loaded scintillators are available at high radiopurity levels [190, 194].

### 5.3.3 Tellurium–loaded water–surfactant–LAB

In order to stably load LAB with Te, a different technique is needed with respect to the organo–metallic loading technique used for Nd. Tellurium is hydrophilic and has to be used in a water solution. Since LAB on the other hand is hydrophobic, a surfactant is needed forming the link between the organic solvent and the water. As a result, the final compound does not only contain the solvent and the metal, but also a non–negligible fraction of water and surfactant, where the fractions grow with the Te concentration [195]. For SNO+, the scintillator will be initially loaded with 0.3% <sup>nat</sup>Te, requiring about (1.5–1.7)% H<sub>2</sub>O and  $\sim$  5% surfactant. Water–surfactant–LAB can be produced with and

---

<sup>5</sup>Solvent–solvent extraction is a technique in which an aqueous solution is brought into contact with an immiscible organic solvent, in order to transfer one or more solutes from the aqueous phase into the organic phase or vice versa.

without Te, enabling amongst others the determination of the influence of the metal on LS properties.

Tellurium is added in form of telluric acid,  $\text{Te}(\text{OH})_6$ . To obtain 0.3% Te in the scintillator, about 0.54% of the telluric acid are needed. The alkyl chain of the aromatic photoreactive surfactant (PRS) used is composed of benzene-1,3-diide ( $\text{C}_6\text{H}_4$ ), sulfonic acid ( $\text{SO}_3\text{H}$ ) and isopropylamines ( $\text{C}_3\text{H}_9\text{N}$ ). Based on the alkyl chain composition, the molecular weight and chemical formula amount to 375.767 g/mol and  $\text{C}_{20.3}\text{H}_{37.6}\text{NSO}_3$  [196]. Considering the natural isotopic abundances of H, C, N, O and S, the densities of the main isotopes in the LS are calculated and listed together with the resulting number fractions in Tab. 5.4. The addition of 15 mg/l bis-MSB or perylene does not change the results at the given accuracy.

**Table 5.4:** Isotope density and number fraction in  $\text{LAB} + 2 \text{ g/l PPO} + 5\% \text{ PRS} + 1.5\% \text{ H}_2\text{O}$ , considering an average composition of  $\text{H}_{28.424}\text{C}_{17.092}\text{N}_{0.052}\text{O}_{0.167}\text{S}_{0.050}$  and an average LS density of  $0.875 \text{ g/cm}^3$  (columns 2 and 3). Isotope density and number fraction in  $\text{LAB} + 2 \text{ g/l PPO} + 5\% \text{ PRS} + 1.5\% \text{ H}_2\text{O} + 0.54\%\text{Te}(\text{OH})_6$ , considering an average composition of  $\text{H}_{28.290}\text{C}_{16.989}\text{N}_{0.052}\text{O}_{0.203}\text{S}_{0.050}\text{Te}_{0.006}$  and an average LS density of  $0.887 \text{ g/cm}^3$  (columns 4 and 5). Only isotopes with densities  $\geq 1 \times 10^{18} / \text{cm}^3$  are used. The number fractions are relative to the sum of the listed isotopes. The LS densities are the average over all constituents.

Isotope	Density	Number fraction	Density	Number fraction
	$[\times 10^{22} / \text{cm}^3]$	[%]	$[\times 10^{22} / \text{cm}^3]$	[%]
$^1\text{H}$	6.2846	62.075	6.3504	62.048
$^2\text{H}$	0.0007	0.007	0.0007	0.007
$^{12}\text{C}$	3.7381	36.921	3.7723	36.857
$^{13}\text{C}$	0.0416	0.411	0.0420	0.410
$^{14}\text{N}$	0.0115	0.114	0.0117	0.114
$^{16}\text{O}$	0.0369	0.364	0.0455	0.445
$^{32}\text{S}$	0.0105	0.104	0.0107	0.104
$^{34}\text{S}$	0.0005	0.004	0.0005	0.005
$^{126}\text{Te}$	—	—	0.0003	0.002
$^{128}\text{Te}$	—	—	0.0004	0.004
$^{130}\text{Te}$	—	—	0.0005	0.004

It should be noted that neither water nor the PRS used scintillate. As a net result, wsLAB has a slightly lower light yield than LAB. On the other hand, Te-loaded wsLAB has a higher light yield than Nd-loaded LAB at the same concentration [185], due to the earlier mentioned absorption lines inherent to Nd, which is advantageous for the  $0\nu\beta\beta$  search of SNO+. In order to maintain the high light yield also at high Te concentrations,

further techniques are being investigated at BNL.

In conclusion, metal-loading of organic liquid scintillators using water-surfactant binding is a novel technique that has been developed and successfully applied with various metals at BNL [185, 195]. Investigations are still ongoing, though, to optimize the scintillator properties at different stages of loading. All wsLAB samples used and explicitly presented in Sec. 6 are state-of-the-art, but may differ from the final SNO+ compound.

### 5.3.4 Bis-MSB and perylene

Te-loaded LS will not only contain PPO as primary solute, but also a secondary solute. The two currently investigated fluors are bis-MSB and perylene, aromatic hydrocarbons with the molecular formulas C<sub>24</sub>H<sub>22</sub> and C<sub>20</sub>H<sub>12</sub>, respectively. Both secondaries shift the light emitted from PPO to wavelengths at which the quantum efficiency of the SNO+ PMTs is increased. The efficiency is highest between about (350–500) nm with a maximum around ∼ 450 nm [197]. In comparison, the PPO emission spectrum peaks at about 360 nm, the bis-MSB spectrum around 430 nm and the perylene spectrum around 480 nm. The final admixture is not fixed yet.

## 5.4 Scintillator purification

In order to accomplish the physics goals of SNO+, a high radiopurity of all scintillator components is necessary. The background target levels for pure LAB scintillator with PPO are  $1.6 \times 10^{-17}$  g<sub>238U</sub>/gLS, corresponding to 13 cpd of <sup>214</sup>Bi, and  $6.8 \times 10^{-18}$  g<sub>232Th</sub>/gLS, corresponding to ∼ 2 cpd of <sup>228</sup>Ac. To reach these levels, a purification plant, which joins different purification steps in a single-stage system, is currently being installed in the underground laboratory. First, a highly concentrated master solution with 120 g/l PPO is prepared in batches and prepurified. The concentrated PPO solution and LAB are distilled in parallel before blending the scintillator in order to remove heavy metals and to improve the UV transparency. In a next step, volatile contaminants of the LAB-PPO scintillator like Rn, Kr, Ar and O<sub>2</sub> are removed by a N<sub>2</sub>/steam stripping process. Furthermore, water extraction and metal scavenging will remove elements like Ra, K, Bi and Pb. To remove dust, the scintillator will pass through micro-filtration. While the detector is operating, it will be possible to re-purify the scintillator in a recirculation process. Details about the purification system are found in [198].

During the phase with Te-loaded wsLAB, the additional scintillator components introduce new contaminations, worsening the purity. The target levels for this phase are  $2.5 \times 10^{-15}$  g<sub>238U</sub>/gTeLS and  $3.0 \times 10^{-16}$  g<sub>232Th</sub>/gTeLS. The purification system for the telluric acid and the PRS are under development. The telluric acid will be purified in a two-stage procedure, where the first stage is conducted on surface and the second underground. On surface, U and Th contaminations as well as cosmogenic isotopes in Te [199] will be

strongly reduced using nitric acid re-crystallization and ethanol rinse. After the first stage of purification, a few hours can elapse before the sample is send underground. In this time, short living isotopes are produced in the telluric acid by cosmic neutron and proton activation. To remove cosmogenic isotopes and further purify the sample underground, it is dissolved in water at 80°C and cooled to re-crystallize without rinsing in this second purification step. This procedure keeps half of the Te, while the other half remains in solution, which is recycled in the surface plant. Additional cooling down underground further reduces cosmogenic backgrounds. Having passed the two stages of purification and six months of cooling down after one year of exposure to the cosmic flux at sea level, less than one cosmogenic background event per year is expected in the ROI for the  $0\nu\beta\beta$  search [200].

## 5.5 Physics goals

SNO+ is a multipurpose detector and has a large physics program, which is beyond the scope of this thesis. Further information about physics goals besides those mentioned here are found in [201, 202, 203], for instance.

### 5.5.1 Double beta decay search

The  $0\nu\beta\beta$  decay described in Sec. 4.3 results in two electrons in the final state, each carrying the full  $Q$ -value of the single decay, since no further particle is emitted. The signal of the  $0\nu\beta\beta$  decay thus is a mono-energetic line at the  $Q$ -value, opposed to the normal  $\beta$ -decay spectral shape of the  $2\nu\beta\beta$  decay, both broadened by the energy resolution of the detector. The observable is the half life of the  $0\nu\beta\beta$  decay  $T_{1/2}^{0\nu}$ , which is related to the effective Majorana mass  $|m_{\beta\beta}|$ , following Eq. 4.53. SNO+ will undertake the  $0\nu\beta\beta$  search using  $^{130}\text{Te}$  and with an initial scintillator loading of 0.3%  ${}^{\text{nat}}\text{Te}$  by mass. With about 0.78 kt of LS and a natural  $^{130}\text{Te}$  abundance of 34.08% [204] this results in around 800 kg of the double beta decaying isotope. With this, it is expected to reach after 5 y of data taking a  $T_{1/2}^{0\nu}$  sensitivity of  $> 9 \times 10^{25}$  y at 90% C.L. (see Fig. 5.2), corresponding to a  $|m_{\beta\beta}|$  sensitivity of  $< 70$  meV. Recent developments suggest that loadings to the percentage level are possible, pushing the sensitivity to the bottom of the inverted hierarchy (see Fig. 4.5).

The expected energy spectrum around the  $^{130}\text{Te}$   $Q$ -value of  $\sim 2.53$  MeV (see Tab. 4.2) is presented in Fig. 5.3. The ROI for the  $0\nu\beta\beta$  search ranges from  $-0.5\sigma$  to  $+1.5\sigma$ , which corresponds to an energy interval of about (2.47–2.69) MeV. The figure shows the  $0\nu\beta\beta$  signal, assuming  $|m_{\beta\beta}| = 200$  meV, and the expected background spectra coming from the  $2\nu\beta\beta$  decay,  $^8\text{B}$  neutrinos from the Sun,  $(\alpha, n)$  reactions and decays within the natural uranium and thorium chains (see Fig. A.1) in the scintillator as well as external backgrounds. The latter are backgrounds from sources outside of the scintillator volume.  $^{238}\text{U}$ ,  $^{232}\text{Th}$  and their daughters are intrinsic to the scintillator, though strongly reduced by the purification techniques outlined in Sec. 5.4. Assuming the target levels given in that

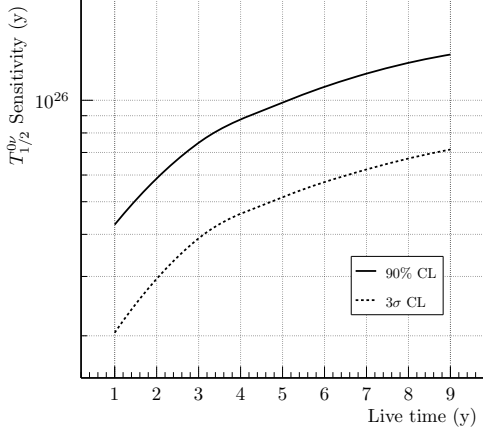


**Figure 5.2:**  $0\nu\beta\beta$  half life  $T_{1/2}^{0\nu}$  sensitivity of SNO+ over live time (Courtesy of the SNO+ collaboration, September 2014).

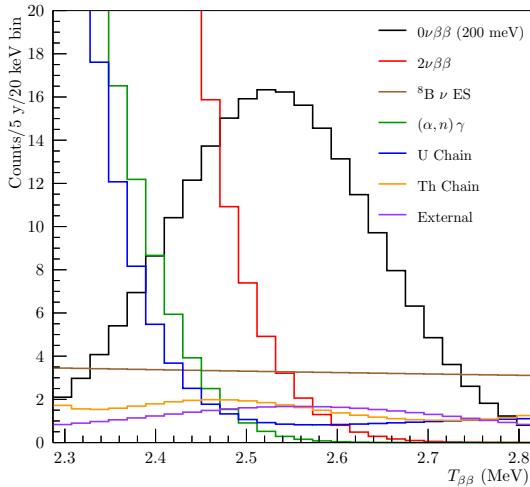


**Figure 5.3:** Expected SNO+ energy spectrum for the  $^{130}\text{Te}$   $0\nu\beta\beta$  decay search after background suppression (Courtesy of the SNO+ collaboration, September 2014). A 20% fiducial volume cut, 0.3%  $^{nat}\text{Te}$  loading, a Gaussian energy resolution with  $\sigma(E) = \sqrt{E[\text{MeV}]/200}$ , the  $2\nu\beta\beta$  half life  $T_{1/2}^{2\nu} = 7 \times 10^{20} \text{ y}$  and an effective Majorana mass of 200 meV are assumed. The nuclear matrix element used is  $M^{0\nu} = 4.03$  (IBM-2). Information about the backgrounds are found in the text.

subsection, Fig. 5.3 is obtained after the application of a  $> 99.99\%$  and  $> 98\%$  efficient coincident tag for  $^{214}\text{Bi}$ - $^{214}\text{Po}$  (U chain) and  $^{212}\text{Bi}$ - $^{212}\text{Po}$  (Th chain) backgrounds. The external backgrounds within a 3.5 m fiducial radius are suppressed by a factor of two due to a likelihood ratio cut. Backgrounds from cosmogenic induced nuclides in Te are not shown, since they are negligible after the purification of Te on surface and underground, as discussed above.

$^{214}\text{Bi}$ - $^{214}\text{Po}$  and  $^{212}\text{Bi}$ - $^{212}\text{Po}$  events from the U and Th chain in the LS form the largest background contribution in the ROI. If these events are not efficiently cut, SNO+ is not sensitive to the current limit of  $|m_{\beta\beta}| < (190 - 450) \text{ meV}$  (90% C.L.) set by EXO-200 [181], or even less able to lower it. For an efficient reduction of these backgrounds, the knowledge of the  $\alpha$ -particle quenching strength, which is measured within this work and presented in Sec. 6, is inevitably necessary. While it is unlikely that  $\alpha$ -particle events from  $^{214}\text{Po}$  and  $^{212}\text{Po}$  itself fall into the ROI, it is very likely that  $\beta$ -particle events from their mothers,  $^{214}\text{Bi}$

and  $^{212}\text{Bi}$ , do. The time coincidence between the mother and the short-living daughter is used together with a visible energy cut on the  $\beta-$  and  $\alpha-$ particle events to suppress the Bi–Po background in the ROI. This suppression is only efficient, if the visible  $\alpha-$ particle energy is known, which strongly deviates from the kinetic energy due to ionization quenching (see Sec. 2.6.3). Furthermore, since the half-live of  $^{212}\text{Po}$  is with 298 ns shorter than the SNO+ trigger window, lasting 400 ns, the majority of  $^{212}\text{Po}$  decays occurs within the same trigger window as  $^{212}\text{Bi}$ . The visible sum energy of these Po+Bi events, which are likely to fall into the ROI, is also defined by the  $\alpha-$ particle quenching strength. The same argument is true for  $^{214}\text{Po}$  and  $^{214}\text{Bi}$ , though to a smaller extend, since the half-live of  $^{214}\text{Po}$  is larger with 164.3  $\mu\text{s}$ . To conclude, a successful search by SNO+ for the  $0\nu\beta\beta$  of  $^{130}\text{Te}$  builds upon the measurements of the strongly quenched, visible  $\alpha-$ particle energy as a function of kinetic energy in the novel Te-loaded LS, which were performed within this works.

### 5.5.2 Supernova neutrinos

With the observation of in total 24  $\bar{\nu}_e$  candidates from the SN 1987A, the Kamiokande II and IMB Cherenkov experiments as well as the Baksan Scintillator Telescope provided important information about the mechanisms of a supernova burst [42, 43, 44], described in Sec. 3.3. Although the Baksan telescope is also a scintillation detector, it was due to its high detector threshold of 10 MeV most sensitive to  $\bar{\nu}_e$  neutrinos undergoing inverse beta decay, like the two Cherenkov detectors.

Liquid scintillation detectors with a low trigger threshold, like SNO+, are sensitive to both, charged and neutral currents, and have in total a larger variety of reactions than the three named detectors. The golden channel for SN neutrino detection of all flavors is neutrino–proton elastic scattering, as this NC reaction is the only channel providing spectral information about all neutrino flavors that also has a relatively high cross section. The proton recoil energy, however, is strongly quenched and nearly all events have visible energies below 2 MeV, assuming a standard CCSN. The spectral sensitivity of SNO+ to the  $\overset{(-)}{\nu}_\mu$ 's,  $\overset{(-)}{\nu}_\tau$ 's of a galactic SN that undergo  $\nu$ - $p$  elastic scattering is determined within this work, based on the measured proton quenching parameters. The details are presented in Sec. 7. Finally, it should be mentioned that SNO+ will participate in the Supernova Early Warning System SNEWS [205].



# Chapter 6

## Ionization quenching in LAB based scintillators

### 6.1 Motivation

The energy dependent light yield of liquid scintillator (LS) varies for different particles, as described in detail in Sec. 2, and is lower the higher the mass of the charged particle is. Thus, in an energy sum spectrum, as recorded in SNO+–like detectors, also the expected number of events in each light yield bin strongly depends on the particle type and energy. Both, signal and background model, are reliant upon a precise knowledge of the light response function to electrons, protons and  $\alpha$ -particles, as well as even heavier ions, if detectable. All discussions within this chapter refer only to the energy range of interest for low energy LS detectors, i.e. a few keV up to about 100 MeV. While the electron light yield raises approximately linear with the particle energy above a few hundred keV, the proton and  $\alpha$ -particle light output is expected to raise non-linearly over several MeV, following Birks' law Eq. 2.12. The response to protons and  $\alpha$ -particles of scintillators based on LAB has not been published before the presented work had been accomplished. Moreover, whether the Birks parameter  $kB$  in Eq. 2.12 is the same for the same LS but for different ions is still under discussion, as already pointed out in Sec. 2.6.3. Hence a determination of both, proton and alpha quenching, within the same measurement, is the ideal way to test this controversy. To determine the non-linear scintillator response due to ionization quenching, the best approach is to use internal particles, as is done within this work, in order to avoid surface effects. If organic scintillators were instead excited from external ionizing particles with a residual range as short as  $< 8$  mm air equivalent range [5] in the compound, excitation energy could escape and the observed total light yield would be less than expected and varies non-linearly with the range. A common method to measure proton quenching is the use of recoiling protons from neutron–proton elastic scattering in which the maximum proton energy equals the neutron energy. Also alpha quenching in organic scintillators can be measured in a neutron field via the  $^{12}\text{C}(n,\alpha)^9\text{Be}$  reaction, in which the maximum  $\alpha$ -particle energy can be calculated, assuming the  $^{12}\text{C}$

atom is at rest. Thus, using neutrons, as done for the presented measurements, proton and alpha quenching can be measured simultaneously with the same detector and data acquisition (DAQ) system and consequently under the same measurement conditions.

The measurements were taken in four individual campaigns C1, C2, C3 and C4. They are not only valuable for SNO+, but for an increasing number of experiments. LAB is employed for novel liquid scintillators which are used or planned as the neutrino target in recently commissioned, upcoming and potential future neutrino experiments like Daya Bay, RENO<sup>1</sup> [206], SNO+ and JUNO<sup>2</sup> [207]. Also further potential experiments like LENS<sup>3</sup> [208] and HANOHANO<sup>4</sup> [209] are considering LAB as possible solvent for their scintillator. Additionally, water–surfactant–LAB (wsLAB) scintillators are being developed [185] to enable loading of a broad range of isotopes. For these scintillators this work delivers the first proton and alpha quenching measurements worldwide. This chapter presents the measurements of the light response functions in different LAB and wsLAB scintillators for protons and  $\alpha$ -particles relative to the electron response function, carried out at the PTB Ion Accelerator Facility (PIAF) of the Physikalisch–Technische Bundesanstalt (PTB), Braunschweig. The presented method, utilizing gamma sources to determine the electron response and a white neutron beam for the alpha and proton response, was already used successfully at the PTB for the characterization of NE213<sup>5</sup>, BC501A<sup>6</sup> and BC501 scintillation detectors [210, 211, 212, 213]. Results of the quenching measurements are partly published [32, 189] and passages of the text in this chapter are identical to text in the publication, since their author is the same. The data presented in [32] was evaluated in two independent analyses by two of the authors. The resulting quenching parameters are the same within their uncertainties.

This chapter is organized as follows. In Sec. 6.2, the compositions of the ten different, investigated LAB based scintillators are specified. The experimental set–up is described in Sec. 6.3, including the relevant details about the neutron field. This section is followed by the description of the gamma source calibrations and presentation of the resulting electron light responses in Sec. 6.4. The beam data analysis is discussed in detail in Sec. 6.5, concluded with the determined proton and alpha light responses relative to the respective electron light response. These measurement results are fit with Birks’ law Eq. 2.12, as described in Sec. 6.6. The resulting Birks’ parameters  $kB$  and  $C$  for protons and  $\alpha$ -particles in the various LAB based scintillators are presented and discussed within this section. For these results, a linear electron light response function is assumed, which is a typical approximation justified by the smallness of the non–linearity of the electron light response. The variation of the fit results in the presence of a non–linearity is investigated in Sec. 6.7.

---

<sup>1</sup>Reactor Experiment for Neutrino Oscillation.

<sup>2</sup>Jiangmen Underground Neutrino Observatory.

<sup>3</sup>Low Energy Neutrino Spectroscopy.

<sup>4</sup>Hawaii Anti–Neutrino Observatory.

<sup>5</sup>Provided by Nuclear Enterprise Ltd. .

<sup>6</sup>Provided by Saint–Gobain Ceramics & Plastics, Inc. .

Different extents of the non-linearity are considered. The strength of the alpha quenching has been measured in two further, independent experiments. One experiment was conducted using the SNO+ detector by members of the SNO+ collaboration and one was performed at the Helmholtz-Zentrum Dresden Rossendorf (HZDR). The results from those measurements are compared to the results of this thesis in Sec. 6.8. Finally, the proton and alpha quenching parameters determined are directly compared in Sec. 6.9 per scintillator, addressing the question of whether the same compound has equal or different Birks parameters. The chapter is concluded in Sec. 6.10 by a short summary and outlook.

## 6.2 Liquid scintillator compositions

The composition of all LS samples used for the measurements at PTB is given in Tab. 6.1. Six different LAB based samples are used, termed LAB1 through LAB6, four wsLAB samples, termed wsLAB1 through wsLAB4, and one PC based sample, termed PC1. The PC measurement is analyzed in [215] and only touched on here for comparison. The first two categories, LAB and wsLAB, correspond to the initial intention of SNO+ to search for the  $0\nu\beta\beta$  of  $^{150}\text{Nd}$  using LAB and the directional change towards the search for the  $0\nu\beta\beta$  of  $^{130}\text{Te}$ , which requires wsLAB. These two categories contain metal-loaded and unloaded samples. Moreover, different fractions of primary and secondary solute are tested. As explained in Sec. 2.6.3, ionization quenching is mainly a primary process and thus different primary solute concentrations as well as the addition of a secondary solute are not expected to change the measured quenching parameters. To control this expectation, measurements using LAB with different PPO concentrations as well as with and without secondary solute are conducted (LAB1–4 in Tab. 6.1). In the case of the Nd loaded samples, no bis-MSB is added, since Nd has intrinsic absorption lines leading to more color quenching (see Sec. 2.6.1) in the range of bis-MSB emission than in PPO emission. The corresponding absorption and emission spectra, measured within the work at hand, are shown in Fig. 6.1.

Within the measurements using wsLAB scintillators, two different secondary wavelength shifters are tested, bis-MSB and perylene (wsLAB2–3 in Tab. 6.1). These secondary solutes are two candidates for the water–surfactant–compound of SNO+. Within these measurements, water and PRS tremendously worsened the measurement conditions, as will be shown and explained within this chapter, and data with a high bis-MSB concentration of 45 mg/l is additionally taken to slightly improve the resolution.

The average density  $\bar{\rho}$  as well as the hydrogen to carbon ratio  $N_H/N_C$ , both influencing the gamma and neutron scattering event rate, are calculated for each scintillator sample from the individual density and number of H and C atoms of the constituents (see Tab. 5.1) and their respective fraction (see Tab. 6.1). The resulting values are summarized in Tab. 6.2. The LAB solvent in all LAB based samples is provided by Petresa Canada Inc., Canada, Bécancour, and has a density of  $(0.858 - 0.868) \text{ g/cm}^3$  at  $15^\circ\text{C}$  [188, 192].

**Table 6.1:** Mass fractions in percent of the solvent (LAB or PC), primary solute (PPO), secondary solute (bis-MSB or perylene), isotope (Nd or Te) and, if any, molecules necessary for element loading (PRS and water) of each liquid scintillator sample used for measurement. In sample wsLAB1, 0.54%  $\text{Te(OH)}_6$  (telluric acid) yield a natural Te loading of 0.3%. All wsLAB samples and isotope loaded samples are prepared by M. Yeh and S. Hans at the Brookhaven National Laboratory.

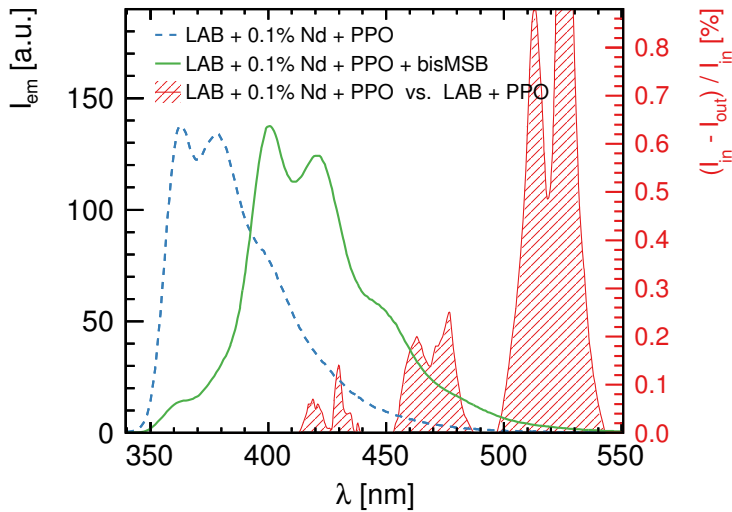
Sample	Fraction by weight			
	LAB	PPO	bis-MSB	Nd
LAB1	99.766	0.232	0.002	—
		( $\approx 2 \text{ g/l}$ )	( $\approx 15 \text{ mg/l}$ )	
LAB2	99.768	0.232	—	—
LAB3	99.650	0.348	0.002	—
		( $\approx 3 \text{ g/l}$ )		
LAB4	99.652	0.348	—	—
LAB5	99.668	0.232	—	0.100
LAB6	99.552	0.348	—	0.100

Sample	Fraction by weight						
	LAB	PPO	bis-MSB	perylene	PRS	water	Te acid
wsLAB1	92.666	0.232	0.002	—	5.00	1.50	0.54
wsLAB2	93.266	0.232	0.002	—	5.00	1.50	—
wsLAB3	93.266	0.232	—	0.002	5.00	1.50	—
wsLAB4	93.263	0.232	0.005	—	5.00	1.50	—
			( $\approx 45 \text{ mg/l}$ )				

Sample	Fraction by weight		
	PC	PPO	bis-MSB
PC1	99.828	0.170	0.002
		( $\approx 1.5 \text{ g/l}$ )	



**Figure 6.1:** Absorption and emission spectra of Nd-loaded LAB. The emission of LAB + 0.1% Nd + 3 g/1PPO (+15 mg/l bis-MSB) is induced with an excitation wavelength of  $\lambda_{ex} = 320$  nm (345 nm) in a Perkin Elmer Luminescence Spectrometer [214]. The light is collected by the spectrometer over  $80\ \mu\text{s}$ . The resulting intensity  $I_{em}$  is shown in arbitrary units (a.u.). The absorption spectrum is given as relative difference between incident light intensity  $I_{in}$  and transmitted light intensity  $I_{out}$ , in 1 cm of LAB + 0.1% Nd + 3 g/1PPO relative to LAB + 3 g/1PPO.

Before measurement, each solution is purified from oxygen by bubbling with Ar for 30 min, to reduce the effect of oxygen quenching, as explained in Sec. 2.6.2. The bubbled LS is filled into the detector cell without further contact to air. The measurements were performed at about 19°C, which is slightly above the temperature of 15°C at which the LAB density is known from the provider [188, 192]. This uncertainty enters the later calculation of the material stopping power.

## 6.3 Experimental set-up

### 6.3.1 Neutron field

To obtain a proton light output function over an energy range as large as possible as well as internal  $\alpha$ -particles with several different energies in a single experiment, a neutron beam with a continuous spectral distribution is used. The white neutron field is produced at PIAF, partly sketched in Fig. 6.2, by bombarding a 3 mm thick stopping-length Be target with a 19 MeV proton beam from the isochronous CV28 cyclotron [216, 217]. Neutrons are predominantly produced by the  ${}^9\text{Be}(p,n){}^9\text{B}^*$  reaction, where the kinematic limit of the  ${}^9\text{Be}(p,n){}^9\text{B}$  ground state transition has a  $Q$ -value of ca.  $-1.850$  MeV. The maximum

**Table 6.2:** Calculated average density  $\bar{\rho}$  at 15°C and hydrogen to carbon ratio  $N_H/N_C$  of all liquid scintillator samples used for measurement and listed in Tab. 6.1. The LAB values are based on [188, 192]. The value for PC1 is taken from [193].

Sample	$\bar{\rho}$ [g/cm <sup>3</sup> ]	$N_H/N_C$
LAB1	0.863	1.649
LAB2	0.863	1.649
LAB3	0.864	1.648
LAB4	0.864	1.648
LAB5	0.870	1.649
LAB6	0.870	1.648
wsLAB1	0.887	1.665
wsLAB2	0.875	1.663
wsLAB3	0.875	1.663
wsLAB4	0.875	1.663
PC1	0.880	1.332

energy of the neutrons is thus about 17.15 MeV at an emission angle of 0°. The minimum energy of neutrons escaping from the target along the beam axis is below 1 MeV.

To enable neutron time-of-flight (TOF) spectroscopy, a fast internal beam-pulsing system is incorporated into the cyclotron providing isolated single beam pulses with adjustable repetition frequency [216]. The cyclotron operated at a frequency  $f_{cyc}$  of approximately 23 MHz during all measurements. The repetition frequency of the isolated pulses is defined by a pulse selector which deflects the unwanted pulses within the first orbit. The accepted single pulses are further accelerated in the cyclotron. The frequency of the selector  $f_{sel}$ , respectively of the beam pulses, is  $f_{sel} = f_{cyc}/n$ , where  $n = 2, 3, 4, \dots, 79$  is scalable. In order to reduce the presence of incompletely deflected pulses before and after the main beam pulse, so-called satellite pulses, and in order to shorten the main pulse, an electric capacitor purges the head and the tail of the main pulse. The shortened pulses have a full width at half maximum of  $\sim 1.5$  ns [216, 217]. Though satellites are mitigated with the pulse shortener, they are not fully suppressed.

The compact cyclotron is placed on a movable,  $\sim 5$  m long swivel arm, as shown in Fig. 6.2, with the target close to the pivot. A fixed heavy collimator system consisting of a polyethylene pre-collimator, water tanks and concrete provides five different possible flight paths to five neutron detector stations with low background from backscattered neutrons.

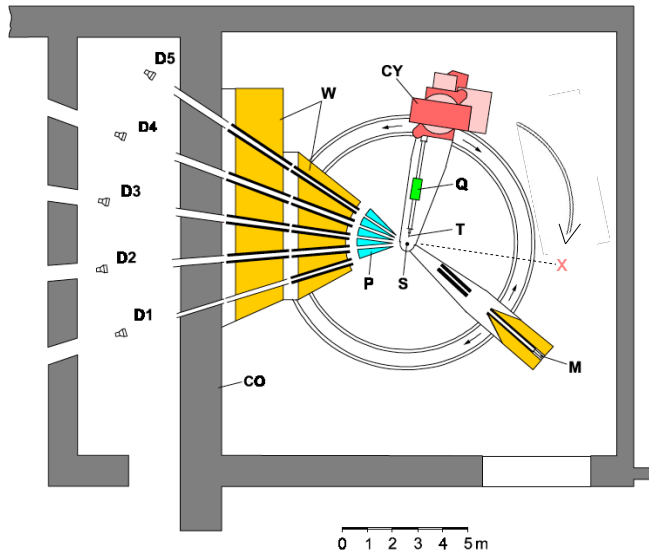


**Figure 6.2:** Time-of-flight spectrometer at PIAF with a cyclotron (CY), quadrupole magnet (Q), target (T), scattering probe and pivot of cyclotron movement (S), monitor (M), polyethylene shields (P), water tanks (W), concrete shield (CO) and five detector stations (D<sub>1</sub>...5). The polyethylene shields, water tanks and concrete shield form a massive neutron shield and collimator system. For quenching measurements, no scattering probe is placed at the pivot and the CY is at position X. The figure is taken from [216].

**Table 6.3:** Selector frequency  $f_{sel}$ , proton beam current  $I_b$  and distance  $d$  between the center of the Be target and of the scintillator volume for the different measurement campaigns. The distance between target and detector cell is measured with an accuracy of  $\pm 2$  mm.

Campaign	Samples	$f_{sel}$ [kHz]	$I_b$ [nA]	$d$ [m]
C1	LAB1-3, LAB6	481.3	50	12.1100
C2	LAB4	959.4	100	12.2109
C3	LAB5	957.4	180	12.2144
C4	wsLAB1-4, PC1	477.2	45	12.2409

The LAB scintillator detector was installed at position D3 in Fig. 6.2 at a distance of approximately 12 m (see Tab. 6.3) in all measurements. The cyclotron was placed such that the detector is on the proton beam axis to collect data within the largest possible neutron energy interval. The approximate neutron energy distribution at the detector position is shown in Fig. 6.3. During gamma calibration data taking, the beam is blocked.

To avoid an overlap of the slowest neutrons from one pulse with the fastest neutrons from the succeeding pulse, also called time-frame-overlap, the selector frequency was restricted to less than 1 MHz. The exact values are listed in Tab. 6.3. Given the distance  $d$  between the Be target center and the scintillator volume center as well as the frequency  $f_{sel}$ , the critical neutron velocity  $v_c$ , at which time-frame-overlap occurs, is

$$v_c = \frac{d}{\frac{d}{v_{\max}} + \frac{1}{f_{sel}}}, \quad (6.1)$$

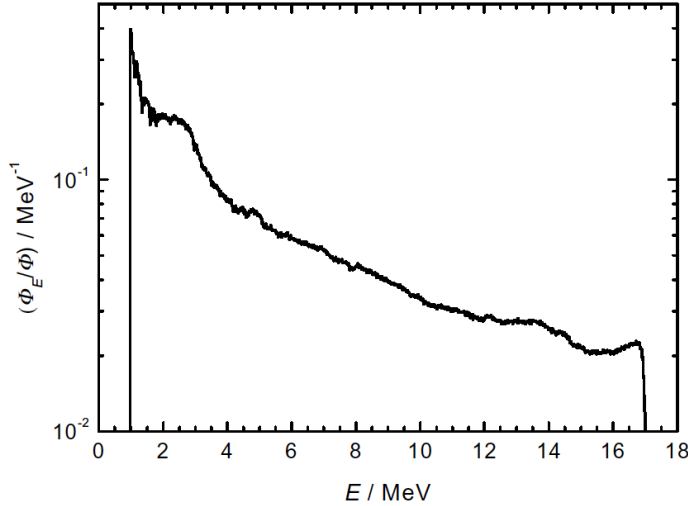


**Figure 6.3:** Relative spectral neutron fluence distribution of  ${}^9\text{Be}(p,n){}^9\text{B}$  reactions, from 19 MeV protons impinging on a thick Be target, at a distance of 27.39 m from the center of the target. The figure is taken from [211].

where

$$v_{\max} = \sqrt{1 - \frac{1}{\frac{E_{\max}}{m_n c^2}}} \cdot c \quad (6.2)$$

is the neutron velocity at maximal kinetic neutron energy  $E_{\max} = 17.15$  MeV,  $m_n$  is the neutron mass and  $c$  the speed of light in vacuum. The resulting critical neutron energy

$$E_c = m_n c^2 \left( \sqrt{\frac{1}{1 - \frac{v_c^2}{c^2}}} - 1 \right) \quad (6.3)$$

is 0.493 MeV with the settings of campaign C3. Consequently, recoiling protons from neutron–proton scattering in the scintillator reach maximally the same energy. The light produced by protons in organic liquids at these low energies is typically reduced by more than a factor of 5 compared to electrons, as will be confirmed for LAB in Sec. 6.5.5, yielding  $< 100$  keV electron-equivalent energy. The maximum possible kinetic energy of heavier charged particles is even lower, while the light reduction is even stronger. With a hardware threshold of 200 keV electron energy, corresponding to  $\sim 1$  MeV proton recoil energy, time-frame overlap can thus be safely neglected in C3 as well as in the other campaigns, which all have an even lower critical energy.

To avoid signal pile-up due to multiple neutron interactions in the detector within one time period  $1/f_{sel}$ , the beam current  $I_b$  had to be limited to about 100 nA. The trigger rate of the constant fraction discriminator (CFD) module is about  $3 \times 10^3 \text{ s}^{-1}$  for a threshold set close to the electronic noise. With the individual values for  $I_b$  listed in Tab. 6.3, the rate of neutrons  $R_n$  incident on the detector front face spans from about  $7 \times 10^3 \text{ s}^{-1}$  in C4 to about  $27 \times 10^3 \text{ s}^{-1}$  in C3. After a neutron interaction has triggered the detector, the probability for a second neutron in the detector within the duration of one beam pulse is  $R_n/f_{sel}$  and thus about 2.8% in C3, the highest probability of the four cases. The average

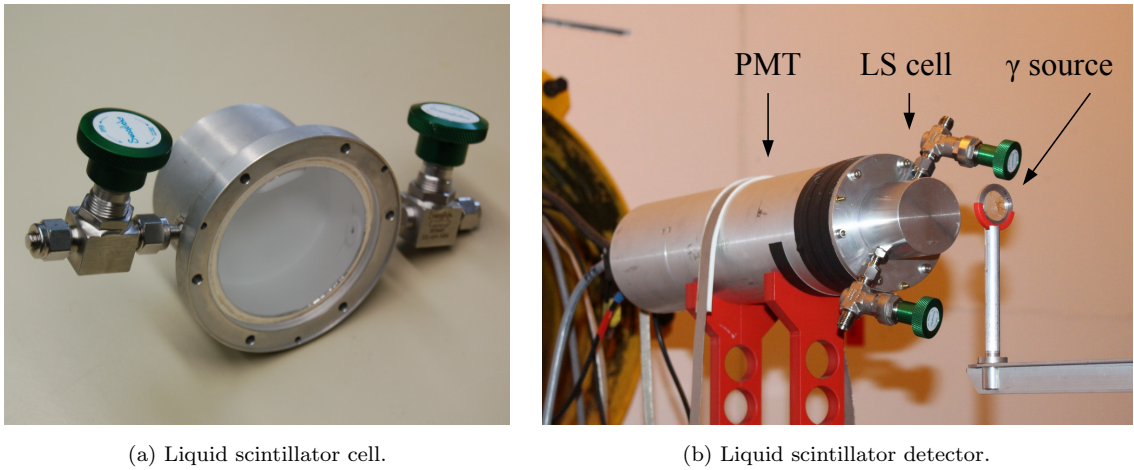


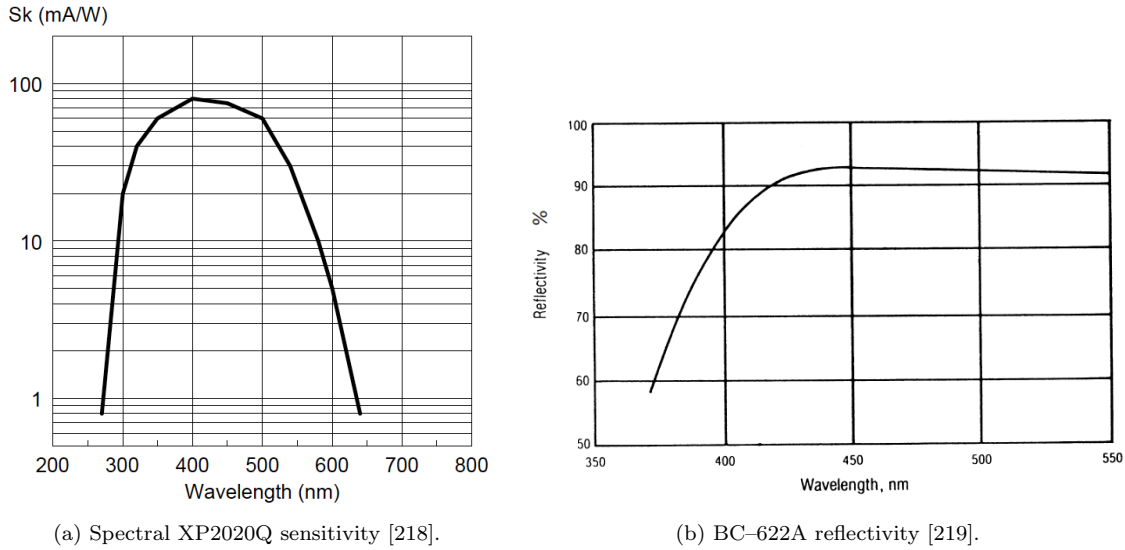
**Figure 6.4:** Liquid scintillator (LS) cell (a) and assembled LS detector (b). The detector is installed at one of the measuring units of the PTB time-of-flight spectrometer. A gamma calibration source is placed a few centimeters in front of the cell.

neutron detection efficiency in a NE213 detector of the same dimensions and threshold as the detector used here is determined to be below 25% [217]. Assuming a similarly good efficiency in the case of the presented measurements, the probability for multiple neutron interactions within one beam pulse is  $\leq 0.7\%$  in all campaigns. The amount of events with falsely measured pulse-height (PH) at a certain TOF is thus not statistically significant and, moreover, the value of the false PH is randomly distributed. Pile-up thus does not cause an observable deterioration of the shape of the PH spectra.

### 6.3.2 Liquid scintillator detector

The scintillation detector consists of a cylindrical dural cell (see Fig. 6.4a) with one port covered by a window made of ground and polished fused silica for higher UV transparency and an XP2020Q PMT [218], also equipped with a fused silica window. Two identical cells have been produced at the mechanical workshop of the TU Dresden. The diameter and inner height of each cell is 50.8 mm and the bottom wall has a thickness of 2.5 mm. At PTB, silica window and cell were joined by an indium gasket and coupled to the PMT by a conical UV transparent poly(methyl methacrylate) (PMMA) light guide<sup>7</sup>. The inner walls of the cell and the light guide are coated with BC-622A [219] reflective paint to increase the light collection efficiency. Both, the PMT sensitivity as well as the paint reflectivity, depend on the wavelength as shown in Fig. 6.5. The bialkali photocathode of the PMT has a peak sensitivity at 420 nm [218] and the paint reflectivity is maximal above about 430 nm. The PMT is surrounded by a mu-metal cylinder with the same potential as the cathode to compensate the influence of the Earth magnetic field. PMT and base are housed in an aluminum casing and the whole detector is tested to be light-tight. A picture of the assembled detector at position D3 is shown in Fig. 6.4b.

<sup>7</sup>Provided by Evonik Röhm GmbH.



(a) Spectral XP2020Q sensitivity [218].

(b) BC-622A reflectivity [219].

**Figure 6.5:** Wavelength dependence of the PMT sensitivity (a) and the paint reflectivity (b).

The detector is equipped with an LED gain stabilization system regulating the drift of the PMT gain for temperature variations between 5°C and 40°C and countrate-dependent drifts with time constants below 1 s [220]. The LED is operated in a triggered mode such that light pulses with durations of a few nanoseconds are produced. These light pulses are directed to the photocathode. The signals produced by the LED pulses are identified electronically and the high voltage is regulated to keep the PH of the LED signals constant. The maximum drift of the gain is kept below 1%. Additionally, capacitors are integrated in the last dynodes to avoid a voltage drop in the case of high dynode currents and thus a gain variation. An effect, which cannot be compensated by external means, however, is the non-linearity of the amplification between dynodes due to space charge effects. In this instance the field of secondary electrons from one dynode affects the fast following electrons from the preceding dynode, partly shielding the dynode voltage. This non-linearity can only be avoided by a decrease of the amplification or by signal extraction before the last dynode. In the used set-up, the latter solution is applied and a slow signal from the ninth PMT dynode out of twelve is read out via a coupling capacitor.

### 6.3.3 Read-out system

The detector is connected to a NIM-standard read-out system, which provides three signal types: PH, pulse-shape (PS) and TOF. In the case of beam measurements, the signals are delayed such that they are registered coincidentally by a multi-parameter DAQ system [221]. This system contains a set of analog-to-digital converters (ADCs) and the signals are stored event-by-event. During the acquisition of calibration data, only PH information is available and the system is switched from coincidence-mode to independent single-mode. The DAQ system allows for online data analysis and sequentially stores the

ADC data, permitting an extensive offline analysis.

The PH is the peak amplitude of an analog pulse, extracted from the ninth dynode of the PMT. The PH signal is then passed through a preamplifier and a delay line amplifier. The integrated charge signal, which is proportional to the number of scintillation photons and thus the light yield, is tested against threshold in a time single channel analyzer (TSCA). The threshold is set to about 200 keV electron energy. Using the delay line amplifier, the PH is regulated such that in the first series of measurements with a particular LS sample, the full dynamic range is registered. In a second series with the same sample, the PH is amplified such that the region at low PHs, which is important for the  $\alpha$ -quenching measurement, is better resolved. In this series, only the full PH spectrum of neutrons with up to about 5 MeV energy is registered. At higher neutron energies, the high PH end of the spectrum is outside the measuring range. In the following, the first amplification mode is referred to as low gain (LG) and the second one as high gain (HG) mode. Each measurement is performed in both modes. The PH scale is calibrated by means of standard gamma sources in order to translate PH, measured in ADC channels, into light yield  $L$  in electron-equivalent energy, as will be described in detail in Sec. 6.4. The proton and  $\alpha$ -particle light response measurements are thus relative to the electron light response.

The PS signal is independent from the pulse amplitude and thus extracted from the anode of the PMT. It is determined for pulse-shape discrimination (PSD) between gamma-induced background events and neutron-induced events. The respective module, as described in detail in [222], uses the zero crossing method to derive a timing marker from the trailing edge of the anode pulse. Therefore the anode pulse is first integrated with an R-C circuit and then differentiated with an active pole-zero compensated differentiator circuit. The time when the integral is maximal, and thus its derivative zero, depends on the amount of light from the slow scintillation component. The more late light, the later the derivative is zero. The time difference between zero crossing and a second marker, the TOF timing marker derived from the fast leading edge of the anode pulse, is measured with a time-to-amplitude converter (TAC). It is related to the decay time of the scintillation light and therefore to the ionization density of the charged particle producing the event.

The TOF signal is derived from the fast anode pulse. The TOF timing marker is determined with a CFD and serves as the start signal. A delayed signal from a capacitive beam pick-up unit (BPU) between the quadrupole magnet and the target (see Fig. 6.2) provides the stop signal. Start and stop signal are passed through a TAC and the resulting TOF signal is forwarded to an ADC of the DAQ system. The TOF measurement is calibrated with a time calibration module which produces a set of pulses with a period of 40 ns. The pulses are measured in TOF channels, as shown in Fig. 6.6. The calibration factor  $c_{\text{cal}}$  is the slope obtained in a linear fit of the pulse number over the pulse position multiplied by 40 ns. The variations of the peak positions from the nominal values  $\Delta p$  quan-

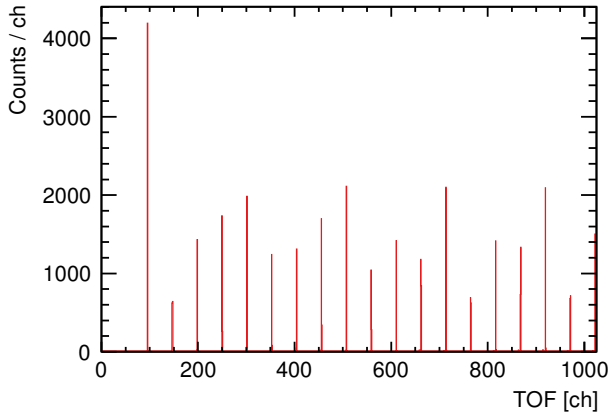


**Figure 6.6:** Spectrum of the time calibration module in TOF channels (ch), measured in campaign C1. The pulses are produced every 40 ns.

tify the non-linearity of the TAC converter and are determined to be smaller than  $\pm 0.2$  TOF channels in average. The results of each calibration are listed in Tab. 6.4. The time calibration has a relative uncertainty of  $\pm 0.05\%$ , which is determined by comparison with a DCF77 10 MHz reference signal.

**Table 6.4:** Results of the time calibration translating TOF channels into units of time. The calibration module produces a set of pulses with a period of 40 ns, measured in TOF channels.  $c_{\text{tcal}}$  is the resulting time calibration factor.  $\Delta p$  is the difference between the nominal and the measured peak position of each pulse. The maximum difference within the set of pulses is denoted as  $\Delta p_{\text{max}}$  and the average difference of all pulses as  $\langle \Delta p \rangle$ .

Campaign	$\langle \Delta p \rangle$ [ch]	$\Delta p_{\text{max}}$ [ch]	$c_{\text{tcal}}$ [ns/ch]
C1	$\pm 0.11$	$\pm 0.3$	0.7765
C2	$\pm 0.15$	$\pm 0.5$	0.7749
C3	$\pm 0.14$	$\pm 0.3$	0.7765
C4	$\pm 0.19$	$\pm 0.5$	1.5625

## 6.4 Gamma calibration

### 6.4.1 Measurement

The energy calibration of the PH spectra and determination of the light response to electrons is obtained with standard gamma calibration sources that create secondary electrons in the organic liquid. Also the electrons are thus internal particles. The sources are subsequently placed in front of the scintillator cell, as shown in Fig. 6.4b, and the electron PH spectra induced by three gamma sources with a total of six  $\gamma$ -lines, namely  $^{137}\text{Cs}$

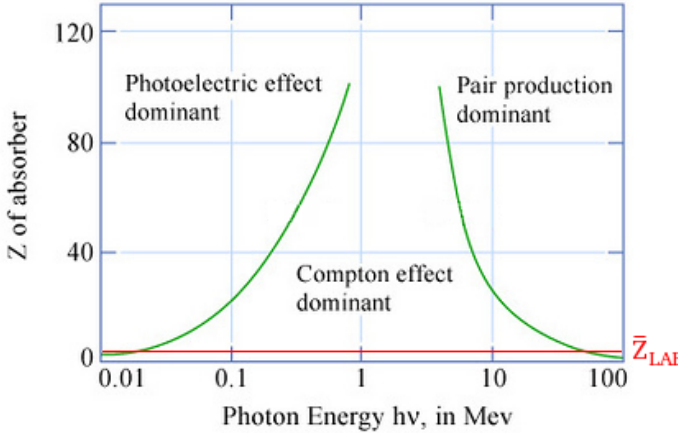


**Figure 6.7:** Relevance of the three main types of gamma interactions depending on the atomic number  $Z$  of the absorber and the gamma energy  $h\nu$ . The green solid lines represent the values of the co-ordinate pairs at which the neighboring effects are equally strong [223]. The red solid line indicates the average atomic number  $\bar{Z} \approx 2.9$  of LAB.

( $E_\gamma = 0.662$  MeV),  $^{22}\text{Na}$  ( $E_\gamma = 0.511$  MeV,  $E_\gamma = 1.275$  MeV) and  $^{207}\text{Bi}$  ( $E_\gamma = 0.570$  MeV,  $E_\gamma = 1.064$  MeV,  $E_\gamma = 1.770$  MeV) are measured. After source data taking and while the beam is still blocked, random background is measured. The background measurement is normalized over time to every source and beam measurement individually and subtracted from it. The amount of detected scintillation light strongly depends on the specific composition of the scintillator and the experimental settings. Therefore the PH calibration of the detector and background measurement are repeated for each filling and amplification mode. In this subsection, measured PH spectra are shown exemplarily for one compound with comparatively good and one with comparatively bad PH resolution.

Though gamma radiation creates secondary electrons in basically three interaction mechanisms, Compton scattering, photoelectric absorption and pair production, the latter two are negligible. There is virtually no photoelectric cross section for gammas of the given energies due to the low mean atomic number  $\bar{Z} \approx 2.9$  of LAB based scintillators with an average molecular formula of  $\text{C}_{17.1}\text{H}_{28.3}$ . Also pair production plays a subordinate role until about 3 MeV gamma energy are reached [224], though in principle possible in the  $^{22}\text{Na}$  and  $^{207}\text{Bi}$  measurements. Compton scattering is the prevailing interaction over the full given energy range from 0.511 MeV to 1.770 MeV in LAB, as illustrated in Fig. 6.7. As a result, no full-energy or escape peaks are observed and the PH spectrum of a single  $\gamma$ -line takes the form of a Compton continuum with a maximum electron energy of

$$E = \frac{2E_\gamma^2}{m_e c^2 + 2E_\gamma} \quad (6.4)$$

at the Compton edge. In this equation,  $m_e$  is the electron rest mass,  $E_\gamma$  the gamma energy and  $c$  the speed of light in vacuum. Multiple gamma scattering enhances the spectrum above the sharp edge. Furthermore, the typical shape of the Compton (sum) PH spectrum is slightly distorted due to wall effects, like the escape of electrons, before they fully deposited their energy or the entrance of external electrons from Compton scattering in the

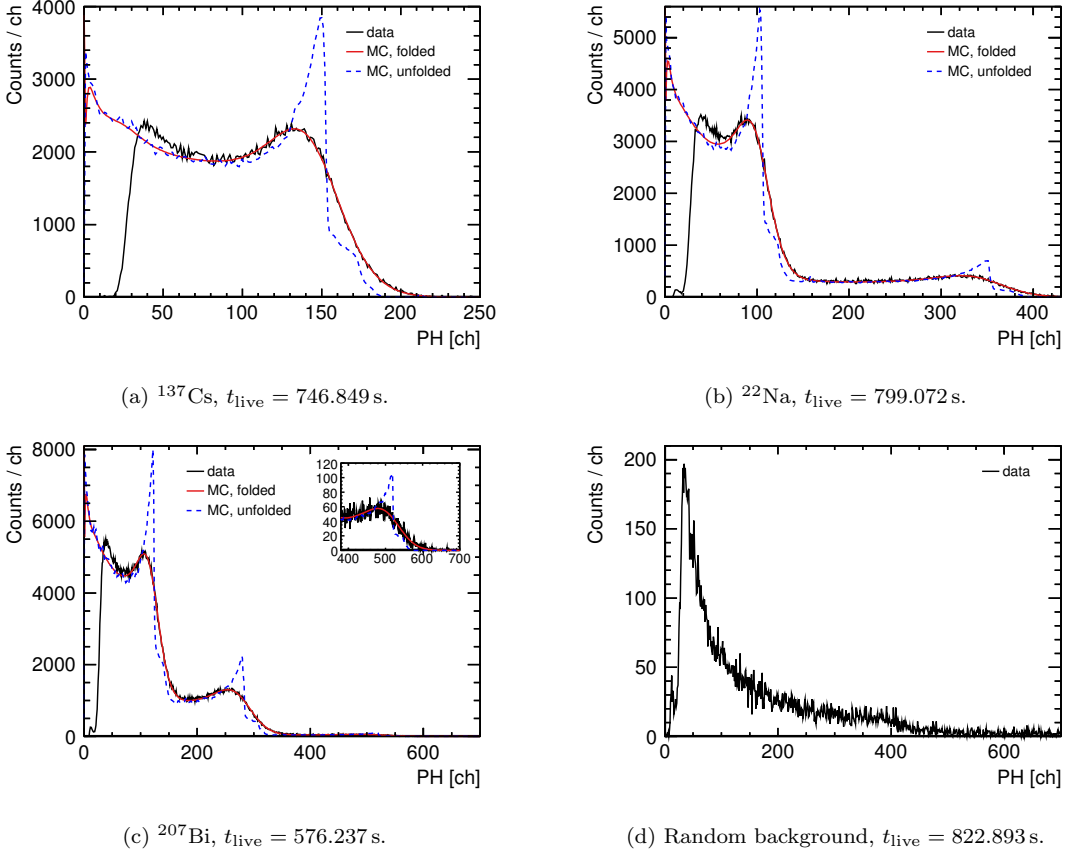


**Figure 6.8:** Pulse-height spectra in ADC channels (ch) of all used calibration sources (a-c) and of background only (d). The third  $\gamma$ -line of  $^{207}\text{Bi}$  is shown enlarged in the inset of (c). The background is subtracted from the source measurements after normalization to the respective livetime  $t_{\text{live}}$ . The data is taken with LAB + 2 g/l PPO + 15 mg/l bis-MSB (LAB1) in HG mode.

surrounding material, depositing their residual energy in the active medium. Also escaping electrons may be scattered back into the scintillator volume. Wall effects mainly lead to additional counts in the low PH region and their importance depends on the dimensions of the detector and surrounding material and is consequently expected to be of the same order for all measurements and mostly independent from the scintillator. The position of each Compton edge in the PH spectra, instead, depends amongst others on the individual scintillator properties. Also the impact of the detector resolution on the shape of the measured spectra differs for the different scintillator cocktails. A finite resolution veils the exact channel position of the Compton edges, as observable in Fig. 6.8 and 6.9, and MC calculations become necessary to determine each position and thus the ADC channel to electron energy relation. The spectra in Fig. 6.8 are an example for measurements with high PH resolution and detected light yield and those in Fig. 6.9 for measurements with low resolution and detected light yield, both in relation to all calibration measurements taken within this work. The remaining spectra are shown in the appendix B.1.

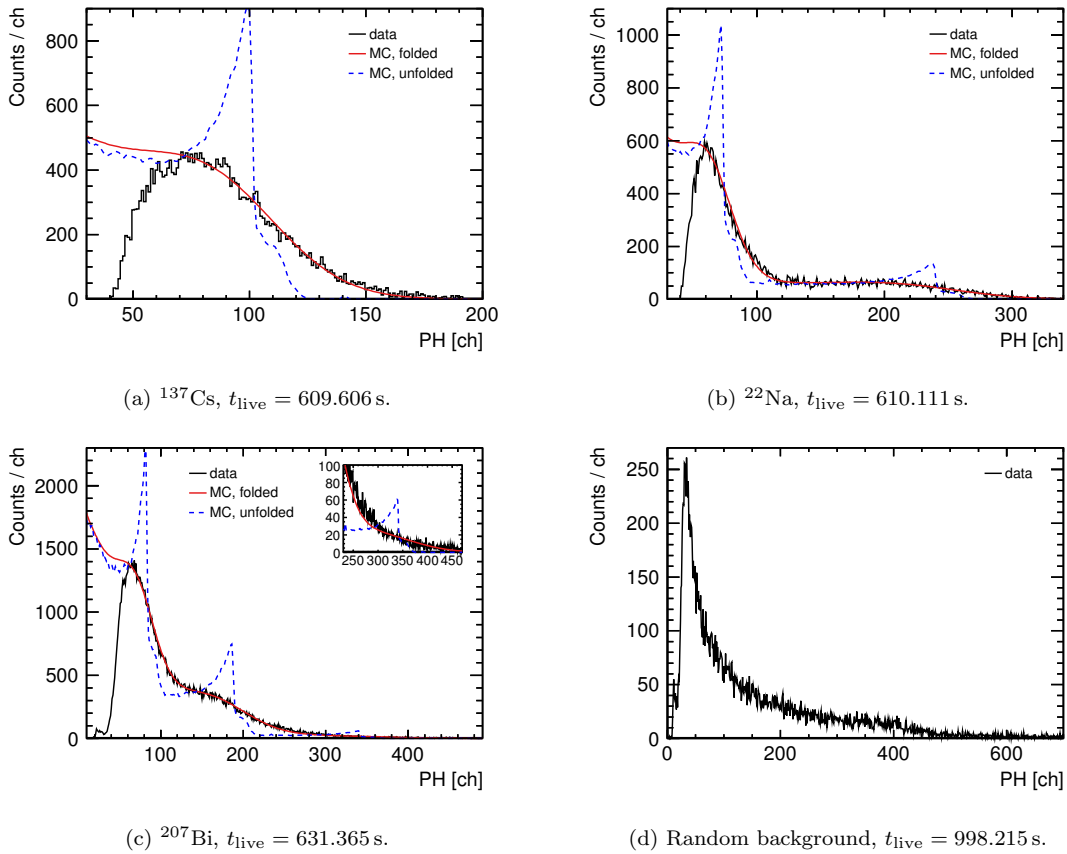


**Figure 6.9:** Pulse–height spectra in ADC channels (ch) of all used calibration sources (a–c) and of background only (d). The third  $\gamma$ -line of  $^{207}\text{Bi}$  is shown enlarged in the inset of (c). The background is subtracted from the source measurements after normalization to the respective livetime  $t_{\text{live}}$ . The data is taken with LAB + 3 g/1PPO + 0.1% Nd (LAB6) in HG mode.

#### 6.4.2 Simulation of the gamma response with GRESP7

The PH distribution produced by the gamma source is simulated with the three-dimensional gamma transport code GRESP7 [225] that was developed for calibration purposes. It follows the course of gammas from an external source within the scintillator volume, aluminum cell walls and light guide until the gamma escapes or its energy reaches the cut-off energy of 2 keV after scattering. Thus multiple gamma scattering is accounted for, which leads to the pile-up events above each Compton edge visible in the unfolded simulated distribution in Fig. 6.8, for instance. The interaction mechanisms included are photoelectric absorption and Compton scattering. Pair production is not considered since only gamma sources with energies up to 2.75 MeV were investigated at the time of development, which is not in conflict with the presented experiments, as explained above. Also Bremsstrahlung is not taken into account. It is assumed that the energy of the secondary electrons is fully deposited within the LS volume, provided that the distance between the interaction and the LS surface is greater than the mean range in the continuous–slowing–

down-approximation [224]. This simplified description of surface effects leads to less counts at low PHs in the simulation compared to data, as can be seen in Fig. 6.8. However, for the purpose of calibration, which only needs the position of the Compton edge, this description is fully sufficient. The Compton edges are very well reproduced, as also visible in Fig. 6.8. This is also the case for scintillators with a poor light yield as for instance LAB + 3 g/lPPO + 0.1% Nd, for which the calibration spectra are shown in Fig. 6.9. The marked difference between simulation and data right above zero is merely due to the fact that GRESP7 assumes zero threshold and thus does not model the low PH cut off due to a detector threshold. The detector threshold is irrelevant for the Compton edge position.

Despite the listed approximations, gamma spectra simulated with GRESP7 are in good agreement with measured spectra from calibration sources with energies up to about 3 MeV and a detector of appropriate geometry as also demonstrated in other experiments [225]. The specific dimensions are adjustable in an input file, as well as the density and H to C ratio of the light guide and specific scintillator. The energy distribution of gammas is simulated with infinite resolution and with a single gamma energy per calculation. The response of sources with multiple  $\gamma$ -lines is obtained by summing the individual spectra according to their percent gamma yield per decay. The particular detector PH resolution is determined in an iterative process, as explained in the following subsection.

#### 6.4.3 Data analysis

Having simulated the detector response to the calibration sources, each  $\gamma$ -line is evaluated independently in the first iteration. A fit interval is specified around the Compton shoulder in the measured spectrum and the simulation is adapted to that region in the horizontal and vertical scale after folding the distribution with a Gaussian resolution function. Within the adaption process, the full width at half maximum (FWHM)  $\Delta PH$  of the PH resolution is stepwise increased until the best agreement between simulation and data is found within a small interval around the Compton shoulder. The obtained scaling factors are applied to the unfolded spectrum and the Compton edge is located within the PH spectrum. Knowing the edge position, the relative resolution  $\Delta PH/PH$  at the respective PH is obtained. This procedure is repeated for each  $\gamma$ -line resulting in six data points  $\Delta PH/PH(PH)$ . The global PH resolution is parameterized by

$$\frac{\Delta PH}{PH} = \sqrt{\alpha^2 + \frac{\beta^2}{PH} + \frac{\gamma^2}{PH^2}}, \quad (6.5)$$

where  $\alpha$ ,  $\beta$  and  $\gamma$  are associated with the contributions from spatial dependence of the light collection efficiency, Poisson fluctuations of the photoelectron yield and electronic noise, respectively [225]. The intermediate values of  $\alpha$ ,  $\beta$  and  $\gamma$  are determined by a fit to the data points.

For the second iteration, the calculated spectrum is folded with the best fitting function Eq. 6.5 and only the normalization as well as the calibration of the pulse-height are

adjusted. Figures 6.8 and 6.9 demonstrate the good agreement between simulation and data after adaption for the two example LAB samples, except at the aforementioned mismodeled low PHs. The unfolded and rescaled GRESP7 distribution is as in the first iteration used to determine the PH at the sharp Compton edge and thus of electrons with energy  $E$  according to Eq. 6.4. This way, six data points  $PH_i(E_i)$  are determined per scintillator and gain setting, which are shown in Fig. 6.10 and 6.11, and a linear fit,

$$PH = m \cdot E + a, \quad (6.6)$$

is used for the analytic description of the relation between PH and electron energy.

The gain of the PMT was fixed by the LED stabilization module. Therefore, the calibration factor  $m$ , for which the best fit values are listed in Tab. 6.5, is also a measure of the light output, i.e. the detected light yield per unit deposited energy. Thus, in order to compare the influence of the scintillator on the observed light output, the calibration results are grouped together in one subfigure of Fig. 6.10 and 6.11, if the experimental settings were identical. In campaign C1 (Fig. 6.10a and 6.10b), the highest light output is observed for the scintillators with bis-MSB as second fluor additional to PPO. This instance is explained with the good PMT sensitivity and reflectivity of the internal detector cell coating (Fig. 6.5) around 430 nm, the peak emission wavelength of bis-MSB (Fig. 2.2), and the reduced sensitivity and reflectivity around 360 nm, the peak emission wavelength of PPO. The addition of Nd to LAB with PPO additionally suppresses the high energy tail of the PPO emission spectrum (Fig. 6.1), the wavelength region which matches the detector properties best, and thus further reduces the light output. LAB with 3 g/l PPO as well as LAB with 2 g/l PPO and 0.1% Nd, shown in Fig. 6.10c to 6.10f, are measured independently, thus the light outputs are not comparable with any other scintillator. The LAB based scintillators with water and PRS on the other hand have all been measured in the same campaign (C4) and the calibration lines are displayed together in Fig. 6.11a and 6.11b. The measurement with perylene (wsLAB4), instead of bis-MSB, as second wavelength shifter reveals the lowest light output, which is explicable with a mismatch between the emission spectrum of PPO and absorption spectrum of perylene, leading to a residual emission around 360 nm, as shown in Fig. 6.12. Not all PPO light is shifted to higher wavelengths at which the detector is more sensitive. The samples with bis-MSB instead show a comparatively high light output, where the one of LAB + 5% PRS + 1.5% water + 2 g/l PPO + 45 mg/l bis-MSB (wsLAB4) is higher than the one with 15 mg/l bis-MSB (wsLAB2) due to the higher secondary concentration. The scintillator with 0.3% Te + 5% PRS + 1.5% water + 2 g/l PPO + 15 mg/l bis-MSB (wsLAB1), however, has a slightly higher light output than expected. Te does not absorb light in the wavelength region of interest, thus a light output as in the case of wsLAB2 is to be expected, since the only difference is the isotope loading. A possible explanation is an uncertainty in the bis-MSB concentrations. A respective uncertainty has no influence on the comparison between wsLAB2 and wsLAB4, since wsLAB4 is gained from wsLAB2 by adding  $\sim 30$  mg/l bis-MSB, while it does affect a direct comparison between the

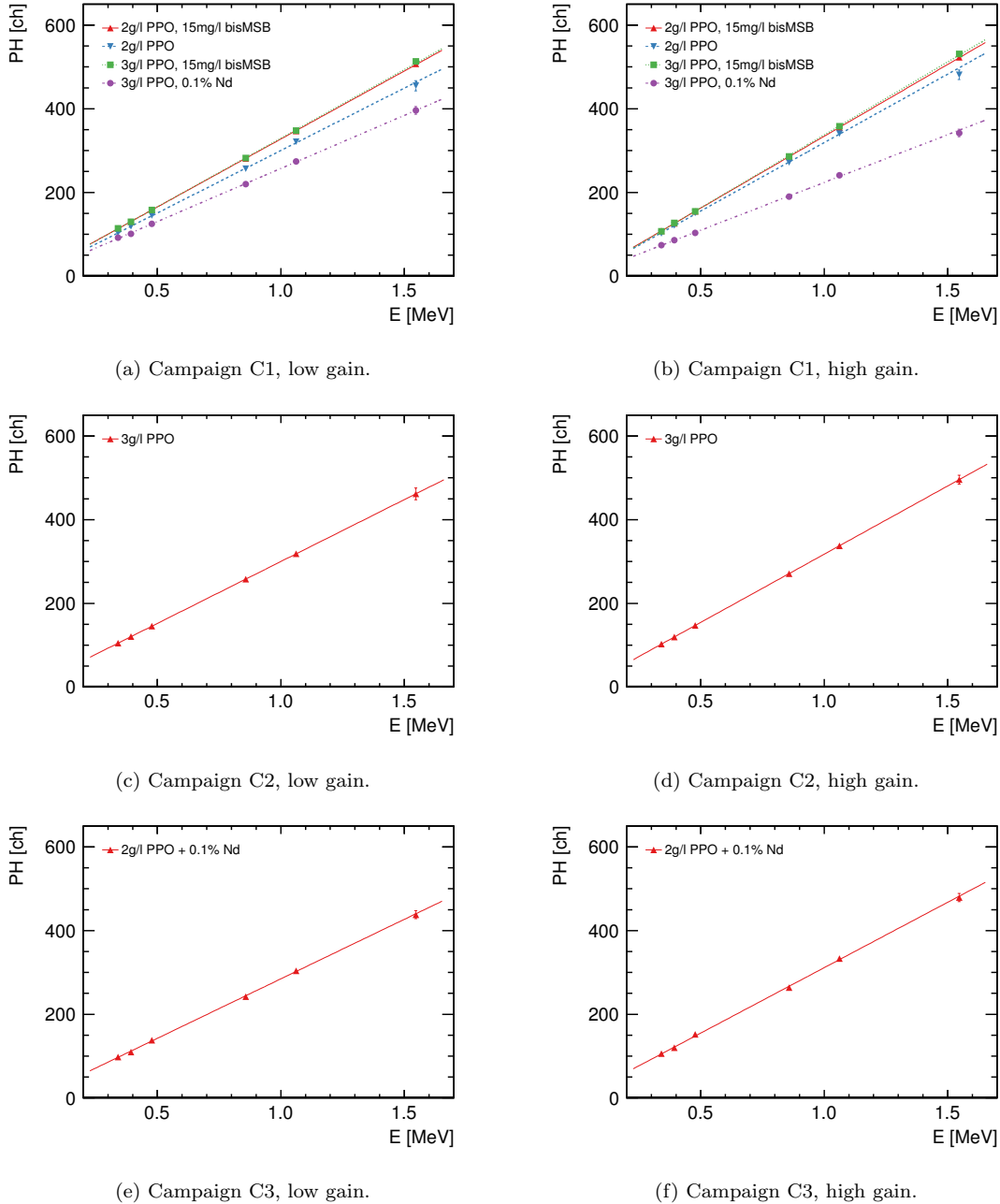


**Figure 6.10:** Pulse-height in ADC channels (ch) as function of electron energy  $E$  in LAB based scintillators. Shown is the data (markers) from all LAB measurements. The respective fluors are listed in the plot legends. The total uncertainties (the quadratic sum of the single contributions) are smaller than the markers, if not visible. The LG PH is measured with a range factor of 1 mV/ch, the HG PH with 4 mV/ch. A straight line is fitted to the data points (lines). The fit parameters are summarized in Tab. 6.5.

**Table 6.5:** Calibration factor  $m$  and PH offset  $a$  of all conducted measurements, obtained from a fit of Eq. 6.6 to the data points shown in Fig. 6.10 and 6.11. Given are the  $1\sigma$  uncertainties from the fit to data. The LG PH measurements are performed with a range factor of 1 mV/ch, while the HG PH and all PH measurements in the neutron field are performed with 4 mV/ch. Therefore, all LG fit results are divided by a factor of 4 before entering the table.

Scintillator	Gain	$m$	$a$	$\chi^2/\text{ndf}$
		[ch/MeV]	[ch]	
LAB1	LG	$81.2 \pm 0.9$	$0.7 \pm 0.5$	0.3/4
	HG	$343.2 \pm 3.7$	$-9.0 \pm 2.0$	0.1/4
LAB2	LG	$74.6 \pm 1.1$	$0.4 \pm 0.6$	1.0/4
	HG	$327.2 \pm 4.4$	$-8.1 \pm 2.1$	6.1/4
LAB3	LG	$81.9 \pm 1.0$	$0.4 \pm 0.5$	0.9/4
	HG	$348.3 \pm 3.8$	$-11.1 \pm 2.1$	1.1/4
LAB4	LG	$73.7 \pm 0.5$	$1.0 \pm 1.0$	3.3/4
	HG	$325.1 \pm 2.5$	$-1.0 \pm 3.0$	0.5/4
LAB5	LG	$71.1 \pm 1.0$	$0.1 \pm 0.5$	4.0/4
	HG	$312.6 \pm 4.4$	$-1.2 \pm 2.5$	4.6/4
LAB6	LG	$63.4 \pm 1.1$	$0.9 \pm 0.7$	2.0/4
	HG	$228.2 \pm 4.1$	$-4.3 \pm 2.5$	2.2/4
wsLAB1	LG	$77.6 \pm 0.6$	$0.2 \pm 0.4$	2.1/4
	HG	$612.4 \pm 1.1$	$-19.6 \pm 1.0$	0.7/4
wsLAB2	LG	$70.4 \pm 0.3$	$0.4 \pm 0.3$	0.6/4
	HG	$553.8 \pm 1.5$	$-15.7 \pm 1.9$	0.5/4
wsLAB3	LG	$57.7 \pm 0.4$	$0.2 \pm 0.3$	1.5/4
	HG	$450.4 \pm 2.9$	$-16.6 \pm 2.0$	2.4/4
wsLAB4	LG	$75.8 \pm 0.3$	$0.4 \pm 0.4$	1.0/4
	HG	$587.6 \pm 1.5$	$-13.8 \pm 1.9$	0.9/4

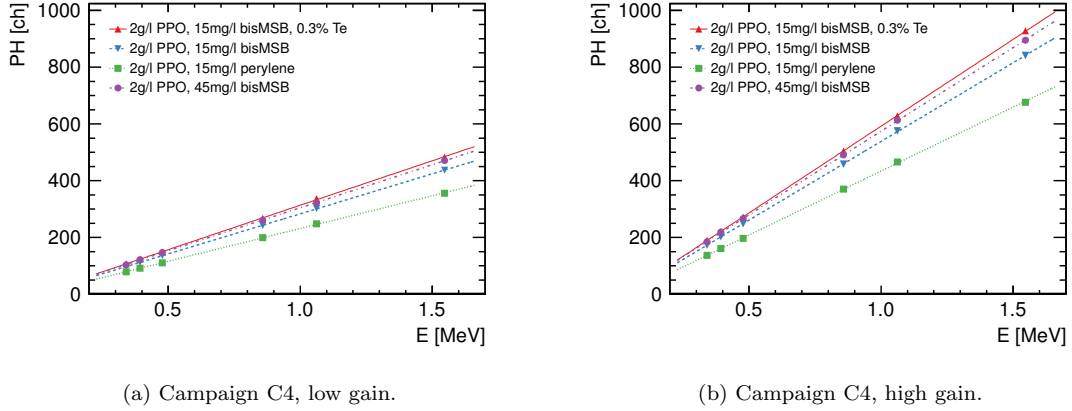


**Figure 6.11:** Pulse-height (PH) in ADC channels (ch) as function of electron energy  $E$  in wsLAB scintillators with 5% PRS and 1.5% water. Shown is the data (markers) from all wsLAB measurements. The respective fluors are listed in the plot legends. The total uncertainties (the quadratic sum of the single contributions) are smaller than the markers, if not visible. The LG PH is measured with a range factor of 1 mV/ch, the HG PH with 4 mV/ch. A straight line is fitted to the data points (lines). The fit parameters are summarized in Tab. 6.5.

Te-loaded wsLAB with the unloaded scintillators with bis-MSB.

The parameter  $a$  is included in the fit function Eq. 6.6 to account for the slightly non-linear behavior at low electron energies [33, 212, 226], not covered by the sources used in this calibration and leading to a small energy offset  $E_0$ , as well as systematic effects, such as a remaining electronic offset of the amplifiers  $PH_{\text{off}}$ , resulting in

$$a = PH_{\text{off}} + E_0. \quad (6.7)$$

A non-physical shift of the PH scale needs to be corrected during data analysis. In the presented measurements, though, a respective shift cannot be separated from the energy offset  $E_0$  due to the electron response non-linearity and external measurements of  $E_0$  for wsLAB scintillators do not exist yet. Thus  $E_0$  is taken to be zero in the following and the causes of a finite  $E_0$  and its influence on heavy particle ( $m \gg m_e$ ) ionization quenching measurements is discussed in Sec. 6.7.

For the analysis of beam data and its experiment independent comparability, the PH is converted into light yield  $L$  in units of electron-equivalent energy. The linear region of the electron light response  $L_e$  is described by

$$L_e(E) = S \cdot (E - E_0), \quad (6.8)$$

where  $S$  is an arbitrary scaling factor. It is set to  $S = 1$ , to obtain the scale in electron-equivalent energy, and  $L_e$  is determined from measurement using Eq. 6.6. In the special case of  $E_0 = 0$ , Eq. 6.8 simplifies to  $L_e(E) = E$ . The subscript in  $L_e$  is added to emphasize

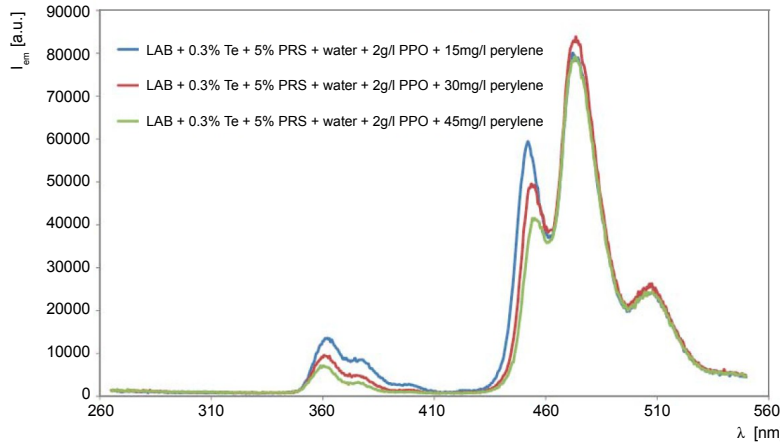


**Figure 6.12:** Emission spectra of wsLAB + 0.3% Te + 2g/l PPO and different concentrations of perylene, as specified in the plot legend. The emission is stimulated with an excitation wavelength  $\lambda_{ex} = 260\text{ nm}$  and its intensity  $I_{em}$  is shown in arbitrary units (a.u.) (Courtesy of M. Yeh).

that Eq. 6.8 is only valid for electrons, it does not introduce a new variable. Expressing the PH scale in light yield, Eq. 6.5 is given in its universal form

$$\frac{\Delta L}{L} = \sqrt{\alpha^2 + \frac{\beta^2}{L} + \frac{\gamma^2}{L^2}}, \quad (6.9)$$

which allows a comparison of light output resolutions from different measurement campaigns.

The final resolution parameters  $\alpha$ ,  $\beta$  and  $\gamma$  are determined by an adaption of Eq. 6.9 to  $\Delta L/L$ . Figures 6.13 and 6.14 show the resulting data points and resolution functions for all scintillator samples and amplification modes as a function of the light output and the fit results are summarized in Tab. 6.6. The grouping in Fig. 6.13 and 6.14 follows the grouping in Fig. 6.10 and 6.11, where results of the same measurement campaign and amplification mode are shown in the same subfigure. However, while in the case of calibration lines a comparison is only possible within one campaign and gain mode, a general comparison is possible in this case, which reveals a similar behavior for scintillators with the same secondary solutes. Scintillators with only PPO as fluor have a relative light yield resolution from about 60% to 40%, the scintillator with perylene as second fluor has a resolution from about 40% to 30% and the scintillators with bis-MSB have a resolution from about 30% to 20%. This observation is consistent with the fact that the PPO emission spectrum matches the wavelength dependent sensitivity of the detector the least, an instance improved by the addition of perylene, which shifts a substantial part of PPO light to higher wavelengths and thus detector sensitivity, and eradicated by an addition of bis-MSB, which shifts all PPO light to higher wavelengths. A conclusion to be drawn from Fig. 6.14 compared to Fig. 6.13 is that 5% PRS and 1.5% water content does not significantly change the resolution in small scale detectors, where different scattering lengths have less or even negligible impact. Also the total light yields of pure LAB and LAB with 5% PRS and 1.5% water differ only by about one standard deviation [189], a difference that is not resolved within the uncertainties of the resolution measurement. It

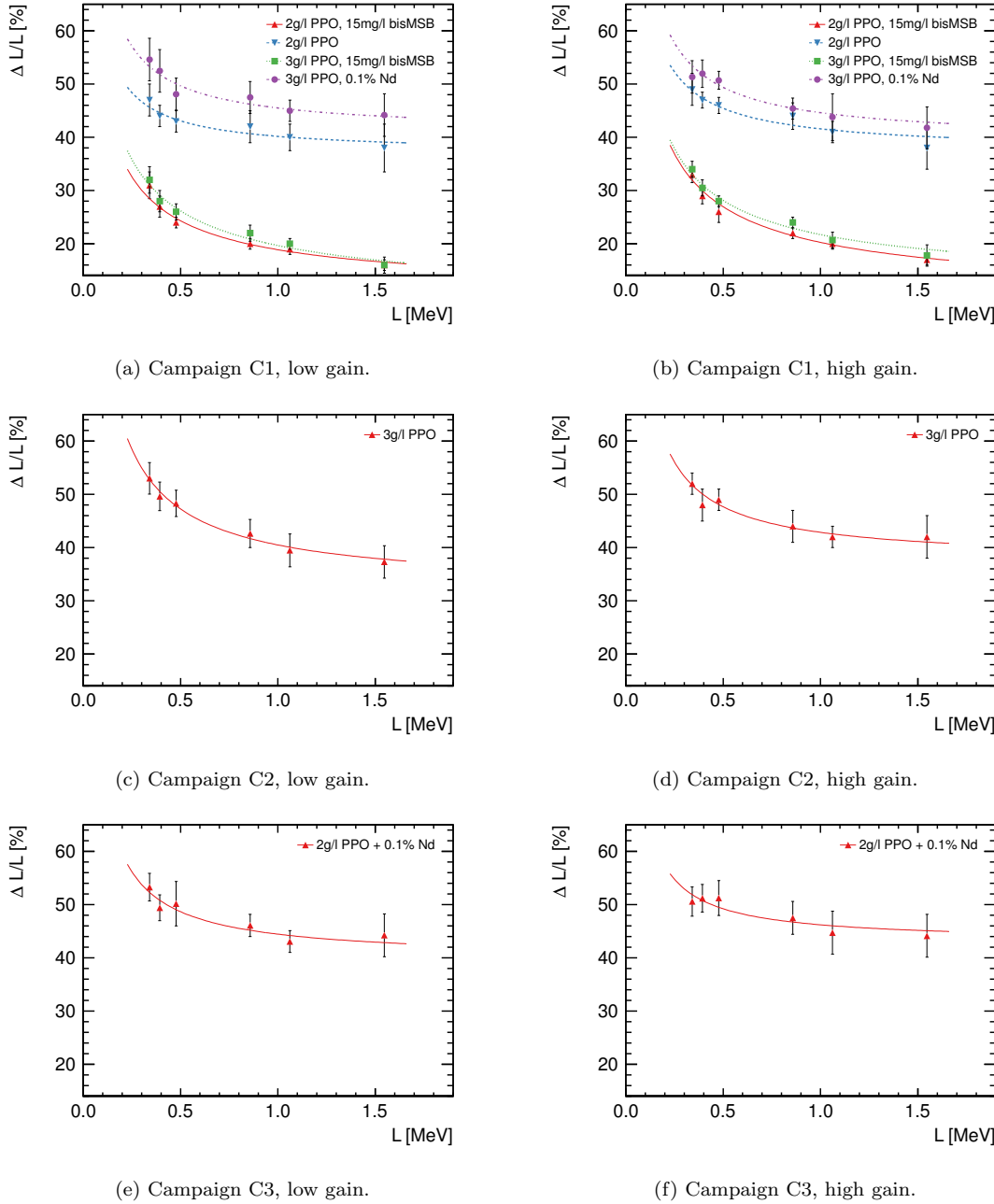


**Figure 6.13:** Relative light output resolution  $\Delta L/L$  as a function of light output for gamma-induced events in LAB based scintillators measured during campaigns C1–C3. The respective fluors to LAB are listed in the plot legends. The shown total uncertainties are the quadratic sum of the single contributions. The lines follow a fit of Eq. 6.9 to the data. The fit results are summarized in Tab. 6.6.

**Table 6.6:** Light output resolution parameters  $\alpha$ ,  $\beta$ ,  $\gamma$  from fitting Eq. 6.9 to data (see Fig. 6.13 and 6.14).  $\gamma$  is fixed to 0.5%, a value known to be between 0.2% and 0.5% from a wide range of measurements at PIAF using scintillators with better resolution [212, 225, 227]. Fixing  $\gamma$  to 0.2% showed no difference in the results.

Scintillator	Gain	$\alpha$	$\beta$	$\gamma$	$\chi^2/\text{ndf}$
		[%]	[%]	[%]	
LAB1	LG	$11.1 \pm 2.2$	$15.3 \pm 1.2$	0.5	2.0/4
	HG	$9.8 \pm 2.1$	$17.7 \pm 0.9$	0.5	1.8/4
LAB2	LG	$37.1 \pm 3.2$	$15.5 \pm 3.8$	0.5	0.6/4
	HG	$37.4 \pm 2.7$	$18.3 \pm 2.8$	0.5	0.9/4
LAB3	LG	$9.5 \pm 2.5$	$17.2 \pm 1.2$	0.5	2.4/4
	HG	$12.4 \pm 2.5$	$17.9 \pm 1.1$	0.5	2.7/4
LAB4	LG	$32.4 \pm 3.5$	$24.3 \pm 2.6$	0.5	0.4/4
	HG	$37.5 \pm 2.8$	$20.8 \pm 2.7$	0.5	0.8/4
LAB5	LG	$39.8 \pm 2.7$	$19.8 \pm 3.1$	0.5	1.2/4
	HG	$43.0 \pm 3.6$	$16.9 \pm 4.5$	0.5	0.8/4
LAB6	LG	$40.9 \pm 3.1$	$19.9 \pm 4.1$	0.5	0.8/4
	HG	$39.3 \pm 3.4$	$21.1 \pm 3.4$	0.5	0.9/4
wsLAB1	LG	$17.8 \pm 3.4$	$14.9 \pm 2.1$	0.5	0.9/4
	HG	$16.5 \pm 3.5$	$17.1 \pm 1.8$	0.5	1.1/4
wsLAB2	LG	$17.0 \pm 3.3$	$15.6 \pm 1.9$	0.5	0.1/4
	HG	$15.4 \pm 3.8$	$18.7 \pm 1.7$	0.5	0.8/4
wsLAB3	LG	$18.8 \pm 5.3$	$22.4 \pm 2.5$	0.5	0.1/4
	HG	$23.6 \pm 4.5$	$21.5 \pm 2.5$	0.5	3.0/4
wsLAB4	LG	$14.5 \pm 4.9$	$14.9 \pm 2.7$	0.5	0.3/4
	HG	$14.9 \pm 4.7$	$15.2 \pm 2.4$	0.5	0.8/4

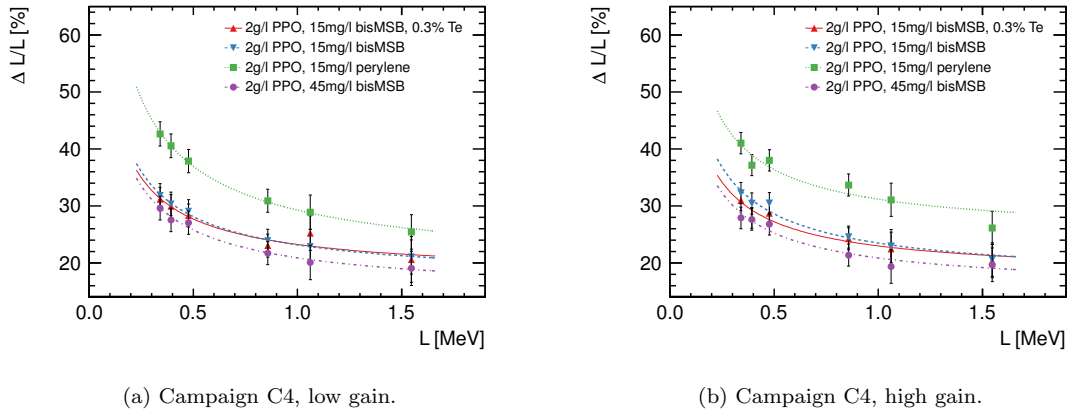


**Figure 6.14:** Relative light output resolution  $\Delta L/L$  as a function of light output for gamma-induced events in wsLAB scintillators with 5% PRS and 1.5% water measured during campaign C4. The respective fluors to wsLAB are listed in the plot legends. The shown total uncertainties are the quadratic sum of the single contributions. The lines follow a fit of Eq. 6.9 to the data. The fit results are summarized in Tab. 6.6.

is worthwhile mentioning that the electron light output resolution observed with LAB based scintillators is much lower than the resolution observed with NE213 scintillator in detectors of the same geometry and dimension, as presented for instance in [212, 225, 227].

## 6.5 Beam data analysis

The analysis of the beam data is subdivided into four main steps: data cleaning, determination of the relative light output resolution in case of neutron-induced events, determination of the proton light output function and determination of the  $\alpha$ -particle light output function. The latter step, however, is not possible for all scintillators listed in Tab. 6.1. The resolution of LAB based scintillators without bis-MSB, i.e. LAB2, LAB4, LAB5 and LAB6, is too low for the respective analysis and no alpha quenching parameters can be determined with the collected data. Furthermore, the cyclotron performance during the measurement of wsLAB3 and wsLAB4 in C4 was severely unstable and the timing structure corrupted. These two samples are only usable for comparisons of PSD capabilities. Except for these two specimens, the proton quenching parameters are determined for all scintillators with high accuracy and the alpha quenching parameters for two LAB based scintillators and two wsLAB scintillators are determined. The behavior of the proton response within the different samples and the subset in which also alpha quenching is measured allows to formulate an expectation of the alpha responses also for those samples, for which an alpha quenching analysis was not possible.

### 6.5.1 Data cleaning

Data cleaning comprises the online discrimination of gamma-induced events and the offline reduction of satellite pulse events and random background. The necessity of a so-called time-walk correction due to the dependence of the TOF measurement on the PH has been investigated.

#### Time-walk correction

The time-walk is a PH dependent shift of the measured neutron TOF values towards neighbouring TOF channels, which shows up in particular at small pulse-heights. It is caused by imperfections in the constant fraction timing technique employed in the CFD module, as described in [211]. Time-walk leads to a distortion of the TOF-PH parameter space and consequently in the extracted proton recoil spectra at low PHs. A correction of the TOF-PH matrices of LAB + 2 g/l PPO + 15 mg/l bis-MSB revealed a deviation of only about 0.7765 ns in the TOF spectrum, while the smallest TOF window width, selected for the PH spectra extraction from the TOF-PH matrix, has a width of 3.8825 ns. This width is chosen at high neutron energies, where the detector resolution allows the narrowest TOF window. At low neutron energies, and thus low resolution, the window width is enlarged to 19.4125 ns. In the evaluation of LAB + 2 g/l PPO + 15 mg/l bis-MSB, a walk-correction of 0.7765 ns showed no significant influence on the results. This scintillator has the highest light output resolution of all the investigated LAB based samples and therefore the smallest possible TOF window widths. Thus, the time-walk effect is also expected to be negligible for the all other samples. Because of these findings and since a correction of the TOF-PH matrices can bring in new artifacts due to the binned structure of the data, no time-walk correction is performed within these analyses.

#### Pulse-shape discrimination

The PS is related to the decay time of the light pulse and thus to the incident particle passing the scintillator. Electrons have a smaller intensity ratio of the slow and the fast scintillation component than ions and the light pulse decays faster, resulting in a smaller PS value. Due to this behavior, a separation in the PH-PS parameter space occurs between gamma-induced events, i.e. electrons, and neutron-induced events, which are mainly protons and  $\alpha$ -particles, as clearly visible in the PH-PS matrix of PC + 1.5 g/l PPO + 15 m/l bis-MSB shown in Fig. 6.15. A discrimination of events with a PS signal below the indicated line reduces  $\gamma$ -induced background events in the PH signal spectra of  $n$ -induced events. The strength of this separation and thus the capability of PSD depends on the PH resolution and on the difference in the signal waveforms of electron and ion light pulses.

Figure 6.16 shows PH versus PS for different LAB and wsLAB scintillators over the full dynamic range and therefore in LG mode. The remaining figures in LG mode are attached in Fig. B.19. The influence of the PH resolution is clearly recognizable. The best

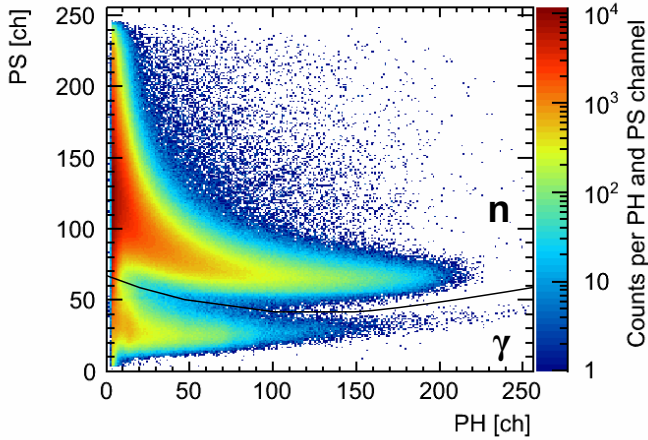


**Figure 6.15:** PH–PS parameter space of all events detected with PC + 1.5 g/l PPO + 15 mg/l bis-MSB during beam run in LG mode. The structures labeled with ‘ $n$ ’ and ‘ $\gamma$ ’ are caused by charged particles resulting from neutron interactions with the scintillator and by Compton electrons from photon interactions, respectively. The cut used to separate  $n$ - and  $\gamma$ -induced events is indicated by the black solid line.

separation occurs in the LAB sample with bis-MSB (Fig. 6.16a), followed by the LAB sample with only PPO as fluor (Fig. 6.16b) in which the separation is already strongly blurred. In case of the sample without bis-MSB but with Nd (Fig. 6.16c), a separation between  $n$ -induced and  $\gamma$ -induced events is only indicated faintly,  $n/\gamma$ -discrimination is not feasible anymore. This observation is confirmed in the measurements using wsLAB scintillators, in which the scintillator with the lowest resolution, the one with perylene as second fluor, has the least PSD capability (Fig. 6.16f). The difference in the overall pattern between LAB and wsLAB scintillators cannot be explained at this point. Obviously the addition of water and PRS worsens the PSD. For a conclusive statement, however, measurements of the individual waveforms from electrons, protons and  $\alpha$ -particles would be necessary and had to be compared quantitatively.

A comparison with Fig. 6.15 reveals that PC with PPO and bis-MSB shows a more prominent separation than all LAB and wsLAB scintillators, which is amongst others attributed to a higher light output, and thus PH resolution, of PC. Within all measurement campaigns, the PC scintillator had the highest light yield, manifesting itself in the lowest necessary delay line amplification. However, also in this case, the individual waveforms would have to be compared for a quantitative statement.

To summarize, PSD is less efficient, and partly even not feasible, for all LAB based scintillators compared to PC and a loss of signal or remaining background is unavoidable. The  $\gamma$ -induced background originates from ambient background, which is measured individually, from prompt gammas produced in inelastic scattering in the Be target, which are discriminated via TOF and from inelastic scattering in the scintillator and detector housing. Only the last class of gammas cannot be suppressed by other means and needs to be considered in the evaluation of PH spectra.

These investigations also reveal that  $n/\gamma$ -PSD using the zero crossing technique is not

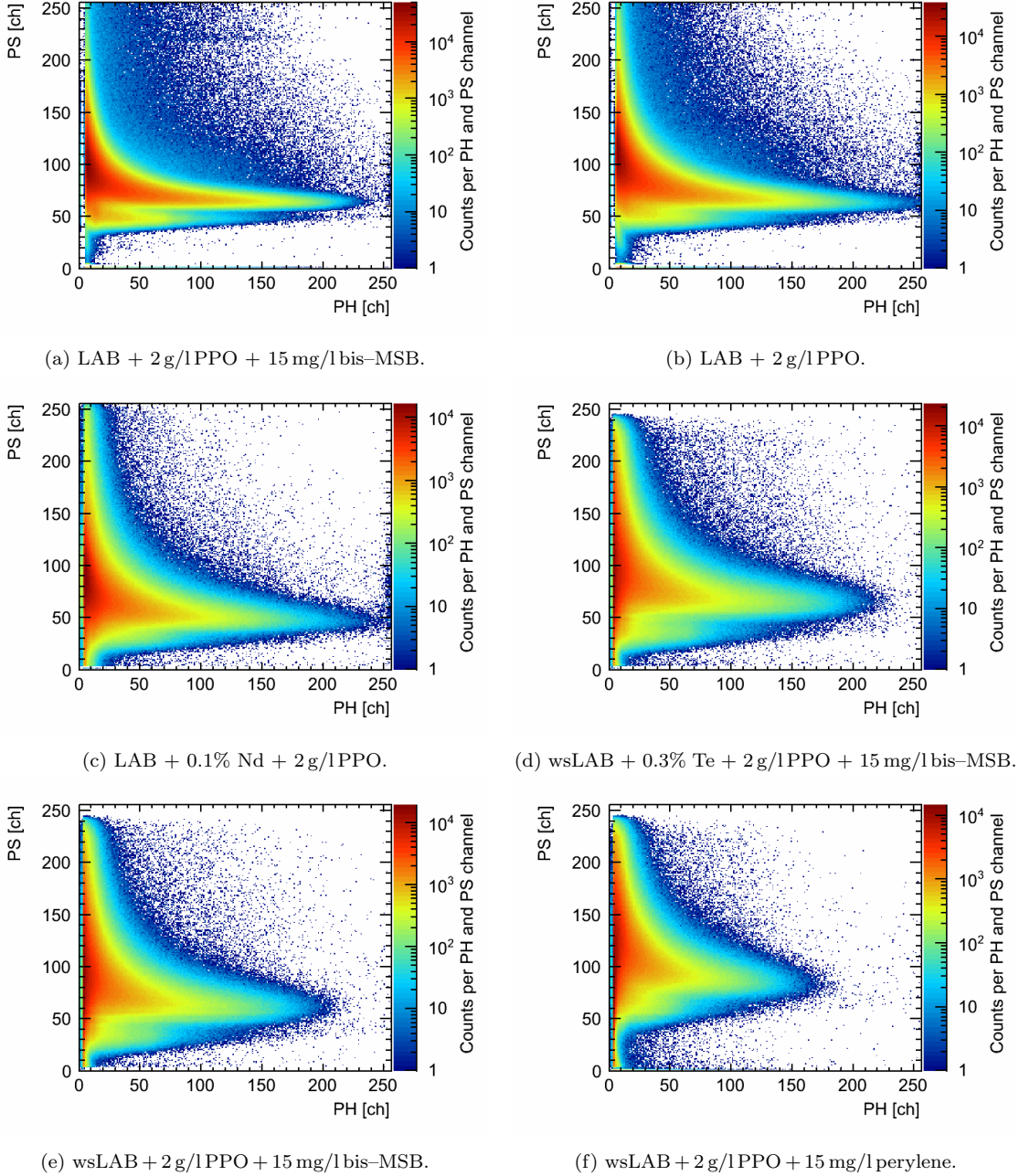


**Figure 6.16:** PH-PS parameter space of all events detected with LAB and wsLAB scintillators during beam run in LG mode. The individual compositions are written in the subcaptions. The wsLAB contains 5% PRS and 1.5% water.

promising for LAB based scintillators. For experiments in which  $n/\gamma$ -PSD is more crucial than in the given one, the use of an alternative method is strongly recommended. A compilation of methods is presented in [228], for instance. These findings are not contradictory to the good  $\alpha/\beta$ -PSD capability of LAB presented in [229].  $n/\gamma$ -PSD involves not only the separation between  $\alpha$ - and  $\beta$ -particles, but between all  $n$ - and  $\gamma$ -induced events and thus also protons. Protons are less ionizing than  $\alpha$ -particles and therefore have a smaller slow scintillation component than  $\alpha$ -particles. The signal waveform is more similar to the one of  $\beta$ -particles and while the difference in the shape of the waveform can still be strong enough for  $\alpha$ -particles, the same is not necessarily true anymore for protons.

### Satellite pulse event reduction

The parameter space of interest for the determination of the proton and alpha responses is the TOF-PH parameter space, displayed in Fig. 6.17. The slide-shaped main distribution is caused by neutrons of different energies. The fastest neutrons reach the highest TOF value ( $\sim 740$  ch in the given figure) and lead to the maximum possible proton recoil energy and thus PH. The slower the neutrons, the lower the observed maximum PH, which is equivalent to the proton recoil edge to be determined. Thus a sharp border of the distribution is desirable.  $\alpha$ -particles instead cause low PH events, thus also the region well below the edge is of importance.

Spurious events caused by satellite pulses can compromise the determination of the position of the recoil proton edge and  $\alpha$ -particle structures, depending on the satellite event yield. Figures 6.17a and 6.17b demonstrate close to ideal measurements in this regard, while Fig. 6.17c and 6.17d show additional faint distributions from satellites, shifted in TOF relative to the main distribution. Since satellite pulses cannot be entirely suppressed using the pulse shortener, an offline correction is performed, if the intensity of satellites in the ROI is too high. The spectral distribution of satellite neutron fields is assumed to be the same as of the main one. A reduction can thus be achieved by normalizing the main distribution to the satellite distribution, shifting the result in the horizontal direction to the position of the respective satellite distribution and subtracting it from it. An exemplary TOF-PH matrix before and after this procedure is displayed in Fig. 6.18. To obtain the normalization factor for a specific satellite pulse, the integral of its distributions is calculated over a PH interval in which no further distribution is present. The interval chosen for the correction presented in Fig. 6.18 ranges from 300 ch to 1024 ch on the PH axis. Additionally, the integral of the main pulse distribution is calculated over the same PH interval. The ratio of the two integrals yields the ratio of the satellite and the main pulse intensities and thus the normalization factor.

This procedure has a clear deficit. The full main pulse distribution is normalized and subtracted from the satellite pulses. However, not the full main distribution is isolated, but overlapping with satellites at low PH. Also the satellite distributions are overlapping

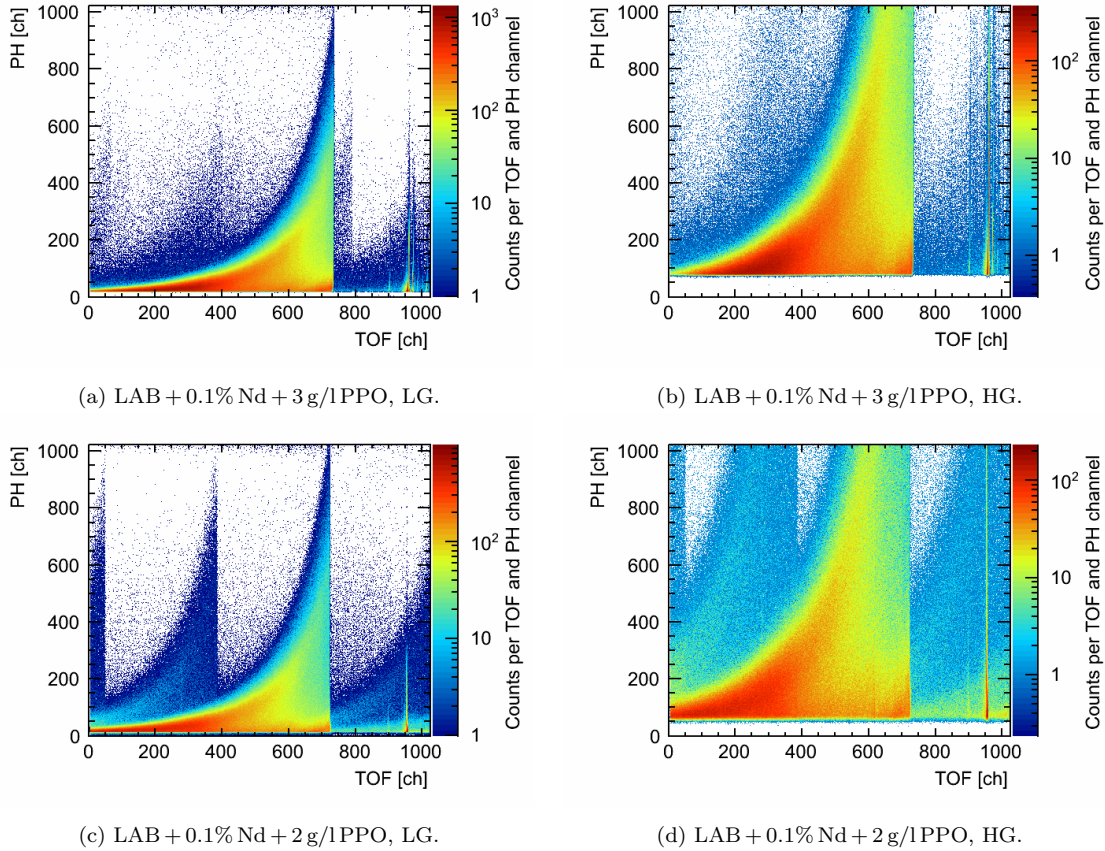


**Figure 6.17:** TOF–PH parameter space of all events detected with LAB4 (a, b) and LAB5 (c, d) during beam run in LG and HG mode. In the measurements shown in (a) and (b), satellite proton bunches were efficiently suppressed, while in (c) and (d) distributions caused by satellites are clearly recognizable.

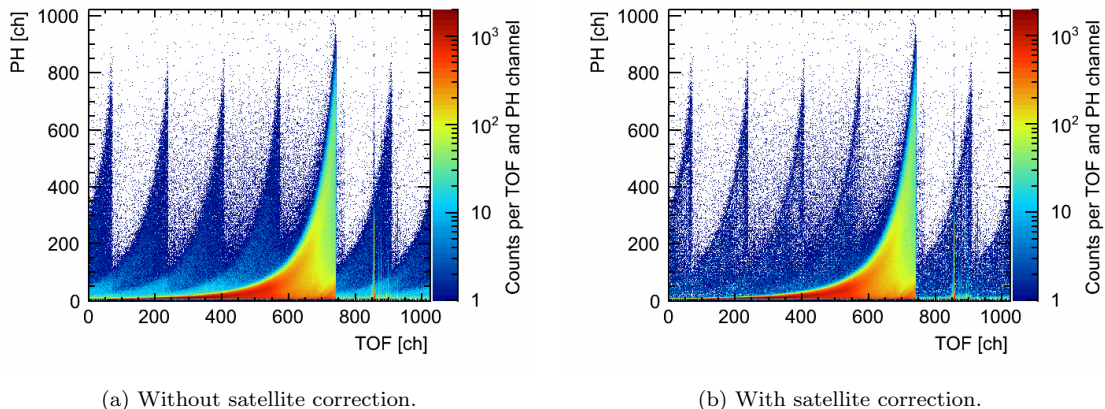


**Figure 6.18:** TOF–PH parameter space of events detected with wsLAB + 0.3% Te + 2 g/lPPO + 15 mg/lbis-MSB in LG mode, before (a) and after (b) offline satellite correction.

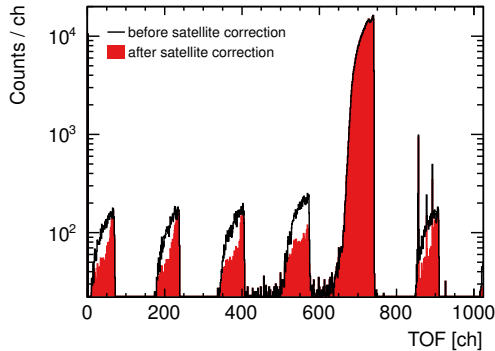


**Figure 6.19:** TOF distribution of events with PHs above 300 ch in wsLAB + 0.3% Te + 2 g/l PPO + 15 mg/l bis-MSB before and after a slight offline satellite correction.

with other satellite distributions, as clearly visible in Fig. 6.18a. Since the satellite events within the main pulse distribution are necessarily normalized with the same factor as main pulse events, their intensity is reduced too much compared to the satellite events of one satellite pulse within the distribution of another satellite. The suppression is thus incomplete in the overlap regions. Furthermore, to avoid new artifacts due to the binned data structure, as mentioned for the case of time-walk correction, only a partial correction is performed. This means, a higher normalization factor is used, than obtained from the satellite to main pulse to intensity ratio.

The projection of the PH interval on the TOF axis before and after partial satellite correction is shown in Fig. 6.19. It should be noted that in all measurements the intensity of satellites is about two orders of magnitude lower than the main beam pulse intensity, except in the measurements with LAB5 (Fig. 6.17c, 6.17d), in which the intensity is between one and two orders of magnitude lower, and wsLAB3 and wsLAB4 with only about one order of magnitude lower satellite intensity. This exceptionally large satellite intensity was caused by technical problems with the pulse selection system. However, LAB5 is only used for proton quenching evaluation due to the poor resolution of LAB without bis-MSB, which makes an alpha quenching evaluation impossible. The determination of the proton edge, instead, is feasible despite the low resolution and is less sensitive to satellite background. Moreover, above TOF channel 400, the proton edge is free from satellites for this LS, as clearly visible in Fig. 6.17c. 400 ch correspond to a neutron energy of about 3.5 MeV in the respective measurement, while neutron energies from about 1.5 MeV to about 17 MeV are used for the quenching analysis. Thus most of the analysis of LAB5 data remains unaffected by satellites.

Although in the case of wsLAB3 and wsLAB4, the resolution is high enough to measure also the  $\alpha$ -particle light response, intense satellites (see the HG measurements Fig. 6.20), complicate the analysis, since the tail of the satellite ahead of the main distribution overlaps with the PH region of  $\alpha$ -particle events, which occur at low PHs. At this point, the alpha quenching analysis for these two scintillators is already questionable. Furthermore, the timing structure of the data from all runs was tested thoroughly, which

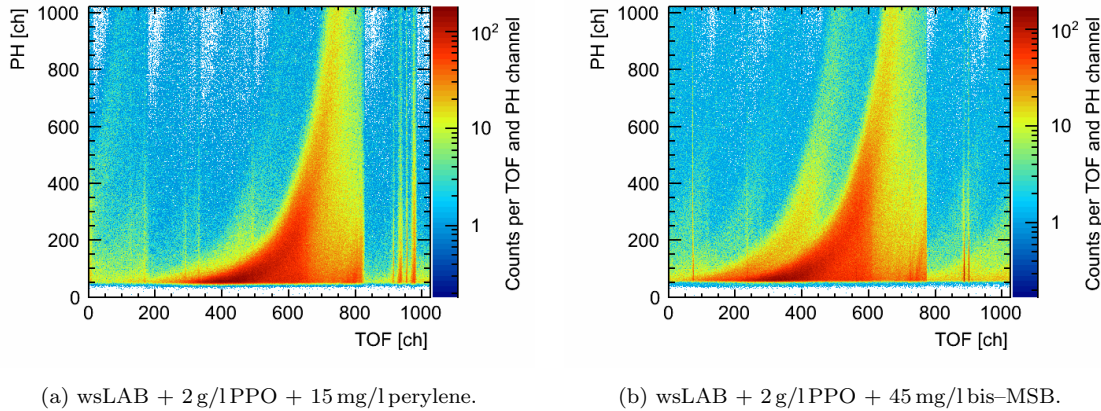


**Figure 6.20:** TOF–PH parameter space of events detected with wsLAB3 (a) and wsLAB4 (b) in HG mode with enhanced occurrence of satellites.

revealed that it is corrupted in the case of these two runs. The corresponding sets of neutron beam data thus do not provide reliable neutron energy information and are not considered for the following analyses anymore.

The prominent line ahead of the main neutron distribution, visible in all TOF–PH matrices, is caused by prompt gammas that are produced simultaneously with the neutrons in the Be target through inelastic scattering. They cause the earliest signal in time and consequently entries well above the highest neutron TOF value. Depending on the cyclotron performance, gammas that are produced elsewhere in the cyclotron due to a misalignment may emerge and cause additional but less intense lines (see e.g. Fig. 6.17a, 6.17b). Only in the measurement with wsLAB3 (Fig. 6.20a), also these gamma lines are very intense, because of the technical problems mentioned above. Also satellite proton bunches generate prompt gammas, which can cause additional gamma-induced background in the region of the main neutron distribution, depending on the time difference between main pulse and subsequent satellite(s). These events do not affect the location of the proton recoil edge, but they can fall in the region of  $\alpha$ -particle structures. PSD does not fully suppress gamma-induced events. However, the location of prompt gammas in the TOF spectrum is known from the TOF difference between the sharp TOF edge at maximum neutron energy and gammas traveling at the speed of light, which is the same for satellites and the main distribution. In the presence of intense satellites, this part of the TOF spectrum is not included in the alpha response evaluation.

### Random background reduction

Random background are registered signals that are neither produced by calibration source gammas nor by particles produced in the target. They are mainly due to ambient gammas from the walls. Random background is expected to be uniformly distributed over all TOF channels and to be higher the lower the PH. Background only measurements are performed

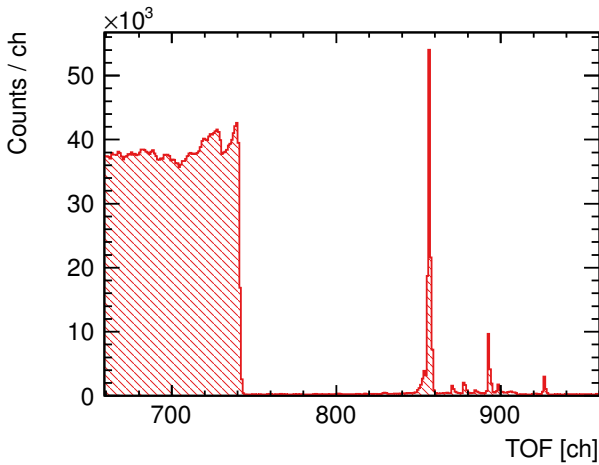


**Figure 6.21:** TOF distribution in wsLAB + 0.3% Te + 2 g/l PPPO + 15 mg/l bis-MSB, measured in LG mode, after satellite and random background correction. The high energy part of the neutron continuum is visible, ending in channel 741. The broadened (see text) prompt gamma line is at higher TOF with the centroid at  $(855.7 \pm 1.0)$  ch.

in the course of calibrations (see e.g. Fig. 6.8d), lasting about 10 min, and are scaled to the individual source and beam measurements. In case of a negligible presence of satellites, the random background collected over the entire beam measurement duration of  $\gtrsim 1$  h is known from the signal free region between the fastest neutrons and prompt gammas. This region refers in Fig. 6.17 to the TOF channel interval from about 750 ch to 900 ch. These figures, however, demonstrate that satellite events superpose possible random background events. For this reason, random background is subtracted using the background measurements, taking into account that PHs were recorded at 1 mV/ch during LG calibrations and background measurements, while they were recorded at 4 mV/ch during all other measurements.

### 6.5.2 Extraction of pulse-height spectra from quasi mono-energetic neutrons

Precondition of the analysis of proton and alpha PH spectra, and thus light responses, is the knowledge of the particle energy and thus of the incoming neutron energy. Therefore, small consecutive TOF windows, each around a value corresponding to a particular neutron energy, are set in the TOF-PH parameter space. The projection of a single TOF interval on the PH axis yields the desired spectrum of a quasi mono-energetic neutron. The TOF, or energy, window width is always kept smaller than the energy window corresponding to the light output resolution. Since the light output resolution for neutron induced events is not known from the beginning, but estimated from existing measurements with other scintillators, the entire analysis is an iterative process. The TOF channel containing neutrons with the energy of interest is determined using the TOF difference between neutrons and prompt gammas and the time calibration parameter  $c_{\text{tcal}}$  quoted in Tab. 6.4:

$$p_n = p_{pg} - \left( \frac{d}{v_n} - \frac{d}{c} \right) \cdot c_{\text{tcal}}^{-1}, \quad (6.10)$$

**Table 6.7:** Prompt  $\gamma$ -peak centroid in LG and HG TOF measurements. The total uncertainty is dominated by the uncertainty from the choice of the TOF interval included in the centroid calculation, as explained in the text.

Sample	$p_{pg}$ (LG) [ch]	$p_{pg}$ (HG) [ch]	Interval (LG) [ch]	Interval (HG) [ch]
LAB1	$955.0 \pm 0.9$	$954.7 \pm 0.9$	[936,962]	[936,962]
LAB2	$956.5 \pm 0.9$	$956.1 \pm 0.9$	[938,964]	[938,964]
LAB3	$956.7 \pm 0.8$	$956.7 \pm 0.8$	[938,964]	[938,964]
LAB4	$956.6 \pm 0.6$	$956.4 \pm 0.6$	[935,964]	[935,964]
LAB5	$953.7 \pm 0.6$	$953.4 \pm 0.6$	[940,960]	[940,960]
LAB6	$957.5 \pm 0.9$	$958.1 \pm 0.9$	[938,964]	[938,964]
wsLAB1	$855.7 \pm 0.8$	$855.7 \pm 0.8$	[840,862]	[840,862]
wsLAB2	$877.4 \pm 0.7$	$876.4 \pm 0.7$	[865,882]	[865,882]

where  $p_n$  is the neutron position in the TOF spectrum and  $p_{pg}$  the prompt gamma position. The neutron velocity  $v_n$  is calculated following Eq. 6.2, the target to cell distance  $d$  of each campaign is recorded in Tab. 6.3. A finite time resolution of the accelerator leads to a broadening of the prompt  $\gamma$ -line in the TOF spectrum, as exemplarily shown in Fig. 6.21, and the centroid position

$$p_{pg} = \sum_i \frac{c_i \cdot y_i}{Y} \quad (6.11)$$

of the resulting  $\gamma$ -peak is used. The TOF distributions of all samples are attached in Fig. B.20. In this,  $y_i$  is the number of counts recorded in the  $i$ -th TOF channel  $c_i$  and  $Y$  is the sum of all counts within the peak area

$$Y = \sum_i y_i. \quad (6.12)$$

The uncertainty of the centroid peak position is determined from

$$\sigma_{p_{pg}} = \frac{\sigma_{c_i}}{\sqrt{Y}} \quad (6.13)$$

with

$$\sigma_{c_i} = \sqrt{\sum_i \frac{y_i(c_i - p_{pg})^2}{Y}}. \quad (6.14)$$

The centroid peak positions of all samples are listed in Tab. 6.7 for both gain modes together with the TOF interval used for the centroid calculation. The magnitude of the uncertainties is owed to the dependence on the TOF interval boundaries set close around the  $\gamma$ -peak and the influence of the tails of adjacent  $\gamma$ -peaks. This uncertainty

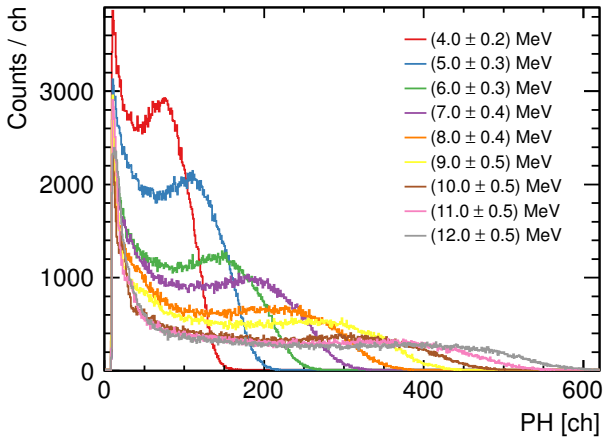


**Figure 6.22:** PH spectra of quasi mono-energetic neutrons in wsLAB + 0.3% Te + 2 g/l PPO + 15 mg/l bis-MSB measured in LG mode. The respective incoming neutron energy is given in the plot legend. The uncertainty corresponds to the TOF window width used for extraction. The window width is larger at lower energy due to a lower resolution.

is determined by a stepwise enlargement of the interval, which is used for the centroid calculation. The interval is only enlarged until it is obvious by eye that the adjacent  $\gamma$ -peak is reaching into the interval. The centroid position is calculated for each choice of interval boundaries and the maximum shift of the centroid position equals the uncertainty on the position, ranging from  $\sim (0.6 - 2.0)$  ch. In comparison, the uncertainty in a selected TOF interval calculated from Eq. 6.14 is smaller than 0.02 ch. LG and HG measurements were always taken during the same cyclotron run, wherefore the position of the centroids is expected to be the same. This is observed for all samples listed in Tab. 6.7, confirming a stable cyclotron performance.

From all of the listed data sets, between 30 and 40 PH spectra are extracted per scintillator sample, covering the full energy region from about 1 MeV to 17 MeV. HG data is used for neutron energies below  $\sim 5$  MeV and LG data for energies above about 3 MeV. The overlap region is evaluated to probe the consistency of the results. Figure 6.22 exemplarily shows a subset of PH spectra measured with wsLAB1 in LG mode. Clearly visible is the shift of the proton recoil shoulder to higher PHs with higher incoming neutron energy. The exact position of the proton edge, as well as of characteristics  $\alpha$ -particle structures, is not discernible due to a finite light output resolution and is determined with the help of simulations, as will be discussed in the next section.

### 6.5.3 Simulation of the neutron response with NRESP7

The NRESP7 [230] MC code was provided by PTB, which has the advantage of a good description of the  $(n,\alpha x)$  reactions on C, which is necessary for the  $\alpha$  quenching data analysis. NRESP7 is a code used for the calculation of detector response to fast neutrons in the energy range from 0.05 MeV to 20 MeV. For neutron energies above 5 MeV, relativistic kinematics are used. The neutron source is treated in NRESP7 as a point source, where the user defines the distance between the detector and the neutron source as well as the angle between the beam-axis and the scintillator cylinder. The incident neutron

distribution can be set by the user to be mono–energetic, Gaussian with adaptable FWHM or rectangular with adaptable width. The code is developed for organic liquid scintillators in an aluminum housing covered by a light guide, equivalent to the design of the detector cells used in the present work. The specific detector dimensions are adjustable by the user, as well as the H to C ratio and density of the scintillator and light pipe. NRESP7 models all interactions of neutrons in the scintillator volume and surrounding material, including the production of secondary charged particles, and calculates the induced light output. As in the GRESP7 code (see Sec. 6.4.2), multiple scattering and wall effects are taken into account for this calculation as well as a finite PH resolution following Eq. 6.5. The resolution is quantified or omitted by the user. The non–linear light yield from different charged particles is simulated by NRESP7 using a set of predefined light output functions, which are stored in an external file and iteratively adapted to the data. Any set is selectable by the user as first approximation and the file is extendable with new data.

The proton light output function is given in table format in the energy range from 0 MeV to 8 MeV, with a step size of 10 keV from 0 MeV to 0.6 MeV and a step size of 20 keV from 0.6 MeV to 8 MeV. The proton light output  $L_p(E)$  above 8 MeV is described analytically by

$$L_p(E) = d_0 + d_1 E. \quad (6.15)$$

The  $\alpha$ –particle light output function is described in NRESP7 by two analytic expressions, namely

$$L_\alpha(E) = c_0 E^{c_1} \quad E < 6.76 \text{ MeV}, \quad (6.16)$$

$$L_\alpha(E) = c_2 + c_3 E \quad E \geq 6.76 \text{ MeV}. \quad (6.17)$$

The parameters  $c_0$  through  $c_3$  are stored together with the proton response information. Also the response of Be, B and C ions is described analytically in NRESP7. Their light output, however, is quenched too strongly to be observed in the presented experiments. For these particles, the initial light output functions are not adapted to LAB based scintillators.

Not taken into account within NRESP7 are interactions of de–excitation photons, e.g. from the first excited state in  $^{12}\text{C}$  at 4.439 MeV, resulting from inelastic neutron scattering. Instead, it is assumed that these events are suppressed by PSD, since the code was originally written for NE213 scintillator fulfilling this requirement. As this background is not entirely suppressed by PSD in LAB based scintillators, the simulated spectra lack the signals from residual de–excitation photons in the data. The influence on the proton and alpha quenching analysis, though, is marginal as will be discussed in the respective sections.

#### 6.5.4 Light output resolution measured with neutron induced events

The light output resolution is already determined within the calibration data analysis and the results are presented in Fig. 6.13, Fig. 6.14 and Tab. 6.6. However, only six data

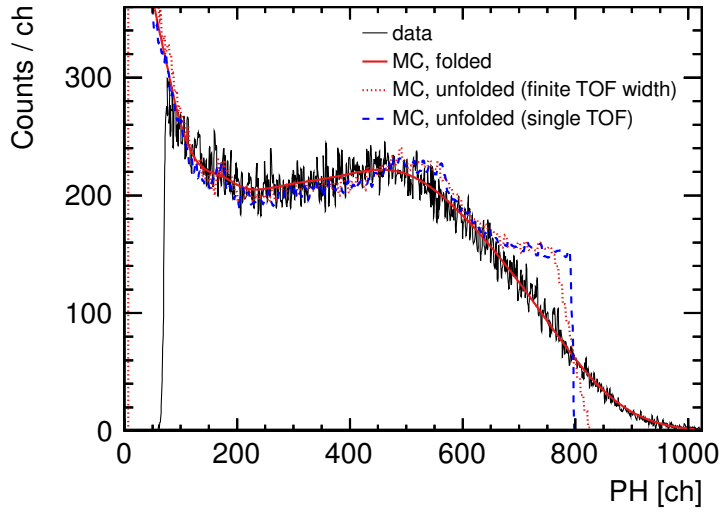


**Figure 6.23:** Measured and simulated PH spectrum in LAB + 5% PRS + 1.5% water + 2 g/l PPO + 15 mg/l bis-MSB + 0.3% Te and HG mode for neutrons with  $E_n = 3.5$  MeV. Simulated is the spectrum of mono-energetic 3.5 MeV neutrons without resolution and quasi mono-energetic neutrons considering a finite TOF window around 3.5 MeV of the same width as used for data extraction. The red solid line is the red dashed line folded with the detector resolution. The sharp blue dashed edge refers to protons with  $E = E_n$ .

points are available and only electron energies between about 0.3 MeV and 1.6 MeV are accessible with the used gamma calibration sources. To reduce the uncertainties on the resolution parameters  $\alpha$  and  $\beta$ , the light output resolution is also determined with beam data, with which a large set of data points over a wide range of energies is accessible. The determined light output resolution functions using calibration data and beam data are expected to agree.

Using the calibration parameters listed in Tab. 6.5, the PH scale of measured PH spectra, as shown in Fig. 6.22, is translated into light output  $L$  in electron-equivalent energy using Eq. 6.6 and 6.8 and thus

$$L = \frac{PH - a}{m}. \quad (6.18)$$

The simulation of each spectrum is performed twice. Once a rectangular neutron distribution around the neutron energy of interest is assumed, with a width corresponding to the TOF window used for data extraction, and once the neutrons are assumed to be mono-energetic. In both cases, no resolution function is applied. An example of these two spectra is presented in Fig. 6.23 (dashed lines). The further evaluation follows the same procedure as in the case of gamma calibration data. A fit interval is defined around the proton recoil edge and the best fit FWHM  $\Delta L$  of a Gaussian distribution, with which the

**Table 6.8:** Light output resolution parameters  $\alpha$ ,  $\beta$ ,  $\gamma$  from fitting Eq. 6.9 to data from neutron induced events (see Fig. 6.24).  $\gamma$  is fixed at 0.5% as in the case of gamma induced events (see Tab. 6.6).

Scintillator	$\alpha$ [%]	$\beta$ [%]	$\gamma$ [%]	$\chi^2/\text{ndf}$
LAB1	$16.6 \pm 0.6$	$16.3 \pm 1.2$	0.5	9.2/15
LAB2	$34.8 \pm 0.5$	$21.4 \pm 2.2$	0.5	4.3/28
LAB3	$18.1 \pm 0.5$	$18.4 \pm 1.8$	0.5	10.8/28
LAB4	$38.9 \pm 0.6$	$19.9 \pm 2.1$	0.5	4.4/14
LAB5	$38.3 \pm 0.5$	$23.7 \pm 2.8$	0.5	15.4/27
LAB6	$41.0 \pm 0.8$	$29.4 \pm 2.2$	0.5	4.0/14
wsLAB1	$19.5 \pm 0.7$	$24.2 \pm 0.9$	0.5	16.6/32
wsLAB2	$21.4 \pm 0.5$	$25.5 \pm 0.8$	0.5	11.0/28

simulation is folded, is determined. Simultaneously, the vertical and the horizontal scale of the spectrum is adapted to the data. In this step, two scaling factors,  $f_h$  and  $f_v$ , are evaluated, with which the simulation is multiplied in the horizontal and in the vertical direction, respectively, yielding the best agreement between simulation and data.

For the adaption, only the simulation of a rectangular neutron distribution is used. The resulting scaling factors are subsequently applied to the MC spectrum of monoenergetic neutrons and the position of the sharp edge in the  $L$  spectrum is identified. Thus  $\Delta L/L(L)$  is determined. Additionally the first approximation of the proton light output  $L(E)$  at a proton energy  $E$  is obtained, knowing that  $E$  at the recoil edge equals the incoming neutron energy. A set of data points is determined in this way for each scintillator sample, using HG data for the first few MeV and LG data for the energies above and up to about 17 MeV. The obtained data points are shown in Fig. 6.24, where the uncertainties are determined by a reasonable alteration of the fit interval boundaries around the recoil edge. Also shown in this figure is a fit of Eq. 6.9 to each set. The fit results of the resolution parameters  $\alpha$ ,  $\beta$  and  $\gamma$  are summarized in Tab. 6.8. As in the case of gamma calibration and for the same reason, the parameter  $\gamma$ , accounting for electronic noise, is fixed at 0.5%.

The results from the beam data analysis, shown in Fig. 6.24, confirm the earlier findings from the calibration data analysis, shown in Fig. 6.13 and 6.14: The scintillators with only PPO as secondary have a relative light output resolution from about 50% to slightly less than 40%, the scintillators with additional bis-MSB content have a resolution from about 30% to 20% and a content of 5% PRS and 1.5% water in wsLAB does not significantly affect the resolution in this detector. The values of the resolution parameters listed in Tab. 6.8 are

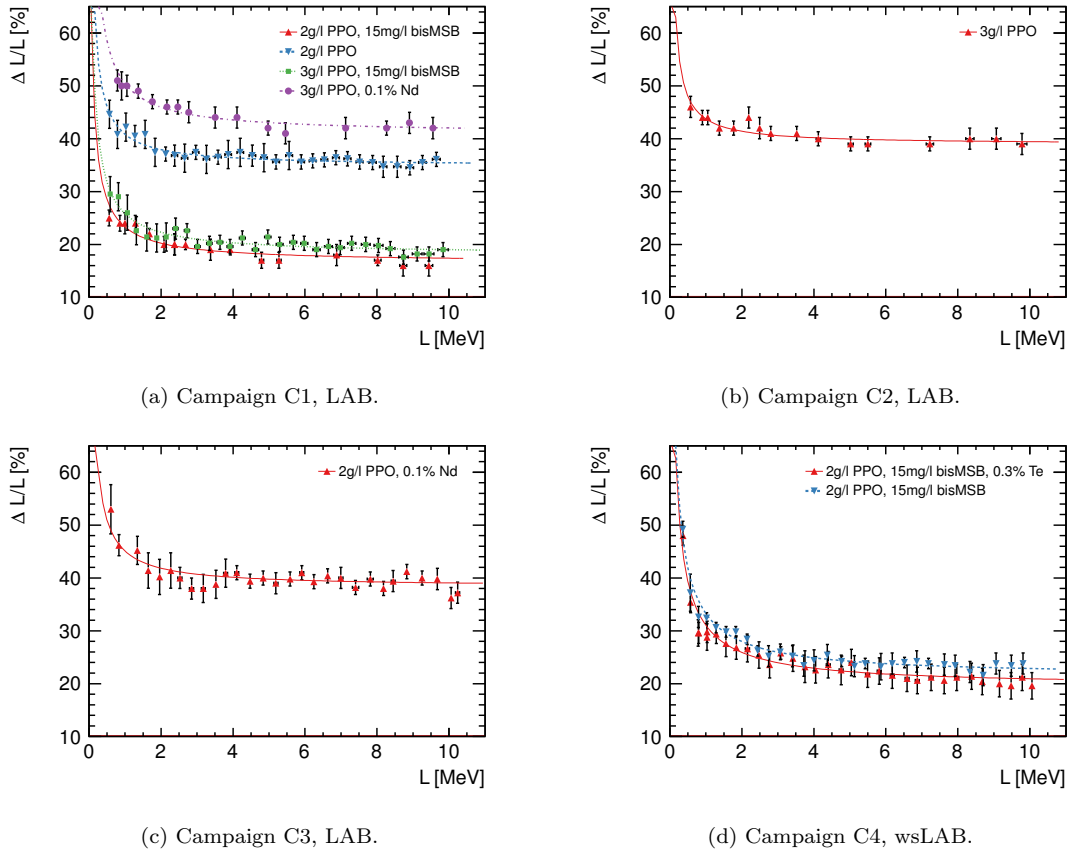


**Figure 6.24:** Relative light output resolution  $\Delta L/L$  as a function of light output for neutron-induced events in (a-c) LAB and (d) wsLAB scintillators. The respective fluors are listed in the plot legends. wsLAB scintillators contain 5% PRS and 1.5% water. The shown uncertainties are explained in the text. The lines follow a fit of Eq. 6.9 to the data (markers). The fit results are summarized in Tab. 6.8.

used for the further analysis of beam data. Figure 6.23 shows exemplarily the agreement between simulation and measurement after folding the simulation with Eq. 6.9 using the resolution parameters for wsLAB1. The agreement for all other sets is comparable.

### 6.5.5 Proton response

Besides the example proton recoil spectrum shown in Fig. 6.23, induced by 3.5 MeV neutrons, four further spectra are shown in Fig. 6.25, using the same scintillator but LG data. In each of them, the idealized proton PH spectrum from mono-energetic neutrons shows the sharp edge at the maximum proton energy mentioned earlier, which equals the incoming neutron energy. As soon as the position of the edge is located in the measured PH spectrum, the correlation between proton energy  $E$  and PH is thus revealed at that PH and consequently  $L(E)$ , using Eq. 6.18.

In the measurements of 5 MeV and 6.5 MeV neutron PH spectra, shown in Fig. 6.25b

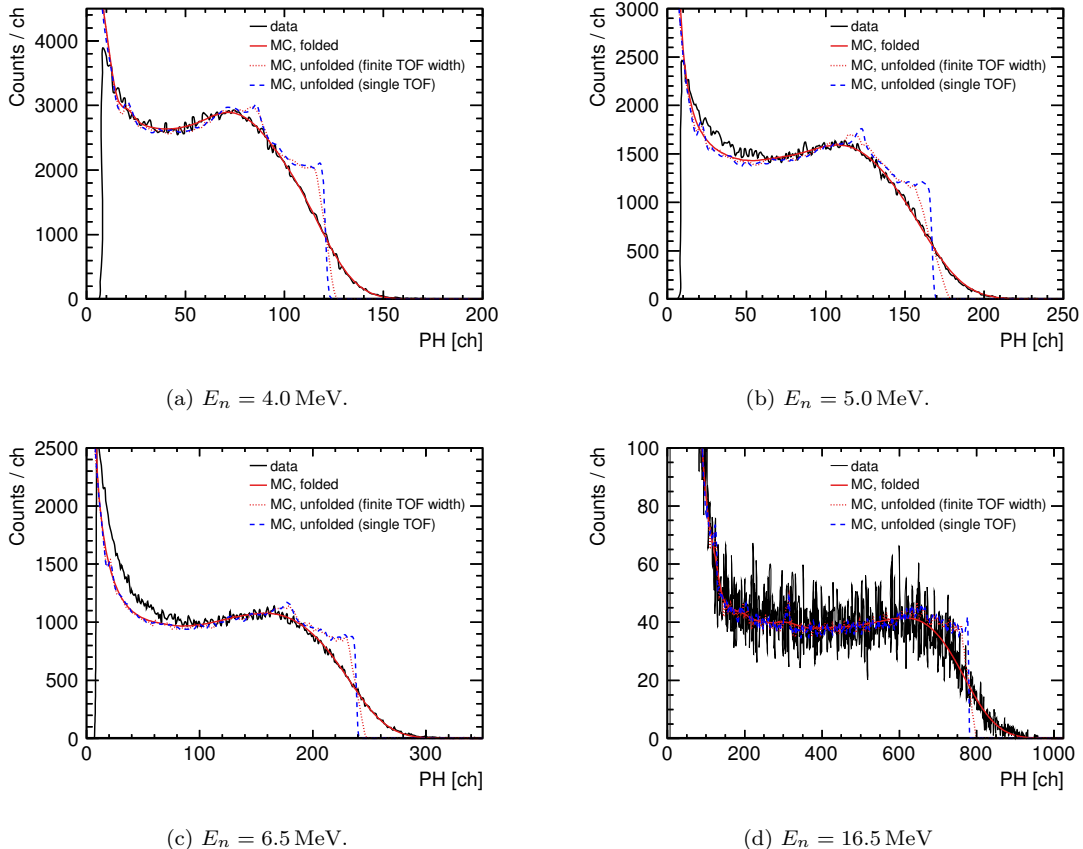


**Figure 6.25:** Measured and simulated PH spectrum in LAB + 5% PRS + 1.5% water + 2g/lPPO + 15 mg/l bis-MSB + 0.3% Te and LG mode for neutrons with different energies  $E_n$ . Simulated is the spectrum of mono-energetic neutrons without resolution and quasi mono-energetic neutrons considering a finite TOF window as used for data extraction. The red solid line is the red dashed line folded with the detector resolution. The sharp blue dashed edge refers to protons with  $E = E_n$ .

and 6.25c, a disagreement between simulation and data is apparent at low PHs, which is not present in the other two examples using 4.0 MeV and 16.5 MeV neutrons, shown in Fig. 6.25a and 6.25d. The explanation was already approached earlier: NRESP7 does not consider de-excitation gammas and PSD does not fully suppress this background in LAB based scintillators. Thus excitations and subsequent de-excitations of isotopes in the scintillator, the cell walls and window, as well as the light guide potentially lead to an excess in the data compared to the simulation. For this reason, the important isotopes in the named detector parts are discussed in this paragraph and the most probable candidate, responsible for the mismatch between simulation and data, is identified.

The main elements are, in the order of occurrence, H with  $\sim 9 \times 10^{24}$  atoms and C

with  $\sim 5 \times 10^{24}$  atoms in the scintillator<sup>8</sup> and PMMA<sup>9</sup> light guide, Al with  $\sim 1 \times 10^{24}$  atoms in the dural cell walls and O with  $\sim 7 \times 10^{23}$  atoms and Si with  $\sim 3 \times 10^{23}$  atoms in the fused silica<sup>10</sup> window. All numbers are derived from the volume of the individual detector parts, the molecular formula of the material and the respective density at room temperature. Only two decimal places of the densities in units of g per cm<sup>3</sup> are used to yield an approximation of the number of atoms over a wide range of temperatures. H is not further discussed, since it does not emit gamma-rays and thus does not contribute to gamma-induced background. O and Si amount to about an order of magnitude less than C and the effective number is further reduced by more than 50%, assuming that the same amount of gammas leaves the quartz glass window on either side and given that the window diameter is larger than the scintillator volume diameter, while the total neutron scattering cross sections around the individual excitation energies are of the same order of magnitude and around (1–10) b [231]. Al atoms occur about five times less than C atoms and the effective number is reduced as well by about a factor of two due to gammas not entering the scintillator volume. The first excited state of <sup>27</sup>Al, the only stable isotope of aluminum, is at 843.76 keV, followed by a large amount of higher excited states, with a spacing between about 1 keV and 1.2 MeV. No corresponding data excess is observed, however, as exemplarily demonstrated in Fig. 6.25a, which shows data and simulation resulting from 4.0 MeV neutrons. At 4 MeV neutron energy, C is not yet excited, turning <sup>27</sup>Al into the major background source, whose total neutron–<sup>27</sup>Al scattering cross section at the respective excitation levels is also around (1–10) b [231]. The isotope of highest natural abundance of C is <sup>12</sup>C (98.90%) and its first excited state is at 4.439 MeV, which is de-excited by gamma emission. All higher excited states primarily decay via charged particle emission. While the neutron energy is too low in Fig. 6.25a to excite <sup>12</sup>C, it is already high enough in Fig. 6.25b, where a mismatch between data and MC is observed first. <sup>12</sup>C has the highest occurrence within the relevant detector parts and the highest fraction of gammas traversing the active medium, since it is a constituent of the scintillator itself, which makes it the main source of gamma-induced background events, when  $E_n \geq 4.439$  MeV. Gammas from low energy neutron moderation  $n(p, d)\gamma$  in the cell are negligible given the smallness of the cell.

A simulation of the PH spectrum induced by 4.439 MeV gammas in wsLAB + 0.3% Te + 2 g/l PPO + 15 mg/l bis-MSB is shown in Fig. 6.26. Within the LG MC spectrum in Fig. 6.26a, corresponding to the PH spectra in Fig. 6.25, the event yield strongly increases below about 150 ch. At the same time, the PSD efficiency increases with increasing PH, as reported in section 6.5.1. The data excess in Fig. 6.25b and 6.25b is therefore only notable below about 100 ch. In Fig. 6.25d, the background is well within the fast rising

---

<sup>8</sup>All given numbers are valid for LAB and wsLAB scintillators. The number of H atoms per volume unit is almost identical in LAB, water and PRS as well as the number of C atoms in LAB and PRS. The total additional number of O atoms in wsLAB is  $\sim 6 \times 10^{22}$ . N and S in PRS amount to  $< 1 \times 10^{22}$  atoms each.

<sup>9</sup>The molecular formula of PMMA is  $(C_5O_2H_8)_n$ .

<sup>10</sup>The molecular formula of silica is SiO<sub>2</sub>.

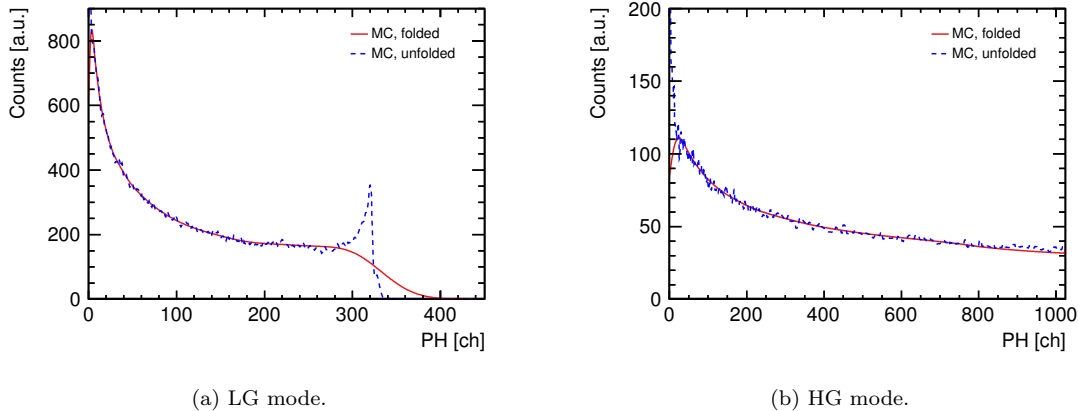


**Figure 6.26:** PH spectrum of  $^{12}\text{C}$  4.439 MeV gammas in LAB + 5% PRS + 1.5% water + 0.3% Te + 2 g/l PPPO + 15 mg/l bis-MSB, simulated with GRESP7. The spectrum is calculated considering a range factor of 4 mV/ch for both, LG (a) and HG (b) amplification, corresponding to the settings in beam measurements. Note that GRESP7 does not calculate pair productions, which are possible at a gamma energy of 4.4 MeV. Thus a small double escape peak is missing, expected at 265 ch in (a). The probability for a single escape peak, located at 305 ch, is vanishingly low due to a mean free path of  $\gtrsim 9\text{ cm}$  of 511 keV photons in LAB. This peak is not expected to be visible in the spectrum due to the low PH resolution.

low energy part of the recoil spectrum and thus not visible in the given figure. For the adaption of the simulation to data, a cut is set below the observed recoil shoulder, as soon as the neutron energy exceeds the threshold for  $^{12}\text{C}$  excitation, and only the remaining part of the recoil spectrum is used. With this cut, the proton recoil shoulder is very well reproduced (see Fig. 6.25), despite the deficit of NRESP7 and despite the poor PSD in the investigated scintillators.

The localization of the proton recoil edge follows the same technique that is used to determine the local PH or light output resolution, described earlier in Sec. 6.5.4. The only difference is that the idealized simulation of quasi mono-energetic neutrons is folded with Eq. 6.9 and the resolution parameters listed in Tab. 6.8, instead of using a Gaussian resolution function with a fixed width valid only for a limited range of PH channels. Thus the dependency on the choice of the fit interval is much lower and can be optimized with respect to the gamma-induced background.

As mentioned above, in the process of adapting the simulation to data, two scaling factors  $f_h$  and  $f_v$  are specified with which the horizontal and vertical scales of the simulation are adapted to the scales of the data spectrum. Having determined these scaling factors, the MC spectrum of mono-energetic neutrons is scaled accordingly, the recoil edge position  $PH(E)$  is read out and its value converted into units of electron-equivalent energy, yielding  $L(E)$ . The described procedure is repeated for in total  $\sim 30$  PH spectra from neutrons with different energies for each tested scintillator. This way a large set of data points is created over an energy range from about 1 MeV to 17 MeV, demonstrated in

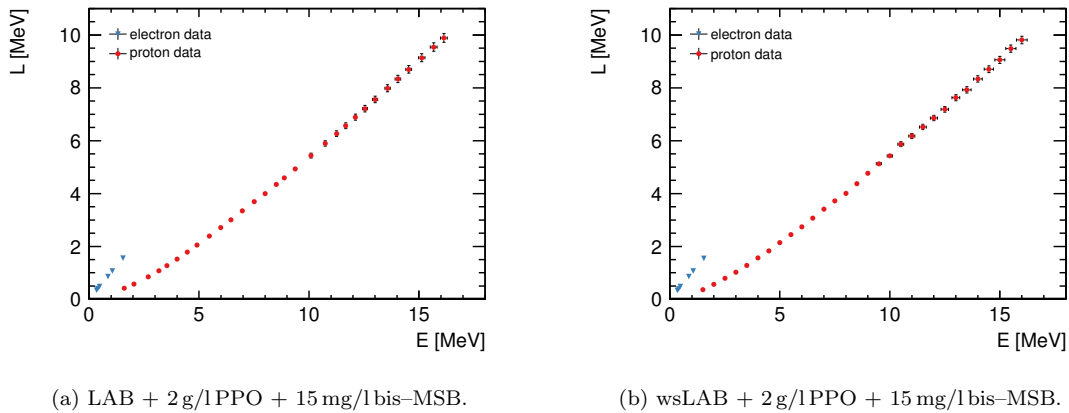


**Figure 6.27:** Light output  $L$  in electron-equivalent energy, measured in LAB1 (a) and wsLAB2 (b) for different electron and proton energies. Both, electrons and protons are internal, resulting from scattering reactions induced by gammas and neutrons respectively. In the shown total uncertainties, the single contributions (see Tab. 6.9) are added quadratically.

Fig. 6.27 for LAB and wsLAB with 2 g/lPPO and 15 mg/lbis-MSB. The quenched light response of protons compared to electrons is in evidence as well as its non-linearity.

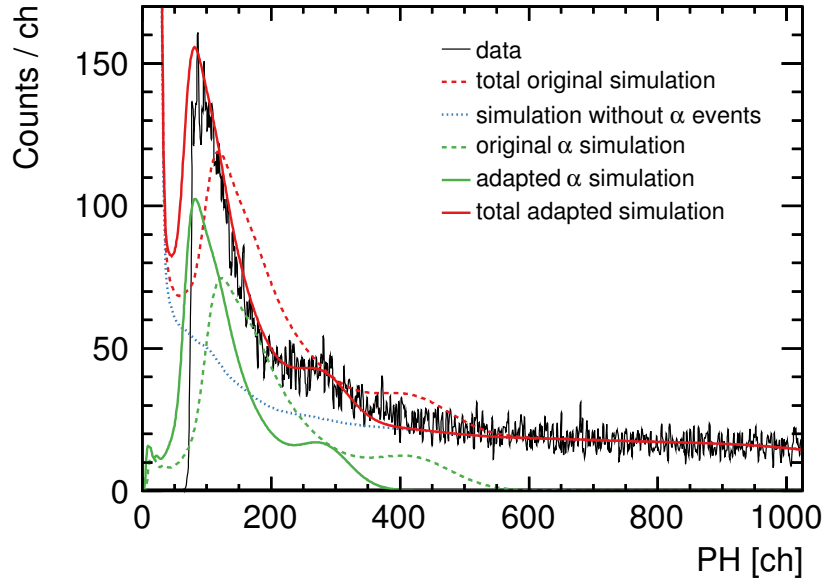
The scaling factor  $f_h$  can be interpreted as a measure of the deviation of the assumed light output function, used in NRESP7, from the true light output function of the LS sample, where  $f_h = 1$  implies that the proton response is properly described. If the input light output function is deviating by more than 2%, i.e.  $f_h \notin [0.98, 1.02]$  at any recoil edge, a new NRESP7 input table is generated by an extrapolation between data points below 8 MeV particle energy and new parameters  $d_0$ ,  $d_1$  are determined for the analytic description above 8 MeV by a fit of Eq. 6.15 to the data points of respective energies. The NRESP7 data base is conclusively updated. The scaling factor  $f_v$  merely adapts the number of counts and has no further physical meaning.

Since the proton light output function in NRESP7 is partly analytical, assuming linearity above 8 MeV proton energy, it is not used for the determination of the quenching parameters  $kB$  and  $C$  in the extended BIRKS law Eq. 2.12. Instead, the final set of data points, as shown in Fig. 6.27, is used. All final sets are presented in Sec. 6.6 in this context.

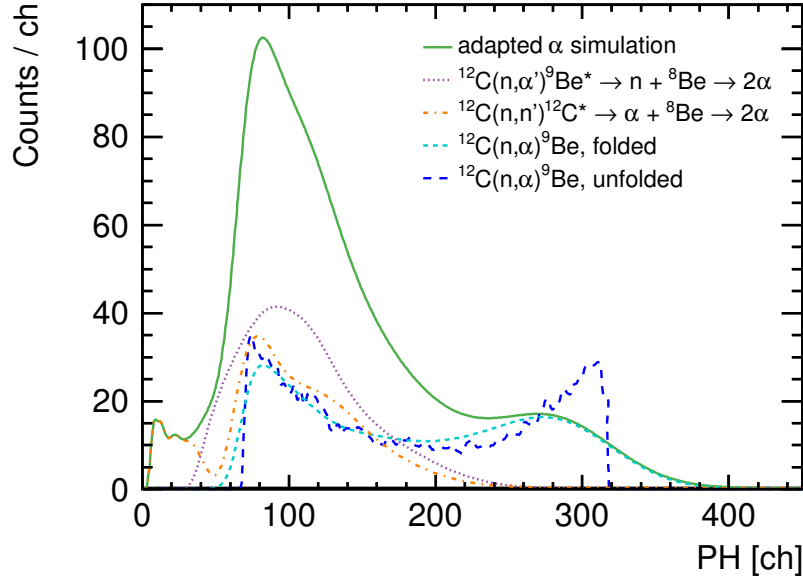
### 6.5.6 Alpha response

Together with the proton quenching data, alpha quenching data is taken, which has the advantage that both quenching measurements are subject to the same conditions and a difference in the quenching parameters for protons and  $\alpha$ -particles, if any, cannot be attributed to different measurement conditions. In this measurement, the  $\alpha$ -particles of interest are produced in the reaction





(a) Measurement and simulation of all events.



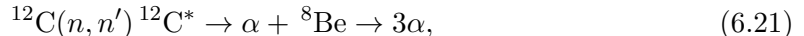
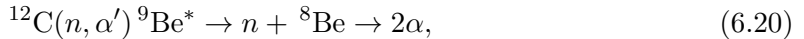
(b) Simulation of the individual α-particle interactions.

**Figure 6.28:** Measured and simulated PH spectrum in LAB + 5% PRS + 1.5% water + 2 g/l PPO + 15 mg/l bis-MSB + 0.3% Te and HG mode for quasi mono-energetic neutrons with  $E_n = 11.2$  MeV (a). Shown is the simulated alpha response before and after adaption of the  $\alpha$ -particle light yield, the sum of non- $\alpha$ -particle events (mainly proton recoils) and the sum of all events before and after adaption of the  $\alpha$ -particle light yield. All simulated spectra are folded with the measured resolution function. (b) shows the contributions of the different  $\alpha$ -particle interactions to the  $\alpha$ -particle sum spectrum. Additionally shown is the  $^{12}\text{C}(n,\alpha)^9\text{Be}$  spectrum from mono-energetic neutrons and without considering the detector resolution. The high energy edge at  $\sim 320$  ch in this spectrum refers to  $\alpha$ -particles with  $E_\alpha = 5.326$  MeV.

Thus the  $\alpha$ -particles are internal, like the protons and electrons, and surface effects that need to be considered for external sources, do not play a role here. Furthermore, the extraction of measured PH spectra follows the same procedure as described in section 6.5.5 for the case of the proton response measurements, since the PH spectra are a sum of all interactions of neutrons with a given TOF. The simulation of the sum PH spectra is performed with NRESP7 after insertion of the newly determined proton light output function for the investigated scintillator. The initial  $\alpha$ -particle light output function in NRESP7 remains unchanged for the first iteration. The PH resolution function, determined within the proton quenching analysis, is also directly applied.

The threshold of the  $^{12}\text{C}(n,\alpha)^9\text{Be}$  reaction is 6.19 MeV and leads to a characteristic structure in the PH spectra, as soon as the light yield is high enough to overcome the detector threshold. This is the case after about 9.5 MeV neutron energy in the investigated data sets. In the example shown in Fig. 6.28a, the characteristic structure is found between 200 ch and 400 ch. The shoulder of this structure refers to the maximum  $\alpha$ -particle energy  $E_\alpha$ , as demonstrated in Fig. 6.28b, which is calculated from kinematics (see App. C), knowing  $E_n$  and assuming  $^{12}\text{C}$  at rest. This assumption is correct within the measurement uncertainties. With the knowledge of the  $\alpha$ -particle energy, the relation between  $L$  and  $E$  follows from the position of the sharp high energy edge in the PH spectrum, shown in Fig. 6.28b, and the conversion of the PH into  $L$  in units of electron-equivalent energy, using Eq. 6.18.

Two further reactions contribute to the  $\alpha$ -particle event yield:



where reaction Eq. 6.20 has a threshold of 8.81 MeV and reaction Eq. 6.21 has a threshold of 8.29 MeV. These reactions have more than one  $\alpha$ -particle in the final state and no characteristic spectral feature that is assigned to a distinct  $\alpha$ -particle energy (see Fig. 6.28b). Above  $\sim$ 11.5 MeV neutron energy, these two interactions dominate [230] and no structure can be identified with  $\alpha$ -particles of known energy. Only above  $\sim$ 14 MeV, the maximum  $\alpha$ -particle energy from  $^{12}\text{C}(n,\alpha)^9\text{Be}$  is high enough to be well outside the other two spectra and faintly visible in the total spectrum. As a consequence, only a limited set of PH spectra can be evaluated to obtain the light output function  $L(E)$  for  $\alpha$ -particles, of which a subset is presented in Fig. 6.29.

In all these spectra, simulated  $\alpha$ -particle and non- $\alpha$ -particle events are separated to adapt the  $\alpha$ -particle light response independently. As in the case of the proton response analysis, the scaling factor  $f_h$  is equivalent to a correction of the initial light output function, while  $f_v$  corresponds to a normalization factor. The normalization suffers from the poor knowledge of the individual neutron cross sections on carbon [230] and

the  $\alpha$ -particle simulation is scaled in  $y$ -direction to best match only the region of the  $(n,\alpha)$  shoulder in the data spectrum. As a consequence, the  $\alpha$ -particle event yield is overestimated in the presence of background events. The location of the edge position, though, is not affected, as long as the background is featureless.

Figures 6.29a–6.29c show PH spectra from neutrons with energies between about 9.5 MeV and 11.5 MeV and the good agreement between data and simulation right at the visible structure. In Fig. 6.29d, a shoulder is barely recognizable, though it is still significant, if background can be excluded as source of this structure. For this reason, the previous discussion about backgrounds in Sec. 6.5.5 is extended at this point. The requirement for a visible shoulder in the PH spectra is a high enough yield of secondary charged particles with identical energy from neutron interactions. Prompt gammas are outside the TOF neutron range, regions with satellite prompt gammas are excluded and ambient background is measured individually and subtracted, as mentioned in section 6.4.1. Since the light yield of recoiling ions heavier than  $\alpha$ -particles, like Be, B or C, is below threshold, the only remaining background source are de-excitation gammas from isotopes within the scintillator and the surrounding material. A Compton edge, full energy or escape peak following gamma interactions have the potential to mimic the  $\alpha$ -particle shoulder. As discussed in Sec. 6.5.5, of all elements in the scintillator, the cell walls and window, as well as the light guide, the only isotope of considerable amount that has additionally only a small amount of energy levels in the neutron energy range is  $^{12}\text{C}$ .  $^{27}\text{Al}$ , the second most abundant isotope in the relevant detector parts, has a large amount of nearby levels and not the capability to create one discrete and observable shoulder. The  $^{12}\text{C}$  background is discussed using the example of the HG PH spectrum of wsLAB1 in Fig. 6.28a. The first excited state of  $^{12}\text{C}$  is at 4.439 MeV and thus causes a maximum Compton electron energy of 4.20 MeV. Using  $m$  for the wsLAB1 HG measurement from Tab. 6.5, the edge is expected at  $PH > 2500\text{ ch}$ , far away from the observed structure and above the last ADC channel 1024 (see also Fig. 6.26b). The double escape pulse from pair production and subsequent annihilation has an energy of  $2 \times 1.71\text{ MeV}$  resp. a PH of  $> 2000\text{ ch}$  and is therefore still way beyond the shoulder region. The Compton spectrum in Fig. 6.26b is rising in the ROI, but it is even and shows no structure able to mimic the observed shoulder in Fig. 6.28a. As a consequence,  $^{12}\text{C}$  de-excitations can explain the data excess in the vicinity of the observed structure in Fig. 6.28a, as well as Fig. 6.29, but they cannot cause the structure itself. Two isotopes that have also a limited amount of excitation levels within the neutron energy range, and with the first excited state at lower energy than the one of  $^{12}\text{C}$ , are  $^{14}\text{N}$  and  $^{32}\text{S}$ , isotopes that are part of the PRS present in wsLAB1 and wsLAB2. Their total neutron scattering cross sections around the excitation energies are of the same order of magnitude as the one of  $^{12}\text{C}$  [231]. However, each of them amounts to only about 0.2% of the  $^{12}\text{C}$  content and is thus too low in concentration and none of them is part of standard LAB used in Fig. 6.29. Moreover, while the  $\alpha$ -particle shoulder shifts towards higher PHs with higher neutron energy, gammas from a particular background source remain at the same PH. In summary, also de-excitation gammas are

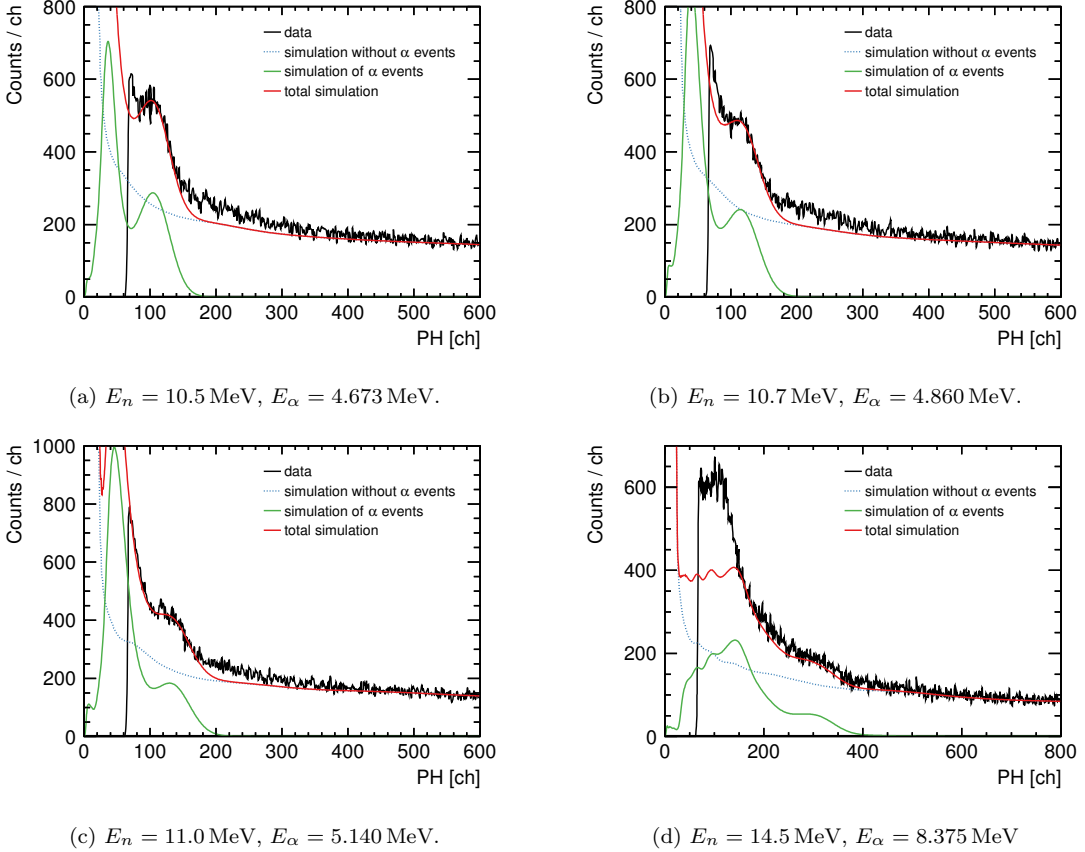


**Figure 6.29:** Measured and simulated PH spectrum in LAB + 2 g/l PPO + 15 mg/l bis-MSB and HG mode for quasi mono-energetic neutrons with different energies  $E_n$ . Simulated is the spectrum excluding  $\alpha$ -particle events, the spectrum of  $\alpha$ -particle events only and the sum spectrum of all events. The high energy shoulder within the  $\alpha$ -particle spectrum is formed by  $\alpha$ -particles with maximum energy  $E_\alpha$  from  $^{12}\text{C}(n,\alpha)^9\text{Be}$  reactions.

safely excluded as cause of the observed shoulder in the PH spectra.

The entire analysis is only possible, if the  $\alpha$ -particle structures are resolved. As discussed in Sec. 6.4.3 and 6.5.4, the PH resolution of LAB based scintillators is comparatively low. Only samples with bis-MSB content just reach high enough resolution, shown in Fig. 6.24, leaving only four data sets that are suitable for the determination of the alpha response function, the ones of LAB1, LAB3, wsLAB1 and wsLAB2. For each of these four scintillators, up to ten PH spectra can be evaluated, yielding the respective number of data points  $L_i(E_i)$ , as shown for LAB and wsLAB with 2 g/l PPO and 15 mg/l bis-MSB in Fig. 6.30. The remaining results are presented in the following section. The  $\alpha$ -particle light responses in Fig. 6.30 are stronger quenched than the proton responses in Fig. 6.27, as expected, and the functional behavior is also non-linear, especially since the origin of ordinates has to be included. In order to complete the update in the NRESP7 input file, Eq. 6.16 and 6.17 are fit to the respective data points and the resulting parameters  $c_{0-3}$

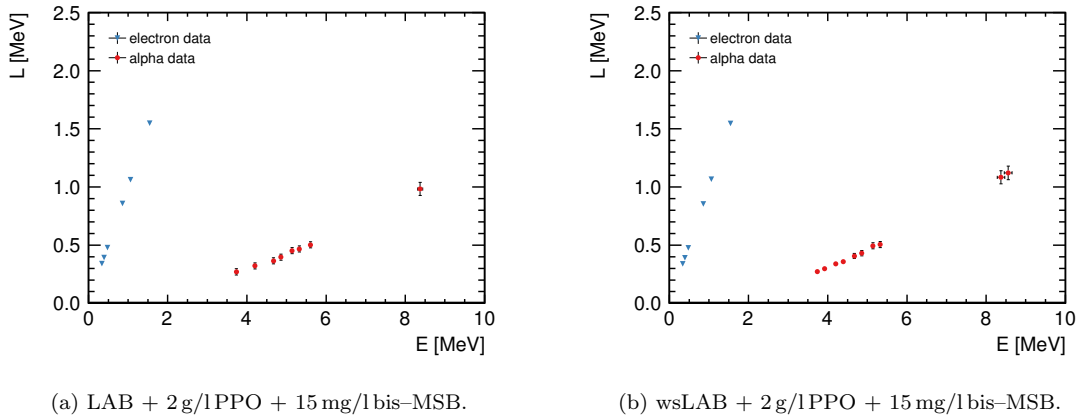


**Figure 6.30:** Light output  $L$  in electron-equivalent energy, measured in LAB1 (a) and wsLAB2 (b) for different electron and  $\alpha$ -particle energies. Both, electrons and  $\alpha$ -particles are internal, resulting from scattering reactions induced by gammas and neutrons respectively. In the shown total uncertainties, the single contributions (see Tab. 6.9) are added quadratically.

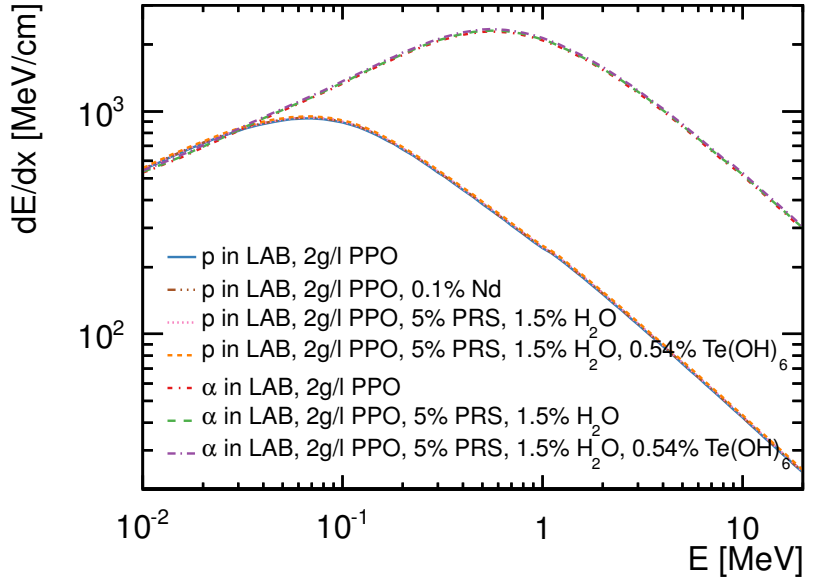
are updated in the set of light responses of the corresponding scintillator.

## 6.6 Adaption of Birks' law to the measured light responses

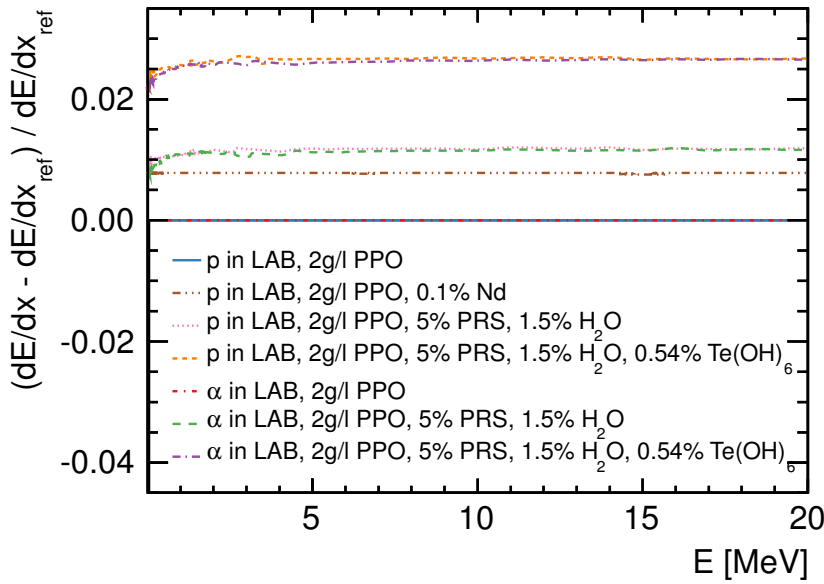
The most popular analytical description for the energy dependency of the light output is given by the semi-empirical Birks' law Eq. 2.11, assuming ionization quenching to be the reason for the reduced light output observed in Fig. 6.27 and 6.30. For the description of the measured light output of protons and  $\alpha$ -particles, the generalized form of Birks' law Eq. 2.12, including the quadratic correction term parameterized by  $C$  [37] is used, as well as the original law, in which  $C = 0$ . Electron, proton and  $\alpha$ -particle light output functions of a particular scintillator are measured within the present work under identical conditions, so that the scaling factor  $S$  for proton and  $\alpha$ -particle data is the same as the one for electron data, i.e.  $S = 1$  (see Sec. 6.4.3). Birks' parameter  $kB$  and the parameter  $C$  of all LAB based scintillators are obtained by means of a  $\chi^2$  fit of the theoretically expected light output  $L^{\text{theo}}$  using Eq. 2.12 at each of the  $N$  experimentally determined values  $L^{\text{exp}}$  presented, for instance, in Fig. 6.27 and 6.30.  $N$  is between 30 and 49 in proton quenching evaluations and between 8 and 11 in alpha quenching evaluations. The total stopping power  $dE/dx$  for protons and  $\alpha$ -particles is calculated using the code SRIM [232] and displayed in Fig. 6.31. Also shown in that figure is the relative difference of Nd-loaded LAB to LAB as well as of Te-loaded and unloaded wsLAB to LAB which is  $\lesssim 3\%$ .

The  $\chi^2$  calculation is carried out following the pull approach [233], where

$$\chi^2(kB, C, \xi_k) = \sum_{n=1}^N \frac{\left[ L_n^{\text{exp}} - L_n^{\text{theo}} \left( 1 + \sum_{k=1}^K \xi_k f_n^k \right) \right]^2}{u_n^2} + \sum_{k=1}^K \xi_k^2. \quad (6.22)$$



(a) Stopping power.



(b) Relative stopping power difference.

**Figure 6.31:** (a) Total stopping power  $dE/dx$  as function of energy for protons and  $\alpha$ -particles of various LAB based scintillators and (b) their relative difference to the stopping power of LAB + 2 g/l PPO, denoted as  $dE/dx_{ref}$  (b). The stopping powers are calculated with SRIM using the densities listed in Tab. 6.1. Bis-MSB is not included in the calculations due to its negligible concentration. 0.54%  $\text{Te}(\text{OH})_6$  correspond to 0.3% Te loading.

**Table 6.9:**  $1\sigma$  values of the experimental uncertainties within the relative light output measurements. Time-walk of the CFD, satellite pulses, multiple neutron events and time-frame overlap have a minor effect (see Sec. 6.3.1 and 6.5.1) and are neglected as source of uncertainty. The uncertainty of the distance between target and detector is the quadratic sum of the distance measurement uncertainty, half target thickness and half depth of the scintillator volume. The extracted edge positions carry two uncertainties, a statistical and a systematic. The statistical one is the uncertainty on the scaling factors  $f_{x,y}$  from the fit of the simulated to the measured PH spectrum. An additional systematic uncertainty comes from the choice of the fit interval, since different interval boundaries shift the edge position by more than  $1\sigma_{\text{stat}}$ . This uncertainty is determined at each data point individually. Only the highest uncertainty of all data points is listed here, while the right number for each scintillator is used when fitting the light output function to data. For  $\alpha$ -particle light output measurements, only HG data sets are used.

Nr.	Systematic uncertainty	$1\sigma_{\text{sys}}$
1	Prompt $\gamma$ -peak centroid position	$\leq 0.9 \text{ ch}$ (see Tab. 6.7)
2	TAC non-linearity $\langle \Delta p \rangle$	$< 0.2 \text{ ch}$ (see Tab. 6.4)
3	Time calibration	$\pm 0.05\%$
4	Target – detector distance	$\pm 25.5 \text{ mm}$
5	Gain stabilization	$\pm 0.5\%$
6	HG calibration factor $m$	(see Tab. 6.5)
7	LG calibration factor $m$	(see Tab. 6.5)
8	HG pulse-height offset $a$	(see Tab. 6.5)
9	LG pulse-height offset $a$	(see Tab. 6.5)
10a	Edge position (protons)	$\leq 5 \text{ ch}$
10b	Edge position ( $\alpha$ -particles)	$\leq 9 \text{ ch}$
Statistical uncertainty		$1\sigma_{\text{stat}}$
Edge position		$< 0.02\%$

Within this calculation  $K = 10$  ( $K = 8$ ) independent sources of systematic uncertainties in the proton ( $\alpha$ -particle) light output measurements, listed in Tab. 6.9, are included as nuisance parameters. The  $\alpha$ -particle measurement has two sources of uncertainty less than the proton measurement, since only HG data is used in the first case, eliminating the two uncertainties from the LG calibration Nr. 7 and Nr. 9 in Tab. 6.9. The factor  $f_n^k$  in Eq. 6.22 describes the fractional change of the  $n$ -th value of  $L^{\text{theo}}$  if the  $k$ -th source of systematics is varied by  $1\sigma_k$  and  $\xi_k$  is a standard normal deviate. The normalization condition for the  $\xi_k$ 's is realized through quadratic penalties, summed over the  $K$  sources of systematics. The statistical uncertainty, denoted by  $u$ , is also indicated in Tab. 6.9 and is below 0.02%, hence the measurements are dominated by systematics.

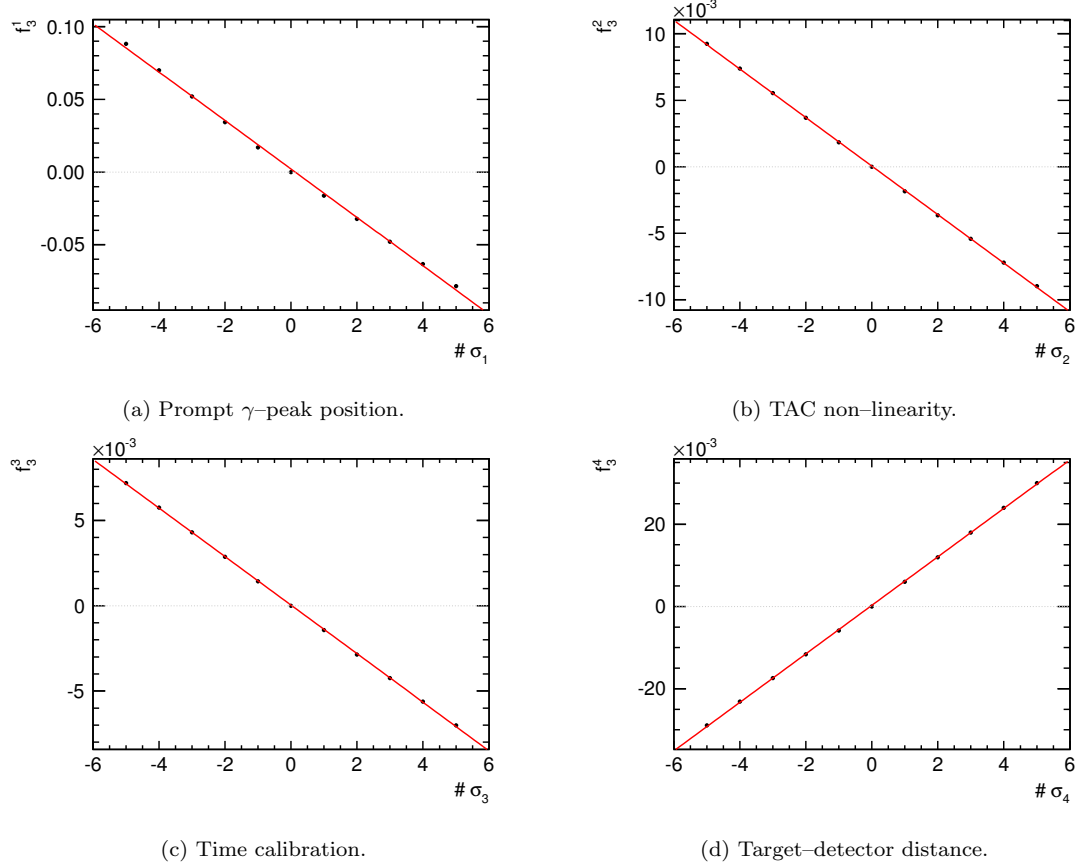


**Figure 6.32:** Fractional change  $f_n^k$  of the  $n$ -th value of the theoretical light output  $L^{\text{theo}}$  under the variation of the  $k$ -th source of systematics by an integer multiple of  $\sigma_k$ . Shown is  $f_n^k$  for the theoretical value expected at the third data point ( $n = 3$ ) of the proton response measurement with wsLAB + 2g/lPPO + 15mg/lbis-MSB, shown in Fig. 6.27b. The source of the altered systematic effect is given in the subcaption.

Since the nuisance parameters  $\xi_k$  are assumed to have Gaussian constraints centered on zero, the requirement for the applicability of Eq. 6.22 is a linear variation of  $L^{\text{theo}}$  with the variation of the systematic uncertainties, that is the  $f_n^k$ 's have to be linear. For this reason, the effect on  $L$  caused by the first four sources of systematics, listed in Tab. 6.9, is tested. The remaining uncertainties are directly multiplied with  $L$  in the calculation of its variation, linearity is thus trivially given. Figure 6.32 shows the dependence of  $f_n^k$  on the number of sigmas by which the  $k$ -th source of systematics is changed for one data point of one response function and scintillator, showing excellent agreement with a linear behavior. These figures are representative for all measurements, since a measurement of campaign C4 was chosen, in which the time calibration factor is  $c_{\text{tcal}} \approx 1.6 \text{ ns/ch}$  instead of  $c_{\text{tcal}} \approx 0.8 \text{ ns/ch}$  (see Tab. 6.4). Thus the uncertainty of the  $\gamma$ -peak position and the TAC non-linearity have the largest effect on  $L$  in this campaign.

The minimum of the  $\chi^2$  function with respect to  $kB$ ,  $C$ , as well as all nuisance parameters, is calculated with the MINUIT [234] implementation in the ROOT analysis

framework [235].  $C$ , introduced in [37], is a simple higher order correction term without a physical interpretation (see Sec. 2.6.3). Thus  $C$  is also not limited and negative values are possible, as observed for example in [236] for EJ-200 plastic scintillator. In most of the cases, though,  $C$  is found to be positive (e.g. [237, 238, 239, 240, 241, 242]). Each  $\chi^2$  minimization is therefore performed up to three times: Once  $C$  is allowed to float freely, once  $C$  is constrained to positive values including zero and once  $C = 0$  is fixed, yielding a fit of the original Birks' law Eq. 2.11 with one fit parameter. If  $C$ , fit as a free parameter, is at least  $1\sigma$  greater than zero, the constrained fit is not executed.

The number of degrees of freedom (ndf) is calculated as per

$$\text{ndf} = N - J + K' - M, \quad (6.23)$$

where  $N$  is the number of data points considered in Eq. 6.22.  $J$  is the number of model parameters and  $M$  is the number of effective constraints. The number  $K$  of nuisance parameters has to be accounted for, since these parameters contribute to  $\chi^2$  with their Gaussian constraints. However, some nuisance parameters have the same effect on  $L^{\text{theo}}$  and the minimization procedure adjusts the respective parameters in the same way. They are fully correlated. These nuisance parameters do not contribute to  $\chi^2$  independently and have to be counted together as one parameter. This is twice the case: The TAC non-linearity (Nr. 2 in Tab. 6.9) and the uncertainty on the prompt  $\gamma$ -peak position (Nr. 1 in Tab. 6.9) affect the TOF measurement equivalently and the edge position uncertainty (Nr. 10a, b in Tab. 6.9) and the PH offset uncertainty (Nr. 8, 9 in Tab. 6.9) affect the PH measurement equivalently. Thus only a reduced number  $K' = K - 2$  is considered as additional degrees of freedom. It should be noted that for the proton quenching evaluation, in which HG and LG data sets are used, the PH offset uncertainty in HG measurements (Nr. 8 in Tab. 6.9) and in LG measurements (Nr. 9 in Tab. 6.9) are not correlated, since they do not affect the same data points (see Sec. 6.5.5).

The model parameter uncertainties are extracted from the  $\chi^2$  projections on  $kB$  and  $C$  respectively. If the best fit value has a two-sided  $1\sigma$  limit, the corresponding parameter values at  $\chi^2 - \chi^2_{\min} = 1$  are read out. If only an upper limit can be achieved, the limit at 95% C.L. is determined, referring to  $\chi^2 - \chi^2_{\min} = 1.645$ .

The value and uncertainty of the parameters  $kB$  and  $C$  in Birks' law Eq. 2.12 are additionally correlated with the material's stopping power  $dE/dX$  and the theoretical uncertainty within the stopping power calculation. With the SRIM code, a determination of the stopping power for all elemental materials is possible with an accuracy of "a few percent" [232, 243], thus the described fitting procedure is repeated for  $dE/dx + \sigma_{dE/dx}$  and  $dE/dx - \sigma_{dE/dx}$ , assuming a shift of 3%. Note that this uncertainty covers also the uncertainty from the calculated densities of Tab. 6.2, introduced from an about 4°C higher ambient temperature than used for the table. This theoretical uncertainty is added quadratically to the experimental one. All fit results are presented and discussed in the following

two sections.

### 6.6.1 Fit results using proton light responses

Figures 6.33 and 6.34 show the experimentally determined proton light output data points using different LAB and wsLAB scintillators, respectively, together with the adapted Birks law Eq. 2.12. In these figures the fit with unconstrained  $C$  is shown as well as the fit with  $C = 0$ . Both curves agree, hence qualitatively  $C$  has no impact on the predicted light response behavior. The numerical values resulting from these fits, as well as from a fit of Birks' law omitting negative values for  $C$ , are listed in Tab. 6.10. As mentioned in Sec. 6.1, two independent analyses have been performed using a subset of the data (LAB1–4). The results of the earlier analysis are published in [32] and do not differ from the results presented here within one standard deviation. Regarding Tab. 6.10, again no significant influence of  $C$  is observed. For each scintillator sample, Birks' parameter  $kB$  is the same within the uncertainties independent of the fit condition imposed on  $C$  and, comparing the goodness of each fit, none of the three fit conditions is to be favored. With  $C$  floating freely, the fit converges twice at a negative value of  $C$ , once for LAB + 2 g/lPPO + 15 mg/lbis-MSB (LAB1) and once for LAB + 2 g/lPPO (LAB2). Given the respective  $1\sigma$  uncertainties, however, both values are consistent with zero. In total, only in the fit using LAB + 2 g/lPPO + 0.1% Nd (LAB5),  $C$  deviates with  $(2.0 \pm 1.6) \times 10^{-6} \text{ cm}^2/\text{MeV}^2$  from zero by slightly more than  $1\sigma$ .

### 6.6.2 Discussion of the measured proton Birks' parameters

Concluding from the above observations, inserting an extra model parameter  $C$  is not necessary and the proton light response functions are well-described by the original Birks law Eq. 2.11. For the ease of comparison, the corresponding  $kB$  values are summarized in Fig. 6.35, showing an agreement between the Birks parameters of all investigated LAB based scintillators. In the following paragraphs, the influence of the individual additives to the LAB solvent on the  $kB$  measurements is discussed, where the aspect of electron affinity is discussed separately at the end.

#### Influence of solutes

According to current knowledge, ionization quenching processes are primary processes in the scintillator, in other words processes that transfer ionization energy to excitation energy of the solvent. As explained in Sec. 2.6.3, ionization quenching suppresses the excitation of the solvent molecules into  $\pi$ -electron singlet states and enhances the population of their  $\pi$ -electron triplet states. This circumstance changes the light yield as well as the waveform of the scintillation pulse emitted by the solvent, independent of the solute content. Direct excitations or ionizations of secondary molecules are negligible primary processes due to the low molecule concentrations [12]. The transfer of the emitted light to the solutes is subject to secondary processes. Consequently, for scintillators with the same solvent, the magnitude of ionization quenching is expected to be the same, independent of possible solutes

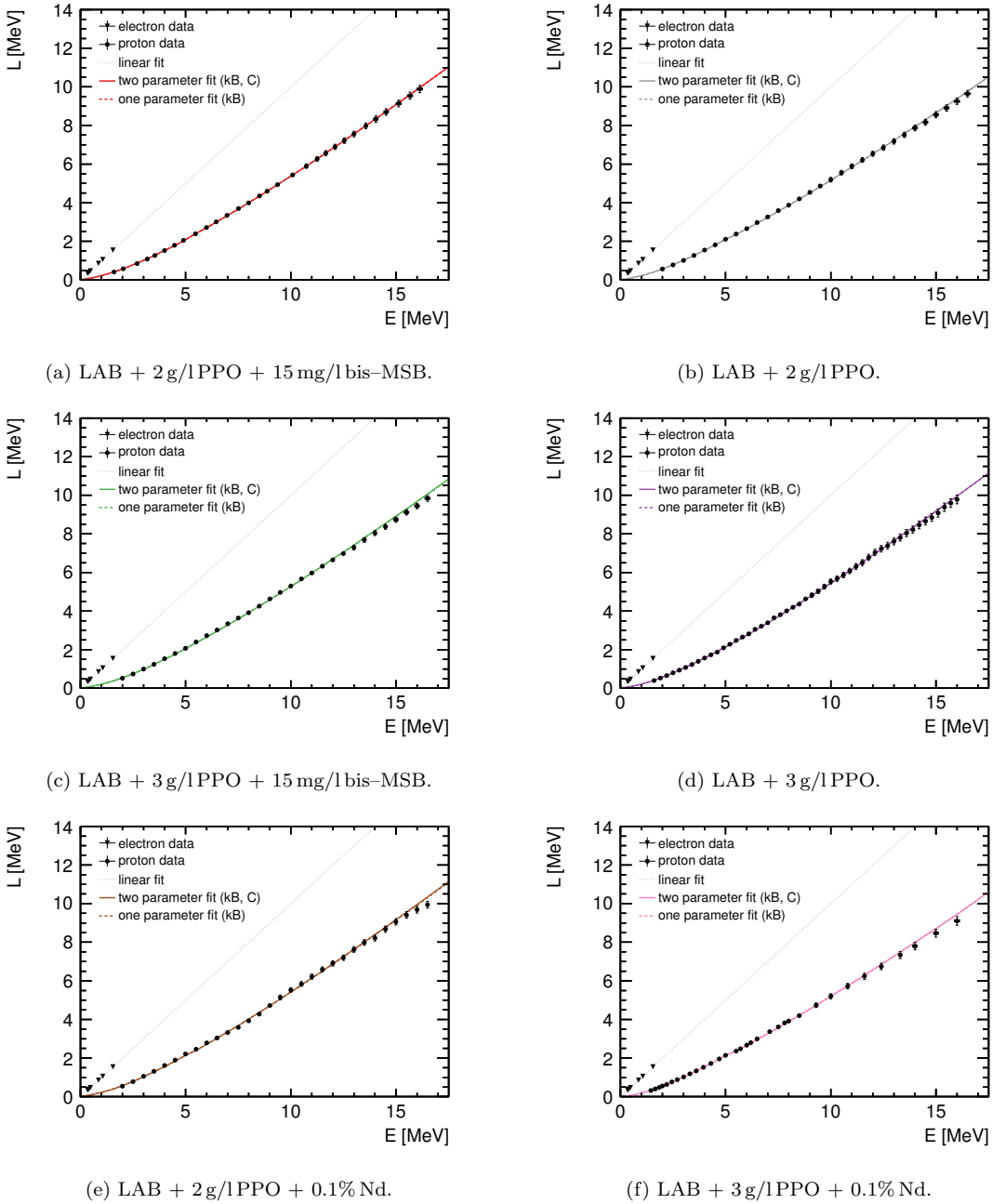


**Figure 6.33:** Light output  $L$  in electron-equivalent energy as function of kinetic energy  $E$ .  $L$  is shown for electrons and protons in different LAB based scintillators, specified in the subcaptions (a-f). Electron data is fitted with Eq. 6.8 and proton data with Eq. 2.12 including all systematic effects, listed in Tab. 6.9, as nuisance parameters. Once both quenching parameters ( $kB, C$ ) are allowed to float freely and once  $C = 0$  is fixed. No difference in the resulting light responses is observed. In the shown total uncertainties, the single contributions in Tab. 6.9 are added quadratically.

**Table 6.10:** Proton quenching parameters  $kB$  and  $C$  and their total  $1\sigma$  uncertainty resulting from a fit of Eq. 2.12 to data (see Fig. 6.33 and 6.34) using different LAB and wsLAB scintillators. Upper limits are given for a confidence level of 95%. The number of degrees of freedom ndf is calculated according to Eq. 6.23. The detailed scintillator descriptions are given in Tab. 6.1.

sample	$kB$ [cm/MeV]	$C$ ( $\times 10^{-6}$ ) [cm $^2$ /MeV $^2$ ]	$C$ , fit condition	$\chi^2/\text{ndf}$
LAB1	$0.0099 \pm 0.0005$	$-1.6 \pm 2.2$	free	4.52/36
	$0.0096 \pm 0.0003$	$\leq 2.7$	constrained	5.03/35
	$0.0096 \pm 0.0003$	0.0	fixed	5.03/37
LAB2	$0.0095 \pm 0.0007$	$-1.0 \pm 3.2$	free	9.82/36
	$0.0093 \pm 0.0003$	$\leq 8.3$	constrained	9.92/35
	$0.0093 \pm 0.0004$	0.0	fixed	9.92/37
LAB3	$0.0095 \pm 0.0004$	$1.3 \pm 1.7$	free	26.17/36
	$0.0095 \pm 0.0004$	$\leq 2.1$	constrained	26.17/35
	$0.0097 \pm 0.0003$	0.0	fixed	26.82/37
LAB4	$0.0090 \pm 0.0004$	$0.5 \pm 1.3$	free	14.86/55
	$0.0090 \pm 0.0003$	$\leq 1.5$	constrained	14.86/54
	$0.0091 \pm 0.0003$	0.0	fixed	15.01/56
LAB5	$0.0087 \pm 0.0004$	$2.0 \pm 1.6$	free	36.71/36
	$0.0092 \pm 0.0003$	0.0	fixed	38.33/37
LAB6	$0.0090 \pm 0.0005$	$0.2 \pm 2.3$	free	34.04/39
	$0.0090 \pm 0.0007$	$\leq 18.1$	constrained	34.04/38
	$0.0090 \pm 0.0004$	0.0	fixed	34.04/40
wsLAB1	$0.0086 \pm 0.0006$	$1.6 \pm 1.9$	free	6.55/36
	$0.0086 \pm 0.0006$	$\leq 2.4$	constrained	6.55/35
	$0.0090 \pm 0.0003$	0.0	fixed	7.29/37
wsLAB2	$0.0089 \pm 0.0005$	$1.6 \pm 1.9$	free	6.96/36
	$0.0089 \pm 0.0006$	$\leq 2.4$	constrained	6.96/35
	$0.0093 \pm 0.0003$	0.0	fixed	7.74/37

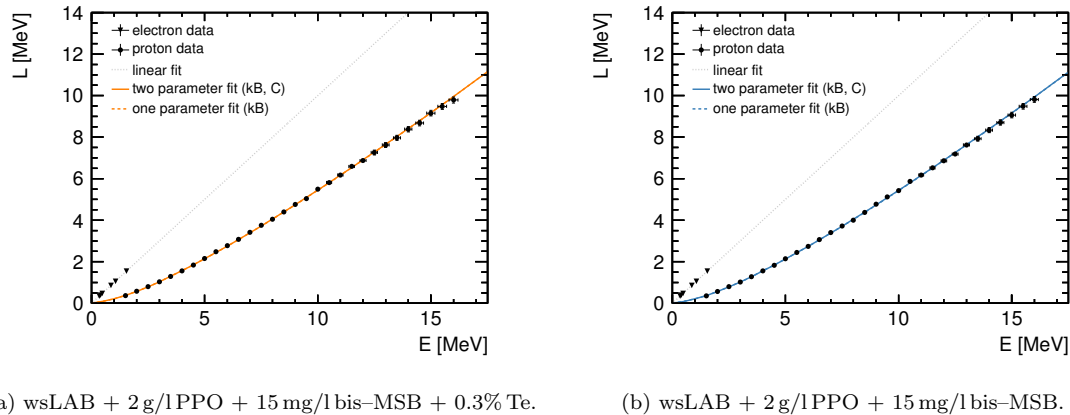


**Figure 6.34:** Light output  $L$  in electron-equivalent energy as function of kinetic energy  $E$ .  $L$  is shown for electrons and protons in wsLAB scintillator, with (a) and without (b) Te-loading. Electron data is fitted with Eq. 6.8 and proton data with Eq. 2.12 including all systematic effects (see Tab. 6.9) as nuisance parameters. Once both quenching parameters ( $kB$ ,  $C$ ) are free and once  $C = 0$  is fixed. No difference in the resulting light responses is observed. The PRS and water content in wsLAB are 5% and 1.5%, respectively. In the shown total uncertainties, the single contributions in Tab. 6.9 are added quadratically.

Within the presented proton quenching measurements, no significant deviation from these considerations is observed, comparing the  $kB$  values in Fig. 6.35 of the binary and ternary LAB based scintillators LAB1 through LAB4, which only differ in the solute concentrations.

### Influence of metals

The addition of the non-scintillating metals, Nd or Te, leads to impurity quenching and, in the case of Nd, to color quenching, as described in Sec. 2.6.1 and Sec. 6.2. These types of quenching affect electrons and ions in the same way, in contrast to ionization quenching. The proton light response relative to the electron light response is not expected to change, even with high loadings. Nonetheless, the measured Birks parameter will vary, when the isotope concentrations become high enough to significantly change the total stopping power, due to their correlation in Eq. 2.12, even if the relative proton light output does not change. Thus great care has to be taken with the interpretation of Birks' parameter  $kB$  and the parameter  $C$ , i.e. the quenching parameters. More conclusive is a material property independent parameterization of the quenching function – the ratio of the ion light response function to the electron response function – as for instance presented in [38]. In the tested samples, however, the Nd (Te) concentration of 0.1% (0.3%) changes the stopping powers compared to unloaded LAB (wsLAB) by less than 2% (see Fig. 6.31), well within the assumed uncertainty of the stopping power calculation using SRIM. As a consequence, the measured Birks' parameters are not expected to be affected within their total uncertainties, which is confirmed by the agreement between the Birks parameters of loaded (LAB5, LAB6, wsLAB1) and unloaded (LAB1–4, wsLAB2) LAB based scintillators presented in Fig. 6.35.

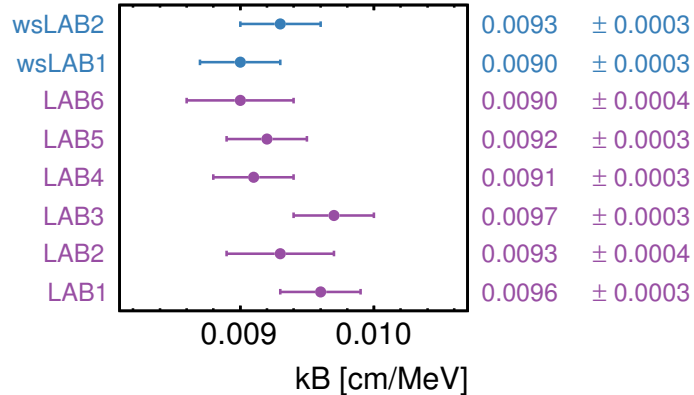


**Figure 6.35:** Measured Birks' parameter  $kB$ , parameterizing proton quenching in different LAB (violet) and wsLAB (blue) scintillators. The values are taken from Tab. 6.10 with  $C = 0 \text{ cm}^2/\text{MeV}^2$ . The detailed scintillator descriptions are given in Tab. 6.1.

SNO+ plans to increase the Te-loading from the initial loading of 0.3% to the percent level. Depending on the loading level achieved, the presented fit has to be repeated with the newly calculated stopping power of the scintillator. Since a higher loading is expected to increase  $dE/dx$ , the quenching parameters are expected to decrease. Depending on the increase of the water and PRS component, necessary for the higher Te-loading, a new measurement is recommended for the reason given in the following paragraph.

### Influence of water and PRS

Since bound water and PRS are only present together in the used samples, they also have to be discussed together. Water is, like Nd or Te, non-scintillating and from this point of view an impurity quencher. However, it produces Cherenkov light, if the charged particle is fast enough. While the Cherenkov threshold for electrons in water is around 260 keV, it is  $> 1 \text{ GeV}$  for protons. The electron energy range observed in the presented measurements is 393 keV–1547 keV and the maximum proton energy is about 17 MeV. Thus an additional light component added up to the scintillation light of wsLAB scintillators, when the electron light output was measured, which is not present, in the proton light output measurements. Compared to standard LAB based scintillators, the proton light yield relative to the electron light could thus be lower, resulting in a higher value of  $kB$ . However, the water concentration of 1.5% in the investigated wsLAB scintillators is very small, in this context, and the Cherenkov light yield of water for 1 MeV electrons is about 50 times lower than the corresponding LAB scintillation light yield [189, 244]. This makes the additional Cherenkov light yield smaller than the statistical fluctuations of the scintillation light yield and no significant effect is expected on the measured ionization quenching parameters.

These considerations motivate a systematic study of the variation of  $kB$  with an increasing water concentration, beyond the statistical fluctuations of the scintillation light yield. This is in particular interesting for SNO+ in the view of higher Te-loadings.

Also the aromatic PRS used (see Sec. 5.3.3) does not scintillate, since it has no system of delocalized  $\pi$ -electrons. The total light yield is reduced. The O contained in PRS is bound in the molecule and thus not contributing to oxygen quenching induced by free O<sub>2</sub> (see Sec. 2.6.2). Thus, in summary, also PRS is not expected to affect ionization quenching but only to reduce the total light output of all particles identically.

A direct comparison of the determined  $kB$  values for LAB + 2 g/lPPO + 15 mg/lbis-MSB (LAB1) and wsLAB + 2 g/lPPO + 15 mg/lbis-MSB (wsLAB2), given in Fig. 6.35, does not reveal a difference in the results within the uncertainties. Additionally, also the deviation in the respective stopping powers is  $\sim 1\%$  (see Fig. 6.31) and thus too small to shift the quenching parameters beyond at least one standard deviation. Thus, the same  $kB$  value leads to the conclusion that the proton ionization quenching behavior does not change, when water at a concentration of 1.5% and PRS at a concentration of 5% is added to LAB, in agreement with the expectations.

### Electron affinities

In this discussion so far, it was assumed that none of the addends, Nd, Te(OH)<sub>6</sub>, PRS or H<sub>2</sub>O, attracts electrons. Since trapped electrons, however, are not available anymore for recombination processes and thus for secondary LS molecule excitations (see Sec. 2.4.1), this aspect is shortly addressed here. To illustrate the effect of lost electrons on the observed quenching factor Eq. 2.13, the following equations are used:

$$Q_i = \frac{L_i}{L_e} = \frac{{}^1l_{i,p} + {}^1l_{i,s} + {}^3l_{i,s}}{{}^1l_{e,p} + {}^1l_{e,s} + {}^3l_{e,s}}, \quad (6.24)$$

$$Q_i^* = \frac{{}^1l_{i,p} + ({}^1l_{i,s} - \frac{1}{4}n) + ({}^3l_{i,s} - \frac{3}{4}n')}{{}^1l_{e,p} + ({}^1l_{e,s} - \frac{1}{4}m) + ({}^3l_{e,s} - \frac{3}{4}m')}, \quad (6.25)$$

in which the ion light output  $L_i$  and electron light output  $L_e$  are split up into light components  $l$  from singlet and triplet excited states after primary and secondary excitations. The superscript denotes the multiplicity of the excited state, analog to Sec. 2.5, and the additional subscript denotes whether it is a primary excitation or a secondary excitation after ion electron recombination. In Eq. 6.24 it is assumed that none of the free electrons in the LS are lost and thus available for recombination processes. In Eq. 6.25 it is assumed that electrons are absorbed by non-scintillating electron acceptors, where  $n^{(i)}$  and  $m^{(i)}$  quantify the consequent amount of lost light. The partitioning of the light losses corresponds to the 25%:75% population probability of singlet compared to triplet exited states

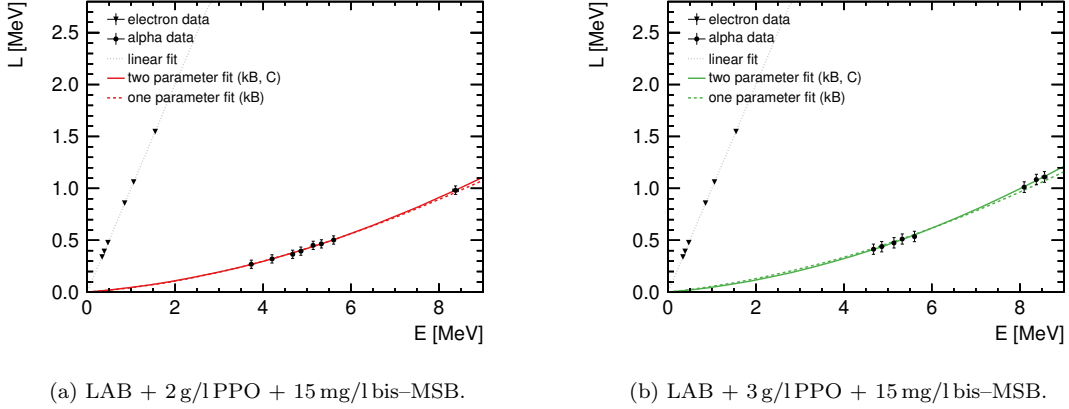


**Figure 6.36:** Light output  $L$  in electron-equivalent energy as function of kinetic energy  $E$ .  $L$  is shown for electrons and  $\alpha$ -particles in LAB scintillator with 15 mg/l bis-MSB and 2 g/l (a) or 3 g/l (b) PPO. Electron data is fitted with Eq. 6.8 and  $\alpha$ -particle data with Eq. 2.12 including all systematic effects, listed in Tab. 6.9, as nuisance parameters. Once both quenching parameters ( $kB, C$ ) are free and once  $C = 0$  is fixed. In the shown total uncertainties, the single contributions in Tab. 6.9 are added quadratically.

after recombination (see Sec. 2.4.1). Since the quantum efficiencies of singlet and triplet state de-excitation differ, the same amount of lost electrons leads to a different amount of lost light, and thus  $n, m \neq n', m'$ . Comparing Eq. 6.24 and 6.25 shows that  $Q_i \approx Q_i^*$  is only true, if the primary light output component is much larger than the sum of the secondary light output components, i.e.  ${}^1l_p \gg ({}^1l_s + {}^3l_s)$ , or if the light losses are much smaller than the secondary light yields, i.e.  $n, n', m, m' \ll {}^1l_{i,s}, {}^3l_{i,s}, {}^1l_{e,s}, {}^3l_{e,s}$ . If instead the light losses are statistically significant, then  $Q_i \neq Q_i^*$ , which means the ionization quenching strength is modified by the addition of a strong electron acceptor. The agreement of all  $kB$  values within the uncertainties, presented in Fig. 6.35, hence means that none of the non-scintillating addends has a high enough electron affinity to significantly change the observed light output given the detector light output resolution and uncertainties of the results.

### 6.6.3 Fit results using $\alpha$ -particle light responses

The experimentally determined  $\alpha$ -particle light output in various LAB and wsLAB scintillators as well as the model Eq. 2.12, fitted once with unconstrained and once with fixed  $C$ , are presented in Fig. 6.36 and Fig. 6.37. In contrast to the case of the proton responses, the two model curves slightly deviate from each other, where the difference increases with energy. This deviation is the strongest for wsLAB + 2 g/l PPO + 15 mg/l bis-MSB, which is shown in Fig. 6.37b. In all four measurements, adding one more free parameter improves the fit, as evident from the reduced  $\chi^2$  values listed together with the best fit quenching parameters in Tab. 6.11, especially for wsLAB + 2 g/l PPO + 15 mg/l bis-MSB (wsLAB2). A fit with the condition  $C \geq 0$  is not performed, since the  $C$  values resulting from an unconstrained fit are all well-above zero. Despite the improvement of the fit, when  $C$  is

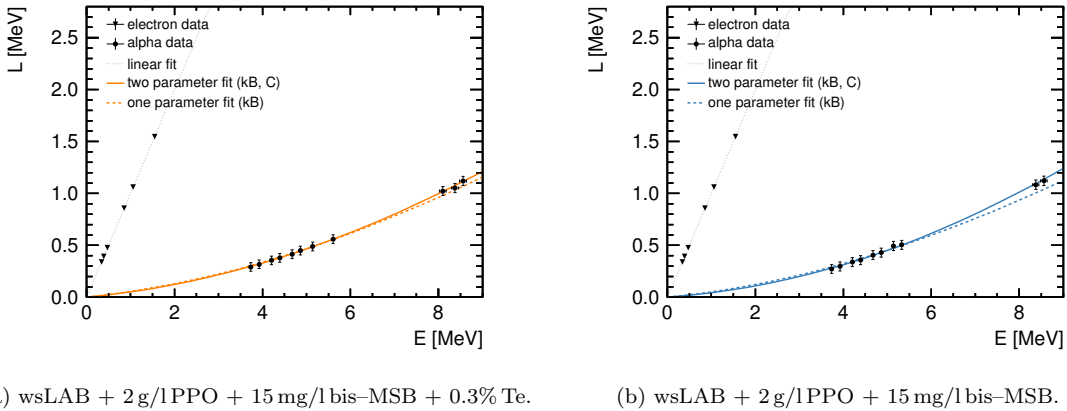


**Figure 6.37:** Light output  $L$  in electron-equivalent energy as function of kinetic energy  $E$  for electrons and  $\alpha$ -particles in wsLAB scintillator with (a) and without (b) Te-loading. Electron data is fitted with Eq. 6.8 and  $\alpha$ -particle data with Eq. 2.12 including all systematic effects (see Tab. 6.9) as nuisance parameters. Once both parameters ( $kB$ ,  $C$ ) are free, once  $C = 0$  is fixed. The PRS and water content are 5% and 1.5%, respectively. In the shown total uncertainties, the single contributions in Tab. 6.9 are added quadratically.

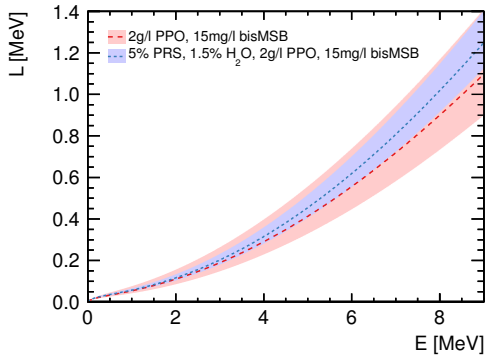


**Figure 6.38:** Light output  $L$  as function of energy  $E$  (see Eq. 2.12) of  $\alpha$ -particles traversing different LAB based scintillators. The admixtures to LAB are noted in the plot legend, referring to LAB1 (red dashed line) and wsLAB2 (blue dotted line). Also shown are the error bands resulting from the  $1\sigma$  fit uncertainties of the free parameters  $kB$  and  $C$ , listed in Tab. 6.11.

included as a free parameter, the difference between the two resulting light output functions becomes noticeable only at  $\alpha$ -particle energies above  $\sim 6$  MeV. At 8.95 MeV, the highest  $\alpha$ -particle energy within the natural U and Th chains ( $^{212}\text{Po} \rightarrow ^{208}\text{Pb} + \alpha$ , see Fig. A.1), the difference of  $L$  is  $\sim 9\%$  in wsLAB + 2 g/l PPO + 15 mg/l bis-MSB (see Fig. 6.37b) and at least a factor of two smaller in the three other samples (see Fig. 6.36 and 6.37a).

#### 6.6.4 Discussion of the measured Birks' parameters of $\alpha$ -particles

Following the discussion about proton quenching in Sec. 6.6.2, it also for  $\alpha$ -particles expected that the relative light output functions behave the same throughout the different samples, since the arguments given above are the same for both particle species. The difference in this subsection is the fact that the extended Birks law, which includes the quadratic correction term  $C$ , is preferred, comparing the values for  $\chi^2/\text{ndf}$  in Tab. 6.11. Since, however,  $kB$  and  $C$  are strongly anti-correlated, a direct comparison between the values of these parameters, resulting from measurements with different samples, is

**Table 6.11:**  $\alpha$ -particle quenching parameters  $kB$  and  $C$  and their total  $1\sigma$  uncertainty, following Eq. 2.12, determined for different LAB and wsLAB scintillators. Upper limits are given for a confidence level of 95%.

sample	$kB$ [cm/MeV]	$C$ ( $\times 10^{-6}$ ) [cm $^2$ /MeV $^2$ ]	$C$ , fit condition	$\chi^2/\text{ndf}$
LAB1	$0.0059 \pm 0.0010$	$2.0 \pm 1.1$	free	5.69/12
	$0.0076 \pm 0.0003$	0.0	fixed	9.47/13
LAB3	$0.0052 \pm 0.0007$	$1.9 \pm 0.9$	free	2.68/12
	$0.0071 \pm 0.0003$	0.0	fixed	17.63/13
wsLAB1	$0.0054 \pm 0.0005$	$1.4 \pm 0.4$	free	2.76/15
	$0.0070 \pm 0.0004$	0.0	fixed	24.27/16
wsLAB2	$0.0042 \pm 0.0005$	$2.6 \pm 0.4$	free	9.27/14
	$0.0072 \pm 0.0004$	0.0	fixed	71.48/15

not conclusive. This is to say, a disagreement between the values of  $kB$  and/or  $C$  of different samples within one standard deviation, as is the case for wsLAB2 compared to the other three samples listed in Tab. 6.11, does not necessarily mean, the light output functions disagree. This is demonstrated in Fig. 6.38, where the light output function of wsLAB + 2 g/lPPO + 15 mg/lbis-MSB (wsLAB2) and the one of LAB + 2 g/lPPO + 15 mg/lbis-MSB (LAB1) are shown. Also shown are the error bands of the light output functions considering the  $1\sigma$  total uncertainty resulting from the uncertainties of  $kB$  and  $C$ . Both light output functions agree within the total uncertainty. The curves from the other two samples lie between the two presented ones and are thus also in agreement with both of them and with each other.

Prominent in Fig. 6.38 is the large uncertainty of the  $\alpha$ -particle light response of LAB1, an instance that would be improved by a second high energy data point around  $E \approx 8$  MeV. Using this scintillator sample, however, only one data point could be safely extracted in this energy range.

Finally, comparing the fit results for  $kB$  listed in Tab. 6.11 from the one-parameter fit, shows that no significant difference between the values is observed in this case. Since the relative differences in the  $\alpha$ -particle stopping powers (see Fig. 6.31b) are also for  $\alpha$ -particles smaller than the considered 3% uncertainty on  $dE/dx$ , an agreement between the values of  $kB$  means an agreement between the different light output functions.

To conclude, the results from the  $\alpha$ -quenching measurements reveal no significant difference between the ionization quenching behavior in the two LAB and two wsLAB

samples. This observation is in agreement with the results from the proton quenching measurements.

## 6.7 Influence of the non-linearity of the electron light response

As mentioned in Sec. 6.4, the slight non-linearity of the electron light yield in LS leads to a small negative energy offset  $E_0$  (see Eq. 6.8), in case the electron light yield behavior is assumed to be strictly linear. Any assumption with respect to the electron light yield has a direct impact on the measured proton and  $\alpha$ -particle ionization quenching parameters, since the information of interest is the ion light yield compared to the electron light yield in the same scintillator.

In contrast to the ion response, the electron response consists of two components, scintillation light and additionally Cherenkov light. Equation 2.12 approximates  $L = S \cdot E$  for small  $dE/dx$ , thus the non-linearity from the scintillation component alone is expected to be very small. This is confirmed by [226], measuring the electron light yield below and above the Cherenkov threshold, and by [34], measuring exclusively below the Cherenkov threshold. Extrapolation of the displayed scintillation light functions yields  $E_0 \approx 5$  keV in [34]. In [226], the offset is too small to be resolved and close to 0 keV.

The onset of Cherenkov light causes a total offset of  $E_0 \approx 100$  keV for LAB based scintillators and  $E_0 \approx 80$  keV for EJ301, in [226] and thus is presumably the main cause of the observed electron non-linearity. The Cherenkov photon yield itself depends on the refractive index of the scintillator. The fraction of observed Cherenkov light generally depends on the detector, since the emitted Cherenkov photons are concentrated in the near UV wavelength region, where typically the sensitivity of detectors strongly decreases. The detected Cherenkov component is even strongly suppressed, if, for instance, the PMT window and the light guide are not UV transparent. On the other hand, if the detector is large compared to the absorption and re-emission length scale, a fraction of the Cherenkov light can be absorbed and re-emitted at higher wavelengths, with the efficiency depending on the absorption spectrum of the scintillator. In summary, the amount of observed Cherenkov photons depends on the wavelength dependent sensitivity and possibly the size of the detector, as well as on the primary wavelength shifter.

As a consequence, also the slope of the observed total electron response function above the Cherenkov threshold, consisting of scintillation plus Cherenkov light, depends on the detector as well as the scintillator secondaries and refractive index. These dependencies are propagated into the ionization quenching measurements of heavy charged particles, when the light response functions are given relative to the one of electrons, even though for example the process of ionization quenching itself is competing with primary processes

in the scintillator [11] and thus mostly independent of the secondaries.

Ideally, the deviation from linearity of the electron response, parameterized by  $E_0$ , is determined in the same detector. This is not always possible in which case assumptions on  $E_0$  have to be made. References [32, 237, 238], for instance, consider strict linearity and therewith  $E_0 = 0 \text{ keV}$ , whereas [213] assumes  $E_0 = 5 \text{ keV}$ , a figure known from dedicated electron response measurements [245]. The value  $E_0 = 5 \text{ keV}$  was measured for NE213 small scale detectors of various volumes and shapes [212, 245], which all agreed. NE213, however, consists like EJ301 of 93% xylene and 7% naphthalene doped with activators and POPOP, thus  $E_0$  should be comparable to the one of EJ301, but is  $E_0 \approx 80 \text{ keV}$  in the measurements reported in [226]. This difference confirms that  $E_0$  is at best determined in the detector used for the ion measurements as well.

In order to study the influence of  $E_0$  on the quenching parameters  $kB$  and  $C$ , fits using LAB + 5% PRS + 1.5% water + 2 g/l PPO + 15 mg/l bis-MSB + 0.3% Te are repeated for  $E_0 = 0, 5, 50, 100 \text{ keV}$  and the results are listed in Tab. 6.12. No nuisance parameters are included in this study. A shift of the order of 5 keV does not significantly change the resulting best fit values, only the reduced  $\chi^2$  increases slightly, which is also given in Tab. 6.12. A shift of 100 keV, though, leads to a shift by more than  $4\sigma_{kB}$  in the one-parameter fit for protons and more than  $8\sigma_{kB}$  in the one-parameter fit for  $\alpha$ -particles and the proton and  $\alpha$ -particle Birks constants are closer together. However, in the corresponding fits, the reduced  $\chi^2$  becomes  $\sim 11$  for protons and  $\sim 46$  for  $\alpha$ -particles. This means, the Birks model cannot properly describe the data anymore without the quadratic correction term, and thus  $C$ , in which case the reduced  $\chi^2$  becomes  $\sim 2$  and  $\sim 4$ , respectively. In conclusion, the treatment of the electron non-linearity during ionization quenching measurements can significantly influence the resulting quenching parameters  $kB$  and  $C$ .

## 6.8 Comparison of the alpha quenching results with independent LAB measurements

NE213, and its equivalents BC501A and EJ301, are one of the most investigated liquid scintillators and a multitude of ionization quenching measurements exist [226, 238, 240, 241, 242, 246]. Comparing the quenching parameters for the same particle reveals disagreements and it is an open discussion [36], how strongly the determined quenching parameter(s)  $kB$  (and  $C$ ) depend on the measurement conditions, experimental set-up and analysis method, as partly addressed in the above section. Within the following section, the presented neutron beam alpha quenching measurements are compared with two further alpha quenching measurements using the same solvent, LAB, but different detectors and experimental approaches.

**Table 6.12:** Proton and alpha quenching parameters  $kB$  and  $C$  and their total uncertainties resulting from a fit of Birks' law Eq. 2.12 to the measured light output of LAB + 5% PRS + 1.5% water + 2 g/l PPO + 15 mg/l bis-MSB + 0.3% Te after applying a shift of  $E_0$  to the light output scale.

particle	$E_0$ [MeV]	$kB$ [cm/MeV]	$C$ ( $\times 10^{-6}$ ) [cm $^2$ /MeV $^2$ ]	$\chi^2/\text{ndf}$
proton	0.000	$0.0090 \pm 0.0003$	$0.5 \pm 0.9$	9.22/28
	0.000	$0.0091 \pm 0.0002$	—	9.47/29
	0.005	$0.0089 \pm 0.0003$	$1.1 \pm 1.0$	9.98/28
	0.005	$0.0091 \pm 0.0002$	—	11.29/29
	0.050	$0.0084 \pm 0.0003$	$7.5 \pm 1.1$	21.60/28
	0.050	$0.0096 \pm 0.0002$	—	78.34/29
	0.100	$0.0076 \pm 0.0003$	$17.2 \pm 1.2$	53.27/28
	0.100	$0.0104 \pm 0.0002$	—	319.31/29
$\alpha$ -particle	0.000	$0.0054 \pm 0.0004$	$1.4 \pm 0.3$	2.78/9
	0.000	$0.0072 \pm 0.0002$	—	33.62/11
	0.005	$0.0053 \pm 0.0004$	$1.6 \pm 0.3$	3.09/9
	0.005	$0.0073 \pm 0.0002$	—	41.47/11
	0.050	$0.0038 \pm 0.0004$	$3.5 \pm 0.3$	9.41/9
	0.050	$0.0082 \pm 0.0002$	—	172.39/11
	0.100	$0.0014 \pm 0.0004$	$6.7 \pm 0.3$	34.45/9
	0.100	$0.0097 \pm 0.0002$	—	507.02/11

One approach uses a 28 ml cuvette filled with  $^{nat}\text{Sm}$ -loaded LAB scintillator, which includes the  $\alpha$ -particle emitting isotope  $^{147}\text{Sm}$ , observed by two PMTs. This experiment is referred to in the following as Sm-experiment. Another approach uses a  $\sim 1\text{l}$  acrylic flask, also called bucket source, deployed in the water-filled SNO(+)<sup>11</sup> detector, using radioactive backgrounds as  $\alpha$ -particle sources. This experiment is from here on referred to as bucket source experiment. Common to all three experiments, including the one performed with in this thesis and referred to as neutron beam experiment, is the use of small scintillator volumes and UV transparent materials as well as of PMTs with similar wavelength sensitivity. Furthermore, the primary solute is in all cases PPO. The Sm-experiment was conducted by L. Neumann [247] and T. Kögler in 2013 and the bucket

<sup>11</sup>The bucket source was deployed in 2008, in the transition period from SNO to SNO+.

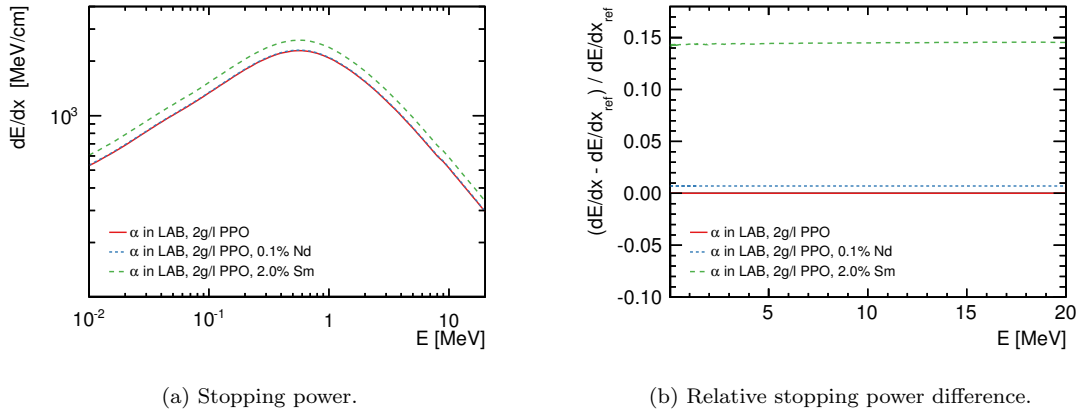


**Figure 6.39:** (a) Total stopping power  $dE/dx$  as function of energy for  $\alpha$ -particles of unloaded and loaded LAB based scintillators and (b) their relative difference to the stopping power of LAB + 2 g/l PPO, denoted as  $dE/dx_{ref}$ . The stopping powers are calculated with SRIM using the densities listed in Tab. 6.1 for the unloaded and Nd-loaded LAB scintillator and 0.997 g/cm<sup>3</sup> for the Sm-loaded LAB scintillator.

source analysis was performed by H. S. Wan Chan Tseung and H. M. O’Keeffe in 2009 within the SNO+ collaboration. Both measurements are described in more detail in the following.

For the ease of comparison, only  $kB$  is considered within this section, i.e. the original Birks’ law. The samples from the neutron beam experiment used for comparison are LAB + 2 g/l PPO + 15 mg/l bis-MSB (LAB1) and LAB + 3 g/l PPO + 15 mg/l bis-MSB (LAB3) and the respective fit results are summarized in Tab. 6.11. Though the two-parameter fit, which includes  $C$ , is favored, the one-parameter fit still yields a very good description in case of these two samples, with a reduced  $\chi^2$  of 0.73 and 1.36, respectively.

### 6.8.1 Alpha quenching measurement with Sm-loaded LAB

Natural Sm contains 14.99(18)%  $^{147}\text{Sm}$ , which decays under the emission of a 2.233 MeV  $\alpha$ -particle. At BNL, LAB was loaded with natural Sm at a concentration of 2% using TMHA, as in the procedure of Nd-loading (see Sec. 5.3.2). By loading the scintillator with the  $\alpha$ -particle source, the source is intrinsic and again surface effects are avoided. The final scintillator contains 2 g/l PPO as fluor. The high concentration of Sm increases the compound’s density to about 0.997 g/cm<sup>3</sup> responsible for nearly a 15% difference in the stopping power of loaded and unloaded LAB (see Fig. 6.39). The density is calculated on the basis of LAB2 from table Tab. 6.2.

At HZDR, a detector was set-up to measure the PMT charge  $Q$ , integrated over about 200 ns, which is induced by a charged particle traversing the scintillator volume.  $Q$  is proportional to the total light yield and measured in arbitrary units. To reduce noise, signals are identified by coincidence tagging using two PMTs (see Fig. 6.40). The measured

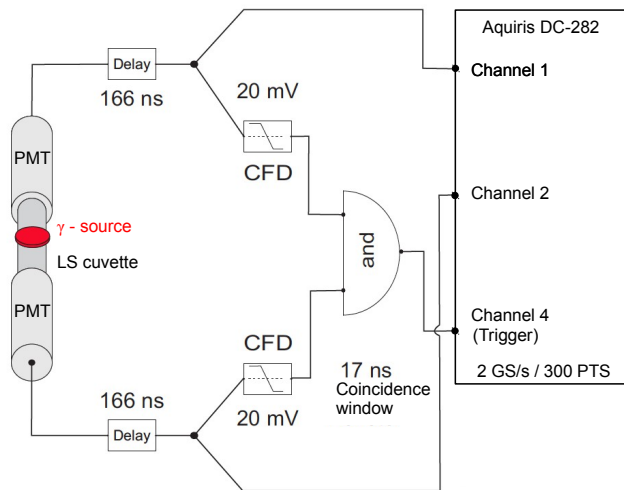


**Figure 6.40:** Schematic set-up at HZDR for the measurement of alpha quenching using Sm-loaded LAB scintillator [247, 14] (PMT: photomultiplier tube, LS: liquid scintillator, CFD: constant fraction discriminator).

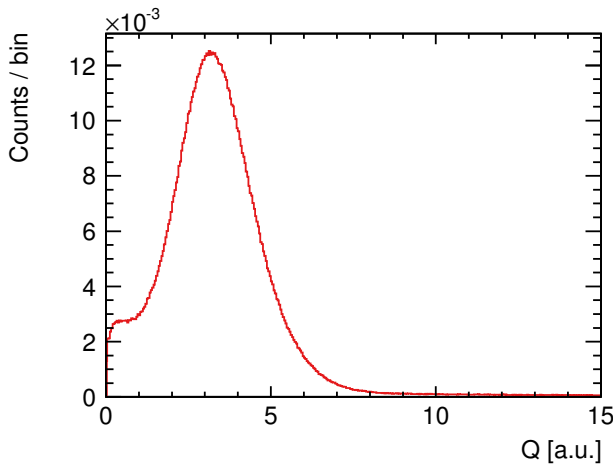


**Figure 6.41:** Normalized charge  $Q$  spectrum in arbitrary units (a.u.) of  $^{nat}\text{Sm}$  loaded LAB, measured within [247]. The prominent peak is induced by 2.233 MeV  $\alpha$ -particles from  $^{147}\text{Sm}$  decays.

charge spectrum of the deoxygenated Sm-loaded LAB is shown in Fig. 6.41 with an  $\alpha$ -peak mean value at  $Q = (3.2 \pm 0.3)$  a.u.. The charge scale is calibrated analogous to Eq. 6.6 as per

$$Q(E) = m \cdot E + a. \quad (6.26)$$

$E$  is the maximum Compton electron energy observed in charge spectra from different  $\gamma$ -sources ( $^{137}\text{Cs}$ ,  $^{166m}\text{Ho}$ ,  $^{60}\text{Co}$ ), successively placed on the center of the cuvette. The calibration factor  $m$  and intercept  $a$ , resulting from a fit of Eq. 6.26 to the calibration data, are  $(0.0396 \pm 0.0021)$  a.u./keV and  $(-3.39 \pm 1.9)$  a.u., respectively. The resulting  $\alpha$ -particle energy in electron-equivalent energy is  $E = (166.7 \pm 49.4)$  keV and is thus quenched by a factor of  $13.4 \pm 4.0$ .

### 6.8.2 Alpha quenching measurement using SNO+ bucket source data

The bucket source, shown in Fig. 6.42, is manufactured to hold about 11 of LS and was deployed into the SNO(+) detector in 2008 to study various optical properties of different



**Figure 6.42:** Acrylic vessel, or *bucket source*, with a hollow space of  $\sim 11$  for liquid scintillator. The vessel was build for deployment in the water-filled SNO(+) detector to test optical properties of LAB scintillator. The picture is taken from [248].

LAB samples with 2g/l PPO. The samples used are raw LAB, Nd-loaded LAB and distilled LAB, where raw LAB refers to Petresa LAB without further processing, while distilled LAB is purified. Only the results from the measurements using raw LAB are discussed here, since it is the same kind of LAB used for the alpha quenching measurements in the presented work.

To determine the light yield of electrons, an Am–Be source was attached to the bucket, producing neutrons and 4.4 MeV gammas. After thermalization, neutrons are mostly captured on  $^1\text{H}$ , producing a deuteron and a 2.2 MeV gamma. Compton scattering of the two types of gammas again lead to two distinct Compton edges of known electron energy, enabling the calibration of the light yield scale, using

$$N_{\text{corr}}(E) = m \cdot E + a. \quad (6.27)$$

The electron light yield was measured at first instance in units of NHits, that is the number of PMTs that fired in an event with a trigger window of 400 ns. This number  $N$  is corrected, accounting for the number of working PMTs and the number of PMTs that were hit more than once during one event, resulting in  $N_{\text{corr}}$ . Originally,  $N_{\text{corr}}$  measured at the two Compton edges was additionally reduced by the number of NHits attributed to the Cherenkov light contribution of the scintillator in order to determine exclusively the scintillation light yield, resulting<sup>12</sup> in  $m = (483 \pm 3)$  NHits/MeV and  $a = (-27 \pm 8)$  NHits. However, neither in the neutron beam experiment nor in the Sm-experiment this contribution is subtracted. Instead, the  $\alpha$ -particle light yield is compared to the total electron light yield. Since the quenching factor, and thus Birks' parameter, is sensitive to this difference in the electron light scale, the calibration factor  $m$  and the intercept  $a$  are re-evaluated here including the Cherenkov component, resulting in  $m = (489 \pm 3)$  NHits/MeV and  $a = (-28.6 \pm 8.5)$  NHits. Without this re-evaluation, a comparison between the three measurements would be subject to different assumptions

<sup>12</sup>Internal note by H. M. O'Keeffe, SNO+-doc-484, version 1.

and potentially leading to a misinterpretation.

As  $\alpha$ -particle source, intrinsic  $\alpha$ -particle backgrounds are used, resulting from dissolved  $^{222}\text{Rn}$  gas.  $^{222}\text{Rn}$  itself emits  $\alpha$ -particles with 5.49 MeV, producing  $^{218}\text{Po}$  which majorily also decays under the emission of an  $\alpha$ -particle. The  $^{218}\text{Po}$   $\alpha$ -particle has an energy of 6.00 MeV. The third kind of  $\alpha$ -particles, identified within the bucket source data, are  $\alpha$ -particles with 7.69 MeV energy from decaying  $^{214}\text{Po}$ , a daughter nuclide further down the natural decay chain (see the full  $^{238}\text{U}$  chain in Fig. A.1).

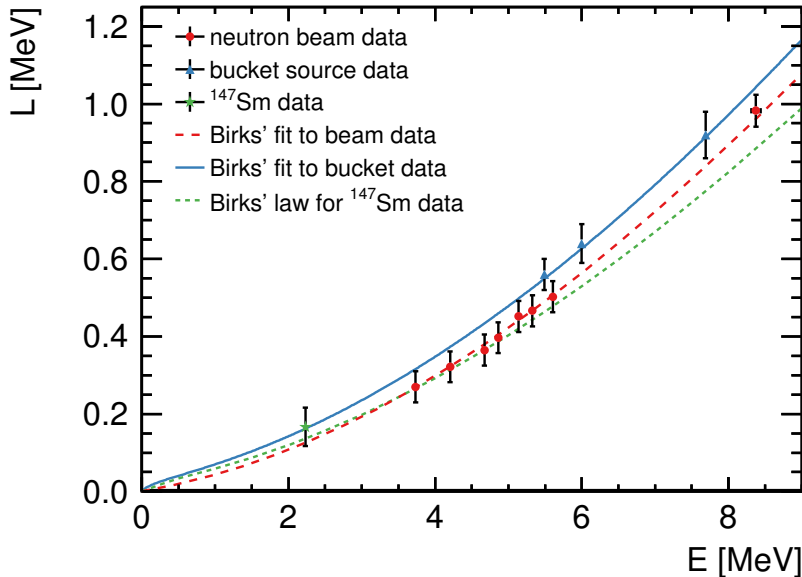
The mean  $\alpha$ -particle light yield  $N_{\text{corr}}$  are measured in NHits, yielding  $(246.4 \pm 2.2)$  NHits,  $(284.2 \pm 2.1)$  NHits and  $(422.2 \pm 2.6)$  NHits for  $^{222}\text{Rn}$ ,  $^{218}\text{Po}$  and  $^{214}\text{Po}$ , respectively. These values are in the original internal note<sup>13</sup> translated into electron-equivalent energy, dividing it by  $m = 483$  Nhits/MeV. The resulting Birks' parameter is  $kB = (0.0079 \pm 0.0004)$  cm/MeV. To compare Birks' parameter with the other two experiments, however, the value including the Cherenkov component  $m = (489 \pm 3)$  NHits/MeV needs to be used, as aforementioned, and the intercept  $a$  has to be taken into account to yield the same boundary conditions for the analysis as in the other two experiments: In the neutron beam and Sm-experiment, no exclusive measurement of the electron non-linearity was possible, which is needed to disentangle the physical intercept from a systematic bias, and  $E_0 = 0$  keV was assumed. Not subtracting  $a$  in case of the bucket source experiment would imply instead  $E_0 = 58$  keV, considering the total electron light yield from scintillation and Cherenkov light.

Within the present work, the bucket source  $\alpha$ -particle data was re-evaluated, inserting  $m = (489 \pm 3)$  NHits/MeV and  $a = (-28.6 \pm 8.5)$  NHits in Eq. 6.27, as well as the measured light yield  $N_{\text{corr}}$ , resulting in the  $\alpha$ -particle light yield in electron-equivalent energy. With these values a new fit, using MINUIT and the stopping power of LAB with 2 g/l PPO calculated with SRIM (see Fig. 6.31a), is performed, resulting in  $kB = (0.0072 \pm 0.0003)$  cm/MeV. The difference to the previously determined Birks' parameter underlines the importance of the knowledge about the assumptions made concerning the electron response, before quenching parameters can be interpreted. Along with the  $kB$  value, it is necessary to quote, whether the ion light yield is measured relative to the electron scintillation light yield or to the total electron light yield as well as the value of  $E_0$  assumed or measured.

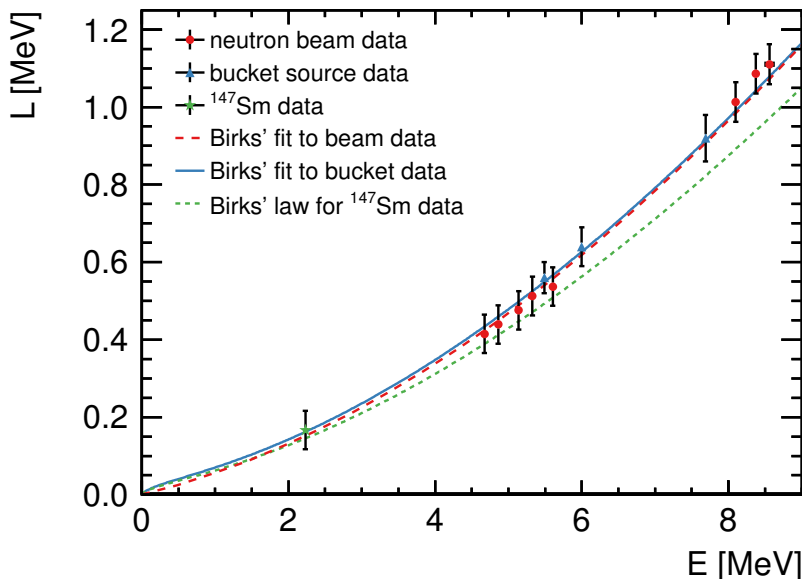
### 6.8.3 Comparison of the results from the three alpha quenching experiments

The data points measured with the three presented experiments and scaled to the same light yield scale are shown in Fig. 6.43. The results from both LAB samples, LAB1 and LAB3, used for the neutron beam experiment are compared to the other two experiments individually. Additionally shown are the light response functions, following Birks' law

<sup>13</sup>Internal note by H. S. Wan Chan Tseung, SNO+-doc-905, version 1.



(a) Neutron beam data, using LAB + 2 g/l PPO + 15 mg/l bis-MSB.



(b) Neutron beam data, using LAB + 3 g/l PPO + 15 mg/l bis-MSB.

**Figure 6.43:** Light yield  $L$  of  $\alpha$ -particles in electron-equivalent energy over kinetic energy  $E$ . Shown are data points from two different neutron beam measurements in (a) and (b), as indicated in the subcaptions. Furthermore shown are the data points, extracted from bucket source data, as well as one data point from an intrinsic  $^{147}\text{Sm}$  source within the Sm-experiment. Also shown is Birks' law Eq. 2.11, once fitted to beam data and once to bucket data, as well as Birks' law, using the Birks parameter  $kB$  from the fit to neutron beam data, but together with the stopping power of Sm-loaded LAB (see text).

Eq. 2.11 with  $kB$  as only quenching parameter. The fit of the light response function to the neutron beam data includes all known systematic uncertainties as nuisance parameters (see Sec. 6.6). The fit to the bucket source data is performed within this work with  $kB$  as only free parameter. No fit is performed to the single  $^{147}\text{Sm}$  data point. In this case it is instead verified, whether the Birks parameter  $kB = (0.0076 \pm 0.0003) \text{ cm/MeV}$  ( $kB = (0.0071 \pm 0.0003) \text{ cm/MeV}$ ), determined for LAB1 (LAB3), can properly model the Sm-loaded LAB light yield, using the stopping power calculated for the Sm-loaded scintillator (see Fig. 6.39).

In both figures, Fig. 6.43a and 6.43b, the  $\alpha$ -particle light response function for Sm-loaded LAB, calculated with the LAB1 or LAB3  $kB$  value, is in good agreement with the light yield at 2.233 MeV  $\alpha$ -particle energy measured in the Sm-experiment. Also noticeable is, that the response functions of Sm-loaded and the unloaded LAB1 (LAB3) differ, although the same Birks parameter was applied. This results from the different stopping powers of the two scintillators, as demonstrated in Fig. 6.39.

The neutron beam data using LAB + 3 g/l PPO + 15 mg/l bis-MSB is in excellent agreement with the bucket source data, using raw LAB + 2 g/l PPO (see Fig. 6.43b) and also the fitted light output functions agree remarkably well. Also the neutron beam data using LAB + 2 g/l PPO + 15 mg/l bis-MSB agrees with the bucket source data within their  $1\sigma$  uncertainties (see Fig. 6.43a). The fitted light output functions are not overlapping in this case. However, the corresponding  $kB$  values agree with  $kB = (0.0076 \pm 0.0003) \text{ cm/MeV}$ , from the neutron beam experiment, and  $kB = (0.0072 \pm 0.0003) \text{ cm/MeV}$ , from the bucket source experiment, within  $1\sigma$  and thus the light output functions within their  $1\sigma$  error band.

To conclude, all four measurements of the light yield caused by intrinsic  $\alpha$ -particles in LAB, taken with three different experiments, but evaluated under the same assumptions concerning the electron energy scale, yield comparable Birks' parameters or can be modeled with the same Birks' parameter, if an individual fit is not reasonable. This is the case in the Sm-experiment, from which only one data point can be extracted.

## 6.9 Comparison between the proton and alpha quenching parameter results

A further longstanding question is, whether Birks' constant is the same for different ions in the same scintillator or whether it varies. This issue is already addressed in the original work by J. B. Birks [11], where the Birks' parameter describing the alpha response in anthracene crystals cannot properly reproduce the proton response in the same scintillator (see also Sec. 2.6.3). Also measurements using organic liquids revealed different  $kB$  values for different particles in the same scintillator, as for instance in [242].

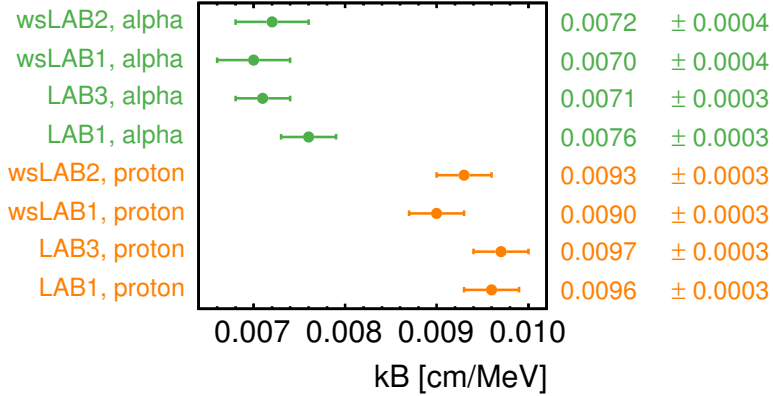


**Figure 6.44:** Measured Birks' parameters  $kB$ , parameterizing proton (orange) and alpha (green) quenching in the same LAB based scintillator. The values are taken from Tab. 6.10 and 6.11 with  $C = 0 \text{ cm}^2/\text{MeV}^2$ . The detailed scintillator descriptions are given in Tab. 6.1.

The presented work provides ideal conditions to test this hypothesis, since the proton and alpha quenching data was taken simultaneously with the same detector, filling and DAQ system and was analyzed using the same method and assumptions. Neither temperature changes, nor a different amount of impurities like oxygen, nor different aging are subject to the measurement of one sample. Furthermore, protons and  $\alpha$ -particles are both created inside the scintillator volume, avoiding surface effects.

For comparability with publications, the comparison of proton and alpha quenching parameters is also here reduced to  $kB$ , determined in the one-parameter fit. All respective values are presented in Fig. 6.44. While the presented results all agree for the same particle type measured with different scintillators based on the same solvent, the  $kB$  values for protons and  $\alpha$ -particles in the same sample deviate by about  $5\sigma$ . The two particle types cannot be described by the same Birks parameter.

In [249], an example is given of two measurements of PC scintillator with 1.5 g/L PPO, one for proton [250] and one for alpha [251] quenching, in which the resulting Birks parameters  $kB$  in a one-parameter fit [249] excellently agree. However, in this case, the  $\alpha$ -particle measurement was taken in a small laboratory measurement of equivalent size as the one presented here and the proton measurement was done with the Borexino detector, a multi-tonne detector. Thus, the measurement conditions were very different. Furthermore, information is missing about the details of the analysis, relevant to judge the comparability of the two measurements (as discussed in Sec. 6.8.3). In [242] instead, the same detector was used for both, alpha and proton quenching measurement using NE213. The results are  $kB_{\text{proton}} = 0.0091 \text{ g/cm}^2\text{MeV}$  and  $kB_{\alpha} = 0.0051 \text{ g/cm}^2\text{MeV}$  in a one-parameter fit (the uncertainties are not provided in [242]). In this case, the

quenching parameters do not agree for different charged particles in the same scintillator.

These contradictory results motivate further investigations, using a larger set of ions. Therefore, an experiment with a very low detector threshold and high ion energies is mandatory, which could be realized at an accelerator facility.

## 6.10 Summary and outlook

In this chapter, the measurements of proton and  $\alpha$ -particle light responses in various LAB and wsLAB scintillators are presented as well as the resulting ionization quenching parameters  $kB$  and  $C$ , using the extended Birks' law Eq. 2.12 for the analytical description. The agreements between the quenching parameters for the same particle in the different LAB based scintillators, all measured with the same detector and analyzed identically, confirm that ionization quenching is a primary process and its strength defined by the solvent, not the solutes. However, even if the solutes do not influence the ionization quenching processes itself, the primary solute can have an impact on the electron light scale, and thus the resulting quenching parameters, depending on the solute's re-absorption efficiency of Cherenkov light, as discussed in Sec. 6.7. Within this work, all measurements are performed with the same detector and primary solute and the direct comparison of the results is not affected. When it comes to comparisons with other experiments, however, the electron scale used for the relative ion response measurements has to be as similar as possible. The values of  $kB$  and  $C$  are naturally sensitive to whether only scintillation light from electrons or scintillation plus Cherenkov light are considered, since the electron light yield is used for calibration, as discussed in Sec. 6.8.3. Consequently, also the amount of observed Cherenkov light has an impact. This quantity is influenced by the detector's wavelength sensitivity, as well as potentially its size (see Sec. 6.7). The influence of the size of the scintillator volume on the observed electron response function, and thus the quenching parameters, is not known yet. This dependency can be well-investigated in a MC study in a first step. Depending on the results, an experiment which enables the variation of the scintillator volume without changing the DAQ system, place of the experiment and source of the ionizing particles would be of high interest for large scale detectors like SNO+ in order to reduce systematic uncertainties coming from externally measured quenching parameters.

Another aspect during calibration is the handling of the slight electron non-linearity at low energies leading to a small energy offset  $E_0$ . Neglecting the observed offset or correcting the measurements for the entire offset yield two different assumptions. The first attributes the entire offset to the electron non-linearity, not controlling a potential non-physical systematic shift. The second assumes the electron response to be fully linear. Until the non-linearity is quantified, the second approach is recommended, since the assumption made yields a fixed physical parameter  $E_0 = 0 \text{ MeV}$ , while in the first

approach the effective size of  $E_0$  is unknown and can vary. The influence of the Cherenkov light on the observed quenching parameters could be measured in a future study, using differently efficient UV filters, for instance. Also this experiment is very valuable for the transfer of results from one experiment to another.

To conclude, the quenching parameter  $kB$ , and eventually  $C$ , determined for a specific solvent is not universally valid for this solvent, but is related to the experimental set-up and data analysis. Proper documentation, though, allows the adaption of the results to the same boundary conditions necessary for a comparison or transfer of the results. The successful transfer of the results from this work to the SNO+ detector was demonstrated in this chapter for standard LAB. Ionization quenching in water–surfactant–LAB, with and without Te content, has never been measured before this work and the presented measurements form the basis of the radioactive background rejection techniques for the  $0\nu\beta\beta$  decay search of  $^{130}\text{Te}$  in SNO+. They are mandatory for the achievement of a successful measurement.

It is stated in [36] that the Birks' parameter  $kB$ , often referred to as Birks' constant, should not be considered as a true constant of a specific material, since its value can vary if the measurement conditions and analyses differ. All above observations support this argument. The second assumption, addressed in [36], that the same quenching parameters of a scintillator properly describe different ions in the otherwise identical detector, are not confirmed within the presented work. The Birks' parameter  $kB$  determined for protons and  $\alpha$ -particles under exactly the same measurement and analysis conditions and using the identical scintillator deviate by about  $5\sigma$ , as shown in Sec. 6.9. These results are essential and strongly encourage the measurement of the quenching parameters of heavier ions. It would be of great interest to determine, whether the dependency of Birks' parameter on the ionizing particle could be, for instance, related to its mass. This way, results from the easier to realize proton quenching measurements could be transferred to e.g. the  $\alpha$ -particle or deuterium light response.

Due to the form of Birks' law Eq. 2.11 and 2.12, which correlates the parameters  $kB$  and  $C$  with the stopping power  $dE/dx$ , identical quenching parameters do not necessarily imply the same light response function  $L(E)$  and vice versa. This fact is demonstrated in Fig. 6.43 in which the same Birks parameter is used for LAB and Sm-loaded LAB. The resulting light response curves differ, since the respective stopping powers deviate due to the high loading with Sm. It is thus not possible to compare the quenching strength of two different scintillators by the mere comparison of the quenching parameters, unless the stopping powers are known to be very similar. The quenching strength at a certain particle energy is only conclusively described by the ratio of ion light yield to electron light yield, also known as quenching factor.

A deep understanding of the scintillator light responses to different particles is crucial

for the interpretation of signal and background in LS detectors. It is thus important, to individually study the magnitude of different impacts, partly addressed above, to improve ionization quenching experiments and to facilitate the transfer of the results. In the view of the physics goals of SNO+, it is additionally recommended to test the variation of the quenching parameters with high Te-loading, which is accompanied by a high water and surfactant concentration. The samples used within this work were loaded with 0.3% Te, the initial SNO+ concentration, which had no impact on the quenching parameters. However, it is not excluded that high Te–water–surfactant loadings do have an impact. A systematic study with increasing concentrations is thus strongly motivated.

A direct application from results of this chapter is presented in the next chapter, in which the  $\nu + p \rightarrow \nu + p$  reaction is used to observe the spectral distribution of SN neutrinos. Without the knowledge of the proton quenching parameter in the respective scintillator, the reconstruction of the  $\nu$  energy would not be possible.



## Chapter 7

# Sensitivity of LAB scintillator detectors to supernova neutrinos

Core collapse supernovae (CCSNe) are an exceptional source of neutrinos, as described in Sec. 3. Even from the  $\sim 50$  kpc distant SN 1987A, 24 events in total were observed, all associated with inverse beta decay (IBD) events of  $\bar{\nu}_e$  [42, 43, 44]. The observations are in agreement with general model characteristics, like the total energy emitted in neutrinos and the burst duration [252], and commenced the era of neutrino astronomy. The next measurement of SN neutrinos is expected to shed light on the still not fully understood explosion mechanism, depending on the event statistics and the sensitivity of the available detection channels to the spectral shape of all incoming neutrino fluxes, where the  $\bar{\nu}_\mu$ 's and  $\bar{\nu}_\tau$ 's are typically summarized as  $\nu_x$ . Massive underground high-purity liquid scintillator (LS) detectors, like SNO+, offer a rich sample of detection channels, low backgrounds and a large amount of target particles and nuclei. They are thus promising detectors in this quest. The aim of this chapter is the determination of the sensitivity of LAB based scintillator detectors to the spectral shape of SN  $\bar{\nu}_e$  and  $\nu_x$  under the assumption that the neutrino energy spectra are described by a quasi-thermal distribution. The LAB masses considered are  $m_{\text{LAB}} = 0.45$  kt and  $m_{\text{LAB}} = 16.80$  kt in agreement with a realistic fiducial volume (FV) of SNO+ and the proposed kilotonne-scale JUNO experiment, respectively.

The shape of the SN  $\nu_\alpha$  ( $\nu_\alpha = \nu_e, \bar{\nu}_e, \nu_x$ ) energy spectra is expected to approximate a thermal spectrum (see Sec. 3.3) in the absence of neutrino flavor changing mechanisms. In this case, the energy spectra are usually parameterized by the neutrino mean energy  $\langle E_\alpha \rangle$ , a shape parameter  $\beta_\alpha$  and the neutrino luminosity  $\mathcal{L}_\alpha$  or its time-integrated equivalent, the neutrino total energy<sup>1</sup>  $\varepsilon_\alpha$ , following Eq. 3.15 and 3.22. At postbounce times  $t \lesssim 1$  s, the flavor changes are reduced to those induced by the well-known MSW effect in a quasi-static environment (see Sec. 4.2.2). Though this is also a flavor changing mechanism, it is well understood and moreover does not introduce pronounced spectral features in

---

<sup>1</sup>The total SN neutrino energy is typically given in units of foe, where foe stands for (ten to the power of) fifty-one ergs and thus  $1 \text{ foe} = 10^{51}$  erg (see also Tab. A.1).

this early time of the SN, as will be shown in Sec. 7.6, which cannot be reproduced by the named parameterization. At later times a multitude of further effects interfere (see Sec. 4.1), which are highly non-trivial and partly still lacking full understanding and a consistent analytical treatment. Thus, sensitivity studies to the spectral parameters  $\mathbf{a}_\alpha = (\langle E_\alpha \rangle, \beta_\alpha, \varepsilon_\alpha)$  are only meaningful at present for maximally the first second of the burst. In this time span, half of all neutrinos are estimated to be emitted [253], an information which is used in this work to approximate the normalization of the neutrino fluence in the first second of a reference SN. Note that this approximation only affects the statistics, not the shape of the spectrum. The reference SN will be introduced, amongst others, in Sec. 7.1. The neutrino fluence, gained from the SN models of the Garching group and introduced in Sec. 3.5.1, is only available for the first 500 ms after the core bounce. However, figures 3.9–3.11 suggest a higher neutrino emission in the first 500 ms than in the second, where the partitioning is not known quantitatively, an information also not known for the reference SN. Thus, for the spectral sensitivity studies on the basis of the reference SN, presented in Sec. 7.4 and 7.5, the full first second is used. Instead, the event yield study in Sec. 7.6, comparing amongst others the yields from different progenitors and equations of state (EOSs) that were simulated by the Garching group, is based on the first 500 ms after the core bounce.

The intention of Sec. 7.1 is the determination of the event yields and of the visible energy distributions of all detection channels in 1 kt of LAB based scintillator, using the full reference SN neutrino fluence. Throughout the more generic discussion in Sec. 7.1 of the available SN detection channels in LS, the entire reference SN fluence is applied for the ease of comparison with publications like [92, 93]. Since both, the event yields and the visible spectra, are modified if neutrino flavor changes occur, the results in this section are only a benchmark, providing a general idea of the capabilities of kilotonne-scale LS detectors. Of particular interest in the context of LS detectors is the shape of the  $\nu_x$  energy spectrum, which is as of today only accessible with this detector type and through  $\nu$ - $p$  elastic scattering (ES) [92, 254]. A further promising channel is the IBD reaction, which is exclusively sensitive to  $\bar{\nu}_e$ 's, carries spectral information and can be tagged with high efficiency. These two channels are used for the spectral sensitivity studies in this thesis.

A set of reaction channels, which is often not mentioned or if, only discussed rudimentarily [93, 254], are inclusive  $^{12}\text{C}$  transitions after neutrino excitation with a free nucleon in the final state. Since these knockout protons and neutrons are a potential background to the detection of  $\nu$ - $p$  ES and IBD events, respectively, and since the expected visible spectra of the individual inclusive reactions are not existent in publications, also these channels are discussed in more detail within Sec. 7.1.

Backgrounds in general to the two detection channels of interest in this work,  $\nu$ - $p$  ES and IBD, are described in Sec. 7.2. This section shows that backgrounds not induced by the SN itself are negligible for the IBD channel, while they have to be well-measured

for the  $\nu$ - $p$  ES channel and thoroughly subtracted in the event of a real SN. It will be demonstrated that, despite the high neutrino flux during a SN, the backgrounds expected for SNO+ partly exceed the  $\nu$ - $p$  ES signal. Since the main physics goal of large-scale LS detectors like SNO+ is usually not the observation of SN neutrinos, also the energy ROI of the main goal might be different from the one for SN  $\nu$ - $p$  ES and thus the focus of background measurements. This section is aimed to highlight the energy region, which is the most important in terms of  $\nu$ - $p$  ES backgrounds and which needs background measurement with high precision. Besides non-SN backgrounds, backgrounds induced by SN neutrinos are discussed in this section.

The reconstruction of the incoming SN neutrino spectra from visible  $\nu$ - $p$  ES and IBD event spectra is described in Sec. 7.3. To these spectra, the parametric description mentioned above is fitted in order to determine the spectral sensitivities. The concept of the fit is optimized for each of the two detection channels individually and explained within Sec. 7.4 for the IBD channel and within Sec. 7.5 for the  $\nu$ - $p$  ES channel. The fit results yielding the spectral  $\bar{\nu}_e$  and  $\nu_x$  sensitivity of SNO+ and JUNO sized detectors are also presented in Sec. 7.4 and 7.5, respectively. Section 7.5 additionally discusses the influence of the uncertainty of the quenching parameter  $kB$ , as determined within this work, on the  $\nu_x$  sensitivity. All results are related to the reference SN and the corresponding event yield.

Section 7.6 presents how the event yield varies with varying SN models, as simulated by the Garching group, and neglecting or including the MSW effect. It also shows the small influence of the MSW effect on the neutrino energy spectrum in this early phase of the SN. The findings from this section are compared to the reference SN, which enables a generalization of the results from the  $\mathbf{a}_{\bar{\nu}_e}$  and  $\mathbf{a}_{\nu_x}$  sensitivity studies in Sec. 7.4 and 7.5.

This chapter works out the potentials and hurdles of a spectral SN neutrino IBD and  $\nu$ - $p$  ES analysis, which are resumed in Sec. 7.7. These measurements are highly interesting in order to test fundamental SN hypotheses like the equipartitioning of the progenitor's binding energy, emitted in neutrinos, amongst all neutrino flavors and types. Tests like this are only possible, if all three SN flux components can be measured individually. The present work shows the potentials of SNO+ and JUNO to constrain the  $\mathbf{a}_{\bar{\nu}_e}$  and  $\mathbf{a}_{\nu_x}$  parameter spaces. Sensitivity studies to  $\mathbf{a}_{\nu_e}$  are beyond the scope of this work, but motivated in Sec. 7.7, together with further outlooks.

Throughout the entire chapter, a resolution of the visible energy  $E_{\text{vis}}$  of  $\sigma_{E_{\text{vis}}} = 6\%/\sqrt{E_{\text{vis}}(\text{MeV})}$  is assumed. This resolution is slightly better than the one of the KamLAND detector [255] and in agreement with expectations for SNO+. Furthermore a trigger threshold of 200 keV is used for the sensitivity studies in Sec 7.4 and 7.5. This threshold is motivated by a strongly increased background rate below this value, as will be discussed in Sec. 7.2.2. This trigger threshold is above the energy where the trigger

efficiency reaches about 100%. The Borexino<sup>2</sup> experiment, which is similar to SNO+, reports a trigger efficiency of effectively 100% above about 80 keV, while it significantly drops at lower energies, reaching nearly 0% efficiency at about 30 keV [193]. SNO+ expects a comparable turn on curve in the pure LS phase. Thus, within this thesis the lowest trigger threshold considered is at 100 keV in Sec. 7.6 in the context of  $\nu$ - $p$  ES event yield studies.

## 7.1 Interaction channels in liquid scintillator

Supernova neutrinos can undergo a multitude of different interactions in LS detectors, which are all listed in Tab. 7.1. The advantage of this diversity is the sensitivity to different parts of the total neutrino flux using the same detector. The disadvantage is the fact that some channels form a background to each other. To develop an idea of the relative event yields in 1 kt of LAB, the yields are calculated within this section for the full course of the reference SN and without flavor changes. The SN is assumed to occur at a distance of 10 kpc, as motivated in Sec. 3.4. This distance is used for all calculations performed throughout this chapter and is considered to be known from, for instance, the detection of the electro-magnetic radiation released in the SN event. The binding energy released in the form of neutrinos is assumed to amount to 300 foe, which is equipartitioned amongst all six flavors and types. The time-integrated neutrino flux of the reference SN follows the parameterization Eq. 3.29, which assumes the same constant shape parameter  $\beta = 3$  for all flavors and is deduced from Eq. 3.26. The mean energies chosen are 12 MeV for  $\nu_e$ , 15 MeV for  $\bar{\nu}_e$  and 18 MeV for  $\nu_x$ , following [92]. These are generic mean SN neutrino energies [144], consistent with the findings from SN 1987A [253]. These spectral parameter values are summarized in Tab. 7.2 and the resulting  $\nu_e$ ,  $\bar{\nu}_e$  and  $\nu_x$  fluences are shown in Fig. 7.1. The event yields derived from the entire reference SN per LS detection channel are added to Tab. 7.1.

All neutrino interaction total cross sections used within this work are shown in Fig. 7.2. Comparing Fig. 7.1 and Fig. 7.2 reveals the dominance of the IBD and  $\nu$ - $p$  ES cross sections in the neutrino energy region of interest. The total and differential cross sections of the individual detection channels are described within this section. They are used to determine the visible energy distributions, exemplarily shown in the following for the reference SN and each channel. The integral over each visible energy distribution yields the respective total event yield listed in Tab. 7.1.

### 7.1.1 Neutrino-proton elastic scattering ( $\nu$ - $p$ ES)

Elastic scattering on protons,  $\nu + p \rightarrow \nu + p$ , is possible for all (anti-)neutrinos and the resulting proton recoil spectrum provides spectral information about the incoming neutrino flux. This instance makes this NC channel unique. Moreover, though the total cross section for elastic scattering on protons is about a factor of three smaller than the one for IBD (see

---

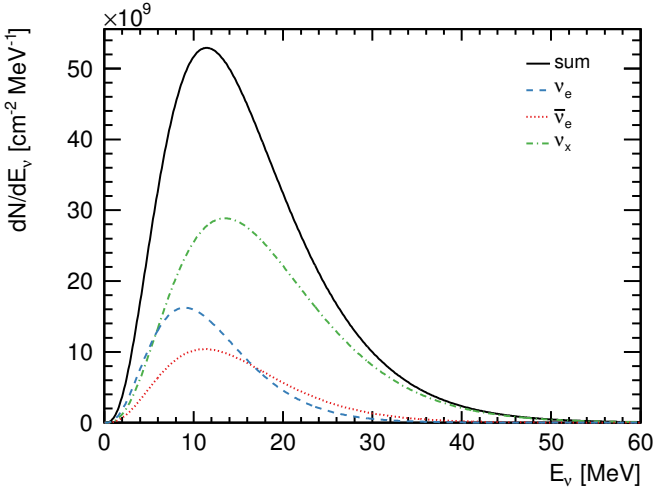
<sup>2</sup>Borexino is the Italian diminutive of BOREX, which stands for BORon solar neutrino EXperiment.

**Table 7.1:** Supernova neutrino interaction channels in liquid scintillator. The target densities assume LAB only as solvent. The event rates assume 1 kt of LAB and an incoming neutrino fluence as shown in Fig. 7.1 from the reference SN at 10 kpc distance. No flavor changing mechanisms are considered. The total cross section of each channel is shown in Fig. 7.2. The uncertainties on the event rates only comprises the cross section uncertainties, which are given in the text. <sup>†</sup>This rate assumes a trigger threshold of 200 keV visible energy. \*The Standard Model cross section uncertainty is < 1%.

Nr.	Current	Process	Target density [10 <sup>22</sup> /cm <sup>3</sup> ]	Events [1/kt]
1	NC	$\nu + p \rightarrow \nu' + p$	6.275	$550.1 \pm 15.4$ $(152.4 \pm 4.3)^{\dagger}$
2	CC	$\bar{\nu}_e + p \rightarrow n + e^+$	6.275	$249.6 \pm 1.3$
3	CC	$\bar{\nu}_e + {}^{12}\text{C} \rightarrow {}^{12}\text{B}_{\text{g.s.}} + e^+$	3.763	$9.0 \pm 0.9$
4	CC	$\nu_e + {}^{12}\text{C} \rightarrow {}^{12}\text{N}_{\text{g.s.}} + e^-$	3.763	$3.5 \pm 0.4$
5	NC	$\nu + {}^{12}\text{C} \rightarrow {}^{12}\text{C}^*(15.11 \text{ MeV}) + \nu'$	3.8	$56.2 \pm 11.2$
6	CC	$\nu_e + {}^{12}\text{C} \rightarrow {}^{11}\text{C} + p + e^-$	3.763	$0.2 \pm 0.1$
7	CC	$\bar{\nu}_e + {}^{12}\text{C} \rightarrow {}^{11}\text{B} + n + e^+$	3.763	$0.2 \pm 0.1$
8	NC	$\nu + {}^{12}\text{C} \rightarrow {}^{11}\text{B} + p + \nu'$	3.763	$2.1 \pm 0.6$
9	NC	$\nu + {}^{12}\text{C} \rightarrow {}^{11}\text{C} + n + \nu'$	3.763	$0.6 \pm 0.2$
10	NC/CC	$\nu_e + e^- \rightarrow \nu'_e + e^-$	29.08	$8.2^*$
11	NC	$\bar{\nu}_e + e^- \rightarrow \bar{\nu}'_e + e^-$	29.08	$3.5^*$
12	NC	$\nu_x + e^- \rightarrow \nu'_x + e^-$	29.08	$2.7^*$
13	NC	$\bar{\nu}_x + e^- \rightarrow \bar{\nu}'_x + e^-$	29.08	$2.4^*$
Total				$888.3 \pm 30.2$ $(490.6 \pm 19.1)^{\dagger}$

**Table 7.2:** Spectral parameters of the reference SN neutrino fluence, where  $\langle E \rangle$  mean energy,  $\beta$  the shape parameter and  $\varepsilon$  the total neutrino energy, which is equivalent to the time-integrated luminosity.  $\varepsilon$  is once given for the full duration of the SN and once for the first second, following the estimate of [253] that this amounts to half the number of neutrinos. Equipartitioning amongst all flavors is supposed. These values are following the assumptions of [92]. The value of  $\varepsilon_{\nu_x}$  is the sum from all four contributing neutrino types.

Flavor	$\langle E_\alpha \rangle$ [MeV]	$\beta_\alpha$	$\varepsilon_\alpha$ [foe]	$\varepsilon_\alpha$ [foe]
			first second	
$\nu_e$	12.0	3.0	25.0	50.0
$\bar{\nu}_e$	15.0	3.0	25.0	50.0
$\Sigma\nu_x$	18.0	3.0	100.0	200.0



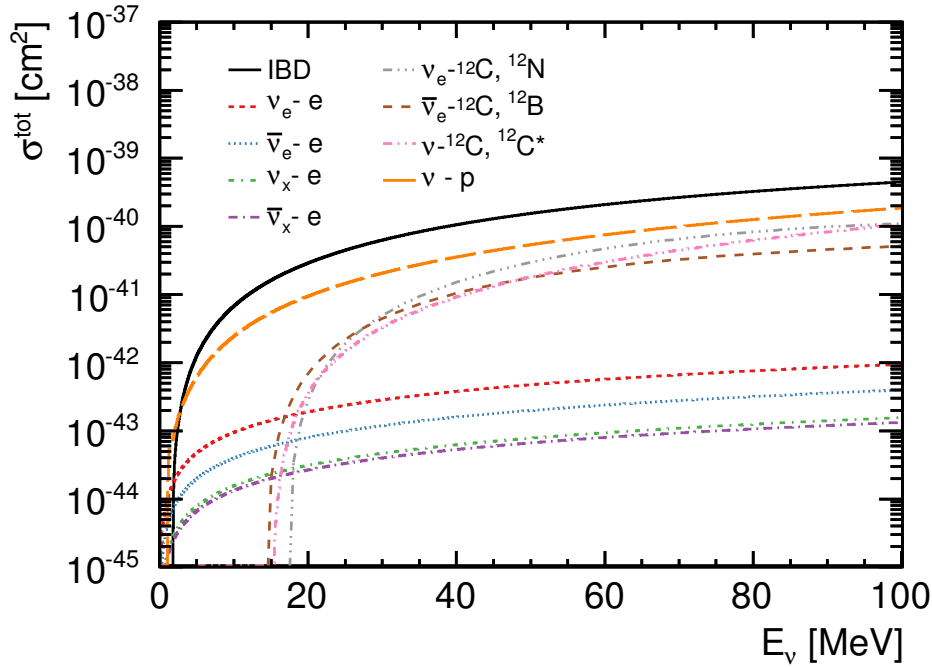
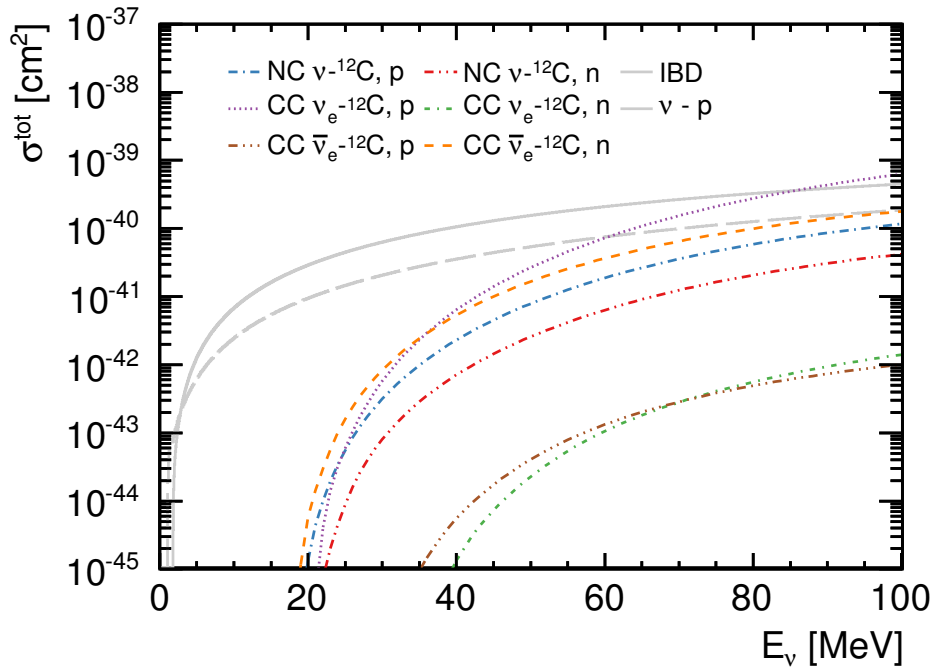
**Figure 7.1:** Reference SN neutrino fluence  $dN/dE_\nu$  as function of neutrino energy  $E_\nu$ , following the analytical description Eq. 3.29. A distance of 10 kpc from the SN and a total neutrino energy of 300 foe are assumed. The individual spectral parameters are given in Tab. 7.2.

Fig. 7.2) this channel reaches the highest total event yield, since all six neutrinos take part and no kinematic threshold energy has to be overcome. The cross section is predicted by the standard model and the full formula can be found in e.g. [256, 257]. At SN neutrino energies, the calculations strongly simplify and the differential cross section as function of the incoming neutrino energy  $E_\nu$  and proton recoil energy  $E_p$  reduces to

$$\frac{d\sigma}{dE_p}(E_\nu) = \frac{G_F^2 m_p}{2\pi E_\nu^2} [(c_V \pm c_A)^2 E_\nu^2 + (c_V \mp c_A)^2 (E_\nu - E_p)^2 - (c_V^2 - c_A^2)m_p E_p], \quad (7.1)$$

where the upper sign of  $c_A$  refers to neutrinos, the lower to anti-neutrinos [254].  $c_A$  and  $c_V$  are the axial-vector and vector coupling constants between the exchanged  $Z^0$  boson and the proton with

$$c_V = \frac{1 - 4\sin^2\theta_W}{2} \quad (7.2)$$

(a) IBD, elastic scattering on protons ( $\nu$ - $p$ ) and electrons ( $\nu$ - $e$ ) and exclusive  $^{12}\text{C}$  transitions.(b) Inclusive  $^{12}\text{C}$  transitions (IBD and elastic scattering on protons are shown for comparison).

**Figure 7.2:** Total cross sections  $\sigma^{\text{tot}}$  of neutrino interactions in liquid scintillator (see Tab. 7.1).  $E_\nu$  is the neutrino energy. Shown are in (a) inverse beta decay (IBD),  $\nu$ - $e$  and  $\nu$ - $p$  elastic scattering and exclusive  $^{12}\text{C}$  transitions. In (b) the total cross sections for inclusive  $^{12}\text{C}$  transitions are shown, where the nucleon added to the legend denotes the knocked out nucleon. The  $\nu_e$ -induced  $p$  knockout (violet dotted line) is dominated by Eq. 7.24, the  $\bar{\nu}_e$ -induced  $n$  knockout (orange dashed line) by Eq. 7.25 and the  $\nu$ -induced  $p$  (blue dashed dotted line) and  $n$  (red dashed dotted line) knockout by Eq. 7.26 and 7.27.

and

$$c_A = \frac{g_A(0) \cdot (1 + \eta)}{2}. \quad (7.3)$$

$\theta_W$  is the effective weak mixing angle with  $\sin^2 \theta_W = 0.23155$  and  $g_A(0) = 1.267$  is the axial proton form-factor [152]. The axial current further depends on the proton strangeness  $\eta$ , which is the strange-quark contribution to  $g_A(0)$  [258].  $\eta$  is related to the often used strangeness contribution to the proton spin  $\Delta s$  via  $\eta \equiv -\Delta s/g_A(0)$ . The currently best available measurement yields  $\eta = 0.12 \pm 0.07$  [257], in agreement with the theoretical prediction [259, 260, 261].

The total cross section, shown in Fig. 7.2, is obtained by integrating Eq. 7.1

$$\sigma_{\text{tot}}(E_\nu) = \int_0^{E_p^{\max}} \frac{d\sigma}{dE_p}(E_\nu) dE_p, \quad (7.4)$$

where

$$E_p^{\max} = \frac{2E_\nu^2}{m_p + 2E_\nu} \quad (7.5)$$

is the maximum proton recoil energy, reached when the neutrino is scattered backwards. The uncertainty on the total cross section due to the uncertainty of  $\eta$  is  $\sim 13\%$ . If the proton strangeness is neglected, i.e.  $\eta = 0$ , the total cross section is about 25% lower than the one presented in Fig. 7.2 over the energy region shown in that figure [258]. The event yield thus strongly depends on the assumptions made on  $\eta$ . The influence of  $\eta$  on the  $\nu$ - $p$  ES event spectrum was investigated in preparation of the sensitivity studies presented in Sec. 7.5, where only the scale was found to significantly vary with  $\eta$ , not the shape: At the relevant kinetic particle energies, Eq. 7.1 approximates a linear function of  $E_p$  because of  $(E_\nu - E_p)^2 \approx E_\nu^2$ . In this approximation,  $\eta$  enters the intercept and the slope of the linear function, where the slope is  $\propto E_\nu^{-2}$  and dominated by this quantity. The intercept, instead, has no varying quantity and is sensitive to changes in  $\eta$ . A change in the intercept, but not the slope, results only in an increase or decrease of the event yield. The shape remains unchanged.

An important aspect to be considered for  $\nu$ - $p$  ES is that the visible energy  $E_{\text{vis}}$  from the recoiling protons is strongly quenched with respect to the kinetic proton energy  $E_p$  (see Sec. 6). The visible spectrum is thus determined as per

$$\frac{dN}{dE_{\text{vis}}}(E_\nu) = N_p \frac{dE_p}{dE_{\text{vis}}} \int_{E_\nu^{\min}}^{\infty} \frac{d\sigma}{dE_p}(E_\nu) \frac{dN}{dE_p} dE_\nu, \quad (7.6)$$

where the true proton recoil spectrum is multiplied with a quenching function  $dE_p/dE_{\text{vis}}$ . In this work, the quenching function follows Birks' parameterization Eq. 2.12 with  $kB = (0.0096 \pm 0.0003) \text{ cm/MeV}$  and  $C \equiv 0 \text{ m}^2/\text{MeV}^2$  (see Tab. 6.10, LAB1).  $N_p$  is the number of target protons (see Tab. 5.3) and the minimum required energy  $E_\nu^{\min}$  to reach a distinct  $E_p$  is

$$E_\nu^{\min} = \frac{E_p + \sqrt{E_p(E_p + 2m_p)}}{2}. \quad (7.7)$$

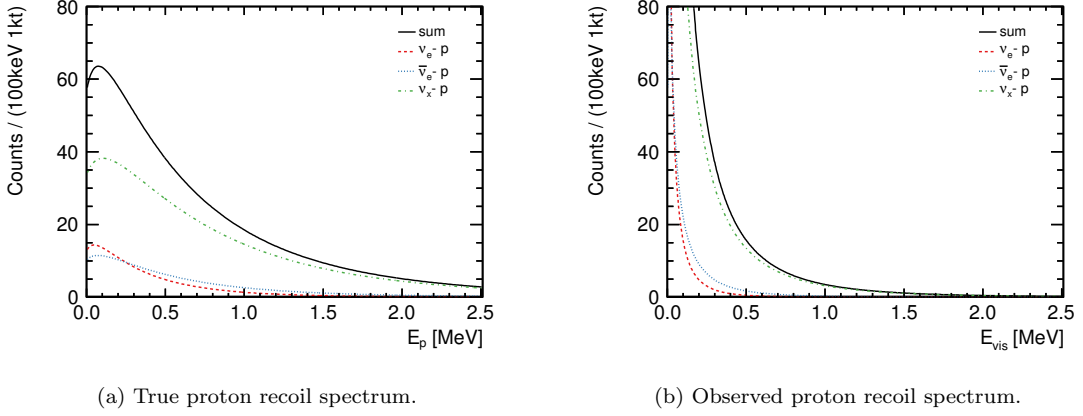


**Figure 7.3:** True (a) and observed (b) proton recoil spectrum in LAB. The SN neutrino fluence is assumed to follow Fig. 7.1. The observed proton spectrum takes ionization quenching with  $kB = 0.0096 \text{ cm/MeV}$  and an energy resolution of  $6\%/\sqrt{E_{\text{vis}}(\text{MeV})}$  into account, where the latter detector effect has no visible impact in this case.

The  $E_p$  and  $E_{\text{vis}}$  distributions of the reference SN neutrino spectrum, shown in Fig. 7.3, demonstrate that most of the scattering events are shifted below  $\sim 500 \text{ keV}$  electron-equivalent energy. However, below about  $200 \text{ keV}$  the background rate tremendously increases, as will be discussed in Sec. 7.2, and the detector threshold is typically set around that energy in order to keep the trigger and/or data rate reasonably low. As a consequence, the detected event spectrum is only a small fraction of the total event spectrum, in numbers  $\sim 30\%$ , assuming a threshold energy of  $E_{\text{thr}} = 200 \text{ keV}$  (see Tab. 7.1). Though detectors like SNO+ will be capable of instantaneously lowering the detector threshold down to about  $100 \text{ keV}$  with the occurrence of a SN for a short time, the backgrounds between this lower trigger threshold and the default trigger threshold are not measured with the same statistical precision as the backgrounds above the default trigger threshold.

### 7.1.2 Inverse beta decay (IBD)

The inverse beta decay reaction,

$$\bar{\nu}_e + p \rightarrow n + e^+, \quad (7.8)$$

has a comparatively high and theoretically clean cross section, a threshold of

$$E_{\text{thr}} = \frac{(m_n + m_e)^2 - m_p^2}{2m_p} \approx 1.806 \text{ MeV} \quad (7.9)$$

and the visible energy is directly related to the incoming neutrino energy  $E_{\bar{\nu}_e}$ . The total cross section shown in Fig. 7.2 follows the simple, but at SN neutrino energies to the per-mille level accurate, approximation [262]

$$\sigma_{\text{tot}}(E_{\bar{\nu}_e}) = 10^{-43} \text{ cm}^2 p_{e^+} E_{e^+}^{\text{tot}} E_{\bar{\nu}_e}^{-0.07056 + 0.02018 \ln E_{\bar{\nu}_e} - 0.001953 \ln^3 E_{\bar{\nu}_e}}, \quad (7.10)$$

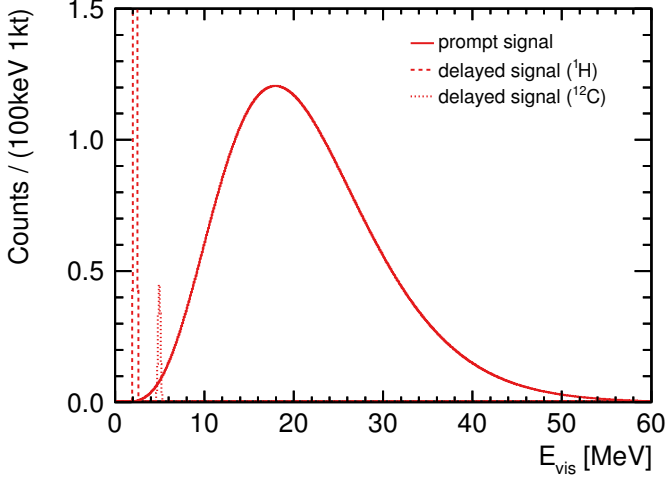


**Figure 7.4:** Visible inverse beta decay spectrum in LAB. The incoming SN neutrino fluence is assumed to follow Fig. 7.1. The prompt signal is the kinetic and annihilation energy of the positron, the delayed signals are the de-excitation  $\gamma$ -rays after neutron capture on  ${}^1\text{H}$  or  ${}^{12}\text{C}$ . An energy resolution of  $6\%/\sqrt{E_{\text{vis}}(\text{MeV})}$  is assumed.

where  $p_{e^+}$  is the momentum of the positron and

$$E_{e^+}^{\text{tot}} \approx E_{\bar{\nu}_e} - (m_n - m_p) \quad (7.11)$$

its total energy. The average neutron recoil energy is of  $\mathcal{O}(10\text{ keV})$  [263] and is neglected in the evaluation of  $E_{e^+}^{\text{tot}}$ . All energies in Eq. 7.10 are given in MeV. The full calculation of the cross section, to which Eq. 7.10 is the approximation, also has an uncertainty, which is  $< 0.4\%$  up to 50 MeV, according to a conservative estimate in [262], which is used to calculate the event yield uncertainty given in Tab. 7.1.

The energy  $E_{\text{vis}}^p$ , promptly visible in the detector, is the sum of the kinetic positron energy  $E_{e^+}$  and its annihilation energy

$$E_{\text{vis}}^p = E_{e^+} + 2m_e = E_{\nu} - (m_n - m_p) - m_e + 2m_e, \quad (7.12)$$

making use of Eq. 7.11. The neutrino energy is thus given by  $E_{\nu} \approx E_{\text{vis}}^p + 0.782\text{ MeV}$ . The prompt positron signal is followed by the (200–260)  $\mu\text{s}$  [263, 264] delayed capture of the thermalized neutron on hydrogen, producing a characteristic 2.223 MeV de-excitation  $\gamma$ -ray. More than 99% of the neutrons capture on  ${}^1\text{H}$ , while less than 1% capture on  ${}^{12}\text{C}$  [263]. In the latter case, the de-excitation  $\gamma$  has an energy of 4.945 MeV. The prompt and delayed visible energy spectra are shown in Fig. 7.4 assuming the reference SN neutrino fluence.

The neutron typically travels around 50 cm in the LS before it is captured. Time and space coincidence permit, together with energy cuts, an efficient tagging of IBD events. Therefore, the delayed candidate events are selected by a cut on the delayed visible energy  $E_{\text{vis}}^d$ . The prompt event has to have occurred within a time  $\Delta t$  before the delayed candidate event and within a spherical volume  $\Delta V$  around the vertex of the delayed event. The radius of  $\Delta V$  is defined by the reconstructed distance  $\Delta r$  between the two events.

The KamLAND collaboration reaches with the conditions  $2.04 \text{ MeV} < E_{\text{vis}}^d < 2.82 \text{ MeV}$ ,  $0.5 \mu\text{s} < \Delta t < 660 \mu\text{s}$  and  $\Delta r < 1.6 \text{ m}$  a total detection efficiency of  $0.940 \pm 0.006$  [265].

This high tagging efficiency of IBD events is reached, as long as the event rate  $R_{\text{IBD}}$  is

$$R_{\text{IBD}} \leq \frac{1}{\Delta t_{\max} \Delta V_{\max} \rho}, \quad (7.13)$$

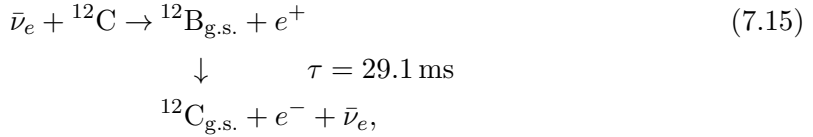
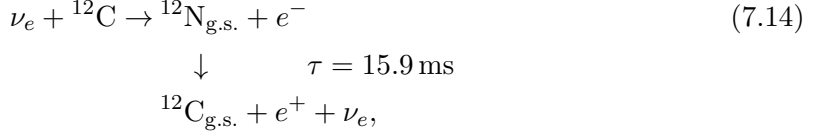
where  $\Delta t_{\max}$  and  $\Delta V_{\max}$  are the maximum values of the trigger conditions and  $\rho$  is the scintillator density. This inequality means that after a prompt-like signal occurred, maximally one neutron capture candidate event meets the trigger conditions. Using the maximum values of the given KamLAND time and space intervals for Eq. 7.13 and  $\rho = 0.86 \text{ g/cm}^3$  for LAB based scintillator (see Tab. 6.2), the IBD event rate has to be  $R_{\text{IBD}} \lesssim 1.03 \times 10^5 \text{ kt}^{-1}\text{s}^{-1}$ . This rate is enormous and while the condition Eq. 7.13 is easily fulfilled in reactor and geo neutrino experiments, a near-by SN potentially exceeds this limit. This is for instance the case, if the SN is at  $\lesssim 350 \text{ pc}$ , extrapolating the IBD event yield of  $249.6 \text{ kt}^{-1}$  from the  $10 \text{ kpc}$  distant reference SN (see Tab. 7.1) and assuming that half of all neutrinos are emitted within the first second, as noted in the introduction. The CCSN candidate Betelgeuse, mentioned in Sec. 3.4, is  $(197 \pm 45) \text{ pc}$  away from Earth [96] and thus not fulfilling the inequality Eq. 7.13 anymore.

### 7.1.3 Neutrino–nucleus reactions on $^{12}\text{C}$

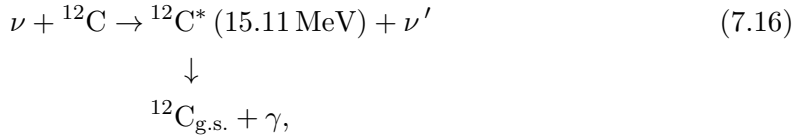
Organic scintillators are rich in  $^{12}\text{C}$  (see Tab. 5.3) and a large fraction of SN neutrinos reaches high enough energies to decompose  $^{12}\text{C}$  via neutrino–nucleus reactions. In these reactions, light elements up to N are produced, partially accompanied by the knockout of at least one nucleon. The respective total cross sections for the production of the individual isotopes and the release of nucleons from  $^{12}\text{C}$  are calculated in [266] in the context of nuclear network calculations. For consistency, all relevant production rate calculations due to  $\nu-^{12}\text{C}$  scattering in this chapter are based on this one reference. The processes considered for the presented work are those that notably contribute to the visible event spectrum. These are the exclusive transitions to the  $A = 12$  isospin triplet (i.e.  $^{12}\text{N}_{\text{g.s.}}$ ,  $^{12}\text{B}_{\text{g.s.}}$ ,  $^{12}\text{C}_{15.11 \text{ MeV}}^*$ ) and the inclusive transitions to excited continuum states  $^{12}\text{N}^*$ ,  $^{12}\text{B}^*$  and  $^{12}\text{C}^*$ .

### Exclusive transitions

Neutrino– $^{12}\text{C}$  interactions with a considerably high total cross section are the two superallowed charged currents



followed by the  $\beta$  decay of the final state isotope, and the superallowed neutral current



followed by the emission of a 15.11 MeV de-excitation  $\gamma$ . The NC reaction does not contribute to stellar nucleosynthesis, hence the cross section is not part of the network calculations in [266]. The cross section shown in Fig. 7.2a is taken from [267, 268] and known to an accuracy of about 20% [93]. The mono-energetic character of the  $\gamma$  leads to an observable spectral feature in the visible sum energy spectrum, despite the high reaction threshold. This channel, however, carries no neutrino flavor or spectral information.

The theoretical cross section of the charged current Eq. 7.14 from [266], shown in Fig. 7.2a, is in very good agreement with measurements by KARMEN<sup>3</sup> and LSND<sup>4</sup> [269, 270, 271, 272]. The measurement uncertainties of the neutrino flux averaged cross sections are  $\sim 10\%$  [271, 270], which is considered for the event yield calculation as uncertainty for both CC interactions. A theoretical uncertainty is not published in [266].

The reactions Eq. 7.14 and 7.15 have a threshold energy

$$E_{\text{thr}} = \frac{(m_{12\text{N}/\text{B}} + m_e)^2 - m_{12\text{C}}^2}{2m_{12\text{C}}} \quad (7.17)$$

of 17.86 MeV and 13.89 MeV, respectively. They are thus only sensitive to the high energy fraction of the  $\nu_e$  and  $\bar{\nu}_e$  spectra in Fig. 7.1. The advantage of these reactions are the short-living final state nuclei, which provoke a delayed signal, enabling a time and spatial coincidence tag together with the prompt  $e^\mp$  signal, as successfully performed in [270].

---

<sup>3</sup>Karlsruhe Rutherford Medium Energy Neutrino experiment.

<sup>4</sup>Liquid Scintillator Neutrino Detector.

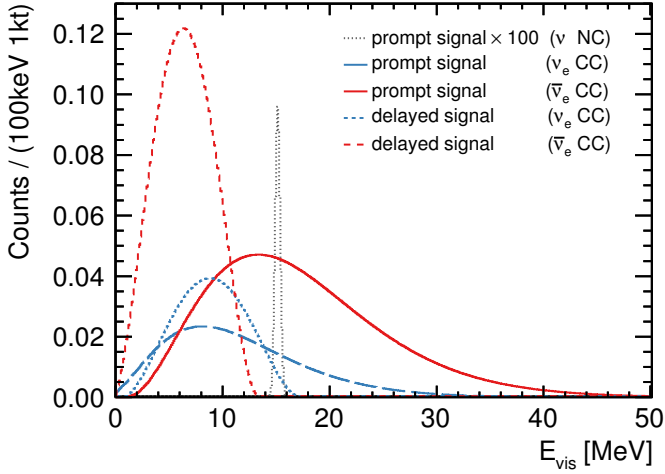


**Figure 7.5:** Visible energy spectra of exclusive neutral current (NC) and charged current (CC) transitions of  $^{12}\text{C}$  in LAB. The incoming SN neutrino fluence is assumed to follow Fig. 7.1. The resulting prompt and delayed signals are explained in the text (Eq. 7.18–7.21). The NC signal is downscaled by a factor 100 for display purposes. An energy resolution of  $6\%/\sqrt{E_{\text{vis}}(\text{MeV})}$  is assumed.

The visible energy distributions of the prompt and delayed signal from both interactions are shown in Fig. 7.5 together with the NC reaction Eq. 7.16.

The visible prompt energy is

$$E_{\text{vis}}^p = E_{e^-} \quad (\nu_e - {}^{12}\text{C}), \quad (7.18)$$

$$E_{\text{vis}}^p = E_{e^+} + 2m_e \quad (\bar{\nu}_e - {}^{12}\text{C}), \quad (7.19)$$

including the immediate ( $\tau < 1 \text{ ns}$ ) annihilation of the positron after the  $\bar{\nu}_e - {}^{12}\text{C}$  charged current reaction. The kinetic energy  $E_e$  of the prompt  $e^\mp$  is directly related to the incoming neutrino energy  $E_\nu$  as per  $E_e = E_\nu - E_{\text{thr}}$ , since the recoil energy of the final state nucleus is negligible. The visible energy of the delayed signal is

$$E_{\text{vis}}^d = E_{\beta^+} + 2m_e \quad ({}^{12}\text{N decay}), \quad (7.20)$$

$$E_{\text{vis}}^d = E_{\beta^-} \quad ({}^{12}\text{B decay}), \quad (7.21)$$

including the pair annihilation of the  $\beta^\pm$  in the case of  ${}^{12}\text{N}$  decay.  $E_\beta$  is the kinetic energy of the emitted  $\beta^\pm$ . The distribution of the kinetic energy follows

$$N(E_\beta) = (1 + aE_\beta^{\text{tot}} + b(E_\beta^{\text{tot}})^2) p_\beta E_\beta^{\text{tot}} (Q - E_\beta)^2 F(Z, E_\beta), \quad (7.22)$$

where  $E_\beta^{\text{tot}} = E_\beta + m_e$  is the total energy and  $p_\beta = \sqrt{(E_\beta^{\text{tot}})^2 - m_e^2}$  the momentum of the  $\beta$  particle. The shape correction factor  $a$  is measured to be  $a({}^{12}\text{N}) = (-0.38 \pm 0.09) \times 10^{-2} \text{ MeV}^{-1}$  and  $a({}^{12}\text{B}) = (0.71 \pm 0.11) \times 10^{-2} \text{ MeV}^{-1}$  at  $b = 0$  [273]. The  $Q$ -value of the  ${}^{12}\text{N}$  and  ${}^{12}\text{B}$  decays to  ${}^{12}\text{C}_{\text{g.s.}}$  are  $\sim 17.338 \text{ MeV}$  and  $\sim 13.369 \text{ MeV}$  [274], respectively, and the Fermi function  $F(Z, E_\beta)$  is approximated by

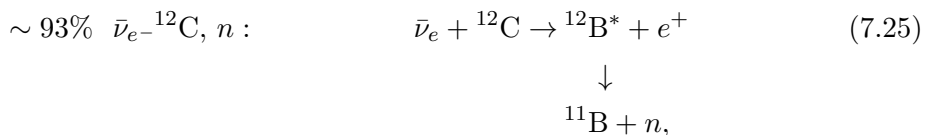
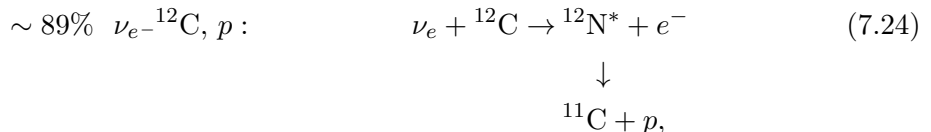
$$F(Z, E_\beta) \approx \frac{2\pi\zeta}{(e^{2\pi\zeta} - 1)}, \quad (7.23)$$

where  $\zeta = \mp \alpha Z E_\beta^{\text{tot}} / p_\beta$  ( $-$  for  $\beta^+$ ,  $+$  for  $\beta^-$ ). In the latter equality,  $\alpha$  is the fine structure constant and  $Z = 6$  the charge of the final state isotope. The use of the non-relativistic Primakoff–Rosen approximation Eq. 7.23 was found to have a negligible effect on the results.

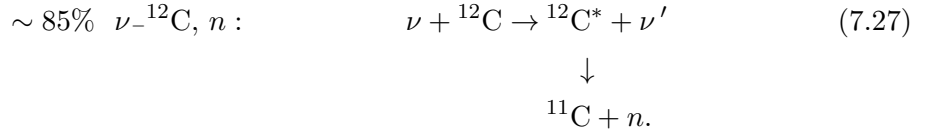
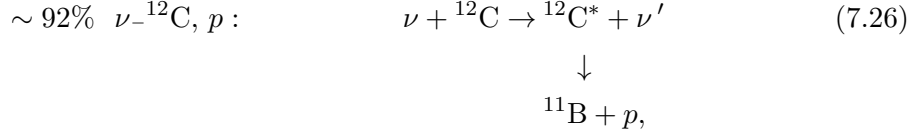
Since the lifetimes of the  $^{12}\text{N}$  and  $^{12}\text{B}$  decays differ, it is recommended to investigate the efficiency of  $\nu_e$  and  $\bar{\nu}_e$  event identification by coincidence tagging with multi-kilotonne targets as proposed for JUNO and RENO–50. An efficient event classification would render an exclusive spectral shape measurement of  $\nu_e$  possible, an opportunity that no further channel in Tab. 7.1 provides. With this, a single detector, using LS, would be sensitive to spectral information from all flux components:  $\bar{\nu}_e$ ,  $\nu_x$  and  $\nu_e$ . A strong enhancement of the flavor sensitivity is achievable if electrons can be discriminated against positrons, as suggested in [195]. However, these investigations are beyond the scope of this thesis and only mentioned here as outlook.

### Inclusive transitions

In the context of SN neutrino measurements with LS, not only the superallowed reactions Eq. 7.14–7.16 are relevant, but also forbidden  $\nu$ –induced interactions on  $^{12}\text{C}$  with free nucleons in the final state due to inclusive transitions. Knockout protons and recoil protons, induced by knockout neutrons, form a background to  $\nu$ – $p$  ES events. The thermalized knockout neutrons furthermore result in IBD background events, since their capture leads to a similar prompt–delayed signal coincidence as used for IBD identification. All CC and NC nucleon production cross sections over the relevant neutrino energy range are shown in Fig. 7.2b. The cross sections for neutron release in  $\nu_e$ – $^{12}\text{C}$  charged currents and proton release in  $\bar{\nu}_e$ – $^{12}\text{C}$  charged currents are very small and the reaction thresholds considerably high with respect to the expected neutrino energy range Fig. 7.1. These channels do not notably contribute to the observed SN neutrino spectrum and thus not discussed here. The  $\nu$ – $^{12}\text{C}$  reactions predominantly contributing to the remaining four nucleon knockout channels are the charged currents



and the neutral currents



The description of the nucleon knockout reactions in a two-step process, incorporating nuclear excitation above the continuum threshold, follows [275]. Since the excited states are above the separation energy of a nucleon, the nucleus decays by particle emission into a residual nucleus. It is assumed that the cross sections in Fig. 7.2b entirely apply to the above reactions, a good approximation in view of the smallness of the event yields (see Tab. 7.1) and the expected uncertainty of the cross sections. No theoretical uncertainties are quoted in [266], but a comparison of the results for Eq. 7.26, for instance, with the calculations in [276] reveal a difference of about 30% [93]. An uncertainty of at least this order is thus likely and used to estimate the event yield uncertainties given in Tab. 7.1. The differential cross sections, and hence the energy distribution of the outgoing nucleons and leptons, are not available in [266]. For this reason, the approximated analytical shape of the differential cross section

$$\frac{d\sigma}{dE_N} \propto \sqrt{E_N} (\sqrt{s} - m_N - m_I - E_N)^2, \quad (7.28)$$

deduced from basic phase space considerations, is adopted from [93]. In this expression,  $E_N$  is the kinetic energy of the outgoing nucleon and  $\sqrt{s}$  is the center of mass energy with  $s = m_{^{12}\text{C}}^2 + 2m_{^{12}\text{C}}E_\nu$ . The masses  $m_{^{12}\text{C}}$ ,  $m_N$  and  $m_I$  are the masses of the initial state  ${}^{12}\text{C}$  nucleus and the final state nucleon  $N$  and isotope  $I$ , respectively. The accuracy of the spectral shape is sufficient, again with respect to the smallness of the event statistics. The outgoing nucleon energy spectrum follows with Eq. 7.28 from

$$\frac{dN}{dE_N}(E_\nu) = N_{^{12}\text{C}} \int_{E_\nu^{\min}}^{\infty} A \frac{d\sigma}{dE_N}(E_\nu) \frac{dN}{dE_\nu} dE_\nu, \quad (7.29)$$

where  $N_{^{12}\text{C}}$  is the number of target  ${}^{12}\text{C}$  nuclei (see Tab. 5.3).  $A$  is a normalization factor, adapting the integral of Eq. 7.28 over the nucleon energy, taken from [93], to the total cross section, calculated in [266] and shown in Fig. 7.2b. The minimal incoming neutrino energy  $E_\nu^{\min}$  necessary to yield  $E_N$  is

$$E_\nu^{\min} = \frac{\left( \sqrt{m_I^2 + 2m_N E_N + E_N^2} + m_L + m_N + E_N \right)^2 - m_{^{12}\text{C}}^2}{2m_{^{12}\text{C}}}, \quad (7.30)$$

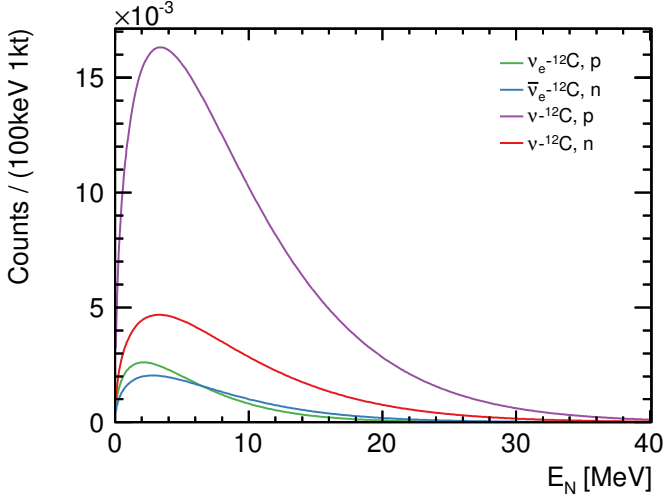


**Figure 7.6:** Time-integrated kinetic energy  $E_N$  distribution of knockout nucleons in LAB produced by SN neutrinos. The neutrino fluence is assumed to follow Fig. 7.1. The individual reactions are explicitly given in Eq. 7.24–7.27.

which follows from kinematics with the outgoing lepton at rest. The resulting nucleon energy distributions of all four reactions are shown in Fig. 7.6. Reaction Eq. 7.26 has the highest event rate since it has with  $E_{\text{thr}} = 15.46 \text{ MeV}$  the lowest energy threshold. The threshold energies of reactions Eq. 7.24, 7.25 and 7.27 are  $17.95 \text{ MeV}$ ,  $17.26 \text{ MeV}$  and  $18.73 \text{ MeV}$ , respectively. All thresholds are calculated as per

$$E_{\text{thr}} = \frac{(m_I + m_N + m_L)^2 - m_{^{12}\text{C}}^2}{2m_{^{12}\text{C}}}, \quad (7.31)$$

where  $m_L$  is the mass of the final state lepton  $L$ .

The kinetic lepton energy  $E_L$  is given by  $E_L = E_\nu - E_{\text{thr}} - E_N$ , since the outgoing nucleon and lepton share the initial neutrino energy that exceeds the threshold energy. With the knowledge of  $E_L$  and  $E_N$ , the visible energy is determined for the individual inclusive transitions, where a prompt signal follows all transitions and a delayed signal follows only the neutron knockout reactions. The visible prompt energy  $E_{\text{vis}}^p$  is

$$E_{\text{vis}}^p = E_{e^-} + E_{p,\text{vis}} \quad (\nu_{e^-}{}^{12}\text{C}, p), \quad (7.32)$$

$$E_{\text{vis}}^p = E_{e^+} + 2m_e + E_{n,\text{vis}} \quad (\bar{\nu}_{e^-}{}^{12}\text{C}, n), \quad (7.33)$$

$$E_{\text{vis}}^p = E_{p,\text{vis}} \quad (\nu_-{}^{12}\text{C}, p), \quad (7.34)$$

$$E_{\text{vis}}^p = E_{n,\text{vis}} \quad (\nu_-{}^{12}\text{C}, n), \quad (7.35)$$

including the positron annihilation energy in Eq. 7.33 after the  $\bar{\nu}_{e^-}{}^{12}\text{C}$  charged current reaction. The visible proton energy  $E_{p,\text{vis}} = L(E_N)$  is the quenched nucleon energy  $E_N$ , using Birks' law Eq. 2.12 and the quenching parameters mentioned in Sec. 7.1.1, measured within this work. In the case of inclusive  ${}^{12}\text{C}$  transitions, also the knockout neutrons produce a prompt signal due to the high kinetic energies reached (see Fig. 7.6). At these energies, neutrons mainly deposit their energy in the scintillator by  $n-p$  ES and inelastic scattering on  ${}^{12}\text{C}$ , where  $n-p$  ES dominates. The visible neutron energy  $E_{n,\text{vis}}$  is thus

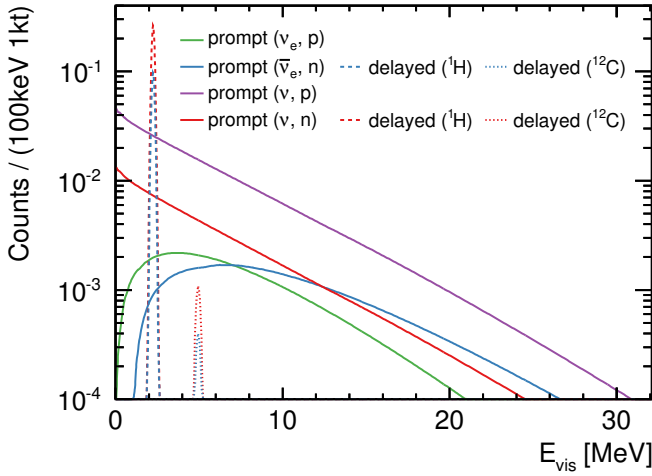


**Figure 7.7:** Visible energy spectra of inclusive transitions of  $^{12}\text{C}$  in LAB induced by SN neutrinos. The neutrino fluence is assumed to follow Fig. 7.1. The resulting prompt and delayed signals are explained in Eq. 7.32–7.35 and in the text. An energy resolution of  $6\%/\sqrt{E_{\text{vis}}(\text{MeV})}$  is assumed.

primarily composed of the sum of quenched proton recoil energies and, in the case of  $^{12}\text{C}$  excitation, the respective de-excitation energy. Also contributions of  $\alpha$ -particles from  $^{12}\text{C}(n, \alpha)^9\text{Be}$  reactions were considered in this step, but the reaction rate was found to be too low and the highly quenched light yield too small to change the resulting visible energy. Finally, the prompt signals of the neutron knockout reactions Eq. 7.25 and 7.27 are, as in the case of the IBD of free protons (see Sec. 7.1.2), followed by the delayed capture of the thermalized neutron on  $^1\text{H}$  or  $^{12}\text{C}$ , releasing a 2.223 MeV or 4.945 MeV de-excitation  $\gamma$ -ray, respectively. The prompt and delayed visible energy spectra of the four transitions Eq. 7.24–7.27 are shown in Fig. 7.7 assuming the reference SN neutrino fluence in Fig. 7.1.

The total SN neutrino event yields of all relevant inclusive  $^{12}\text{C}$  transitions together with the complete illustration of the respective visible spectra have not been publicly available so far, but are important to estimate the relevance of these transitions as  $\nu$ - $p$  ES and IBD backgrounds. The final state nuclei,  $^{11}\text{B}$  and  $^{11}\text{C}$ , do not enable time coincidence tagging, since  $^{11}\text{B}$  is stable and  $^{11}\text{C}$  has a lifetime of  $\tau = 29.42$  min. The inclusive  $^{12}\text{C}$  reactions can thus not be reliably identified and rejected. Their contribution to the background spectrum will be discussed in Sec. 7.2.

#### 7.1.4 Neutrino-electron elastic scattering

Elastic scattering on electrons is possible for all neutrinos and neutrino energies and the cross sections of the purely leptonic process are known to better than 1% within the SM. The total cross sections shown in Fig. 7.2a follow

$$\sigma_{\text{tot}}(E_\nu) = \frac{G_F^2 2m_e E_\nu}{\pi} \left[ c_1 \cdot \left( \frac{1}{2} \pm \sin^2 \theta_W \right)^2 + c_2 \cdot \sin^4 \theta_W \right], \quad (7.36)$$

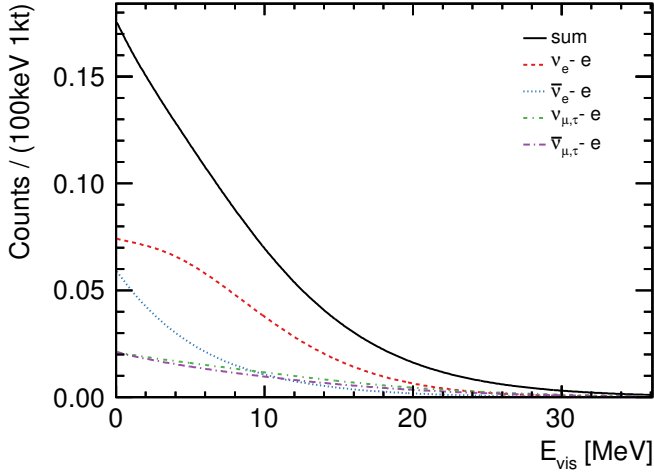


**Figure 7.8:** Visible energy spectra of  $\nu$ - $e$  elastic scattering in LAB induced by SN neutrinos. The neutrino fluence is assumed to follow Fig. 7.1 and an energy resolution of  $6\%/\sqrt{E_{\text{vis}}(\text{MeV})}$  is assumed. Since  $\nu$ - $e$  elastic scattering events, induced by neutrinos of different flavors and types, are indistinguishable, only the sum spectrum is observed.

where the "+" sign is for electron flavor and the "−" sign for muon and tau flavor neutrinos. The factors  $c_{1,2}$  depend on the neutrino type and are  $c_1^{(\nu)} = c_2^{(\bar{\nu})} = 1$  and  $c_1^{(\bar{\nu})} = c_2^{(\nu)} = 1/3$ . The total cross section is small compared to all other relevant cross sections (see Fig. 7.2). The visible signal is induced by the scattered electron and the visible energy distribution, shown in Fig. 7.8, determined by the differential cross section

$$\frac{d\sigma}{dE_e}(E_\nu, E_e) = \frac{G_F^2 2m_e}{\pi} \left[ g_1^2 + g_2^2 \left( 1 - \frac{E_e}{E_\nu} \right)^2 - g_1 g_2 \frac{m_e E_e}{E_\nu^2} \right]. \quad (7.37)$$

The dependence on  $\theta_W$  is expressed by the quantities  $g_1$  and  $g_2$ , which are correlated with the neutrino flavor and type:  $g_1^{(\nu_e)} = g_2^{(\bar{\nu}_e)} = 1/2 + \sin^2 \theta_W$ ,  $g_2^{(\nu)} = g_1^{(\bar{\nu})} = \sin^2 \theta_W$  and  $g_1^{(\nu_x)} = g_2^{(\bar{\nu}_x)} = -1/2 + \sin^2 \theta_W$ .

Neither for  $\nu$ - $e$  ES nor for  $\nu$ - $p$  ES coincidences exist to permit special tagging methods. Discrimination between these two channels is only possible through pulse-shape discrimination (PSD), though the efficiency is low for LAB based scintillators, as discussed in Sec. 6.5.1. Without PSD, this channel is an irreducible background to  $\nu$ - $p$  ES.

### 7.1.5 Summary

A summary of all visible spectra from the individual SN neutrino interaction channels in LAB based scintillator is shown in Fig. 7.9. As above, the reference SN Fig. 7.1 at 10 kpc distance is used. Figure 7.9 demonstrates the dominance of  $\nu$ - $p$  ES at low visible energies and of IBD at high visible energies. In case of the exclusive and inclusive  $^{12}\text{C}$  transitions only the respective sum spectra are shown.

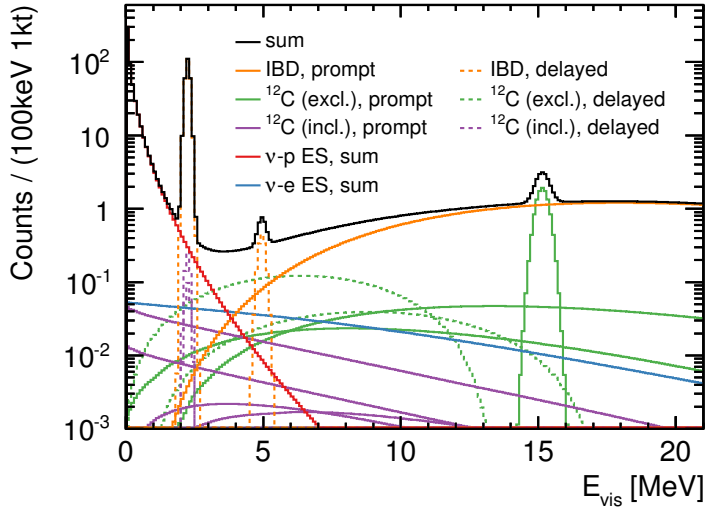


**Figure 7.9:** Visible energy spectra of all detection channels in liquid scintillator listed in Tab. 7.1. The events are induced by SN neutrinos with a fluence following Fig. 7.1. LAB as scintillator and an energy resolution of  $6\%/\sqrt{E_{\text{vis}}(\text{MeV})}$  are assumed. Details about the individual spectra are shown in Fig. 7.3–7.8.

## 7.2 Backgrounds

A standard galactic CCSN leads for a short time to a relatively high neutrino event rate, reaching  $\mathcal{O}(100 \text{ kt}^{-1} \text{s}^{-1})$  in the case of the IBD and  $\nu$ -*p* ES reactions (see Tab. 7.1). Most of the usual background sources to the observation of typical low energy neutrinos, like solar, atmospheric, reactor and geo neutrinos, have several orders of magnitudes lower rates and are fully negligible. At SN event rates, the IBD detection channel is virtually background free, also including the backgrounds induced by the SN itself, as will be outlined in Sec. 7.2.1. Different from the case of IBD, not all non-SN backgrounds are negligible for  $\nu$ -*p* ES. Subsection 7.2.2 will underline the importance of a well-measured background spectrum in the ROI for  $\nu$ -*p* ES, which may be different from the well-studied ROI of the main physics goal of a detector like SNO+, which is not an exclusive SN detector. If the background is indeed measured with vanishing statistical uncertainty in the long-term phases without a SN, background subtraction is expected to be highly efficient, which is supposed for the  $\nu$ -*p* ES sensitivity studies in Sec 7.5.

### 7.2.1 Backgrounds to IBD events

Two types of events generally contribute to the background of IBD events: true and mimicked IBD events. Both types have contributions from non-SN and SN events. The highest non-SN IBD rate in underground LS detectors is induced by reactor plus geo neutrinos,

reaching  $\mathcal{O}(10^{-5}) \text{ kt}^{-1}\text{s}^{-1}$  [263, 264, 277]. This rate by itself is already seven orders of magnitude lower than the SN IBD event rate and fully negligible. All backgrounds corresponding to reactor and geo neutrino measurements in underground LS detectors have comparable or lower rates [263, 264, 277] and their sources are not further discussed here. Only random coincidence events are shortly mentioned, since the energy range for the coincidence tag of SN  $\bar{\nu}_e$  differs from the one for reactor and geo  $\bar{\nu}_e$ . Besides this, the next paragraphs hence only cover SN induced backgrounds to IBD.

### True IBD events

The SN  $\bar{\nu}_e$ -induced inclusive  $^{12}\text{C}$  transition Eq. 7.25 (Nr. 7 in Tab. 7.1) is an IBD reaction. Since the final state neutron gains a finite kinetic energy after  $^{12}\text{B}^*$  excitation in this case, the incoming neutrino energy  $E_\nu$  is not unambiguously designated to a certain positron energy  $E_{e^+}$  as in the case of the IBD of a free proton (see Eq. 7.12). Moreover, the fast knockout neutron creates an additional prompt signal via scattering on protons and C atoms, adding up to the visible positron signal. Due to an undetermined combination of positron signal and quenched proton recoil signal, also no distinct promptly visible energy  $E_{\text{vis}}^p$  can be assigned to  $E_\nu$ . The event signatures, on the other hand, are identical in the neutron knockout reaction Eq. 7.25 and in the IBD Eq. 7.8. Reaction Eq. 7.25 thus is a background source. Following Tab. 7.1, the event rate of this reaction from a standard CCSN is  $R \approx 0.1 \text{ kt}^{-1}\text{s}^{-1}$  in the first second of the burst.

### Mimicked IBD events

Mimicked IBD events arise from scattering of SN  $\nu$  on  $^{12}\text{C}$  and from random coincidences of uncorrelated events. In the inclusive  $^{12}\text{C}$  transition Eq. 7.27 (Nr. 9 in Tab. 7.1) a fast neutron is released, which produces a prompt signal via proton or  $^{12}\text{C}$  scattering and the delayed neutron capture signal, when the neutron is thermalized. The expected rate from a standard CCSN is  $R \approx 0.3 \text{ kt}^{-1}\text{s}^{-1}$  in the first second of the burst, under the conditions set for Tab. 7.1. This background is the largest background to SN  $\bar{\nu}_e$ -induced IBDs.

The rate of uncorrelated events that coincidentally fulfill the IBD coincidence trigger conditions, i.e. of random coincidence events, depends on the event rates and on the trigger conditions itself. The observed coincidence rate from non-SN events is  $< 10^{-6} \text{ kt}^{-1}\text{s}^{-1}$  in the large-scale LS detectors Borexino [277] and KamLAND [263]. The energy window considered in this case is optimized for geo and reactor  $\bar{\nu}_e$  tagging and is much smaller than for SN  $\bar{\nu}_e$ 's, since the maximal visible energy is below about 10 MeV [263, 277] in the first case, while it reaches several tens of MeV (see Fig. 7.4) in the second case. However, since above about 5 MeV the contribution from radioactive contaminations significantly drops, the coincidence rate due to non-SN events is not expected to increase to an extend relevant for SN neutrino observation.

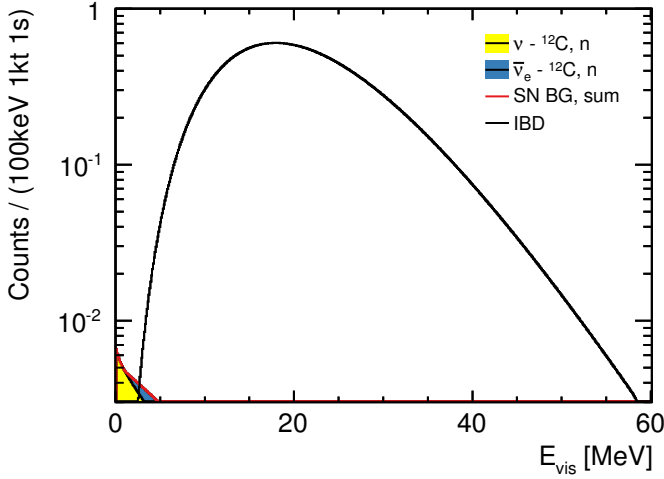


**Figure 7.10:** Visible energy spectra of signal and background events in LAB induced by SN neutrinos and integrated over the first second of the burst. The signal is formed by inverse beta decays (IBD) and the background by neutron knockout reactions (see text). The neutrino fluence is assumed to follow Fig. 7.1 and an energy resolution of  $6\%/\sqrt{E_{\text{vis}}(\text{MeV})}$  is considered.

The rate of random coincidences in the presence of SN events from all detection channels listed in Tab. 7.1 depends mainly on the distance to the SN. For an estimate of the random coincidence rate of SN events, the event yields in Tab. 7.1 are used, which are calculated for the reference SN at 10 kpc. The event yield is doubled for those detection channels, which have a prompt and a delayed signal (see Fig. 7.9). It is again assumed that half of the total yield corresponds to the event rate per second in the first second of the burst. Applying the trigger conditions  $\Delta t_{\text{max}} = 660 \mu\text{s}$  and  $\Delta r_{\text{max}} = 1.6 \text{ m}$  from Sec. 7.1, the rate of non-IBD events in the time and space coincidence window becomes  $R_{\text{random}} \approx 2.4 \times 10^{-3} \text{ kt}^{-1}\text{s}^{-1}$ . With an additional cut on the delayed energy, with  $1.7 \text{ MeV} < E_{\text{vis}}^d < 2.8 \text{ MeV}$  for  $n$  capture on H and  $4.3 \text{ MeV} < E_{\text{vis}}^d < 5.6 \text{ MeV}$  for  $n$  capture on C, this rate further reduces to  $R_{\text{random}} \approx 6.4 \times 10^{-5} \text{ kt}^{-1}\text{s}^{-1}$ . This estimate is conservative, since no additional tagging techniques are considered to reject the non-IBD events initiated by the SN. The estimated rate is nearly seven orders of magnitude lower than the IBD signal rate and thus negligible.

To conclude, the highest background rates, relevant for SN-induced IBDs in LS detectors, arise from the inclusive  $^{12}\text{C}$  transitions Nr. 7 and 9 in Tab. 7.1, leading to a still small sum rate of  $R = (0.4 \pm 0.1) \text{ kt}^{-1}\text{s}^{-1}$  in the first second of the burst. The uncertainty solely considers the cross section uncertainty mentioned in Sec. 7.1.3. The prompt signals from these two reactions, depicted as blue and red solid lines in Fig. 7.7, form the visible sum background spectrum to SN  $\bar{\nu}_e$  IBD events, as shown in Fig. 7.10. The majority of this background is easily rejected by a low energy cut at  $E_{\text{vis}} = 5 \text{ MeV}$ . This corresponds to an incoming neutrino energy of  $E_{\nu} \approx 5.8 \text{ MeV}$  (see Sec. 7.1.2). The remaining background amounts to less than 1% in the energy region common to signal and background and is neglected within the sensitivity studies in Sec. 7.4.

### 7.2.2 Backgrounds to $\nu-p$ ES scattering events

Neutrino–proton elastic scattering does not offer specific tagging possibilities and PSD against signals from electrons, positrons or gammas is challenging with LAB based scintillator. PSD between protons and  $\alpha$ -particles has not been explicitly tested for LAB based scintillators yet. It is thus conservatively assumed that PSD is not possible in general and all events that are not associated with a specific reaction, contribute to the background spectrum.

The rates of the corresponding background spectra shown in this subsection are based on expected or targeted SNO+ levels<sup>5</sup>. The non-SN background sum spectrum is shown at the end of this subsection in comparison to the signal spectrum. Also the composition of the SN-induced background sum spectrum is described here and shown at the end of this passage. The details of the contributing SN neutrino reactions are given in Sec. 7.1.

There are basically three non-SN background categories: Detector intrinsic radioactivity, solar plus atmospheric neutrinos and cosmic muons plus cosmogenics. Detector intrinsic radioactivity is further classified as external, surface and internal background. External backgrounds are all events that are generated by radioactive decays outside the scintillator, for example in the PMTs, but not on the inner surface of the LS housing, which is in case of SNO+ the AV. The only external background events possibly occurring in the scintillator are induced by  $\gamma$ -rays. Those background events that are caused by decays of contaminants on the inner surface of the LS housing are called surface backgrounds. Internal backgrounds originate from radioactive contaminants within the LS itself. The largest background contribution in the case of SNO+ comes from internal backgrounds, which reaches and partly even excesses the signal spectrum. External and surface backgrounds sum up on internal backgrounds and are thus also presented here.

#### Detector intrinsic radioactivity

The number of **external backgrounds** is strongly reduced by position reconstruction and the definition of a FV. The size and shape of the FV depends on the analysis to be performed and on the detector. The most generic FV for a quasi radial symmetric detector like SNO+, or JUNO, is a sphere with a fiducial radius  $r_{\text{FV}}$ . A small FV cut is normally sufficiently suppressing the external backgrounds for the observation of SN neutrinos. For SNO+, a radius of  $r_{\text{FV}} = 5.0 \text{ m}$  is chosen in this chapter, which results in a distance between the AV surface and the FV of 1 m and a fiducial mass of 0.45 kt. The same radius reduction by 1 m in case of a 20 kt spherical LAB volume, the mass proposed for JUNO, results in a 16.80 kt FV. These are the two FVs considered throughout the

---

<sup>5</sup>All values used are determined by the SNO+ Background Working Group for the pure LAB phase and internally available in SNO+-doc-507, version 24. The document was latest accessed for this work January 2015.

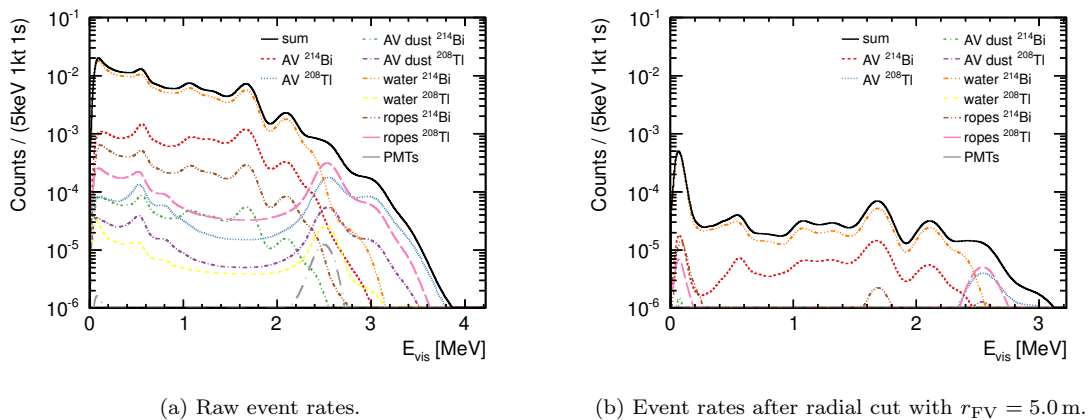


**Figure 7.11:** Expected event rates in LAB based scintillator from external  $\gamma$  ray backgrounds. The visible energy ( $E_{\text{vis}}$ ) distributions are simulated with RAT by members of the SNO+ collaboration. Within this thesis, the spectra are normalized according to SNO+ expectations within the full scintillator volume (a) and within a spherical FV with  $r_{\text{FV}} = 5.0 \text{ m}$  (b). All spectra are convolved with an energy resolution of  $6\%/\sqrt{E_{\text{vis}}(\text{MeV})}$ .

sensitivity studies in Sec. 7.4 and 7.5. The smaller FV is additionally used for the event yield calculations in Sec. 7.6.

The external background rates per kilotonne and second expected in SNO+ due to the water shielding, the rope system supporting the AV, dust and the AV itself are shown in Fig. 7.11 before and after the FV cut. All individual rates within the FV are  $< 10^{-2} \text{ kt}^{-1}\text{s}^{-1}$ , summing up to a total external background rate of  $\sim 0.02 \text{ kt}^{-1}\text{s}^{-1}$ .

Also **surface backgrounds** are reduced by a FV cut, though to a smaller extend. The level of surface backgrounds, backgrounds coming from the inner surface of the scintillator housing, strongly depends on the history of the material. The original SNO detector was build for neutrino energies above about 3.5 MeV and radioactive backgrounds played a subordinate role. After SNO data taking, the empty detector, including the inner AV, was exposed to mine air before it was insulated. Mine air is highly contaminated with  $^{222}\text{Rn}$  and also long-term insulation only eradicated the shorter living Rn daughters (see the  $^{238}\text{U}$  decay chain in Fig. A.1). The longer living  $\beta$  emitter  $^{210}\text{Pb}$  remains, which tends to adsorb on surfaces. As a consequence, the inner AV surface is notably contaminated with its two radioactive daughters  $^{210}\text{Bi}$  and  $^{210}\text{Po}$ . These backgrounds slowly leach into the liquid in contact with the surface, i.e. water in the initial water phase of SNO+ and LAB based scintillator in the subsequent LS phase. The surface background rate is reduced by leaching, while the internal background rate is consequently increased.

While the surface background rate in dedicated low-background detectors, using ultra-pure materials, is indeed fully negligible for SN  $\nu$  observations (see e.g. [193]), the  $\alpha$ - and  $\beta$ -event rates from decays of  $^{210}\text{Pb}$ ,  $^{210}\text{Bi}$  and  $^{210}\text{Po}$  expected in SNO+ are high. The

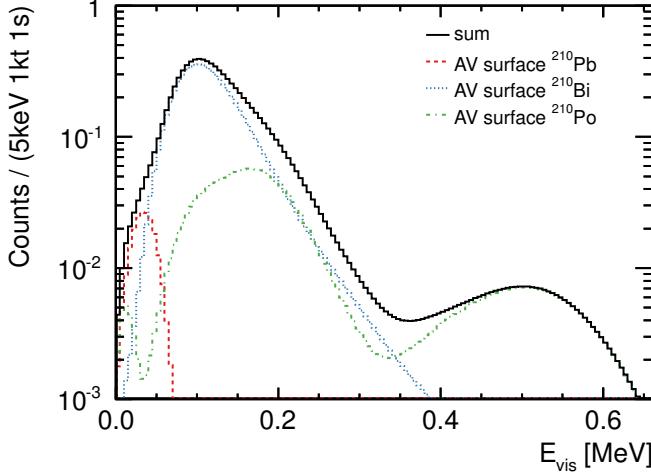


**Figure 7.12:** Visible energy,  $E_{\text{vis}}$ , spectra of surface backgrounds expected in SNO+ including leaching (see text). The reconstructed  $E_{\text{vis}}$  distributions are simulated with RAT by the SNO+ collaboration. A radial cut with  $r_{\text{FV}} = 5.0 \text{ m}$  is applied and an energy resolution of  $6\%/\sqrt{E_{\text{vis}}(\text{MeV})}$  is considered.

respective surface background rate expectations depend on the rate of the isotope leaching from the AV surface into the liquid inside the AV and the duration of the filled AV phases. Based on leaching rate measurements, it is expected that after 9 months of ultra-pure water in the AV and thorough cleaning of its surface after draining, the rate of  $^{210}\text{Pb}$ ,  $^{210}\text{Bi}$  and  $^{210}\text{Po}$  in the LAB phase is about  $0.2 \text{ kt}^{-1}\text{s}^{-1}$ ,  $6.6 \text{ kt}^{-1}\text{s}^{-1}$  and  $1.8 \text{ kt}^{-1}\text{s}^{-1}$ , respectively, after the FV cut. The residual rate within the FV is determined via simulations with the SNO+ MC code RAT and the corresponding simulated residual visible energy,  $E_{\text{vis}}$ , spectra are shown in Fig. 7.12. Though the  $\alpha$ - and  $\beta$ -particles from these decays are typically stopped before they reach the FV, their events are not fully suppressed by the cut due to a reduced vertex reconstruction efficiency close to the AV. The efficiency further decreases at visible energies as low as the ones of  $^{210}\text{Pb}$ , which maximally emits  $\beta$ 's with a kinetic energy of 17 keV and 63 keV. All other surface background rates are already before any cut  $< 10^{-2} \text{ kt}^{-1}\text{s}^{-1}$  and thus not individually mentioned here.

In the case of **internal backgrounds**, the only backgrounds worthwhile mentioning in the given context are  $\beta$ -decays of  $^{14}\text{C}$  and again the  $\alpha$ - and  $\beta$ -decays of  $^{210}\text{Pb}$ ,  $^{210}\text{Bi}$  and  $^{210}\text{Po}$  in the presence of leaching from the AV into the LS. All other internal backgrounds, arising from the natural  $^{238}\text{U}$  and  $^{232}\text{Th}$  chains (see Fig. A.1) and the potential ingress of further contaminants during filling or calibration procedures, have a sum rate of  $< 10^{-2} \text{ kt}^{-1}\text{s}^{-1}$ . The respective backgrounds are added for completeness to the internal background sum spectrum following in this section, but are not further discussed here. The interested reader is referred to e.g. [193], which provides an extensive discussion of typical internal backgrounds in low-background LS detectors.

The four named, relevant isotopes are given in Tab. 7.3 together with their expected rates, considering leaching. The leached isotopes are assumed to be homogeneously distributed in the LS volume and their rates are based on the same assumptions as made

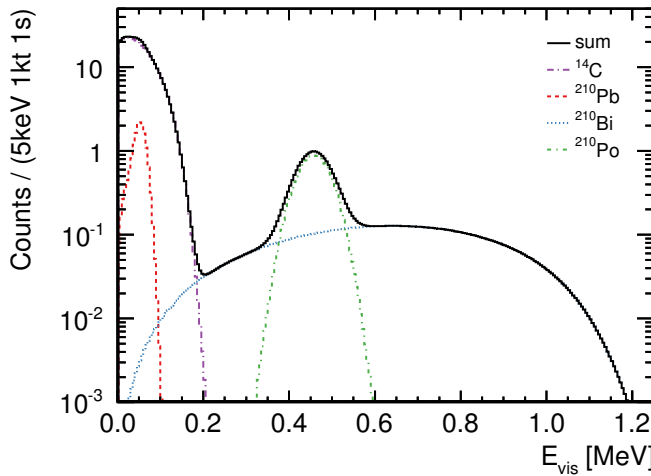


**Figure 7.13:** Visible energy,  $E_{\text{vis}}$ , spectra of internal backgrounds expected in SNO+ including leaching (see text). The  $E_{\text{vis}}$  distributions are calculated analytically, considering an energy resolution of  $6\%/\sqrt{E_{\text{vis}}(\text{MeV})}$ .

**Table 7.3:** Internal background isotopes with their branching ratio (BR) and lifetime  $\tau$ , relevant for the SN neutrino observation via  $\nu$ - $p$  ES in SNO+.  $E$  is in case of  $\alpha$  decay, the particle energy and in case of  $\beta$  decay the endpoint energy of the spectrum.  $R_{\text{SNO+}}$  is the rate derived from expected SNO+ background levels, converted into units of kilotonnes and seconds. The  ${}^{210}\text{Pb}/{}^{210}\text{Bi}/{}^{210}\text{Po}$  values include contaminations leaching from the inner AV surface into the LS. For these values, 9 months of ultra-pure water in the AV, followed by additional surface cleaning, before the LS phase are assumed.

Isotope	$\tau$	Decay	$E$	$R_{\text{SNO+}}$
		(BR [%])	[keV]	[ $\text{kt}^{-1}\text{s}^{-1}$ ]
${}^{14}\text{C}$	$8.27 \times 10^3 \text{ y}$	$\beta$ (100)	156.5	391.46
${}^{210}\text{Pb}$	32.2 y	$\beta$ (81, 19)	17, 63	15.68
${}^{210}\text{Bi}$	7.23 d	$\beta$ (99)	1161	15.68
${}^{210}\text{Po}$	200 d	$\alpha$ (99)	5.305	16.49
Total				439.31

in the context of surface backgrounds. The corresponding  $E_{\text{vis}}$  spectra are calculated analytically and shown in Fig. 7.13. The reduction of the trigger efficiency below about 80 keV is not considered, since the precise behavior of the turn on curve is not yet known for the considered detectors, SNO+ and JUNO.

Also shown in this figure is the most relevant non-SN background:  ${}^{14}\text{C}$ .  ${}^{14}\text{C}$  is a  $\beta$  emitter with a lifetime of  $8.27 \times 10^3 \text{ y}$ , which is short from the geological point of view. It is, however, constantly reproduced through cosmic and cosmogenic neutron interactions and generally present even in geologically old organic materials. The relative abundance depends on the history of the material and can differ by orders of

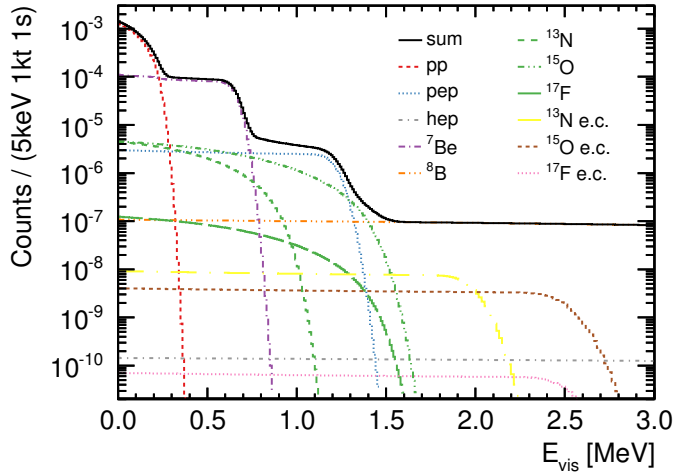


**Figure 7.14:** Visible, unoscillated energy distribution of electron neutrinos from the Sun in LAB based scintillator, where e.c. stands for electron capture. An energy resolution of  $6\%/\sqrt{E_{\text{vis}}(\text{MeV})}$  is taken into account.

magnitudes.  $^{14}\text{C}$  and  $^{12}\text{C}$  are chemically identical, omitting the removal of  $^{14}\text{C}$  from the LS by purification. So far only the Borexino collaboration achieved a measurement of the very low  $^{14}\text{C}$  content in high-purity LS using the Counting Test Facility (CTF) [278], yielding  $\propto 10^{-18} \text{g-14C/g-12C}$ . The  $^{14}\text{C}$  rate observed in the Borexino detector is  $R_{14\text{C}} = (400.46 \pm 10.42) \text{ kt}^{-1}\text{s}^{-1}$  [193]. Assuming the same isotopic abundance of  $^{14}\text{C}$  in LAB based scintillator as in PC scintillator, but accounting for the lower  $^{12}\text{C}$  mass percent fraction of  $\sim 87\%$  in LAB + PPO compared to  $\sim 89\%$  in PC + PPO, results in a rate of  $R_{14\text{C}} = 391.46 \text{ kt}^{-1}\text{s}^{-1}$ . Despite the low abundance, the comparatively short lifetime typically turns  $^{14}\text{C}$  into by far the largest background in underground organic LS detectors, as obvious from Tab. 7.3. This instance generally imposes a low energy analysis threshold, or even trigger threshold, around 200 keV, depending in the latter case amongst others on the data rate capacity of the detector. This is the motivation for the stated 200 keV trigger threshold used for the sensitivity studies presented in Sec. 7.4 and Sec. 7.5.

### Backgrounds from solar and atmospheric neutrinos

Elastic scattering of solar neutrinos with electrons in the scintillator is irreducible. The resulting spectra of the different neutrino species from the Sun are presented in Fig. 7.14, including the sum spectrum. Though this background cannot be suppressed, the respective rate is low compared to the neutrino rate arising from a SN. The total rate, and thus the rate in the ROI, in LAB based scintillator on Earth is  $< 0.03 \text{ kt}^{-1}\text{s}^{-1}$ . The total rate of atmospheric neutrinos is  $\lesssim 10^{-5} \text{ kt}^{-1}\text{s}^{-1}$  [280] and thus neglected.

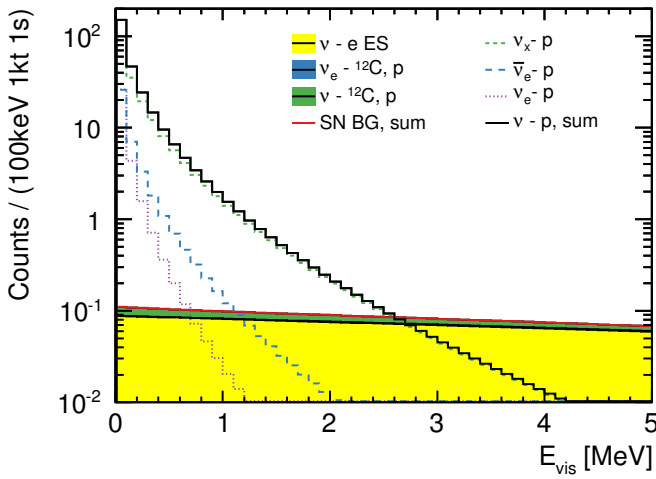


**Figure 7.15:** Visible energy,  $E_{\text{vis}}$ , spectra of signal and background events in LAB induced by SN neutrinos, integrated over the first second of the burst. The signal is formed by  $\nu$ - $p$  elastic scattering and the background by  $\nu$ - $e$  elastic scattering and inclusive  $^{12}\text{C}$  transitions with a free proton in the final state (see text). The reference SN is used and an energy resolution of  $6\%/\sqrt{E_{\text{vis}}(\text{MeV})}$  is assumed.

### Backgrounds from cosmic muons, cosmogenic isotopes and neutrons

The cosmic muon rate  $R_\mu$ , and thus also the rate of cosmogenic backgrounds, depends on the site of the experiment. The muon flux measured in SNOLAB is  $\Phi_\mu = (3.31 \pm 0.09) \times 10^{-10} \text{ cm}^{-2}\text{s}^{-1}$  [279]. With the given rate, SNO+ expects  $(3.74 \pm 1.02) \times 10^{-4}$  muons per second in the entire 780 t scintillator volume, corresponding to  $(4.79 \pm 1.31) \times 10^{-4} \text{ kt}^{-1}\text{s}^{-1}$ , which does not cause a problem in the time span of a SN neutrino burst. The total muon induced radioactive isotope rate in LS is lower than the muon rate itself [255] and thus, together with the cosmic muons, neglected in the presented studies.

Also the expected rate of muon induced neutrons in the liquid is slightly lower than the cosmic muon rate [255] and thus  $< 4.79 \times 10^{-4} \text{ kt}^{-1}\text{s}^{-1}$ . Added to that, cosmogenic neutrons produced in the surrounding rock and reaching the scintillator are expected at a rate of  $< 10^{-7} \text{ kt}^{-1}\text{s}^{-1}$ , derived from expectations of the former SNO experiment. And finally, the expected sum rate<sup>6</sup> of neutrons produced in the AV and scintillator due to spontaneous fission of  $^{238}\text{U}$ , photodisintegration on deuterium and carbon isotopes and reactions of energetic alpha particles on  $^{13}\text{C}$  and  $^{18}\text{O}$ , i.e.  $(\alpha, n)$  reactions, is  $\sim 1 \times 10^{-4} \text{ kt}^{-1}\text{s}^{-1}$ , of which  $\sim 99\%$  occur near the AV. The total neutron background thus amounts to  $< 10^{-3} \text{ kt}^{-1}\text{s}^{-1}$  and is consequently also neglected.

### Backgrounds from other SN detection channels

The visible  $\nu$ - $p$  ES sum spectrum is shown in Fig. 7.9 together with all other SN interaction channels in LS (see Tab. 7.1). Those channels, which have a prompt and delayed signal, are expected to be efficiently rejected by coincidence tagging and to not form a background to  $\nu$ - $p$  ES. The exclusive NC transition of  $^{12}\text{C}$  Eq. 7.16 produces a

<sup>6</sup>Internal note SNO+-doc-2497.

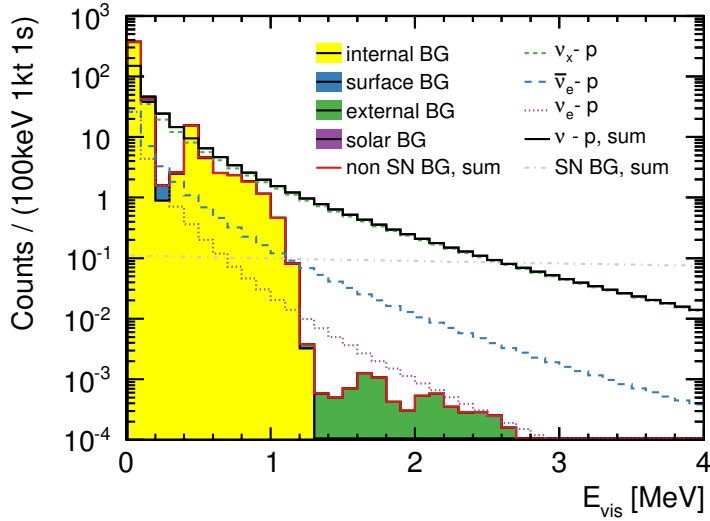


**Figure 7.16:** Expected event rates in LAB based scintillator from all backgrounds (BG) that are not induced by the SN itself. The summed SN induced BG spectrum is shown for comparison. The BG levels of SNO+, after a decent spherical FV cut with  $r_{\text{FV}} = 5.0\text{ m}$ , are assumed including leaching of contaminants from the AV into the scintillator. All spectra are convolved with an energy resolution of  $6\%/\sqrt{E_{\text{vis}}(\text{MeV})}$  and ionization quenching is taken into account.

15.11 MeV  $\gamma$  ray and thus a  $\gamma$  peak above the signal spectrum (see Fig. 7.9). This channel does not contribute to the background neither. The remaining channels, which are the  $\nu-e$  ES reaction and the two inclusive  $^{12}\text{C}$  transitions with a free proton in the final state Eq. 7.24 and 7.26, cannot be distinguished from the signal. Only PSD could suppress at least the first kind of events. The summation of the visible energy spectra is shown in Fig. 7.15 together with the individual  $\nu-p$  ES spectra.

The main background contribution comes from  $\nu-e$  ES interactions, followed by a small contribution from the NC inclusive  $^{12}\text{C}$  transition Eq. 7.26. The contribution from the CC inclusive transition Eq. 7.24 is too small to be resolved in Fig. 7.15. The sum of these SN induced backgrounds are below the  $\nu_x$  signal up to about  $E_{\text{vis}} \approx 2.6\text{ MeV}$ , as visible in Fig. 7.9. Their individual background contribution to each signal energy bin is known from the ratio of the respective differential signal and background reaction cross sections and assumed to be subtracted from the measurement for the sensitivity studies within this chapter.

## Summary

Figure 7.16 summarizes the contributions from the different background classes to  $\nu-p$  ES events of SN neutrinos, described above. These are backgrounds from external, surface and internal radioactivity, from solar neutrinos and from SN neutrinos themselves. The

sum spectrum corresponding to the last named background source is shown independently from the non-SN induced backgrounds. All other backgrounds are stepwise summed up, where the expected SNO+ rates including leaching are used. The contribution from solar neutrinos is too small to be resolved. The highest background rate is observed at energies below about 200 keV due to internal  $^{14}\text{C}$ . At higher energies, internal backgrounds form the major background up to about 1.2 MeV visible energy, partly exceeding the signal. This figure demonstrates the importance of a precise background measurement over the  $\nu$ - $p$  ES ROI and a thorough background subtraction from the signal in the event of real data.

For this work, it is supposed that the sum spectrum of non-SN background events above 200 keV visible energy has been measured precisely in the period without a SN and is subtracted from the observed sum spectrum. The SN induced backgrounds are assumed to be subtracted, using the respective cross section ratios.

## 7.3 Reconstruction of neutrino energy spectra from IBD and $\nu$ - $p$ ES

### 7.3.1 True neutrino and visible energy distributions

The neutrino fluence on Earth is assumed to be described by the reference SN neutrino distribution, as before. For the aforementioned reasons, only the first second of the neutrino flux is used in this and the following sections, which reduces the total number of neutrinos by a factor of two, compared to the fluence of the entire burst, for all calculations. Based on this flux, the energy ( $E_\nu^{\text{true}}$ ) distribution of the SN neutrinos that have interacted in the detector is calculated. This distribution is the product of the neutrino flux at the detector site, the total interaction cross section of the interaction of interest and the corresponding number of targets. The targets are in the case of both signal reactions,  $\nu$ - $p$  ES and IBD, protons.

The visible energy ( $E_{\text{vis}}$ ) distributions of  $\nu$ - $p$  ES and IBD using the reference SN neutrino fluence and 1 kt of LAB are shown in Fig. 7.10 and 7.15 together with the corresponding SN induced backgrounds. All spectra are scaled for the following sensitivity studies to a fiducial SNO+ and JUNO mass of 0.45 kt and 16.80 kt, respectively. The detector effects considered are, as before, an energy resolution of  $6\%/\sqrt{E_{\text{vis}}(\text{MeV})}$  and the ionization quenching of the proton signal using Eq. 2.12 and the results of the constrained fit for LAB1 from Tab. 6.10. The uncertainties of these quantities contribute to the systematic uncertainties of the fit parameters.

All sources of systematic uncertainty, considered within the thesis at hand, as well as their uncertainties are summarized in Tab. 7.4. The information whether the shape or the scale of the visible energy spectrum is affected, is important for the propagation

**Table 7.4:** Parameters and  $1\sigma$  systematic uncertainties propagated for the determination of the systematic uncertainties of the fitted spectral parameters. The last column denotes whether the scale or the shape of the visible signal energy spectrum is affected. If only one of the two signals,  $\nu$ -p ES or IBD, is affected, the respective channel is given in brackets.

Quantity	Variable	Value	$1\sigma_{\text{sys}}$	Affected property
Fiducial mass	$m_{\text{FV}}$	0.45 kt / 16.80 kt	1.9%	scale
Proton density	$\rho_p$	$6.266 \times 10^{22} / \text{cm}^3$	0.2%	scale
Energy resolution	$\sigma_{E_{\text{vis}}}$	$\frac{6\%}{\sqrt{E_{\text{vis}}(\text{MeV})}}$	$\frac{2\%}{\sqrt{E_{\text{vis}}(\text{MeV})}}$	shape
Birks' parameter	$k_B$	0.0096 MeV/cm	0.0003 MeV/cm	shape ( $\nu p$ ES)
Proton strangeness	$\eta$	0.12	0.07	scale ( $\nu p$ ES)
IBD tagging efficiency	$\epsilon_{\text{IBD}}$	94.0%	0.6%	scale (IBD)
IBD cross section	$\sigma_{\text{IBD}}$	–	0.4%	scale (IBD)

of uncertainties in Sec. 7.4 and 7.5. The uncertainty of the energy resolution is chosen conservatively large, to demonstrate the smallness of its influence on the detector sensitivity in the presented studies. The uncertainty of the fiducial mass  $m_{\text{FV}}$  includes a relative uncertainty of 1.8% due to the position reconstruction uncertainty on  $r_{\text{FV}}$  and a relative uncertainty of 0.59% from the uncertainty on the LS density. The LS density uncertainty itself is the quadratic sum of the uncertainty from the LAB density range at 15 °C, amounting to 0.58% [188, 192], and an approximate uncertainty of 0.1% from temperature and pressure variations [281, 282, 283]. The temperature and pressure variation influence on the density, also added quadratically, as well as the influence of the position reconstruction uncertainty are adopted from KamLAND [263, 281], since the situation in SNO+ is expected to be similar in this context. The uncertainty of the proton number density  $\rho_p$  considers only an estimated uncertainty from dissolved gases [281] and from the molecular LAB composition itself, since the LS density uncertainties are already accounted for within the  $m_{\text{FV}}$  uncertainty.

The  $m_{\text{FV}}$  and  $\rho_p$  uncertainties affect the number of protons  $N_p$ , and thus the scale of the spectrum, in the same way and are added quadratically yielding a total proton number uncertainty of  $\sigma_{N_p} = 2\%$ . As discussed in Sec. 7.1.1 for  $\nu$ -p ES, also the proton strangeness  $\eta$  only affects the scale, where the scale varies by  $\pm 13\%$ . The total scale uncertainty in the case of  $\nu$ -p ES reactions is the quadratic sum of this variation and  $\sigma_{N_p}$  and thus  $\sigma_{\text{scale}} = 13.2\%$ . In the case of IBDs,  $\sigma_{\text{scale}}$  is the quadratic sum of  $\sigma_{N_p}$ , the uncertainty on the assumed tagging efficiency  $\epsilon_{\text{IBD}}$  and the uncertainty on the cross

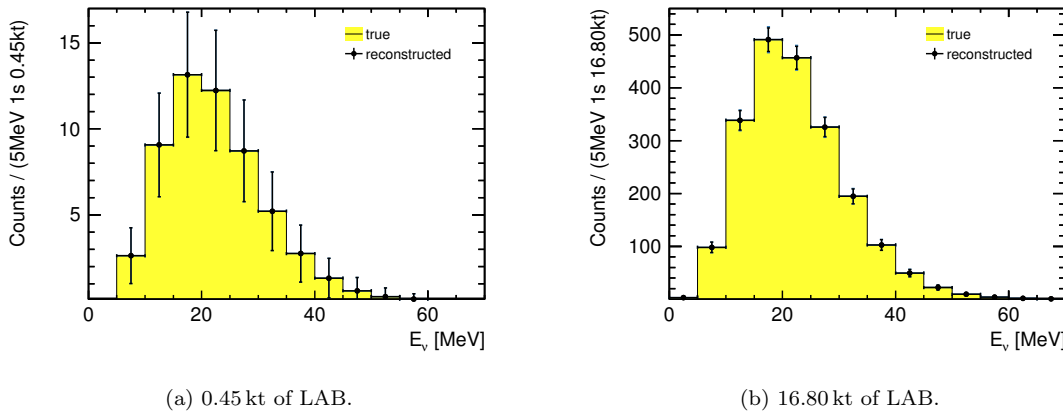


**Figure 7.17:** Reconstructed and true SN neutrino energy distribution of the IBD detection channel in LAB based scintillator. The spectra assume the neutrino  $\bar{\nu}_e$  flux in the first second of the reference SN, a distance of 10 kpc and the two different LAB fiducial masses shown in (a) and (b). The uncertainties shown in black are the statistical uncertainty. The total uncertainties, i.e. the quadratic sum of the statistical and the systematic uncertainties, are drawn in blue. However, the contribution from systematics is too small to be resolved.

section  $\sigma_{\text{IBD}}$ , yielding  $\sigma_{\text{scale}} = 2.1\%$ .

### 7.3.2 Reconstructed neutrino energy distributions

The reconstruction of the incoming  $E_\nu^{\text{true}}$  spectrum from the  $E_{\text{vis}}$  spectrum is straightforward in the case of IBD, while ionization quenching and the differential cross section turn the reconstruction in the case of  $\nu$ - $p$  ES more complex. The IBD reconstruction is discussed here first. The reconstructed neutrino energy is denoted as  $E_\nu^{\text{rec}}$ .

The  $E_\nu$  reconstruction from IBD events is a mere shift of about 0.782 MeV in energy, following Eq. 7.12. In order to account for the energy resolution, the visible spectrum in principal has to be additionally unfolded. However, the influence of the energy resolution on the visible IBD spectral shape was investigated within this thesis and found to be negligible. No significant deviation from the results of a fit to the  $E_\nu^{\text{rec}}$  spectrum, folded with the energy resolution, was observed after a fit to the  $E_\nu^{\text{true}}$  spectrum. The true and reconstructed  $E_\nu$  distributions are shown for the IBD channel in Fig. 7.17.

In the case of  $\nu$ - $p$  ES, four major aspects have to be taken into account for the  $E_\nu$  reconstruction. First, due to ionization quenching the visible energy of the proton is not identical to its kinetic energy, but is strongly and non-linearly reduced (see Fig. 7.3), which is analytically described by Birks' law Eq. 2.12. Second, a particular  $E_\nu$  can result in different  $E_{\text{vis}}$ , depending on the differential cross section Eq. 7.1. As a consequence, considering binned data, one  $E_\nu$  bin is reconstructed from the contents of several  $E_{\text{vis}}$  bins and the reconstructed bin contents are strongly correlated. This is aggravated by the fact that not

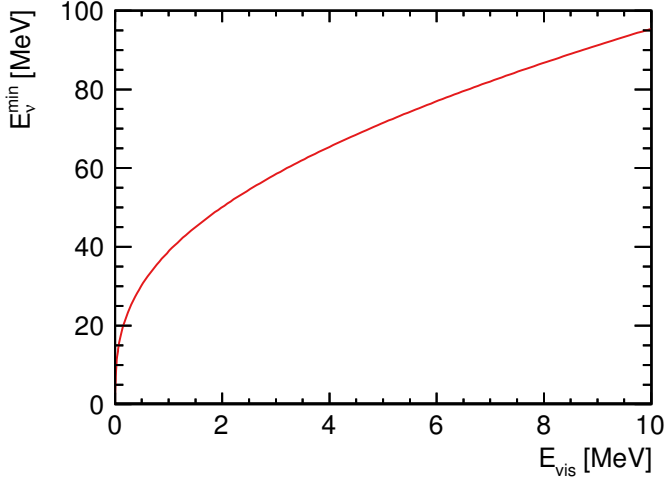


**Figure 7.18:** Minimal neutrino energy  $E_{\nu}^{\text{min}}$  necessary to yield a certain visible energy  $E_{\text{vis}}$  from  $\nu$ - $p$  elastic scattering, resulting from kinematics and taking ionization quenching with  $kB = 0.0096 \text{ cm/MeV}$  into account.

the entire  $E_{\text{vis}}$  spectrum can be measured, due to the non-zero trigger threshold, the third aspect to be considered within the  $E_{\nu}$  reconstruction. The minimal neutrino energy  $E_{\nu}^{\text{min}}$ , necessary to reach a certain  $E_{\text{vis}}$ , is determined using Birks' law and Eq. 7.7, resulting in the notably non-linear functional behavior shown in Fig. 7.18. Following this calculation, the minimal neutrino energy corresponding to the trigger threshold of  $E_{\text{vis}} = 200 \text{ keV}$  is  $E_{\nu}^{\text{min}} = 21.88 \text{ MeV}$ . This energy is thus the lower limit of the  $E_{\nu}^{\text{rec}}$  spectrum, which is for the reference SN just above the peak of the distribution. The fourth, and last, major aspect to be considered is the energy resolution, which is  $\propto 1/\sqrt{E_{\text{vis}}(\text{MeV})}$ . The variation of the resolution over energy at energies near, and especially below, the 200 keV threshold is thus very large. This leads amongst others to the migration of reconstructed events from below the threshold to higher energies due to a mis-reconstruction of  $E_{\nu}^{\text{true}}$ . The bin to bin migration increases with decreasing threshold. To sum up, the differential cross section, the detector threshold, ionization quenching and the energy resolution have to be taken into account within the  $E_{\nu}$  reconstruction from  $\nu$ - $p$  ES events. This reconstruction is achieved with an unfolding matrix  $\mathbf{A}$ , which is calculated on the basis of these four aspects.

Within this thesis, the TUnfold algorithm [284] is used in order to calculate  $\mathbf{A}$ , where  $\mathbf{A}$  is an  $n \times m$  matrix with  $n < m$ . This means, the number  $n$  of  $E_{\nu}^{\text{rec}}$  bins has to be smaller than the number  $m$  of  $E_{\text{vis}}$  bins. Besides this, the binning can be chosen freely. Upon the calculation of  $\mathbf{A}$ , the covariance matrix  $\mathbf{V}_{\text{cov}}^{\text{bins}}$  of the reconstructed bins is determined, which results from the unfolding matrix. TUnfold is an implementation of standard unfolding. Besides this standard approach, numerical methods exist to determine  $\mathbf{A}$ , which may form an advantage in special cases. A numerical approach for the unfolding of SN  $\nu$ - $p$  ES event spectra is suggested in [92], which was tested within this work. However, thorough investigations revealed that the unfolding matrix entries strongly depend on the numerical integration method that is used (see Sec. D of the appendix). Since not only the  $E_{\nu}^{\text{rec}}$  bin contents are calculated using the unfolding matrix, but also the covariance matrix

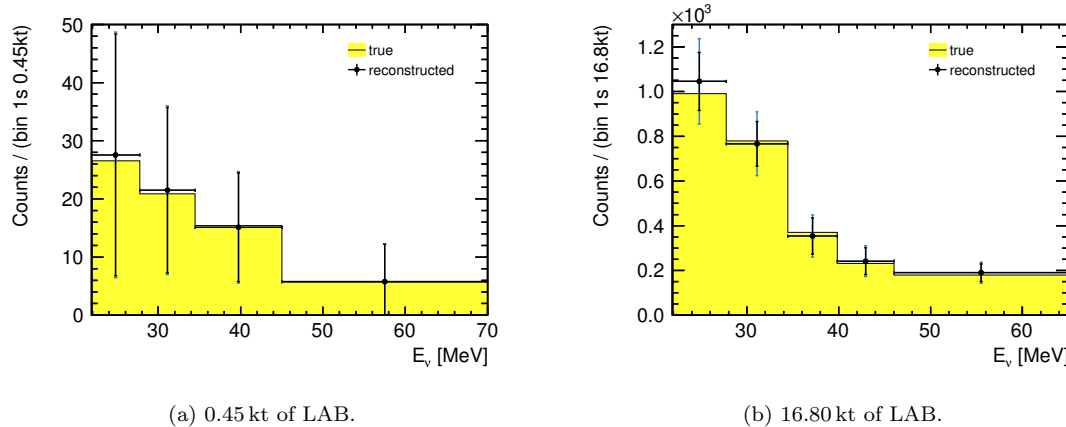


**Figure 7.19:** Reconstructed and true SN neutrino energy distribution of the  $\nu$ - $p$  ES detection channel in LAB based scintillator. The shown spectra are the sum of the  $\nu_e$ ,  $\bar{\nu}_e$  and  $\nu_x$  spectra, considering their flux in the first second of the reference SN. The distance to the SN is assumed to be 10 kpc and the two different LAB fiducial masses are considered, shown in (a) and (b), respectively. The uncertainties shown in black are the statistical uncertainty. The uncertainties shown in blue are the total uncertainties including the systematic uncertainty added in quadrature. In (a) the contribution from systematics is too small to be resolved.

$\mathbf{V}_{\text{cov}}^{\text{bins}}$  of the correlated, reconstructed energy bins, this dependence is further propagated into the uncertainties of the reconstructed bin content and ultimately into the determined detector sensitivity. For the determination of the LAB detector sensitivities to spectral SN  $\nu_x$  parameters, the TUnfold framework is thus preferred over the numerical approach in [92] and used within this chapter. Note that in either case, the necessary wide binning of the  $E_{\text{vis}}$  spectrum on the one hand and the strong correlations between the reconstructed bins on the other hand, limits the accuracy of the reconstruction. The  $E_{\nu}^{\text{rec}}$  binning in case of  $m_{\text{LAB}} = 0.45 \text{ kt}$  is chosen such that each bin has at least 5 events.

The obtained  $E_\nu^{\text{rec}}$  spectrum is shown in Fig. 7.19 together with the  $E_\nu^{\text{true}}$  spectrum. The number of events in the lowest bin is slightly overestimated, due to the bin-to-bin migrations caused by the finite energy resolution. Also shown in the figures are the statistical and total systematic uncertainties. In this case, the statistical uncertainty per bin is not the square root of the bin content, since the observable is not the  $E_\nu^{\text{rec}}$  bin content, but the  $E_{\text{vis}}$  bin content. Different from the case of the IBD, these contents are not identical, but one  $E_{\text{vis}}$  bin populates usually more than one  $E_\nu^{\text{rec}}$  bin. As a consequence, the statistical uncertainty of a  $E_\nu^{\text{rec}}$  bin can be larger than its content. The uncertainties drawn in Fig. 7.19 are the square root of the diagonal elements of  $\mathbf{V}_{\text{cov}}^{\text{bins}}$ .

## 7.4 Fit to reconstructed neutrino energy spectra from IBD and sensitivities to spectral $\bar{\nu}_e$ parameters

The sensitivity of a SNO+ and JUNO-like detector to the set of parameters  $\mathbf{a} = (\langle E_{\bar{\nu}_e} \rangle, \beta_{\bar{\nu}_e}, \varepsilon_{\bar{\nu}_e})$  is determined by fitting the analytical description of the SN neutrino fluence  $d\Phi(\mathbf{a})/dE$ , Eq. 3.26, multiplied with the total IBD cross section  $\sigma_{\text{tot}}$ , Eq. 7.10, to the reconstructed  $\bar{\nu}_e$  spectrum. In view of the small event statistics in 0.45 kt of LAB, as visible in Fig. 7.17a, an unbinned fit is performed, making use of the unique relation between  $E_{\text{vis}}$  and  $E_{\nu}^{\text{rec}}$ , in order to reduce possible biases in the fit results.

The best fit values of  $\mathbf{a}$  are obtained from the minimization of an unbinned negative log-likelihood function  $-2 \ln L(\mathbf{a})$ . Since one of the parameters defines the normalization of the distribution, namely  $\varepsilon_{\alpha}$ , an extended log-likelihood function is used:

$$-2 \ln L(\mathbf{a}) = -2 \cdot \left[ \sum_{j=1}^J \ln(g(E_{\nu,j}|\mathbf{a})) - \int_0^{E_{\nu}^{\max}} g(E'_{\nu}|\mathbf{a}) dE_{\nu} \right]. \quad (7.38)$$

In this equation,  $g(E_{\nu,j}|\mathbf{a})$  is the probability density function (PDF) of the reconstructed neutrino energies, normalized to the number of expected events  $K$  according to

$$\int_0^{E_{\nu}^{\max}} g(E'_{\nu}|\mathbf{a}) dE_{\nu} = K. \quad (7.39)$$

The normalized PDF reads

$$\begin{aligned} g(E_{\nu}|\mathbf{a}) dE_{\nu} &= \epsilon_{\text{IBD}} \cdot \frac{N_p}{4\pi d^2} \cdot \frac{d\Phi_{\bar{\nu}_e}(\mathbf{a})}{dE} \cdot \sigma_{\text{tot}} \\ &= \epsilon_{\text{IBD}} \cdot \frac{N_p}{4\pi d^2} \cdot \varepsilon_{\bar{\nu}_e} \frac{(1 + \beta_{\bar{\nu}_e})^{1+\beta_{\bar{\nu}_e}}}{\Gamma(1 + \beta_{\bar{\nu}_e})} \frac{E^{\beta_{\bar{\nu}_e}}}{\langle E_{\bar{\nu}_e} \rangle^{\beta_{\bar{\nu}_e}+2}} \exp\left[-(\beta_{\bar{\nu}_e} + 1)\frac{E}{\langle E_{\bar{\nu}_e} \rangle}\right] \cdot \sigma_{\text{tot}}, \end{aligned} \quad (7.40)$$

where  $N_p$  is the number of protons in the scintillator volume and  $\epsilon_{\text{IBD}}$  the IBD tagging efficiency. The minimization is performed with MINUIT [234]. The  $E_{\nu}^{\text{rec}}$  region below 5.8 MeV is excluded from the fit, which rejects nearly the entire IBD background spectrum discussed in Sec. 7.2.1.

Log-likelihood estimates are typically Gaussian distributed and unbiased for a large number of events  $K$  and thus statistics. For small statistics, however, as in the case of the 0.45 kt FV, a bias is likely, although reduced by the realization of an unbinned log-likelihood fit instead of a binned fit. In order to correct for biases, the log-likelihood function Eq. 7.38 is minimized with respect to the fit parameters in 5 000 toy MC event spectra, yielding an equally large set of best estimators  $\hat{\mathbf{a}}$ . The distribution of the 5 000 best estimates per parameter is used to determine the fit results as well as the statistical parameter uncertainties, as will be demonstrated in the course of this section.

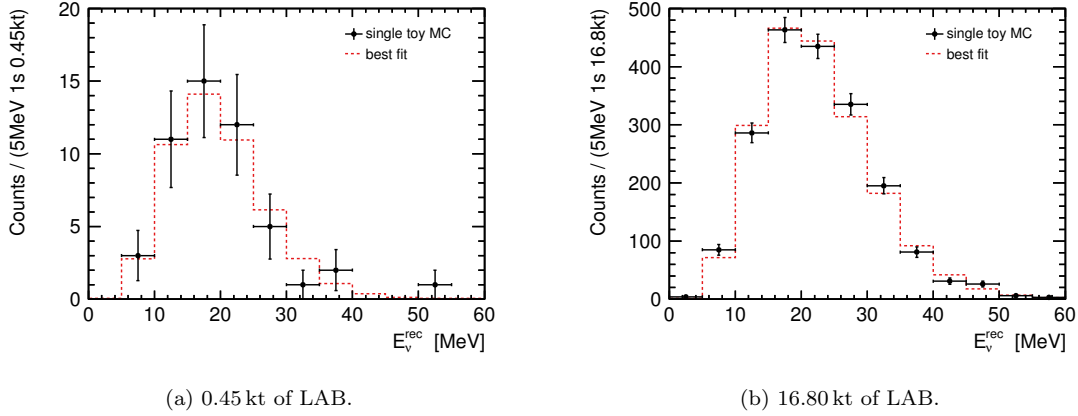


**Figure 7.20:** Exemplary single spectrum out of 5 000 toy MC  $E_\nu^{\text{rec}}$  spectra from IBD. The reference SN at 10 kpc distance is assumed and two different fiducial masses in figures (a) and (b).

In the toy MC, the  $E_\nu^{\text{rec}}$  spectrum per pseudo-experiment is simulated by randomly distributing the  $K$  events of the calculated  $E_\nu^{\text{rec}}$  spectrum, complying with Poisson statistics. One single example spectrum out of the 5 000 toy MC spectra is shown for each LAB based scintillator mass in Fig. 7.20 together with the corresponding best fit  $E_\nu$  distribution. The resulting correlation matrix of the fit parameters  $\boldsymbol{a}$  for this one example shown in Fig. 7.20a reads:

$$\begin{aligned} \mathbf{V}_{\text{corr}}^a &= \begin{pmatrix} v(\langle E \rangle, \langle E \rangle) & v(\langle E \rangle, \beta) & v(\langle E \rangle, \varepsilon) \\ v(\beta, \langle E \rangle) & v(\beta, \beta) & v(\beta, \varepsilon) \\ v(\varepsilon, \langle E \rangle) & v(\varepsilon, \beta) & v(\varepsilon, \varepsilon) \end{pmatrix} \\ &= \begin{pmatrix} 1.000 & 0.889 & -0.481 \\ 0.889 & 1.000 & -0.351 \\ -0.481 & -0.351 & 1.000 \end{pmatrix}. \end{aligned} \quad (7.41)$$

The matrix shows strong correlations between all three parameters. The strongest correlation is between  $\langle E \rangle$  and  $\beta$  and imposed by the analytical expression of  $\beta$ , Eq. 3.24, into which  $\langle E \rangle$  enters.

The normalized  $\hat{\boldsymbol{a}}$  distributions after 5 000 fits, assuming  $m_{\text{LAB}} = 0.45 \text{ kt}$ , are shown in Fig. 7.21. Most striking in these figures is the distinct asymmetry of the  $\langle E_{\bar{\nu}_e} \rangle$  and  $\beta_{\bar{\nu}_e}$  distributions in Fig. 7.21a and 7.21b, respectively. The asymmetry of the  $\beta_{\bar{\nu}_e}$  distribution is a result of two circumstances coming together: First, the log-likelihood function rises very fast with negative  $\beta$  values, due to the factor  $E^{\beta_{\bar{\nu}_e}}$  in the PDF Eq. 7.40. Thus, though  $\beta < 0$  is not forbidden, neither from the analytical nor the physical point of view, the fit does not converge at negative values. Second, the low statistics lead to a wide spread of the best estimators. Just from the width of the  $\beta_{\bar{\nu}_e}$  distribution, negative values of  $\beta_{\bar{\nu}_e}$

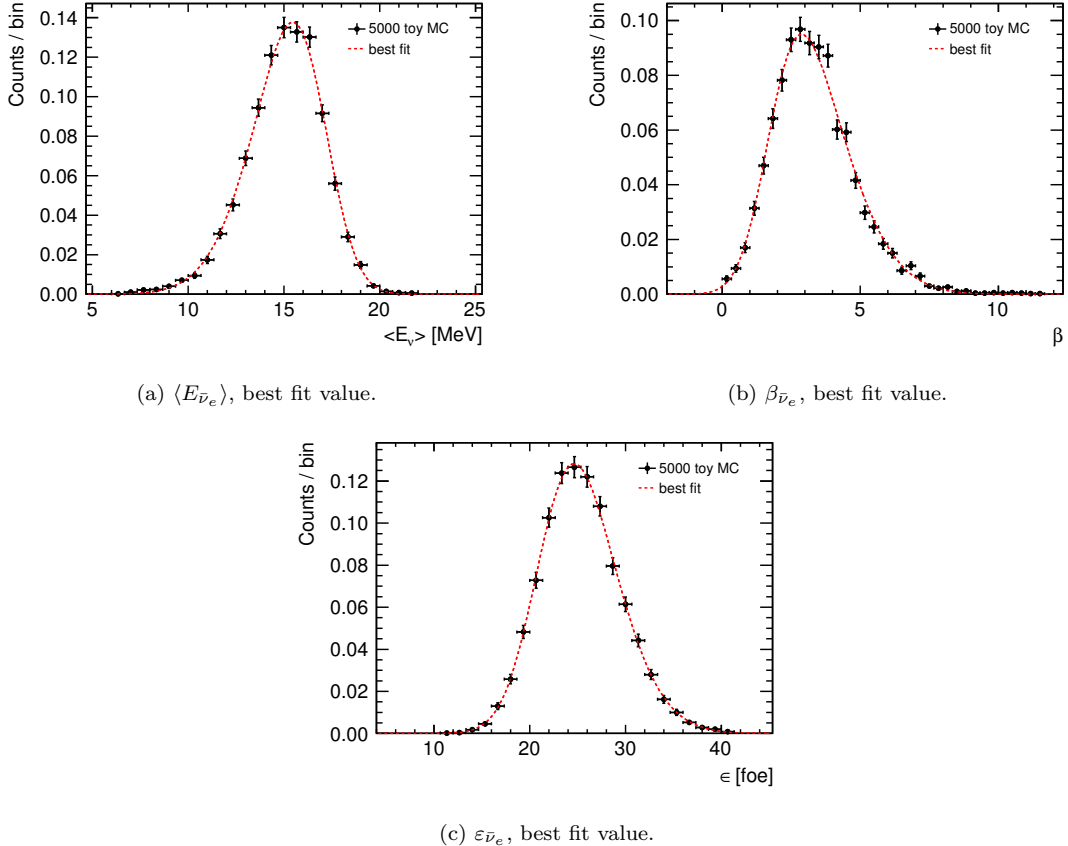


**Figure 7.21:** Best fit (a)  $\langle E_{\bar{\nu}_e} \rangle$ , (b)  $\beta_{\bar{\nu}_e}$  and (c)  $\varepsilon_{\bar{\nu}_e}$  distributions, resulting from fits to 5 000 IBD toy MC  $E_{\nu}^{\text{rec}}$  spectra. A LAB mass of 0.45 kt is considered. The distributions are normalized. Details about the fit are given in the text.

would be reached, if the fit would not strongly disfavor this region. The asymmetry of the  $\langle E_{\bar{\nu}_e} \rangle$  distribution is a consequence of the strong correlation between  $\beta_{\bar{\nu}_e}$  and  $\langle E_{\bar{\nu}_e} \rangle$ . Also the best fit value distribution of  $\varepsilon_{\bar{\nu}_e}$ , shown in Fig. 7.21c, is slightly affected by the correlations, though to a smaller extend. The correlations between  $\varepsilon_{\bar{\nu}_e}$  and the other two parameters are similarly strong (see Eq. 7.41), which widen the  $\varepsilon_{\bar{\nu}_e}$  distribution in opposite directions as can be inferred from Fig. 7.21a and 7.21b.

Due to the asymmetry of the  $\hat{\alpha}$  distributions, using 0.45 kt of LAB, the mean and the mode, i.e. the position of the maximum, of each distribution are not identical and the results thus biased, if the final best fit parameters are deduced from the mean values. Additionally, the width of each distribution and thus the statistical uncertainties on  $\hat{\alpha}$  cannot be obtained from a standard Gaussian fit. Both instances are accounted for by fitting a skew normal distribution

$$f(x) = \frac{e^{-\frac{(x-\mu)^2}{2\sigma^2}} \operatorname{erfc}\left[-\frac{\alpha(x-\mu)}{\sqrt{2}\sigma}\right]}{\sqrt{2\pi}\sigma} \quad (7.42)$$

**Table 7.5:** Fit results using the reference SN  $E_\nu^{\text{rec}}$  distribution from IBDs in 0.45 kt of LAB. A neutrino energy cut of  $E_\nu^{\text{rec}} \geq 5.8$  MeV is applied, corresponding to  $E_{\text{vis}} \gtrsim 5$  MeV. The results are obtained by minimizing Eq. 7.38 with respect to 5 000 toy MCs (see text).

Parameter	Unit	Expectation	Best fit	$1\sigma_{\text{stat}}$	$1\sigma_{\text{sys}}$
0.45 kt of LAB					
$\langle E_{\bar{\nu}_e} \rangle$	MeV	15.0	15.47	+1.54 -2.43	+0.02 -0.04
$\beta_{\bar{\nu}_e}$	—	3.0	2.88	+1.90 -1.01	+0.03 -0.06
$\varepsilon_{\bar{\nu}_e}$	foe	25.0	24.64	+4.96 -3.53	+0.45 -0.72

to each  $\hat{\mathbf{a}}$  distribution shown in Fig. 7.21. In the case of a symmetric distribution,  $\alpha$  becomes zero and the skew normal distribution recovers the Gaussian distribution. The fit parameters  $\mu$ ,  $\sigma$  and  $\alpha$  are the location, scale and shape parameter of the distribution, from which the mean

$$\omega = \mu + \sigma \frac{\alpha}{\sqrt{1+\alpha^2}} \sqrt{\frac{2}{\pi}} \quad (7.43)$$

and the variance

$$v = \sigma \left( 1 - \frac{2 \left( \frac{\alpha}{\sqrt{1+\alpha^2}} \right)^2}{\pi} \right), \quad (7.44)$$

follow. The value of the mode is the parameter value, at which the first derivative of the best fitting skew normal distribution becomes zero. The difference between mode and mean is an estimate of the size of the bias.

If the distributions were Gaussian, the statistical uncertainties would be the square root of the variance and symmetric. In the given case, however, the uncertainty towards the broader side of the distribution, which is in e.g. Fig. 7.21a to the left of the mode, is the square root of the variance plus the difference between mode and mean. The uncertainty towards the narrower side is accordingly the square root of the variance minus the difference between mode and mean.

The fit of Eq. 7.42 to the  $\hat{\mathbf{a}}$  distributions is shown in Fig. 7.21. The mode of each best fit skew normal distribution is given in Tab. 7.5, representing the final best fit value of the respective parameter. The size of the statistical uncertainties are also given in the table and calculated as described above. In order to determine the systematic uncertainties on the best fit parameters, the entire fitting procedure is repeated after varying the source of each systematic independently by plus and minus  $1\sigma$ . The resulting shift of the mode of the skew normal distribution, after adaption to the new  $\hat{\mathbf{a}}$  distributions, yields the corresponding one sigma systematic uncertainty. Since applying an energy

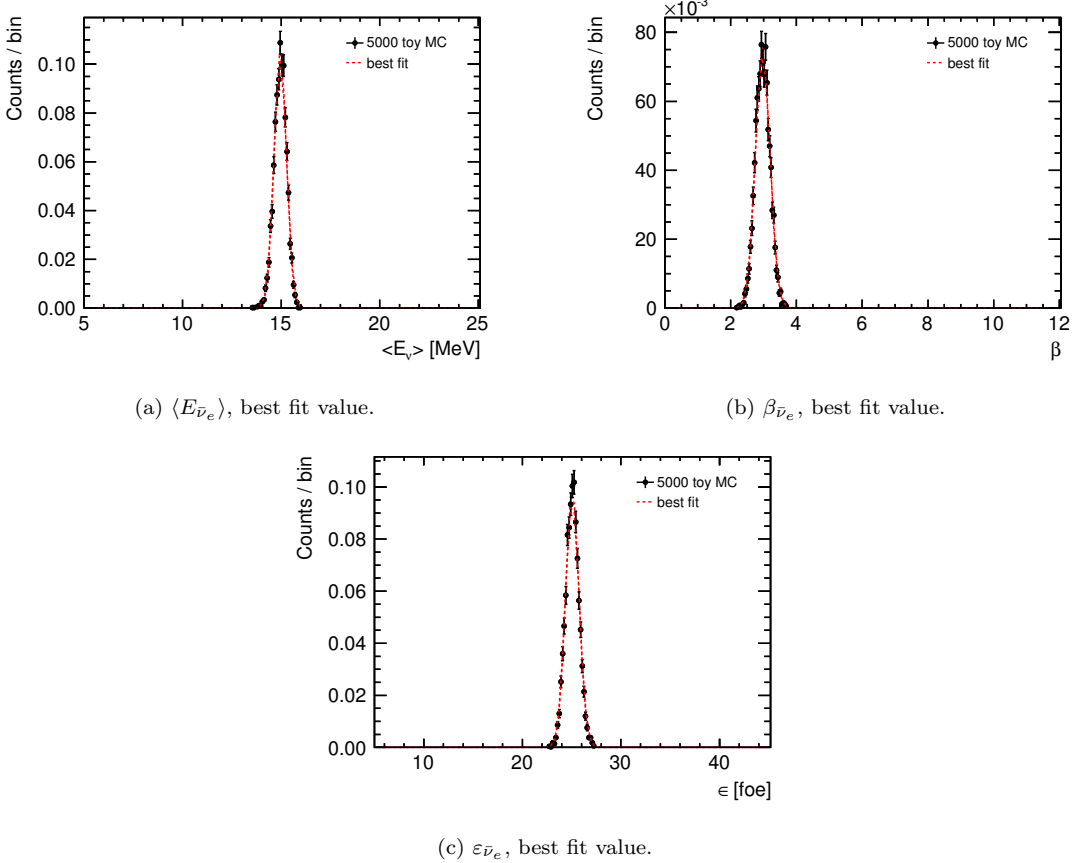


**Figure 7.22:** Best fit (a)  $\langle E_{\bar{\nu}_e} \rangle$ , (b)  $\beta_{\bar{\nu}_e}$  and (c)  $\varepsilon_{\bar{\nu}_e}$  distributions, resulting from fits to 5 000 IBD toy MC  $E_{\nu}^{\text{rec}}$  spectra. A LAB mass of 16.80 kt is considered. The distributions are normalized.

resolution of  $6\%/\sqrt{E_{\text{vis}}(\text{MeV})}$ , or not, to the IBD spectrum has no significant effect on the best fit values of the spectral neutrino parameters, also a variation of the resolution by  $\pm 2\%/\sqrt{E_{\text{vis}}(\text{MeV})}$  does not affect the results. Only  $1\sigma_{\text{scale}}$  amounting to 2.1% (see Sec. 7.3.1) contributes to the total systematic uncertainty, given in Tab. 7.5. Since the respective sources of systematic uncertainty affect only the scale, the resulting relative systematic uncertainty is the largest for  $\varepsilon_{\bar{\nu}_e}$ , which is the normalization factor of the neutrino fluence.

Increasing the statistics by using 16.80 kt of LAB, instead of 0.45 kt, results as expected in much narrower  $\hat{\alpha}$  distributions, which are shown in Fig. 7.22. Fitting Eq. 7.42 to these distributions reveals that they are nearly symmetric, since  $\alpha \propto 10^{-1} - 10^{-3}$ , and thus the distributions approximately Gaussian. The final best fit values together with their statistical and systematic uncertainties are listed in Tab. 7.6. Using 16.80 kt of LAB, the expectation value of  $\beta_{\bar{\nu}_e}$  is more than  $13\sigma_{\text{stat}}$  away from zero and thus not skewed anymore.

**Table 7.6:** Fit results using the reference SN  $E_\nu^{\text{rec}}$  distribution from IBDs in 16.80 kt of LAB. A neutrino energy cut of  $E_\nu^{\text{rec}} \geq 5.8$  MeV is applied, corresponding to  $E_{\text{vis}} \gtrsim 5$  MeV. The results are obtained by minimizing Eq. 7.38 with respect to 5 000 toy MCs (see text).

Parameter	Unit	Expectation	Best fit	$1\sigma_{\text{stat}}$	$1\sigma_{\text{sys}}$
16.80 kt of LAB					
$\langle E_{\bar{\nu}_e} \rangle$	MeV	15.0	14.97	$\pm 0.31$	$+0.01$ $-0.02$
$\beta_{\bar{\nu}_e}$	–	3.0	2.98	$\pm 0.22$	$+0.01$ $-0.02$
$\varepsilon_{\bar{\nu}_e}$	foe	25.0	25.05	$+0.69$ $-0.64$	$+0.56$ $-0.51$

In summary, the fit parameters  $\boldsymbol{a}$  are strongly correlated. The sensitivity to these parameters in a scintillation detector with  $m_{\text{LAB}} = 0.45$  kt is clearly dominated by the statistical uncertainty. The statistical uncertainties of especially  $\beta_{\bar{\nu}_e}$  and  $\langle E_{\bar{\nu}_e} \rangle$  are furthermore considerably asymmetric. The sources of considered systematic uncertainties only affect the scale of the neutrino energy distribution and thus result in the largest relative systematic uncertainty for the total neutrino energy  $\varepsilon_{\bar{\nu}_e}$ , yielding of about (2–3)%. The total relative  $1\sigma$  uncertainty of  $\langle E_{\bar{\nu}_e} \rangle$ ,  $\beta_{\bar{\nu}_e}$  and  $\varepsilon_{\bar{\nu}_e}$  is < 16%, < 66% and < 21%, respectively.

Increasing the detector mass from 0.45 kt to 16.80 kt raises the statistics by about a factor 37. Thus the statistical uncertainties are each reduced by about a factor of  $\sqrt{37} \approx 6$ , comparing the results in Tab. 7.5 and 7.6. Note that the sensitivities are still limited by the statistics, but the statistical uncertainties become approximately symmetric. The total relative uncertainty of  $\langle E_{\bar{\nu}_e} \rangle$ ,  $\beta_{\bar{\nu}_e}$  and  $\varepsilon_{\bar{\nu}_e}$  at the  $1\sigma$  level is  $\sim 2\%$ ,  $\sim 7\%$  and  $\sim 4\%$ , respectively. The IBD detection channel allows large-scale LS detectors to significantly constrain the spectral parameter space of  $\bar{\nu}_e$ 's from a galactic CCSN.

## 7.5 Fit to reconstructed neutrino energy spectra from $\nu$ - $p$ ES and sensitivities to spectral $\nu_x$ parameters

In case of the  $\nu$ - $p$  ES detection channel, the  $E_\nu^{\text{rec}}$  spectrum is binned. An unbinned fit is hence not possible. The reconstructed bins are moreover strongly correlated (see Sec. 7.3.2) and the covariance matrix has to be taken into account. Thus the covariance approach of a standard, binned  $\chi^2$  fit is followed, reading

$$\chi_{\text{cov}}^2 = \sum_{i,j=1}^I (O_i^{\text{exp}} - O_i^{\text{theo}}) [\sigma_{i,j}^2]^{-1} (O_j^{\text{exp}} - O_j^{\text{theo}}). \quad (7.45)$$

$O_{i,j}^{\text{exp}}$  and  $O_{i,j}^{\text{theo}}$  are the experimental and theoretically expected contents in bin  $i$  and  $j$ , respectively, and  $[\sigma_{i,j}^2]^{-1}$  is the corresponding entry in the inverse of the covariance matrix

$\mathbf{V}_{\text{cov}}^{-1}$ . The  $I \times I$  covariance matrix is determined within the TUnfold algorithm upon the unfolding of the  $E_{\text{vis}}$  spectrum, where  $I$  is the number of  $E_{\nu}^{\text{rec}}$  bins.  $O_i^{\text{theo}}$  is calculated as per

$$O_i^{\text{theo}}(\mathbf{a}) = \frac{N_p}{4\pi d^2} \cdot \int_{E_0}^{E_1} \sum_{\alpha} \varepsilon_{\alpha} \frac{(1 + \beta_{\alpha})^{1+\beta_{\alpha}}}{\Gamma(1 + \beta_{\alpha})} \frac{E^{\beta_{\alpha}}}{\langle E_{\alpha} \rangle^{\beta_{\alpha}+2}} \exp \left[ -(\beta_{\alpha} + 1) \frac{E}{\langle E_{\alpha} \rangle} \right] \cdot \sigma_{\text{tot}} dE. \quad (7.46)$$

The integral is executed from the lower edge  $E_0$  of bin  $i$  to the corresponding upper edge  $E_1$ .  $\sigma_{\text{tot}}$  is the  $\nu$ - $p$  ES total cross section Eq. 7.4.

The  $E_{\nu}^{\text{rec}}$  spectrum providing  $O_i^{\text{exp}}$ , shown in Fig. 7.19, is the sum of the  $\nu$ - $p$  ES spectra of  $\nu_e$ ,  $\bar{\nu}_e$  and  $\nu_x$ . This sum spectrum is highly degenerate with respect to the nine spectral parameters  $\mathbf{a}_{\nu_e}$ ,  $\mathbf{a}_{\bar{\nu}_e}$  and  $\mathbf{a}_{\nu_x}$  and a fit to the latter set of parameters is only possible if assumptions are made for  $\mathbf{a}_{\nu_e}$  and  $\mathbf{a}_{\bar{\nu}_e}$ . Within this work, it is assumed that  $\mathbf{a}_{\bar{\nu}_e}$  is known from a spectral fit to the reconstructed IBD neutrino spectrum using the same detector, as performed in Sec. 7.4. Concerning  $\mathbf{a}_{\nu_e}$  it has to be assumed that the respective parameters are obtained in a measurement by another detector, which is particularly sensitive to the  $\nu_e$  component of the flux, like HALO-2<sup>7</sup>

Matters are complicated further by the fact that only the energy region above the peak of the  $E_{\nu}$  spectrum is reconstructed due to the trigger threshold of 200 keV. The peak itself lies below the minimal  $E_{\nu}^{\text{rec}}$ , using the reference SN. Note that the reference SN is already optimistic in this context, since it assumes with  $\langle E_{\nu_x} \rangle = 18$  MeV a notably higher mean  $\nu_x$  energy than the results from e.g. the Garching simulations presented in Sec. 3.5.1 suggest. A more detailed comparison with the simulated SN neutrino distributions follows in Sec. 7.6. This loss of spectral information strongly enhances the correlations between the three spectral fit parameters  $\mathbf{a}_{\nu_x}$ . The parameter correlation matrix  $\mathbf{V}_{\text{corr}}^a$  (see Eq. 7.41) was calculated in this work in a fit with three free parameters and all off-diagonal elements were found to reach values above  $|\pm 0.95|$ , even using 16.80 kt of LAB. This means all parameters are almost fully (anti-)correlated in this case, rendering a three parameter fit pointless. Also lowering the trigger threshold from 200 keV to 100 keV, does not resolve the peak at the given statistics and the correlations are thus not reduced, while the resolution deteriorates further, enhancing bin to bin migrations. Furthermore, the background rate strongly increases due to <sup>14</sup>C.

For the given reasons, only two parameters at a time are fit to the  $E_{\nu}^{\text{rec}}$  spectrum in case of  $\nu$ - $p$  ES, where once  $\varepsilon_{\nu_x}$  is fixed and once  $\beta_{\nu_x}$ . The minimization of Eq. 7.46 with respect to the two free parameters  $\langle E_{\nu_x} \rangle$  and  $\beta_{\nu_x}$ , or  $\langle E_{\nu_x} \rangle$  and  $\varepsilon_{\nu_x}$ , is performed with MINUIT using a MINOS error analysis [234] to determine the uncertainties of the best fit values.

---

<sup>7</sup>HALO-2 is a kilotonne-scale Pb based detector in the early design phase. It is based on the same principals as the currently running HALO detector, where HALO stands for Helium And Lead Observatory.

Within this analysis, no toy MCs were sampled, since for the  $n \times m$  unfolding matrix  $\mathbf{A}$ , the inequality  $m > n$  has to be fulfilled. This means the  $E_{\text{vis}}$  spectrum has to have more bins than the  $E_{\nu}^{\text{rec}}$  spectrum. Since only non-empty bins are counted, the binning has to be chosen accordingly for each toy MC. In the event of real data, the  $E_{\text{vis}}$  binning would have to be optimized on the basis of the observed spectrum. Within this section, the model  $E_{\text{vis}}$  spectrum is unfolded and the resulting  $E_{\nu}^{\text{rec}}$  spectrum, shown in Fig. 7.19, is used for the fit.

### 7.5.1 Propagation of systematic uncertainties

The systematic uncertainties, listed in Tab. 7.4, are propagated in two different ways, depending on whether they affect the shape of the  $E_{\text{vis}}$  spectrum or its scale. The sources of systematics affecting the scale are the proton strangeness  $\eta$  and the number of target protons  $N_p$ . The sources, that affect the shape are the ionization quenching parameter  $kB$  and the energy resolution of the detector.

If only the scale is affected, the  $1\sigma$  variation is added to the corresponding variable within the calculation of the theoretical expectation Eq. 7.46, once using  $+1\sigma$ , once using  $-1\sigma$ . The fit is repeated for each variation and the shift of the best fit values with respect to the fit considering statistics only is, as usual, equivalent to the corresponding plus or minus  $1\sigma_{\text{sys}}$  value. The systematic uncertainty of each  $E_{\nu}^{\text{rec}}$  bin content is analogously determined from the shift of the bin content compared to the value calculated, when only the statistic uncertainty is considered. The square of these values correspond to the diagonal elements of a covariance matrix with otherwise zero entries.

In order to propagate a systematic uncertainty, which affects the spectral shape, the unfolding matrix  $\mathbf{A}$ , and with it the covariance matrix  $\mathbf{V}_{\text{cov}}^{\text{bins}}$ , is recalculated, having varied the respective variable by  $\pm 1\sigma$ . Thus, in total four additional matrices  $\mathbf{V}_{\text{cov}}^{\text{bins}}$  are determined, two for  $kB$  and two for the resolution. The fit is repeatedly performed using each of the matrices and extracting the  $1\sigma_{\text{sys}}$  value from the shift of the best fit value.

A third class of source of systematic uncertainty are the parameters  $\mathbf{a}_{\nu_e}$  and  $\mathbf{a}_{\bar{\nu}_e}$ . Though  $\beta$  and  $\langle E \rangle$  affect the shape of the observed spectrum, their uncertainties, as well as the one of  $\varepsilon$ , are propagated by varying the corresponding parameters in Eq. 7.46 and repeating the fit. These parameters are parameters of the theoretical model and thus only enter the theoretical expectation calculation, not the reconstruction. The values of the uncertainties are taken from Tab. 7.5 and 7.6 for the parameters  $\bar{\nu}_e$  and the appropriate LAB mass. The uncertainties of  $\mathbf{a}_{\nu_e}$  are assumed to be close to the ones of SNO+ for  $\bar{\nu}_e$  and  $\sigma_{\langle E \rangle} = \pm 2.5 \text{ MeV}$ ,  $\sigma_\beta = \pm 2$  and  $\sigma_\varepsilon = \pm 5 \text{ foe}$ .

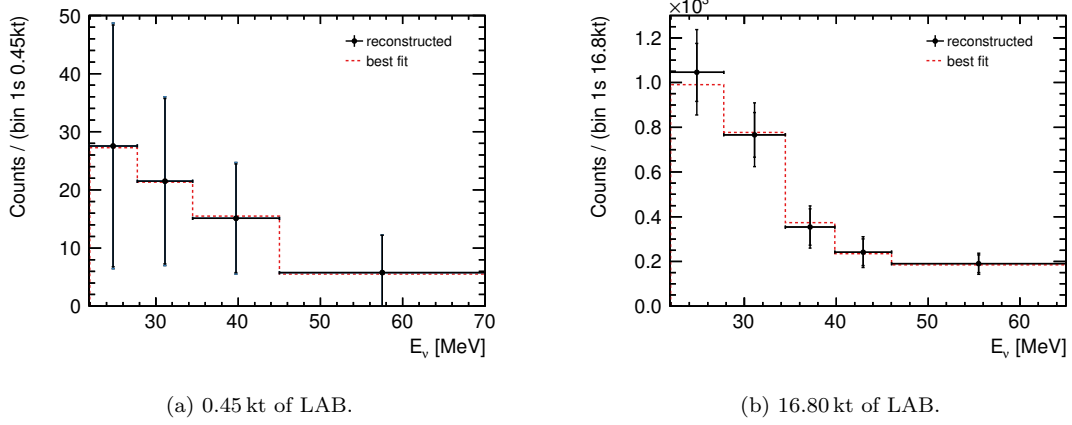


**Figure 7.23:** Reconstructed neutrino energy  $E_\nu$  spectrum and best fit spectrum from a two parameter fit with  $\varepsilon_{\nu_x}$  being fixed at its expectation value of 100 foe and with  $\langle E_{\nu_x} \rangle$  and  $\beta_{\nu_x}$  as free parameters. The spectrum results from  $\nu$ - $p$  ES of all flavors in two different LAB masses (a) and (b). The neutrino fluence is assumed to be the reference SN fluence. The trigger threshold is at 200 keV visible energy.

### 7.5.2 Fit results

Within this subsection, two scenarios are pursued: once  $\varepsilon_{\nu_x}$  is fixed and once  $\beta_{\nu_x}$ . The first scenario assumes that the mass of the SN progenitor, and thus its total binding energy, is known and that  $\varepsilon_{\bar{\nu}_e}$  and  $\varepsilon_{\nu_e}$  are determined from other detection channels or by other experiments. In this case  $\varepsilon_{\nu_x}$  can be calculated and fixed in the fit, given the hypothesis that  $\sim 99\%$  of the binding energy are emitted in the form of neutrinos (see Sec. 3.3). The second scenario, in which  $\beta_{\nu_x}$  is fixed, assumes that  $\beta$  is the same for the different flavors within the measurement uncertainties and  $\beta_{\nu_x}$  is thus known from a measurement of e.g.  $\beta_{\bar{\nu}_e}$ . This assumption is supported by simulations, which predict that  $\beta$  changes after the neutronization burst by less than a factor of two with the neutrino flavor, as deducible from Figures 3.19 to 3.21. Within both scenarios, the influence of  $\sigma_{kB}$  on the detector sensitivity is investigated.

The best fit values of the free parameters are determined from a fit of Eq. 7.46 to each bin of the  $E_\nu^{\text{rec}}$  spectrum shown in Fig. 7.19a, assuming  $m_{\text{LAB}} = 0.45 \text{ kt}$ , and to the one shown in Fig. 7.19b, assuming  $16.80 \text{ kt}$  of LAB. The statistical uncertainties of the fit parameters are determined from a fit with  $\mathbf{V}_{\text{cov}}^{\text{bins}}$ , calculated without having varied any source of systematic uncertainty. Each systematic uncertainty is subsequently propagated as described in Sec. 7.5.1. The best fit spectrum, resulting from a fit with  $\varepsilon_{\nu_x}$  being fixed at the reference value of 100 foe, is presented in Fig. 7.23. The reconstructed and the best fit spectrum agree very well within the uncertainties. The best fit spectrum is not additionally shown for the second fit scenario with  $\beta_{\nu_x} = 3$  being fixed, since the resulting spectra are qualitatively the same. The quantitative results of the fits for both scenarios and both considered LAB masses are summarized in Tab. 7.7 and discussed in the following.

**Table 7.7:** Results from a two-parametric fit to the neutrino spectrum from  $\nu$ - $p$  ES (see text). The third parameter is fixed. Given are for each fitted parameter the model expectation, the best fit value, the statistical uncertainty  $\sigma_{\text{stat}}$ , the systematic uncertainty  $\sigma_{\text{sys}}^{kB}$ , resulting from the uncertainty on the quenching parameter  $kB$ , and the total systematic uncertainty  $\sigma_{\text{sys}}^{\text{tot}}$ , which is the quadratic sum of all propagated systematic uncertainties. LAB masses of 0.45 kt and 16.80 kt are considered.

Parameter	Unit	Expectation	Best fit	$1\sigma_{\text{stat}}$	$1\sigma_{\text{sys}}^{kB}$	$1\sigma_{\text{sys}}^{\text{tot}}$
0.45 kt of LAB						
$\langle E_{\nu_x} \rangle$	MeV	18.0	18.10	$+3.33_{-4.82}$	$< 10^{-3}$	$+2.57_{-2.55}$
$\beta_{\nu_x}$	–	3.0	3.12	$+4.22_{-3.12}$	$< 10^{-4}$	$+1.39_{-1.04}$
$\varepsilon_{\nu_x}$	foe	100.0	<i>fixed</i>	–	–	–
16.80 kt of LAB						
$\langle E_{\nu_x} \rangle$	MeV	18.0	17.81	$+3.48_{-3.00}$	$< 10^{-3}$	$+0.22_{-0.75}$
$\beta_{\nu_x}$	–	3.0	<i>fixed</i>	–	–	–
$\varepsilon_{\nu_x}$	foe	100.0	102.53	$+82.26_{-42.20}$	$< 10^{-3}$	$+16.24_{-13.03}$
16.80 kt of LAB						
$\langle E_{\nu_x} \rangle$	MeV	18.0	17.66	$+0.66_{-0.72}$	$\pm 0.01$	$+2.42_{-2.48}$
$\beta_{\nu_x}$	–	3.0	2.77	$+0.48_{-0.45}$	$< 10^{-3}$	$+1.21_{-0.95}$
$\varepsilon_{\nu_x}$	foe	100.0	<i>fixed</i>	–	–	–
$\langle E_{\nu_x} \rangle$	MeV	18.0	18.15	$+0.52_{-0.50}$	$\pm 0.01$	$+0.19_{-0.50}$
$\beta_{\nu_x}$	–	3.0	<i>fixed</i>	–	–	–
$\varepsilon_{\nu_x}$	foe	100.0	96.05	$+8.79_{-7.96}$	$\pm 0.01$	$+15.10_{-11.98}$

### Influence of the quenching parameter uncertainty on the spectral sensitivities

The best fit results in Tab. 7.7 show a good agreement with the expectation values, despite the reconstruction bias in the lowest  $E_{\nu}^{\text{rec}}$  (see Fig. 7.19b). The value of  $\sigma_{\text{sys}}^{kB}$  is listed individually in this table and shortly discussed here, since the uncertainty being propagated is the uncertainty achieved in the ionization quenching measurements with LAB based scintillator within this work, as presented in Sec. 6. Table 7.7 shows that  $\sigma_{\text{sys}}^{kB}$  is very small compared to  $\sigma_{\text{stat}}$  and negligible in the case of the lower LAB mass of 0.45 kt, where the statistical uncertainty dominates.

Besides the  $1\sigma$  uncertainties given in Tab. 7.7, the allowed region at 95% C.L. of the two parameter spaces is determined. In order to obtain the total covariance matrix, all individual covariance matrices are added, which is only reasonable, if the additional

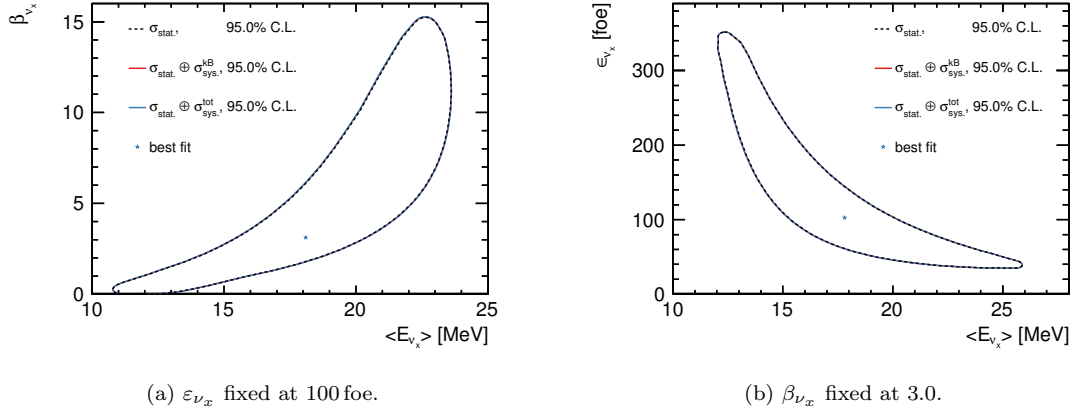


**Figure 7.24:** Constraints at 95% C.L. on the parameter space after a two-parametric fit to the neutrino spectrum from  $\nu$ - $p$  ES (see text). A LAB mass of 0.45 kt is assumed. The third parameter is fixed at the value given in the subcaptions (a) and (b). Shown are the contours considering only the statistical uncertainty  $\sigma_{\text{stat}}$  (black dashed line), considering the quadratic sum of  $\sigma_{\text{stat}}$  and the systematic uncertainty  $\sigma_{\text{sys}}^{kB}$  from the uncertainty on the quenching parameter  $kB$  (red solid line) and considering the quadratic sum of  $\sigma_{\text{stat}}$  and the total systematic uncertainty  $\sigma_{\text{sys}}^{\text{tot}}$ . All three contours coincide, since the measurement is completely dominated by statistics.

off-diagonal entries due to the remaining systematics are zero or negligibly small. This is fulfilled here, since also in the case of the resolution uncertainty, for which  $\mathbf{V}_{\text{cov}}^{\text{bins}}$  was calculated with TUnfold, the systematic contributions to the off-diagonal entries are very small. They are at or below the permille level compared to the entries due to statistics. However, the impact of the resolution uncertainty becomes more important, when the trigger threshold is lowered. The lower the energy is, the worse the resolution. Thus, bin to bin migrations increase, which enhances on the other hand the correlations between the bins.

Having determined the covariance matrices, the two-dimensional contours at 95.0% C.L. are calculated within the minimization of Eq. 7.46. The results are shown in Fig. 7.24 for  $m_{\text{LAB}} = 0.45 \text{ kt}$  and in Fig. 7.25 for  $m_{\text{LAB}} = 16.80 \text{ kt}$  and for both fit scenarios in each case. The contour is determined three times: First, only the statistical uncertainty is included. Second, the statistical uncertainty together with the uncertainty from  $kB$  is considered. Third, the statistical uncertainty together with the total systematic uncertainty is accounted for. These results confirm the conclusions drawn in the context of Tab. 7.7. The uncertainty on  $kB$  obtained within this work does not influence the sensitivity of a LAB based scintillator detector with 0.45 kt fiducial mass like SNO+ to the spectral parameters  $\langle E_{\nu_x} \rangle$ ,  $\beta_{\nu_x}$  and  $\epsilon_{\nu_x}$ , as obvious from Fig. 7.24. Also the other systematic uncertainties considered show no impact in these figures. The measurement is in this case clearly dominated by statistics.

In the case of a JUNO-like detector with a 16.80 kt fiducial mass, shown in Fig. 7.25,

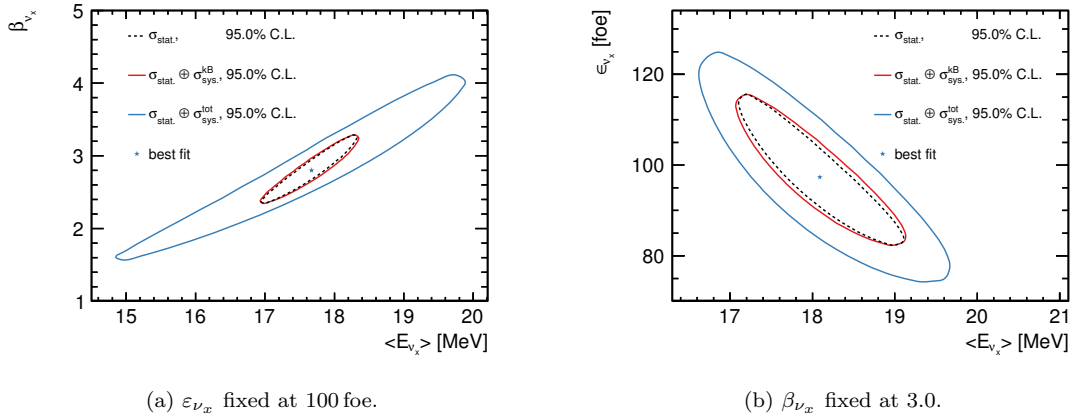


**Figure 7.25:** Constraints at 95% C.L. on the parameter space after a two-parametric fit to the neutrino spectrum from  $\nu$ - $p$  ES (see text). A LAB mass of 16.80 kt is assumed. The third parameter is fixed at the value given in the subcaptions (a) and (b). Shown are the contours considering only the statistical uncertainty  $\sigma_{\text{stat}}$  (black dashed line), considering the quadratic sum of  $\sigma_{\text{stat}}$  and the systematic uncertainty  $\sigma_{\text{sys}}^{kB}$  from the uncertainty on the quenching parameter  $kB$  (red solid line) and considering the quadratic sum of  $\sigma_{\text{stat}}$  and the total systematic uncertainty  $\sigma_{\text{sys}}^{\text{tot}}$ . The measurement is dominated by systematics.

the contour including  $\sigma_{\text{sys}}^{kB}$  is slightly widened with respect to the contour using only  $\sigma_{\text{stat}}$ . The projection on the  $\langle E \rangle$  axis, the  $\beta$  axis or the  $\varepsilon$  axis, however, is only slightly affected. This observation is confirmed by the results given in Tab. 7.7 for 16.80 kt of LAB, where  $1\sigma_{\text{sys}}^{kB}$  is very small compared to  $1\sigma_{\text{stat}}$  for all three fit parameters. However, the contour in Fig. 7.25 including all systematic uncertainties is significantly wider than the contour from statistics only. With the increased detector mass, the measurement becomes dominated by systematics, where the largest contribution comes from the proton strangeness  $\eta$ , which varies the total event yield by about  $\pm 13\%$  (see Sec. 7.1.1). The next largest systematic uncertainty comes from the uncertainty on the three parameters  $\nu_e$ , whose uncertainties were assumed to be close to the ones of  $\bar{\nu}_e$  as measured by SNO+.

### Spectral sensitivity at 68.3%, 95% and 99.73% confidence level

On the basis of the total covariance matrix including all considered systematic uncertainties and analogue to the above determination of the respective contour at 95.0% C.L., the contours at 68.3% and 99.73% C.L. are calculated. All three obtained allowed regions are shown for  $m_{\text{LAB}} = 0.45$  kt in Fig. 7.26 and for both fit scenarios with once fixed  $\varepsilon_{\nu_x} = 100$  foe (Fig. 7.26a) and once fixed  $\beta_{\nu_x} = 3.0$  (Fig. 7.26b). The strong correlations between the fit parameters are conspicuous. Furthermore, as was also observed in the case of the IBD detection channel in Sec. 7.4, the shape parameter  $\beta$  is the parameter which is affected the most by low statistics. The contours shown in Fig. 7.26 are obtained for the reference SN at 10 kpc and a trigger threshold of 200 keV visible energy, resulting in about 35  $\nu$ - $p$  ES events above threshold in the first second of the SN. Of these, about 29

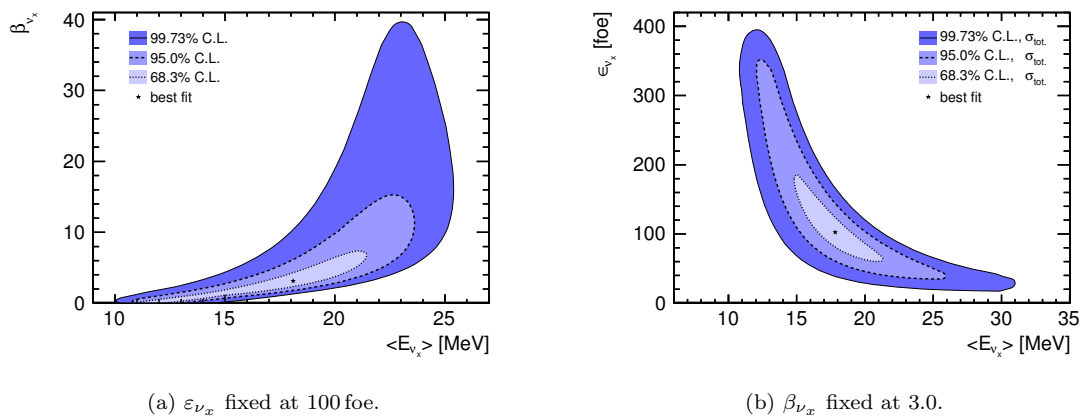


**Figure 7.26:** Constraints at 68.3%, 95.0% and 99.73% C.L. on the parameter space after a two-parametric fit to the neutrino spectrum from  $\nu$ - $p$  ES (see text). A LAB mass of 0.45 kt is assumed. The third parameter is fixed at the value given in the subcaptions (a) and (b). The contours include the total uncertainty  $\sigma_{\text{tot}}$ , which is the quadratic sum of the statistical uncertainty  $\sigma_{\text{stat}}$  and the total systematic uncertainty  $\sigma_{\text{sys}}^{\text{tot}}$ .

events are from  $\bar{\nu}_x$ . Given these poor statistics for a spectral fit, the strong correlations between the parameters, the strong correlations between the  $E_\nu^{\text{rec}}$  bins and the fact that not the entire  $E_{\text{vis}}$  spectrum is available for the  $E_\nu$  reconstruction, the constraint on all three parameters at the 68.3% and 95.0% C.L. is noteworthy. All three contours are closed after the fit with fixed  $\beta_{\nu_x}$ , shown in Fig. 7.26b and even a fit with fixed  $\varepsilon_{\nu_x}$  allows a measurement of  $\langle E_{\nu_x} \rangle$  at  $3\sigma$ , as visible in Fig. 7.26a. No further local minimum is encountered in any of the two parameter spaces. The total relative uncertainties of the parameters are high, though. They are for  $\langle E_{\nu_x} \rangle$ ,  $\beta_{\nu_x}$  and  $\varepsilon_{\nu_x}$  at the  $1\sigma$  level  $< 30\%$ ,  $< 143\%$  and  $< 82\%$ , respectively, where the value for  $\langle E_{\nu_x} \rangle$  is the result from the first fit scenario. The total relative uncertainty from the second fit scenario, in which  $\beta_{\nu_x}$  is fixed, reaches  $\sim 19\%$  and is thus the preferred scenario. The improvement in the latter case is explained by the slightly stronger correlation between  $\langle E_{\nu_x} \rangle$  and  $\beta_{\nu_x}$ , compared to  $\langle E_{\nu_x} \rangle$  and  $\varepsilon_{\nu_x}$ .

Increasing the statistics, using 16.80 kt of LAB instead of 0.45 kt, further constrains the allowed regions for both scenarios, as shown in Fig. 7.27. The total relative uncertainties for  $\langle E_{\nu_x} \rangle$ ,  $\beta_{\nu_x}$  and  $\varepsilon_{\nu_x}$  at the  $1\sigma$  level become  $< 15\%$  ( $< 4\%$ ),  $< 47\%$  and  $< 18\%$ , respectively, where the value for  $\langle E_{\nu_x} \rangle$  is the result from the first (second) fit scenario. The constraints of the parameter spaces are in this case dominated by systematic uncertainties, where the main contribution comes from the uncertainty of the proton strangeness  $\eta$ . A measurement of  $\eta$  with a higher precision would thus strongly improve the fit parameter constraints. The only further relevant systematic uncertainty comes from the uncertainties of the parameters  $\nu_e$ , which are assumed to be close to the ones of  $\bar{\nu}_e$ , obtained with  $m_{\text{LAB}} = 0.45$  kt. Thus also a measurement of the parameters  $\nu_e$  with small uncertainties is of high interest for the determination of  $\nu_x$ , which motivates

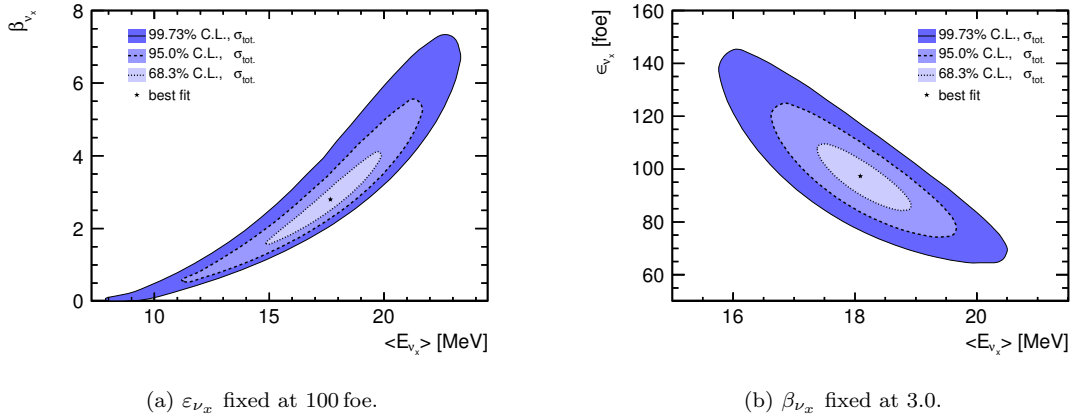


**Figure 7.27:** Constraints at 68.3%, 95.0% and 99.73% C.L. on the parameter space after a two-parametric fit to the neutrino spectrum from  $\nu$ - $p$  ES (see text). A LAB mass of 16.80 kt is assumed. The third parameter is fixed at the value given in the subcaptions (a) and (b). The contours include the total uncertainty  $\sigma_{\text{tot}}$ , which is the quadratic sum of the statistical uncertainty  $\sigma_{\text{stat}}$  and the total systematic uncertainty  $\sigma_{\text{sys}}^{\text{tot}}$ .

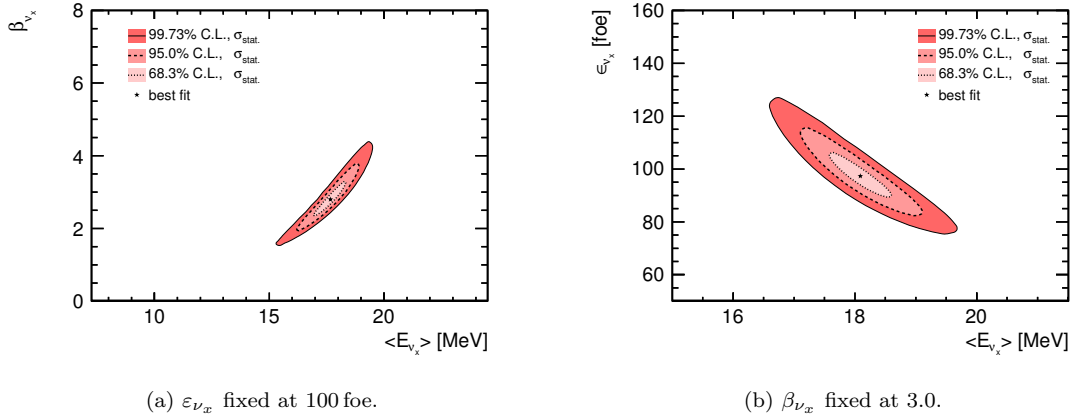


**Figure 7.28:** Constraints at 68.3%, 95.0% and 99.73% C.L. on the parameter space after a two-parametric fit to the neutrino spectrum from  $\nu$ - $p$  ES (see text). A LAB mass of 16.80 kt is assumed. The third parameter is fixed at the value given in the subcaptions (a) and (b). The contours include only the statistical uncertainty  $\sigma_{\text{stat}}$ .

sensitivity studies on the  $\nu_e$  spectral shape. The improvement possible, if these two sources of systematics are strongly reduced, is demonstrated in Fig. 7.28, for which it is assumed that the measurement is dominated by statistics. In this case, the relative  $3\sigma$  uncertainty of  $\beta_{\nu_x}$ , obtained from the projection of the 99.73% contour on the  $\beta$  axis, reaches 50% and the relative  $1\sigma$  uncertainty reaches 16%. The relative  $3\sigma$  and  $1\sigma$  uncertainty of  $\varepsilon_{\nu_x}$  is below 30% and 10%, respectively. The parameter which is constrained the strongest is  $\langle E_{\nu_x} \rangle$ , whose relative  $3\sigma$  uncertainty is pushed below 15%, fixing  $\varepsilon_{\nu_x}$ , and below 10%, fixing  $\beta_{\nu_x}$ . The corresponding values at  $1\sigma$  are  $< 4\%$  and  $< 3\%$ . The relative uncertainties on all three parameters are remarkably small, underlining the inter-

est in a precisely known  $\nu-p$  ES cross section and well-determined spectral parameters  $\mathbf{a}_{\nu_e}$ .

## 7.6 Influence of the trigger threshold, MSW effect, progenitor and equation of state on the $\nu-p$ ES event yield

The previous sections have demonstrated that the sensitivities of a detector with a 0.45 kt LAB fiducial mass, like SNO+, to spectral SN  $\bar{\nu}_e$  parameters and especially to  $\nu_x$  parameters is limited by statistics. Only the latter parameters are discussed here, since in this case the  $\nu-p$  ES detection channel is used, which is strongly affected by the trigger threshold and thus its event yield more prone to varying assumptions.

For all results shown above, the reference SN is used, which is summarized in Tab. 7.2. This model is very useful for sensitivity studies, as presented within this chapter, since it is commonly used [92, 93, 94, 285]. However, it is an optimistic model in terms of the event yields with respect to state-of-the-art simulations, as will be shown here. Furthermore, the MSW effect influences the spectral shapes and thus amongst others the event yield above threshold, which is also shortly discussed in this section. Further flavor changing mechanisms are not relevant for the time span considered for the presented studies. Since the MSW effect affects neutrinos and anti-neutrinos differently (see Fig. 4.3), it breaks the degeneracy of the  $\nu_{\mu,\tau}$  and  $\bar{\nu}_{\mu,\tau}$  spectra. For this reason, the  $\bar{\nu}_x$ 's are distinguished from the  $\nu_x$ 's throughout this section even if the MSW is not considered, for consistency.

### Trigger threshold

The  $\nu-p$  ES event yield above threshold is evidently influenced by the trigger threshold itself. Experiments like SNO+ aim at a threshold below 200 keV visible energy, at least on the short time basis for a SN. The increase of the  $\nu-p$  ES event yields, lowering the trigger threshold, is thus summarized in Tab. 7.8. Note that below about 100 keV, the trigger efficiency is expected to drop, following the turn on curve of the detector. Thus only thresholds of 100 keV, 150 keV and 200 keV compared to no threshold are considered. At these three thresholds, the total yield amounts to about 45%, 35% and 28% of the total yield above zero threshold and the  $(\bar{\nu})_x$  yield amounts to about 50%, 40% and 33% of the  $(\bar{\nu})_x$  yield above zero threshold, respectively. Thus also at the lowest considered trigger threshold only half of the  $\nu-p$  ES events are observed. Furthermore, the  $(\bar{\nu})_x-p$  ES event yield is increased by maximally a factor of  $\sim 1.5$ , lowering the threshold from 200 keV to 100 keV, while the disadvantage of lowering the threshold remains: the correlations are higher between the lowest  $E_\nu^{\text{rec}}$  bins. Furthermore, also at 100 keV the peak of the  $E_\nu^{\text{true}}$  distribution cannot be resolved and thus the fit parameter correlations not significantly reduced.

**Table 7.8:**  $\nu$ - $p$  ES event yield above a trigger threshold at the indicated visible energy value. The yields are determined for the analytical reference SN.

Flavor	Event yield above			
	0 keV	100 keV	150 keV	200 keV
$\nu_x$	44.6905	22.5375	17.8791	14.5799
$\bar{\nu}_x$	44.6905	22.5375	17.8791	14.5799
all	123.6046	55.6007	43.0691	34.5109

### Deduction of supernova neutrino spectra from Garching simulations

The simulations provide for each SN model used a set of flux tables, which contain the time-binned mean energy  $\langle E \rangle$ , luminosity  $\mathcal{L}$  and the second and third energy moment  $\langle E^2 \rangle$  and  $\langle E^3 \rangle$  (see Sec. 3.5.1). The time-integrated energy spectra are calculated by summing up  $N$  weighted spectra  $\sum_{i=0}^N w_i S_i$ , where each spectrum  $S_i$  is described by Eq. 3.25, and the parameters used to calculate the respective spectrum are taken from a parabolic interpolation<sup>8</sup> of  $\mathcal{L}(t_i)$ ,  $\langle E \rangle(t_i)$  and  $\beta(t_i)$ .  $w_i$  is given by the time step  $w_i = \Delta t_i = t_i - t_{i-1}$ . After summation, the spectra are normalized via  $S = \sum_{i=0}^N w_i S_i / \sum_{i=0}^N w_i$ . The summation is performed using an energy binning of 0.1 MeV and  $S_i$  is numerically integrated inside the bin edges. The time steps are adaptive, since they are varying in the tables and are typically between 0.2 ms and 2 ms. The time binning also differs between the various SN models. While the energy-binning is motivated by computational simplicity only, the time-binning is intrinsically limited by the provided tables and the interpolation method. The spectra obtained by the described method are shown in Fig. 7.29 for an example model which uses a  $15.0 M_\odot$  progenitor and the **ls220** EOS. The  $15.0 M_\odot$  progenitor is chosen, as its time-dependent spectral parameters are neither particularly high nor low with respect to all other available models (see Fig. 3.12 to 3.21). The spectra are integrated from 50 ms to 500 ms, in order to exclude the deleptonization burst. The focus of this chapter lies on the spectral parameters from the SN neutrino flux parameterization Eq. 3.26, which is guided by an approximately thermal distribution. During the deleptonization burst, the  $\nu_e$ 's do not thermalize (see Sec. 3.3), rendering this parameterization unfavorable for this phase. Since flavor changes due to the MSW effect propagate this behavior to the time distributions of the other flavors, the same time cut is applied to all flavors. This time cut reduces the total  $\bar{\nu}_x$  yield by  $\lesssim 1.5\%$  and is applied to every simulated spectrum throughout this section.

<sup>8</sup>The spline-interpolation for  $\beta_\alpha(t_i)$  is performed by first calculating  $\beta_\alpha$  for all time steps given in the respective table and interpolating the resulting  $\beta_\alpha$  values and not by interpolating  $\langle E \rangle(t_i)$  and  $\langle E^2 \rangle(t_i)$  and calculating  $\beta_\alpha$  using these interpolated values.

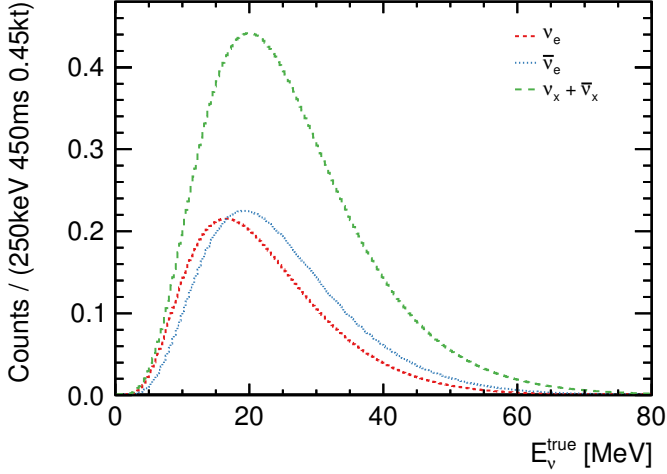


**Figure 7.29:** True SN neutrino energy,  $E_\nu^{\text{true}}$ , distributions of the  $\nu$ - $p$  ES detection channel in 0.45 kt of LAB based scintillator, derived from the Garching flux tables [46]. The progenitor has a mass of  $15 M_\odot$  and the **ls220** EOS is used in the simulation. The neutrino fluxes are integrated from 50 ms to 500 ms postbounce time. A SN distance of 10 kpc is assumed. The  $\nu_x$  and  $\bar{\nu}_x$  spectra are identical and thus summed up.

For a direct comparison of the simulated neutrino fluence with the analytical reference SN of this chapter, the values of the spectral parameters  $\boldsymbol{a} = (\langle E_\alpha \rangle, \beta_\alpha, \varepsilon_\alpha)$  are additionally calculated here for this example simulation model. The total energies  $\varepsilon_\alpha$ , emitted in a particular time span, are calculated from the flux tables by summing up  $I$  luminosity entries  $\sum_{i=0}^I \Delta t_i \mathcal{L}_{\alpha,i}$ , weighted by the corresponding time step  $\Delta t_i$ . The time-averaged mean energies and second energy momenta are obtained from  $(\sum_{i=0}^I N_{\alpha,i} \langle E_{\alpha,i}^{(2)} \rangle) / N_\alpha$ , where  $N_{\alpha,i}$  is the number of emitted neutrinos during  $\Delta t_i$ , calculated using Eq. 3.16.  $N_\alpha$  is the total number of emitted neutrinos. The time-averaged  $\beta_\alpha$  is finally derived from the time-averaged  $\langle E_\alpha \rangle$  and  $\langle E_\alpha^2 \rangle$  (see Eq. 3.24). The results for the example model are summarized in Tab. 7.9. Also in this case, only times from 50 ms to 500 ms are included in the calculations.

**Table 7.9:** Time-averaged mean energy  $\langle E \rangle$  and shape parameter  $\beta$  as well as time-integrated luminosity  $\varepsilon$  derived from the Garching supernova neutrino flux tables [46] (see also Sec. 3.5.1). The values are calculated exemplarily for the progenitor with  $15.0 M_\odot$  and the **ls220** equations of state. The value of  $\varepsilon_{\nu_x}$  is the value for one of the two contributing neutrino types. The same is true for  $\varepsilon_{\bar{\nu}_x}$ .

Flavor	$\langle E_\alpha \rangle$ [MeV]	$\beta_\alpha$	$\varepsilon_\alpha$ [foe]	$\varepsilon_\alpha / \varepsilon_{\nu_x}$
$\nu_e$	13.4555	2.82813	22.1710	1.97
$\bar{\nu}_e$	15.9436	3.05365	21.7909	1.93
$\nu_x$	15.6242	2.15489	11.2810	1.00
$\bar{\nu}_x$	15.6242	2.15489	11.2810	1.00

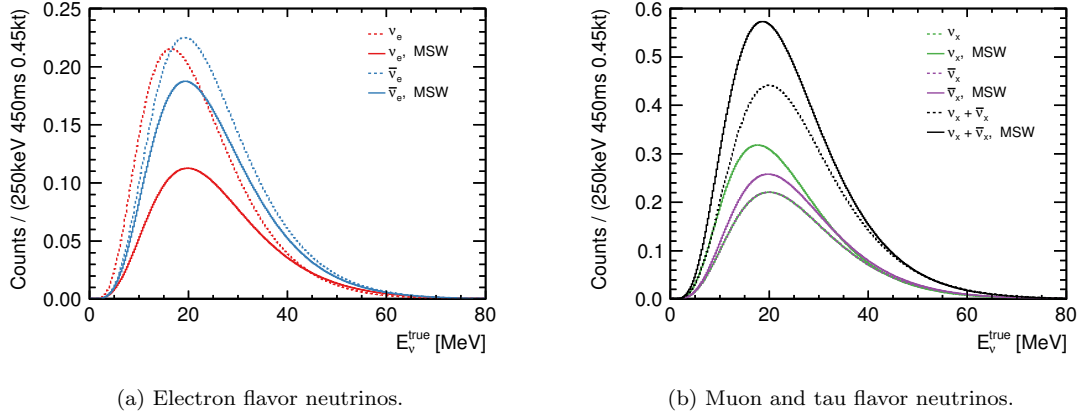


**Figure 7.30:** True SN neutrino energy,  $E_\nu^{\text{true}}$ , distributions of the  $\nu$ - $p$  ES detection channel in 0.45 kt of LAB based scintillator, derived from the Garching flux tables [46]. The progenitor has a mass of  $15 M_\odot$  and the **ls220** EOS is used in the simulation. The neutrino fluxes are integrated from 50 ms to 500 ms postbounce time. A SN distance of 10 kpc is assumed. The distributions are once shown without considering the MSW effect in the SN and once taking it into account, assuming normal hierarchy (NH). The  $\nu_e$  and  $\bar{\nu}_e$  distributions are shown in (a) and the  $\nu_x$  and  $\bar{\nu}_x$  distributions as well as their sum in (b). The  $\nu_x$  distribution is without the MSW effect identical to the  $\bar{\nu}_x$  distribution and they thus fully overlap.

The tabulated values neither confirm a  $\langle E_\alpha \rangle$  hierarchy, nor equipartitioning, nor the same  $\beta_\alpha$  for all flavors, the assumptions made for the reference SN. These disagreements with standard SN hypotheses are also discussed in e.g. [117]. Especially the  $\nu_x$  mean energy is with  $\langle E_{\nu_x} \rangle \approx 15.6$  MeV notably lower than the reference value of 18 MeV. Furthermore, the results in Tab. 7.9 show that  $\beta_\alpha$  is not equal to 3.0 for all neutrino flavors. The value is with  $\sim 2.15$  the smallest for  $\bar{\nu}_x$ , which yields a relative difference of about 30% to the reference value of 3.0 used in this work and in e. g. [92, 93, 254]. Thus, if the systematic uncertainties can be reduced within a  $\nu$ - $p$  ES measurement in a detector like JUNO, such a detector is expected to be sensitive to this difference at the  $1\sigma$  level due to a relative statistical uncertainty of about 25%. This relative statistical uncertainty takes into account that the simulated value  $\varepsilon_{\nu_x} = 11.281$  foe is about a factor of 2.2 smaller than the reference value, which is 25 foe.

### MSW effect

The neutrino fluences including the MSW effect in the early SN phase are calculated using Eq. 4.47. The flip probability matrix  $\mathcal{P}_f$ , used in this equation, is given for both neutrino mass hierarchies and for neutrinos and anti-neutrinos in Eq. 4.49. Given these flip probabilities, the only oscillation parameters entering the calculation are  $\theta_{12}$  and  $\theta_{13}$ .

Figure 7.30 shows exemplarily the  $E_\nu^{\text{true}}$  distributions from  $\nu$ - $p$  ES for the above mentioned  $15.0 M_\odot$  progenitor model and a LAB mass of 0.45 kt, again without flavor changes, as in Fig. 7.29, and additionally considering the MSW effect assuming NH. This

**Table 7.10:**  $\nu$ - $p$  ES event yield variation due to the MSW effect above a trigger threshold of 200 keV. The yields are determined assuming three different progenitors and two different equations of state (EOS) [46]. The decimal digit within the name of the simulation models gives the progenitor mass in units of  $M_\odot$ . The MSW effect is calculated with normal (NH) and inverted (IH) hierarchy using the parameters from Tab. 4.1.

SN model	Flavor	no MSW	no MSW	MSW, NH	MSW, IH	
		<b>shen</b>	<b>ls220</b>			
s11.2	$\nu_x$	1.4547	1.9145	1.5139	1.6285	
	$\bar{\nu}_x$	1.4547	1.9145	1.9579	2.0437	
	all	4.0580	5.4654	5.4654	5.4654	
s15.0	$\nu_x$	4.0037	5.6967	6.2298	6.0774	
	$\bar{\nu}_x$	4.0037	5.6967	6.3830	7.7400	
	all	14.0192	19.7308	19.7308	19.7308	
s25.0	$\nu_x$	6.1762	8.9232	9.5798	9.3920	
	$\bar{\nu}_x$	6.1762	8.9232	9.8403	11.6537	
	all	21.3944	30.2412	30.2412	30.2412	

figure illustrates how the MSW effect breaks the degeneracy of the  $\nu_{\mu,\tau}$  and  $\bar{\nu}_{\mu,\tau}$  spectra. It however also shows that the spectral splitting, visible in Fig. 7.30b, is too weak to generate a characteristic feature in the shape of the  $\langle \bar{\nu}_x \rangle$  sum spectrum that is not in agreement with a quasi-thermal distribution. This is in contrast to later phases, where prominent spikes or dents can appear due to, for instance, collective effects (see Fig. 4.1). This observation confirms the motivation within this chapter to only use the first second of the reference SN for the sensitivity studies, which are based on the quasi-thermal analytical description Eq. 3.26. It should be noted, though, that also in this first second, considering the MSW effect, the interpretation of a shape parameter  $\beta_\alpha$  in the context of pinching, obtained from fitting Eq. 3.26 to the neutrino spectrum, is not straight forward anymore. A deviation from the value in local thermodynamic equilibrium (LTE),  $\beta_\alpha \approx 2.3$  (see Sec. 3.6) is possible, even if the original neutrino spectra were in LTE.

In the context of expected  $\langle \bar{\nu}_x \rangle$ - $p$  ES event yields above the trigger threshold, the most interesting observation in Fig. 7.30 is the fact that the total number of  $\nu_x$ 's and  $\bar{\nu}_x$ 's increases. Assuming the standard trigger threshold of this chapter at 200 keV, the event yield is calculated for the model progenitor as well as for two further progenitors:

one with a mass of  $11.2 M_{\odot}$  and one with a mass of  $25.0 M_{\odot}$ . The first progenitor shows the lowest spectral parameters over time in Fig. 3.12 to Fig. 3.21, while the second has amongst the highest spectral parameters. Also in these two cases, the models calculated with **ls220** are chosen. The event yields above threshold are listed in Tab. 7.10, with and without the MSW effect and once assuming normal and once inverted hierarchy. In all cases the  $(\overline{\nu}_x)_p$  ES event yield increases, with one exception: The  $\nu_x$  event yield of the  $11.2 M_{\odot}$  progenitor slightly decreases. This is due to the fact, that the mean energy of the  $\nu_x$  distribution, which is before the MSW effect already only about 13.2 MeV, is shifted towards the lower energies of the  $\nu_e$  after the MSW effect. This shift occurs also using the other progenitors, however in these cases the gain above threshold due to the increased number of neutrinos is higher than the loss due to the shift of the mean energy to lower energies. The highest increase are  $\sim 2.7$  additional events to  $\sim 8.9$   $\bar{\nu}_x$ - $p$  ES events in case of the  $25.0 M_{\odot}$  progenitor and IH, which is an increase of about 31%.

Besides the event yield increase due to the MSW effect, the low event yields of the smallest progenitor are striking. This progenitor produces only about 5  $\nu$ - $p$  ES events from all flavors above threshold. In this case, a spectral fit is impossible, even if the full first second was twice the yield of the first 500 ms. The largest progenitor, instead, approximates with  $\sim 30$  events the total yield that results from the analytical reference SN, which is about 35 events in the first second. Since the total yield of the  $25.0 M_{\odot}$  progenitor is  $\sim 30$  events in 450 ms, the yield after 1 s is most probably even higher than the reference yield. Note, however, that the fraction of  $(\overline{\nu}_x)_p$  is lower in case of the simulated SN, where it reaches maximally  $\sim 70\%$ , compared to the reference SN, where the fraction is above 80%. This difference is due to the pronounced neutrino mean energy hierarchy in case of the reference SN (see Tab. 7.2), which is not observed for the simulated SNe (see Tab. 7.9). All progenitors and both EOSs provided at [46], totaling 21 models, have been investigated within this work and for each of these models the mean energy ordering was found to be  $\langle E_{\nu_e} \rangle < \langle E_{\nu_e} \rangle \approx \langle E_{\nu_x} \rangle$ . Furthermore, the highest mean energy was observed for the  $25.0 M_{\odot}$  **ls220** model, reaching only  $\langle E_{\nu_x} \rangle \approx 16$  MeV. Nonetheless, due to the high yield and still high mean energy, a SN similar to this model is promising for a spectral  $\nu$ - $p$  ES measurement and a parameter constraint comparable to the results presented in Sec. 7.4 and 7.5 expectable.

Additionally given in Tab. 7.10 and conclusively dealt with are the  $\nu$ - $p$  ES event yields, considering the **shen** EOS, neglecting the MSW effect. The use of this stiffer EOS, compared to the soft **ls220**, reduces the event yield. In this case, the  $25.0 M_{\odot}$  progenitor, for instance, leads to only about 21  $\nu$ - $p$  ES events above threshold in total, compared to the above mentioned  $\sim 30$  events. It is still not excluded that the yield in the full first 1 s reaches the yield of about 35 events from the reference SN. To conclude, the results from the sensitivity studies of this chapter are for an optimistic, but not unrealistic scenario.

The difference between the event yields from different EOSs motivates to investigate

the power of large-scale LS detectors to reject the EOS that was not used to simulate the  $E_\nu$  spectrum, depending on the progenitor mass. In the view of the very small event yields, resulting from some of the Garching SN models, it should also be investigated, which information about the SN could be gained from a measurement without considering the shape, but only the event yield and for instance the highest energy observed. So far, SN  $\overset{(-)}{\nu}_x$  have never been observed and even a measurement of only a few  $\overset{(-)}{\nu}_x$ 's is an important source of information.

## 7.7 Summary and outlook

Within this chapter, the sensitivities of two LAB based scintillator detectors to the spectral parameters  $\mathbf{a}_{\bar{\nu}_e} = (\langle E_{\bar{\nu}_e} \rangle, \beta_{\bar{\nu}_e}, \varepsilon_{\bar{\nu}_e})$  and  $\mathbf{a}_{\nu_x} = (\langle E_{\nu_x} \rangle, \beta_{\nu_x}, \varepsilon_{\nu_x})$  of CCSN neutrinos were determined. The analytical description of the SN neutrino spectra, based on these parameters, is expected to follow Eq. 3.26 in the first second after core bounce. The two fiducial LAB masses considered are 0.45 kt, corresponding to SNO+, and 16.80 kt, corresponding to JUNO. The detection channels in LS used for spectral analyses are the IBD, which allows to constrain the parameters  $\mathbf{a}_{\bar{\nu}_e}$ , and  $\nu$ - $p$  ES, which allows to constrain the parameters  $\mathbf{a}_{\nu_x}$ . A trigger threshold of 200 keV is assumed.

The reconstruction of the incoming neutrino energy spectrum from the visible signal spectrum is very complex for  $\nu$ - $p$  ES due to the differential cross section of the process, the non-linear behavior of ionization quenching, the non-zero trigger threshold and the increased impact of the energy resolution at the lowest observed energies. The circumstance that no one-to-one relationship between the visible energy and the true neutrino energy exists, demands spectral unfolding. The resulting reconstructed neutrino energy spectrum shows strong bin-to-bin correlations and the peak of the neutrino energy distribution is not resolved due to the trigger threshold. This is in contrast to the IBD neutrino energy reconstruction, where the entire visible spectrum can be reconstructed and where one distinct visible energy corresponds to one distinct neutrino energy.

The concept of the fit of Eq. 3.26 to the determined  $E_\nu^{\text{rec}}$  spectrum was optimized for the two signal channels. In case of the NC  $\nu$ - $p$  ES channel, only the sum event spectrum from all flavors is detected. The fit thus depends on measurements of the parameters  $\mathbf{a}_{\bar{\nu}_e}$  and  $\mathbf{a}_{\nu_e}$ . The first set of parameters is known from the IBD measurement with the same detector. The uncertainties resulting from the respective IBD fit are thus propagated within the  $\nu$ - $p$  ES fit. For the parameters  $\mathbf{a}_{\nu_e}$  it is assumed that similar parameter uncertainties as resulting from the SNO+ IBD fit are achieved by a measurement with another detector, like HALO-2.

The total relative  $1\sigma$  uncertainties on  $\langle E_{\bar{\nu}_e} \rangle$ ,  $\beta_{\bar{\nu}_e}$  and  $\varepsilon_{\bar{\nu}_e}$ , resulting from a three-parametric fit to the  $E_\nu^{\text{rec}}$  spectrum using IBD, are for 0.45 kt of LAB: < 16%, < 66% and < 21%, where the larger value of the asymmetric uncertainties is used. The corresponding

values using 16.80 kt of LAB are:  $\sim 2\%$ ,  $\sim 7\%$  and  $\sim 4\%$ .

The total relative  $1\sigma$  uncertainties on  $\langle E_{\nu_x} \rangle$ ,  $\beta_{\nu_x}$  and  $\varepsilon_{\nu_x}$ , resulting from a two-parametric fit to the  $E_{\nu}^{\text{rec}}$  spectrum using  $\nu$ - $p$  ES, are for 0.45 kt of LAB:  $< 30\%$  ( $< 19\%$ ),  $< 143\%$  and  $< 82\%$ , where the value for  $\langle E_{\nu_x} \rangle$  refers to the fit with  $\varepsilon_{\nu_x}$  ( $\beta_{\nu_x}$ ) being fixed at the expectation value. The larger value of the asymmetric uncertainties is used to calculate the relative uncertainty. The corresponding values using 16.80 kt of LAB are:  $\sim 15\%$  ( $< 4\%$ ),  $\sim 47\%$  and  $\sim 18\%$

The results from the sensitivity studies to the parameters  $a_{\bar{\nu}_e}$  and  $a_{\nu_x}$  in case of the smaller detector SNO+ reveal – partly strongly – asymmetric uncertainties. This is a consequence of the small statistics on the one hand and high fit parameter correlations on the other hand, which partly exceed  $| \pm 0.9 |$ . Moreover, it was demonstrated that SNO+ is in both measurements limited by the statistical uncertainty. In order to enhance the spectral sensitivity of this detector to the  $\nu_x$  component of the SN neutrino flux, a parameterization based on parameters with smaller correlations would be of great interest. It should be furthermore tested, how basic progenitor properties like its mass can be constrained only on the basis of  $\nu$ - $p$  ES event yields above the trigger threshold, including possibly the information about the maximum visible energy observed. These studies could be supported by the information gained from other detection channels, like the exclusive NC transition of  $^{12}\text{C}$  Eq. 7.16, which yields a prominent peak in the SN sum spectrum.

The fit results of JUNO show that also in this case the statistical uncertainties dominate, using the IBD channel, but the influence of the fit parameter correlations are negligible and the resulting uncertainties symmetric, or nearly symmetric. Using  $\nu$ - $p$  ES, however, the measurement is limited by the systematic uncertainties, which are dominated by the uncertainty of the  $\nu$ - $p$  ES cross section, arising from the uncertainty of the proton strangeness  $\eta$ , followed by the uncertainties on the parameters  $a_{\nu_e}$ . The systematic uncertainty due to the quenching parameter  $kB$ , measured within this work, was proven to be very small. If the systematic uncertainties due to  $\eta$  and  $a_{\nu_e}$  can be reduced, such that the 16.80 kt measurement is dominated by statistics, the relative uncertainties of  $\langle E_{\nu_x} \rangle$ ,  $\beta_{\nu_x}$  and  $\varepsilon_{\nu_x}$  strongly improve, yielding  $< 4\%$  ( $< 3\%$ ),  $\sim 16\%$  and  $< 10\%$ , respectively, where the value for  $\langle E_{\nu_x} \rangle$  refers to the fit with  $\varepsilon_{\nu_x}$  ( $\beta_{\nu_x}$ ) being fixed at the expectation value. To reduce  $\eta$ , an external experiment is necessary. The corresponding measurement, though, is highly non-trivial and not promising to be achieved in the near future. However, the cross section information is only necessary after data extraction. Thus the data can be re-analyzed, as soon as  $\eta$  is known with higher precision.

In the context of future studies, the precision achieved with 16.80 kt of LAB for  $a_{\bar{\nu}_e}$  via IBD and for  $a_{\nu_x}$  via  $\nu$ - $p$  ES, under the assumption, the systematics can be reduced, motivates a time-binned analysis over the entire course of the SN to reveal strong deviations from a quasi-thermal spectral distribution. In the event of a real SN, it could

be tested in combination with the IBD channel, whether non-thermal features appear at the same times and/or energies in the different spectra, attributing non-thermality to neutrino properties, not to SN properties. This investigation could be strongly supported by the measurement of the  $\nu_e$  spectrum. Thus, it is also in this context of high interest to study the spectral sensitivities of different detectors to the  $\nu_e$  component of the SN neutrino flux. One opportunity is offered by LS detectors themselves, if they have a LS mass of  $\mathcal{O}(10\text{ kt})$ . In this case the event statistics of the two exclusive CC transitions of  $^{12}\text{C}$  (Eq. 7.14 and 7.15) could become high enough for a spectral analysis of the resulting  $\nu_e$  and  $\bar{\nu}_e$  spectra, shown in Fig. 7.5. Both channels have a prompt and delayed signal, allowing coincidence tagging. In case the two channels can only be poorly discriminated from each other, due to their similarity of the signals, the measured parameters  $\mathbf{a}_{\bar{\nu}_e}$  could also in this case be used, in order to enhance the sensitivity to the parameters  $\mathbf{a}_{\nu_e}$ .

The results from this chapter strongly encourage the expansion of the sensitivity studies, including further LS detection channels and further detectors using different technologies, like the Pb based HALO(-2) detector or liquid Ar detectors. Both detector types are especially sensitive to  $\nu_e$  due to inelastic neutrino–nucleus scattering [94, 285, 286].

## Chapter 8

# Conclusions

This thesis presents the measurement of the proton and  $\alpha$ -particle light yield functions in eight different LAB based scintillators relative to the electron light yield. These measurements are indispensable for SNO+ for the search of the  $0\nu\beta\beta$  decay of  $^{130}\text{Te}$ , its main physics goal, and for the spectral analysis of supernova neutrinos of all flavors, one of its secondary physics goals. The light yield functions vary due to ionization quenching, an effect which reduces the light yield the stronger the higher the ionization energy loss of a particle is. All measurement results were parameterized individually, using Birks' law, with one parameter  $kB$  or two parameters  $kB$  and  $C$ . The set of many different LAB based scintillators was used to thoroughly investigate the influence of various contributions to the solvent itself. The results of this work, providing the first publication of quenching parameters in LAB, are thus not only viable for SNO+, but for all current and future liquid scintillator detectors, using or considering LAB as solvent, like Daya Bay, RENO, RENO-50, JUNO, LENS and HANOHANO. The systematic uncertainties introduced, when the parameters measured in this work are applied to another liquid scintillator experiment, arising from for instance different operating temperatures or detector sizes, can be reduced by a measurement of the temperature dependency of the quenching parameters and a systematic study of the influence of the detector size. In case of the latter it is of particular interest to investigate the influence of the scintillator volume on the observed Cherenkov light component, which ultimately affects the electron scale and thus the relative proton and  $\alpha$ -particle light yield, as emphasized within this work.

The knowledge of the  $\alpha$  quenching parameters, obtained in this work, enables SNO+ to develop reliable tagging techniques to efficiently reduce backgrounds from radioactive isotopes. Especially without the strong reduction of background events in the signal region from  $^{214}\text{Bi}$ - $^{214}\text{Po}$  and  $^{212}\text{Bi}$ - $^{212}\text{Po}$   $\beta$ - $\alpha$  coincidence events, SNO+ would not be sensitive to the current limit of  $|m_{\beta\beta}| < (190 - 450) \text{ meV}$  (90% C.L.) [181]. The quenching parameters in LAB, loaded with water, an amine based surfactant and 0.3%  $^{\text{nat}}\text{Te}$ , determined in this thesis, are  $kB = (0.0054 \pm 0.0005) \text{ cm/MeV}$  and  $C = (1.4 \pm 0.4) \times 10^{-6} \text{ cm}^2/\text{MeV}^2$  in a two parameter fit or  $kB = (0.0070 \pm 0.0004) \text{ cm/MeV}$  in a one parameter fit. The fluors used

in this compound are 2 g/lPPO and 15 mg/lbis-MSB. Ionization quenching in this newly developped metal-loaded liquid scintillator, using water and a surfactant, was measured for the first time within this thesis.

The proton quenching parameters are mandatory for the analysis of events from  $\nu$ - $p$  elastic scattering, the only supernova neutrino interaction in liquid scintillator with a high enough cross section that additionally provides spectral information about  $\nu_x$ 's ( $\nu_x = \nu_\mu, \bar{\nu}_\mu, \nu_\tau, \bar{\nu}_\tau$ ). This information was not accessible during the SN 1987A, but is vitally important to understand the mechanisms driving the explosion, which can not yet be conclusively explained. The proton quenching parameters obtained in this work for pure LAB with 2 g/lPPO and 15 mg/lbis-MSB are  $kB = (0.0096 \pm 0.0003)$  cm/MeV and  $C \leq 2.7 \times 10^{-6}$  cm<sup>2</sup>/MeV<sup>2</sup> (95% C.L.) in a two parameter fit or  $kB = (0.0096 \pm 0.0003)$  cm/MeV in a one parameter fit.

Based on the quoted proton quenching parameters, the sensitivity of SNO+ and a JUNO-sized detector to supernova  $\nu_x$  using  $\nu$ - $p$  elastic scattering was investigated within the present work. The results show that, under reasonable assumptions for the supernova, a measurement with SNO+ will be statistically dominated, while a measurement with JUNO will be limited by systematic uncertainties, where the dominating source of systematic uncertainty is the reaction cross section. The sensitivity of SNO+ to the  $\nu_x$  mean energy is  $\langle E_{\nu_x} \rangle = 17.81^{+3.48}_{-3.00}{}^{+0.22}_{-0.75}$  and to the respective total neutrino energy is  $\varepsilon_{\nu_x} = 102.53^{+82.26}_{-42.20}{}^{+16.24}_{-13.03}$ , determined within this work in a two parameter fit with  $\beta_{\nu_x} = 3.0$  being fixed. The first uncertainty is the statistical and the second the systematic  $1\sigma$  uncertainty. The sensitivity studies to the inverse beta decay spectrum, also performed within this work, yield  $\langle E_{\bar{\nu}_e} \rangle = 15.47^{+1.54}_{-2.43}{}^{+0.02}_{-0.04}$  for the mean  $\bar{\nu}_e$  energy,  $\varepsilon_{\bar{\nu}_e} = 24.64^{+4.96}_{-3.53}{}^{+0.45}_{-0.72}$  for the corresponding total energy, and  $\beta_{\bar{\nu}_e} = 2.88^{+1.90}_{-1.01}{}^{+0.03}_{-0.06}$  for the shape parameter in a three parameter fit. In case of a JUNO-sized detector, the statistical uncertainties improve by about a factor of six and become nearly symmetric. These studies represent the first sensitivity study of a combined  $\nu$ - $p$  elastic scattering and inverse beta decay measurement.

Finally, this thesis provides a direct comparison of the proton and  $\alpha$ -particle quenching parameters, measured simultaneously and thus under exactly the same conditions. First, while  $C$  is found to be consistent with zero in all proton quenching measurements and the one parametric model is sufficient, the two parametric model is preferred in the case of  $\alpha$  quenching measurements with a non-zero  $C$ . Second, a comparison of the  $kB$  values obtained in a one parameter fit in both cases reveals a  $\sim (4 - 5)\sigma$  difference between the proton and  $\alpha$ -particle  $kB$  values for all compounds used. These results strongly disfavor the hypothesis that different ions in the same liquid scintillator can be described by the same quenching parameters.

## Appendix A

# Natural decay chains and constants and non-SI units

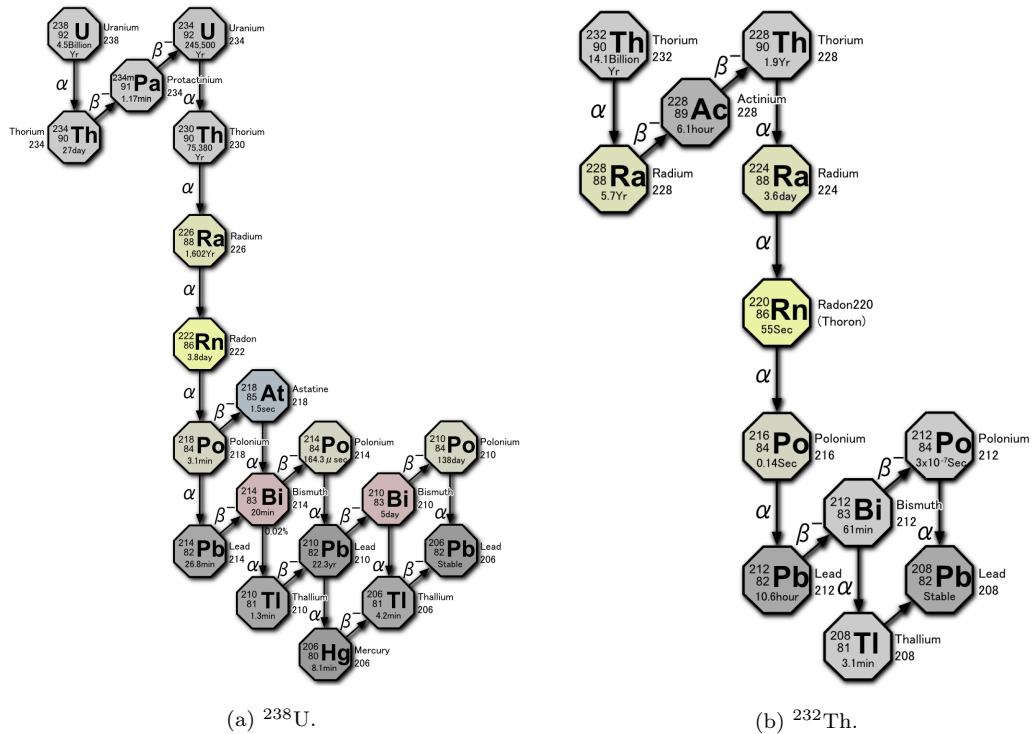


**Figure A.1:** Natural uranium (a) and thorium (b) decay chains<sup>1</sup>.

---

<sup>1</sup>(a) "Decay chain(4n+2, Uranium series)", (b) "Decay chain(4n, Thorium series)" by Tosaka is licensed under CC-BY-3.0.

**Table A.1:** Natural constants and non-SI units [152].

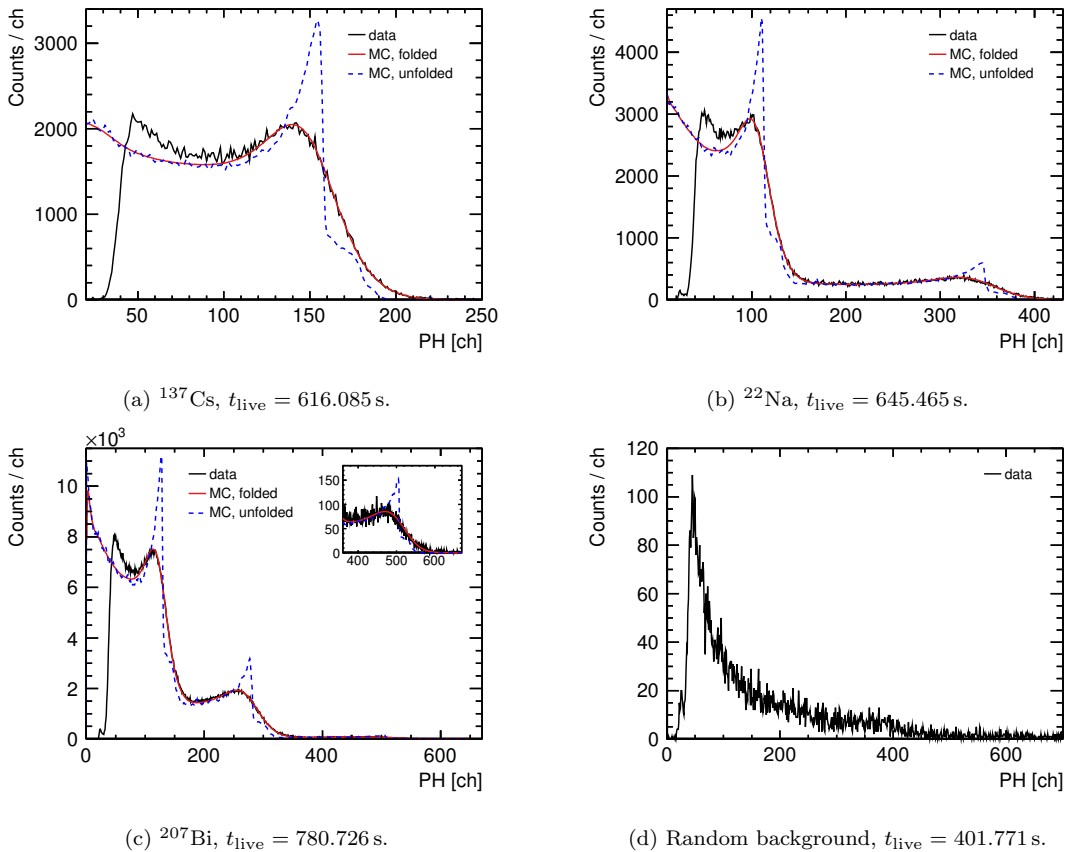
Quantity/Name	Symbol/Equation	Value
Neutron mass	$m_n$	939.565379(21) MeV/c <sup>2</sup>
Proton mass	$m_p$	938.272046(21) MeV/c <sup>2</sup>
Electron mass	$m_e$	0.510998928(11) MeV/c <sup>2</sup>
Solar mass	$M_\odot$	1.9885(2) $\times 10^{30}$ kg
Ergon	erg	$0.1 \times 10^{-6}$ kg m <sup>2</sup> /s <sup>2</sup>
Fifty one erg	foe	$1 \times 10^{51}$ erg = 1 Bethe
Parsec	pc	$3.0856776 \times 10^{16}$ m $\approx 3.262$ ly
Light year (deprecated unit)	ly	$0.946053... \times 10^{16}$ m
Fermi constant	$G_F$	$8.9618756 \times 10^{-44}$ MeV cm <sup>3</sup>
Speed of light in vacuum	$c$	299 792 458 m s <sup>-1</sup>
Conversion constant	$\hbar c$	$197.3269631 \times 10^{-13}$ MeV cm
Conversion constant	$G_F/(\hbar c)^3$	$1.1663788 \times 10^{-11}$ MeV <sup>-2</sup>
Effective weak mixing angle	$\sin^2\theta_W$	0.23155(5)

## Appendix B

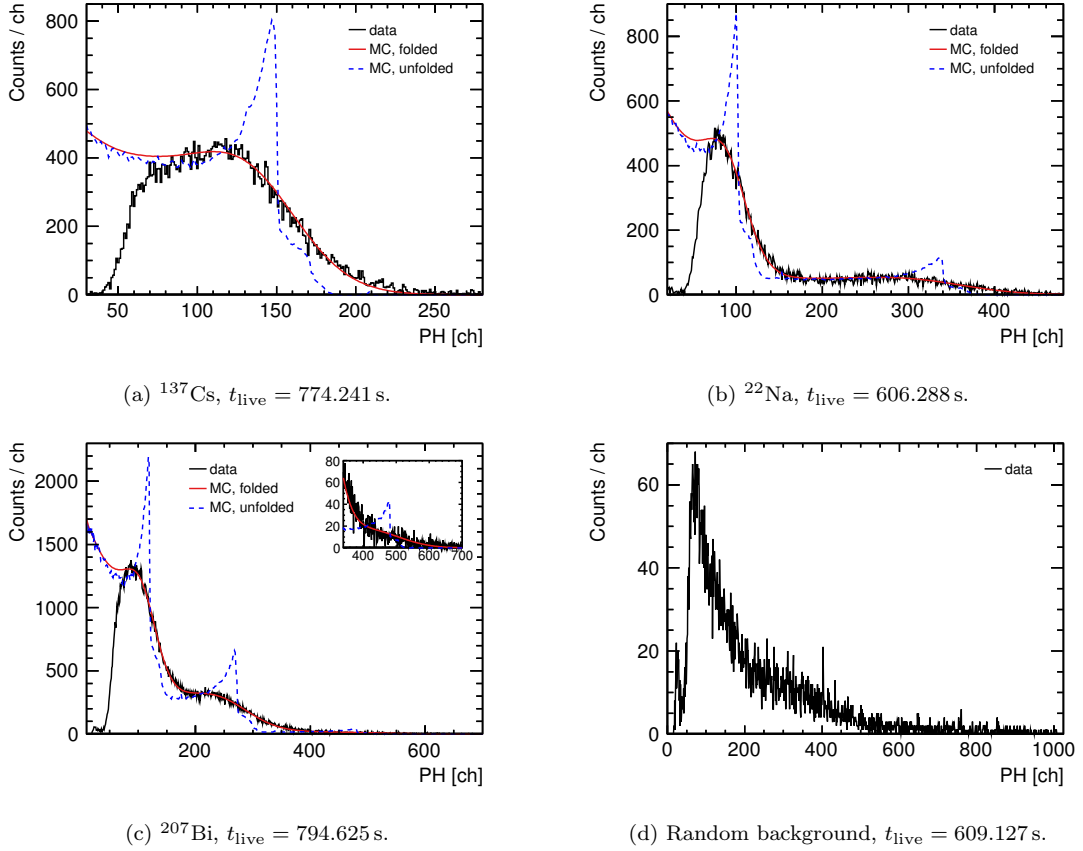
# Spectra taken within the ionization quenching measurements

### B.1 Gamma calibration spectra

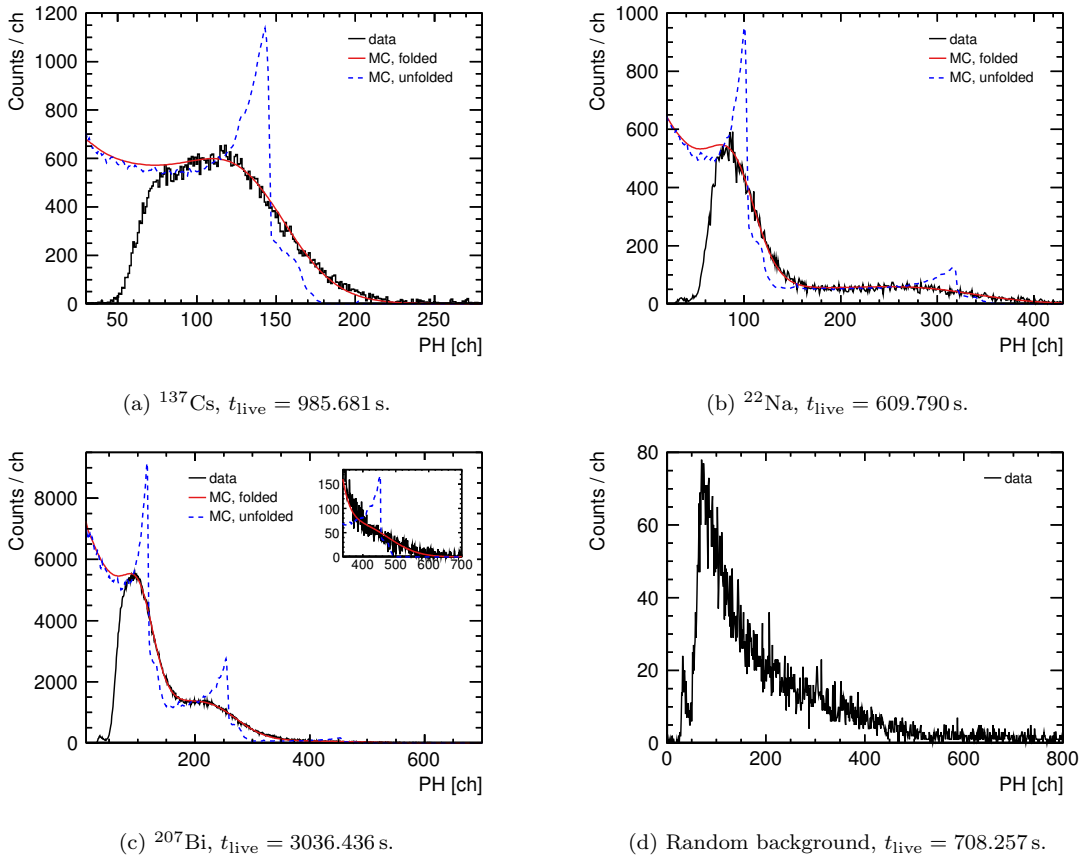
This section shows the remaining gamma calibration spectra from all linear alkylbenzene (LAB) and water–surfactant–LAB (wsLAB) samples that were not shown in Sec. 6.4.1. For each sample, the calibration was performed in high gain (HG) and in low gain (LG) mode.



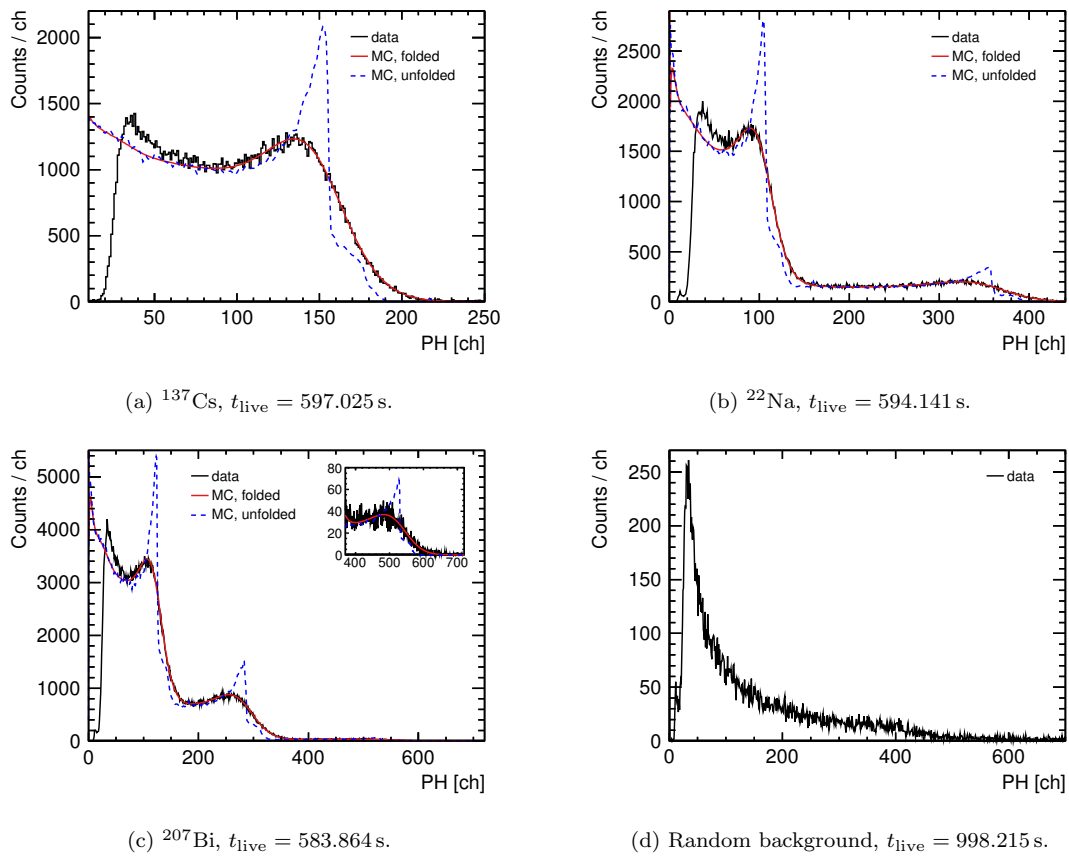
**Figure B.1:** Pulse-height spectra in ADC channels (ch) of all used calibration sources (a-c) and of background only (d). The third  $\gamma$ -line of  $^{207}\text{Bi}$  is shown enlarged in the inset of (c). The background is subtracted from the source measurements after normalization to the respective livetime  $t_{\text{live}}$ . The data is taken with LAB + 2 g/l PPO + 15 mg/l bis-MSB (LAB1) in LG mode.



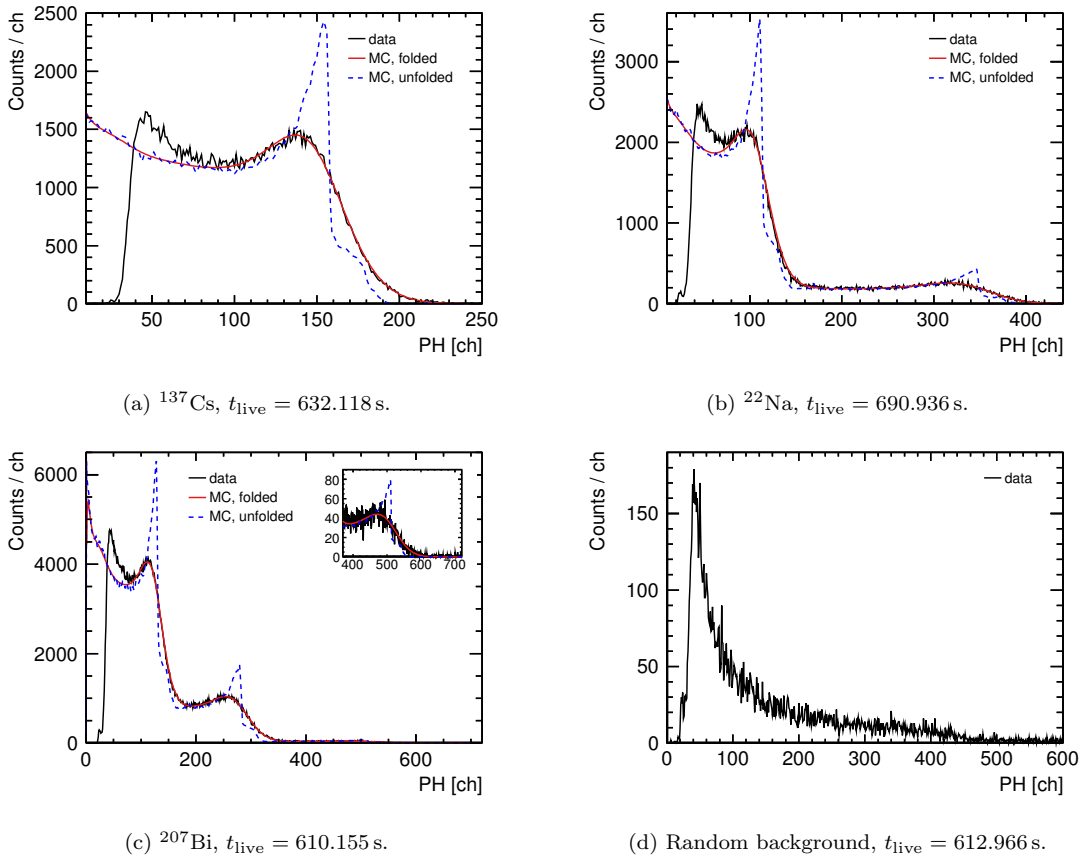
**Figure B.2:** Pulse-height spectra in ADC channels (ch) of all used calibration sources (a-c) and of background only (d). The third  $\gamma$ -line of  $^{207}\text{Bi}$  is shown enlarged in the inset of (c). The background is subtracted from the source measurements after normalization to the respective livetime  $t_{\text{live}}$ . The data is taken with LAB + 2g/1PPO (LAB2) in HG mode.



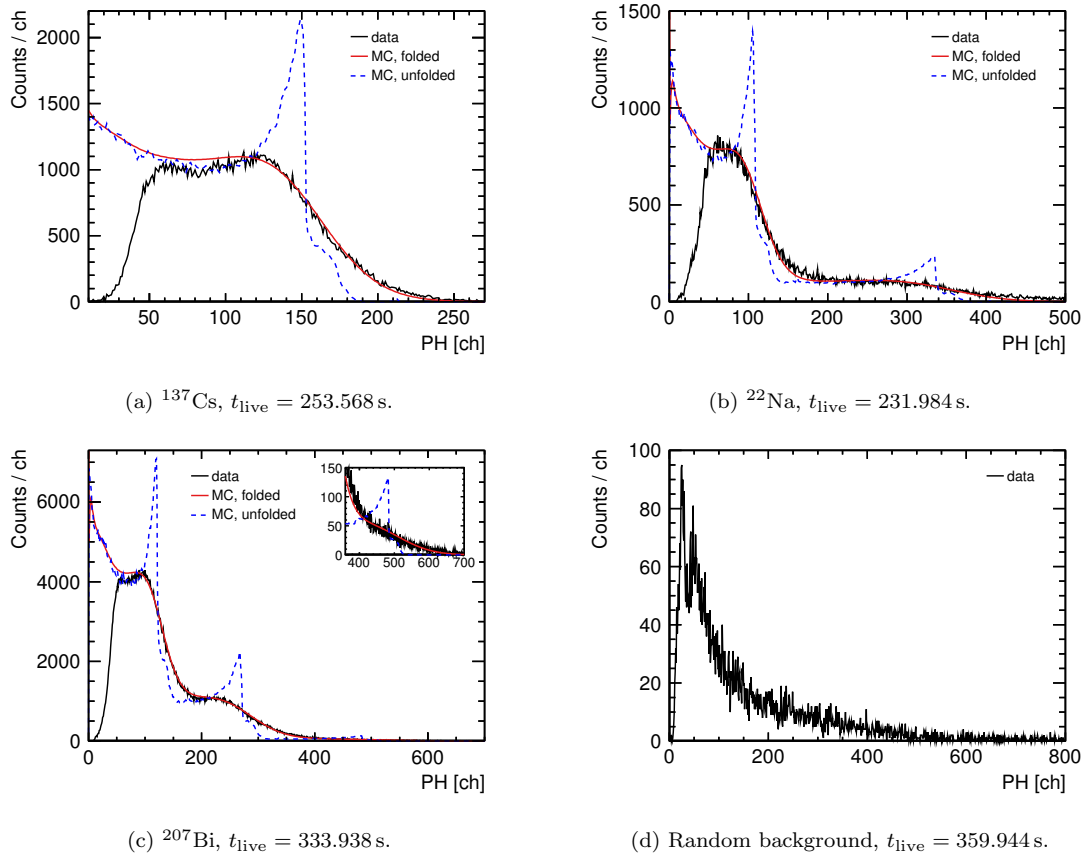
**Figure B.3:** Pulse-height spectra in ADC channels (ch) of all used calibration sources (a-c) and of background only (d). The third  $\gamma$ -line of  $^{207}\text{Bi}$  is shown enlarged in the inset of (c). The background is subtracted from the source measurements after normalization to the respective livetime  $t_{\text{live}}$ . The data is taken with LAB + 2g/1PPO (LAB2) in LG mode.



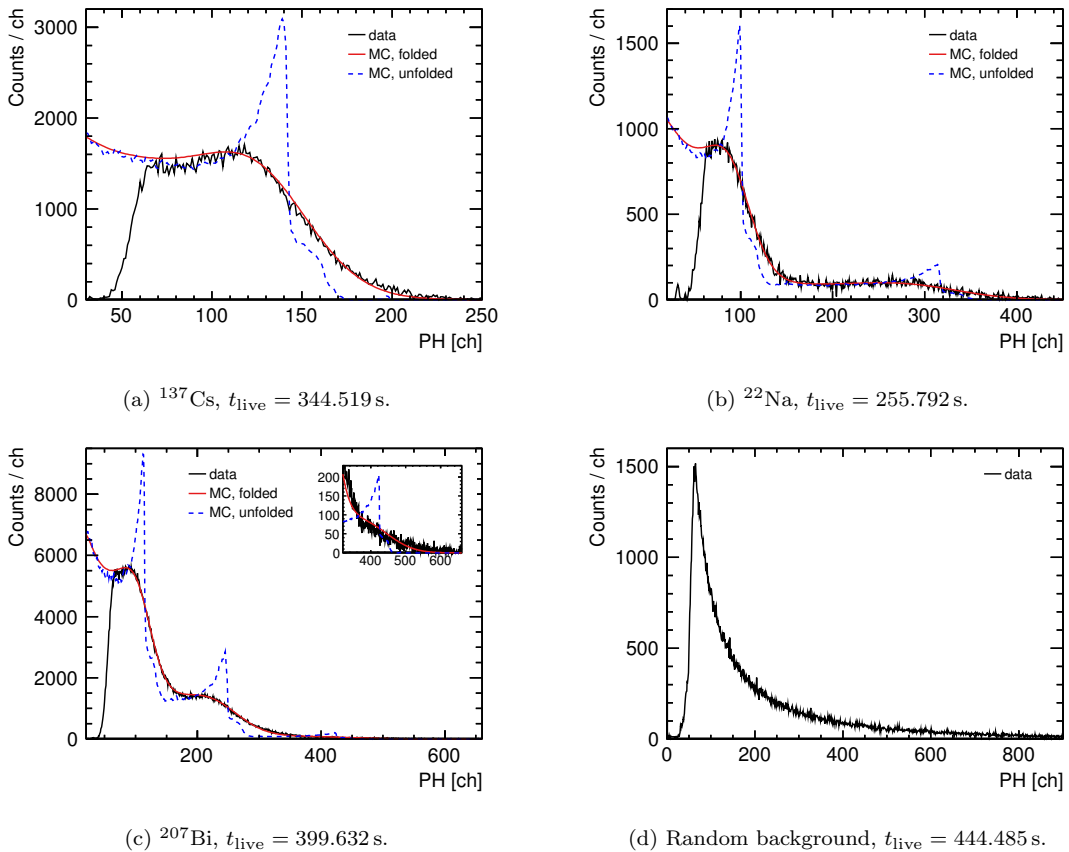
**Figure B.4:** Pulse-height spectra in ADC channels (ch) of all used calibration sources (a-c) and of background only (d). The third  $\gamma$ -line of  $^{207}\text{Bi}$  is shown enlarged in the inset of (c). The background is subtracted from the source measurements after normalization to the respective livetime  $t_{\text{live}}$ . The data is taken with LAB + 3 g/lPPO + 15 mg/lbis-MSB (LAB3) in HG mode.



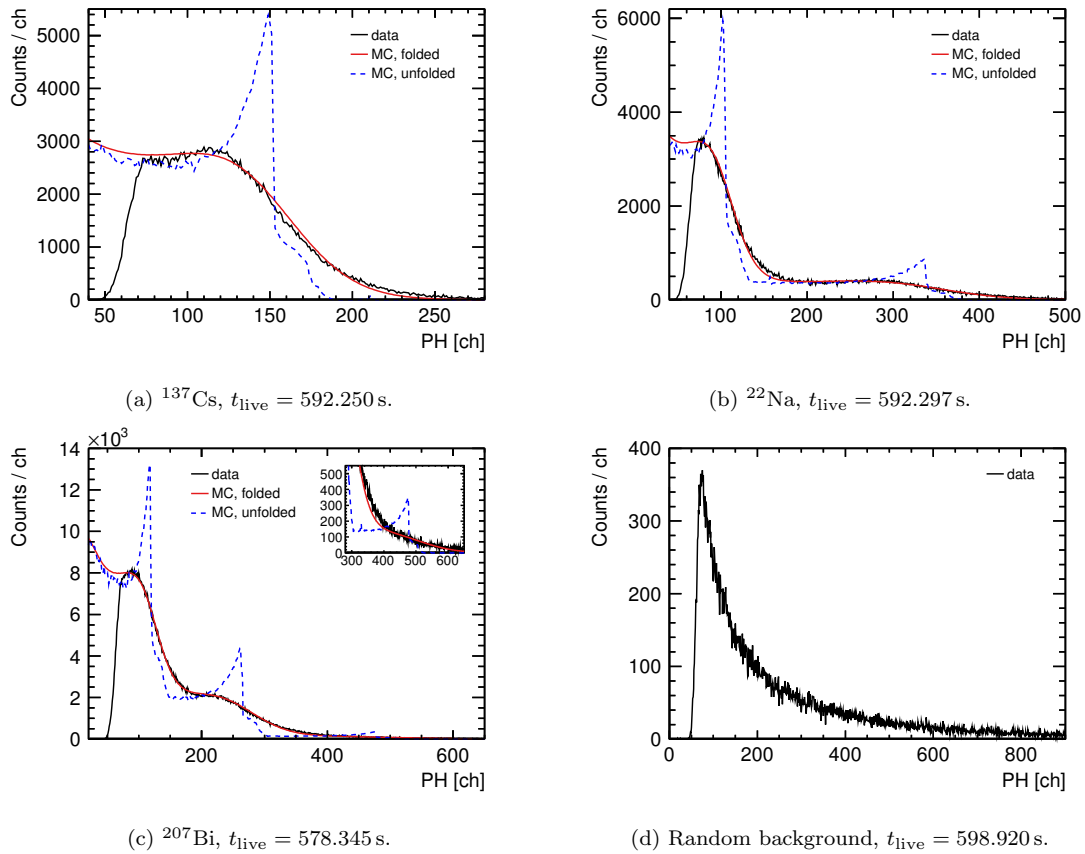
**Figure B.5:** Pulse-height spectra in ADC channels (ch) of all used calibration sources (a-c) and of background only (d). The third  $\gamma$ -line of  $^{207}\text{Bi}$  is shown enlarged in the inset of (c). The background is subtracted from the source measurements after normalization to the respective livetime  $t_{\text{live}}$ . The data is taken with LAB + 3 g/l PPO + 15 mg/l bis-MSB (LAB3) in LG mode.



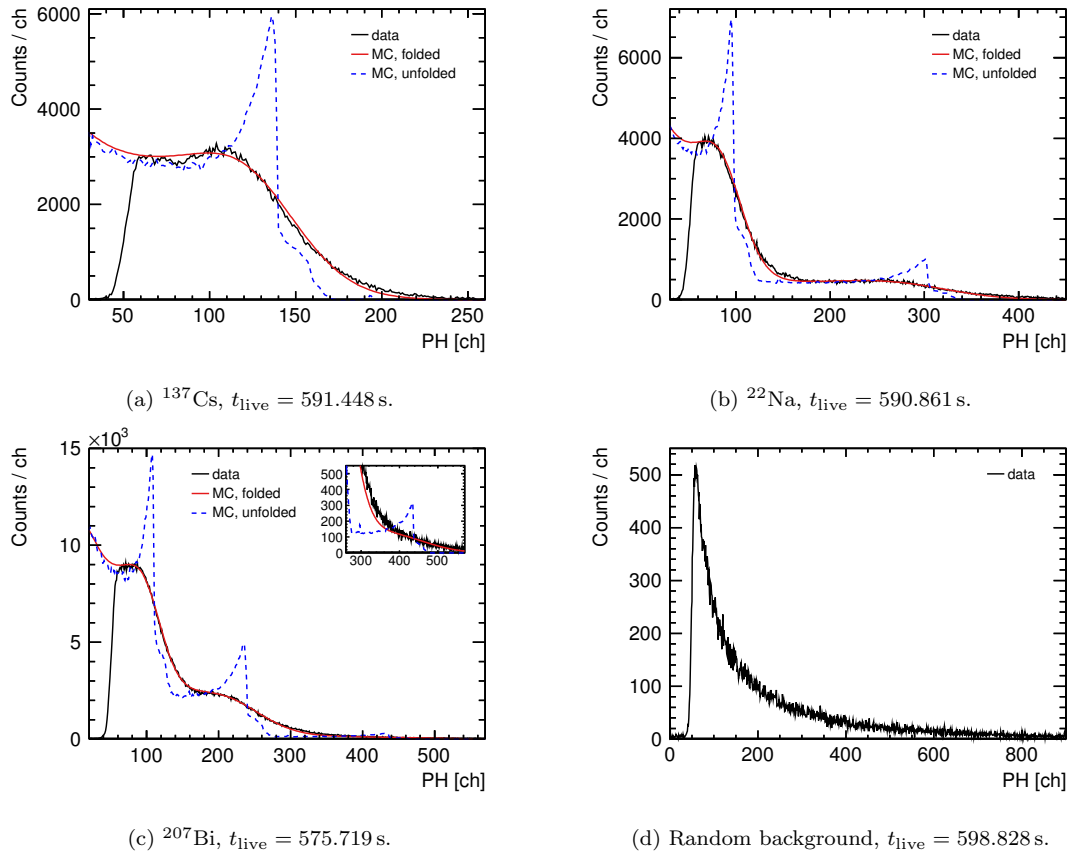
**Figure B.6:** Pulse-height spectra in ADC channels (ch) of all used calibration sources (a-c) and of background only (d). The third  $\gamma$ -line of  $^{207}\text{Bi}$  is shown enlarged in the inset of (c). The background is subtracted from the source measurements after normalization to the respective livetime  $t_{\text{live}}$ . The data is taken with LAB + 3g/1PPO (LAB4) in HG mode.



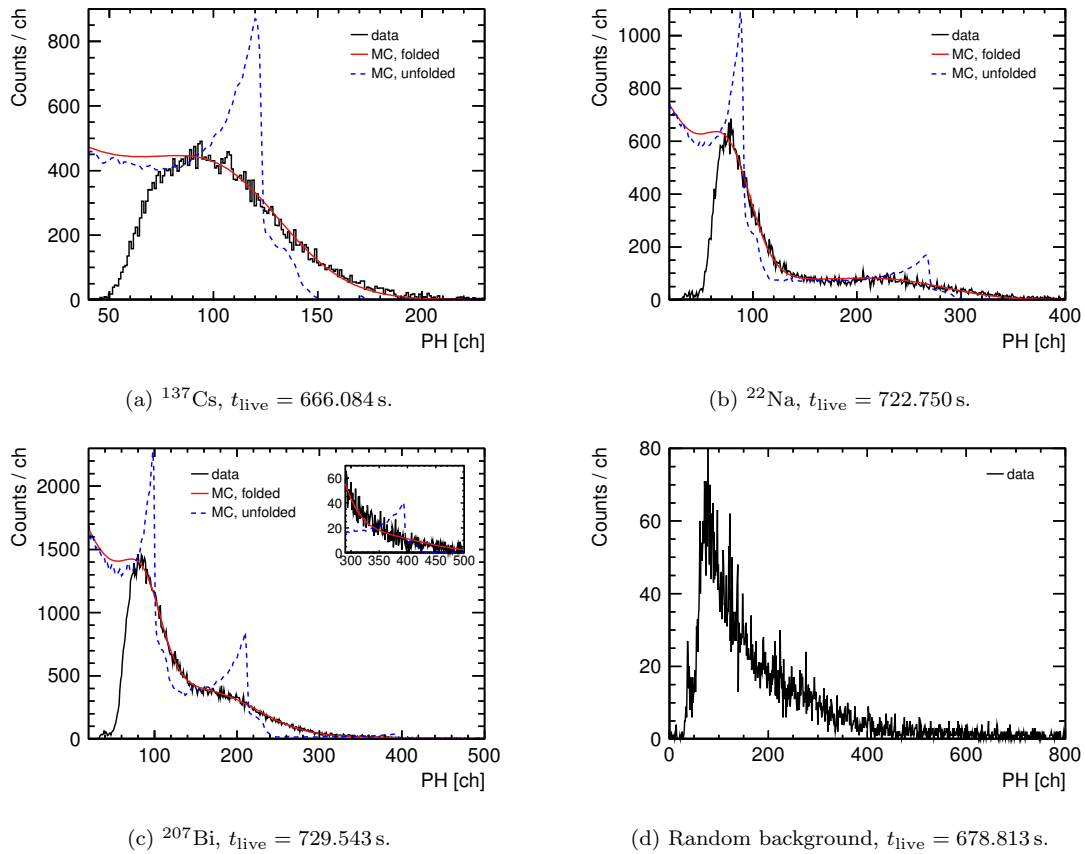
**Figure B.7:** Pulse-height spectra in ADC channels (ch) of all used calibration sources (a-c) and of background only (d). The third  $\gamma$ -line of  $^{207}\text{Bi}$  is shown enlarged in the inset of (c). The background is subtracted from the source measurements after normalization to the respective livetime  $t_{\text{live}}$ . The data is taken with LAB + 3g/1PPO (LAB4) in LG mode.



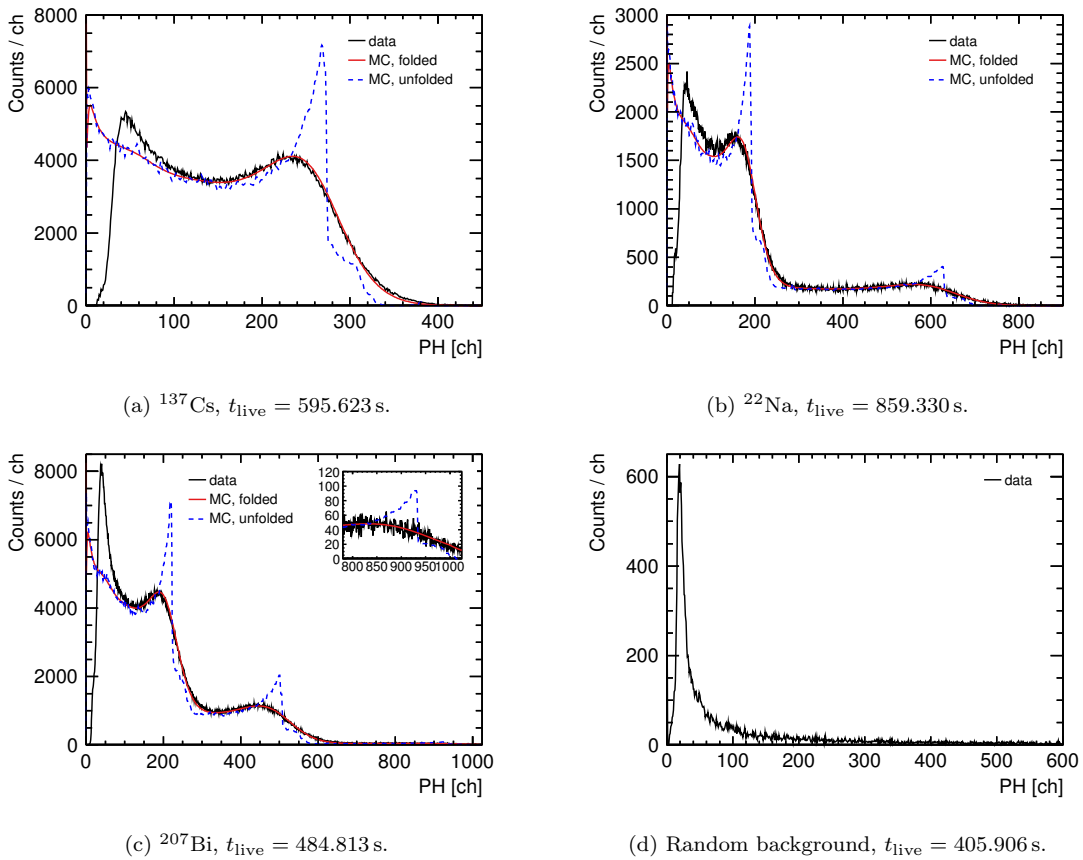
**Figure B.8:** Pulse-height spectra in ADC channels (ch) of all used calibration sources (a-c) and of background only (d). The third  $\gamma$ -line of  $^{207}\text{Bi}$  is shown enlarged in the inset of (c). The background is subtracted from the source measurements after normalization to the respective livetime  $t_{\text{live}}$ . The data is taken with LAB + 2g/1PPO + 0.1% Nd (LAB5) in HG mode.



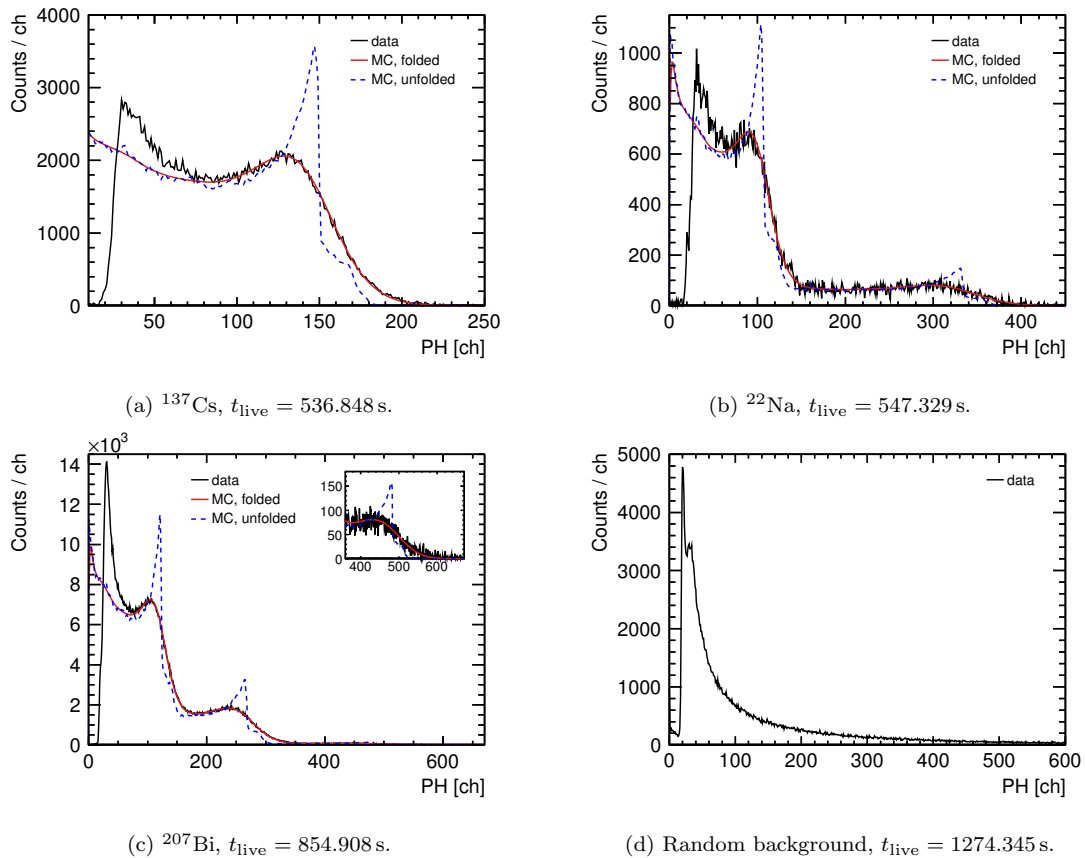
**Figure B.9:** Pulse-height spectra in ADC channels (ch) of all used calibration sources (a-c) and of background only (d). The third  $\gamma$ -line of  $^{207}\text{Bi}$  is shown enlarged in the inset of (c). The background is subtracted from the source measurements after normalization to the respective livetime  $t_{\text{live}}$ . The data is taken with LAB + 2 g/1PPO + 0.1% Nd (LAB5) in LG mode.



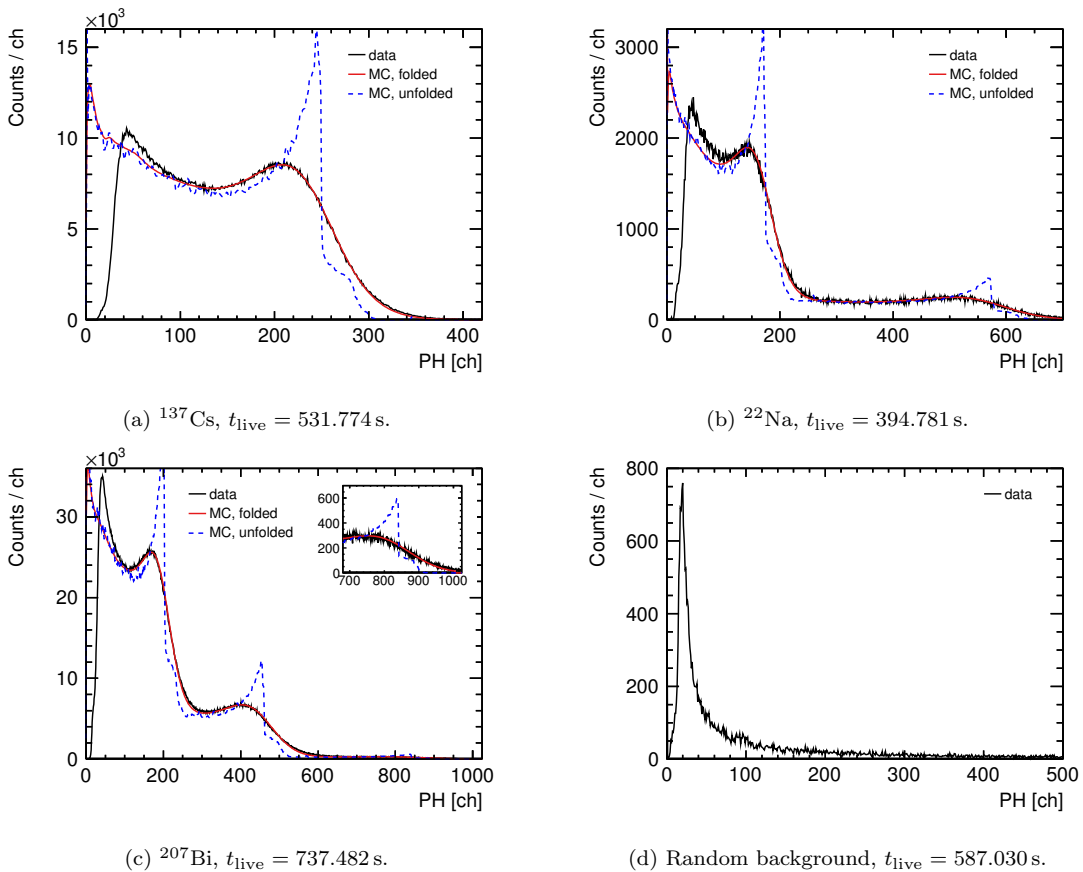
**Figure B.10:** Pulse-height spectra in ADC channels (ch) of all used calibration sources (a-c) and of background only (d). The third  $\gamma$ -line of  $^{207}\text{Bi}$  is shown enlarged in the inset of (c). The background is subtracted from the source measurements after normalization to the respective livetime  $t_{\text{live}}$ . The data is taken with LAB + 3g/1PPO + 0.1% Nd (LAB6) in LG mode.



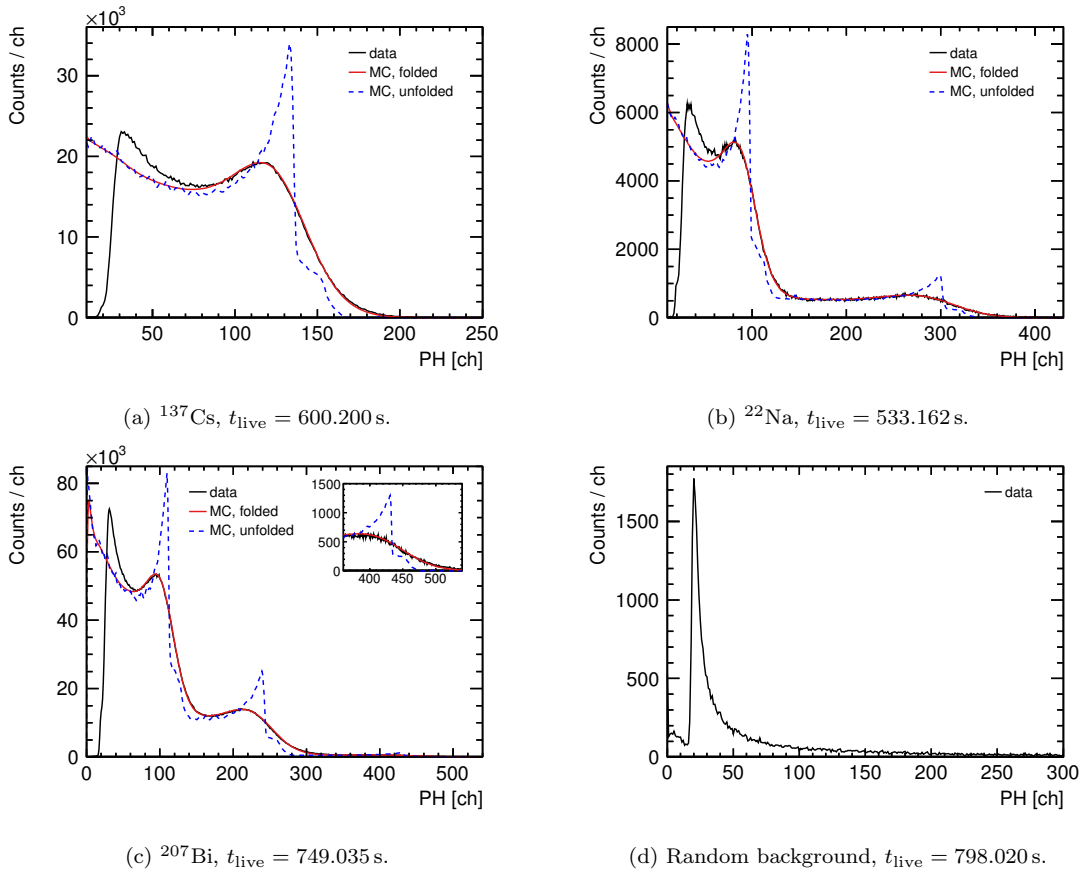
**Figure B.11:** Pulse-height spectra in ADC channels (ch) of all used calibration sources (a-c) and of background only (d). The third  $\gamma$ -line of  $^{207}\text{Bi}$  is shown enlarged in the inset of (c). The background is subtracted from the source measurements after normalization to the respective livetime  $t_{\text{live}}$ . The data is taken with LAB + 5% PRS + 1.5% water + 2 g/l PPO + 15 mg/l bis-MSB + 0.3% Te (wsLAB1) in HG mode.



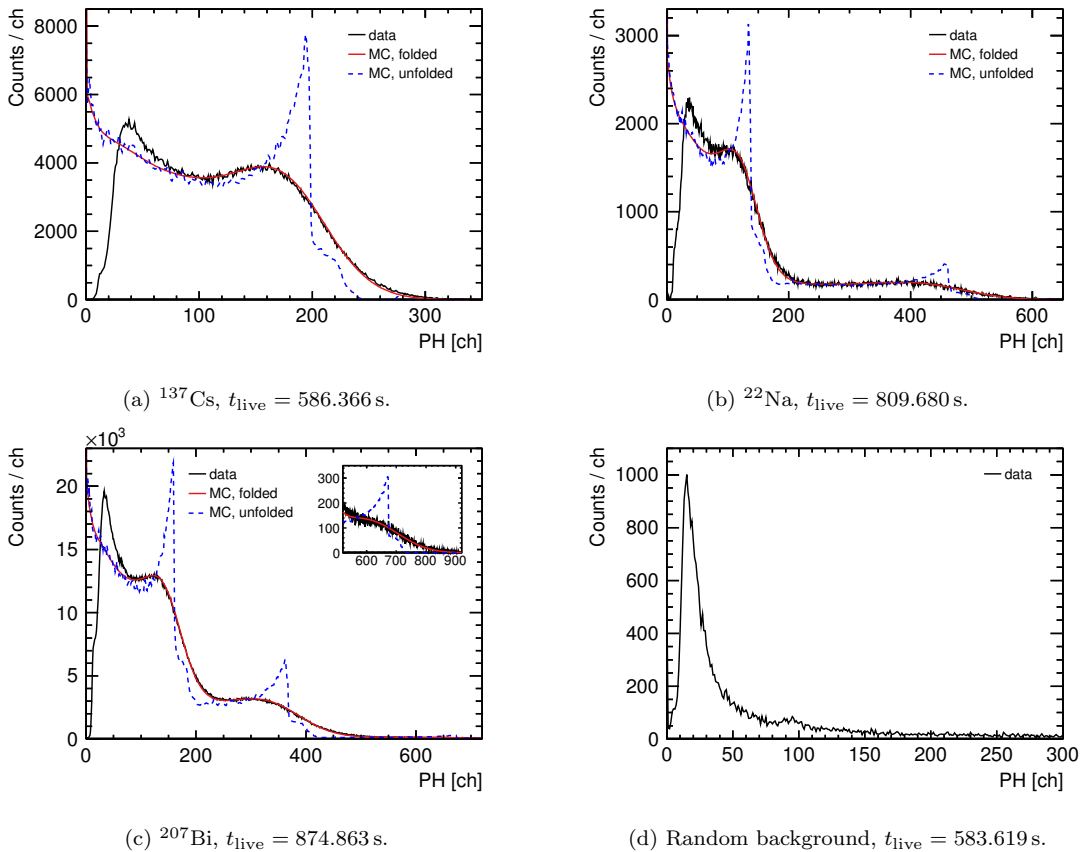
**Figure B.12:** Pulse-height spectra in ADC channels (ch) of all used calibration sources (a-c) and of background only (d). The third  $\gamma$ -line of  $^{207}\text{Bi}$  is shown enlarged in the inset of (c). The background is subtracted from the source measurements after normalization to the respective livetime  $t_{\text{live}}$ . The data is taken with LAB + 5% PRS + 1.5% water + 2 g/l PPO + 15 mg/l bis-MSB + 0.3% Te (wsLAB1) in LG mode.



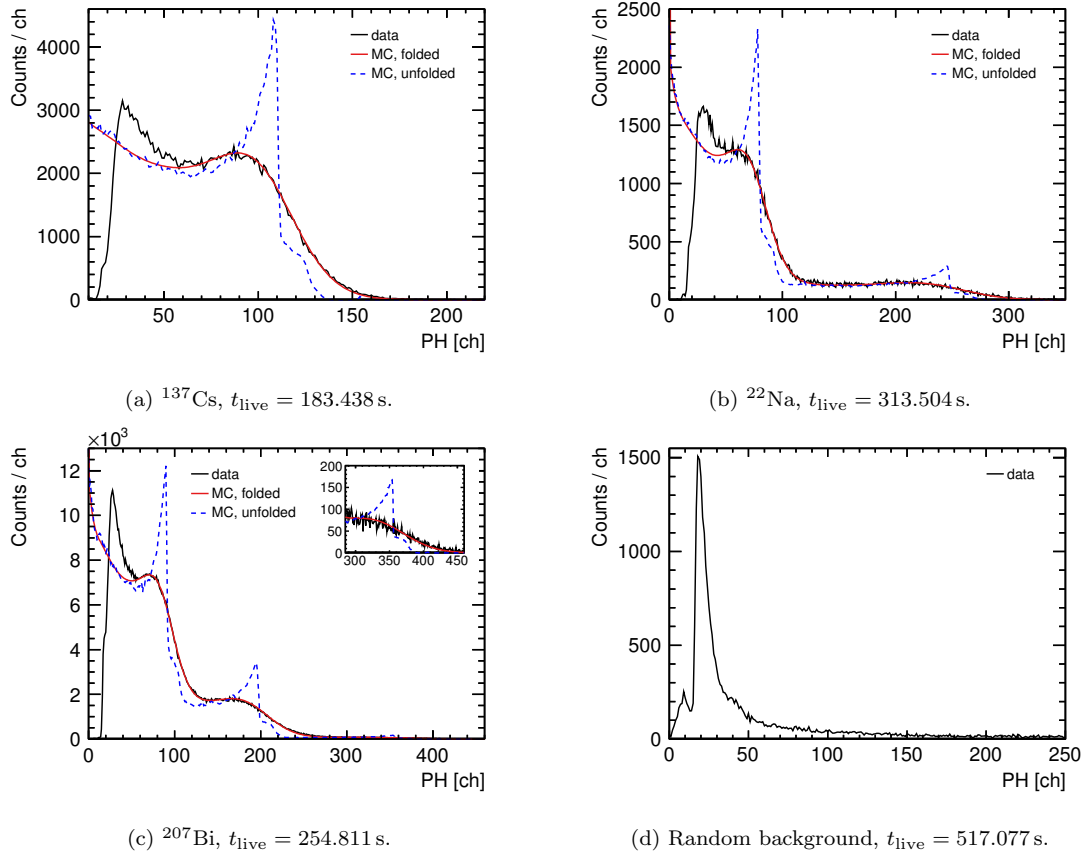
**Figure B.13:** Pulse-height spectra in ADC channels (ch) of all used calibration sources (a-c) and of background only (d). The third  $\gamma$ -line of  $^{207}\text{Bi}$  is shown enlarged in the inset of (c). The background is subtracted from the source measurements after normalization to the respective livetime  $t_{\text{live}}$ . The data is taken with LAB + 5% PRS + 1.5% water + 2 g/l PPO + 15 mg/l bis-MSB (wsLAB2) in HG mode.



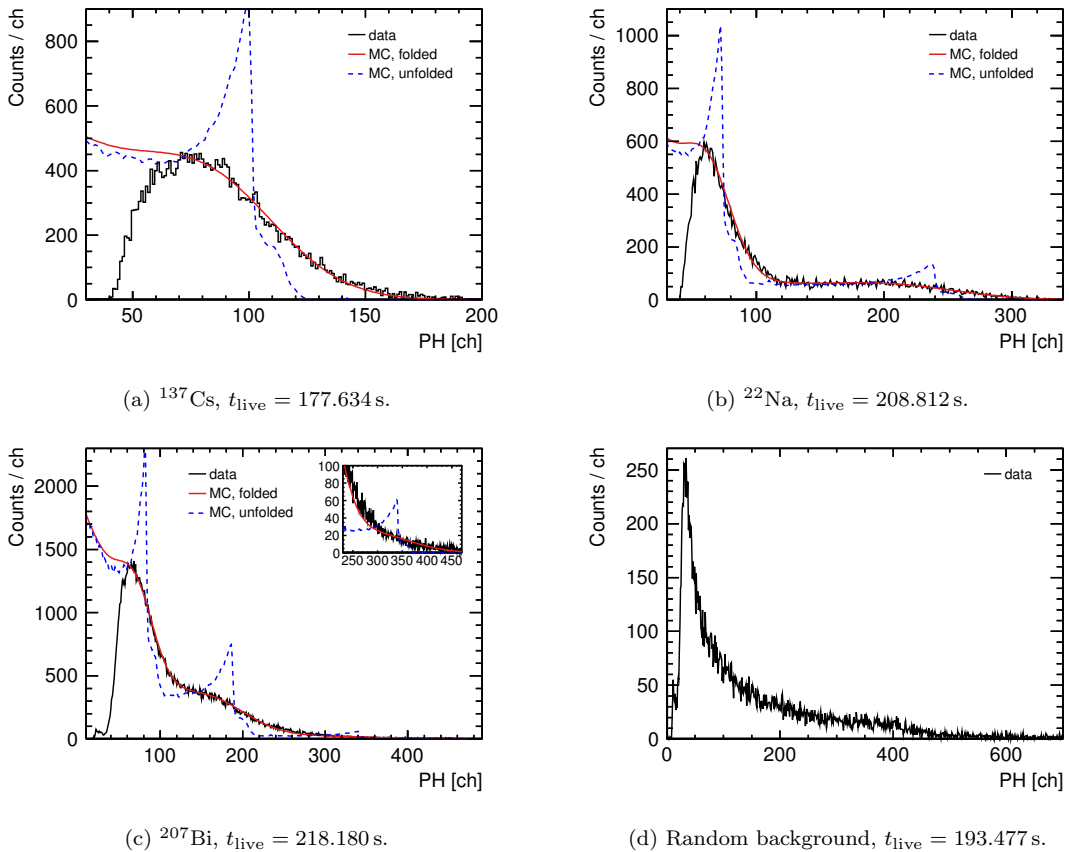
**Figure B.14:** Pulse-height spectra in ADC channels (ch) of all used calibration sources (a-c) and of background only (d). The third  $\gamma$ -line of  $^{207}\text{Bi}$  is shown enlarged in the inset of (c). The background is subtracted from the source measurements after normalization to the respective livetime  $t_{\text{live}}$ . The data is taken with LAB + 5% PRS + 1.5% water + 2g/1PP0 + 15mg/l bis-MSB (wsLAB2) in LG mode.



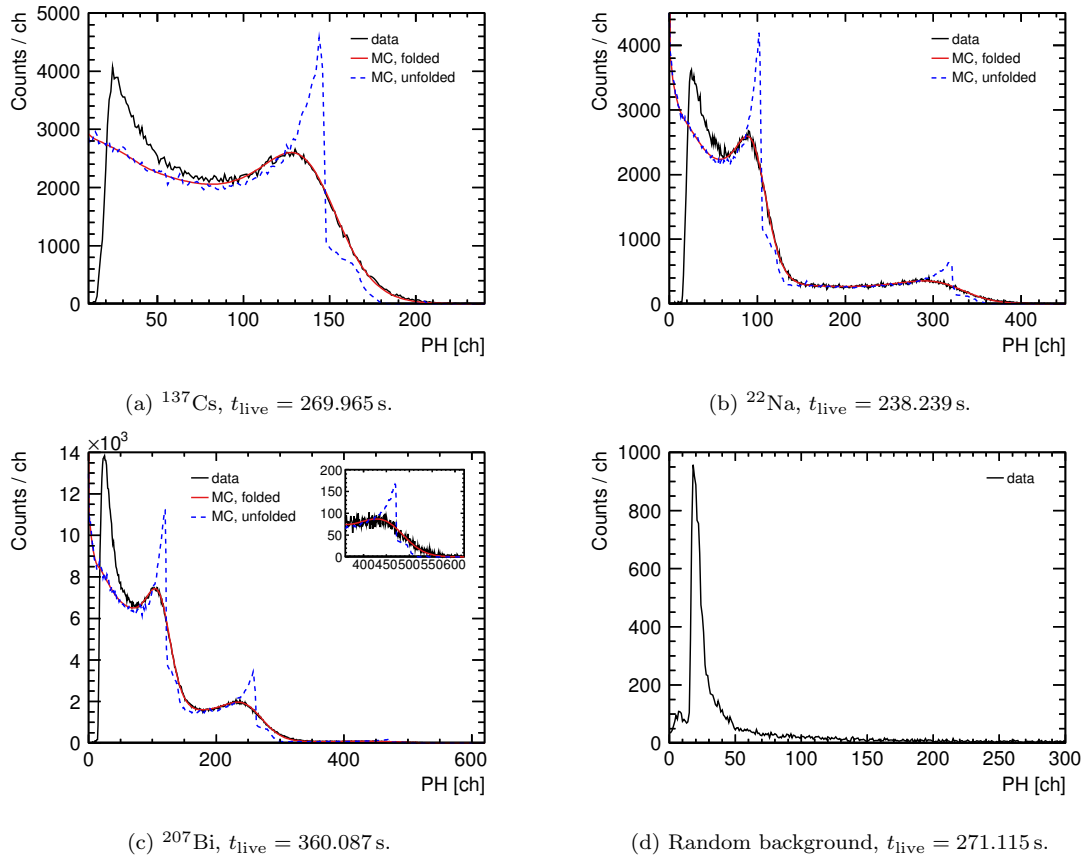
**Figure B.15:** Pulse-height spectra in ADC channels (ch) of all used calibration sources (a-c) and of background only (d). The third  $\gamma$ -line of  $^{207}\text{Bi}$  is shown enlarged in the inset of (c). The background is subtracted from the source measurements after normalization to the respective livetime  $t_{\text{live}}$ . The data is taken with LAB + 5% PRS + 1.5% water + 2 g/l PPO + 15 mg/l perylene (wsLAB3) in HG mode.



**Figure B.16:** Pulse-height spectra in ADC channels (ch) of all used calibration sources (a-c) and of background only (d). The third  $\gamma$ -line of  $^{207}\text{Bi}$  is shown enlarged in the inset of (c). The background is subtracted from the source measurements after normalization to the respective livetime  $t_{\text{live}}$ . The data is taken with LAB + 5% PRS + 1.5% water + 2g/1PPO + 15mg/l perylene (wsLAB3) in LG mode.



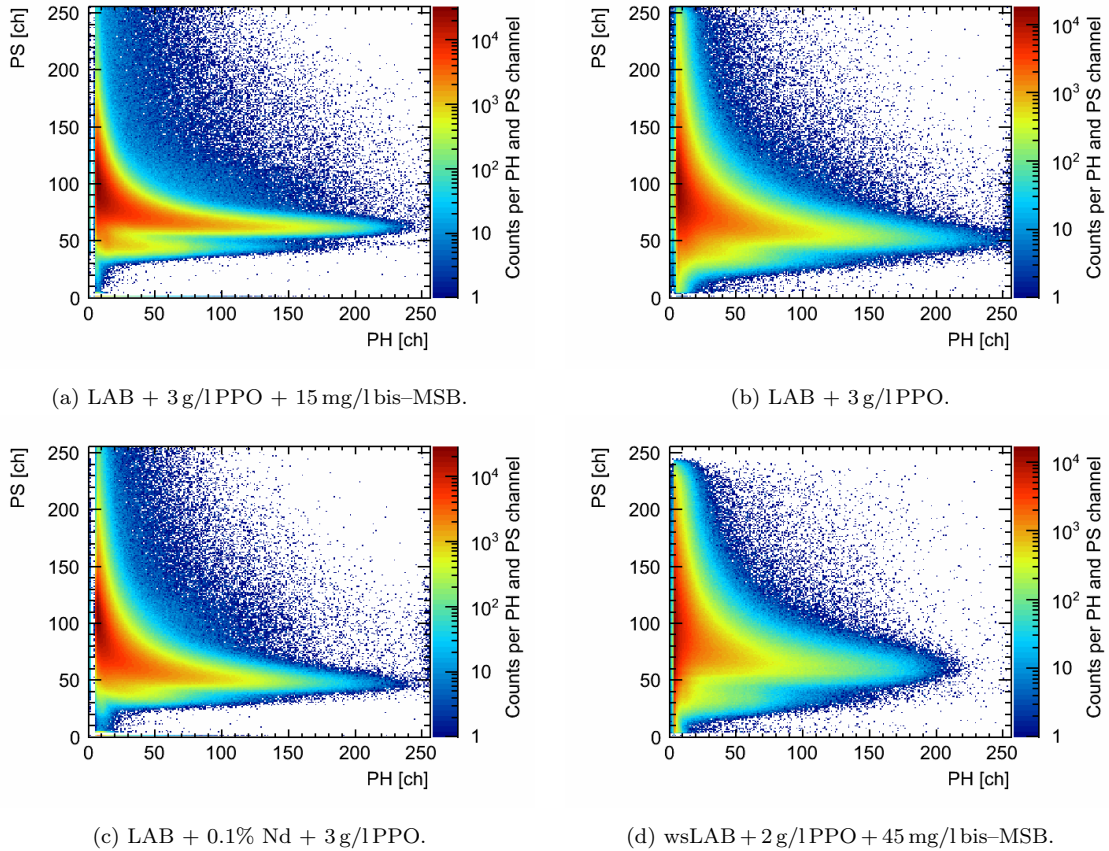
**Figure B.17:** Pulse-height spectra in ADC channels (ch) of all used calibration sources (a-c) and of background only (d). The third  $\gamma$ -line of  $^{207}\text{Bi}$  is shown enlarged in the inset of (c). The background is subtracted from the source measurements after normalization to the respective livetime  $t_{\text{live}}$ . The data is taken with LAB + 5% PRS + 1.5% water + 2 g/l PPO + 45 mg/l bis-MSB (wsLAB4) in HG mode.



**Figure B.18:** Pulse-height spectra in ADC channels (ch) of all used calibration sources (a-c) and of background only (d). The third  $\gamma$ -line of  $^{207}\text{Bi}$  is shown enlarged in the inset of (c). The background is subtracted from the source measurements after normalization to the respective livetime  $t_{\text{live}}$ . The data is taken with LAB + 5% PRS + 1.5% water + 2g/1IPPO + 45mg/l bis-MSB (wsLAB4) in LG mode.

## B.2 Pulse-height over pulse-shape distributions

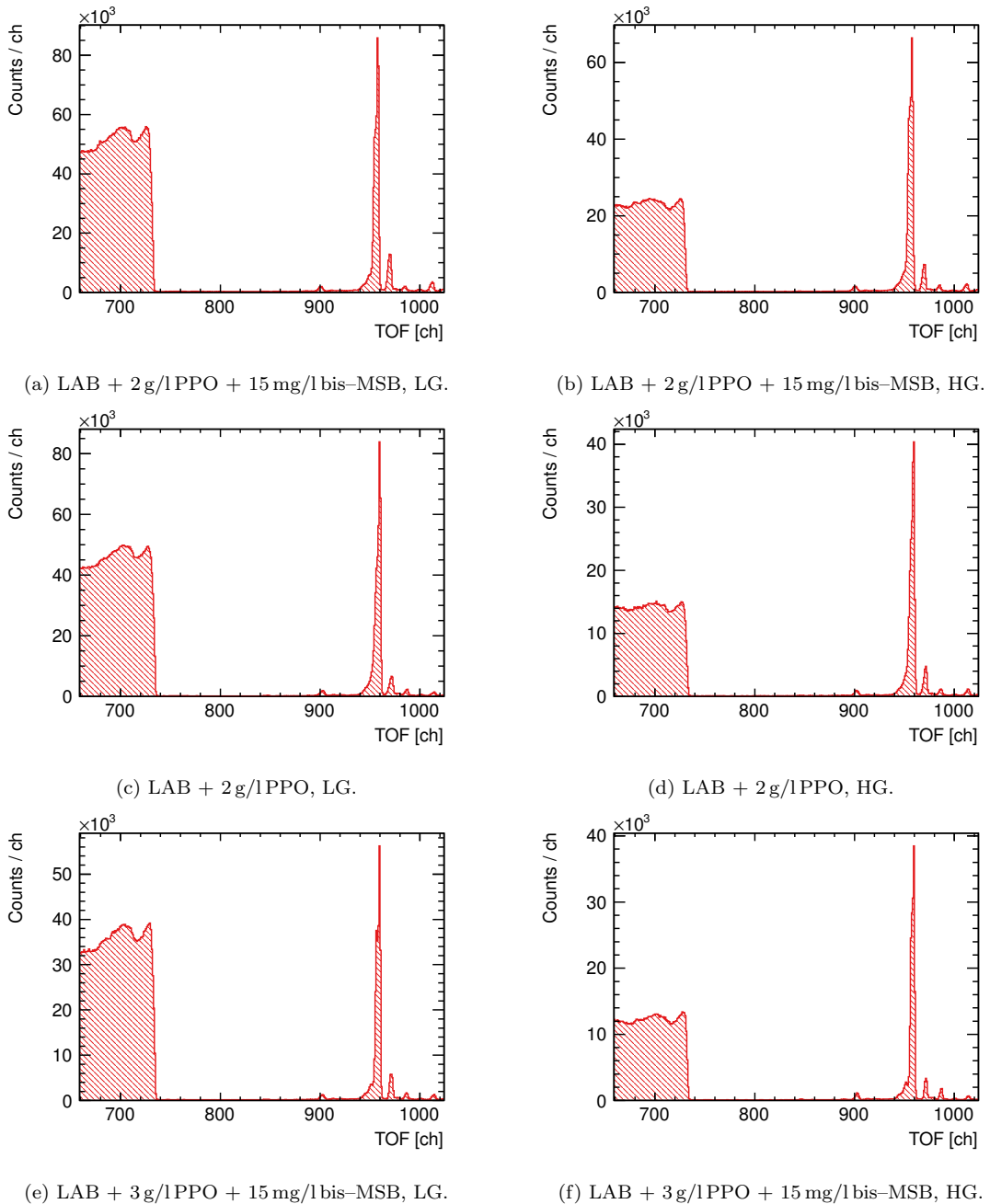
Within this section the remaining pulse-shape (PS) over pulse-height (PH) distributions from all linear alkylbenzene (LAB) and water-surfactant-LAB (wsLAB) samples are presented that were not shown in Sec. 6.5.1. These distributions were measured in the white neutron field described in Sec. 6.3.1 and are used for pulse-shape discrimination. Only low gain (LG) mode data is shown. Qualitatively, the high gain (HG) distributions are an enlargement of the LG distributions at low PHs.

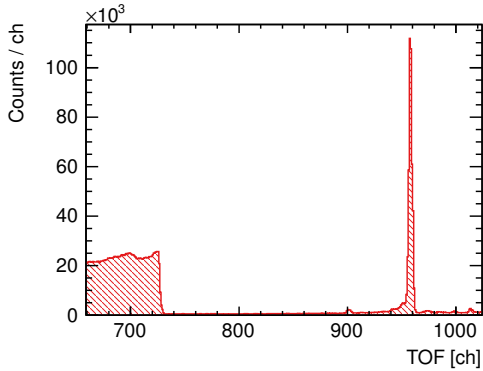


**Figure B.19:** PH–PS parameter space of all events detected with LAB and wsLAB scintillators during beam run in LG mode. The individual compositions are written in the subcaptions. The wsLAB contains 5% PRS and 1.5% water.

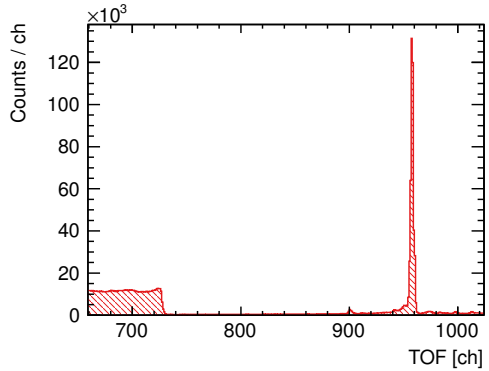
### B.3 Time-of-flight distributions

All time-of-flight (TOF) distributions, measured in the white neutron field with linear alkylbenzene (LAB) and water-surfactant-LAB (wsLAB), that were not shown in Sec. 6.5.1 are presented in this section. The distributions are shown before satellite correction to underline the good performance of the cyclotron in most of the cases in contrast to the rejected measurements using wsLAB3 and wsLAB4, shown in Fig. B.20q to B.20t. High gain (HG) and low gain (LG) data is presented.

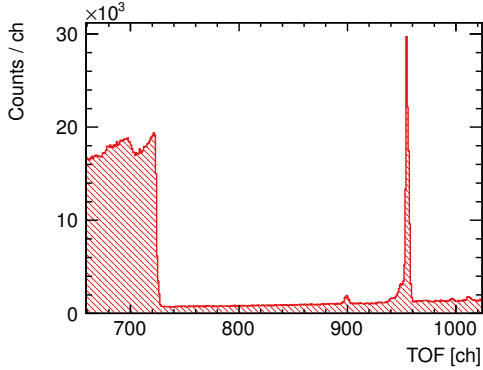




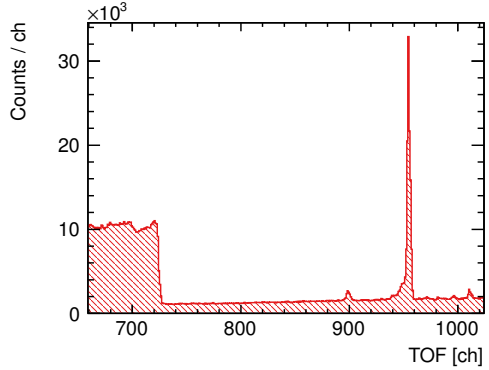
(g) LAB + 3 g/lPPO, LG.



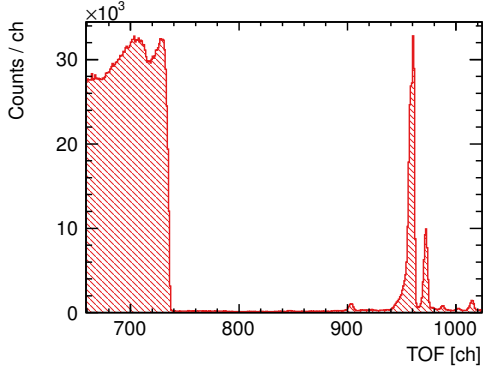
(h) LAB + 3 g/lPPO, HG.



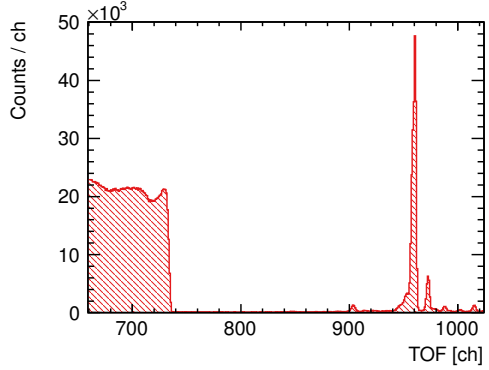
(i) LAB + 2 g/lPPO + 0.1% Nd, LG.



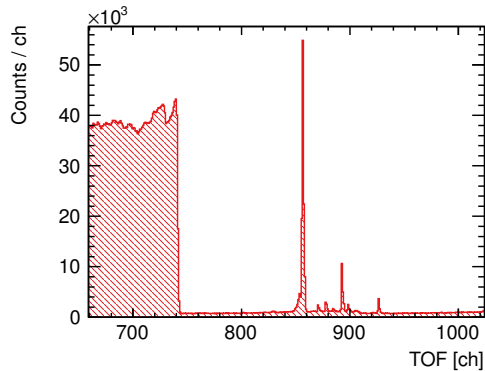
(j) LAB + 2 g/lPPO + 0.1% Nd, HG.



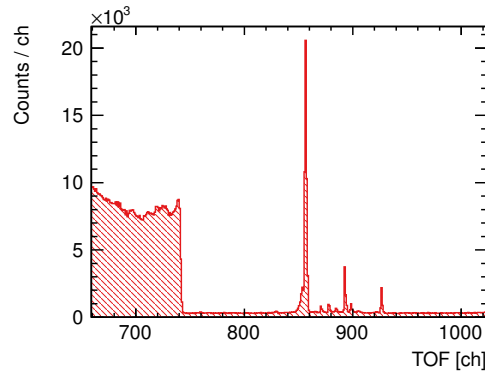
(k) LAB + 3 g/lPPO + 0.1% Nd, LG.



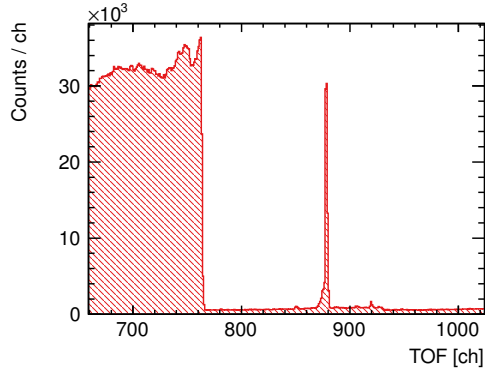
(l) LAB + 3 g/lPPO + 0.1% Nd, HG.



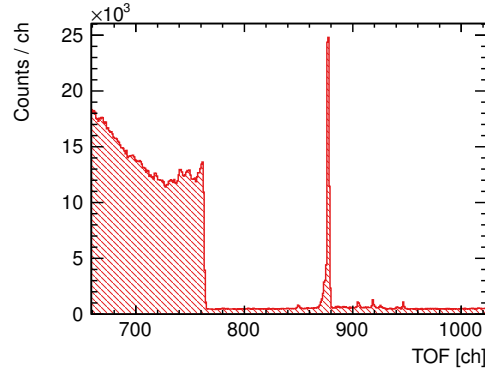
(m) wsLAB + 2 g/l PPO + 15 mg/l bis-MSB + 0.3% Te, LG.



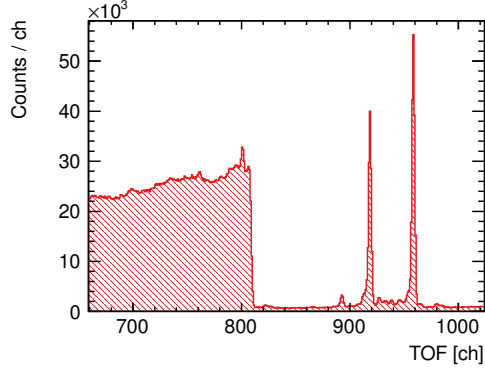
(n) wsLAB + 2 g/l PPO + 15 mg/l bis-MSB + 0.3% Te, HG.



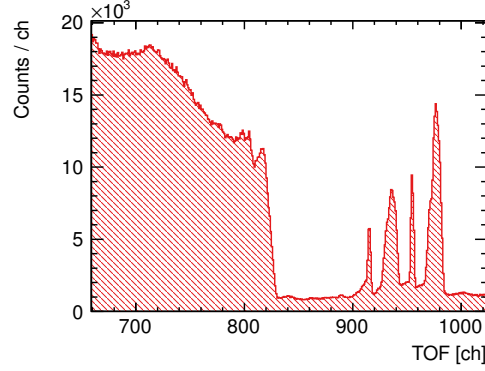
(o) wsLAB + 2 g/l PPO + 15 mg/l bis-MSB, LG.



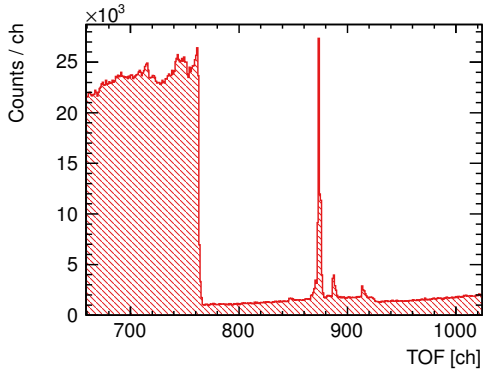
(p) wsLAB + 2 g/l PPO + 15 mg/l bis-MSB, HG.



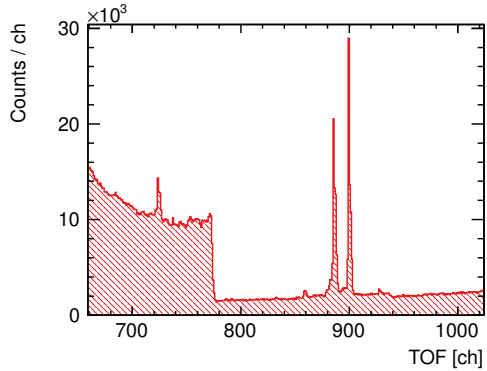
(q) wsLAB + 2 g/l PPO + 15 mg/l perylene, LG.



(r) wsLAB + 2 g/l PPO + 15 mg/l perylene, HG.



(s) wsLAB + 2 g/l PPO + 45 mg/l bis-MSB, LG.



(t) wsLAB + 2 g/l PPO + 45 mg/l bis-MSB, HG.

**Figure B.20:** TOF distribution in LAB and wsLAB scintillators measured during beam time before satellite correction. The specific scintillator and amplification mode is given in the subcaptions. The PRS and water content in wsLAB is 5% and 1.5%, respectively.

## Appendix C

# Relativistic kinematics of the two-body $^{12}\text{C}(n,\alpha)^9\text{Be}$ reaction

This chapter outlines the relativistic kinematics of the reaction  $^{12}\text{C}(n,\alpha)^9\text{Be}$  that are necessary to determine the maximum kinetic energy of the emitted  $\alpha$ -particle, i.e. of the projectile. The following calculation is based on Lorentz-invariant quantities, where  $s$  denotes the squared invariant mass of the reaction. Quantities in the center-of-mass frame are indexed with 'cm'. The numbering scheme of the four participating particles with mass  $m$  follows  $m_1(m_2, m_3)m_4$ . The total particle energy is denoted with  $E_i$  and  $E'_j$ , the particle momentum with  $p_i$  and  $p'_j$  and the kinetic energy with  $T_i$  and  $T'_j$ , where  $i = (1, 2)$  and  $j = (3, 4)$ . In this scheme, the wanted maximum kinetic  $\alpha$ -particle energy reads  $T'_{3,\max}$ .

The target nucleus  $^{12}\text{C}$  is assumed to be at rest and the incident neutron, i.e. the projectile, has a kinetic energy  $T_2$ . Without loss of generality, the projectile direction is chosen along the positive  $z$ -axis. The four-vectors in the laboratory frame hence are

$$\mathbf{p}_1 = (m_1, 0, 0, 0), \quad (\text{C.1})$$

$$\mathbf{p}_2 = (E_2, 0, 0, p_2), \quad (\text{C.2})$$

$$\mathbf{p}_3 = (E_3, 0, p_3 \sin \theta_3, p_3 \cos \theta_3), \quad (\text{C.3})$$

$$\mathbf{p}_4 = (E_4, 0, p_4 \sin \theta_4, p_4 \cos \theta_4), \quad (\text{C.4})$$

where  $\theta$  is the angle between the particle direction and the  $z$ -axis. The squared invariant mass in the laboratory frame is in this case given by

$$\begin{aligned} s &= \left( \sum_{i=1,2} E_i \right)^2 - \left( \sum_{i=1,2} p_i \right)^2 \\ &= (m_1 + m_2)^2 + 2m_1 T_2, \end{aligned} \quad (\text{C.5})$$

and in the center-of-mass frame by

$$s = \left( \sqrt{m_1^2 + p_{\text{cm}}^2} + \sqrt{m_2^2 + p_{\text{cm}}^2} \right)^2, \quad (\text{C.6})$$

where the initial particle momenta  $p_1$  and  $p_2$  are equal and opposite and  $p_{\text{cm}} \equiv |p_1| = |p_2|$ . Further algebraic manipulation yields the total center–of–mass momentum

$$p_{\text{cm}} = \sqrt{\frac{(s - m_1^2 - m_2^2)^2 - 4m_1^2m_2^2}{4s}}. \quad (\text{C.7})$$

It is analogously derived for the final state particles and is thus

$$p'_{\text{cm}} = \sqrt{\frac{(s - m_3^2 - m_4^2)^2 - 4m_3^2m_4^2}{4s}}. \quad (\text{C.8})$$

A useful quantity to express the Lorentz transformation is the rapidity  $\varphi$ , which is defined such that the Lorentz factor is  $\gamma = \cosh \varphi$  and the relativistic beta is  $\beta = \tanh \varphi$  and thus  $\beta\gamma = \sinh \varphi$ . Using these equalities, the particle energy and momentum read in the center–of–mass frame

$$E_{\text{cm}}^{(\prime)} = \sqrt{m^2 + p_{\text{cm}}^{(\prime)2}} = m \cosh \varphi, \quad (\text{C.9})$$

$$p_{\text{cm}}^{(\prime)} = m \sinh \varphi. \quad (\text{C.10})$$

The back–transformation of the particle energy from the center–of–mass to the laboratory frame in this notation is performed as per

$$E^{(\prime)} = E_{\text{cm}}^{(\prime)} \cosh \varphi + p_{\text{cm},z}^{(\prime)} \sinh \varphi, \quad (\text{C.11})$$

$$= \sqrt{m^2 + p_{\text{cm}}^{(\prime)2}} \cosh \varphi + p_{\text{cm}}^{(\prime)} \cos \theta_{\text{cm}} \sinh \varphi. \quad (\text{C.12})$$

Knowing the rapidity, the ejectile energy thus directly follows from Eq. C.8 and C.12. The rapidity is derived from Eq. C.9, C.10 and the trigonometric equality  $e^\varphi = \sinh \varphi + \cosh \varphi$  and yields

$$\varphi_{\text{cm}} = \ln \left( \frac{p_{\text{cm}} + \sqrt{m_1^2 + p_{\text{cm}}^2}}{m_1} \right). \quad (\text{C.13})$$

The quantity of interest within this chapter is the maximum kinetic energy of the ejectile. The particle reaches the maximum total energy, when  $\cos \theta_{\text{cm}} = 1$  in Eq. C.12, i.e. when the scattering angle towards the  $z$ –axis is zero, which yields

$$E_3^{\max} = \sqrt{m_3^2 + p_{\text{cm}}'^2} \cosh \varphi + p_{\text{cm}}' \sinh \varphi. \quad (\text{C.14})$$

The maximum kinetic energy of the  $\alpha$ –particle can now be calculated from the known kinetic neutron energy  $T_2$ , using the above equations and

$$T'_{3,\max} = E_3^{\max} - m_3. \quad (\text{C.15})$$

## Appendix D

# Numerical neutrino energy reconstruction from the proton recoil spectrum

This chapter describes a numerical approach for the reconstruction of the incoming neutrino energy  $E_\nu$  from the visible energy  $E_{\text{vis}}$  of  $\nu$ - $p$  elastic scattering events. The approach is based on the scheme presented in [92]. The aim of the reconstruction is the inversion of

$$\frac{dN}{dE_{\text{vis}}}(E_\nu) = \int_{E_\nu^{\min}}^{\infty} N_p \frac{dE_p}{dE_{\text{vis}}} \frac{d\sigma}{dE_p}(E_\nu) \frac{dN}{dE_\nu} dE_\nu, \quad (\text{D.1})$$

which describes the calculation of the visible energy spectrum  $dN/dE_{\text{vis}}$  from the incoming neutrino energy spectrum  $dN/dE_\nu$ .  $N_p$  is the number of target protons,  $dE_p/dE_{\text{vis}}$  is the proton response function, commonly described by Birks' law Eq. 2.12, and  $d\sigma/dE_p$  is the differential cross section of the process.  $E_\nu^{\min}$  is the minimal neutrino energy, which is necessary to reach a kinetic proton energy  $E_p$ .

### D.1 Numerical solution of first-kind Volterra integral equations

Equation D.1 is a linear Volterra integral equation of the first kind:

$$g(t) = \int_{a=t}^b K(t, s) f(s) ds, \quad (\text{D.2})$$

where  $g(t)$  is known and  $f(s)$  is the unknown function to be solved for. The function of both variables,  $K(t, s)$ , is also called kernel with

$$K(t, s) = 0 \quad \text{for} \quad s < t. \quad (\text{D.3})$$

To solve integral equations numerically, any kind of quadrature rule

$$\int_a^b y(x)dx \approx \sum_{j=0}^H w_j y(x_j) \quad (\text{D.4})$$

is typically used, where  $w_j$  are weights and  $x_j$  the abscissas of the quadrature rule.

The simplest scheme is given by Newton–Cotes rules, which evaluate the integrand on a grid with constant step size as per

$$x_j = a + jh, \quad j = 0, 1, \dots, H, \quad h \equiv \frac{b-a}{H}. \quad (\text{D.5})$$

In this equation,  $H$  is the number of steps with step size  $h$ . The points of the grid are also known as quadrature points. Two well-known Newton–Cotes rules are the extended trapezoidal rule

$$\int_a^b y(x)dx \approx h \left( \frac{y(x_0)}{2} + \sum_{j=1}^{H-1} y(x_j) + \frac{y(x_H)}{2} \right) \quad (\text{D.6})$$

and the extended midpoint rule

$$\int_a^b y(x)dx \approx h \sum_{j=0}^{H-1} y(x'_j) \quad (\text{D.7})$$

with

$$x'_j = \frac{x_j + x_{j+1}}{2}. \quad (\text{D.8})$$

A comparison of the two rules shows that the trapezoidal rule uses  $H + 1$  abscissas, which are identically equal to the quadrature points, while the midpoint rule uses  $H$  points, which are shifted with respect to the quadrature points. The meaning of this difference will become important in the next section.

Applying Eq. D.4 to Eq. D.2 yields

$$g(t) \approx \sum_{j=0}^H w_j K(t, s_j) f(s_j). \quad (\text{D.9})$$

Evaluating this equation at the quadrature points

$$\begin{aligned} g(t_i) &\approx \sum_{j=0}^H w_{ij} K(t_i, s_j) f(s_j) \\ &= \sum_{j=0}^H \tilde{K}(t_i, s_j) f(s_j) \end{aligned} \quad (\text{D.10})$$

with

$$\tilde{K}(t_i, s_j) = w_{ij} K(t_i, s_j), \quad (\text{D.11})$$

Eq. D.2 can be written in matrix notation:

$$\tilde{\mathbf{K}} \cdot \mathbf{f} \approx \mathbf{g}. \quad (\text{D.12})$$

When  $\mathbf{g}$  is nonzero and  $\tilde{\mathbf{K}}$  is invertible, Eq. D.12 has a unique solution  $\mathbf{f} = \tilde{\mathbf{K}}^{-1} \cdot \mathbf{g}$ , where  $\tilde{\mathbf{K}}^{-1}$  is the matrix inverse. As a consequence of Eq. D.3,  $\mathbf{K}$ , and thus also  $\tilde{\mathbf{K}}$ , is upper triangular with zero entries below the diagonal. Matrix equations of this kind are trivially solvable by backward substitution

$$f_i \approx \frac{1}{\tilde{K}_{ii}} \left[ g_i - \sum_{j=i+1}^H \tilde{K}_{ij} f_j \right]. \quad (\text{D.13})$$

In case the trapezoidal rule Eq. D.6 is used for numerical integration, the approximation of  $f(s)$  at the abscissas is given by

$$f_i \approx \frac{2}{K_{ii}} \left[ \frac{g_i}{h} - \sum_{j=i+1}^{H-1} K_{ij} f_j - \frac{K_{iH} f_H}{2} \right]. \quad (\text{D.14})$$

If, instead, the midpoint rule Eq. D.7 is applied, it is given by

$$f_i \approx \frac{1}{h K_{ii}} \left[ g_i - h \sum_{j=i+1}^{H-1} K_{ij} f_j \right]. \quad (\text{D.15})$$

Note that the values of the vector  $\mathbf{f}(s_i)$  in Eq. D.14 and Eq. D.15 are evaluated at different points and that the entries in the matrix  $\mathbf{K}(t_i, s_j)$  are not identical as the abscissas are shifted from  $s_j$  to  $s'_j$  (see Eq. D.8). Given the trapezoidal rule,  $\mathbf{f}(s_i)$  and  $\mathbf{g}(t_i)$  are of dimension  $n = H + 1$  and  $\mathbf{K}(t_i, s_j)$  is an  $n \times n$  matrix, whereas in case of the midpoint rule  $\mathbf{f}(s_i)$  has the dimension  $m = H$  and  $\mathbf{K}(t_i, s_j)$  is an  $n \times m$  matrix.

### D.1.1 Application to a supernova event spectrum

In this section, the integral Eq. D.1 is solved, using the above methods. The visible spectrum  $dN/dE_{\text{vis}}$  is based on the reference SN (see Sec. 7.1), occurring at a distance from the Earth of 10 kpc and being observed by 1 kt of LAB based scintillator. Furthermore, a trigger threshold of 200 keV visible energy is considered.

The variables  $s$  and  $t$  in the Volterra equation Eq. D.2 are given by the neutrino kinetic energy  $E_\nu$  and the minimal neutrino kinetic energy  $E_\nu^{\min}$  necessary to obtain a proton with a kinetic energy of  $E_p$ , respectively. When a neutrino with a true energy  $E_\nu$  scatters off a proton, the proton kinetic energy ranges from 0 to  $E_p^{\max}$ , where

$$E_p^{\max} = \frac{2E_\nu^2}{m_p + 2E_\nu} \quad (\text{D.16})$$

and hence

$$E_\nu^{\min} = \frac{E_p + \sqrt{2m_p E_p + E_p^2}}{2}, \quad (\text{D.17})$$

where  $m_p$  is the proton mass. Using Eq. D.17 and  $E_p(E_{\text{vis}})$  from the inverse of Birks' law Eq. 2.12, the variable  $E_{\text{vis}}$  in Eq. D.1 is substituted by  $E_\nu^{\min}$ . The measured energy spectrum of recoiled protons  $dN/dE_{\text{vis}}(E_\nu^{\min})$  provides the function  $g(E_\nu^{\min})$ , the kernel is calculated as per

$$K(E_\nu^{\min}, E_\nu) = N_p \frac{dE_p}{dE_{\text{vis}}}(E_\nu^{\min}) \frac{d\sigma}{dE_p}(E_\nu^{\min}, E_\nu) \quad (\text{D.18})$$

and the supernova neutrino fluence  $dN/dE_\nu(E_\nu)$  is the unknown function  $f(E_\nu)$ . Figure D.1a shows the known function  $g(E_\nu^{\min}) = dN/dE_{\text{vis}}(E_\nu^{\min})$  and Fig. D.1b and D.1c show the integrand of Eq. D.2,  $K(E_\nu^{\min}, E_\nu)f(E_\nu)$ , exemplary at  $E_\nu^{\min} = 34.34 \text{ MeV}$  (or  $E_{\text{vis}} = 0.71 \text{ MeV}$ ). These two figures furthermore show the approximation of the integrand using the trapezoidal (Eq. D.6) and the midpoint (Eq. D.7) quadrature rule.

The measuring interval ranges from the trigger threshold of  $E_{\text{vis}} = 200 \text{ keV}$  to  $E_{\text{vis}} = 5.00 \text{ MeV}$ , where the observed proton recoil spectrum drops below 0.1 events/MeV in the given example. This corresponds to a  $E_\nu^{\min}$  interval from 21.90 MeV to 71.66 MeV. Using the trapezoidal rule to conduct the numerical integration, the lower limits  $E_{\nu,i}^{\min}$  to yield the respective value  $g(E_{\nu,i}^{\min})$  run along the same grid as the abscissas used within each integration. Hence  $\mathbf{K}(E_{\nu,i}^{\min}, E_{\nu,j})$  is a  $n \times n$  matrix, as mentioned earlier, whereas the abscissas are shifted in case the midpoint rule is applied and  $\mathbf{K}(E_{\nu,i}^{\min}, E_{\nu,j})$  reduces to a  $n \times m$  matrix (see Fig. D.1b and D.1c).  $\mathbf{K}$  needs to be quadratic though, in order to be invertible. Thus a further abscissa is appended without changing the integral as this step is consistent with adding a zero.

Assuming in the next step that the values  $g(E_{\nu,i}^{\min})$  are known from measurement, the unknown function  $f(E_\nu)$  can be approximated using Eq. D.14 and D.15. The numerical approximation naturally improves with decreasing step size. The minimal step size possible is given by the known values of  $g(E_{\nu,i}^{\min})$  and thus by the bin width of the data. The minimal step size reasonable is given by the statistics in the individual data bins. To enable the assumption of a Gaussian distribution of the bin content, bins with <5 events must be merged, bins with <10 entries should be merged. In the next step, the horizontal axis of the data has to be rescaled, since the proton recoil spectrum  $dN/dE_{\text{vis}}$  is measured as a function of quenched proton energy  $E_{\text{vis}}$ , not as a function of the respective minimal neutrino energy  $E_\nu^{\min}$ . The bin centers finally provide the quadrature points  $E_{\nu,i}^{\min}$ . However, even starting from uniformly binned data, the quadrature points are not equidistant since the translation from  $E_{\text{vis}}$  to  $E_\nu^{\min}$  is not linear. Consequently, Eq. D.14 and D.15 need to be generalized to allow for a variable step size:

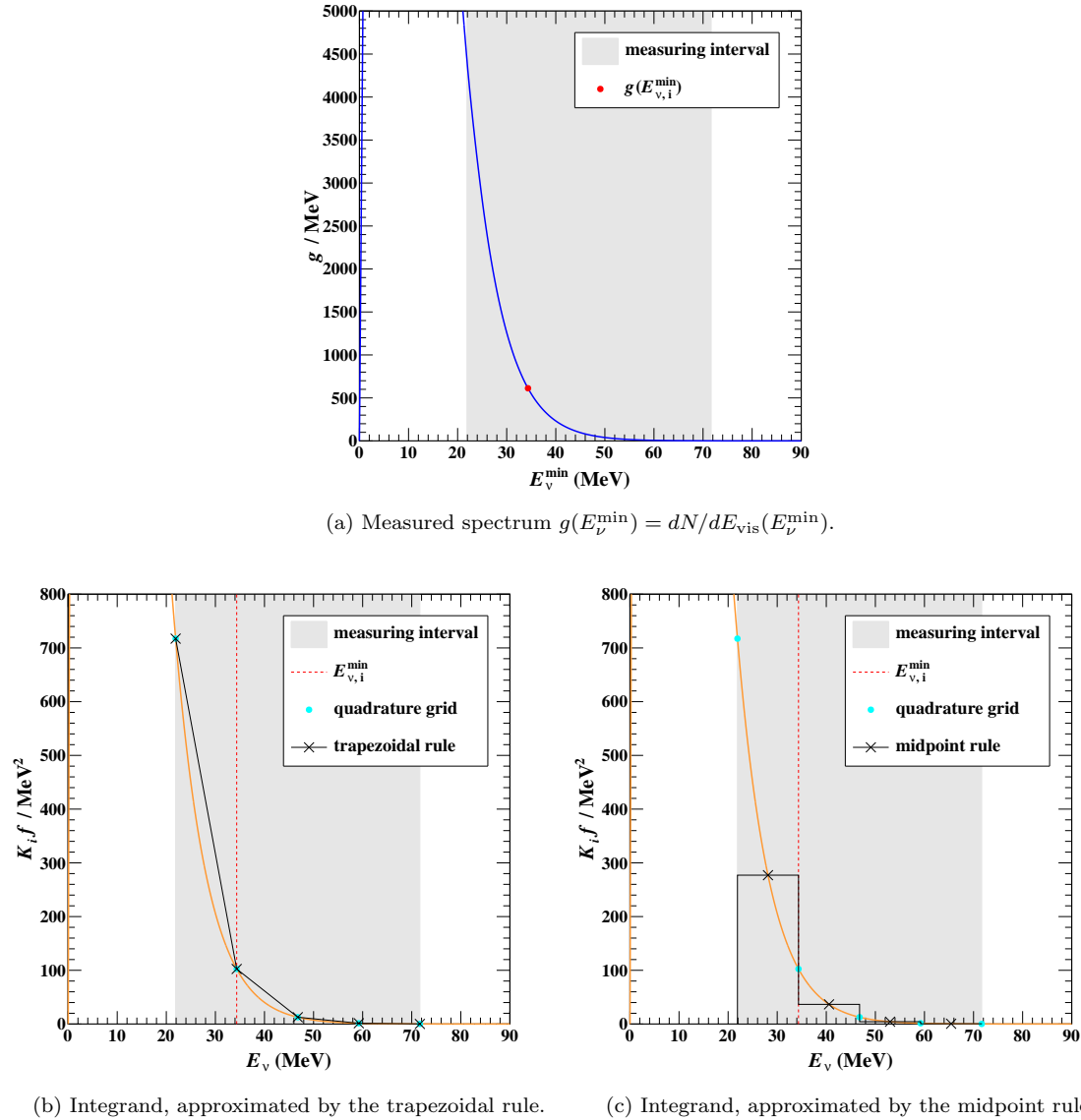


**Figure D.1:** Components of the Volterra integral Eq. D.2, assuming the explicit form Eq. D.1. (a) shows the known function  $g(E_\nu^{\min})$  (blue solid line), i.e. the measurement  $dN/dE_{\text{vis}}$  as function of  $E_\nu^{\min}$ , and marks one distinct value  $E_{\nu,i}^{\min}$  (red point). (b-c) shows the integrand of Eq. D.2, where the kernel entries  $K_i$  at  $E_{\nu,i}^{\min}$  over  $E_\nu$  are described by Eq. D.18 and where the function  $f(E_\nu)$  to be solved for is given by the neutrino energy spectrum  $dN/dE_\nu$ . The red dashed line marks the value of  $E_{\nu,i}^{\min}$ , i.e. the lower limit of the integral to be solved. The cyan points mark the quadrature points used for the numerical integration, the black crosses indicate the abscissas of the quadrature rule and the black solid line indicates the corresponding approximation of the function between two quadrature points. (a) uses the trapezoidal quadrature rule for the approximation and (b) the quadrature midpoint rule. The gray area corresponds to the energy range above the trigger threshold.

$$f_i \approx \frac{2}{K_{ii}h_i} \left[ g_i - \sum_{j=i+1}^{H-1} \left( \frac{h_{j-1} + h_j}{2} \right) K_{ij} f_j - \frac{h_H}{2} K_{iH} f_H \right], \quad (\text{D.19})$$

$$f_i \approx \frac{1}{h_i K_{ii}} \left[ g_i - \sum_{j=i+1}^{H-1} h_j K_{ij} f_j \right]. \quad (\text{D.20})$$

### D.1.2 Propagation of statistical uncertainties

The covariance matrix  $\mathbf{V}_g$  of the vector  $\mathbf{g}(E_\nu^{\min})$  of observables contains at this point only statistical Poisson fluctuations, i.e. the diagonal elements are  $\sigma_{g_i}^2 = N_i$ , the off-diagonal are  $\sigma_{g_i}\sigma_{g_j} = 0$ . The uncertainties within the reconstructed vector  $\mathbf{f}(E_\nu)$  are correlated and the covariance matrix  $\mathbf{V}_f$  is calculated from  $\mathbf{V}_g$  according to

$$\mathbf{V}_f = \tilde{\mathbf{K}}^{-1} \cdot \mathbf{V}_g \cdot \tilde{\mathbf{K}}^{-1 T}. \quad (\text{D.21})$$

In the above section, two different quadrature rules are presented in order to calculate the entries of the weighted kernel  $\tilde{\mathbf{K}}$ , given here in matrix representation. The weights  $w_{ij}$  in this calculation are very different for both rules, while the unweighted kernels  $\mathbf{K}$  agree within the percent level. As a consequence, the derived covariance matrices strongly deviate from each others. This instance, and its impact, will be explained in detail in the following subsection.

#### Simplified example

Starting from a simplified example with three quadrature points and equidistant steps  $h$  along  $s$  within the numerical integration of  $f(s)$  results in a  $3 \times 3$  kernel  $\mathbf{K}$ .  $\tilde{\mathbf{K}}$  is then given by

$$\tilde{\mathbf{K}} = \begin{pmatrix} w_{11}K_{11} & w_{12}K_{12} & w_{13}K_{13} \\ 0 & w_{22}K_{22} & w_{23}K_{23} \\ 0 & 0 & w_{33}K_{33} \end{pmatrix} \quad (\text{D.22})$$

using Eq. D.11. Comparing Eq. D.13 with Eq. D.14 and D.15 shows that in the case of the midpoint rule all weights are identical, with  $w_{ij} = h$ , while the weights using the trapezoidal rule are different on the diagonal and in the last column with  $w_{ii} = w_{iH} = h/2$ . The inverse matrix for the latter case is given by

$$\tilde{\mathbf{K}}^{-1} = \begin{pmatrix} 2 \cdot \frac{1}{hK_{11}} & -4 \cdot \frac{K_{12}}{hK_{11}K_{22}} & 4 \cdot \frac{K_{12}K_{23}}{hK_{11}K_{22}K_{33}} - 2 \cdot \frac{K_{13}}{hK_{11}K_{33}} \\ 0 & 2 \cdot \frac{1}{hK_{22}} & -2 \cdot \frac{K_{23}}{hK_{22}K_{33}} \\ 0 & 0 & 2 \cdot \frac{1}{hK_{33}} \end{pmatrix} \quad (\text{D.23})$$

$$= \begin{pmatrix} 2 \cdot \kappa_{11} & -4 \cdot \kappa_{12} & 4 \cdot \kappa_{13,a} - 2 \cdot \kappa_{13,b} \\ 0 & 2 \cdot \kappa_{22} & -2 \cdot \kappa_{23} \\ 0 & 0 & 2 \cdot \kappa_{33} \end{pmatrix},$$

where the pre-factors (highlighted in red) are all equal to one in the case of the midpoint rule.

Since only statistical uncertainties  $\sigma_{g_i} = \sigma_{g_i,\text{stat}}$  are considered here, the covariance matrix  $\mathbf{V}_g$  of the observables is given by

$$\mathbf{V}_g = \begin{pmatrix} \sigma_{g_1}^2 & 0 & 0 \\ 0 & \sigma_{g_2}^2 & 0 \\ 0 & 0 & \sigma_{g_3}^2 \end{pmatrix}. \quad (\text{D.24})$$

The difference in  $\tilde{\mathbf{K}}^{-1}$  and its transposed further propagates into the covariance matrix  $\mathbf{V}_f$  applying Eq. D.21:

$$\begin{aligned}
 \mathbf{V}_f = & \begin{pmatrix} 4\kappa_{11}^2\sigma_{g_1}^2 + 16\kappa_{12}^2\sigma_{g_2}^2 + (4\kappa_{13,a} - 2\kappa_{13,b})^2\sigma_{g_3}^2 & 0 & 0 \\ 8\kappa_{22}\kappa_{12}\sigma_{g_2}^2 + (8\kappa_{13,a}\kappa_{23} - 4\kappa_{13,b}\kappa_{23})\sigma_{g_3}^2 & 0 & 0 \\ (8\kappa_{13,a}\kappa_{33} - 4\kappa_{13,b}\kappa_{33})\sigma_{g_3}^2 & 0 & 0 \end{pmatrix} \\
 + & \begin{pmatrix} 0 & 8\kappa_{12}\kappa_{22}\sigma_{g_2}^2 + (8\kappa_{13,a}\kappa_{23} - 4\kappa_{13,b}\kappa_{23})\sigma_{g_3}^2 & 0 \\ 0 & 4\kappa_{22}^2\sigma_{g_2}^2 + 4\kappa_{23}^2\sigma_{g_3}^2 & 0 \\ 0 & 4\kappa_{23}\kappa_{33}\sigma_{g_3}^2 & 0 \end{pmatrix} \quad (D.25) \\
 + & \begin{pmatrix} 0 & 0 & (8\kappa_{13,a}\kappa_{33} - 4\kappa_{13,b}\kappa_{33})\sigma_{g_3}^2 \\ 0 & 0 & 4\kappa_{23}\kappa_{33}\sigma_{g_3}^2 \\ 0 & 0 & 4\kappa_{33}^2\sigma_{g_3}^2 \end{pmatrix}.
 \end{aligned}$$

The values of the pre-factors, which additionally enter the covariance matrix  $\mathbf{V}_f$  in case of the trapezoidal rule, become larger with an increasing number of quadrature points, or in other words, with a finer binning of the data set. In the same time, the entries of the unweighted kernels  $\mathbf{K}$  become more and more similar using either of the two rules. Thus the covariance matrices  $\mathbf{V}_f$ , deduced from the two rules, increasingly deviate from each others. As a consequence, not only the correlations between the bins are considered to be differently strong, but also the statistical uncertainty per reconstructed  $E_\nu$  bin derived from the diagonal of  $\mathbf{V}_f$  varies significantly, even though the event statistics is the same.

These findings show that in case of the presented numerical approach, the covariance matrix depends on the numerical integration method. This dependency is further propagated into any sensitivity study to spectral parameters of SN neutrinos, using  $\nu$ - $p$  ES. Thus this approach is not further followed in the context of this thesis, since no conclusive statement about detector sensitivities is possible in this case.

## List of Acronyms

<b>ADC</b>	analog-to-digital converter .....	92
<b>AV</b>	acrylic vessel.....	72
<b>bis-MSB</b>	p-bis-(o-methylstyryl)-benzene	
<b>BNL</b>	Brookhaven National Laboratory .....	71
<b>BPU</b>	beam pick-up unit .....	93
<b>CC</b>	charged current .....	34
<b>CFD</b>	constant fraction discriminator.....	90
<b>CCSN</b>	core collapse supernova .....	23
<b>CMB</b>	cosmic microwave background.....	51
<b>CTF</b>	Counting Test Facility .....	182
<b>DAQ</b>	data acquisition.....	84
<b>EDF</b>	Energy Density Functional method.....	67
<b>EOS</b>	equation of state.....	31
<b>ES</b>	elastic scattering.....	158
<b>FV</b>	fiducial volume .....	157
<b>FWHM</b>	full width at half maximum .....	98
<b>HG</b>	high gain .....	93
<b>HZDR</b>	Helmholtz-Zentrum Dresden Rossendorf .....	85
<b>IBD</b>	inverse beta decay .....	24
<b>IBM-2</b>	Interacting Boson Model-2.....	67
<b>IH</b>	inverted hierarchy.....	57
<b>LAB</b>	linear alkylbenzene.....	1
<b>LG</b>	low gain .....	93
<b>LMC</b>	Large Magellanic Cloud	
<b>LS</b>	liquid scintillator.....	5
<b>LSSM</b>	Large-Scale Shell Model .....	67
<b>LTE</b>	local thermodynamic equilibrium .....	46
<b>MC</b>	Monte Carlo .....	2
<b>MSW</b>	Mikheyev-Smirnov-Wolfenstein .....	52

<b>NC</b>	neutral current .....	23
<b>NH</b>	normal hierarchy .....	57
<b>NME</b>	nuclear matrix element .....	66
<b>NS</b>	neutron star .....	37
<b>NSE</b>	nuclear statistical equilibrium .....	30
<b>PC</b>	pseudocumene (1,2,4-trimethylbenzene)	
<b>PH</b>	pulse-height .....	91
<b>PHFB</b>	Projected Hartree–Fock–Bogoliubov approach .....	67
<b>PIAF</b>	PTB Ion Accelerator Facility .....	84
<b>PMMA</b>	poly(methyl methacrylate) .....	91
<b>PMT</b>	photomultiplier tube .....	72
<b>PNS</b>	protoneutron star .....	33
<b>POPOP</b>	2,2'-p-phenylene-bis-(5-phenyloxazole) .....	6
<b>PPO</b>	2,5-diphenyloxazole	
<b>PDF</b>	probability density function .....	190
<b>PRS</b>	photoreactive surfactant .....	1
<b>PS</b>	pulse-shape .....	92
<b>PSD</b>	pulse-shape discrimination .....	93
<b>PSUP</b>	photomultiplier tube support structure .....	72
<b>PTB</b>	Physikalisch–Technische Bundesanstalt .....	84
<b>QD</b>	quasi degenerate .....	57
<b>QRPA</b>	Quasi-particle Random Phase Approximation .....	67
<b>RAT</b>	Reactor Analysis Tool	
<b>ROI</b>	region of interest .....	69
<b>SASI</b>	standing accretion shock instability .....	37
<b>SM</b>	Standard Model .....	51
<b>SN</b>	supernova .....	23
<b>TAC</b>	time-to-amplitude converter .....	93
<b>TOF</b>	time-of-flight .....	88
<b>TSCA</b>	time single channel analyzer .....	93
<b>UV</b>	ultraviolet .....	8
<b>wSLAB</b>	water–surfactant–LAB .....	74
$0\nu\beta\beta$	neutrinoless double beta .....	1
$2\nu\beta\beta$	two-neutrino double beta .....	68

# List of Figures

2.1	Absorption and fluorescence spectrum of anthracene . . . . .	7
2.2	Absorption and fluorescence spectrum of LAB with and without solutes . . . . .	8
2.3	Molecular orbital formation . . . . .	9
2.4	$sp^3$ hybridization . . . . .	9
2.5	Benzene molecule . . . . .	10
2.6	Jablonski diagram . . . . .	11
2.7	Scintillation light pulse with fast and slow component . . . . .	12
2.8	The scintillation processes in a ternary organic liquid scintillator . . . . .	15
2.9	Measured scintillation time profiles from $\alpha$ - and $\beta$ -particle excitation . . . . .	19
2.10	Differential light yield of anthracene to different charged particles . . . . .	20
2.11	Total light yield of NE102 plastic scintillators to different charged particles	21
2.12	Surface effect on light response . . . . .	22
3.1	Supernova taxonomy . . . . .	24
3.2	Remnants and SN types of massive single stars as function of initial metallicity and mass . . . . .	28
3.3	Schematic shell structure of a supernova progenitor . . . . .	30
3.4	Final stages of massive star evolution . . . . .	31
3.5	Exemplary neutrino luminosity evolution over post-bounce time . . . . .	32
3.6	Neutrino energy- and transportsphere . . . . .	35
3.7	Comparison of pinched and unpinched thermal distributions . . . . .	36
3.8	Supernova distance probability distribution . . . . .	39
3.9	Electron neutrino luminosity over time from simulation . . . . .	43
3.10	Electron anti-neutrino luminosity over time from simulation . . . . .	43
3.11	Muon/tau (anti-)neutrino luminosity over time from simulation . . . . .	43
3.12	Electron neutrino mean energy over time from simulation . . . . .	44
3.13	Electron anti-neutrino mean energy over time from simulation . . . . .	44
3.14	Muon/tau (anti-)neutrino mean energy over time from simulation . . . . .	44
3.15	Electron neutrino second energy moment over time from simulation . . . . .	45
3.16	Electron anti-neutrino second energy moment over time from simulation . . . . .	45
3.17	Muon/tau (anti-)neutrino second energy moment over time from simulation	45
3.18	Comparison of the degeneracy parameter $\eta$ and the shape parameter $\beta$ . . . . .	47

3.19	Electron neutrino energy shape parameter over time from simulation . . . . .	49
3.20	Electron anti-neutrino energy shape parameter over time from simulation . .	49
3.21	Muon/tau (anti-)neutrino energy shape parameter over time from simulation	49
4.1	Supernova neutrino energy spectra before and after collective oscillations . .	52
4.2	Level crossing scheme of the MSW effect . . . . .	62
4.3	Level crossing scheme of the MSW effect in a SN environment . . . . .	63
4.4	Feynman diagram of the $0\nu\beta\beta$ decay . . . . .	67
4.5	Effective Majorana mass as function of the lightest neutrino mass . . . . .	69
4.6	Nuclear matrix elements of $0\nu\beta\beta$ decaying isotopes . . . . .	69
5.1	Schematic view of the SNO+ detector . . . . .	73
5.2	SNO+ $T_{1/2}^{0\nu}$ sensitivity over time . . . . .	80
5.3	SNO+ energy spectrum in the region of interest for $^{130}\text{Te}$ $0\nu\beta\beta$ decay . . .	80
6.1	Absorption and emission spectra of Nd-loaded LAB . . . . .	87
6.2	PIAF time-of-flight spectrometer . . . . .	89
6.3	Spectral neutron distribution from $^9\text{Be}(p,n)^9\text{B}$ . . . . .	90
6.4	Liquid scintillator detector . . . . .	91
6.5	Liquid scintillator detector wavelength dependencies . . . . .	92
6.6	Time calibration spectrum . . . . .	94
6.7	Major gamma interactions . . . . .	95
6.8	Calibration source measurements in LAB1 and HG mode . . . . .	96
6.9	Calibration source measurements in LAB6 and HG mode . . . . .	97
6.10	PH as function of electron energy in LAB scintillators . . . . .	100
6.11	PH as function of electron energy in wsLAB scintillators . . . . .	102
6.12	Emission spectra of Te-loaded wsLAB with perylene . . . . .	103
6.13	Relative light output resolution for gamma-induced events in LAB scintillators	104
6.14	Relative light output resolution for gamma-induced events in wsLAB scin- tillators . . . . .	106
6.15	PH-PS matrix of pseudocumene scintillator . . . . .	108
6.16	PH-PS matrix of LAB and wsLAB scintillators . . . . .	109
6.17	TOF-PH matrix of LAB scintillators . . . . .	111
6.18	TOF-PH matrix of wsLAB1 before and after satellite correction . . . . .	111
6.19	TOF distribution of wsLAB1 before and after a satellite correction . . . . .	112
6.20	TOF-PH matrix of wsLAB3 and wsLAB4 in HG mode . . . . .	113
6.21	Prompt gamma-peak in wsLAB1 . . . . .	114
6.22	Measured PH spectra of neutrons at different energies in wsLAB1 . . . . .	116
6.23	Measured and simulated PH spectrum of 3.5 MeV neutrons in wsLAB1 . . .	118
6.24	Relative light output resolution for neutron-induced events . . . . .	120
6.25	Measured and simulated PH spectrum of neutrons at different energies in wsLAB1 . . . . .	121
6.26	Simulated PH spectrum of $^{12}\text{C}$ 4.439 MeV gammas . . . . .	123

---

6.27	Measured electron and proton light output in LAB1 and wsLAB2 . . . . .	124
6.28	Measured and simulated PH spectrum from protons and $\alpha$ -particles in wsLAB1 . . . . .	125
6.29	Measured and simulated PH spectrum of neutrons at different energies in LAB1 . . . . .	128
6.30	Measured electron and $\alpha$ -particle light output in LAB1 and wsLAB2 . . . . .	129
6.31	Stopping power of various LAB scintillators and their relative difference . .	130
6.32	Test of the linearity of systematic effects . . . . .	132
6.33	Fit of Birks' law to proton data in LAB scintillators . . . . .	135
6.34	Fit of Birks' law to proton data in wsLAB scintillators . . . . .	137
6.35	Birks' parameters for protons in different LAB scintillators . . . . .	138
6.36	Fit of Birks' law to $\alpha$ -particle data in LAB scintillators . . . . .	140
6.37	Fit of Birks' law to $\alpha$ -particle data in wsLAB scintillators . . . . .	141
6.38	$\alpha$ -particle light output functions of LAB1 and wsLAB2 . . . . .	141
6.39	Stopping power of LAB and loaded LAB scintillators and their relative dif- ference . . . . .	146
6.40	Alpha quenching detector for Sm-loaded LAB measurements . . . . .	147
6.41	Charge spectrum of Sm-loaded LAB . . . . .	147
6.42	Bucket source . . . . .	148
6.43	Alpha quenching in LAB from independent measurements . . . . .	150
6.44	Birks' constants for protons and $\alpha$ -particles in different LAB scintillators .	152
7.1	Analytical SN neutrino fluence of a model SN . . . . .	162
7.2	Cross sections of neutrino interactions in liquid scintillator at low energies .	163
7.3	True and visible proton recoil spectrum in a SN burst . . . . .	165
7.4	Visible inverse beta decay spectrum of SN neutrinos . . . . .	166
7.5	Visible energy spectra of exclusive charged current transitions of $^{12}\text{C}$ induced by SN neutrinos . . . . .	169
7.6	Kinetic energy spectra of knockout nucleons produced by SN neutrinos in LAB . . . . .	172
7.7	Visible energy spectra of inclusive transitions of $^{12}\text{C}$ induced by SN neutrinos in LAB . . . . .	173
7.8	Visible energy spectra of $\nu-e$ elastic scattering induced by SN neutrinos in LAB . . . . .	174
7.9	All visible energy spectra induced by SN neutrinos in LAB . . . . .	175
7.10	Background to IBD events from other SN detection channels . . . . .	177
7.11	External backgrounds extrapolated from SNO+ expectations in the AV and within a 5.0 m fiducial radius . . . . .	179
7.12	Surface backgrounds extrapolated from SNO+ expectations within a 5.0 m fiducial radius . . . . .	180
7.13	Internal backgrounds extrapolated from SNO+ expectations . . . . .	181
7.14	Background from solar neutrinos . . . . .	182
7.15	Background to $\nu-p$ ES from other SN detection channels . . . . .	183

7.16 Total background expectation to SN $\nu$ - $p$ elastic scattering in SNO+ . . . . .	184
7.17 Reconstructed and true SN neutrino energy distribution for IBD . . . . .	187
7.18 Minimal neutrino energy necessary to yield a certain visible energy from $\nu$ - $p$ elastic scattering . . . . .	188
7.19 Reconstructed and true SN neutrino energy distribution for $\nu$ - $p$ elastic scattering . . . . .	189
7.20 Fit to single IBD toy MC . . . . .	191
7.21 Best fit parameter distributions after 5 000 toy MC considering 0.45 kt of LAB192	
7.22 Best fit parameter distributions after 5 000 toy MC considering 16.80 kt of LAB . . . . .	194
7.23 Best fit spectrum to the reconstructed neutrino energy spectrum from $\nu$ - $p$ ES198	
7.24 Constraints at 95% C.L. on the spectral parameter space of SN $\nu_x$ by SNO+ .	200
7.25 Constraints at 95% C.L. on the spectral parameter space of SN $\nu_x$ by JUNO .	201
7.26 Constraints at 68.3%, 95.0% and 99.73% C.L. on the spectral parameter space of SN $\nu_x$ by SNO+ . . . . .	202
7.27 Constraints at 68.3%, 95.0% and 99.73% C.L. on the spectral parameter space of SN $\nu_x$ by JUNO . . . . .	203
7.28 Constraints at 68.3%, 95.0% and 99.73% C.L. on the spectral parameter space of SN $\nu_x$ by JUNO using statistical uncertainties only . . . . .	203
7.29 Simulated SN neutrino energy distributions from $\nu$ - $p$ ES without MSW . .	206
7.30 True SN neutrino energy distributions from $\nu$ - $p$ ES after MSW . . . . .	207
 A.1 Uranium and thorium decay chains . . . . .	215
 B.1 Calibration source measurements in LAB1 and LG mode . . . . .	218
B.2 Calibration source measurements in LAB2 and HG mode . . . . .	219
B.3 Calibration source measurements in LAB2 and LG mode . . . . .	220
B.4 Calibration source measurements in LAB3 and HG mode . . . . .	221
B.5 Calibration source measurements in LAB3 and LG mode . . . . .	222
B.6 Calibration source measurements in LAB4 and HG mode . . . . .	223
B.7 Calibration source measurements in LAB4 and LG mode . . . . .	224
B.8 Calibration source measurements in LAB5 and HG mode . . . . .	225
B.9 Calibration source measurements in LAB5 and LG mode . . . . .	226
B.10 Calibration source measurements in LAB6 and LG mode . . . . .	227
B.11 Calibration source measurements in wsLAB1 and HG mode . . . . .	228
B.12 Calibration source measurements in wsLAB1 and LG mode . . . . .	229
B.13 Calibration source measurements in wsLAB2 and HG mode . . . . .	230
B.14 Calibration source measurements in wsLAB2 and LG mode . . . . .	231
B.15 Calibration source measurements in wsLAB3 and HG mode . . . . .	232
B.16 Calibration source measurements in wsLAB3 and LG mode . . . . .	233
B.17 Calibration source measurements in wsLAB4 and HG mode . . . . .	234
B.18 Calibration source measurements in wsLAB4 and LG mode . . . . .	235
B.19 PH-PS matrix of LAB and wsLAB scintillators . . . . .	236

B.20 Prompt gamma-peak in LAB and wsLAB scintillators . . . . .	240
D.1 Components of the Volterra integral applied to $\nu-p$ elastic scattering . . . . .	247



# List of Tables

4.1	Three flavor neutrino oscillation parameters after 2012 . . . . .	58
4.2	Candidate $0\nu\beta\beta$ isotopes . . . . .	68
5.1	Overview over the components of SNO+ scintillators . . . . .	74
5.2	Molecules in the LAB solvent of SNO+ . . . . .	75
5.3	Isotope density and number fraction in SNO+’s LAB with 2 g/l PPO . . . . .	76
5.4	Atom density and number fraction in SNO+’s wsLAB with 2 g/l PPO . . . . .	77
6.1	Constituent mass fractions of the liquid scintillator samples used for measurements . . . . .	86
6.2	Density and H to C ratio of the liquid scintillator samples used for measurements . . . . .	88
6.3	Details of the individual quenching measurement campaigns . . . . .	89
6.4	Time calibration . . . . .	94
6.5	Calibration factor $m$ and PH offset $a$ . . . . .	101
6.6	Light output resolution parameters $\alpha$ , $\beta$ , $\gamma$ for calibration data . . . . .	105
6.7	Prompt gamma–peak centroid . . . . .	115
6.8	Light output resolution parameters $\alpha$ , $\beta$ , $\gamma$ for neutron beam data . . . . .	119
6.9	Systematic and statistic uncertainties of the quenching measurements at PTB131	
6.10	Resulting proton quenching parameters $kB$ and $C$ and their total $1\sigma$ uncertainty . . . . .	136
6.11	Resulting $\alpha$ -particle quenching parameters $kB$ and $C$ and their total $1\sigma$ uncertainty . . . . .	142
6.12	Proton and alpha quenching parameters $kB$ and $C$ after applying a shift of $E_0$ to the light output scale . . . . .	145
7.1	Supernova neutrino interaction channels in liquid scintillator . . . . .	161
7.2	Reference supernova neutrino spectral parameters . . . . .	162
7.3	Internal background isotopes relevant for the SN neutrino obeservation . . . . .	181
7.4	Systematic measurement uncertainties propagated for the determination of the fit parameter systematic uncertainty . . . . .	186
7.5	Fit results for the reference SN, IBD and 0.45 kt of LAB . . . . .	193
7.6	Fit results for the reference SN, IBD and 16.80 kt of LAB . . . . .	195

---

7.7	Results from fits to the reconstructed neutrino spectrum from $\nu$ - $p$ ES . . . . .	199
7.8	$\nu$ - $p$ ES event yield above different trigger thresholds . . . . .	205
7.9	Supernova neutrino spectral parameters from simulation . . . . .	206
7.10	$\nu$ - $p$ ES event yield variation above threshold using different progenitors and EOSs . . . . .	208
A.1	Natural constants and non-SI-units . . . . .	216

## Bibliography

# Bibliography

- [1] H.H. Seliger. Wilhelm Conrad Röntgen and the glimmer of light. *Physics Today*, 48:25–31, 1995.
- [2] S.E. Derenzo, M.J. Weber, E. Bourret-Courchesne, and M.K. Klintenberg. The quest for the ideal inorganic scintillator. *Nucl.Instrum.Meth.*, A505:111–117, 2003.
- [3] I. Broser and H. Kallmann. Über die Anregung von Leuchtstoffen durch schnelle Korpuskularteilchen. 1. (Eine neue Methode zur Registrierung und Energiemessung schwerer geladener Teilchen). *Z. Naturforsch. A - Natur und Technik*, 2:439–440, 1947.
- [4] P.R. Bell. The use of anthracene as a scintillation counter. *Phys. Rev.*, 73:1405, 1948.
- [5] J.B. Birks. Scintillations from naphthalene–anthracene crystals. *Proc. Phys. Soc. A*, 63:1044, 1950.
- [6] H. Kallmann. Scintillation counting with solutions. *Phys. Rev.*, 78:621, 1950.
- [7] M. Ageno, M. Chiozzotto, and R. Querzoli. Scintillations in liquids and solutions. *Phys. Rev.*, 79:720, 1950.
- [8] M.G. Schorr and F.L. Torney. Solid non-crystalline scintillation phosphors. *Phys. Rev.*, 80:474–474, 1950.
- [9] L. Herforth and H. Kallmann. Die Fluoreszensanregung von festem und flüssigem Naphthalin, Diphenyl und Phenanthren durch Alphateilchen, schnelle Elektronen und Gammastrahlung. *Ann. der Physik*, 6:231–245, 1948.
- [10] I. Broser, L. Herforth, H. Kallmann, and U. Martius. Über die Anregung von Leuchtstoffen durch schnelle Korpuskularteilchen. 1. (Eine neue Methode zur Registrierung und Energiemessung schwerer geladener Teilchen). *Z. Naturforsch.*, 3a:6, 1948.
- [11] J.B. Birks. *The Theory and Practice of Scintillation Counting*. Pergamon, New York, USA, 1964.
- [12] E.D. Bransome Jr. et al. *The current status of liquid scintillation counting*. Grune & Stratton, New York, USA, 1970.

- [13] J.R. Lakowicz. *Principles of Fluorescence Spectroscopy*. Springer Science & Business Media, New York, USA, 2006.
- [14] T. Kögler. Pulsformdiskrimination und Lichtausbeutemessungen von LAB-basierten Flüssigszintillatoren, 2011. Diploma thesis. Technische Universität Dresden, Germany.
- [15] Z.H. Cho, I. Ahn, and C.M. Tsai. *IEEE Transactions on Nuclear Science*, NS-21(1):218, 1974.
- [16] C.L. Cowan, Jr., F. Reines, F.B. Harrison, H.W. Kruse, and A.D. McGuire. Detection of the Free Neutrino: A Confirmation. *Science*, 124:103–104, 1956.
- [17] F.P. An et al. Observation of electron-antineutrino disappearance at Daya Bay. *Phys.Rev.Lett.*, 108:171803, 2012, 1203.1669.
- [18] A. Beiser. *Atome, Moleküle, Festkörper*. Vieweg, Braunschweig, 1983. Original edition: *Perspectives of Modern Physics*.
- [19] M. Krammer. Detektoren in der Hochenergiephysik: 5. Szintillatoren. <http://web-docs.gsi.de/~wolle/Schuelerlabor/TALKS/DETEKTOREN/V0-5-Szintillatoren.pdf>. Lecture series, Institute for High Energy Physics ÖAW, Vienna, Austria. Accessed 01 December 2014.
- [20] A. Raviart and V. Koechlin. Analyse per échantillonage sur photon individuelles des liquides fluorescents dans le domaine de la sub-nanoseconds. *Nucl.Instrum.Meth.*, 29:45, 1966.
- [21] B. Bengtson and M. Moszynski. Energy transfer and light-collection characteristics for different types of plastic scintillators. *Nucl.Instrum.Meth.*, 117:227, 1974.
- [22] C.A. Parker and C.G. Hatchard. Delayed fluorescence of pyrene in ethanol. *Trans. Faraday Soc.*, 59:284–295, 1963.
- [23] T. Förster. Zwischenmolekulare Energiewanderung und Fluoreszenz. *Ann.Phys.*, 437:55–75, 1948.
- [24] T. Förster. *Modern Quantum Chemistry* (ed. by O.Sinanoglu), volume III, chapter Delocalized excitation and excitation transfer, page 93. Academic Press, New York, USA, 1965.
- [25] D.L. Horrocks. *Applications of Liquid Scintillation Counting*. Academic Press, New York, USA, 1974.
- [26] E.J. Bowen and A. Norton. The quenching of fluorescence in solution. *Trans. Faraday Soc.*, 35:44–48, 1939.

- [27] C.A. Ziegler and D.J. Cheleck. Ultrasonic Degassing of Liquid Scintillators. *Rev.Sci.Instrum.*, 28:466–467, 1957.
- [28] C. Lan. SNO+ and Geoneutrino Physics, 2007. Master thesis. Queen’s University, Kingston, Ontario, Canada.
- [29] R.W. Pringle, L.D. Black, B.L. Funt, and S. Sobering. A New Quenching Effect in Liquid Scintillators. *Phys.Rev.*, 92:1582–1583, 1953.
- [30] H.-L. Xiao, J.-S. Deng, and N.-Y. Wang. Oxygen quenching in a LAB based liquid scintillator and the nitrogen bubbling model. *Chin.Phys.*, C34(5):571–575, 2010.
- [31] F. Elisei, F. Masetti, U. Mazzucato, F. Gatti, G. Testera, et al. Measurements of liquid scintillator properties for the Borexino detector. *Nucl.Instrum.Meth.*, A400:53–68, 1997.
- [32] B. von Krosigk, L. Neumann, R. Nolte, S. Röttger, and K. Zuber. Measurement of the proton light response of various LAB based scintillators and its implication for supernova neutrino detection via neutrino-proton scattering. *Eur.Phys.J.*, C73:2390, 2013, 1301.6403.
- [33] E. Brannon and G.L. Olde. The existence of a neutron. *Radiat. Res.*, 16:1, 1962.
- [34] C. Aberle, C. Buck, F.X. Hartmann, S. Schönert, and S. Wagner. Light output of Double Chooz scintillators for low energy electrons. *JINST*, 6:P11006, 2011.
- [35] J.B. Birks. Scintillation from organic crystals: specific fluorescence and relative response to different radiations. *Proc. Phys. Soc. A*, 64:874, 1951.
- [36] V.I. Tretyak. Semi-empirical calculation of quenching factors for ions in scintillators. *Astropart.Phys.*, 33:40–53, 2010, 0911.3041.
- [37] C. N. Chou. The nature of the saturation effect of fluorescent scintillators. *Phys. Rev. Lett.*, 87:904–905, Sep 1952.
- [38] A. Grau Malonda and A. Grau Carles. The ionization quench factor in liquid scintillation counting standardizations. *Applied Radiation and Isotopes*, 51:183–188, 1999.
- [39] J.B. Birks and F.D. Brooks. Scintillation response of anthracene to 6-30 kev photoelectrons. *Proc. Phys. Soc. B*, 69:721–730, 1956.
- [40] C.J. Taylor, W.K. Jentschke, M.E. Remley, F.S. Eby, and P.G. Kruger. Response of some scintillation crystals to charged particles. *Phys. Rev.*, 84:1034–1043, 1951.
- [41] Q.R. Ahmad et al. Measurement of the rate of  $\nu_e + d \rightarrow p + p + e^-$  interactions produced by B-8 solar neutrinos at the Sudbury Neutrino Observatory. *Phys.Rev.Lett.*, 87:071301, 2001, nucl-ex/0106015.

- [42] K. Hirata et al. Observation of a Neutrino Burst from the Supernova SN 1987a. *Phys.Rev.Lett.*, 58:1490–1493, 1987.
- [43] T. Haines et al. Neutrinos from SN1987a in the IMB detector. *Nucl.Instrum.Meth.*, A264:28–31, 1988.
- [44] E.N. Alekseev, L.N. Alekseeva, I.V. Krivosheina, and V.I. Volchenko. Detection of the neutrino signal from SN 1987A in the LMC using the INR Baksan underground scintillation telescope. *Phys.Lett.*, B205:209–214, 1988.
- [45] A. Ishihara et al. First observation of PeV-energy neutrinos with IceCube. *e-print*, 2013, astro-ph.HE/1307.0324.
- [46] Hüdepohl, L. and others. Spherically symmetric simulations of the accretion phase for a set of progenitors and EoS. <http://www.mpa-garching.mpg.de/ccsnarchive/data/Huedepohl-1D-Accretion/index.html>, 2013. [Online; accessed 01-March-2014].
- [47] P. D. Serpico, S. Chakraborty, T. Fischer, L. Hüdepohl, H.-T. Janka, et al. Probing the neutrino mass hierarchy with the rise time of a supernova burst. *Phys.Rev.*, D85:085031, 2012, 1111.4483.
- [48] M. Aglietta, G. Badino, G. Bologna, C. Castagnoli, A. Castellina, et al. On the event observed in the Mont Blanc Underground Neutrino observatory during the occurrence of Supernova 1987a. *Europhys.Lett.*, 3:1315–1320, 1987.
- [49] W.D. Arnett, J.N. Bahcall, R.P. Kirshner, and S.E. Woosley. Supernova 1987A. *Ann.Rev.Astron.Astrophys.*, 27:629–700, 1989.
- [50] E. Cappellaro and M. Turatto. Supernova Types and Rates. In D. Vanbeveren, editor, *The Influence of Binaries on Stellar Population Studies*, volume 264 of *Astrophysics and Space Science Library*, page 199, 2001, arXiv:astro-ph/0012455.
- [51] J.C. Niemeyer, M. Reinecke, and W. Hillebrandt. Models of Type Ia supernova explosions. *e-print*, 2002, astro-ph/0203369.
- [52] K. Kotake, K. Sato, and K. Takahashi. Explosion mechanism, neutrino burst, and gravitational wave in core-collapse supernovae. *Rept.Prog.Phys.*, 69:971–1144, 2006, astro-ph/0509456.
- [53] A. Heger, C.L. Fryer, S.E. Woosley, N. Langer, and D.H. Hartmann. How massive single stars end their life. *Astrophys.J.*, 591:288–300, 2003, astro-ph/0212469.
- [54] K. Takahashi, T. Yoshida, and H. Umeda. Evolution of Progenitors for Electron Capture Supernovae. *Astrophys.J.*, 771:28, 2013, 1302.6402.
- [55] S. Chandrasekhar. On Stars, Their Evolution and Their Stability. Technical report, University of Chicago, Chicago, Illinois 60637, USA, 1983. Nobel Prize lecture.

- [56] S.E. Woosley, A. Heger, and T.A. Weaver. The evolution and explosion of massive stars. *Rev.Mod.Phys.*, 74:1015–1071, 2002.
- [57] K. Nomoto, M. Tanaka, N. Tominaga, and K. Maeda. Hypernovae, gamma-ray bursts, and first stars. *New Astronomy Reviews*, 54:191–200, 2010.
- [58] A.J.T. Poelarends, F. Herwig, N. Langer, and A. Heger. The supernova channel of super-agb stars. *The Astrophysical Journal*, 675(1):614, 2008.
- [59] L. Hüdepohl, B. Müller, H.-T. Janka, A. Marek, and G.G. Raffelt. Neutrino Signal of Electron–Capture Supernovae from Core Collapse to Cooling. *Phys.Rev.Lett.*, 104:251101, 2010, 0912.0260.
- [60] T. Fischer, S.C. Whitehouse, A. Mezzacappa, F.-K. Thielemann, and M. Liebendörfer. Protoneutron star evolution and the neutrino driven wind in general relativistic neutrino radiation hydrodynamics simulations. *Astron.Astrophys.*, 517:A80, 2010, 0908.1871.
- [61] S. Wanajo, K. Nomoto, H.-T. Janka, F.S. Kitaura, and B. Mueller. Nucleosynthesis in Electron Capture Supernovae of AGB Stars. *Astrophys.J.*, 695:208–220, 2009, 0810.3999.
- [62] G.G. Raffelt. Neutrinos and the stars. In G. Bellini and L. Ludhova, editors, *Proceedings of the International School of Physics "Enrico Fermi"*, volume 182 of *Neutrino Physics and Astrophysics*, pages 61–xxx, 2011.
- [63] S.E. Woosley and J.S. Bloom. The Supernova Gamma-Ray Burst Connection. *Ann.Rev.Astron.Astrophys.*, 44:507–556, 2006, astro-ph/0609142.
- [64] C.L. Fryer, S.E. Woosley, and A. Heger. Pair instability supernovae, gravity waves, and gamma-ray transients. *Astrophys.J.*, 550:372–382, 2001, astro-ph/0007176.
- [65] S.E. Woosley, S. Blinnikov, and A. Heger. Pulsational pair instability as an explanation for the most luminous supernovae. *Nature*, 450:390, 2007, 0710.3314.
- [66] A. Heger and S.E. Woosley. The nucleosynthetic signature of population III. *Astrophys.J.*, 567:532–543, 2002, astro-ph/0107037.
- [67] H.-T. Janka. Explosion Mechanisms of Core-Collapse Supernovae. *Ann.Rev.Nucl.Part.Sci.*, 62:407–451, 2012, 1206.2503.
- [68] A.C. Phillips. *The Physics of Stars*. John Wiley & Sons, Inc., New York, USA, 1999.
- [69] S. Woosley and H.-T. Janka. The physics of core-collapse supernovae. *Nature Physics*, 2006, astro-ph/0601261.
- [70] R.B. Firestone. LBNL Isotopes Project Nuclear Data Dissemination Home Page. <http://ie.lbl.gov/toi.html>. Retrieved March 11, 2002. Accessed 14 August 2013.

- [71] R. Buras, M. Rampp, H.-T. Janka, and K. Kifonidis. Two-dimensional hydrodynamic core-collapse supernova simulations with spectral neutrino transport. 1. Numerical method and results for a 15 solar mass star. *Astron. Astrophys.*, 447:1049–1092, 2006, astro-ph/0507135.
- [72] H.-T. Janka, K. Langanke, A. Marek, G. Martinez-Pinedo, and B. Mueller. Theory of Core-Collapse Supernovae. *Phys.Rept.*, 442:38–74, 2007, astro-ph/0612072.
- [73] E. O’Connor and C. Ott. The Progenitor Dependence of the Preexplosion Neutrino Emission in Core-Collapse Supernovae. *Astrophys.J.*, 762:126, 2013, astro-ph/1207.1100.
- [74] C. Giunti and C.W. Kim. *Fundamentals of neutrino physics and astrophysics*. Oxford University Press, Oxford, 2007.
- [75] G.G. Raffelt. Muon–neutrino and tau–neutrino spectra formation in supernovae. *Astrophys.J.*, 561:890–914, 2001, astro-ph/0105250.
- [76] H.-T. Janka and W. Hillebrandt. Neutrino emission from type II supernovae – an analysis of the spectra. *Astron. Astrophys.*, 224:49–56, 1989.
- [77] H.-T. Janka et al. Core-Collapse Supernovae: Reflections and Directions. *PTEP*, 2012:01A309, 2012, 1211.1378.
- [78] H.-T. Janka. The Garching Core–Collapse Supernova Research. <http://www.mpa-garching.mpg.de/ccsnarchive/>. Accessed 20 October 2014.
- [79] H.A. Bethe and J.R. Wilson. Revival of a stalled supernova shock by neutrino heating. *Astrophys.J.*, 295:14–23, 1985.
- [80] A. Burrows and J. Gosh. A Theory of supernova explosions. *Astrophys.J.*, 416:L75–L78, 1993.
- [81] A. Arcones, H.-T. Janka, and L. Scheck. Nucleosynthesis-relevant conditions in neutrino-driven supernova outflows. 1. Spherically symmetric hydrodynamic simulations. *Astron. Astrophys.*, 2006, astro-ph/0612582.
- [82] M. Herant, W. Benz, W.R. Hix, C.L. Fryer, and S.A. Colgate. Inside the supernova: A Powerful convective engine. *Astrophys.J.*, 435:339, 1994, astro-ph/9404024.
- [83] H.T. Janka and E. Mueller. Neutrino heating, convection, and the mechanism of Type-II supernova explosions. *Astron. Astrophys.*, 306:167, 1996.
- [84] J.M. Blondin, A. Mezzacappa, and C. DeMarino. Stability of standing accretion shocks, with an eye toward core collapse supernovae. *Astrophys.J.*, 584:971–980, 2003, astro-ph/0210634.

- [85] J. Nordhaus, A. Burrows, A. Almgren, and J. Bell. Dimension as a Key to the Neutrino Mechanism of Core–Collapse Supernova Explosions. *Astrophys.J.*, 720:694–703, 2010, 1006.3792.
- [86] S.M. Adams, C.S. Kochanek, J.F. Beacom, M.R. Vagins, and K.Z. Stanek. Observing the Next Galactic Supernova. *Astrophys.J.*, 778:164, 2013, 1306.0559.
- [87] W. Baade and R. Minkowski. Identification of the Radio Sources in Cassiopeia, Cygnus A, and Puppis A. *Astrophys.J.*, 119:206, 1954.
- [88] D.W. Hughes. Did Flamsteed see the Cassiopeia A supernova? *Nature*, 285:132–133, May 1980.
- [89] Giunti, editor. *Discorso di Lodovico Delle Colombe*, Firenze, 1606. written speech to the archbishop of Florence ([...] la nuova Stella apparita l’Ottobre passato 1604 nel Sagittario [...]).
- [90] S. Reynolds et al. A Deep Chandra Observation of Kepler’s Supernova Remnant: A Type Ia Event with Circumstellar Interaction. *Astrophys.J.*, 668:L135, 2007, 0708.3858.
- [91] J. Kepler. *De Stella nova in pede Serpentarii*. Prague, 1606.
- [92] B. Dasgupta and J.F. Beacom. Reconstruction of supernova  $\nu_\mu$ ,  $\nu_\tau$ , anti- $\nu_\mu$ , and anti- $\nu_\tau$  neutrino spectra at scintillator detectors. *Phys.Rev.*, D83:113006, 2011, 1103.2768.
- [93] C. Lujan-Peschard, G. Pagliaroli, and F. Vissani. Spectrum of Supernova Neutrinos in Ultra-pure Scintillators. *JCAP*, 1407:051, 2014, 1402.6953.
- [94] D. Vaananen and C. Volpe. The neutrino signal at HALO: learning about the primary supernova neutrino fluxes and neutrino properties. *JCAP*, 1110:019, 2011, 1105.6225.
- [95] A. Ianni. Supernova neutrino detection with liquid scintillators. *J.Phys.Conf.Ser.*, 309:012027, 2011.
- [96] G. M. Harper, A. Brown, and E. F. Guinan. A New VLA-Hipparcos Distance to Betelgeuse and its Implications. *Astronom.J.*, 135:1430–1440, April 2008.
- [97] S. Mohamed, J. Mackey, and N. Langer. 3D simulations of Betelgeuse’s bow shock. *Astr. & Astroph.*, 541:A1, May 2012, 1109.1555.
- [98] S.A. Colgate. Citation classic commentary on: The hydrodynamic behavior of supernovae explosions. *Astrophysical J.* 143:626-81, 1966. <http://garfield.library.upenn.edu/classics1981/A1981KX88700001.pdf>, 1981. E. Garfield’s Citation Classics.
- [99] E.M. Burbidge, G.R. Burbidge, W.A. Fowler, and F. Hoyle. Synthesis of the elements in stars. *Rev. Mod. Phys.*, 29:547–650, 1957.

- [100] S.A. Colgate and R.H. White. The Hydrodynamic Behavior of Supernovae Explosions. *Astrophys.J.*, 143:626, 1966.
- [101] J.R. Wilson. A Numerical Study of Gravitational Stellar Collapse. *Astrophys.J.*, 163:209, January 1971.
- [102] W.D. Arnett. Gravitational collapse and weak interactions. *Can. J. Phys.*, 44:2553–2594, 1966.
- [103] W.D. Arnett. Supernovae as Phenomena of High-Energy Astrophysics. *Annals of the New York Academy of Science*, 302:90–100, 1977.
- [104] James R.W. and Ronald W.M. Convection in core collapse supernovae. *Physics Reports*, 163(1-3):63–78, 1988.
- [105] S.W. Bruenn and T. Dineva. The Role of Doubly Diffusive Instabilities in the Core-Collapse Supernova Mechanism. *Astrophys.J.Lett.*, 458:L71, 1996.
- [106] C.L. Fryer. Mass Limits For Black Hole Formation. *Astrophys.J.*, 522:413–418, 1999, arXiv:astro-ph/9902315.
- [107] A. Burrows, E. Livne, L. Dessart, C. Ott, and J. Murphy. A new mechanism for core-collapse supernova explosions. *Astrophys.J.*, 640:878–890, 2006, astro-ph/0510687.
- [108] A. Marek and H.-T. Janka. Delayed neutrino-driven supernova explosions aided by the standing accretion-shock instability. *Astrophys.J.*, 694:664–696, 2009, 0708.3372.
- [109] Y. Suwa et al. Explosion geometry of a rotating  $13 M_{\odot}$  star driven by the SASI-aided neutrino-heating supernova mechanism. *Publ.Astron.Soc.Jap.*, 62:L49–L53, 2010, 0912.1157.
- [110] B. Müller, H.-T. Janka, and A. Marek. A New Multi-Dimensional General Relativistic Neutrino Hydrodynamics Code for Core-Collapse Supernovae II. Relativistic Explosion Models of Core-Collapse Supernovae. *Astrophys.J.*, 756:84, 2012, 1202.0815.
- [111] A. Marek, H. Dimmelmeier, H.-T. Janka, E. Muller, and R. Buras. Exploring the relativistic regime with Newtonian hydrodynamics: An Improved effective gravitational potential for supernova simulations. *Astron.Astrophys.*, 445:273, 2006, astro-ph/0502161.
- [112] B. Müller, H.-T. Janka, and H. Dimmelmeier. A new multi-dimensional general relativistic neutrino hydrodynamics code for core-collapse supernovae. I. Method and code tests in spherical symmetry. *Astrophys.J.Suppl.*, 189:104–133, 2010, 1001.4841.
- [113] M. Liebendoerfer, M. Rampp, H.-T. Janka, and A. Mezzacappa. Supernova simulations with Boltzmann neutrino transport: A Comparison of methods. *Astrophys.J.*, 620:840–860, 2005, astro-ph/0310662.

- [114] S.E. Woosley and T.A. Weaver. The Evolution and explosion of massive stars. 2. Explosive hydrodynamics and nucleosynthesis. *Astrophys.J.Supp.*, 101:181–235, 1995.
- [115] J.M. Lattimer and F.D. Swesty. A Generalized equation of state for hot, dense matter. *Nucl.Phys.*, A535:331–376, 1991.
- [116] H. Shen, H. Toki, K. Oyamatsu, and K. Sumiyoshi. Relativistic equation of state of nuclear matter for supernova and neutron star. *Nucl.Phys.*, A637:435–450, 1998, nucl-th/9805035.
- [117] M.T. Keil, G.G. Raffelt, and H.-T. Janka. Monte Carlo study of supernova neutrino spectra formation. *Astrophys.J.*, 590:971–991, 2003, astro-ph/0208035.
- [118] K.A. Olive et al. The Review of Particle Physics. *Chin.Phys.*, C38:090001, 2014.
- [119] S. Schael et al. Precision electroweak measurements on the  $Z$  resonance. *Phys.Rept.*, 427:257–454, 2006, hep-ex/0509008.
- [120] P.A.R. Ade et al. Planck 2013 results. XVI. Cosmological parameters. *Astron.Astrophys.*, 2014, 1303.5076.
- [121] C.L. Bennett et al. Nine-Year Wilkinson Microwave Anisotropy Probe (WMAP) Observations: Final Maps and Results. *Astrophys.J.Supp.*, 208:20, 2013, 1212.5225.
- [122] J. Dunkley et al. The Atacama Cosmology Telescope: likelihood for small-scale CMB data. *JCAP*, 1307:025, 2013, 1301.0776.
- [123] R. A. Battye and A. Moss. Evidence for Massive Neutrinos from Cosmic Microwave Background and Lensing Observations. *Phys.Rev.Lett.*, 112(5):051303, 2014, 1308.5870.
- [124] B. Dasgupta, A. Mirizzi, I. Tamborra, and R. Tomas. Neutrino mass hierarchy and three-flavor spectral splits of supernova neutrinos. *Phys.Rev.*, D81:093008, 2010, 1002.2943.
- [125] James P. Kneller and Alex W. Mauney. Does the finite size of the proto-neutron star preclude supernova neutrino flavor scintillation due to turbulence? *Phys.Rev.*, D88(4):045020, 2013.
- [126] James P. Kneller and Alex W. Mauney. Consequences of large  $\Theta_{13}$  for the turbulence signatures in supernova neutrinos. *Phys.Rev.*, D88(2):025004, 2013, 1302.3825.
- [127] X.-H. Guo, M.-Y. Huang, and B.-L. Young. Realistic Earth matter effects and a method to measure small  $\theta_{13}$  in the detection of supernova neutrinos. *Phys.Rev.*, D79:113007, 2009, 0806.2720.
- [128] C. Lunardini and A.Y. Smirnov. Supernova neutrinos: Earth matter effects and neutrino mass spectrum. *Nucl.Phys.*, B616:307–348, 2001, hep-ph/0106149.

- [129] L. Wolfenstein. Neutrino Oscillations in Matter. *Phys.Rev.*, D17:2369–2374, 1978.
- [130] S.P. Mikheyev and A.Y. Smirnov. Resonant neutrino oscillations in matter. *Prog.Part.Nucl.Phys.*, 23:41–136, 1989.
- [131] A.S. Dighe and A.Y. Smirnov. Identifying the neutrino mass spectrum from the neutrino burst from a supernova. *Phys.Rev.*, D62:033007, 2000, hep-ph/9907423.
- [132] T.-K. Kuo and J.T. Pantaleone. Neutrino Oscillations in Matter. *Rev.Mod.Phys.*, 61:937, 1989.
- [133] G.L. Fogli, E. Lisi, A. Mirizzi, and D. Montanino. Probing supernova shock waves and neutrino flavor transitions in next-generation water-Cerenkov detectors. *JCAP*, 0504:002, 2005, hep-ph/0412046.
- [134] J. Gava, J. Kneller, C. Volpe, and G.C. McLaughlin. A Dynamical collective calculation of supernova neutrino signals. *Phys.Rev.Lett.*, 103:071101, 2009, 0902.0317.
- [135] J. Xu, M.Y. Huang, X.-H. Guo, and B-L Young. Detection of supernova neutrinos on the earth for large  $\theta_{13}$ . 2013, 1303.0611.
- [136] B. Dasgupta and Am Dighe. Collective three-flavor oscillations of supernova neutrinos. *Phys.Rev.*, D77:113002, 2008, 0712.3798.
- [137] J.T. Pantaleone. Neutrino oscillations at high densities. *Phys.Lett.*, B287:128–132, 1992.
- [138] H. Duan, M. Fuller, G, and Y.-Z. Qian. Collective Neutrino Oscillations. *Ann.Rev.Nucl.Part.Sci.*, 60:569–594, 2010, 1001.2799.
- [139] H. Duan, M. Fuller, G, J. Carlson, and Y.-Z. Qian. Simulation of Coherent Non-Linear Neutrino Flavor Transformation in the Supernova Environment. 1. Correlated Neutrino Trajectories. *Phys.Rev.*, D74:105014, 2006, astro-ph/0606616.
- [140] G.L. Fogli, E. Lisi, A. Marrone, and A. Mirizzi. Collective neutrino flavor transitions in supernovae and the role of trajectory averaging. *JCAP*, 0712:010, 2007, 0707.1998.
- [141] B. Dasgupta, A. Dighe, G.G. Raffelt, and Alexei Yu. Smirnov. Multiple Spectral Splits of Supernova Neutrinos. *Phys.Rev.Lett.*, 103:051105, 2009, 0904.3542.
- [142] S. Sarikas, G.G. Raffelt, L. Hudepohl, and H.-T. Janka. Suppression of Self-Induced Flavor Conversion in the Supernova Accretion Phase. *Phys.Rev.Lett.*, 108:061101, 2012, 1109.3601.
- [143] S. Chakraborty, T. Fischer, A. Mirizzi, N. Saviano, and R. Tomas. Analysis of matter suppression in collective neutrino oscillations during the supernova accretion phase. *Phys.Rev.*, D84:025002, 2011, 1105.1130.

- [144] T. Lund and J.P. Kneller. Combining collective, MSW, and turbulence effects in supernova neutrino flavor evolution. *Phys.Rev.*, D88(2):023008, 2013, 1304.6372.
- [145] E. Borriello, S. Chakraborty, A. Mirizzi, P.D. Serpico, and I. Tamborra. (Down-to-)Earth matter effect in supernova neutrinos. *Phys.Rev.*, D86:083004, 2012, 1207.5049.
- [146] B. Pontecorvo. Mesonium and antimesonium. *Sov. Phys. JETP*, 6:429, 1957.
- [147] A. Bellerive. Review of Solar Neutrino Experiments. *International Journal of Modern Physics A*, 19:1167–1179, 2004, hep-ex/0312045.
- [148] Gian Luigi Fogli, E. Lisi, A. Marrone, and G. Scioscia. A global analysis of the atmospheric neutrino data. *Nucl.Instrum.Meth.*, A451:10–15, 2000.
- [149] J.F. Beacom. The Diffuse Supernova Neutrino Background. *Ann.Rev.Nucl.Part.Sci.*, 60:439–462, 2010, 1004.3311.
- [150] E. Fernandez. Neutrino physics at accelerators. *J.Phys.Conf.Ser.*, 53:83–106, 2006, hep-ex/0607024.
- [151] X. Qian and W. Wang. Reactor neutrino experiments:  $\theta_{13}$  and beyond. *Mod.Phys.Lett.*, A29:1430016, 2014, 1405.7217.
- [152] J. Beringer et al. The Review of Particle Physics. *Phys.Rev.*, D86:010001, 2012.
- [153] G.L. Fogli et al. Global analysis of neutrino masses, mixings and phases: entering the era of leptonic CP violation searches. *Phys.Rev.*, D86:013012, 2012, 1205.5254.
- [154] M.C. Gonzalez-Garcia, M. Maltoni, J. Salvado, and T. Schwetz. Global fit to three neutrino mixing: critical look at present precision. *JHEP*, 1212:123, 2012, 1209.3023.
- [155] T. Ferber. Limits on neutrino oscillations in the CNGS neutrino beam and event classification with the OPERA detector, 2012. Ph.D. thesis. Universität Hamburg, Germany.
- [156] S.P. Mikheev and A.Y. Smirnov. Resonance Amplification of Oscillations in Matter and Spectroscopy of Solar Neutrinos. *Sov.J.Nucl.Phys.*, 42:913–917, 1985.
- [157] S.P. Mikheev and A.Y. Smirnov. Resonant amplification of neutrino oscillations in matter and solar neutrino spectroscopy. *Nuovo Cim.*, C9:17–26, 1986.
- [158] G. Fogli and E. Lisi. Evidence for the MSW effect. *New J.Phys.*, 6:139, 2004.
- [159] C. Volpe. Open issues in neutrino astrophysics. *Annalen Phys.*, 525(8-9):588–599, 2013, 1303.1681.
- [160] D.R. Williams. Sun Fact Sheet. <http://nssdc.gsfc.nasa.gov/planetary/factsheet/sunfact.html>, 2013.

- [161] A.B. Balantekin, J. Gava, and C. Volpe. Possible CP-Violation effects in core-collapse Supernovae. *Phys.Lett.*, B662:396–404, 2008, 0710.3112.
- [162] S.M. Bilenky and Carlo Giunti. Neutrinoless double-beta decay: A brief review. *Mod.Phys.Lett.*, A27:1230015, 2012, 1203.5250.
- [163] A. Dueck, W. Rodejohann, and K. Zuber. Neutrinoless Double Beta Decay, the Inverted Hierarchy and Precision Determination of theta(12). *Phys.Rev.*, D83:113010, 2011, 1103.4152.
- [164] M. Goeppert-Mayer. Double beta-disintegration. *Phys.Rev.*, 48:512–516, 1935.
- [165] Ettore Majorana. Theory of the Symmetry of Electrons and Positrons. *Nuovo Cim.*, 14:171–184, 1937.
- [166] W.H. Furry. On transition probabilities in double beta-disintegration. *Phys.Rev.*, 56:1184–1193, 1939.
- [167] P. Minkowski.  $\mu \rightarrow e \gamma$  at a Rate of One Out of 1–Billion Muon Decays? *Phys.Lett.*, B67:421, 1977.
- [168] R.N. Mohapatra and G. Senjanovic. Neutrino Mass and Spontaneous Parity Violation. *Phys.Rev.Lett.*, 44:912, 1980.
- [169] J. Kotila and F. Iachello. Phase space factors for double- $\beta$  decay. *Phys.Rev.*, C85:034316, 2012, 1209.5722.
- [170] A. Bobyk, W.A. Kaminski, and F. Simkovic. Neutrinoless double beta decay within selfconsistent renormalized quasiparticle random phase approximation and inclusion of induced nucleon currents. *Phys.Rev.*, C63:051301, 2001, nucl-th/0012010.
- [171] F. Simkovic. Neutrinoless double-beta decay and related topics. *Phys.Part.Nucl.*, 42:598–612, 2011.
- [172] T.R. Rodriguez and G. Martinez-Pinedo. Energy density functional study of nuclear matrix elements for neutrinoless  $\beta\beta$  decay. *Phys.Rev.Lett.*, 105:252503, 2010, 1008.5260.
- [173] T.R. Rodriguez and G. Martinez-Pinedo. Neutrinoless double beta decay studied with configuration mixing methods. *Prog.Part.Nucl.Phys.*, 66:436–440, 2011, 1012.1783.
- [174] P.K. Rath, R. Chandra, K. Chaturvedi, P.K. Raina, and J.G. Hirsch. Uncertainties in nuclear transition matrix elements for neutrinoless  $\beta\beta$  decay within the PHFB model. *Phys.Rev.*, C82:064310, 2010, 1104.3965.
- [175] J. Barea and F. Iachello. Neutrinoless double-beta decay in the microscopic interacting boson model. *Phys.Rev.*, C79:044301, 2009.

- [176] J. Menendez, A. Poves, E. Caurier, and F. Nowacki. Disassembling the Nuclear Matrix Elements of the Neutrinoless beta beta Decay. *Nucl.Phys.*, A818:139–151, 2009, 0801.3760.
- [177] J. Menendez. Shell model progress on neutrinoless double beta decay: Nuclear matrix element uncertainties, neutrino exchange mechanism in seesaw models. *J.Phys.Conf.Ser.*, 312:072012, 2011.
- [178] C. Macolino et al. Results on neutrinoless double beta decay from GERDA Phase I. *Mod.Phys.Lett.*, A29(1):1430001, 2014, 1312.0562.
- [179] H.V. Klapdor-Kleingrothaus, I.V. Krivosheina, A. Dietz, and O. Chkvorets. Search for neutrinoless double beta decay with enriched Ge-76 in Gran Sasso 1990-2003. *Phys.Lett.*, B586:198–212, 2004, hep-ph/0404088.
- [180] A. Gando et al. Limit on Neutrinoless  $\beta\beta$  Decay of Xe-136 from the First Phase of KamLAND-Zen and Comparison with the Positive Claim in Ge-76. *Phys.Rev.Lett.*, 110(6):062502, 2013, 1211.3863.
- [181] J.B. Albert et al. Search for Majorana neutrinos with the first two years of EXO-200 data. *Nature*, 510:229–234, 2014, 1402.6956.
- [182] J. Boger et al. The Sudbury neutrino observatory. *Nucl.Instrum.Meth.*, A449:172–207, 2000, nucl-ex/9910016.
- [183] B. Aharmim et al. Determination of the  $\nu_e$  and total  $^8\text{B}$  solar neutrino fluxes with the Sudbury neutrino observatory phase I data set. *Phys.Rev.*, C75:045502, 2007, nucl-ex/0610020.
- [184] M. Yeh. A New Water-based Liquid Scintillator for Large Neutrino Physics. <http://meetings.aps.org/Meeting/APR12/Event/169448>. APS April Meeting 2012, Atlanta, Georgia, USA. Accessed 10 July 2013.
- [185] M. Yeh. Challenges of Liquid Scintillator (water-based & Metal-loaded) for Physics Frontiers. <https://indico.fnal.gov/getFile.py/access?contribId=73&sessionId=7&resId=0&materialId=slides&confId=6050>. Talk at the Joint CPAD and Instrumentation Frontier Community Meeting, Argonne National Laboratory, USA. Accessed 04 April 2014.
- [186] Y.-C. Wu et al. Measurement of Cosmic Ray Flux in China JinPing underground Laboratory. *Chin.Phys.*, C37(8):086001, 2013, 1305.0899.
- [187] P.G. Jones. Background Rejection for the Neutrinoless Double Beta Decay Experiment SNO+, 2011. Ph.D. thesis. Lincoln College, Oxford, UK.
- [188] Petresa Canada Inc. Linear Alkylbenzene, Petrelab 500–Q (P 500–Q), 2009. MSDS.

- [189] B. von Krosigk et al. Scintillation light yield, decay time, and ionization quenching measurements of Tellurium-loaded Linear Alkyl Benzene. 2015. under preparation.
- [190] M. Yeh, A. Garnov, and R.L. Hahn. Gadolinium-loaded liquid scintillator for high-precision measurements of antineutrino oscillations and the mixing angle, Theta(13). *Nucl.Instrum.Meth.*, A578:329–339, 2007.
- [191] X. Zhou et al. Measurements of the densities, isobaric thermal expansion coefficients and isothermal compressibilities of linear alkylbenzene in large liquid scintillator detectors. *Submitted to Chinese Physics C*, 2014, ins-det/1408.0877.
- [192] Petresa Canada Inc. Linear Alkylbenzene, Petrelab 550–Q (P 550–Q), 2011. MSDS, Cod. Cepsa 77767.
- [193] G. Bellini et al. Final results of Borexino Phase-I on low energy solar neutrino spectroscopy. *Phys.Rev.*, D89:112007, 2014, 1308.0443.
- [194] M. Yeh, J.B. Cumming, S. Hans, and R.L. Hahn. Purification of lanthanides for large neutrino detectors: Thorium removal from gadolinium chloride. *Nucl.Instrum.Meth.*, A618:124–130, 2010.
- [195] S. Perasso et al. Measurement of ortho–Positronium Properties in Liquid Scintillators. *e-print*, 2013, 1306.6001.
- [196] S. Hans. Private communication, 2014. BNL.
- [197] B.A. Moffat. The Optical Calibration of the Sudbury Neutrino Observatory, 2001. Ph.D. thesis. Queen’s University, Kingston, Canada.
- [198] R. Ford, M. Chen, O. Chkvorets, D. Hallman, and E. Vazquez-Jauregui. SNO+ scintillator purification and assay. *AIP Conf.Proc.*, 1338:183–194, 2011.
- [199] V. Lozza and J. Petzoldt. Cosmogenic activation of a natural tellurium target. *Astropart.Phys.*, 61:62–71, 2015.
- [200] V. Lozza. The SNO+ Experiment for Neutrinoless Double-Beta Decay. *Nucl. Phys. B (Proc. Suppl.)*, 00:1–6, 2014.
- [201] B. von Krosigk. SNO+ status. *PoS*, HQL2012:025, 2012.
- [202] L. Sibley. SNO+: Physics program and status update. *AIP Conf.Proc.*, 1604:449–455, 2014.
- [203] Christine Kraus and Simon J.M. Peeters. The rich neutrino programme of the SNO+ experiment. *Prog.Part.Nucl.Phys.*, 64:273–277, 2010.
- [204] J.R. de Laeter et al. Atomic weights of the elements: Review 2000. *Pure Appl. Chem.*, 75:683–800, 2000.

- [205] P. Antonioli et al. SNEWS: The Supernova Early Warning System. *New J.Phys.*, 6:114, 2004, astro-ph/0406214.
- [206] J.K. Ahn et al. Observation of Reactor Electron Antineutrino Disappearance in the RENO Experiment. *Phys.Rev.Lett.*, 108:191802, 2012, 1204.0626.
- [207] L. Zhan. Daya Bay II and Future Reactor Experiments. *Nucl.Phys.Proc.Supp.*, 237-238:114–116, 2013.
- [208] V.N. Kornoukhov. Detector LENS as a new tool for solar neutrino spectroscopy. *Part.Nucl.Lett.*, 108:58–67, 2001.
- [209] B. Cicenas and N. Solomey. The HANOHANO Detector and Ongoing Research and Development. *Phys.Procedia*, 37:1324–1331, 2012.
- [210] A. Öhrn, J. Blomgren, H. Park, S. Khurana, R. Nolte, D. Schmidt, and K. Wilhelmsen. Calibration procedure for a neutron monitor at energies below 20 MeV. *Nucl.Instrum.Meth. A*, 592(3):405–413, 2008.
- [211] A. Hildebrand, H. Park, S. Khurana, R. Nolte, and D. Schmidt. Experimental Determination of the Response Matrix of a BC501 Scintillation Detector using a Wide Neutron Spectrum: A Status Report, 2005. PTB Report PTB-6.42-05-1.
- [212] T. Novotný. Photon Spectrometry in Mixed Neutron-Photon Fields using NE 213 Liquid Scintillation Detectors, 1997. PTB Report PTB-N-28.
- [213] D. Schmidt, B. Asselineau, R. Böttger, H. Klein, L. Lebreton, S. Neumann, R. Nolte, and G. Pichenot. Characterization of liquid scintillation detectors. *Nucl.Instrum.Meth. A*, 476:186–189, 2002.
- [214] Perkin Elmer Ltd. LS-55 Luminescence Spectrometer, 2000. User’s Guide.
- [215] J. Thurn. To be announced., 2018. Ph.D. thesis. Technische Universität Dresden, Germany.
- [216] H.J. Brede et al. The Braunschweig accelerator facility for fast neutron research. 1) Building design and accelerators. *Nucl.Instrum.Meth.*, 169:349–358, 1980.
- [217] H.J. Brede et al. Neutron yields from thick Be targets bombarded with deuterons or protons. *Nucl.Instrum.Meth. A*, 274:332–344, 1989.
- [218] Photonis. Photomultiplier XP2020Q, 2007. datasheet.
- [219] Crystals Saint-Gobain. BC-622A Reflector Paint for Liquid Scintillator Tanks, 2005. datasheet.
- [220] K. Tittelmeier and H.J. Barrenscheen. Stabilisierung von Szintillationsdetektoren, 2003. PTB Report.

- [221] H. Klein, H.J. Barrenscheen, G. Dietze, B.R.L. Siebert, and W. Bretfeld. The Braunschweig accelerator facility for fast neutron research. 2) Data acquisition and analysis. *Nucl.Instrum.Meth.*, 169:359–367, 1980.
- [222] P. Sperr, H. Spieler, and M.R. Maier. A simple pulse-shape discrimination circuit. *Nucl.Instrum.Meth.*, 116:55–59, 1974.
- [223] J.A. Coderre. Introduction to Ionizing Radiation. <https://www.flickr.com/photos/mitopencourseware/3706466731/in/photostream/>, 2006. MIT OpenCourseWare.
- [224] P. Marmier and E.. Sheldon. *Physics of nuclei and particles*, volume 1. Academic Press, New York, USA, 1969.
- [225] G. Dietze and H. Klein. Gamma-calibration of NE 213 scintillation counters. *Nucl.Instrum.Meth.*, 193:549–556, 1982.
- [226] H. Wan Chan Tseung, J. Kaspar, and N. Tolich. Measurement of the dependence of the light yields of linear alkylbenzene-based and EJ-301 scintillators on electron energy. *Nucl.Instrum.Meth. A*, A654:318–323, 2011, 1105.2100.
- [227] L. Büermann et al. Response of NE213 liquid scintillation detectors to high-energy photons ( $E_\gamma > 3$  MeV). *Nucl. Instrum. Meth. A*, 332:483–492, 1993.
- [228] G. Ranucci. An analytical approach to the evaluation of the pulse shape discrimination properties of scintillators. *Nucl.Instrum.Meth.*, A354:389–399, 1995.
- [229] H.M O’Keeffe, E. O’Sullivan, and M.C. Chen. Scintillation decay time and pulse shape discrimination in oxygenated and deoxygenated solutions of linear alkylbenzene for the sno+ experiment. *Nucl. Inst. and Meth. A*, 640:119–122, 2011.
- [230] G. Dietze and H. Klein. NRESP4 and NEFF4 Monte Carlo codes for the calculation of neutron response functions and detection efficiencies for NE 213 scintillation detectors, 1982. PTB Report PTB-ND-22.
- [231] OECD/NEA Data Bank. The JEFF-3.2 Nuclear Data Library. *EFF Report 24, OECD/NEA Data Bank*, 2014.
- [232] J.F. Ziegler. SRIM-2012 computer program. <http://www.srim.org/>. Accessed 16 January 2013.
- [233] G.L. Fogli, E. Lisi, A. Marrone, D. Montanino, and A. Palazzo. Getting the most from the statistical analysis of solar neutrino oscillations. *Phys. Rev.*, D66:053010, 2002, hep-ph/0206162.
- [234] F. James and M. Roos. MINUIT - A system for function minimization and analysis of the parameter errors and correlations. *Computer Physics Communications*, 10:343–367, 1975.

- [235] R. Brun and F. Rademakers. ROOT data analysis framework. `root.cern.ch`, 2014.
- [236] F. Giovacchini. Cosmic rays anti-deuteron flux sensitivity of the AMS-02 detector, 2007. Ph.D. thesis. Università di Bologna, Italy.
- [237] R.E. Pywell et al. Light output response of BC-505 liquid scintillator. *Nucl.Instrum.Meth.*, A565:725–730, 2006.
- [238] B. Braizinha, J.H. Esterline, H.J. Karwowski, and W. Tornow. Determination of the proton and alpha-particle light-response functions for the KamLAND, BC-501A and BC-517H liquid scintillators. *Nucl.Instrum.Meth.*, A623:1046–1049, 2010.
- [239] N.R. Tolich. Experimental study of terrestrial electron anti-neutrinos with KamLAND, 2005. Ph.D. thesis. Stanford University - California, USA.
- [240] V.V. Verbinski et al. Light yield and n- $\gamma$  pulse-shape discrimination of liquid scintillators based on linear alkyl benzene. *Nucl.Instrum.Meth.*, 65:8–25, 1968.
- [241] R.L. Craun and D.L. Smith. Analysis of response data for several organic scintillators. *Nucl.Instrum.Meth.*, 80:239–244, 1970.
- [242] S. Mouatassim et al. The Light yield response of NE213 organic scintillators to charged particles resulting from neutron interactions. *Nucl.Instrum.Meth.*, 359A:530–536, 1995.
- [243] J.F. Ziegler. Stopping of energetic light ions in elemental matter. *J. Appl. Phys.*, 85:1249–1272, 1999.
- [244] G.F. Knoll. *Radiation Detection and Measurement*, 3rd ed. John Wiley & Sons, Inc., New Jersey, USA, 2000.
- [245] T. Novotný, L. Büermann, S. Guldbakke, and H. Klein. Response of NE213 liquid scintillation detectors to high-energy photons ( $7 \text{ MeV} < E_\gamma < 20 \text{ MeV}$ ). *Nucl. Instrum. Meth. A*, 400:356–366, 1997.
- [246] T. Kögler et al. Light yield and n- $\gamma$  pulse-shape discrimination of liquid scintillators based on linear alkyl benzene. *Nucl.Instrum.Meth.*, A701:285–293, 2013.
- [247] L. Neumann. Untersuchung der relativen Lichtausbeute für Protonen und alpha-Teilchen in auf linearem Alkylbenzol basierenden Flüssigszintillatoren, 2013. Diploma thesis. Technische Universität Dresden, Germany.
- [248] N. Tolich. Status of the SNO+ experiment. [http://nnn09.colostate.edu/Talks/Session05/Tolich\\_SNO+.pdf](http://nnn09.colostate.edu/Talks/Session05/Tolich_SNO+.pdf). Talk at the NNN-2013 conference, Colorado, USA. Accessed 04. August 2013.
- [249] V.I. Tretyak. Semi-empirical calculation of quenching factors for scintillators: new results. *EPJ Web Conf.*, 65:02002, 2014, 1312.5779.

- [250] The Borexino collaboration. New experimental limits on the pauli-forbidden transitions in  $^{12}\text{C}$  nuclei obtained with 485 days borexino data. *Phys. Rev. C.*, 81:034317, 2010.
- [251] H.O. Back et al. Pulse-shape discrimination with the Counting Test Facility. *Nucl. Instrum. Meth. A*, 584:98–113, 2008.
- [252] I.V. Krivosheina. SN 1987A – Historical view about registration of the neutrino signal with BAKSAN, KAMIOKANDE II and IMB detectors. *Int.J.Mod.Phys.*, D13:2085, 2004.
- [253] G. Pagliaroli, F. Vissani, M.L. Costantini, and A. Ianni. Improved analysis of SN1987A antineutrino events. *Astropart.Phys.*, 31:163–176, 2009, 0810.0466.
- [254] J.F. Beacom, W.M. Farr, and P. Vogel. Detection of supernova neutrinos by neutrino proton elastic scattering. *Phys.Rev.*, D66:033001, 2002, hep-ph/0205220.
- [255] S. Abe et al. Production of Radioactive Isotopes through Cosmic Muon Spallation in KamLAND. *Phys.Rev.*, C81:025807, 2010, 0907.0066.
- [256] S. Weinberg. Effects of a neutral intermediate boson in semileptonic processes. *Phys.Rev.*, D5:1412–1417, 1972.
- [257] L.A. Ahrens, S.H. Aronson, P.L. Connolly, B.G. Gibbard, M.J. Murtagh, et al. Measurement of Neutrino - Proton and anti-neutrino - Proton Elastic Scattering. *Phys.Rev.*, D35:785, 1987.
- [258] G. Pagliaroli, C. Lujan-Peschard, M Mitra, and F. Vissani. Using Low-Energy Neutrinos from Pion Decay at Rest to Probe the Proton Strangeness. *Phys.Rev.Lett.*, 111(2):022001, 2013, 1210.4225.
- [259] J.C. Collins, F. Wilczek, and A. Zee. Low-Energy Manifestations of Heavy Particles: Application to the Neutral Current. *Phys.Rev.*, D18:242, 1978.
- [260] R.N. Mohapatra and G. Senjanovic. Higher-order induced axial-vector isoscalar neutral current in gauge theories. *Phys.Rev.*, D19:2165, 1979.
- [261] L. Wolfenstein. Problem of the isoscalar axial-vector current in neutral-current phenomenology. *Phys.Rev.*, D19:3450, 1979.
- [262] A. Strumia and F. Vissani. Precise quasielastic neutrino/nucleon cross-section. *Phys.Lett.*, B564:42–54, 2003, astro-ph/0302055.
- [263] S. Abe et al. Precision Measurement of Neutrino Oscillation Parameters with KamLAND. *Phys.Rev.Lett.*, 100:221803, 2008, 0801.4589.
- [264] G. Bellini et al. Measurement of geo-neutrinos from 1353 days of Borexino. *Phys.Lett.*, B722:295–300, 2013, 1303.2571.

- [265] S. Abe et al. Measurement of the 8B Solar Neutrino Flux with the KamLAND Liquid Scintillator Detector. *Phys.Rev.*, C84:035804, 2011, 1106.0861.
- [266] T. Yoshida et al. Neutrino-Nucleus Reaction Cross Sections for Light Element Synthesis in Supernova Explosions. *Astrophys.J.*, 686:448–466, 2008, astro-ph/0807.2723.
- [267] B. Armbruster et al. Measurement of the weak neutral current excitation  $^{12}\text{C}(\nu, \nu')^{12}\text{C}^*(15.1\text{ MeV})$  at  $E(\nu) = 29.8\text{ MeV}$ . *Phys. Lett.*, B423:15–20, 1998.
- [268] K. Scholberg et al. SNOWGLOBES: SuperNova Observatories with GLoBES. <http://www.phy.duke.edu/~schol/snowglobes/>. Accessed 23 September 2014.
- [269] C. Athanassopoulos et al. Measurements of the reactions  $^{12}\text{C}(\nu_e, e^-)^{12}\text{N}_{\text{g.s.}}$  and  $^{12}\text{C}(\nu_e, e^-)^{12}\text{N}^*$ . *Phys. Rev. C*, 55:2078–2091, Apr 1997.
- [270] L. B. Auerbach et al. Measurements of charged current reactions of  $\nu_e$  on  $^{12}\text{C}$ . *Phys. Rev. C*, 64:065501, Nov 2001.
- [271] B. Zeitnitz. KARMEN: Neutrino physics at ISIS. *Prog.Part.Nucl.Phys.*, 32:351–373, 1994.
- [272] J. A. Formaggio and G. P. Zeller. From ev to eev: Neutrino cross sections across energy scales. *Rev. Mod. Phys.*, 84:1307–1341, Sep 2012.
- [273] W. Kaina, V. Soergel, H. Thies, and W. Trost. A new measurement of the weak magnetism term in the betaspectra of  $^{12}\text{B}$  and  $^{12}\text{N}$ . *Phys.Lett.*, B70:411–414, 1977.
- [274] B. Pfeiffer, K. Venkataramiah, U. Czok, and C. Scheidenberger. Atomic mass compilation 2012. *Atomic Data and Nuclear Data Tables*, 100(2):403 – 535, 2014.
- [275] E. Kolbe, K. Langanke, S. Krewald, and F.-K. Thielemann. Inelastic neutrino scattering on  $^{12}\text{C}$  and  $^{16}\text{O}$  above the particle emission threshold. *Nucl.Phys.*, A540:599–620, 1992.
- [276] A. Heger, E. Kolbe, W.C. Haxton, K. Langanke, G. Martinez-Pinedo, et al. Neutrino nucleosynthesis. *Phys.Lett.*, B606:258–264, 2005, astro-ph/0307546.
- [277] G. Bellini et al. Observation of Geo-Neutrinos. *Phys.Lett.*, B687:299–304, 2010, 1003.0284.
- [278] The Borexino collaboration. Measurement of the  $^{14}\text{C}$  abundance in a low-background liquid scintillator. *Phys.Lett.B*, 422:349–358, 1998.
- [279] B. Aharmim et al. Measurement of the Cosmic Ray and Neutrino-Induced Muon Flux at the Sudbury Neutrino Observatory. *Phys.Rev.*, D80:012001, 2009, 0902.2776.
- [280] C. Adams et al. The Long-Baseline Neutrino Experiment: Exploring Fundamental Symmetries of the Universe. 2013, 1307.7335.

- [281] L.A. Winslow. First Solar Neutrinos from KamLAND: A Measurement of the  ${}^8\text{B}$  Solar Neutrino Flux, 2008. Ph.D. thesis. University of California, Berkeley, USA.
- [282] T. Araki et al. Measurement of neutrino oscillation with KamLAND: Evidence of spectral distortion. *Phys.Rev.Lett.*, 94:081801, 2005, hep-ex/0406035.
- [283] R.E. Bolz and G.L. Tuve, editors. *CRC Handbook of Tables for Applied Engineering Science, 2nd edition*. CRC Press, Inc, 1991.
- [284] S. Schmitt. TUnfold: an algorithm for correcting migration effects in high energy physics. *JINST*, 7:T10003, 2012, 1205.6201.
- [285] K. Scholberg. Supernova neutrino detection. *Nucl.Phys.Proc.Suppl.*, 91:331–337, 2001, hep-ex/0008044.
- [286] D.B. Cline, F. Sergiampietri, J.G. Learned, and K. McDonald. LANND: A Massive liquid argon detector for proton decay, supernova and solar neutrino studies, and a neutrino factory detector. *Nucl.Instrum.Meth.*, A503:136–140, 2003, astro-ph/0105442.

# Acknowledgement

I would like to express my gratitude to Prof. Dr. Kai Zuber for being my thesis advisor and for encouraging my research. Then I also want to thank Prof. Dr. Lothar Oberauer for his time and effort as my second referee. I owe particular thanks to Dr. Ralf Nolte for his great support during and after every single measurement campaign. On a related note I want to thank Kai Tittelmeier and Dr. Stefan Röttger, as well as the accelerator staff of the PTB and the mechanical workshop of the TU Dresden. Thanks also to my former diploma student, Laura Neumann, who made valuable contributions to the achievement of the results at hand. I am also most grateful for the tireless supply with every kind of metal-loaded scintillators by Dr. Minfang Yeh and Dr. Sunej Hans. All these people helped to make the measurements presented within this work possible. Thank you! In the context of supernova neutrinos, I would like to express my special appreciation to Dr. Torben Ferber for his priceless support, co-work and advice. Thanks also to Dr. Cristina Volpe for helpful discussions and to Dr. Hans-Thomas Janka and Dr. Lorenz Hüdepohl for granting me access to the results of their supernova simulation results. Moreover, I want to thank Dr. Valentina Lozza for suppressing my supernova neutrino backgrounds and for always taking her time for my questions. Moreover, all the many detector shifts would not have been the same without her. This includes the hours-long scraping off flooring and glue from the DCR floor cm by cm the day of my birthday, where she (and Gwen) saved my day with a cake at Perkins and singing and clapping waitresses. Thanks to the both of you! Though this thesis became too long to include any solar neutrino oscillation studies, I would like to greatly acknowledge the fruitful collaboration with Dr. Nuno Barros on this topic. And thank you also for the very nice and entertaining common time in the office. The same words are directed at Björn Lehnert including my thanks for his patience as my office mate in the last weeks of my writing. I will soon get the chance to return this. And last but not least my special thanks to my wonderful parents and sister Hartmut, Elisabeth and Alex and my dear aunt Gunda for being patient with me the entire time.



Hiermit versichere ich, dass ich die vorliegende Arbeit ohne unzulässige Hilfe Dritter und ohne Benutzung anderer als der angegebenen Hilfsmittel angefertigt habe; die aus fremden Quellen direkt oder indirekt übernommenen Gedanken sind als solche kenntlich gemacht. Die Arbeit wurde bisher weder im Inland noch im Ausland in gleicher oder ähnlicher Form einer anderen Prüfungsbehörde vorgelegt.

Die Promotion wurde an der Technischen Universität Dresden, am Institut für Kern- und Teilchenphysik, unter der wissenschaftlichen Betreuung von Prof. Dr. Kai Zuber durchgeführt.

Ich erkenne die Promotionsordnung der Fakultät Mathematik und Naturwissenschaften vom 23.02.2011 an.

Dresden, 12. März 2015

Belina von Krosigk